A Digital Autopilot for the Space Shuttle Vehicle
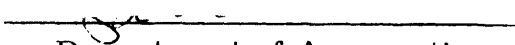
by

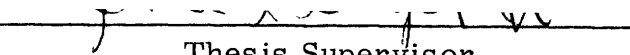Greg L. Zacharias

B.S., M.I.T.

(1967)

SUBMITTED IN PARTIAL FULFILLMENT

OF THE REQUIREMENTS FOR THE

DEGREE OF MASTER OF SCIENCE

at the

MASSACHUSETTS INSTITUTE OF TECHNOLOGY
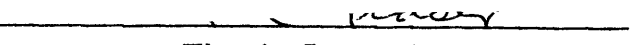
February, 1974

Signature of Author _____

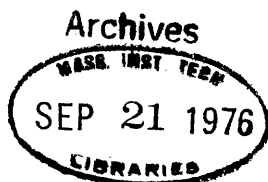Department of Aeronautics
and Astronautics, February 1974

Certified by _____

Thesis Supervisor

Certified by _____

Thesis Supervisor

Accepted by _____

Chairman, Departmental
Graduate Committee

Thesis

A DIGITAL AUTOPILOT FOR THE

SPACE SHUTTLE VEHICLE

by

GREG L. ZACHARIAS

ABSTRACT

A digital autopilot is designed for the Space Shuttle Vehicle (SSV),
for operation during atmospheric entry following deorbit, and system
performance is evaluated by flight simulation. A combination of design
synthesis techniques is used to meet the performance specifications
over the large entry flight envelope, and to ensure satisfaction of design
constraints imposed by control effector characteristics and uncertainties
in vehicle design. Autopilot design is based on a rigid-body, quasi-
static, stability-axis linear model of the vehicle dynamics, which is
derived from the general non-linear equations of motion. The simpli-
city of this dynamic model provides for insight into design trades re-
garding control effector utilization and modes of stability-axis attitude
control. The control laws governing operation of the Attitude Control
Propulsion System (ACPS) are based on this simplified model, and con-
sist of several phase-plane switching logics which reflect the inertial
characteristics of the vehicle during the early portion of the entry. The
control laws governing operation of the Aerodynamic Control Surface
System (ACSS) are also based on the simplified vehicle model, and are
essentially linear networks whose gains are chosen by an analytic closed-
loop pole allocation method. A novel feature of this linear logic is the
deliberate use of turn miscoordination to effect banking maneuvers, a
feature which substantially reduces ACPS fuel expenditures when

2

compared with conventional body-axis control techniques. A non-linear
blending logic incorporated in the autopilot design ensures compatible
operation between the ACPS and ACSS, and provides for a gradual
transition from exoatmospheric flight to flight characterized by conven-
tional aerodynamic forces and torques. Extensive simulation through-
out the flight envelope is used to validate the autopilot design, both for
nominal operation and for operation in the face of vehicle and environ-
mental uncertainties. The results show that the autopilot meets its
design goals, and suggest further avenues of analysis and design effort
needed prior to flight software implementation.

Thesis Supervisors:

John J. Deyst, Jr.

Associate Professor of Aeronautics
and Astronautics

Donald C. Fraser

Lecturer, Department of Aeronautics
and Astronautics

Director, Control and Flight
Dynamics Division, Charles Stark
Draper Laboratory

ACKNOWLEDGEMENTS

4

5

TABLE OF CONTENTS

9

1. Introduction

The objective of this study is to design and evaluate an automatic attitude control system for the Space Shuttle Vehicle (SSV) for use during atmospheric entry after deorbit. It should be recognized that due to the magnitude of the SSV program, several engineering groups are actively involved in the autopilot design effort: The Johnson Spacecraft Center of the National Aeronautics and Space Administration (NASA-JSC), the Space Division of Rockwell International (RI), the Aerospace Division of Honeywell Incorporated (HI), and the C. S. Draper Laboratory (CSDL). This thesis documents a portion of the CSDL effort in the SSV autopilot design area, and it should be noted that both complementary and parallel studies are being conducted by the other groups; in fact, an alternative approach to the entry control problem, developed by RI and HI, is the present baseline design for eventual incorporation into the SSV flight software. The eventual decision to fly this baseline design will, of course, depend on the system's performance in the face of the anticipated changes in vehicle configuration and mission requirements, between this point in time and the time of the first launch (presently scheduled for early 1979). It should also be recognized that all of the groups mentioned above are conducting on-going design efforts; in keeping with this dynamic situation the design discussed here will undoubtedly change to meet new requirements and/or improve performance. However, it is felt that the design is of sufficient maturity to merit the documentation this thesis provides, and that such a "snapshot" view will give the reader a fair insight into the entry control design problem.

The entry flight phase is fairly loosely defined; here it is taken to be initiated when the vehicle's altitude drops below 400,000 ft (at velocities in excess of 26,000 ft/sec) and terminated at an altitude of approximately 75,000 ft (with a velocity of approximately 1500 ft/sec). While there exist several mission profiles

for SSV operation, they are all characterized by an eventual return from orbit to a conventional (dead-stick) airstrip landing, so as to reduce recovery and refurbishment costs. Compared with an Apollo-type ocean recovery, the targeting requirements are relatively stringent; to compensate, the delta-wing vehicle has a higher lift-to-drag ratio than the Apollo command module, so that the SSV may be viewed as more like an airplane than a typical blunt-body entry vehicle. With specific regard to the dynamic properties of the vehicle then, the entry portion of the mission can be viewed as a transition phase from exo-atmospheric operation in which the vehicle's mass properties dominate the dynamic response characteristics, to an atmospheric regime in which the aerodynamic effects become considerably more significant. This factor, combined with the objective of maintaining active attitude control throughout the entry, is perhaps the driving influence in control systems design, and the one which distinguishes this design problem from those encountered in past projects (e.g., passive stabilization of blunt-body rotational dynamics).

The altitude/velocity "corridor" flown by the SSV during entry is basically similar to those flown by other entry vehicles. The similarity stops here though, because of the larger variable lift-to-drag ratio allowing for considerable modulation of the vehicle's flight path. This capability is somewhat similar to X-15 operation, although the latter's flight envelope is significantly smaller due to the lower altitudes and velocities encountered at entry interface. SSV operation differs from X-15 flight in another important aspect: high angle-of-attack operation. This feature is required to provide the necessary drag deceleration; the implications for aerodynamic control of the vehicle are significant, simply because of the lack of flight experience with design-specified high angle-of-attack operation.

The performance requirements placed on the attitude control system stem primarily from guidance specifications, while the design constraints can be traced to the vehicle, sensor, and control effector hardware specifications. In the former case, the guidance system attempts to meet its targeting objectives, while satisfying its design constraints, by modulation of the vehicle's angle-of-attack and bank angle throughout the entry. Thus, the control logic must be capable of commanding the appropriate control effectors, which consist of attitude control thrusters and aerodynamic control surfaces, so as to maneuver the vehicle in a sufficiently responsive manner to satisfy the guidance requests. Naturally, a subsidiary control objective is to maintain or augment vehicle stability throughout the entry envelope. This capability is of course dependent on the actuators available to the control logic (e.g., ACPS thrust levels, auxiliary control surfaces, etc.), and, to a large extent, on the aerodynamic characteristics of the vehicle.

The design philosophy guiding the development of the controller is fairly straightforward: after gaining a strong insight into the fundamental dynamics and constraints involved, break the problem down into easily identifiable design subtasks, and then, for each subtask, use any available design technique which shows promise in providing a solution. This problem-oriented approach naturally leads to an amalgamation of different design characteristics, and it is appropriate here to note some features of the control system design eventually arrived at. The control logic is digital, and is presently implemented in FORTRAN. The design utilizes both non-linear phase-plane switching logics (for control of the attitude jets) and gain-scheduled linear logics (for control of the aerodynamic control surfaces), with a "blending" logic to provide appropriate phasing between the two control effector subsystems. Mode switching and non-linear filtering are used as appropriate, primarily to ensure a continuity of control activity throughout the extensive

12

flight envelope (the magnitude of the flight envelope can be appreciated by referring to the mission histories illustrating Appendix C). Naturally, many of these features will change as the design continues to evolve in response to vehicle/mission/hardware changes; thus, the design presented here is a "snapshot" of the entry control system in one stage of its development.

This study is organized into eight chapters. Chapter 2 provides a more formal definition of the design problem at hand, by summarizing the important vehicle characteristics, flight-envelope parameters, and performance requirements appropriate to control system design definition. Aside from providing a quantitative introduction to the problem, this information serves as a base for a discussion of some of the engineering trades involved in controller design; it also serves as a convenient reference source of data relevant to the analysis and synthesis efforts of later chapters. Chapter 3 then provides a brief overview of the design synthesis effort itself, in an attempt to provide a meaningful introduction to the quantitative material of the next three chapters. This chapter stresses the iterative nature of the design process, with the fundamental feedback provided by a realistic simulator, used in the verification or revision of proposed design techniques.

To gain the necessary understanding of the dynamics involved in the attitude control problem, Chapter 4 derives and discusses a simplified model of the vehicle's rigid-body rotational dynamics. Identified here is the fundamental importance of the stability-axis frame of reference, a frame considerably more appropriate to the design problem than the conventionally utilized body-axis coordinate system. The quasi-static linear model not only provides the insight necessary for intelligent design trades, but also serves as an equation base for the synthesis effort of the next chapter.

13

With such a quantative picture of the vehicle dynamics, Chapter 5 then proceeds with a derivation of the entry control logic. By making maximum use of the simplified vehicle model, an analytic formulation of the logic is presented which allows a considerable degree of configuration independence, and minimizes the amount of trial-and-error testing typical of such design studies. As noted earlier, the design effort makes use of several control synthesis techniques, and does not attempt to "bend" one technique to serve in situations where it is clearly not appropriate. The output of the chapter is a set of related block diagrams and control equations covering all phases of the entry mission, defined as functions of yet to be specified design parameters. The chapter provides a qualitative discussion on parameter selection, which is then utilized in the summary description given in Chapter 6. Here, the control system "sub-units" of Chapter 5 are integrated into comprehensive block diagrams which provide the formal definition of the control logic and illustrate the overall structure. Also specified here are the design parameter values appropriate to this particular vehicle and set of mission requirements.

Chapter 7 then provides some insight into performance of the closed-loop vehicle/controller system, by describing simulation results obtained at various flight conditions throughout the entry, and under various off-nominal conditions. Since the simulator used is a very realistic six degree-of-freedom non-linear model of the vehicle and its entry environment, the results presented here serve both to validate the accuracy of the simplified model derived in Chapter 4 and to justify some of the design choices made in Chapter 5. In addition to showing a generally successful satisfaction of the design objectives, some of the simulation results indicate areas for future work, both in better definition of the design environment and in possible compensatory modifications to the control logic. Chapter 8 concludes the study with a brief

14

summary of the major findings of this effort, and suggests additional areas of design work necessary to the eventual implementation of this control logic into the SSV flight control software.

2. Design Requirements

This chapter provides a formal definition of the attitude control design problem by summarizing the important vehicle characteristics, flight envelope parameters, and performance requirements particularly relevant to the synthesis effort. Three basic objectives motivate this type of presentation. First, by a quantitative description of the vehicle and its flight envelope, a better understanding is gained of the uniqueness of the entry control problem: the vehicle may be the identical vehicle which "cruises" at 20,000 feet, but the entry flight conditions so transform the vehicle so that very few dynamic characteristics can be directly correlated with those associated with a more conventional flight regime. Thus, although the equations of motion may be familiar, it is essential that the numerical properties be intimately involved in any description of the vehicle. A second objective of this description, closely tied with the numerically determined fundamental vehicle characteristics, is to provide a quantitative base for the discussion of the basic trades involved in controller design. Thus, before entering into a detailed design synthesis, it is imperative to determine some of the more obvious implications of the vehicle characteristics on the choice of a particular technique of attitude control. At that, such a discussion is difficult, and misses some of the more important subtleties which strongly determine vehicle performance; however, some obvious conclusions can be drawn from the "raw" vehicle data. A final objective of this chapter is to provide a quantitative base appropriate to discussions in the later chapters covering vehicle modelling, controller synthesis, and performance evaluation. Clearly, a complete data base requires hundreds of pages (see, for example, the aerodynamic data presented in Reference 2); only the more essential features are presented here.

This chapter is organized into five sections. Section 2.1 gives a simplified summary description of the vehicle and its operational envelope, while Section 2.2 concentrates on the two sources of torque authority available for attitude control: the Attitude Control Propulsion System (ACPS) and the Aerodynamic Control Surface System (ACSS). Section 2.3 then defines the operational objectives of the control system by describing both quantitatively and qualitatively the performance

16

requirements of the closed-loop controlled vehicle. To recognize the practical nature of the design problem, from the start of the design effort, Section 2.4 discusses off-nominal considerations which must influence any realistic design choices. Finally, Section 2.5 qualitatively discusses some of the more obvious trades of control system design which can be based on the material already presented in this chapter. This discussion should provide some basis for understanding the motives of the design choices made in later chapters.

2.1 Vehicle and Flight Envelope

This section gives a brief description of the vehicle in terms of its geometric, mass, and aerodynamic properties, and of the entry flight envelope in terms of the basic trajectory parameters. It should be recognized that at the time of this writing the vehicle design is undergoing constant refinement, and thus most of the parameter values presented below will be subject to some change as the design matures.

The double-delta wing orbiter configuration described in Reference 2, and referred to as the 89B vehicle (from the drawing number) is designed to provide the required lift-to-drag ratio necessary for high cross-range, low heat load trajectories, and to provide the capability of trimmed flight over a wide range of angles-of-attack. Table 2-1 gives the vehicle's geometric properties of particular interest to the control system design problem. The empty vehicle weight is approximately 150,000 pounds, with a payload capacity of 25,000 pounds; Table 2-2 gives the vehicle mass properties during entry, appropriate to these two payload conditions. It should be noted that these data are referred to the "fabrication" frame defined by Figure 2-1; also illustrated is the conventional "body-axis" frame used in dynamics analysis, so as to avoid the confusion which inevitably results in a discussion of mass properties. The two frames are simply related by a translation from the datum point of the fabrication frame to the vehicle center-of-gravity, and a 180° rotation about the y-axis.

The entry flight envelope, a "corridor" in the altitude-velocity plane, is shown in Figure 2-2, along with a nominal design mission trajectory. The extremely large range of nominal dynamic pressures

17

Table 2-1: Fundamental Geometric Properties

Property	Symbol	Value
Overall length	–	125 ft
Reference length	ℓ_B	110.7 ft
Reference area	S	2690 ft^2
Wingspan	b	78.1 ft
Mean aerodynamic chord	c	39.6 ft

Table 2-2: Mass Properties

Property	Symbol	No Payload	25K Payload (nominal)	Dimension
Weight	m	156,617	181,617	pounds
CG location	x_{CG}	1106.4	1083.5	inches
	y_{CG}	0.0^2	0.0^2	"
	z_{CG}	373.0	376.7	"
Moment of Inertia	I_{xx}	0.779	0.805	10^6 slug-ft^2
	I_{yy}	5.474	5.849	"
	I_{zz}	5.695	6.067	"
Product of Inertia	I_{xy}	0.0^3	0.0^3	"
	I_{xz}	0.160	0.140	"
	I_{yz}	0.001	0.001	"

Note: 1. Referred to fabrication frame of figure 2-1
       2. Nominal value; tolerance ≈ 2.0 inches
       3. Nominal value; tolerance ≈ 3 x 10^3 slug-ft^2
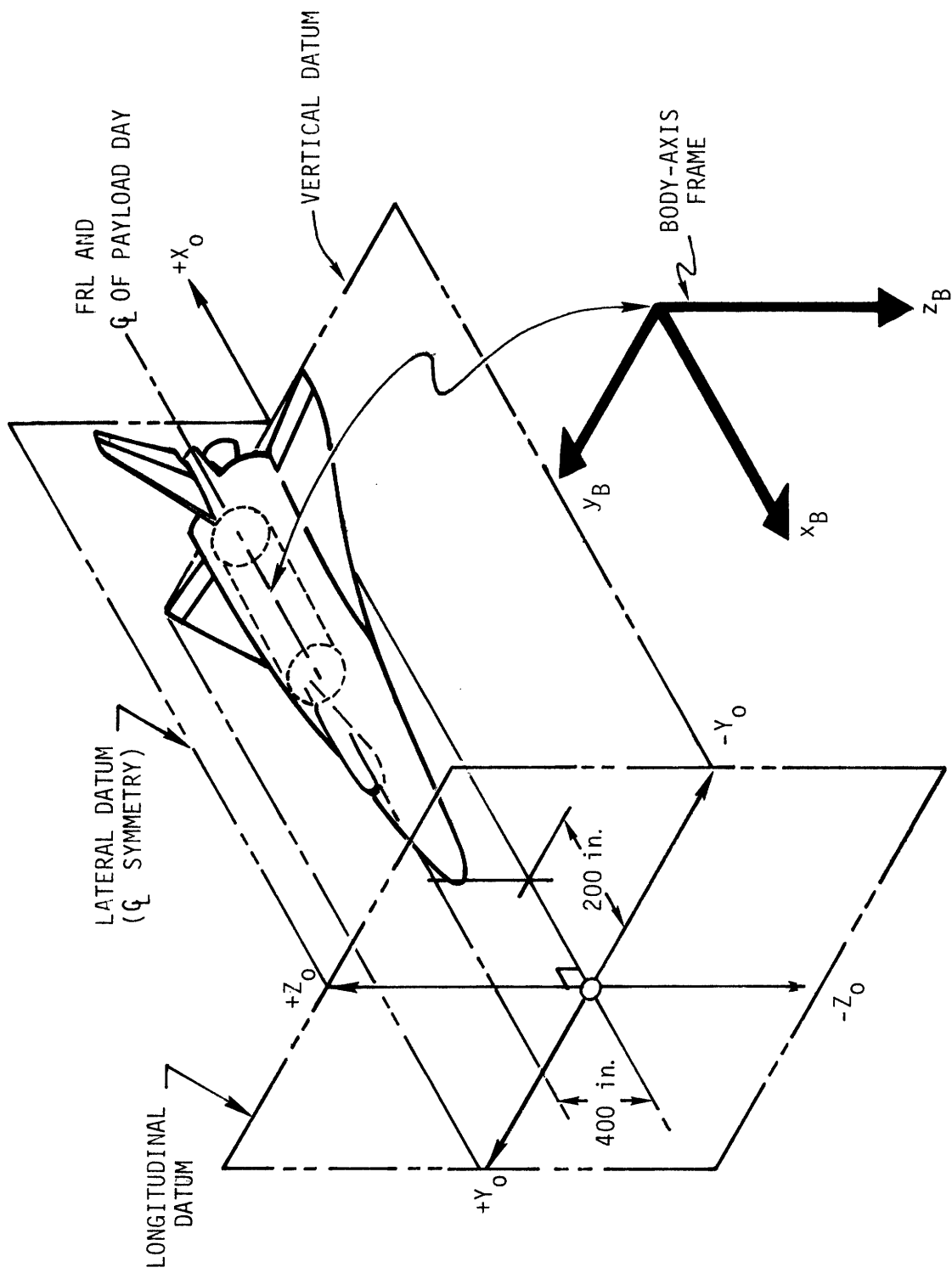
Figure 2-1. Fabrication Reference System and Body-Axis Frame.

19
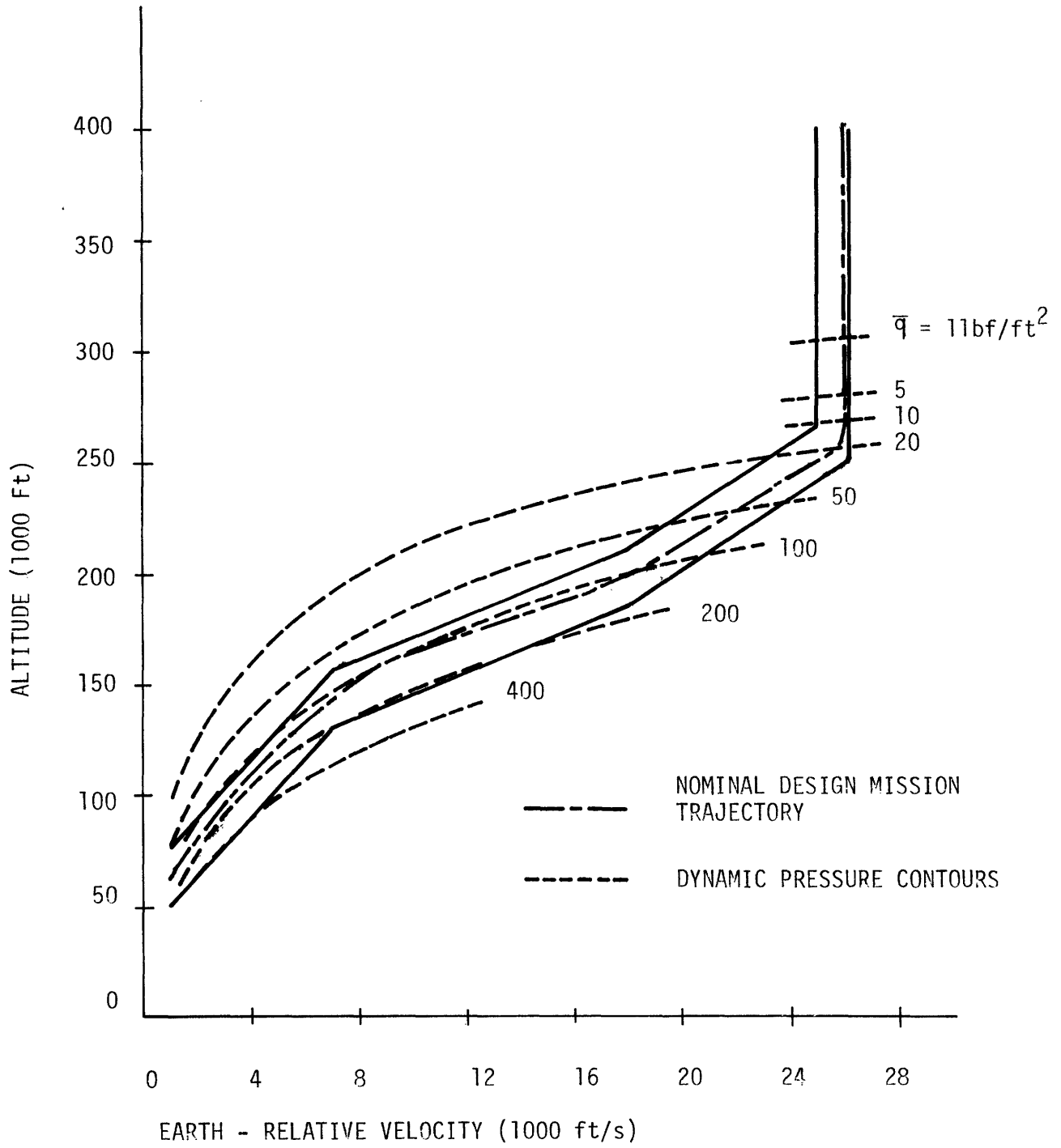
Figure 2-2. Entry Flight Envelope.

$(\equiv \bar{q})$ encountered during the entry is indicated by the contours shown on the figure, and serves to emphasize the necessity for flexibility in any control system operating in this regime.

In order to attain the type of vehicle performance indicated by this envelope, a set of ground rules was developed for the aerodynamic specifications; these are given in Table 2-3, repeated from Reference 2. Three points should be noted. First, the angle-of-attack range is un-specified for the transonic to high supersonic regime, although the pitch trim limits described below place effective operational limits on the angle-of-attack envelope in this regime. Second, as noted above, the longitudinal displacement of the center-of-gravity can range up to 2% of the reference length; the implications of this become quite clear when it is recognized that Reference 2 is, in essence, two aerodynamic data books, one associated with each center-of-gravity extreme. Finally, as will become evident by the discussion given in Chapter 4, the specification on the lateral hypersonic value for the coefficient C_{n_β}' implies that the uncontrolled airframe may be laterally unstable: i.e., divergent instead of simply undamped. Fortunately, in this case, the design specifications are exceeded with sufficient margin to ensure basic stability (see Section 4.4.2).

To gain some idea of the operational constraints in entry trajectory design, Figure 2-3 shows the longitudinal trim control "power" limits of the vehicle, due to fixed elevon deflection limits (see below), center-of-gravity displacement, and changing aerodynamics due to Mach number and angle-of-attack variations. Considerably more constraints are imposed by guidance considerations (e.g., targeting, heating, g-loads, etc.) so that the "velocity/alpha" envelope rapidly narrows. Figure 2-4 shows an operational envelope, repeated from Reference 18, which provides an adequate margin about the nominal entry profile shown to ensure sufficient maneuverability in response to off-nominal guidance commands. Although this type of envelope is appropriate to the specification of control design dependence on the vehicle's aerodynamic properties, a more pertinent flight envelope is used extensively in later chapters: the "Mach number/alpha" envelope. Although this latter envelope is similar to the one shown in Figure 2-4, the use of Mach number in place of

21

Table 2-3: Design Ground Rules, 150K Lightweight Orbiter

Parameter	Value
Angle of Attack	
Hypersonic	25 deg to 40 deg
Transonic	0 deg to 15 deg
Subsonic	-5 deg to 20 deg
Center of Gravity Range	
Maximum Travel	2 percent body length
Design Range	$0.66\,\ell_B - 0.68\,\ell_B$
Landing Performance	
Payload	25,000 pounds
Landing Weight (with payload)	179,000 pounds
Minimum Design Touchdown Speed, V_D	165 knots
Longitudinal Stability	
Minimum Hypersonic Static Margin	Positive
Minimum Subsonic Static Margin (AFT Center of Gravity)	-2 percent ℓ_B

Lateral-Directional Stability

			Value
Hypersonic	Directional	C_{n_β}	≥ -0.001
$\alpha = 34$ deg	Lateral	C_{ℓ_β}	≥ -0.001
	Dynamic	C'_{n_β}	≥ -0.002
Subsonic	Directional	C_{n_β}	≥ 0.001
$\alpha = 13$ deg	Lateral	C_{ℓ_β}	≈ -0.001
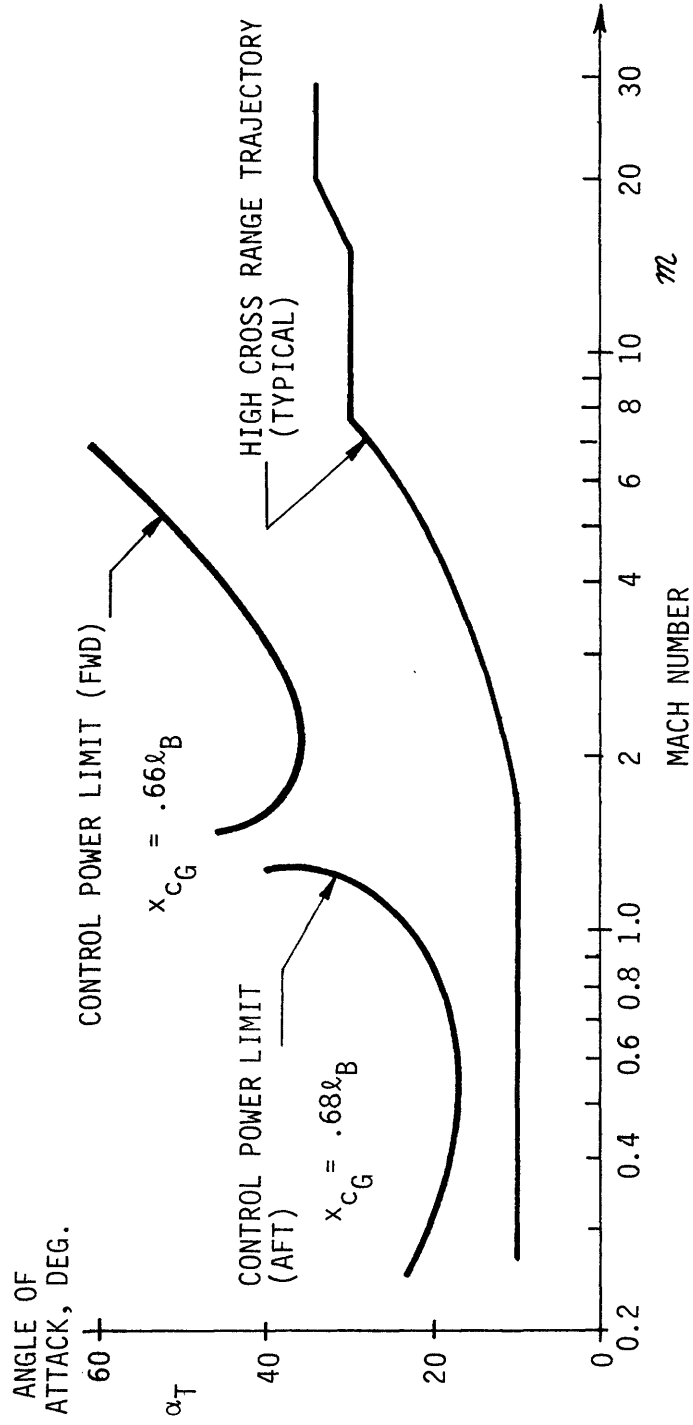
Figure 2-3. Static Trim Boundaries.

23
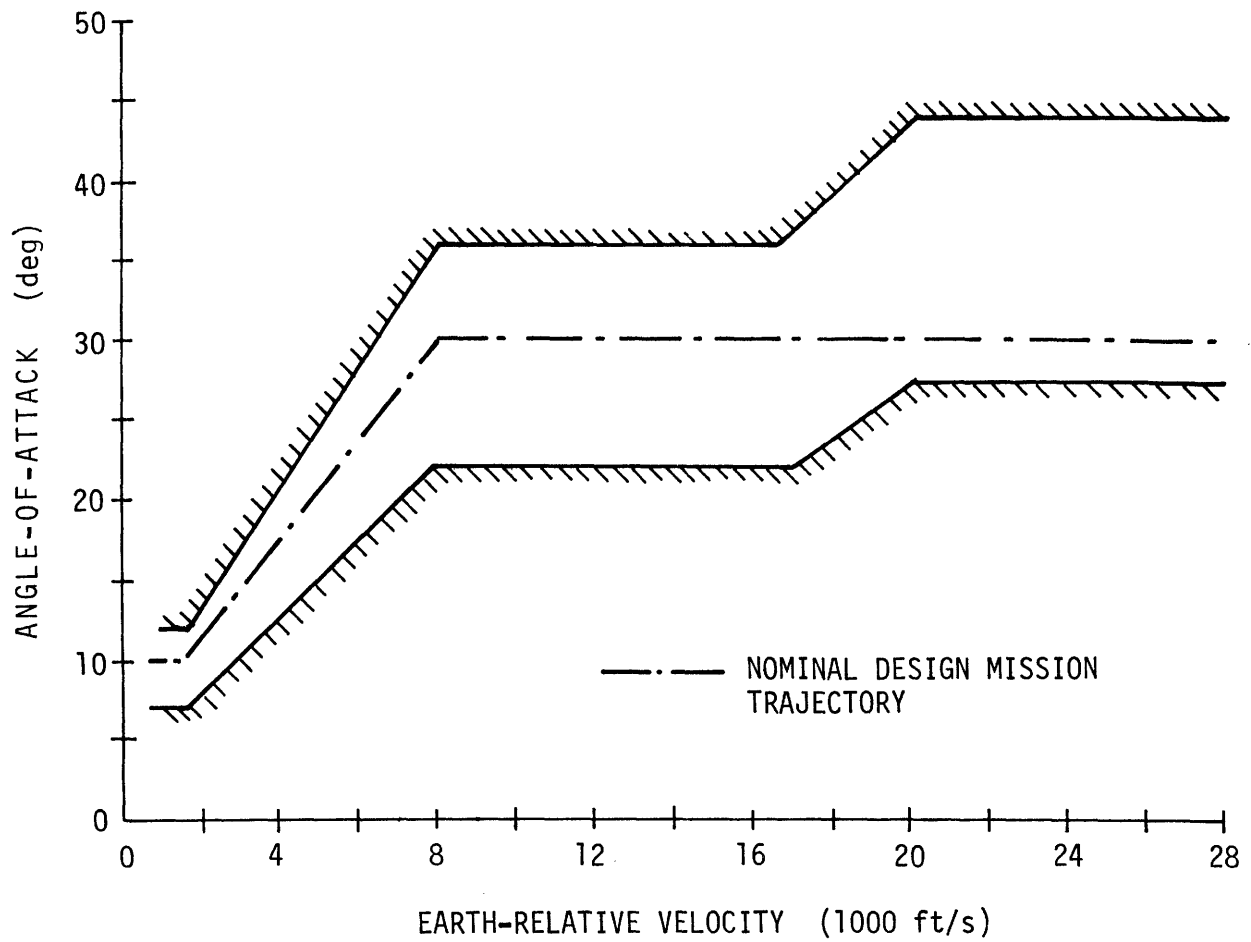
Figure 2-4. Angle-of-Attack Envelope.

earth-relative velocity allows for a more complete specification of the vehicle's aerodynamic properties, since Mach number and angle-of-attack determine all of the trim aerodynamic characteristics of the vehicle.

No attempt will be made here to discuss the detailed characteristics of the bare airframe aerodynamic coefficients, since it is shown in Chapter 4 that a considerably more appropriate coefficient set exists which better defines the vehicle dynamics. In fact, it is shown there how misleading a conventional interpretation of coefficient values can be: thus, a discussion of these parameters is delayed until a proper background is prepared.

2.2   Sources of Control Authority

This section describes the basic characteristics of the two sources of torque authority available for attitude control during entry: the reaction jet ACPS (Attitude Control Propulsion System) and the somewhat conventional surface controls, or the ACSS (Aerodynamic Control Surface System).

2.2.1 ACPS

The ACPS consists of 40 appropriately clustered bipropellant thrusters*, each with a thrust of approximately 1000 lbf and a specific impulse of 230 seconds, implying a mass flow rate of approximately 4.34 lbm/sec. At present, the usable minimum impulse time is estimated to be 20 milliseconds, but as will be seen in Chapter 5, this figure will prove to be a small fraction of the total jet "on-time" for a typical thrust pulse commanded by the control logic; this minimum impulse thus has little impact on the controller design. Sixteen of the thrusters are located behind protective doors near the nose of the vehicle, and, because of heating considerations, are unavailable during the entry. The remaining 24 jets are located in two symmetric tail pods, with no restrictions on operation (see below for a possible exception). All 40 jets can be grouped into 16 "clusters" of co-linearly firing jets; the cluster

---

* Additional low thrust ($\approx$ 25 lbf) "vernier" jets are available for on-orbit use.

25

locations are shown in Figure 2-5, and the thruster identification number assigned with each cluster number is given in Table 2-4. Because of the significant displacement of the thrusters from the vehicle center-of-gravity, and because of the non-colinearity of thrust vectors with body-axes, there is a considerable amount of cross-coupling of torques produced by the jets. Shown in Table 2-5 are the angular accelerations (i.e., torque divided by appropriate moment of inertia) associated with the firing of each jet in the tail pods, for the "forward" center-of-gravity configuration. It should be clear from the data that there exists no thruster whose torque can be said to be essentially about a single body axis, so that it is somewhat misleading to refer to a jet as a pitch, roll, or yaw jet. However, when taken in particular combinations which minimize cross-coupling, it is often appropriate and convenient to use such nomenclature; this will be done occasionally in later chapters, to convey the sense of the basic torque being applied.

Control-axis coupling is not the only objectionable feature of the ACPS; recent studies (see, for example, Reference 22) indicate strong and unexpected coupling due to plume interference with the vehicle's flow patterns, noticeable at sufficiently high dynamic pressures. The net result (dependent, of course, on the particular thruster being considered) is a flight-condition dependent deviation in vehicle response from what is encountered in exo-atmospheric operation. Thus, although it is convenient to view the ACPS as capable of providing idealized torques essentially independent of the flight condition, some caution must be used in a generalization covering the entire entry. In fact, this interference effect may very well preclude jet operation during certain portions of the flight envelope.

2.2.2 ACSS

The set of control surfaces comprising the ACSS consists of left and right elevons, a conventional rudder, a programmed speedbrake, and a trim set body flap. These are illustrated in Figure 2-6 along with a table showing the effects of "positive" deflections of these surfaces. The "derived" deflections of elevator and aileron are based on the fact that the elevons can be operated in tandem to emulate an elevator in its
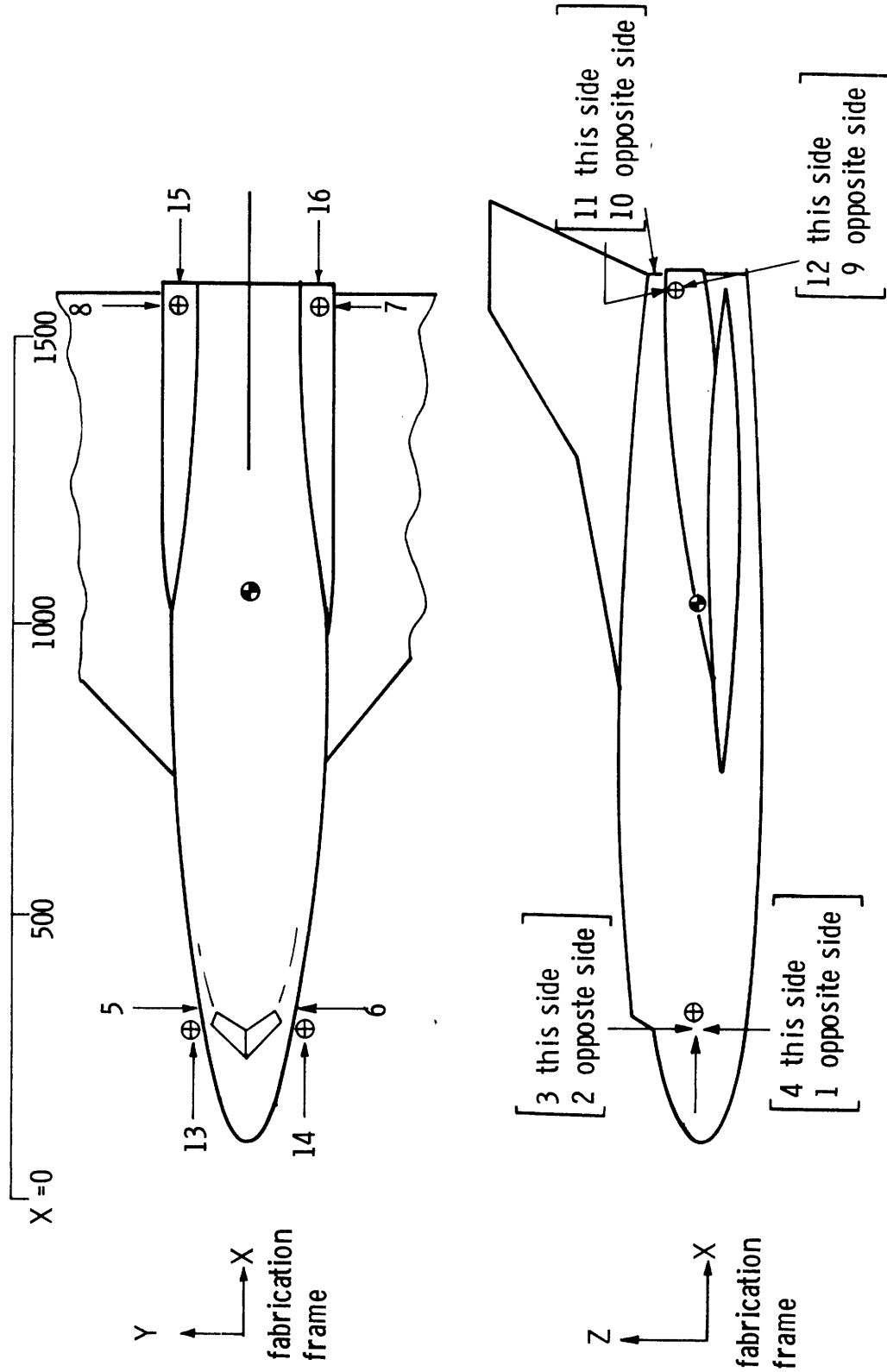
Figure 2-5 Thruster Cluster Locations.

27

Table 2-4: <u>Thruster Cluster Allocations</u>

<u>Cluster Location</u>	<u>Number of Thrusters</u>	<u>Thruster Number</u>
1*	2	10, 12
2*	2	14, 16
3*	2	13, 15
4*	2	9, 11
5*	2	6, 8
6*	2	5, 7
7	4	17, 19, 21, 23
8	4	18, 20, 22, 24
9	3	32, 34, 36
10	3	26, 28, 30
11	3	25, 27, 29
12	3	31, 33, 35
13*	2	2, 4
14*	2	1, 3
15	2	38, 40
16	2	37, 39

* Nose clusters; unavailable for entry

Table 2-5: Angular Accelerations of Tail Pod Thrusters
(about body frame axes)

Thruster Number	Angular Acceleration (deg/sec^2)		
	a_x	a_y	a_z
17	0.459	0.0	-0.530
18	-0.459	0.0	0.530
19	0.535	0.0	-0.529
20	-0.535	0.0	0.529
21	0.601	0.0	-0.528
22	-0.601	0.0	0.528
23	0.688	0.0	-0.526
24	-0.688	0.0	0.526
25	-0.745	0.556	-0.009
26	0.745	0.556	0.009
27	-0.745	0.568	-0.009
28	0.745	0.568	0.009
29	-0.745	0.578	-0.009
30	0.745	0.578	0.009
31	0.693	-0.520	0.028
32	-0.693	-0.520	-0.028
33	0.693	-0.531	0.028
34	-0.693	-0.531	-0.028
35	0.693	-0.544	0.028
36	-0.693	-0.544	-0.028
37	-0.222	0.048	0.120
38	0.222	0.048	-0.120
39	-0.222	0.058	0.120
40	0.222	0.058	-0.120
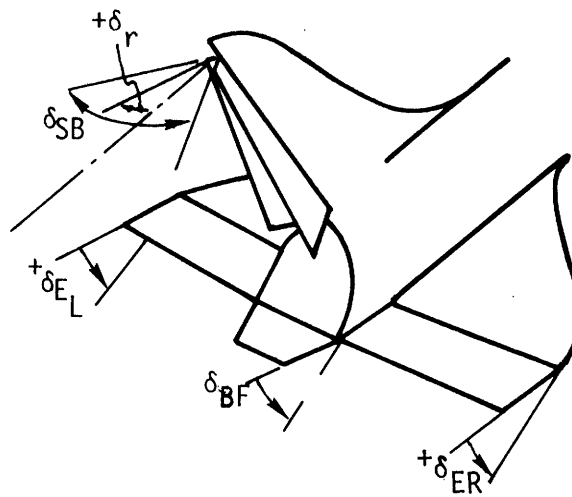
Figure 2-6. Control Surface Conventions.

SURFACE NAME	POSITIVE DEFLECTION OF	PRIMARY VEHICLE RESPONSE**	PRIMARY FORCES AND MOMENTS**
Left Elevon	δ_{E_L}	$+\phi$	$+C_\ell$
Right Elevon	δ_{E_R}	$-\phi$	$-C_\ell$
Rudder	δ_r	$+\beta$, $-\psi$	$+C_y$, $-C_n$
Speedbrake	δ_{SB}	$-V_x$	$+C_D$
Body Flap	δ_{BF}	$-\theta$, $-\alpha$	$-C_M$
Elevator*	δ_e	$-\theta$, $-\alpha$	$-C_M$
Aileron*	δ_a	$+\phi$	$+C_\ell$

*Note: Fictitious surfaces defined by:

$$\delta_e \equiv \tfrac{1}{2}(\delta_{E_L} + \delta_{E_R})$$

$$\delta_a \equiv \tfrac{1}{2}(\delta_{E_L} - \delta_{E_R})$$

**Note: Unfamiliar symbols are defined in chapter 4.

pitch torque capability, and operated differentially to emulate ailerons in roll torque capability. The rudder is actually incorporated with the speedbrake, but independent operation of the two is provided for.

Both the speedbrake and the body flap are surfaces auxiliary to the essential control functions of the ACSS. Specifically, the speedbrake, a vertical controllable flare surface of the dorsal fin, has a pre-programmed deflection schedule through the entry (see Figure 2-7; taken from Reference 2), so as to enhance lateral stability. With slow deflection rates, it may thus be viewed as a weak augmenter of the un-controlled airframe dynamics, as opposed to a control surface available for transient torque applications. Similarly, the body flap, a ventral horizontal trim surface, is set to a fixed deflection depending on the fore-aft displacement of the center of gravity from its nominal forward location (see Figure 2-7). In this manner, the body flap generates a pitch trim torque, so that the trim elevator deflection in the presence of an "aft" center of gravity approximates the trim setting for the nominal forward location (see Reference 2). The point to be recognized is that, as with the speedbrake, the body flap is constrained to low deflection rates and is thus not available for transient attitude control. Thus, both surfaces may be neglected for dynamics analysis by incorporating their static effectiveness into the bare airframe characteristics; this is done in the analysis of the following chapters.

The deflection and deflection rate limits of the elevons and rudder are given in Table 2-5. The mechanical arrangement of the hardware (actuators and surfaces) provides the primary specification on the deflection limits, although, as noted in the table, undesirable heating characteristics may impose further restrictions in range. It should be noted

Table 2-5: Surface Deflection and Rate Limits

Effector	Deflection Limits (deg)	Deflection Rate Limits (deg/sec)
δ_{E_L}	-40, +15(+10*)	±15
δ_{E_R}	-40, +15(+10*)	±15
δ_r	±28	±15
δ_e	-40, +15	-
δ_a	±15	-

* Note: Down deflections may be constrained by heating considerations.

31
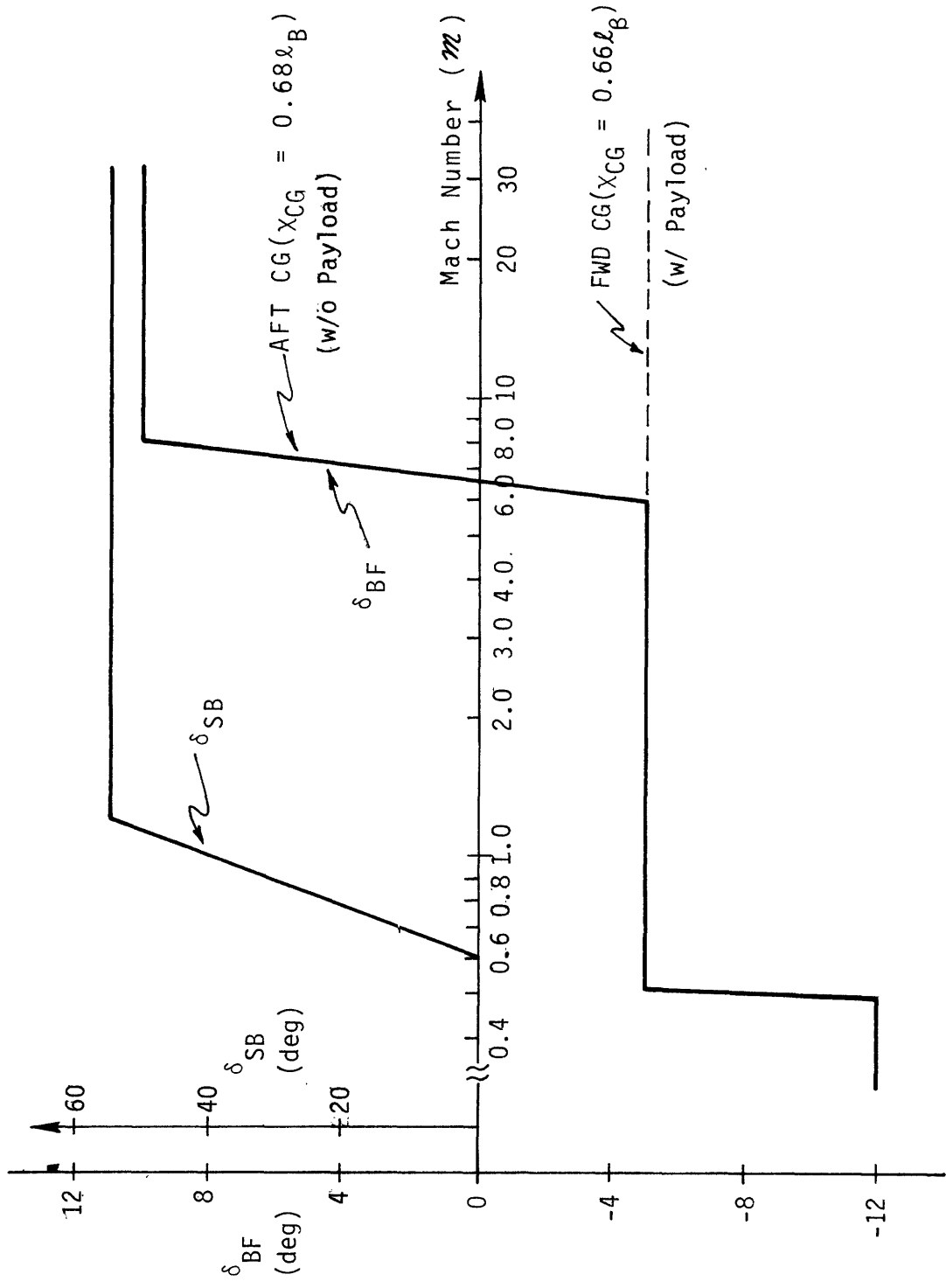
Figure 2-7. Body Flap and Speed Brake Schedules.

that constraints due to heating are still poorly defined, so that the
specification of deflection limits is an open issue. Determination of
maximum _rate_ limits is more difficult, and perhaps even misleading
due to the nature of the limit. Shown in Figure 2-8 is an idealized plot
of surface rate versus hinge-moment, the latter variable being the
torque applied about the surface hinge due to aerodynamic forces acting
on the deflected surface. The curve itself is determined by actuator
torque and horsepower sizing, so that zero rate capability is associated
with a stall hinge-moment, while the no-load condition is associated with
a large rate limit. This would be sufficiently complicated as it stands;
however, the hinge moment itself is a function of dynamic pressure,
Mach number, trim angle-of-attack, and surface deflection magnitude.
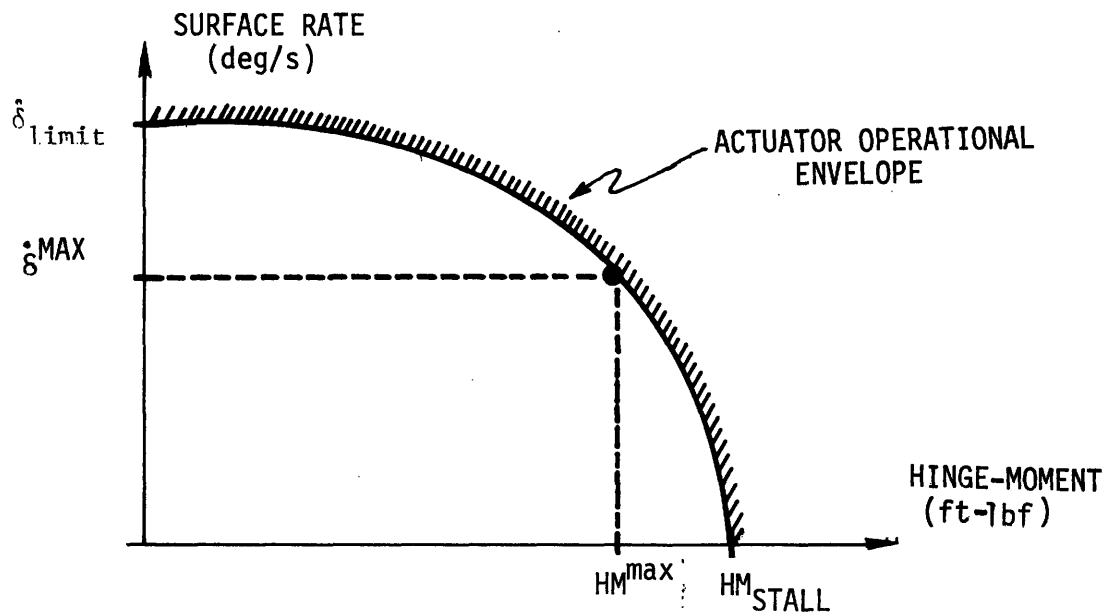
Figure 2-8. Actuator Horsepower Constraint.

The conventional solution to this problem is to estimate a maximum
anticipated hinge-moment in the regime of interest, and then find the
associated maximum rate from the appropriate actuator data. Because
of the lack of readily available actuator data, this approach was not taken
in specifying the values given in the table; they are, instead, conservative
values agreed upon by several workers in the field to be fairly accurate
first estimates which will suffice until better actuator modelling becomes

33

available. Whatever the values, however, it must be remembered that they are, in actuality, not fixed, but instead, variable rate limits dependent on several factors.

Also listed in the table are the "elevator" and "aileron" deflection limits, used for control system design and evaluation. It should be clear from the values given in the table and the transformation equations given in Figure 2-6, that the elevator and aileron limits are inconsistent with the elevon limits. For example, an elevator deflection of +15 degrees (down) implies that both left and right elevons must be at their 15-degree limits, in turn implying no capability for differential deflections which will maintain the desired elevator deflection. Thus, a 15-degree elevator deflection limit is incompatible with any non-zero aileron limit. This discussion is continued in more detail in Section 5.4.2.1, covering control system output processing; for now, however, the inconsistent limit set provides a useful approximation to the actual situation. The rate limit situation is similar; however, in later chapters it will be seen unnecessary to the synthesis effort to specify elevator and aileron rate limits, so that no values are given in the table.

The complete specification of the aerodynamic surface coefficients, used in determining control torques generated by surface deflections, is given in Reference 2; no attempt is made here to repeat this voluminous data. It is, however, appropriate to condense some of this information in a format which helps to better visualize the approximate surface control authority which can be expected during a "nominal" entry. A first approximation to surface effectiveness in producing body-axis torques is obtained by assuming that the elevator is exclusively responsible for pitch torques, the aileron for roll, and the rudder for yaw. That this is not true is seen by the non-zero cross-control effectiveness coefficients of Reference 2; however, for this discussion, a simplified view is adequate, so that the control accelerations about the body axes are given as follows:

$$a_x = \frac{\bar{q}Sb}{I_{xx}} C_{l\delta_a} \delta_a; \quad a_y = \frac{\bar{q}Sc}{I_{yy}} C_{m\delta_e} \delta_e; \quad a_z = \frac{\bar{q}Sb}{I_{zz}} C_{n\delta_r} \delta_r \qquad (2-1)$$

where the mass and geometric properties have been introduced above, and where the aerodynamic surface control coefficients are specified functions of Mach number and trim angle-of-attack. If the trajectory parameters are defined by Figures 2-2 and 2-4, then the ACSS control acceleration effectiveness may be plotted versus velocity by use of (2-1), as shown in Figure 2-9. It should be noted that the normalization used implies, for example, a roll acceleration capability of a_x deg/sec^2 per degree deflection of the aileron.

The obvious influence of low dynamic pressure at the beginning of entry is apparent from the figure. Some of the later modulation in effectiveness is due to dynamic pressure changes; the remainder is due to changes in the aerodynamic coefficients due, in turn, to Mach number and angle-of-attack changes. Perhaps most striking is the very late effectiveness of the rudder; this is due to the "shadow" effect at the relatively high angles-of-attack maintained throughout most of the entry. The implications for control design are discussed in a later section. To gain some appreciation of the acceleration magnitudes, it is instructive to compare the histories of Figure 2-9 with the ACPS acceleration levels of Table 2-5. For example, a positive pitch acceleration of approximately 1.1 deg/sec^2 can be obtained by firing thrusters 25 and 26; in the middle of the entry, a few degrees of elevator can completely cancel this. A similar situation exists for ACPS and aileron induced roll accelerations. Yaw, of course, is not controllable by the rudder until late into the entry, so that a single "yaw" ACPS thruster (e.g., number 17) provides a much higher acceleration level than the rudder, for the majority of the entry. Further discussions comparing ACPS to ACSS control are found in Section 2.5.

2.3 Performance Requirements

As noted earlier, the basic objective of the entry control system is to provide direct control over angle-of-attack and bank angle, in response to guidance system attitude commands, utilizing the ACPS and ACSS within their design constraints. Attitude hold accuracy and maneuver response characteristics must, of course, satisfy the guidance

35
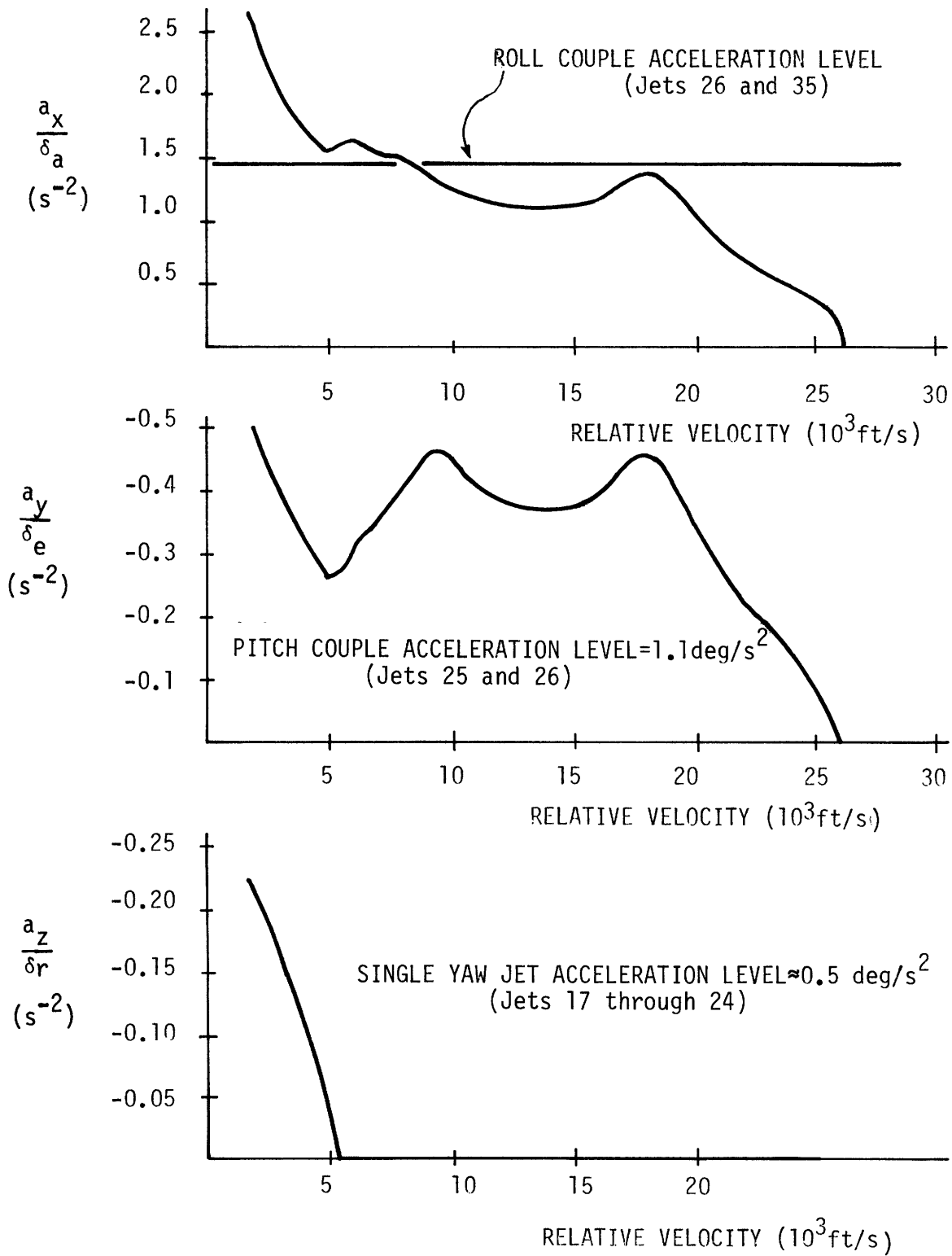
Figure 2-9.   Surface Effectiveness During Entry (Typical).

system requirements, but all other performance specifications not directly associated with subsystem constraints are of secondary importance. In particular, attempting to apply to this problem conventional handling quality specifications (such as those found in References 12 and 18) may lead to the imposition of design constraints superfluous to the mission, whose satisfaction may require increased demands on the controller subsystems and/or degradation of the primary functions of the control system. This is not to suggest that no attempt should be made to satisfy secondary performance requirements; on the contrary, when they can be satisfied in the normal course of the controller design effort it is clearly advantageous to broaden the scope of the system's performance objectives.

The primary performance requirements should specify attitude hold and maneuver characteristics necessary for successful operation with the guidance system. Unfortunately, few guidance studies have concentrated on specifying the required control system performance, and the data that is available is of an informal nature with the expected number of qualifying conditions. From a general consensus, it would appear that a steady-state attitude hold accuracy of approximately 1 degree in angle-of-attack and 3 degrees in bank will satisfy the guidance requirements. Maneuver rates are even less specific, but the indications of Reference 13 imply a bank rate capability in excess of 5 deg/sec in response to a bank reversal occurring at high dynamic pressures. No specific minimum values for angle-of-attack rate have been found in the literature; discussions with workers in the field suggest very low levels, below those which naturally occur in the process of control loop stabilization of the longitudinal dynamics. In this discussion of vehicle attitude specifications, it is appropriate to note that there is, at present, some concern over sideslip induced heating rates, so that an airframe operational constraint may limit sideslip excursions to less than some maximum value. Present indications set this value at 5 degrees; again, it will be seen that maintenance of vehicle stability (in the lateral axes) results in sideslip excursions considerably smaller than this specification. This rather informal discussion is summarized in Table 2-6 ; the reader is cautioned to recognize the approximate nature of this data.

37

Table 2-6: Attitude Control Performance Requirements

	Steady-State Error	Maneuver Rate
Angle-of-attack	$\lesssim 1°$	(low)
Bank angle	$\lesssim 3°$	$\gtrsim 5°/\text{sec}$
Sideslip angle	$< 5°$ (?)	--

The performance requirements imposed by the effector subsystem constraints follow fairly directly from the ACPS and ACSS operational characteristics described in the previous section. Specifically, it is clear that an implicit performance requirement on the controller is low ACPS fuel expenditure so as to stay within an allocated entry budget, presently 700 pounds. Additionally, two other ACPS subsystem oriented requirements may be noted. First, because of the undesirability of high thruster pulse rates, the ACPS torque commands, issued by the control logic, should be at a low frequency, specifically ruling out any attempt at pulse rate modulation. Second, because of the present concern with thruster firings at high dynamic pressures (see Reference 22) an implied requirement on the controller is the minimization of ACPS use in those flight regimes. In a similar fashion, the actuator horsepower and torque characteristics, combined with skin heat rates, limit surface deflections and rates. Thus, the ACSS imposed constraints imply small deflections at low rates. These performance requirements imposed by both ACPS and ACSS constraints and desired operational modes are necessarily qualitative, due to a lack of available data; they must be recognized, however, in any design effort.

2.4 Off-Nominal Considerations

Early attention in a design effort to off-nominal situations is a prerequisite for successful control system operation in a realistic environment. To this end, this section discusses some of the more obvious considerations which are arbitrarily labelled "off-nominal", to distinguish them from the somewhat idealized "nominal" vehicle and

trajectory characteristics commonly used for design synthesis. It should be noted that the definition of the "nominal" parameters defining the control problem (e.g., vehicle aerodynamic coefficients, guided altitude/velocity profile, etc.) is a difficult enough task, let alone the specification of deviations from nominal. Thus, many of the considerations here are qualitative, pending further study and assignment of numerical values specifying ranges of variations on parameter values. The type of considerations directly affecting control system design can be grouped into two categories: those to do with modelling accuracy and vehicle parameter definition, and those associated with subsystem "errors." Both categories are discussed below. A third area which could be considered is associated with the large entry flight envelope; thus, a trajectory within the envelope which is not the "nominal" trajectory (see Figures 2-2 and 2-4) could be considered "off-nominal". Recognizing the fact that the envelope itself is "nominal", the discussion becomes one of more semantics than engineering. The approach taken here is to simply delay this flight envelope discussion to the next section, and discuss its implications there.

2.4.1 Model Accuracy

As will be seen in Chapters 4 and 5, control law synthesis is dependent on the definition of a simplified vehicle model to account for the more fundamental inertial and aerodynamic properties of the vehicle. A dependence on the knowledge of both the aerodynamic coefficients and the mass properties is implicit in this modelling effort, and in fact, in any practical control design effort.

As noted earlier, the "nominal" aerodynamic coefficient values are given in Reference 2 ; given in Reference 1 is a table describing tolerances and variations of the coefficients appropriate to a slightly different vehicle from the design base vehicle of Reference 2 . Assuming that these values are an appropriate indication of the spread to be anticipated in the coefficient values for the vehicle described above, the data from Reference 1 may be summarized as shown in Table 2-7. As may be noted, the table only gives values at two Mach number/

39

Table 2-7: Possible Aerodynamic Coefficient Variations

Coefficient	Mach No.	Angle of Attack	Tolerance	Variation %	Variation Increment
Lift Coefficient, C_L	2	15°	3%	8	±0.04
	10	30°		13	±0.08
Pitching Moment Coefficient, C_{M_o}	2	15°	10%	25	±0.012
	10	30°		25	±0.002
Pitching Moment Slope, $\dfrac{\partial C_M}{\partial C_N}$	2	15°	3%	7	±0.003
	10	30°		3	±0.001
Drag Coefficient, C_D	2	15°	3%	17	±0.04
	10	30°		10	±0.04
Lift-to-Drag Ratio, $\dfrac{L}{D}$	2	15°	6%	6	±0.13
	10	30°		6	±0.07
Side Force Slope, C_{Y_β}	2	15°	10%	20	±0.003
	10	30°		20	±0.001
Yawing Moment Slope, C_{n_β}	2	15°	10%	25	±0.0004
	10	30°		25	±0.0006
Rolling Moment Slope, C_{ℓ_β}	2	15°	10%	50	±0.0006
	10	30°		17	±0.0003
Yaw Moment due to Aileron, $C_{n_{\delta_a}}$	2	15°	10%	30	±0.0001
	10	30°		10	±0.0001
Aileron Effectiveness, $C_{\ell_{\delta_a}}$	2	15°	10%	20	±0.0002
	10	30°		20	±0.0002
Rudder Side Force, $C_{Y_{\delta_r}}$	2	15°	5%	10	±0.0001
	10	30°		*	*
Rudder Effectiveness, $C_{n_{\delta_r}}$	2	15°	5%	10	±0.00006
	10	30°		*	*
Roll Moment due to Rudder, $C_{\ell_{\delta_r}}$	2	15°	5%	10	±0.00004
	10	30°		*	*

* Nominal value approaches zero, variation negligibly small

40

angle-of-attack pairs, so that it is a fairly sparse data set. The last column, which gives the variation, indicates the anticipated maximum difference between the present data book values and the data book values associated with the final frozen configuration; this type of variation is due to design changes and/or improved wind tunnel data. It should be noted that both a percentage variation and an accuracy band is given; this latter is given in units of per degree where appropriate, in contrast to the per radian usage later in the text. The column describing the tolerance is associated with the uncertainty in knowledge of the coefficient; as such, it is a tolerance about the value obtained after the variation of the last column is taken into account.

Two points should be made regarding the data of this table. First, several workers in the field hold that these data are optimistic and that the actual variations encountered may considerably exceed the values given. Unfortunately, placing an uncertainty level on the coefficient variation levels appears to be beyond the scope of present aerodynamic design techniques. The second point is that, even in the face of these "optimistic" values, some of the variations are quite large. As will be seen in Chapter 4, the basic airframe dynamics are specified by C_{M_0} , C_{n_β} , and C_{ℓ_β} , which are particularly subject to large variations, as shown in the table. It is also appropriate to note the relatively large possible variation in the adverse aileron coefficient $C_{n\delta_a}$, a point which has caused considerable confusion in the entry control design area. The details of this discussion are delayed until Chapter 7, after the control system has been described, so as to better explain the source of this confusion in terms of vehicle dynamics and control loop characteristics.

The other aspect of vehicle modelling accuracy is conerned with the specification of the vehicle's mass and inertia characteristics. As seen in Table 2-2, there are two basic sets of mass properties, dependent on the weight of the payload. The major effect of such a mass variation is to change the center-of-gravity location in the axial direction (i.e., along x_B), which, as may be inferred from the data of Reference 2 , changes the trim attitude of the vehicle for a given elevator trim setting. As discussed earlier, the body flap may be used to compensate

for these payload induced trim variations, simply by following an open loop deflection schedule which allows the appropriate trim moment to be applied. Thus, as will be seen in the development to follow, it is convenient to label the 25,000 pound payload/forward CG situation as "nominal", with the no payload/aft CG situation as an off-nominal, small deviation case, with the basic correction being provided for by the body flap.

Of perhaps more importance to the control problem are lateral displacements of the center-of-gravity, which, as shown in Table 2-2, destroy the vehicle's longitudinal plane of symmetry. The two-inch y-axis tolerance shown in the table can be considered as an unknown variation from the nominal geometric plane of symmetry. The effect of such a displacement, as discussed in Section 5.2.2, is to produce a disturbance torque primarily about the body roll axis, which, if uncompensated for, will lead to a divergent bank attitude. As discussed in this section, this imposes a requirement for a lateral trim logic to maintain attitude in the presence of disturbance torques whose values cannot be precisely predicted.

2.4.2 Subsystem Errors

The subsystems which directly affect control system performance are the input subsystems, which provide vehicle state information, and the output subsystems, which translate control system commands into attitude controlling torques.

The vehicle state information can be categorized into two groups: attitude information and trajectory parameter information. At present, the techniques for providing either type are not well-defined, and thus, it is a difficult task to estimate the performance level of the sensor/ estimator subsystems which will eventually be required. Furthermore, control system design work has not matured sufficiently to place well-founded specifications on the accuracy of the input variables, although this is an area of current design effort. Some work has been done, however, on estimation of vehicle attitude (in the stability-axis frame; see

42

Chapter 4 for a complete definition) from processed inertially derived information, and is reported on in References 14 and 24. The former describes estimates of angle-of-attack and sideslip and describes error growth down the trajectory, implying a requirement for additional sensor information during the latter portion of the entry. The latter reference describes angle-of-attack and sideslip estimation, along with bank attitude estimation. Wind and no wind cases are considered; in addition, the incorporation of a lateral accelerometer measurement in the sideslip estimate is described. The findings show that 1-sigma errors on the order of a few tenths of a degree can be expected (specifically, $\sigma_\alpha \lesssim 0.2$ deg, $\sigma_\beta \lesssim 0.2$ deg, and $\sigma_\phi \lesssim 0.4$ deg, for no unmodelled winds). The presence of unknown winds will naturally degrade the accuracy of the inertially derived information, and is discussed further in the reference. As noted above, current effort is directed towards a better definition of both practical estimator performance and anticipated control system requirements.

The second category of state information is trajectory oriented; i.e., Mach number, dynamic pressure, etc. Very little work has been done in this area, and accuracy estimates are very difficult to obtain. Needless to say, trajectory state estimation will require a concerted effort over the next few months of the design period. Similarly, control system accuracy requirements have not been determined, although some indications of vehicle sensitivity have been determined from simulator studies. These are reported on in Section 7.3.4.

Output subsystem errors can be categorized into those associated with the ACPS and those associated with the ACSS. With the former subsystem, the basic uncertainties involved are those of thruster location, thrust level, and pulse timing. As is seen in Chapters 4 and 5, the control law developed here is effectively insulated from these uncertainties by the use of a jet selection logic, to translate control system commands into individual thruster firings. Thus, most of the errors peculiar to the ACPS should have little effect on controller performance, assuming the jet selection logic provides adequate compensation to deal with off-nominal situations. It should be recognized, however, that the

43

oft-discussed design specification of near nominal operation with two jets failed (off) can be a severe constraint, depending on the particular jets failed. For example, it may be seen from Tables 2-4 and 2-5 that a two-jet failure in cluster 7 implies a maximum yaw acceleration capability of less than $1.1°/\sec^2$; clearly, a demand by the control law for a larger acceleration level will be unsatisfiable by the jet select logic.

With the ACSS, the basic uncertainties involved are those of deflection attitude accuracies. Low frequency errors (e.g., static off-sets) will show up as mistrim torques, so that closed-loop control system operation will provide the proper compensation for this type of error. High frequency errors have not been investigated, and their effect on control system operation has, to date, not been examined. Clearly, this is an area for additional work and subsequent subsystem performance specification.

2.5 Implications for Control System Design

Even with the cursory vehicle description and performance requirement specifications given above, certain basic control system design issues can be readily identified; it is the purpose of this section to briefly describe some of these issues by way of commenting on the descriptive material just presented.

Perhaps the most unique characteristic of this design problem is the large range of vehicle/environment parameters encountered during the entry, due to both the large nominal flight envelope (as illustrated in Figures 2-2 and 2-4) and the large number of possible off-nominal situations which can be encountered. This range in the problem "parameter space" must, of necessity, strongly influence the design effort. One of the questions which must be answered concerns the appropriate utilization of both the ACPS and the ACSS in the face of order-of-magnitude changes in dynamic pressure. Clearly, the ACPS must be used early in the entry. From the surface effectiveness histories of Figure 2-9, full conventional aerodynamic control is not possible until very late in the

entry. The area of concern, of course, is in between these extremes. The type of design trade involved is somewhat more obvious if the longitudinal and lateral aspects of the attitude control problem are treated separately, as is done more formally in Chapters 4 and 5. Thus, from the elevator effectiveness history of Figure 2-9, it appears feasible to use the elevator relatively early, and maintain its use down the entry, since a few degrees of elevator deflection provide a control acceleration level comparable to a "pitch" jet firing (e.g., thrusters 25 and 26 shown in Table 2-5). Also supporting early elevator utilization is the desire to minimize ACPS fuel expenditures, the possible unpredictability of thruster effectiveness at high dynamic pressures, and the difficulty of ACPS control law design synthesis at "significant" dynamic pressure levels (see below). On the other hand, early (and, in fact, during any part of the entry) utilization of the elevator may be constrained by actuator hinge-moment/horsepower requirements, skin surface heating rates, and uncertainty in control authority due to both the large Mach/alpha envelope and the significant possible variations in the surface effectiveness coefficient. Clearly, any finalized pitch ACPS/elevator control law must functionally express the design compromise which satisfies both the ACPS and ACSS constraints and the performance specifications placed on the controller.

The lateral control problem involves the same trades, but is complicated by the lack of rudder effectiveness through the majority of the entry. Delaying the use of the aileron until conventional control (i.e., aileron controls roll, rudder controls yaw) is possible is one approach; this of course implies that the aileron authority throughout most of the entry (see Figure 2-9) is not taken advantage of, and, in turn, implies greater ACPS activity with its concommitant possible problems. A more reasonable alternative is to use the aileron during early entry for body-axis roll control, eliminating the requirement for the ACPS to provide roll torques, "yaw" ACPS firings still being required for z_B-axis control. This has the distinct advantage of emulating conventional operation, where the rudder authority is replaced by yaw jet firings; the disadvantage of such an approach is that all the undesirable features

45

of continued ACPS activity are still present and are compounded with the requirement of compatible simultaneous thruster and surface operation. This latter point may prove to be (adversely) decisive once the plume effect of yaw jet firings over the elevon surfaces is better defined (see Figures 2-5 and 2-6 for the geometry involved). A third alternative is to forgo the attempt of conventional lateral control, and provide lateral control with the aileron alone. As will be seen, the disadvantages of such an approach are primarily those of unanticipated dynamic response characteristics, although clearly all of the constraints of surface utilization mentioned above also apply.

The large flight envelope not only results in large variations in control surface authority, but also similarly affects the basic airframe dynamics. Since any control law design effort must either implicity or explicitly model these dynamics, the choice of any particular control technique should consider model variability. For example, in the case of ACPS control law synthesis, an immediate choice of a predictive or non-predictive logic faces the designer. In a predictive logic, such as is used in the ACPS exoatmospheric control laws described in Reference 27, an accurate vehicle model is necessary to predict the jet firing times necessary to perform a particular maneuver; the advantage is one of fuel minimization, although other performance criteria can also be met quite efficiently in this manner. Outside of the atmosphere, however, vehicle modelling is almost a trivial exercise, since only the inertial properties of the vehicle and the jet configuration parameters need be known. This, of course, is in contrast with the growing aerodynamic effects as the vehicle travels down an entry trajectory, making the modelling problem considerably more difficult. The alternative is to use a non-predictive logic in which the appropriate state variables are sampled at relatively high rates to determine the proper jet firing commands for that particular sample instant. This avoids <u>some</u> of the modelling problems (since inertias and thruster torques must be considered for practical gain selection) but has the disadvantage of providing typically less efficient maneuvers and/or attitude hold operation. Further complicating

46

the trade in this particular design effort is the possibility of simultaneous control torques provided by the ACSS, making a predictive logic model more complicated and tending to make a non-predictive feedback gain structure less likely to guarantee specified closed-loop performance. Also involved in the choice is an interposition of a jet selection logic between control law commands and thruster hardware; control law compatibility with such a logic is of prime importance.

A similar situation exists for ACSS control law synthesis: the large flight envelope results in a considerable variation in both surface effectiveness and vehicle responsiveness to surface induced control torques. Here the question is not one of predictive versus non-predictive (since the possible coefficient errors make a predictive approach unfeasible) but one of implicit versus explicit modelling. Implicit modelling is used here to denote the type of design base used for the classic analog-style trial-and-error design synthesis. Typically, the implicit model is a vehicle simulator, "set-up" at a particular point in the flight envelope. Given a feedback structure, the gains may then be chosen so that the desired response is obtained. By repeating this procedure over a large number of points in the envelope, the gains derived by trial-and-error may be "scheduled" against an appropriate trajectory parameter, so that the design may be "flown" continuously down the entry trajectory. The advantage, of course, is that little analysis is required for control law implementation; the obvious disadvantage is the time spent in trial-and-error searches for multiple gains at many flight conditions. A more subtle disadvantage is noted below. The alternative, explicit modelling, is used to denote the use of a simplified vehicle model adequate as a control law design base and appropriate to an _analytic_ derivation of the required control law gains. A more detailed definition of such a model is given in Chapter 4; it suffices to note here, however, that this approach has a greater inherent sensitivity to modelling errors (e.g., coefficient uncertainties) unless particular attention is paid to desensitizing the control law to off-nominal situations. The design synthesis advantage of analytically defined gains should be obvious, however, with

47

the large range of vehicle parameters encountered in the entry envelope.
In addition, it should be recognized that a sufficiently realistic simpli-
fied model aids greatly in understanding the basic dynamics involved,
and, in fact, may point out unanticipated open-loop vehicle response
characteristics which are only recognized in a trial-and-error approach
by the failure of conventional control techniques. That this is the situa-
tion in this entry control problem will be made clear in Chapter 4.

The vehicle data which have been presented in this chapter, coupled
with the closed-loop performance requirements, point out some obvious
design trades to be made. Clearly there are others (as will be shown in
later chapters) and the above few paragraphs are not intended to be ex-
haustive, but merely provide some insight to the basic issues involved.
It should be obvious, however, that even this material is sufficient to
begin a design effort based on the qualitative conclusions which could
have been drawn here and on some trial-and-error simulator-based
design synthesis work. This is not the approach used here however; a
slightly more circuitous path involving vehicle modelling is described
in the next chapter.

3. Design Synthesis Overview

In many design presentations, there is often lacking sufficient discussion explaining the motivation for the choice of a particular approach to the design problem, and this is often frustrating to the reader, especially when there exist other unexercised and apparently feasible design options with their associated advantages and disadvantages. Perhaps the fundamental cause of this is that in any practical design effort, an iterative procedure lies at the base of the final presented product, and it is somewhat tedious, not to mention cumbersome, to report the chronology of the synthesis and simulation effort. This is certainly the case here, and no attempt is made to provide a development history. Instead, it is felt appropriate to outline here the general approach used, recognizing that the basic design trades have already been described in Section 2.5, and that the discussion of more specific design options will be deferred to the next chapter. The purpose of this very brief chapter, then, is to provide an overview description of the design effort, and concommitantly provide an introduction to the material presented in the next three chapters, respectively describing the vehicle model development used in control law synthesis, the design synthesis itself, and the control law description.

Shown in Figure 3-1 is a diagram of the control law development process used in arriving at the control system described in Chapter 6. The initial step is the development of a simplified equation base used to model the vehicle's rigid-body rotational dynamics. The purpose is twofold: to provide a basic understanding of the vehicle dynamics during the entry regime, and to provide an equation base appropriate for later controller synthesis. Clearly a compromise must be struck between a realistic and untractable multi-dimensional, multi-order, non-linear, time-varying representation and a model of such simplicity that the fundamental dynamics are ignored. Fortunately, the solution is more quantitatively bracketed than it sounds, since the vehicle data

49

guidance requirements

vehicle data

trajectory data

DEVELOPMENT OF
SIMPLIFIED VEHICLE
MODEL

performance
requirements

subsystem
constraints

INITIAL CONTROL
LAW DESIGN

vehicle
simulator

SIMULATION AND
EVALUATION

(updated) performance reqmts

(updated) subsystem
constraints

(new) trajectory envelope

(new) vehicle data

MODIFICATIONS TO
IMPROVE CONTROLLER
PERFORMANCE

MORE DETAILED
VEHICLE
MODELING

CONTROL LAW
UPDATE

Fig. 3-1: Control System Development

and trajectory envelope data can be integrated to support many numerical approximations, which, in turn, may be used to simplify the initially quite complicated equation set describing the vehicle. An even more fundamental simplification is possible by an early recognition of the guidance requirements: as noted in the previous chapter, the primary objective of the control system is to maintain the desired "stability-axis" attitude of the vehicle (see the next chapter for a formal definition of the angles defining stability-axis attitude); by recasting the conventional "body-axis" dynamic equations into a stability-axis format, a dramatic simplification of the equations of motion is possible. This is the subject of Chapter 4, which details the equation development, summarizes the simplified vehicle model appropriate to controller synthesis, and discusses its implications on control law synthesis.

The next step in the design synthesis is to integrate the implications of this simplified model with both the required performance of the closed-loop system and the design constraints of the supporting subsystems (e.g., ACPS, ACSS, state estimator, etc.), so as to arrive at an initial, perhaps näive, control law which attempts to satisfy all the requirements and constraints placed on its operation. Clearly, design trades of the type discussed in Section 2.5 and supported by the data of the other sections of Chapter 2 are central to the synthesis effort here. To provide a verification of the validity of the control system design, the next step (shown in Figure 3-1) in the design effort is one of simulation and evaluation; assumed here is the concurrent development of a realistic vehicle simulator, a major effort in itself, and one which will not be described here. It is at this point that inadequacies in the control law make themselves most apparent, providing strong motivation for modifications to improve performance.

Modifications may also be required when the scope of the control system is changed, for example, by attempting control in a previously unstudied region of the flight regime. In addition, as the vehicle design,

51

subsystem constraints, and/or trajectory envelope are continually updated, corresponding modifications to the control system may also be required. Whether or not additional vehicle modeling is necessary to satisfactory performance will depend on the particular situation; all such changes, however, must eventually loop back for additional simulation and evaluation. This, then, is the design iteration basic to the control law development, and any attempt to give a functional non-chronological description of the control law synthesis (as is done in Chapter 5) or a static description of the control law itself (as is done in Chapter 6) can only meet with partial success. '

It is appropriate at this point to note that the design motivation for the results presented in Chapters 5 and 6 is primarily centered around vehicle dynamic response, and there is no attempt to <u>directly</u> address the design problems raised by the possible operational subsystem constraints noted in the previous chapter. For example, the question of ACPS versus ACSS utilization is settled by a consideration of torque authority levels and a desire to minimize fuel expenditures. Clearly, a surface heating constraint may prohibit ACSS utilization during certain portions of the entry, thus invalidating the design choice made on dynamic considerations. There are two points to be recognized, however. First, no <u>known</u> operational constraints are violated by the design presented here, and second, should the design be found to be in violation of some later specified constraint, there exists a considerable amount of flexibility in control parameter choice, so that satisfaction of an additional system constraint is feasible. Thus, rather than attempt to settle the design issued raised in Chapter 2 by a direct argument, the next three chapters will present one design solution, with as much motivation for the design options exercised as possible. The point to recognize is that actual system performance is the final criterion by which the control synthesis validity can be judged, and a fair argument for this particular controls approach is given by the test results of Chapter 7.

4. Vehicle Model

This chapter derives and discusses the simplified equation base
which is used to model the vehicle's rigid-body rotational dynamics
during the entry flight regime. The primary purpose of this model
is to provide a concise description of the fundamental dynamic
characteristics of the vehicle, in a format useful for both stability
and control analyses, and control law synthesis. The model is thus
a compromise between the sophistication required for an accurate
dynamic representation, and the simplicity necessary for successful
control law design. Specifically, the model is limited to describing
the short-period rotational dynamics of the rigid body, in the absence
of off-nominal vehicle characteristics*.

Three basic features of the model presented in this chapter
should be noted. First, in line with classical aircraft stability and
control analyses, the model consists of linear constant-coefficient
differential equations, where the coefficients are treated as quasi-
static functions of the flight regime. The validity of this type of
frequency separation will be apparent in the time histories of the
equation coefficients. Second, in contrast to classical analyses, the
stability-axis reference frame, rather than the body-axis frame,
is used to specify the vehicle's rotations. As will be seen, the use of
stability-axis variables results in a model of appealing simplicity,
and yet retains the fundamental response characteristics of the vehicle.
Finally, as a direct consequence of the previous feature, the model
introduces the notion of "dynamic" derivatives, which are functions
of the vehicle's inertial and aerodynamic properties. Although versions
of these derivatives have appeared sporadically throughout the literature
over the years, it is felt that the model presented here provides a
unifying structure for these variables. In particular, the stability-axis
vehicle model makes clear the importance of the "dynamic derivatives"
in stability analysis and control system design of high-performance
aircraft.

---

*Center-of-gravity displacements are discussed in Sections 5.2.2.2.3
and 7.3.1.

This chapter is organized into four sections. Section 4.1 uses classic linearization techniques to derive the quasi-static equations of motion describing the vehicle's body-axis rotations at a specified equilibrium flight condition. Section 4.2 then defines the stability-axis variables to be used in the remainder of this chapter. With these definitions, section 4.3 then transforms the body-axis equations of 4.1 into the stability-axis frame. It is at this point that the trajectory envelope and the specific airframe properties are used to determine the important dynamic effects, thus significantly simplifying the equation coefficients in a term-by-term comparison of magnitudes. Finally, Section 4.4 summarizes these results and presents typical time histories of the vehicle model parameters. In addition, the section discusses some interesting qualitative aspects of the vehicle model.

4.1 Linearized Equations of Motion

This section presents the detailed development of the linearized equations of motion expressed in the conventional body-axis reference frame (defined below). Section 4.1.1 presents the non-linear equations specifying the vehicle's response to externally applied forces and torques. Sections 4.1.2 and 4.1.3 then linearize these equations about a symmetric flight condition, while Section 4.1.4 linearizes the aerodynamic forces and torques applied to the vehicle. Finally, Section 4.1.5 presents the linearized body-axis equations of motion.

4.1.1 Non-linear Equations of Motion

This section presents the non-linear equations of motion which characterize the vehicle's dynamic response to externally applied forces and torques. Since this is the subject of extensive treatment in several references on aircraft stability and control (for example, see References 7, 8, 11, and 20) the derivation of these equations is not presented here. However, to avoid possible ambiguities, all pertinent variables are defined and the necessary simplifying assumptions are stated.

Two coordinate systems are needed to describe the vehicle dynamics: a reference frame R and a body-axis frame B. Both frames are defined to have their origins located at the vehicle's nominal center-of-gravity*. The B frame, shown in Figure 4-1, and introduced in Chapter 2, is the conventional body frame, chosen to be fixed to the vehicle (which is assumed to be a rigid body). Specifically, assuming a longitudinal plane of symmetry, the y_B-axis is chosen perpendicular to this plane, approximately out the right wing and the x_B-axis is chosen parallel to a longitudinal reference line, approximately out the nose. The reference frame R is the local geographic frame, with the x_R, y_R, and z_R axes aligned with north, east, and down, respectively. The transformation between the two frames is effected by the conventional Euler angle rotations of Ψ, Θ, and Φ as illustrated in Figure 4-2.

The vehicle's mass properties are defined by a mass m and an inertia matrix $\mathcal{J}$ defined in the B frame:

$$
\mathcal{J} \equiv
\begin{bmatrix}
I_{xx} & 0 & -I_{xz} \\
0 & I_{yy} & 0 \\
-I_{xz} & 0 & I_{zz}
\end{bmatrix}
$$

where I_{xy} and I_{yz} are both zero since the x-z plane is a plane of symmetry. The linear and angular velocities of the vehicle, with respect to a fixed inertial reference frame, are $\underline{v}$ and $\underline{\omega}$, respectively. Expressed in B frame coordinates,

$$
\underline{v} \equiv
\begin{bmatrix}
U \\
V \\
W
\end{bmatrix}
\quad ; \quad
\underline{\omega} \equiv
\begin{bmatrix}
P \\
Q \\
R
\end{bmatrix}
$$

The velocities $\underline{v}$ and $\underline{\omega}$ are shown schematically in Figure 4-3.

---

*Center-of-gravity displacement effects are treated in Section 5.2.2.

55
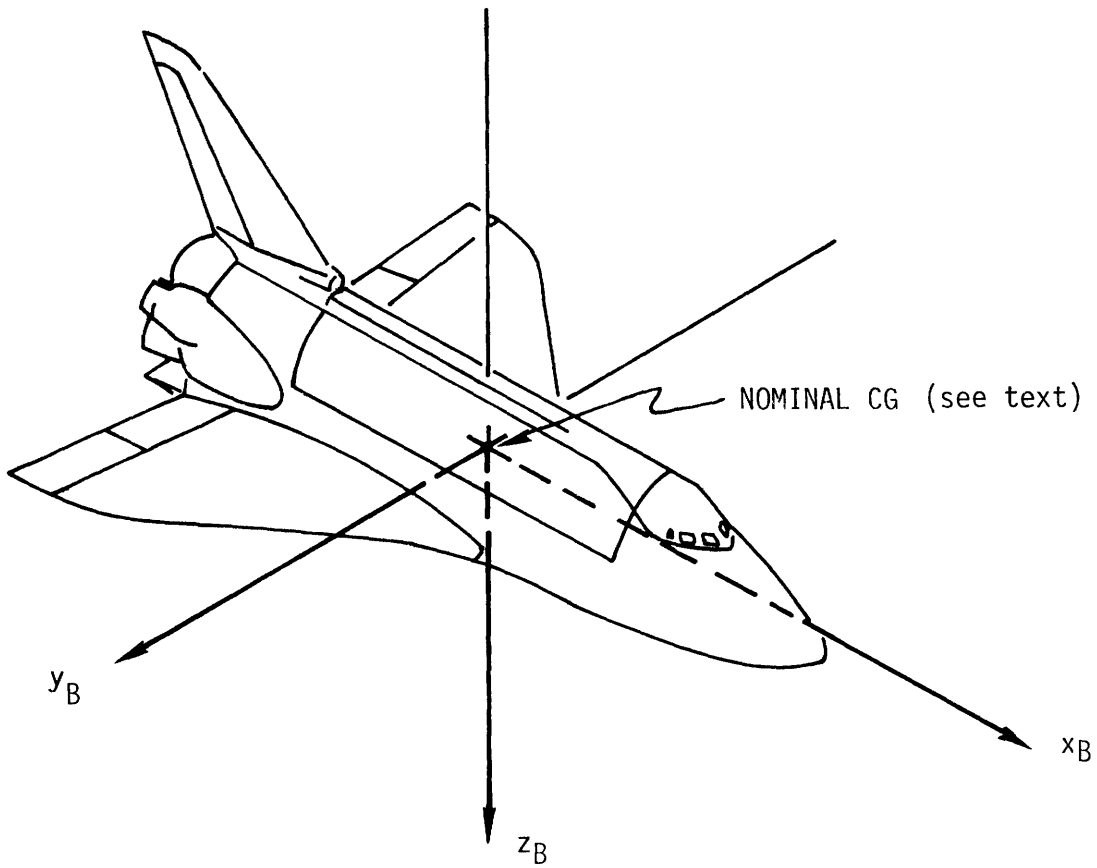
Figure 4-1. Body-axis Reference Frame.
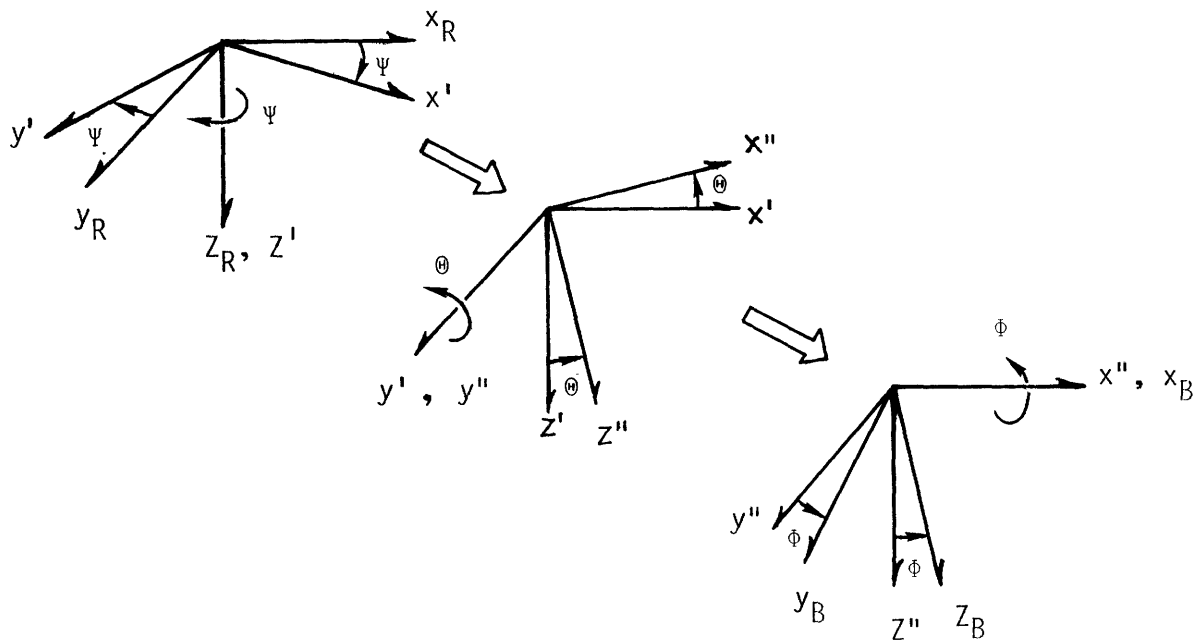
Figure 4-2. Euler Angle Rotation Sequence.
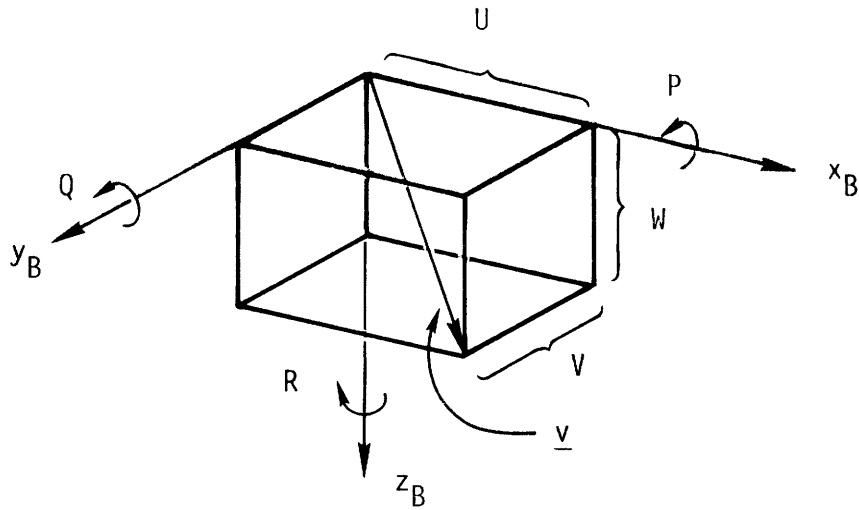
Figure 4-3. Body Frame Velocities.

The forces which act on the vehicle are assumed to be due only to gravity and the vehicle aerodynamics, and are defined as $\underline{g}$ and $\underline{f}$, respectively. The torques which act on the vehicle are assumed to be due only to the vehicle aerodynamics and the ACPS jet firings, and are defined as $\underline{\tau}$ and $\hat{\underline{\tau}}$, respectively. Note that this is equivalent to assuming that the ACPS thrusters are used only as torque couples, which is a fair approximation to the operation of the jet selection logic during entry, as will be seen later in Chapter 5. Expressed in B frame components, the external forces and torques acting on the vehicle are as follows:

$$\underline{f} \equiv \begin{bmatrix} X \\ Y \\ Z \end{bmatrix} \quad ; \quad \underline{\tau} \equiv \begin{bmatrix} L \\ M \\ N \end{bmatrix} \quad ; \quad \hat{\underline{\tau}} \equiv \begin{bmatrix} \hat{L} \\ \hat{M} \\ \hat{N} \end{bmatrix} \quad ; \quad \underline{g} \equiv g \begin{bmatrix} -\sin\Theta \\ \cos\Theta \sin\Phi \\ \cos\Theta \cos\Phi \end{bmatrix}$$

With the above definitions, it is possible to derive the equations of motion defining the vehicle's linear and rotational dynamics as seen in the body frame B. To do this, it is necessary to assume that the reference frame R is inertially non-rotating; this is justified for atti-

tude control purposes, since, in the short time period under consideration, the vehicle will travel along a path subtending a small angle measured at the earth's center. This, in turn, implies that the instantaneous local vertical will not appreciably rotate during the control interval. Note that this assumed lack of rotation is equivalent to a "flat-earth" assumption.

With the above preliminaries, the vehicle's equations of motion may be derived rather directly (see Reference 11).

The three linear momentum equations are:

$$m(\dot{U} + QW - RV) + mg \sin \Theta \quad - X = 0$$
$$m(\dot{V} + RU - PW) - mg \cos \Theta \sin \Phi - Y = 0 \qquad (4-1)$$
$$m(\dot{W} + PV - QU) - mg \cos \Theta \cos \Phi - Z = 0$$

The three angular momentum equations are:

$$I_{xx}\dot{P} - I_{xz}\dot{R} + (I_{zz} - I_{yy})QR - I_{xz}PQ - L = \hat{L}$$
$$I_{yy}\dot{Q} + (I_{xx} - I_{zz})PR + I_{xz}(P^2 - R^2) - M = \hat{M} \qquad (4-2)$$
$$I_{zz}\dot{R} - I_{xz}\dot{P} + (I_{yy} - I_{xx})PQ + I_{xz}QR - N = \hat{N}$$

Finally, the equations relating Euler angle rates to body rates are:

$$\dot{\Theta} - Q \cos \Phi - R \sin \Phi = 0$$
$$\dot{\Phi} - P - Q \sin \Phi \tan \Theta - R \cos \Phi \tan \Theta = 0 \qquad (4-3)$$

The above eight non-linear coupled differential equations thus define the dynamics of the vehicle, in response to force and torque inputs.

4.1.2 Equilibrium Flight Equations

Because of the non-linearities and coupling in (4-1) - (4-3), it is convenient to make use of the concept of equilibrium flight and derive the equations of motion for deviations (perturbations) from equilibrium (nominal). Linearization may be effected by using the conventional

procedure of: (1) replacing each variable by its nominal value plus a perturbation from nominal; (2) neglecting second- and higher-order products of the perturbation quantities; (3) using small angle approximations where appropriate; and (4) subtracting the equilibrium equations from the corresponding perturbed equations. What results, then, is a set of linear differential equations in the perturbation variables.

In the equations below, lower case letters are used to correspond with the previously defined variables: those with a zero subscript denote equilibrium values, while those without denote perturbations. The linearized equations are as follows:

$$m(\dot{u}+q_0 w+w_0 q-r_0 v-v_0 r) + (mg\cos\theta_0)\theta \qquad\qquad -x = 0$$

$$m(\dot{v}+r_0 u+u_0 r-p_0 w-w_0 p) + (mg\sin\theta_0\sin\phi_0)\theta - (mg\cos\theta_0\cos\phi_0)\phi -y = 0$$

$$m(\dot{w}+p_0 v+v_0 p-q_0 u-u_0 q) + (mg\sin\theta_0\cos\phi_0)\theta + (mg\cos\theta_0\sin\phi_0)\phi -z = 0$$

$$(4\text{-}4)$$

$$I_{xx}\dot{p} + (I_{zz}-I_{yy})(q_0 r+r_0 q) - I_{xz}(\dot{r}+p_0 q+q_0 p) - \ell = \hat{\ell}$$

$$I_{yy}\dot{q} + (I_{xx}-I_{zz})(p_0 r+r_0 p) + 2I_{xz}(r_0 r+p_0 p) - m = \hat{m} \qquad (4\text{-}5)$$

$$I_{zz}\dot{r} + (I_{yy}-I_{xx})(p_0 q+q_0 p) - I_{xz}(\dot{p}-q_0 r-r_0 q) - n = \hat{n}$$

$$\dot{\theta} - (\cos\phi_0)q + (q_0\sin\phi_0)\phi - (\sin\phi_0)r - (r_0\cos\phi_0)\phi \qquad\qquad = 0$$

$$\dot{\phi} - p - (\sec^2\theta_0)[q_0\sin\phi_0+r_0\cos\phi_0]\theta - (\tan\theta_0)[q_0\cos\phi_0-r_0\sin\phi_0]\phi$$

$$- [\tan\theta_0\sin\phi_0]q - [\tan\theta_0\cos\phi_0]r = 0$$

$$(4\text{-}6)$$

Note that in the above formulation the perturbation variables $(\hat{\ell}, \hat{m}, \hat{n})$ are equal to the previously introduced ACPS torque variables $(\hat{L}, \hat{M}, \hat{N})$; this is equivalent to stating that ACPS torques are perturbation variables, since the ACPS is nominally inactive for trimmed equilibrium flight.

59

4.1.3 Symmetric Flight Equations

Equations (4-4) - (4-6) describe the vehicle's motion about any given equilibrium flight condition. The particular equilibrium commonly chosen, and the one which will be used here, is that of "symmetric" flight, where:

(a) the nominal angular velocity is zero, or

$$p_o = q_o = r_o = 0$$

(b) the nominal sideslip velocity is zero, or

$$v_o = 0$$

(4-7)

(c) the nominal roll angle is zero, or

$$\phi_o = 0$$

Thus, (4-7) may be used to reduce (4-4), (4-5), and (4-6) to the simplified equations describing perturbations from symmetric flight:

$$m(\dot{u}+w_o q) \quad + (mg\cos\theta_o)\theta - x = 0 \qquad (a)$$

$$m(\dot{v}+u_o r - w_o p) - (mg\cos\theta_o)\phi - y = 0 \qquad (b) \qquad (4-8)$$

$$m(\dot{w}-u_o q) \quad + (mg\sin\theta_o)\theta - z = 0 \qquad (c)$$

$$I_{xx}\dot{p} - I_{xz}\dot{r} - \ell = \hat{\ell} \qquad (a)$$

$$I_{yy}\dot{q} \quad - m = \hat{m} \qquad (b) \qquad (4-9)$$

$$I_{zz}\dot{r} - I_{xz}\dot{p} - n = \hat{n} \qquad (c)$$

$$\dot{\theta} - q \quad = 0 \qquad (a)$$

$$\dot{\phi} - p - (\tan\theta_o)r = 0 \qquad (b) \qquad (4-10)$$

At this point, it is worthwhile to note the tendency toward decoupling in the above equation set. Disregarding the aerodynamic perturbations (which are treated in the next section), it can be seen that equations

(4-8a), (4-8c), (4-9b) and (4-10a) exclusively specify the "longitudinal" rates (linear and angular) u, w, and q, while equations (4-8b), (4-9a), (4-9c), and (4-10b) likewise exclusively specify the "lateral" rates v, p, and r. This characteristic is taken advantage of in Section 4.1.5.

4.1.4 Aerodynamic Perturbations

In order to fully describe the perturbation dynamics expressed in (4-8) - (4-10), it is necessary to relate the aerodynamic perturbations $(x, y, z, \ell, m,$ and $n)$ to the vehicle state variables $(u, v, w,$ etc.).

Following a simplified classical approach (for example, see Reference 8), it is assumed that the aerodynamic forces and torques $(X, Y, Z, L, M,$ and $N)$ are dependent only on the vehicle's linear and angular velocities, and on the aerodynamic control surface deflections (from trim) defined as follows:

$\hat{\delta}_e$ elevator deflection from trim $(\hat{\delta}_e \equiv \delta_e - \delta_{e_T})$

$\hat{\delta}_r$ rudder deflection from trim $(\hat{\delta}_r \equiv \delta_r - \delta_{r_T})$

$\hat{\delta}_a$ aileron deflection from trim $(\hat{\delta}_a \equiv \delta_a - \delta_{a_T})$

The following equation for the x-axis aerodynamic force illustrates this functional dependence:

$$X = X(U, V, W, P, Q, R, \delta_e, \delta_r, \delta_a)$$

Now, to first order, the aerodynamic perturbations are linear functions of the velocity perturbations, or continuing the above example,

$$x \equiv dX = X_u u + X_v v + \ldots + X_{\delta_r} \hat{\delta}_r + X_{\delta_a} \hat{\delta}_a$$

where

$$X_u \equiv \frac{\partial X}{\partial U} \quad , \quad X_v \equiv \frac{\partial X}{\partial V} \quad , \quad \ldots \quad , \quad X_{\delta_r} \equiv \frac{\partial X}{\partial \delta_r} \quad , \quad X_{\delta_a} \equiv \frac{\partial X}{\partial \delta_a}$$

all evaluated at the nominal flight condition of symmetric flight.

Recognizing from (4-1) and (4-2) that there are six dependent variables (X, Y, Z, L, M, and N) and six independent state variables (U, V, W, P, Q, and R), it follows that there are 36 such "stability" derivatives of the above form. In addition, with three more independent control variables (δ_e, δ_r, and δ_a), there are 18 "control" derivatives.

As discussed in Reference 7, symmetry considerations require that half of each set of the above derivatives be identically zero, so that the aerodynamic perturbations may be related to the velocity and control surface perturbations in the following manner:

$$x = X_u u + X_w w + X_q q + X_{\delta_e} \hat{\delta}_e \qquad (a)$$

$$y = Y_v v + Y_p p + Y_r r + Y_{\delta_r} \hat{\delta}_r + Y_{\delta_a} \hat{\delta}_a \qquad (b) \qquad (4\text{-}11)$$

$$z = Z_u u + Z_w w + Z_q q + Z_{\delta_e} \hat{\delta}_e \qquad (c)$$

$$\ell = L_v v + L_p p + L_r r + L_{\delta_r} \hat{\delta}_r + L_{\delta_a} \hat{\delta}_a \qquad (a)$$

$$m = M_u u + M_w w + M_q q + M_{\delta_e} \hat{\delta}_e \qquad (b) \qquad (4\text{-}12)$$

$$n = N_v v + N_p p + N_r r + N_{\delta_r} \hat{\delta}_r + N_{\delta_a} \hat{\delta}_a \qquad (c)$$

For numerical work, it is necessary to relate the above derivatives to the more commonly available non-dimensional stability and control derivatives. This is done in Appendix A (which has been adapted from References 7 and 21 and the relations defining the two sets of derivatives are summarized there.

As in the previous section, it should be noted that (4-11) and (4-12) may be grouped into longitudinal and lateral aerodynamic perturbations, with equations (4-11a), (4-11c) and (4-12b) constituting the longitudinal set (dependent on u, w, q, and $\hat{\delta}_e$), and equations (4-11b), (4-12a), and (4-12c) constituting the lateral set (dependent on v, p, r, $\hat{\delta}_a$, and $\hat{\delta}_r$).

4.1.5 Linearized Dynamics (Body-axis frame)

With the system equations of Section 4.1.3 and the aerodynamic perturbation relations of the previous section, the vehicle dynamics may be expressed in a conventional linear form. The familiar longitudinal and lateral equations of motion may be obtained by substituting (4-11) and (4-12) into (4-8) - (4-10) and collecting terms. In the equations below, the derivative operator (d/dt) is used for clarity.

The longitudinal equations governing (u, w, q, and θ) are:

$$\left[m\frac{d}{dt}-X_u\right]u \quad -X_w w + \left[mu_o-X_q\right]q + \left[mg\cos\theta_o\right]\theta = X_{\delta_e}\hat{\delta}_e \qquad (a)$$

$$-Z_u u + \left[m\frac{d}{dt}-Z_w\right]w - \left[mu_o+Z_q\right]q + \left[mg\sin\theta_o\right]\theta = Z_{\delta_e}\hat{\delta}_e \qquad (b)$$

$$-M_u u \quad -M_w w + \left[I_{yy}\frac{d}{dt}-M_q\right]q \quad = M_{\delta_e}\hat{\delta}_e+\hat{m} \qquad (c)$$

$$q \quad -\left[\frac{d}{dt}\right]\theta = 0 \qquad (d)$$

$$(4-13)$$

The lateral equations governing (v, p, r, and ϕ) are:

$$\left[m\frac{d}{dt}-Y_v\right]v - \left[mw_o+Y_p\right]p + \left[mu_o-Y_r\right]r - \left[mg\cos\theta_o\right]\phi = Y_{\delta_r}\hat{\delta}_r+Y_{\delta_a}\hat{\delta}_a \qquad (a)$$

$$-L_v v + \left[I_{xx}\frac{d}{dt}-L_p\right]p- \left[I_{xz}\frac{d}{dt}+L_r\right]r \quad = L_{\delta_r}\hat{\delta}_r + L_{\delta_a}\hat{\delta}_a + \hat{\ell} \qquad (b)$$

$$-N_v v - \left[I_{xz}\frac{d}{dt}+N_p\right]p+\left[I_{zz}\frac{d}{dt}-N_r\right]r \quad = N_{\delta_r}\hat{\delta}_r + N_{\delta_a}\hat{\delta}_a + \hat{n} \qquad (c)$$

$$-p - \left[\tan\theta_o\right]r + \left[\frac{d}{dt}\right]\phi = 0 \qquad (d)$$

$$(4-14)$$

The above two equation sets may be conveniently normalized by defining the following normalized velocity perturbations:

$$\tilde{u} \equiv u/V_T \quad ; \quad \tilde{v} \equiv v/V_T \quad ; \quad \tilde{w} \equiv w/V_T \qquad (4-15)$$

Further, the ACPS acceleration level may be defined as the appropriate, control torque divided by the corresponding moment of inertia, or*:

$$u_x \equiv \hat{\ell}/I_{xx} \quad ; \quad u_y \equiv \hat{m}/I_{yy} \quad ; \quad u_z \equiv \hat{n}/I_{zz} \tag{4-16}$$

A further simplification results by relating the trim angle-of-attack, α_T, to the equilibrium longitudinal velocities as shown in Figure 4-4. The following relations then hold:

$$\frac{u_o}{V_T} = \cos\alpha_T$$

$$\tag{4-17}$$

$$\frac{w_o}{V_T} = \sin\alpha_T$$
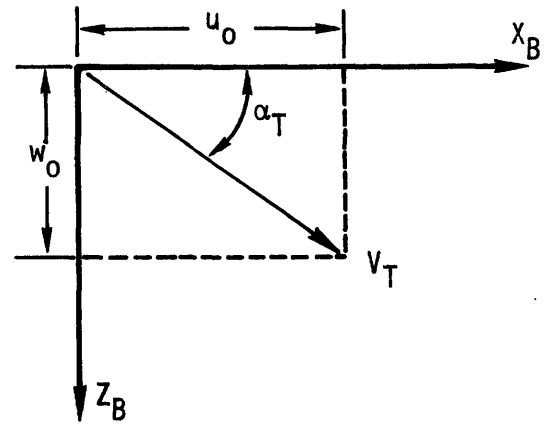
Fig. 4-4: Trim Angle-of-Attack

At this point, (4-13) and (4-14) may be put in a more convenient format by use of the Laplace transform; transformation also allows for the use of (4-13d) and (4-14d) to eliminate θ and ϕ, respectively. With the further use of (4-15) - (4-17) and the assumption of zero initial condition values, the transformed and normalized versions of (4-13) and (4-14) may be used to define the vehicle dynamics. With s as the Laplace transform variable, the longitudinal equations of motion are thus given by:

---

*It should be recognized that (u_x, u_y, u_z) represent the ACPS acceleration levels induced by (any) jet firings, resolved in the body axes. These acceleration levels need not necessarily represent levels attainable through firings of simple jet couples.

$$\left[s - \frac{X_u}{m}\right]\tilde{u} - \left[\frac{X_w}{m}\right]\tilde{w} + \left[\left(\sin\alpha_T - \frac{X_q}{mV_T}\right) + \frac{(g/V_T)\cos\theta_o}{s}\right]q = \frac{X_{\delta_e}}{mV_T}\hat{\delta}_e \quad \text{(a)}$$

$$\left[-\frac{Z_u}{m}\right]\tilde{u} + \left[s - \frac{Z_w}{m}\right]\tilde{w} + \left[-\left(\cos\alpha_T + \frac{Z_q}{mV_T}\right) + \frac{(g/V_T)\sin\theta_o}{s}\right]q = \frac{Z_{\delta_e}}{mV_T}\hat{\delta}_e \quad \text{(b)}$$

$$\left[-\frac{V_T M_u}{I_{yy}}\right]\tilde{u} - \left[\frac{V_T M_w}{I_{yy}}\right]\tilde{w} + \left[s - \frac{M_q}{I_{yy}}\right]q = \frac{M_{\delta_e}}{I_{yy}}\hat{\delta}_e + u_y \quad \text{(c)}$$

$$(4\text{-}18)$$

The lateral equations of motion are similarly defined:

$$\left[s - \frac{Y_v}{m}\right]\tilde{v} - \left[\left(\sin\alpha_T + \frac{Y_p}{mV_T}\right) + \frac{(g/V_T)\cos\theta_o}{s}\right]p + \left[\left(\cos\alpha_T - \frac{Y_r}{mV_T}\right)\right.$$
$$\left. - \frac{(g/V_T)\sin\theta_o}{s}\right]r = \sigma_1 \quad \text{(a)}$$

$$-\left[\frac{V_T L_v}{I_{xx}}\right]\tilde{v} + \left[s - \frac{L_p}{I_{xx}}\right]p - \left[\frac{I_{xz}}{I_{xx}}s + \frac{L_r}{I_{xx}}\right]r = \sigma_2 \quad \text{(b)}$$

$$-\left[\frac{V_T N_v}{I_{zz}}\right]\tilde{v} - \left[\frac{I_{xz}}{I_{zz}}s + \frac{N_p}{I_{zz}}\right]p + \left[s - \frac{N_r}{I_{zz}}\right]r = \sigma_3 \quad \text{(c)}$$

$$(4\text{-}19)$$

where, for convenience, the right-hand side of the above equation set is defined by:

$$\sigma_1 \equiv \frac{Y_{\delta_r}}{mV_T}\hat{\delta}_r + \frac{Y_{\delta_a}}{mV_T}\hat{\delta}_a \quad \text{(a)}$$

$$\sigma_2 \equiv \frac{L_{\delta_r}}{I_{xx}}\hat{\delta}_r + \frac{L_{\delta_a}}{I_{xx}}\hat{\delta}_a + u_x \quad \text{(b)} \qquad (4\text{-}20)$$

$$\sigma_3 \equiv \frac{N_{\delta_r}}{I_{zz}}\hat{\delta}_r + \frac{N_{\delta_a}}{I_{zz}}\hat{\delta}_a + u_z \quad \text{(c)}$$

Equation sets (4-18), (4-19), and (4-20) thus describe the vehicle's longitudinal and lateral dynamics by relating the perturbed linear and angular body-axis velocity components ($\tilde{u}$, $\tilde{v}$, $\tilde{w}$, p, q, and r) to the applied ACPS control accelerations (u_x, u_y, and u_z) and to the aerodynamic control surface deflections ($\hat{\delta}_e$, $\hat{\delta}_a$, and $\hat{\delta}_r$).

4.2 Stability-Axis Variables

The body frame rates of the previous section, in conjunction with (4-18) to (4-20), completely define the vehicle's rotational motion; however, for stability analysis and control law synthesis, it is more appropriate (and more convenient) to introduce the stability-axis variable set to define the vehicle dynamics. Specifically, this section will define: (1) perturbation in angle-of-attack, $\hat{\alpha}$; (2) sideslip angle, β ; and (3) bank angle, ϕ_s . One additional variable, the perturbation in linear velocity magnitude, μ , will be introduced for equation simplicity.

Motivation for the introduction of these additional variables may be found in three areas. First, it must be recognized that the body frame equations of the previous section are extremely useful performance indicators for conventional flight; i.e., for small angles-of-attack along a nearly horizontal flight path*. However, as discussed in Section 2.1, these conditions are not met during the entry flight regime, and thus the body-axis equations are more cumbersome than useful. Second, the guidance requirement of Section 2.3, specifying angle-of-attack and bank angle control, implies that the ultimate objective of any control law will be the maintenance of these particular vehicle states at their commanded values. It thus behooves the control designer to incorporate these angles into a vehicle model, so as to

---

*This is due to the near alignment of the velocity vector with the body x-axis, both approximately in the local horizontal plane. This then allows for the valid use of small angle approximations and concommitant simplifications (see Reference 8 for more details).

better understand their dependence on airframe characteristics. Finally, the vehicle's short-period lateral dynamic response is almost completely specified by the effect sideslip has in inducing coupled aerodynamic roll and yaw torques. An understanding of the sideslip dynamics should thus aid the "inner-loop" or stability augmentation design problem. The remainder of this section will define the stability-axis variables of interest.

The total angle-of-attack, $\tilde{\alpha}$, the total linear velocity, $\tilde{V}$ ($= |\underline{v}|$), and the sideslip angle, $\tilde{\beta}$, are defined by Figure 4-5. Note that this figure is simply a duplication of Figure 4-3, with the addition of the variables $\tilde{\alpha}$ and $\tilde{\beta}$.
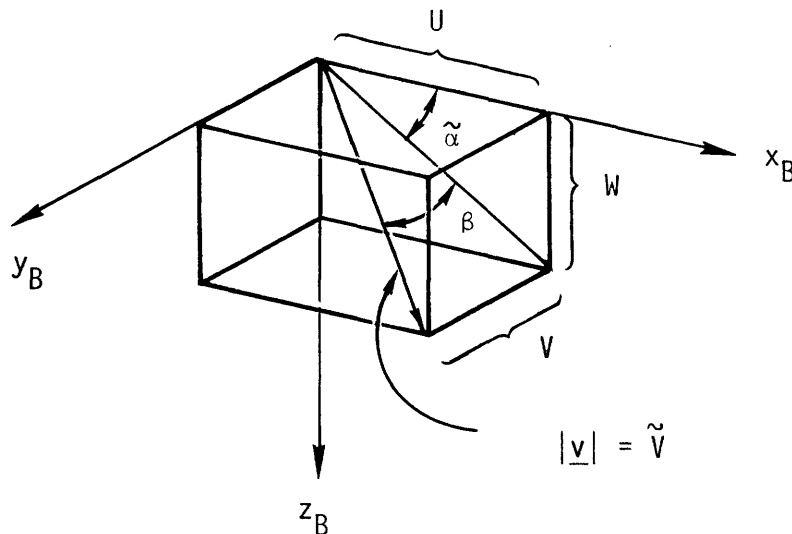
Fig. 4-5: Definition of $\tilde{\alpha}$ and $\tilde{\beta}$

Now, from the figure, it is clear that

$$U = \tilde{V} \cos \tilde{\beta} \cos \tilde{\alpha}$$

$$W = \tilde{V} \cos \tilde{\beta} \sin \tilde{\alpha} \tag{4-21}$$

$$V = \tilde{V} \sin \tilde{\beta}$$

Consistent with the perturbation approach taken in Sections 4.1.2 and 4.1.4, the variables $\tilde{\alpha}$, $\tilde{V}$, and $\tilde{\beta}$ may be expressed as perturbations about nominals, so that

$$\tilde{\alpha} = \alpha_T + \hat{\alpha} \quad ; \quad \tilde{V} = V_T(1 + \mu) \quad ; \quad \tilde{\beta} = \beta \qquad (4\text{-}22)$$

where α_T is the trim angle-of-attack defined by Figure 4-4, and where

$\hat{\alpha} \equiv$ perturbation in angle-of-attack

$V_T \equiv$ total nominal velocity

$\mu \equiv$ perturbation in total velocity (normalized)

$\beta \equiv$ sideslip angle.

Note that it is assumed that the trim sideslip is zero, consistent with symmetric equilibrium flight. The non-zero trim situation (in conjunction with a center-of-gravity displacement from nominal) is treated in Section 5.2. As discussed previously, the linear body rates can be similarly expressed, so that:

$$U = u_o + u \quad ; \quad W = w_o + w \quad ; \quad V = v \qquad (4\text{-}23)$$

Assuming that the perturbing variables are small (so that small angle approximations are valid and perturbation products can be neglected), substitution of (4-22) and (4-23) into (4-21), subtraction of the associated equilibrium equations, and use of (4-15) results in the following relations:

$$\begin{aligned}
\tilde{u} &= \mu\cos\alpha_T - \hat{\alpha}\sin\alpha_T & \text{(a)} & \\
\tilde{w} &= \mu\sin\alpha_T + \hat{\alpha}\cos\alpha_T & \text{(b)} & \qquad (4\text{-}24) \\
\tilde{v} &= \beta & \text{(c)} &
\end{aligned}$$

The above equation set thus relates the perturbations in vehicle velocity ($\tilde{u}$, $\tilde{v}$, $\tilde{w}$) to three of the stability-axis variables ($\hat{\alpha}$, μ, β). The final stability-axis variable, bank attitude (ϕ_s) may be defined as a rotation

of the vehicle about the equilibrium velocity vector. Zero bank is a "wings-level" condition in which the y_B-axis is in the local horizontal plane (and, naturally, the lift vector is pointed "up").[*] Rather than introduce additional reference frames to formally define the bank angle, it is more convenient to consider the bank rate $\dot{\phi}_S$, as a function of the body rates (p, q, r), as shown in Figure 4-6. The bank rate component in the longitudinal plane can be seen to be:

$$\dot{\phi}_S \cos \tilde{\beta} = p \cos \tilde{\alpha} + r \sin \tilde{\alpha} \tag{4-25}$$

Use of (4-22), and the assumption that $\hat{\alpha}$ and β are small, then results in:

$$\dot{\phi}_S = p \cos \alpha_T + r \sin \alpha_T \tag{4-26}$$

Assuming zero initial conditions, use of the Laplace transform then yields:

$$s \phi_S = p \cos \alpha_T + r \sin \alpha_T \tag{4-27}$$
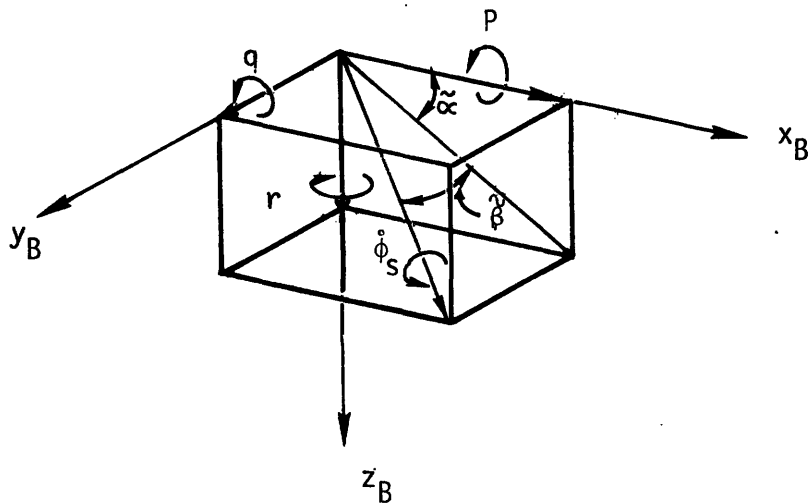
Fig. 4-6: Definition of $\dot{\phi}_S$

---

[*]For a more formal definition of the bank angle, see Section 5.4.1.

With the above type of "rate" definition, it should be noted that the bank angle need not be a small perturbation quantity. This is clearly in conflict with the symmetric flight conditions specified in Section 4.1.3 (where $\phi_0 = 0$) and will be further discussed in Section 7.2.1.8.

To summarize, equations (4-24) and (4-27) relate the body-axis variables $(\tilde{u}, \tilde{v}, \tilde{w}, p, r)$ to the stability-axis variables $(\hat{\alpha}, \mu, \beta, \phi_s)$ through the use of the trim angle-of-attack, α_T. The next section will use these results to transform (4-18) - (4-20), so as to arrive at the equations of motion specifying the vehicle's rotational dynamics, as seen in the stability-axis frame.

4.3 Stability-Axis Rotational Dynamics

The transformation of the body-axis equations of motion of Section 4.1 into equation sets describing the stability-axis rotational dynamics is a fairly straightforward procedure; however, the major objective of this section will be to arrive at a simplified transformed equation set, consistent with the goal of realistic modelling of the vehicle dynamics. Thus, this section will make use of the nominal vehicle aerodynamic, mass, and geometric properties, in conjunction with the anticipated flight envelope, so as to determine the relative importance of various terms in the vehicle model. As will be seen, for the shuttle application, the use of the stability-axis frame is especially appropriate for such numerical approximations.

This section is divided into two subsections: Section 4.3.1 treats the longitudinal dynamics, while Section 4.3.2 covers the lateral dynamics.

4.3.1 Longitudinal Short-Period Dynamics

For convenient reference, it is appropriate to recall the body-axis longitudinal equations of motion derived in Section 4.1, and the transformation set of Section 4.2 relating velocity perturbations to the stability-axis variables:

$$\left[s - \frac{X_u}{m}\right]\tilde{u} - \left[\frac{X_w}{m}\right]\tilde{w} + \left[\left(\sin\alpha_T - \frac{X_q}{mV_T}\right) + \frac{(g/V_T)\cos\theta_o}{s}\right]q = \frac{X_{\delta_e}}{mV_T}\hat{\delta}_e \quad \text{(a)}$$

$$\left[-\frac{Z_u}{m}\right]\tilde{u} + \left[s - \frac{Z_w}{m}\right]\tilde{w} + \left[-\left(\cos\alpha_T + \frac{Z_q}{mV_T}\right) + \frac{(g/V_T)\sin\theta_o}{s}\right]q = \frac{Z_{\delta_e}}{mV_T}\hat{\delta}_e \quad \text{(b)}$$

$$\left[-\frac{V_T M_u}{I_{yy}}\right]\tilde{u} - \left[\frac{V_T M_w}{I_{yy}}\right]\tilde{w} + \left[s - \frac{M_q}{I_{yy}}\right]q = \frac{M_{\delta_e}}{I_{yy}}\hat{\delta}_e + u_y \quad \text{(c)}$$

$$(4\text{-}18)$$

$$\tilde{u} = \mu\cos\alpha_T - \alpha\sin\alpha_T \quad \text{(a)}$$

$$\tilde{w} = \mu\sin\alpha_T + \alpha\cos\alpha_T \quad \text{(b)}$$

$$(4\text{-}24)$$

Two basic equations relating $\hat{\alpha}$ and μ may be obtained in the following manner. First, (4-18a) is multiplied by ($-\sin\alpha_T$) and (4-18b) by ($\cos\alpha_T$) and the results added. Use of (4-24) then results in:

$$s\hat{\alpha} + \frac{1}{m}\left[-X_u\sin^2\alpha_T + (X_w + Z_u)\sin\alpha_T\cos\alpha_T - Z_w\cos^2\alpha_T\right]\hat{\alpha}$$

$$+ \frac{1}{m}\left[X_w\sin^2\alpha_T + (X_u - Z_w)\sin\alpha_T\cos\alpha_T - Z_u\cos^2\alpha_T\right]\mu$$

$$- \left[1 + \frac{1}{mV_T}(Z_q\cos\alpha_T - X_q\sin\alpha_T) + \frac{1}{s}\left(\frac{g}{V_T}\right)(\sin\theta_o\cos\alpha_T - \cos\theta_o\sin\alpha_T)\right]q$$

$$= \frac{1}{mV_T}(Z_{\delta_e}\cos\alpha_T - X_{\delta_e}\sin\alpha_T)\hat{\delta}_e \quad (4\text{-}28)$$

A second relation is obtained by using (4-24) in (4-18c) to obtain:

$$\left(\frac{V_T}{I_{yy}}\right)\left(M_u\sin\alpha_T - M_w\cos\alpha_T\right)\hat{\alpha} - \left(\frac{V_T}{I_{yy}}\right)\left(M_u\cos\alpha_T + M_w\sin\alpha_T\right)\mu + \left(s - \frac{M_q}{I_{yy}}\right)q$$

$$= \frac{M_{\delta_e}}{I_{yy}}\hat{\delta}_e + u_y \quad (4\text{-}29)$$

71

The equation coefficients of the above two equations may be considerably simplified by use of the stability derivative relations presented in Appendix A. After some manipulation, it is found that (4-28) and (4-29) respectively simplify to the following:

$$s\hat{\alpha} + \left(\frac{\bar{q}S}{mV_T}\right)\left(C_D + C_{\mathcal{L}_\alpha}\right)\hat{\alpha} + \left(\frac{\bar{q}S}{mV_T}\right)(2C_{\mathcal{L}})\mu - \left[1 - \left(\frac{\bar{q}Sc}{2mV_T^2}\right)C_{\mathcal{L}_q} + \frac{(g/V_T)\sin\gamma_o}{s}\right]q$$

$$= -\left(\frac{\bar{q}S}{mV_T}\right)\left(C_{\mathcal{L}_{\delta_e}}\cos\alpha_T - C_{D_{\delta_e}}\sin\alpha_T\right)\hat{\delta}_e \qquad (4-30)$$

$$-\left(\frac{\bar{q}Sc}{I_{yy}}\right)C_{M_\alpha}\hat{\alpha} + \left[s - \left(\frac{\bar{q}Sc^2}{2I_{yy}V_T}\right)C_{M_q}\right]q = \left(\frac{\bar{q}Sc}{I_{yy}}\right)C_{M_{\delta_e}}\hat{\delta}_e + u_y \qquad (4-31)$$

where the flight path angle (at zero bank) is introduced as follows:

$$\gamma_o \equiv \theta_o - \alpha_T \qquad (4-32)$$

It is at this point that the numerical properties of the vehicle and its flight envelope may be used to advantage in simplifying the equation development. In particular, Appendix B is devoted to determining the simplifications accruing from comparisons of relative magnitudes of the terms present in the various equations. The detailed assumptions and ground rules are given in the appendix; it suffices to note that the derived inequality relations are specific to the vehicle and flight regime described in Section 2.1 and Reference 2.

As is shown in Appendix B, (4-30) may be solved for the pitch rate q, and then substituted into (4-31) to obtain a single equation in $\hat{\alpha}$ and μ. Further simplification (using term-by-term magnitude comparison) then results in the following dynamic relation (obtained from (B-8)).

$$(s^2 + 2\zeta_\alpha\omega_\alpha s + \omega_\alpha^2)\hat{\alpha} + K_\mu(\tau_\mu s + 1)\mu = K_{\delta_e}(\tau_{\delta_e} s + 1)\hat{\delta}_e + u_y \qquad (4-33)$$

72

where the equation parameters are defined as follows:

$$\omega_\alpha^2 \equiv -\left(\frac{\bar{q}Sc}{I_{yy}}\right)C_{M_\alpha} \tag{a}$$

$$\zeta_\alpha \equiv \frac{1}{2\omega_\alpha}\left(\frac{\bar{q}S}{V_T}\right)\left[\frac{C_D + C_{\mathcal{L}_\alpha}}{m} - \left(\frac{c^2}{2I_{yy}}\right)C_{M_q}\right] \tag{b}$$

$$K_\mu \equiv -\left(\frac{\bar{q}Sc}{mV_T^2}\right)\left(\frac{\bar{q}Sc}{I_{yy}}\right)C_{M_q}C_{\mathcal{L}} \tag{c} \qquad (4\text{-}34)$$

$$\tau_\mu \equiv -\left(\frac{2I_{yy}V_T}{\bar{q}Sc^2}\right)\left(\frac{1}{C_{M_q}}\right) \tag{d}$$

$$K_{\delta_e} \equiv \left(\frac{\bar{q}Sc}{I_{yy}}\right)C_{M_{\delta_e}} \tag{e}$$

$$\tau_{\delta_e} \equiv \left(\frac{I_{yy}}{mcV_T}\right)\left(\frac{C_{D_{\delta_e}}}{C_{M_{\delta_e}}}\sin\alpha_T - \frac{C_{\mathcal{L}_{\delta_e}}}{C_{M_{\delta_e}}}\cos\alpha_T\right) \tag{f}$$

The coupled nature of the longitudinal dynamics should be clear from (4-33). What is important to recognize, however, is that the equation basically specifies the α-dynamics and that the appearance of μ in the equation simply indicates the effect of velocity magnitude perturbations on the α-dynamics through the coupling coefficient K_μ. In fact the coupling is very weak. To see this, note that from (B-9),

$$\left|\left(\frac{\bar{q}Sc}{mV_T^2}\right)C_{M_q}C_{\mathcal{L}}\right| << \left|C_{M_\alpha}\right| \tag{B-9}$$

73

so that use of (4-34a) and (4-34c) results in the following:

$$\left|K_\mu\right| << \left|\omega_\alpha^2\right| \qquad (4-35)$$

With the reasonable assumption that

$$|\mu| \lesssim |\hat{\alpha}| \qquad (4-36)$$

then (4-33) may be further simplified. A second point to note is that perturbations in velocity magnitude are associated with the "phugoid" mode (see Reference 11) which characteristically has a natural frequency orders of magnitude smaller than that of the short-period α-dynamics[*]. Thus, taking advantage of this frequency separation, the rate of the velocity magnitude perturbation, $\dot{\mu}$, can be approximated as zero:

$$\dot{\mu} = 0 \qquad (4-37)$$

Use of (4-35), (4-36), and (4-37) in (4-33) then yields the desired simplified equation approximating the short-period longitudinal dynamics:

$$(s^2 + 2\zeta_\alpha \omega_\alpha s + \omega_\alpha^2)\hat{\alpha} = K_{\delta_e}(\tau_{\delta_e} s + 1)\hat{\delta}_e + u_y \qquad (4-38)$$

where the coefficients are defined by (4-34).

4.3.2 Lateral Short-Period Dynamics

This section derives the simplified Laplace transformed equations which relate the short-period dynamics of sideslip and bank to the control inputs of aileron, rudder, and roll- and yaw-axis ACPS jets. Section 4.3.2.1 considers the sideslip dynamics, while section 4.3.2.2 treats bank. Finally Section 4.3.2.3 presents further simplifications to the bank-sideslip coupled dynamics.

---

[*]For comparative purposes, it is worthwhile to review trajectory studies of the entry mission phase. For example, in Reference 23 it may be seen that the phugoid oscillation period is of the order of 100 seconds, considerably larger than the time periods of interest here.

74

4.3.2.1 Sideslip Dynamics

As was done in the previous section, the body-axis lateral equations of motion may be recalled from Section 4.1, and the transformation relations recalled from 4.2[*]:

$$\left[s - \frac{Y_v}{m}\right]\tilde{v} - \left[\left(\sin\alpha_T + \frac{Y_p}{mV_T}\right) + \frac{(g/V_T)\cos\theta_o}{s}\right]p + \left[\left(\cos\alpha_T - \frac{Y_r}{mV_T}\right) - \frac{(g/V_T)\sin\theta_o}{s}\right]r = \sigma_1 \quad \text{(a)}$$

$$-\left[\frac{V_T L_v}{I_{xx}}\right]\tilde{v} + \left[s - \frac{L_p}{I_{xx}}\right]p - \left[\frac{I_{xz}}{I_{xx}}s + \frac{L_r}{I_{xx}}\right]r = \sigma_2 \quad \text{(b)}$$

$$-\left[\frac{V_T N_v}{I_{zz}}\right]\tilde{v} - \left[\frac{I_{xz}}{I_{zz}}s + \frac{N_p}{I_{zz}}\right]p + \left[s - \frac{N_r}{I_{zz}}\right]r = \sigma_3 \quad \text{(c)}$$

$$\text{(4-19)}$$

$$\tilde{v} = \beta \qquad\qquad \text{(4-24c)}$$

$$s\phi_s = p\cos\alpha_T + r\sin\alpha_T \qquad\qquad \text{(4-27)}$$

In a manner similar to the elimination of the pitch rate in the previous section, the first objective here will be to solve for the body rates p and r, so as to be able to eliminate them later in the development. As shown in Appendix B, (4-19a) and (4-27) may be solved simultaneously for p and r, and the results simplified (by the use of appropriate numerical approximations) to yield:

$$p = \left[s - \frac{Y_v}{m}\right](\beta\sin\alpha_T) + \left[\left(\cos\alpha_T - \frac{Y_r}{mV_T}\right) - \frac{(g/V_T)\sin\theta_o}{s}\right]s\phi_s - \sigma_1\sin\alpha_T \quad \text{(a)}$$

$$r = -\left[s - \frac{Y_v}{m}\right](\beta\cos\alpha_T) + \left[\left(\sin\alpha_T + \frac{Y_p}{mV_T}\right) + \frac{(g/V_T)\cos\theta_o}{s}\right]s\phi_s + \sigma_1\cos\alpha_T \quad \text{(b)}$$

$$\text{(4-39)}$$

---

[*]Recall that the right-hand side of (4-19) is given by (4-20).

With (p, r) thus defined, the "sideslip equation" may be obtained in three steps. First, the resolution of the lateral rotation rates about the sideslip rotation axis is accomplished by multiplying (4-19b) by $(\sin\alpha_T)$ and (4-19c) by $(-\cos\alpha_T)$ and adding, making use of (4-24c). Second, the body rates (p, r) are eliminated by application of (4-39). Finally, the equation is simplified, again by taking advantage of the numerical properties of the vehicle and trajectory. The derivation details are given in Appendix B; given below is the resultant equation approximating the short-period sideslip dynamics:

$$(s^2 + 2\zeta_\beta \omega_\beta s + \omega_\beta^2)\beta + (b_1 s^2 + b_2 s + b_3)\phi_s = \hat{K}_\beta(\lambda'_{\delta_r} s + \lambda_{\delta_r})\hat{\delta}_r + \hat{K}_\beta(\lambda'_{\delta_a} s + \lambda_{\delta_a})\hat{\delta}_a$$

$$+ u_x \sin\alpha_T - u_z \cos\alpha_T \qquad (4\text{-}40)$$

where the equation coefficients are summarized as follows:

$$\omega_\beta^2 \equiv \left(\frac{\bar{q}Sb}{I_{zz}}\right)C'_{n_\beta} \qquad\qquad (a)$$

$$\zeta_\beta \equiv -\frac{1}{2\omega_\beta}\left(\frac{\bar{q}S}{mV_T}\right)\left[C_{y_\beta} + \left(\frac{mb^2}{2I_{zz}}\right)C_{1_\beta}\right] \qquad\qquad (b)$$

$$b_1 \equiv \left(\frac{I_{xz}}{I_{zz}}\cos^2\alpha_T - \frac{I_{xz}}{I_{zz}}\sin^2\alpha_T\right) - \left(\frac{\bar{q}Sb}{2mV_T^2}\right)\left(C_{y_p}\cos\alpha_T + C_{y_r}\sin\alpha_T\right) \qquad (c)$$

$$b_2 \equiv -\left(\frac{g}{V_T}\right) + \left(\frac{\bar{q}Sb^2}{2I_{zz}V_T}\right)C_{1_\phi} \qquad\qquad (d)$$

$$b_3 \equiv \left(\frac{g}{V_T}\right)\left(\frac{\bar{q}Sb^2}{2I_{zz}V_T}\right)C_{1_\beta} \qquad\qquad (e)$$

$$\hat{K}_\beta \equiv \left(\frac{\bar{q}Sb}{I_{zz}}\right) \qquad\qquad (f)$$

$$\lambda'_{\delta_r} \equiv \left(\frac{I_{zz}}{mbV_T}\right)C_{y_{\delta_r}} \quad ; \quad \lambda_{\delta_r} \equiv -C'_{n_{\delta_r}} \qquad\qquad (g)$$

$$(4\text{-}41)$$

$$\lambda'_{\delta_a} \equiv \left(\frac{I_{zz}}{mbV_T}\right) C_{y_{\delta_a}} \qquad ; \qquad \lambda_{\delta_a} \equiv - C'_{n_{\delta_a}} \qquad \text{(4-41h)}$$

where the intermediate variables C_{1_ϕ} and C_{1_β} are defined by:

$$C_{1_\phi} \equiv C'_{n_p} \cos \alpha_T + C'_{n_r} \sin \alpha_T \qquad \text{(a)}$$

$$\text{(4-42)}$$

$$C_{1_\beta} \equiv C'_{n_r} \cos \alpha_T - C'_{n_p} \sin \alpha_T \qquad \text{(b)}$$

In the coefficient definitions of (4-41) and (4-42), it should be noted that "dynamic" derivatives have been introduced into the model description. The general form for their definition is:

$$C'_{n_x} \equiv C_{n_x} \cos \alpha_T - \frac{I_{zz}}{I_{xx}} C_{\ell_x} \sin \alpha_T \qquad \text{(4-43)}$$

where x is replaced by β, p, r, δ_a, or δ_r as appropriate. The five dynamic derivatives defined by (4-43) are all stability-axis yaw derivatives, or more descriptively, sideslip derivatives, since they specify the influence of both vehicle state (β, p, and r) and control surface deflections ($\hat{\delta}_r$ and $\hat{\delta}_a$) on sideslip magnitude. This discussion is continued in the next section.

The obvious sideslip-bank coupling in (4-40) is discussed in Section 4.3.2.3, at which time further simplifications will be made to the sideslip dynamic model.

4.3.2.2 Bank Dynamics

In a manner similar to that of the previous section, the "bank equation" may be obtained in three steps. First, the resolution of the lateral rotation rates about the bank rotation axis (velocity vector) is accomplished by multiplying (4-19b) by $(\cos \alpha_T)$ and (4-19c) by $(\sin \alpha_T)$ and adding, again making use of (4-24c). Second, as before,

the body rates (p, r) are eliminated by using (4-39). Finally, the equation is simplified through the use of numerical approximations. The derivation details are again given in Appendix B; given below is the resultant equation approximating the short-period bank dynamics:

$$(d_1 s^2 + d_2 s + d_3)\beta + (s^2 + e_2 s + e_3)\phi_s = \hat{K}_\phi(\nu'_{\delta_r} s + \nu_{\delta_r})\hat{\delta}_r + \hat{K}_\phi(\nu'_{\delta_a} s + \nu_{\delta_a})\hat{\delta}_a$$

$$+ u_x \cos\alpha_T + u_z \sin\alpha_T \qquad (4\text{-}44)$$

where the equation coefficients are summarized as follows:

$$d_1 \equiv \left(\frac{I_{xz}}{I_{xx}}\cos^2\alpha_T - \frac{I_{xz}}{I_{zz}}\sin^2\alpha_T\right) \qquad (a)$$

$$d_2 \equiv -\left(\frac{\bar{q}Sb^2}{2I_{xx}V_T}\right)C_{2_\beta} \qquad (b)$$

$$d_3 \equiv -\left(\frac{\bar{q}Sb}{I_{xx}}\right)C'_{\ell_\beta} \qquad (c)$$

$$e_2 \equiv -\left(\frac{g}{V_T}\right)\left[\sin\gamma_0 - \left(\frac{I_{xz}}{I_{zz}}\sin\alpha_T\sin\theta_0 - \frac{I_{xz}}{I_{xx}}\cos\alpha_T\cos\theta_0\right)\right] - \left(\frac{\bar{q}Sb^2}{2I_{xx}V_T}\right)C_{2_\phi} \qquad (d)$$

$$e_3 \equiv -\left(\frac{g}{V_T}\right)\left(\frac{\bar{q}Sb^2}{2I_{xx}V_T}\right)C_{2_\beta} \qquad (e)$$

$$\hat{K}_\phi \equiv \left(\frac{\bar{q}Sb}{I_{xx}}\right) \qquad (f)$$

$$\nu'_{\delta_r} \equiv \left(\frac{I_{xz}}{mbV_T}\right)\left(\cos^2\alpha_T - \frac{I_{xx}}{I_{zz}}\sin^2\alpha_T\right)C_{y_{\delta_r}} \quad ; \quad \nu_{\delta_r} \equiv C'_{\ell_{\delta_r}} \qquad (g)$$

$$\nu'_{\delta_a} \equiv \left(\frac{I_{xz}}{mbV_T}\right)\left(\cos^2\alpha_T - \frac{I_{xx}}{I_{zz}}\sin^2\alpha_T\right)C_{y_{\delta_a}} \quad ; \quad \nu_{\delta_a} \equiv C'_{\ell_{\delta_a}} \qquad (h)$$

$$(4\text{-}45)$$

where the intermediate variables C_{2_ϕ} and C_{2_β} are defined by:

$$C_{2_\phi} \equiv C'_{\ell_p} \cos\alpha_T + C'_{\ell_r} \sin\alpha_T \qquad \text{(a)}$$

$$\text{(4-46)}$$

$$C_{2_\beta} \equiv C'_{\ell_r} \cos\alpha_T - C'_{\ell_p} \sin\alpha_T \qquad \text{(b)}$$

As before, the introduction of dynamic derivatives in (4-45) and (4-46) facilitates a more compact model description. The general form for their definition is:

$$C'_{\ell_x} \equiv C_{\ell_x} \cos\alpha_T + \frac{I_{xx}}{I_{zz}} C_{n_x} \sin\alpha_T \qquad \text{(4-47)}$$

where, as before, x is replaced by β, p, r, δ_a, or δ_r as appropriate. The derivatives specified by (4-47) are stability-axis roll derivatives, or, more descriptively, bank derivatives. Thus, the above equation and (4-43) define the lateral dynamic derivative set, and together provide a compact description of the vehicle's lateral aerodynamic and inertial characteristics.

The sideslip-bank coupling evident in (4-44) is discussed in the next section, and further simplifications are made to the bank equation.

4.3.2.3 Sideslip-Bank Short-Period Dynamics

The objective of this section is to provide further simplifications to the approximate lateral equations of (4-40) and (4-44), and, as a consequence, provide the motivation for their original labelling as "sideslip" and "bank" equations, respectively. For convenient reference, the equations are repeated below:

$$(s^2 + 2\zeta_\beta s + \omega_\beta^2)\beta + (b_1 s^2 + b_2 s + b_3)\phi_s = \hat{K}_\beta(\lambda'_{\delta_r} s + \lambda_{\delta_r})\hat{\delta}_r + \hat{K}_\beta(\lambda'_{\delta_a} s + \lambda_{\delta_a})\hat{\delta}_a$$

$$+ u_x \sin\alpha_T - u_z \cos\alpha_T \qquad \text{(4-40)}$$

79

$$(d_1 s^2 + d_2 s + d_3)\beta + (s^2 + e_2 s + e_3)\phi_s = \hat{K}_\phi(\nu'_{\delta_r} s + \nu_{\delta_r})\hat{\delta}_r + \hat{K}_\phi(\nu'_{\delta_a} s + \nu_{\delta_a})\hat{\delta}_a$$

$$+ u_x \cos\alpha_T + u_z \sin\alpha_T \qquad (4\text{-}44)$$

As the equations stand, the only obvious motivation for the sideslip-bank nomenclature choice lies in the resolution of the ACPS accelerations along the respective sideslip and bank rotation axes. This section will make the distinction clearer by further simplification of the equations, particularly in the dynamic cross-coupling terms.

The coefficients b_1, b_2, and b_3 may be regarded as coupling terms in (4-40), indicating the effect of bank acceleration, rate, and attitude (respectively) on the second-order β-dynamics. From Appendix B, it may be noted that:

$$|b_1| \ll 1 \qquad (B\text{-}59)$$

$$10^2 |b_3| \ll |\omega_\beta^2| \qquad (B\text{-}60)$$

Now, if it is assumed that the control system maintains a small sideslip attitude in comparison with the nominal bank attitude, and further, that the vehicle's accelerations in both bank and sideslip are of the same order of magnitude,[*] then

$$|\beta| \sim 10^{-2} |\phi_s| \qquad \text{(a)}$$
$$\qquad\qquad\qquad\qquad\qquad (4\text{-}48)$$
$$|\ddot{\beta}| \sim |\ddot{\phi}_s| \qquad \text{(b)}$$

Thus, the bank and bank acceleration terms may be dropped from (4-40). A further simplification arises by assuming that the surface deflection and rate magnitudes are comparable, so that

$$|\dot{\hat{\delta}}_r| \sim |\hat{\delta}_r| \qquad \text{(c)}$$
$$\qquad\qquad\qquad\qquad\qquad (4\text{-}48)$$
$$|\dot{\hat{\delta}}_a| \sim |\hat{\delta}_a| \qquad \text{(d)}$$

---

[*]The validity of these assumptions, summarized in (4-48), is demonstrated in Section 7.2.1.

With the following relations from Appendix B relating the surface coefficients,

$$|\lambda'_{\delta_r}| << |\lambda_{\delta_r}| \quad ; \quad |\lambda'_{\delta_a}| << |\lambda_{\delta_a}| \qquad \text{(B-61)}$$

then both surface rate terms may also be dropped from (4-40). The sideslip dynamics may thus be obtained in simplified form from (4-40), in the following approximated form:

$$(s^2 + 2\zeta_\beta \omega_\beta s + \omega_\beta^2)\beta + K_\phi s\phi_s = K_{\beta_{\delta_r}}\hat{\delta}_r + K_{\beta_{\delta_a}}\hat{\delta}_a + u_x \sin\alpha_T - u_z \cos\alpha_T \qquad \text{(4-49)}$$

where, from (4-41), the model parameters are given by:

$$\omega_\beta^2 \equiv \left(\frac{\bar{q}Sb}{I_{zz}}\right)C'_{n_\beta} \qquad \text{(a)}$$

$$\zeta_\beta \equiv -\frac{1}{2\omega_\beta}\left(\frac{\bar{q}S}{mV_T}\right)\left[C_{y_\beta} + \left(\frac{mb^2}{2I_{zz}}\right)C_{1_\beta}\right] \qquad \text{(b)}$$

$$K_\phi \equiv -\left(\frac{g}{V_T}\right) + \left(\frac{\bar{q}Sb^2}{2I_{zz}V_T}\right)C_{1_\phi} \qquad \text{(c)} \qquad \text{(4-50)}$$

$$K_{\beta_{\delta_r}} \equiv -\left(\frac{\bar{q}Sb}{I_{zz}}\right)C'_{n_{\delta_r}} \qquad \text{(d)}$$

$$K_{\beta_{\delta_a}} \equiv -\left(\frac{\bar{q}Sb}{I_{zz}}\right)C'_{n_{\delta_a}} \qquad \text{(e)}$$

An entirely analogous procedure may be used to simplify (4-44). In this case, d_1, d_2, and d_3 may be regarded as coupling terms indicating the effect of sideslip acceleration, rate, and attitude (respectively) on the second-order ϕ_s-dynamics. From Appendix B, it is shown that:

$$|d_1| << 1 \qquad \text{(B-62)}$$

$$10^2|e_3| << |d_3| \qquad \text{(B-63)}$$

so that use of (4-48a) and (4-48b) allows for the sideslip acceleration and bank attitude terms to be dropped from (4-44). An additional simplification may be made by assuming sideslip and sideslip rate to be of the same order of magnitude:

$$|\dot{\beta}| \sim |\beta| \qquad \text{(4-48e)}$$

With the following result from Appendix B,

$$|d_2| \ll |d_3| \qquad \text{(B-64)}$$

then the sideslip rate term may also be dropped from (4-48). Finally, with the specifications on surface deflections and rate magnitudes of (4-48c) and (4-48d), and with the following relations shown in Appendix B,

$$|\nu'_{\delta_r}| \ll |\nu_{\delta_r}| \quad ; \quad |\nu'_{\delta_a}| \ll |\nu_{\delta_a}| \qquad \text{(B-65)}$$

then both surface rate terms may also be dropped from (4-44). The bank dynamics may thus be obtained in simplified form from (4-44), approximated in the following manner:

$$K_\beta \beta + (s + 1/\tau_\phi) s \phi_s = K_{\phi_{\delta_r}} \hat{\delta}_r + K_{\phi_{\delta_a}} \hat{\delta}_a + u_x \cos\alpha_T + u_z \sin\alpha_T \qquad \text{(4-51)}$$

where, from (4-45), the model parameters are given by:

$$K_\beta \equiv - \left(\frac{\bar{q}Sb}{I_{xx}}\right) C'_{\ell_\beta} \qquad \text{(a)}$$

$$\frac{1}{\tau_R} \equiv - \left(\frac{g}{V_T}\right)\left[\sin\gamma_0 - \left(\frac{I_{xz}}{I_{zz}}\sin\alpha_T \sin\theta_0 - \frac{I_{xz}}{I_{xx}}\cos\alpha_T \cos\theta_0\right)\right] - \left(\frac{\bar{q}Sb^2}{2I_{xx}V_T}\right)C_{2_\phi} \qquad \text{(b)}$$

$$\text{(4-52)}$$

$$K_{\phi_{\delta_r}} \equiv \left(\frac{\bar{q}Sb}{I_{xx}}\right) C'_{\ell_{\delta_r}} \qquad \text{(c)}$$

$$K_{\phi_{\delta_a}} \equiv \left(\frac{\bar{q}Sb}{I_{xx}}\right) C'_{\ell_{\delta_a}} \qquad \text{(d)}$$

This then completes the derivation of the simplified stability-axis vehicle model of the lateral dynamics. It should be noted that any large deviation from the assumptions made on vehicle state, as expressed in (4-48), may invalidate the dynamic model specified by (4-49) and (4-51). The characteristics of this model are discussed in the next section.

4.4 Simplified Model Summary

At this point it is worthwhile to summarize the results of the preceeding section, and, in particular, briefly describe some of the important qualitative aspects of the simplified model which has been derived. As will be shown, these features greatly aid in understanding the basic rotational dynamics of the vehicle, and, perhaps more germanely, provide a solid basis for rational control law synthesis.

For convenient reference, the one longitudinal and two lateral equations of motion comprising the simplified vehicle model are recalled below:

$$(s^2 + 2\zeta_\alpha \omega_\alpha s + \omega_\alpha^2)\hat{\alpha} = K_{\delta_e}(\tau_{\delta_e} s + 1)\hat{\delta}_e + u_y \tag{4-38}$$

$$(s^2 + 2\zeta_\beta \omega_\beta s + \omega_\beta^2)\beta + K_\phi s\phi_s = K_{\beta_{\delta_r}}\hat{\delta}_r + K_{\beta_{\delta_a}}\hat{\delta}_a + u_x \sin\alpha_T - u_z \cos\alpha_T \tag{4-49}$$

$$K_\beta \beta + (s + 1/\tau_\phi)s\phi_s = K_{\phi_{\delta_r}}\hat{\delta}_r + K_{\phi_{\delta_a}}\hat{\delta}_a + u_x \cos\alpha_T + u_z \sin\alpha_T \tag{4-51}$$

The model parameters, in this case the equation coefficients, are defined by (4-34), (4-50), and (4-52) respectively, and, as mentioned previously, are treated as quasi-static variables. This fictitious time-invariance of the coefficients has been carried throughout the model development: from the initial use of the equilibrium flight condition introduced in the equation development for the body-axis rates, to the extensive simplifications and approximations of the

previous section. The simplified model is thus a "snap-shot" of the rotational dynamics at a particular flight condition; alternatively, it may be viewed as a set of differential equations whose coefficients are "slowly" varying with time. In either case, it is important to gain some insight as to the numerical values involved, their ranges, and their rates of change.

Shown in Figures 4-7 through 4-20 are velocity histories of the model parameters, generated from the data of a simulated entry. The calculation of the model parameter values follows directly from the appropriate defining equations of the previous section, in conjunction with the required vehicle and flight condition trajectory parameter values. Example histories of this latter set of trajectory parameters (e.g., $\bar{q}$, V_T, etc.) are given in Appendix C, and clearly may be used in a model parameter calculation effort. For computational convenience, however, the model parameters were calculated from a simulated entry used to test system operation and described in Section 7.2.3. For reference, histories of the vehicle's altitude, velocity, dynamic pressure, Mach number, and trim angle-of-attack are given in Figures 7-34a through d. The overall flight envelope spanned by the parameter histories is as described previously, in Section 2.1. It suffices to note that the model parameter histories shown below are typical of previous vehicle configurations and entry profiles, and it is anticipated that future changes in configuration and/or mission envelope will not substantially alter the conclusions to be made here.

4.4.1 Longitudinal Dynamics

Several points regarding the longitudinal dynamics may be noted from the parameter histories of Figures 4-7 through 4-10. First, as should be obvious from the form of the parameter definitions of (4-34), during a considerable initial portion of the
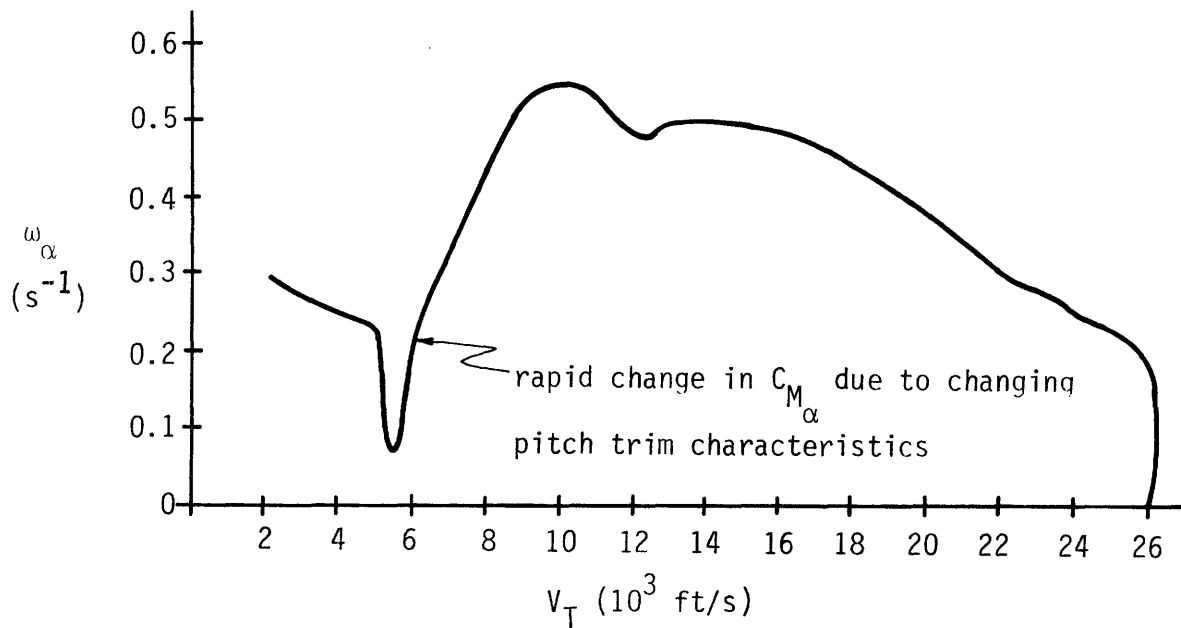
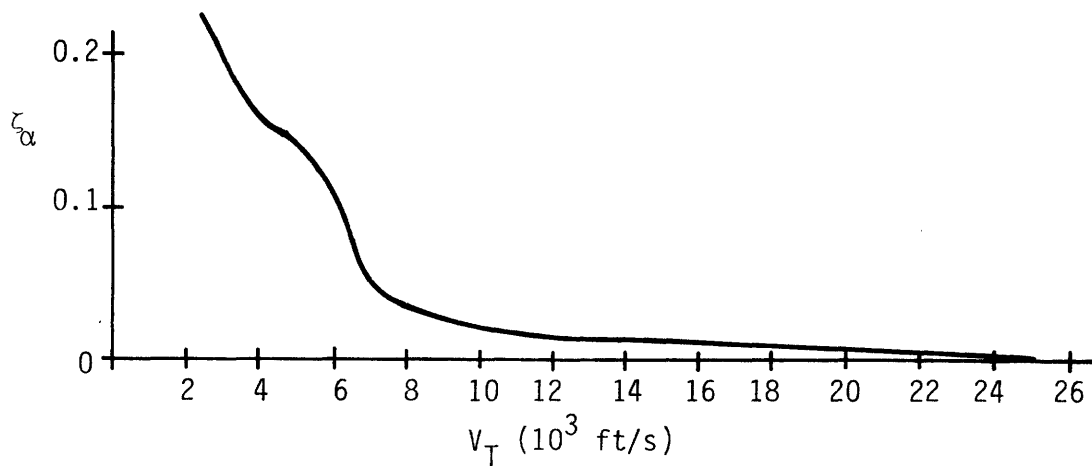Figure 4-7. Natural Frequency in Pitch.
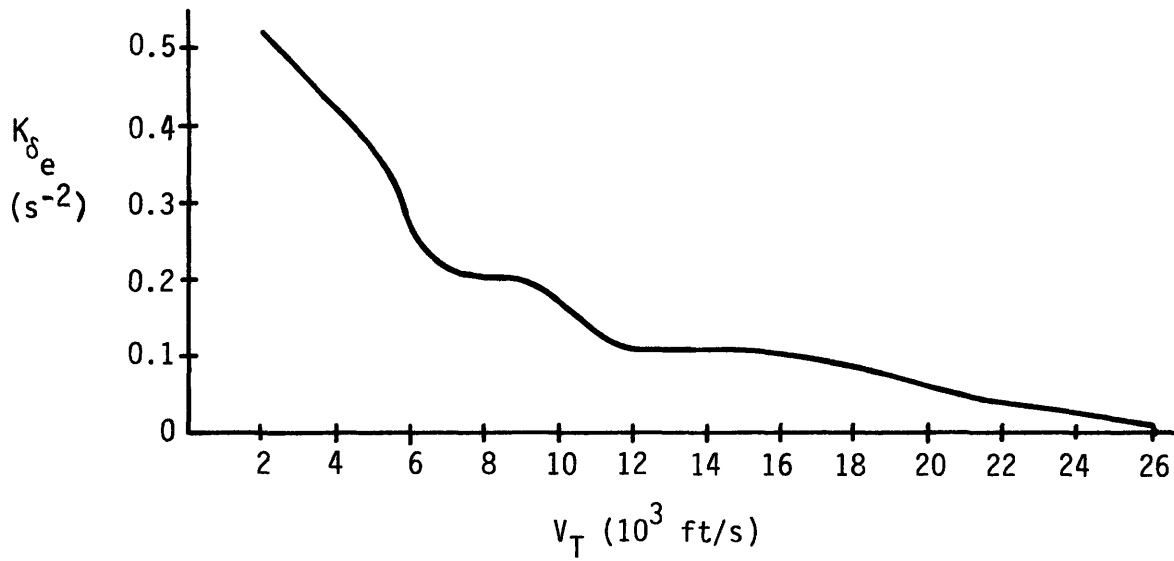

Figure 4-8. Damping Ratio in Pitch.

Figure 4-9. Elevator Effectiveness in Pitch.

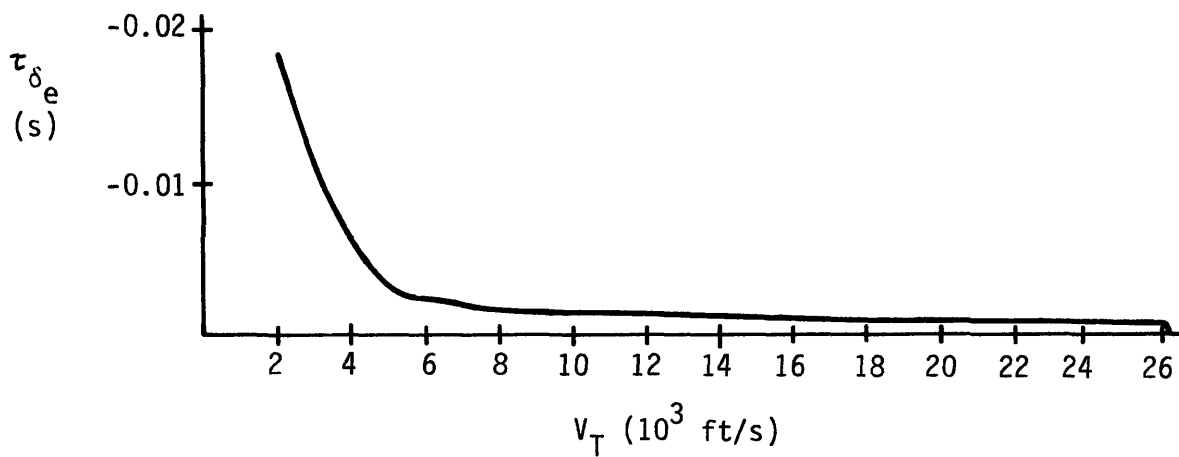
Figure 4-10. Elevator Time Constant.

entry, the vehicle has effectively no aerodynamic properties (i.e.,
the coefficients are insignificantly small), and thus can be viewed
(for control purposes) as a simple mass with specified inertial
properties. This of course follows from the dynamic pressure
dependence of the parameters shown in (4-34), and the typical
dynamic pressure history of Figure C-3, of Appendix C. The
implications for control are similarly obvious: an all-ACPS
attitude control loop must be used, similar to what would be expected
for rotational control while in orbit.

As the vehicle enters an environment more strongly influenced
by aerodynamic effects, the parameter histories take on more
significance. In particular, Figures 4-7 and 4-9 illustrate the
relatively large variations in the natural frequency, ω_α , and
elevator effectiveness, K_{δ_e} , encountered during the entry. Both
parameters exhibit better than an order-of-magnitude increase
over the velocity range considered, while the natural frequency
also exhibits a similar reduction in magnitude late in the entry,
due to variations in pitch trim characteristics (Figure 4-7).
Perhaps more fundamental to the understanding of the basic vehicle
dynamics is the behavior of the damping ratio, ζ_α , and elevator
time constant, τ_{δ_e} , illustrated in Figures 4-8 and 4-10. It is
seen that the damping ratio has a maximum value of about 0.2,
clearly reflecting the low damping available from the locked surface
airframe. This situation is graphically illustrated in the Laplace
s-plane pole locus of Figure 4-11, which displays the travel of the
(upper half-plane) pole defined by the (ζ_α , ω_α) pair; note that the
negative real axis has been expanded by a factor of 10, because
of the small ζ_α values encountered. Figure 4-11 also shows the
travel of the longitudinal transfer function zero (defined by $1/\tau_{\delta_e}$),
along the positive real axis and toward the origin as the entry
progresses. The large distance from the origin should be clear
by recognizing that the positive real axis has been compressed

[NOTE: DIFFERENT SCALES FOR EACH AXIS]

$$\frac{\hat{\alpha}(s)}{\hat{\delta}_e(s)} = \frac{K\delta_e(\tau_{\delta e}s + 1)}{s^2 + 2\zeta_\alpha \omega_\alpha s + \omega_\alpha^2}$$
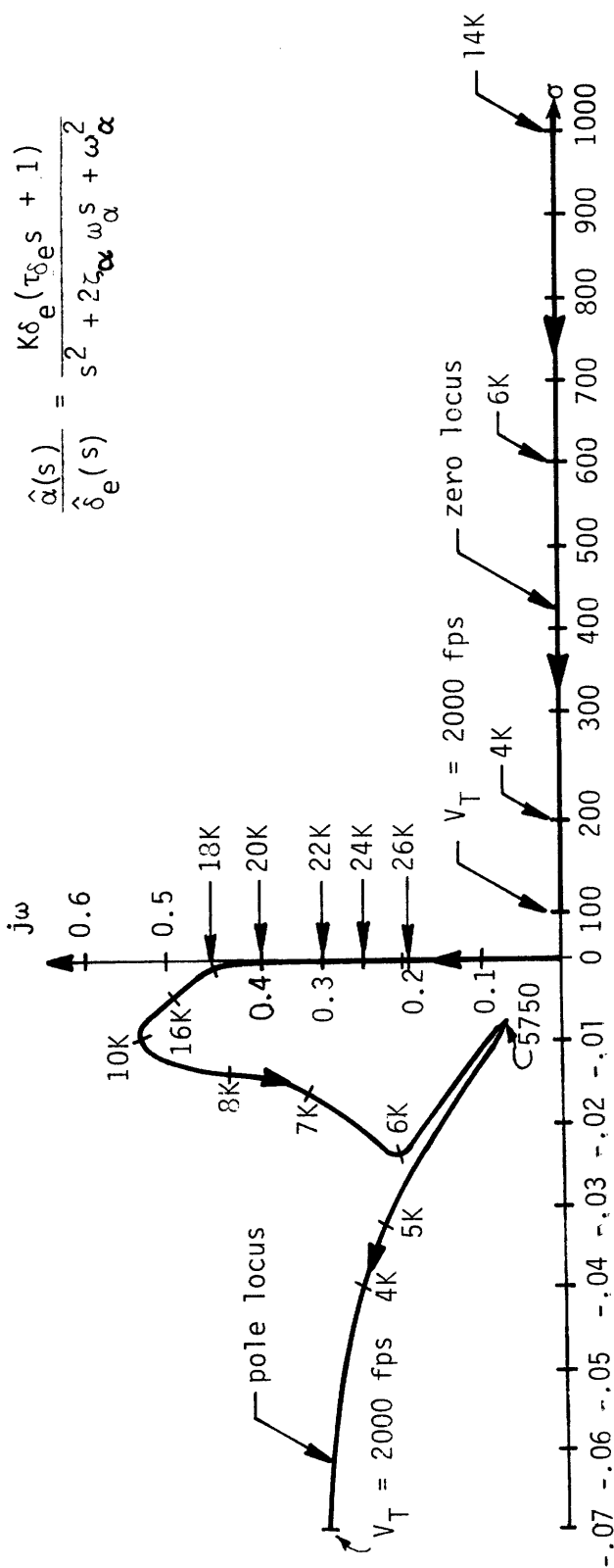
Figure 4-11. Open-Loop Longitudinal Pole-Zero Loci.

88

by a factor of 10,000 (in comparison to the negative axis). The
fact that this zero is so far from the origin is of course due to the
small magnitude of τ_{δ_e} (see Figure 4-10), with a maximum value
of less than 0.02 seconds. Thus, with a realistic magnitude limit
on the elevator deflection rate (see, for example, Section 2.2.2),
this term will contribute little to the overall pitch acceleration.
Both this "fast" elevator-associated time-constant and the inherent
low damping of angle-of-attack deviations thus strongly support a
simple undamped oscillator model of the longitudinal dynamics in
the "aerodynamic" flight regime. At the very least, they imply
that the fundamental dynamics are oscillatory; the implications
for elevator control law synthesis will be made clear in the next
chapter.

4.4.2 Lateral Dynamics

Analogous, although somewhat less obvious, observations
may be made for the lateral dynamics, by referring to the parameter
histories shown in Figures 4-12 through 4-20. Naturally, the
aerodynamic effects are minimal during the initial portion of the
entry, as evidenced by the essentially null values for the model
parameters. Deep into the atmosphere, however, the relative
magnitudes of the parameters become more significant. In
particular, it may be noted that the sideslip damping ratio, ζ_β,
shown in Figure 4-13, never exceeds 0.05, so that similar to the
case of angle-of-attack mistrims, a sideslip rate (the $\dot{\beta}$ term in
(4-49)) contributes effectively nothing to damping sideslip
oscillations. In addition, the effect of bank rate on the sideslip
dynamics is also negligible, as evidenced by the history of the
bank-into-sideslip coupling term K_ϕ, shown in Figure 4-15.
Specifically, with a maximum magnitude of less than 0.003 sec^{-1}
this coupling term provides essentially no acceleration in the
sideslip channel at low bank rates ($\lesssim 1°/\text{sec}$). At high maneuver
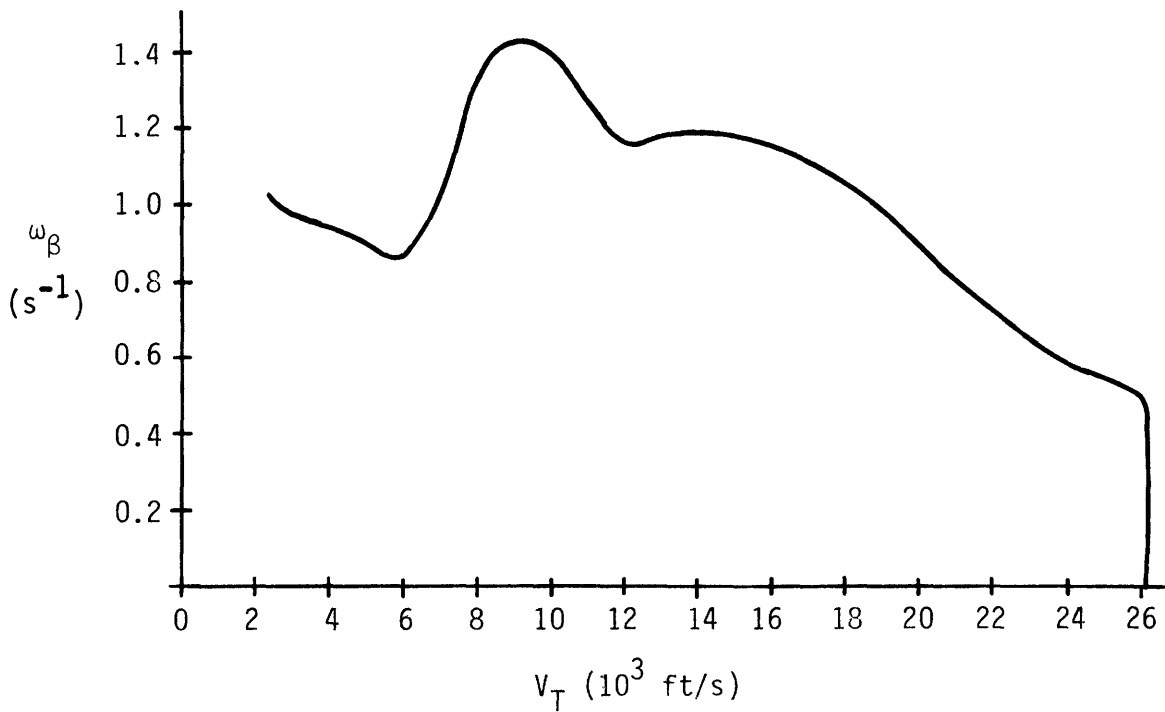
Figure 4-12.   Natural Frequency in Sideslip.

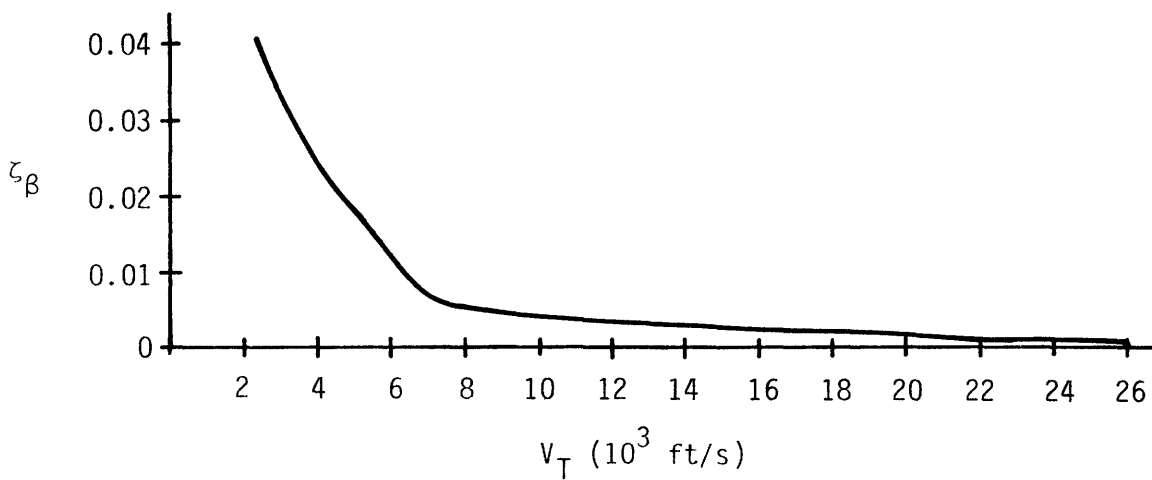Figure 4-13.   Damping Ratio in Sideslip.

90
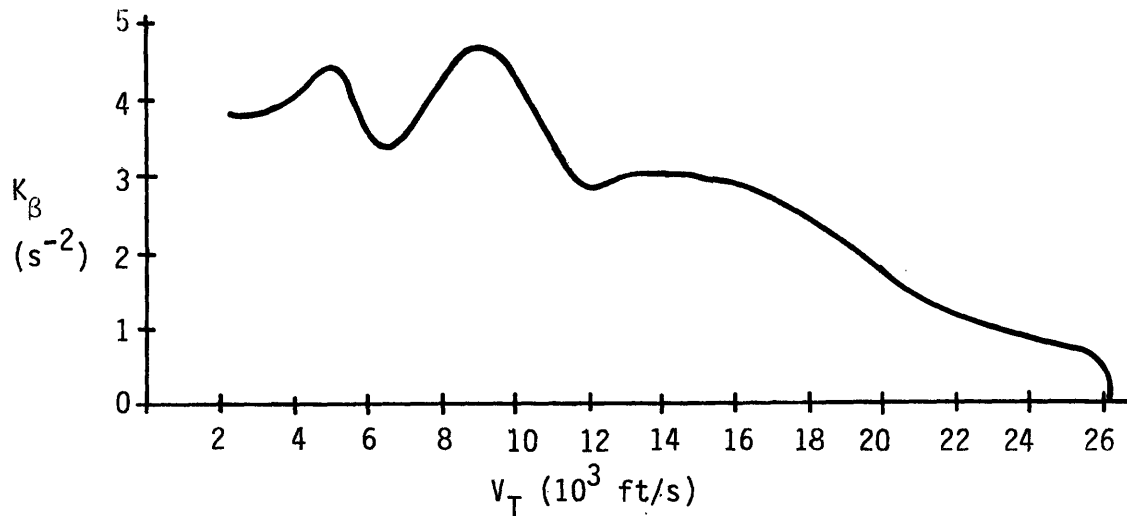
Figure 4-14. Sideslip-into-Bank Coupling Coefficient.
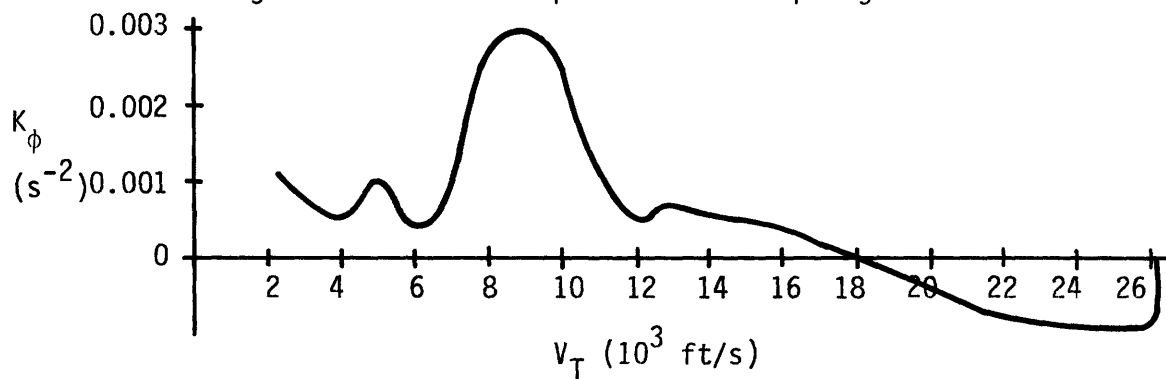
Figure 4-15. Bank-into-Sideslip Coupling Coefficient.
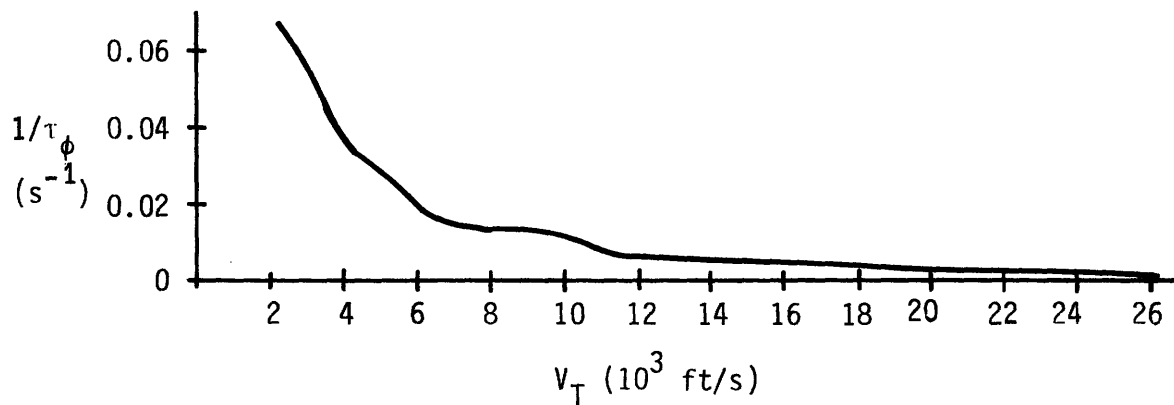
Figure 4-16. Bank Time Constant (Reciprocal).
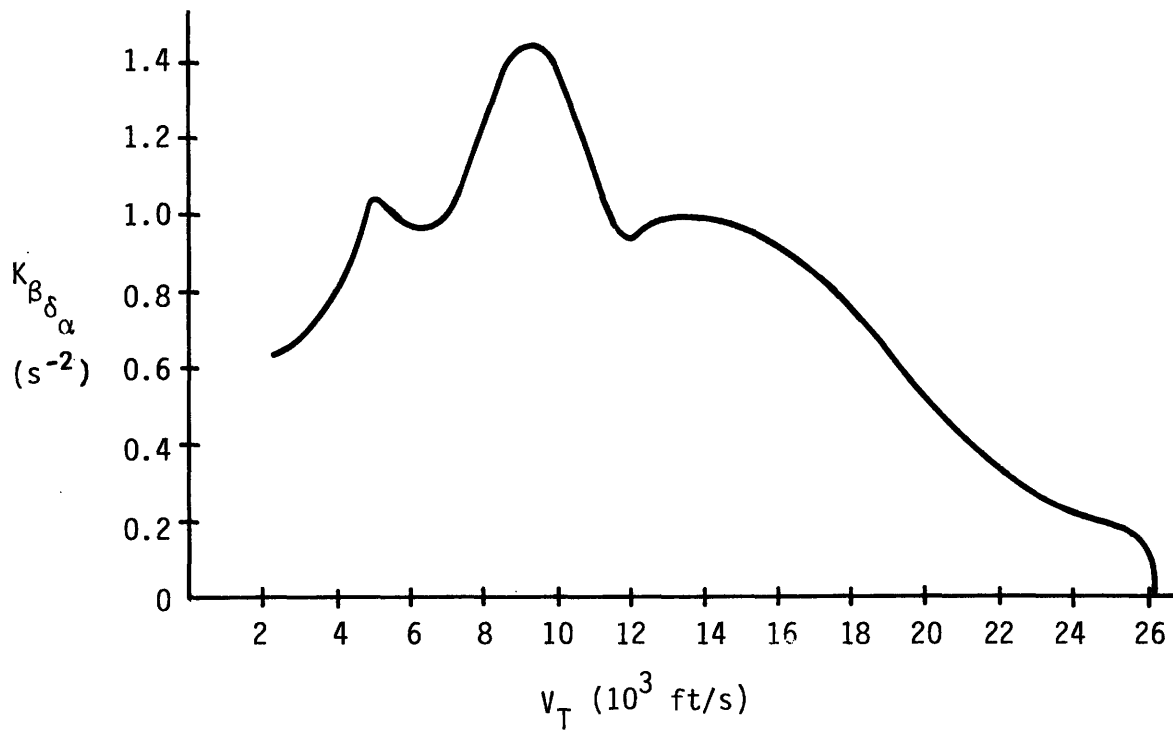
Figure 4-17. Aileron Effectiveness in Sideslip.
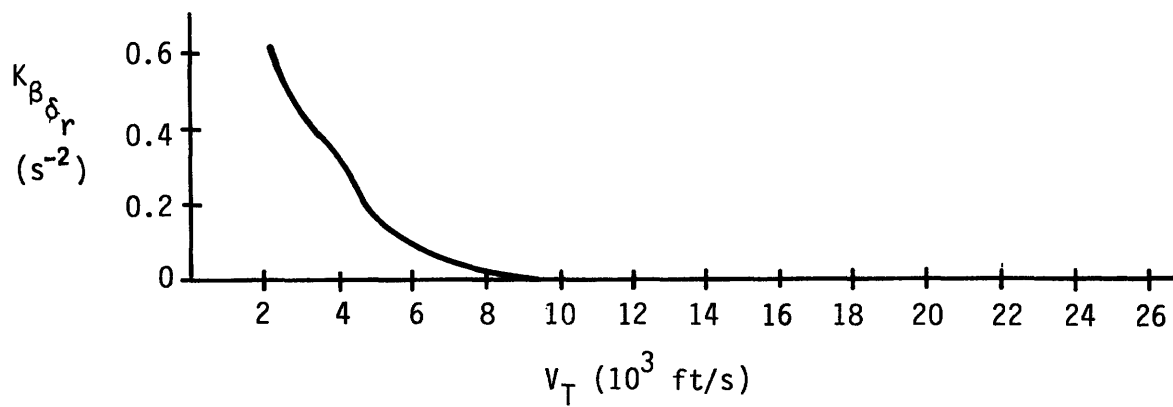
Figure 4-18. Rudder Effectiveness in Sideslip.
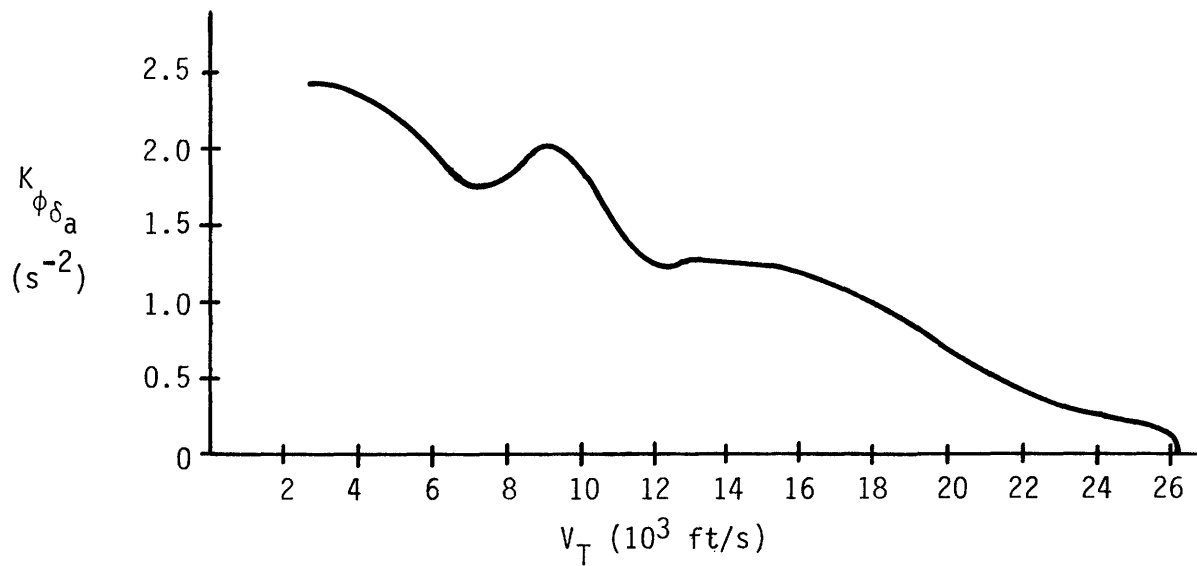
Figure 4-19. Aileron Effectiveness in Bank.
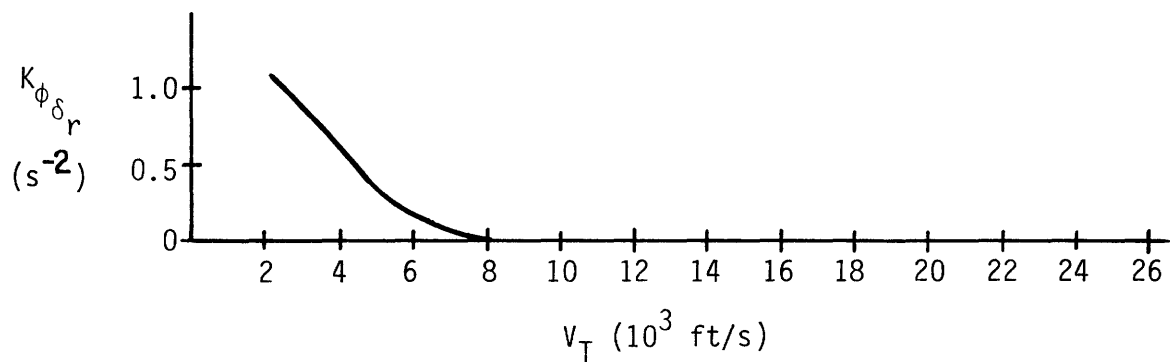
Figure 4-20. Rudder Effectiveness in Bank.

93

rates ($\dot{\phi} \sim 10°$/sec) the coupling induced acceleration is likely to be swamped out by extremely small surface deflection magnitudes (compare K_ϕ history with those for $K_{\beta \delta_r}$ and $K_{\beta \delta_a}$), so as to have little noticeable effect on the sideslip dynamics. Thus, the sideslip dynamics may be modelled in a manner similar to the angle-of-attack mistrim dynamics: both the weak bank-into-sideslip coupling and the essentially zero rate-damping due to sideslip strongly motivate the use of an undamped oscillator model for the sideslip dynamics in the "aerodynamic" flight regime.

A similar simplified view may be taken of the bank dynamics as expressed in (4-51). The inverse bank time constant, $1/\tau_\phi$, whose history is shown in Figure 4-16, attains a maximum magnitude of less than 0.01 $\sec^{-1}$ for the greater part of the entry mission ($V_T \gtrsim 8000$ fps), implying a bank time constant in excess of 100 seconds. Clearly, this type of dynamic information can be neglected for the short-time periods of relevance to the attitude control problem. For the latter part of the entry ($V_T \lesssim 8000$ fps), however, $1/\tau_\phi$ grows by almost an order-of-magnitude, reflecting a time-constant reduction to approximately 10 seconds. This clearly forces a trade to be made between accuracy of representation and simplicity in modelling the bank dynamics; the latter course is chosen here so as to simplify both the control law synthesis procedure and the resulting control loop configuration*. Referring to (4-51), it should be clear that the result of this choice to neglect $1/\tau_\phi$ is a double integrator modelling of the bank dynamics, with a strong sideslip-into-bank coupling due to K_β (see Figure 4-14).

At this point it is appropriate to consider the lateral surface effectiveness terms, shown in Figures 4-17 through 4-20. As mentioned previously, early in the entry, the surfaces are

---

*The effect of neglecting this term is illustrated in the simulation histories of Section 7.2.1.8.

94

ineffective due to the low dynamic pressures encountered. Thus, as in the longitudinal case, the implications for control are fairly straightforward: an all-ACPS attitude control loop designed to stabilize the vehicle about the desired bank attitude. The particular choice of control axes is not so obvious, however, and the motivation for the technique eventually chosen is discussed in greater detail in the next chapter. Later in the entry, it should be clear from Figures 4-17 and 4-19 that the aileron is capable of providing a very healthy control acceleration to the vehicle. For example, a few hundred seconds into the entry (when $V_T \approx 24,500$ ft/sec) when the dynamic pressure is only 25 lbf/ft^2, a 5° aileron deflection will induce a bank acceleration of greater than 1 deg/sec^2 (see Figure 4-19), a level comparable to that available from the ACPS jets. The other point to note is that the rudder is relatively ineffective until quite late in the trajectory ($V_T \lesssim 6000$ fps), and thus one should not be misled by the presence of the rudder effectiveness terms, $K_{\beta \delta_r}$ and $K_{\phi \delta_r}$, of (4-49) and (4-51). Clearly, however, the rudder can be of considerable use during the latter portion of the entry, due to its gradually increasing effectiveness.

4.4.3 Simplified Model Block Diagrams

The above discussion of the longitudinal and lateral dynamics may be conveniently summarized in block diagram form as shown in Figures 4-21 and 4-22. The first figure represents the simplified aerodynamic model defined by (4-38), (4-49), and (4-51), where the ACPS control torque inputs have been omitted for simplicity. The second figure indicates the central features of this model, when the relative magnitudes of both the longitudinal and lateral model parameters are taken into consideration. It is this paring down to essentials that greatly aids the control system design effort described in the next Chapter.
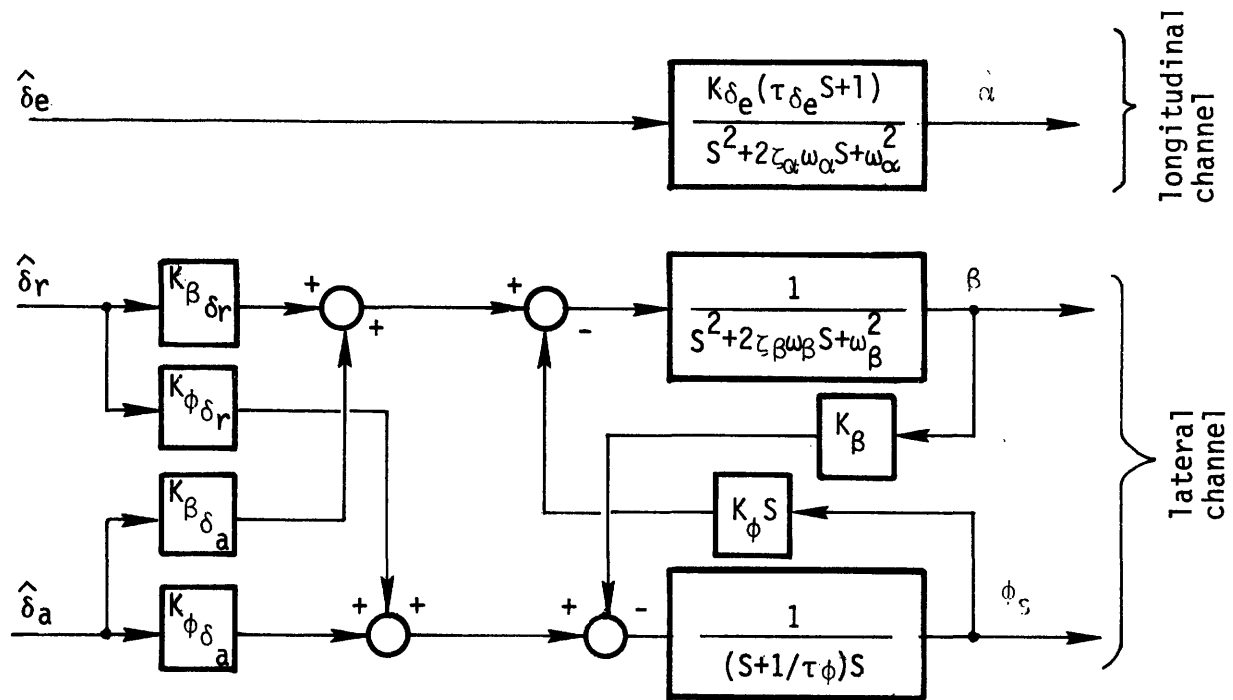
Figure 4-21. Simplified Dynamic Model (ACPS omitted).
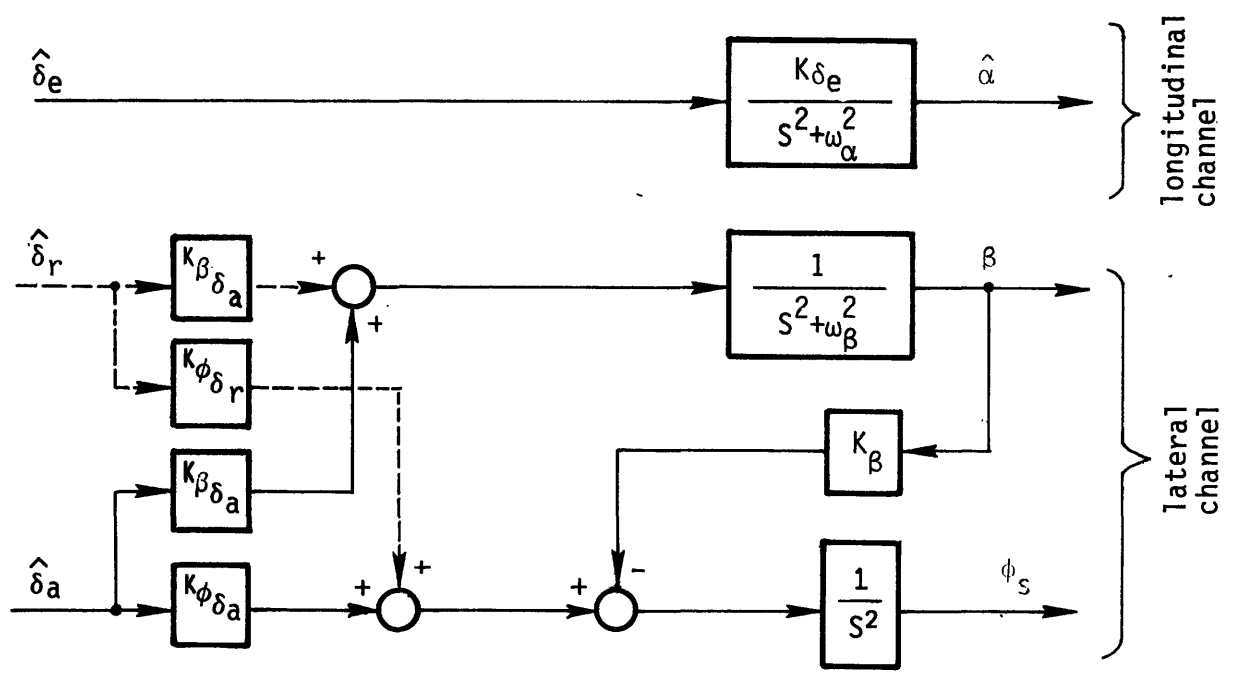
Figure 4-22. Essential Features of Simplified Dynamic
Model (ACPS omitted).

96

4.4.4 Implications for Lateral Control

The conclusions reached above regarding the essential
characteristics of the vehicle dynamics and their implications for
control strategy were reached on the basis of a simple inspection
of the model parameter histories. A more detailed discussion of
the dynamics involved reveals some characteristics of the model
which are especially appropriate to the design synthesis effort,
and this section will consider these control-oriented aspects of
the lateral dynamic model.

As may be recalled from conventional aircraft stability
analyses (see, for example, Reference 8), the vehicle's short-
period sideslip oscillations are deemed stable if the weathercock
stability term, C_{n_β}, is positive.[*] What is interesting to note is
that in a large portion of the entry envelope this derivative is
negative for this particular vehicle, and yet the vehicle
displays no divergent tendencies whatsoever. This apparently
contradictory situation has been an item of some confusion in the
past; however, it is easily explained in the context of the simplified
model developed above. As shown in Figure 4-22, sideslip motions
will be essentially oscillatory (undamped), so that disregarding
control torque inputs, sideslip deflections can be modelled as
follows:

$$\ddot{\beta} = -\omega_\beta^2 \beta \qquad\qquad (4\text{-}53)$$

where, from Section 4.3,

$$\omega_\beta^2 \equiv \left(\frac{\bar{q}Sb}{I_{zz}}\right)C_{n_\beta}' \quad ; \quad C_{n_\beta}' \equiv C_{n_\beta}\cos\alpha_T - \frac{I_{zz}}{I_{xx}}C_{\ell_\beta}\sin\alpha_T \qquad \begin{matrix}(4\text{-}50a);\\(4\text{-}43)\end{matrix}$$

---

[*]and the rotary derivatives are small.

Clearly, for (4-53) to be non-divergent, the dynamic derivative C'_{n_β} must be positive. Note that there is no requirement for the stability derivative C_{n_β} to be positive, so long as the dihedral coefficient, C_{ℓ_β}, is sufficiently negative to cancel out any destabilizing tendencies. This is of course the case for the present vehicle, as evidenced by the positive values of C'_{n_β} throughout the flight envelope, as shown in Figure B-9 of Appendix B. The point being made here is that the weathercock coefficient, C_{n_β}, does not determine lateral stability, but the dynamic derivative C'_{n_β} does.

One additional comment on lateral stability is appropriate at this point. From the definition of C'_{n_β}, it should be clear that as the angle-of-attack grows smaller, then:

$$\lim_{\alpha_T \to 0} C'_{n_\beta} = \lim_{\alpha_T \to 0} \left[C_{n_\beta} - \frac{I_{zz}}{I_{xx}} C_{\ell_\beta} \alpha_T \right] = C_{n_\beta} \tag{4-54}$$

The intermediate expression is clearly a valid expression for C'_{n_β} at small α_T, but its indiscriminate use at large angles-of-attack clearly invites misrepresentation of the vehicle dynamics. The importance of C_{n_β} in determining stability should also be clear from the above expression: most conventional analyses are for low angle-of-attack flight, and thus the dominant term is the weathercock stability coefficient. This of course is not the case in the entry regime.

The stabilizing effect of the dihedral coefficient has already been mentioned; of equal importance is its effect on the bank dynamics. Again, recalling conventional stability analysis results, the dihedral induced body-axis roll acceleration is directly proportional to both the dihedral coefficient, C_{ℓ_β}, and the sideslip mistrim. The coefficient is normally negative so that the induced roll acceleration takes on the opposite sign of the sideslip angle.

This same essential feature holds in the simplified model derived above, except that the effect can be stated in more general terms due to the use of the stability-axis framework. To see this, reference to Figure 4-22 shows that the sideslip-into-bank coupling term K_β drives the bank angle as follows:

$$\ddot{\phi}_s = -K_\beta \beta \qquad (4\text{-}55)$$

where, from Section 4.3,

$$K_\beta = -\left(\frac{\bar{q}Sb}{I_{xx}}\right)C'_{\ell_\beta} \quad ; \quad C'_{\ell_\beta} \equiv C_{\ell_\beta}\cos\alpha_T + \frac{I_{xx}}{I_{zz}}C_{n_\beta}\sin\alpha_T \qquad \begin{matrix}(4\text{-}52a); \\ (4\text{-}47)\end{matrix}$$

With the dynamic derivative C'_{ℓ_β} negative over the entry flight regime (as shown in Figure B-14), then K_β is positive, implying from (4-55) that the induced <u>bank</u> acceleration takes on the opposite sign of the sideslip angle. As can be seen, this is a more general statement of the dihedral effect, because of the following limiting behavior of C'_{ℓ_β}:

$$\lim_{\alpha_T \to 0} C'_{\ell_\beta} = \lim_{\alpha_T \to 0}\left[C_{\ell_\beta} + \frac{I_{xx}}{I_{zz}}C_{n_\beta}\alpha_T\right] = C_{\ell_\beta} \qquad (4\text{-}56)$$

Thus, as angle-of-attack approaches zero, the dynamic derivative C'_{ℓ_β} "collapses" to the stability derivative C_{ℓ_β}. Further, the bank angle itself "collapses" to body-axis roll attitude as $\alpha_T \to 0$ (from Figure 4-6). Thus, the dihedral induced <u>body-axis roll</u> acceleration is just a special case ($\alpha_T = 0$) of the more general induced <u>bank</u> acceleration due to C'_{ℓ_β}.

In addition to the functional form of this dihedral effect, it is important to consider the numerical aspects. In particular, by referring to the history of the coupling constant K_β, given in Figure 4-14 and comparing it with the history of the aileron

99

effectiveness in bank, $K_{\phi \delta_a}$, given in Figure 4-19, it becomes clear
that a sizeable torque is available from small sideslip mistrims:
a degree of sideslip provides approximately twice the bank accelera-
tion generated by a comparable aileron deflection.

At this point it is appropriate to consider one last direct
implication of the simplified vehicle model on the dynamics of
maneuvering. Shown in Figure 4-23 is an attempt to depict the
three-dimensional aspects of a body-axis roll maneuver contrasted
with those of a body-axis yaw maneuver. Assuming the vehicle
initially starts the maneuver with zero sideslip, then, due to the
way in which the vehicle's longitudinal plane is rotated, a non-zero
sideslip angle is generated: specifically, a positive roll will result
in a positive sideslip as shown, while a positive yaw results in
negative sideslip. This geometry of body-axis maneuvers may then
be combined with the dihedral effect discussed above, as shown in
Figure 4-24, so as to illustrate the sequence of events induced by
a body-axis torque. It is seen that a body-axis roll torque eventually
results in an opposing, or adverse, roll torque caused by positive
sideslip and negative dihedral, while a body-axis yaw torque has a
quite different effect, in that it gives rise to a roll torque of the
same sign, thus promoting a coordinated maneuver. This should
make clear that the conventional approach of using body-axis roll
torques (i.e., aileron and/or roll jets) to bank the vehicle may
prove to be entirely inappropriate for control during the entry
mission.

To illustrate the implications of the above discussion,
Figure 4-25 presents simulation results which display the effect of
a positive aileron pulse on the open-loop airframe dynamics. The
simulator is discussed later in Chapter 7; it suffices to note here
that this is a six-degree-of-freedom simulation of the complete,
non-linear equations of motion, at Mach 5, where the dynamic pressure
is 155 lbf/ft^2 and the trim angle-of-attack is 20°. As can be seen,

100
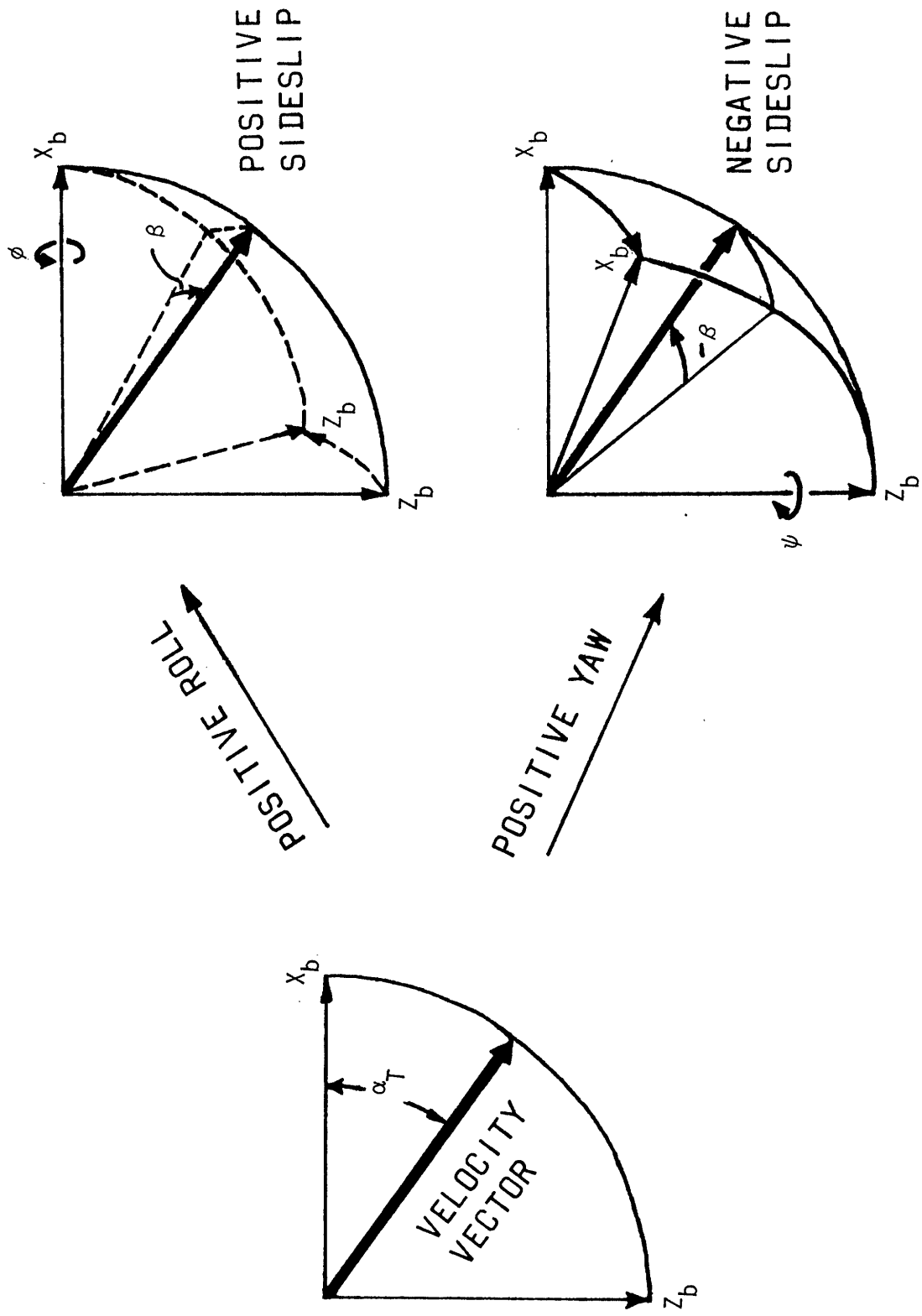
Figure 4-23. Vehicle Attitude Geometry.

101

EFFECT OF POSITIVE ROLL TORQUE

$+T_\phi \rightarrow$ VEHICLE DYNAMICS $\xrightarrow{+\phi}$ GEOMETRY $\xrightarrow{+\beta}$ DIHEDRAL EFFECT $\xrightarrow{-T_\phi}$ CREATES NEGATIVE ROLL TORQUE

WEATHERCOCK STABILITY
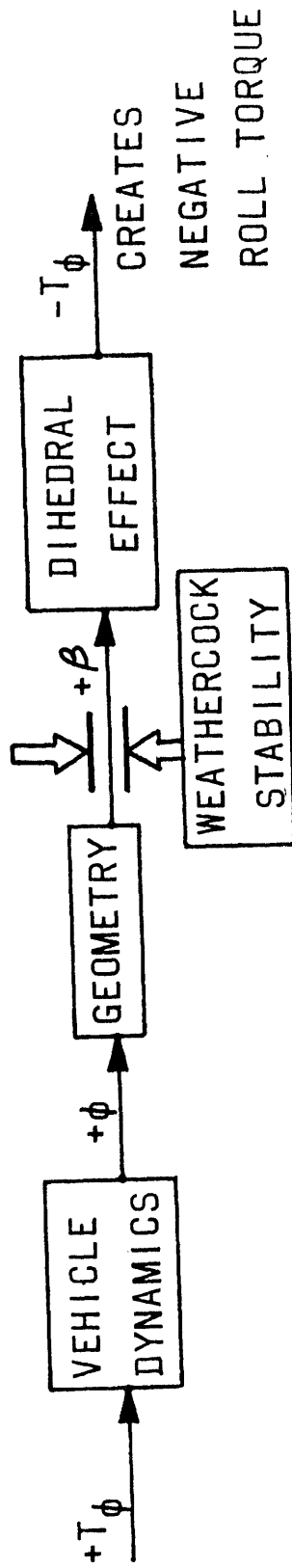
EFFECT OF POSITIVE YAW TORQUE

$+T_\psi \rightarrow$ VEHICLE DYNAMICS $\xrightarrow{+\psi}$ GEOMETRY $\xrightarrow{-\beta}$ DIHEDRAL EFFECT $\xrightarrow{+T_\phi}$ CREATES POSITIVE ROLL TORQUE

WEATHERCOCK STABILITY
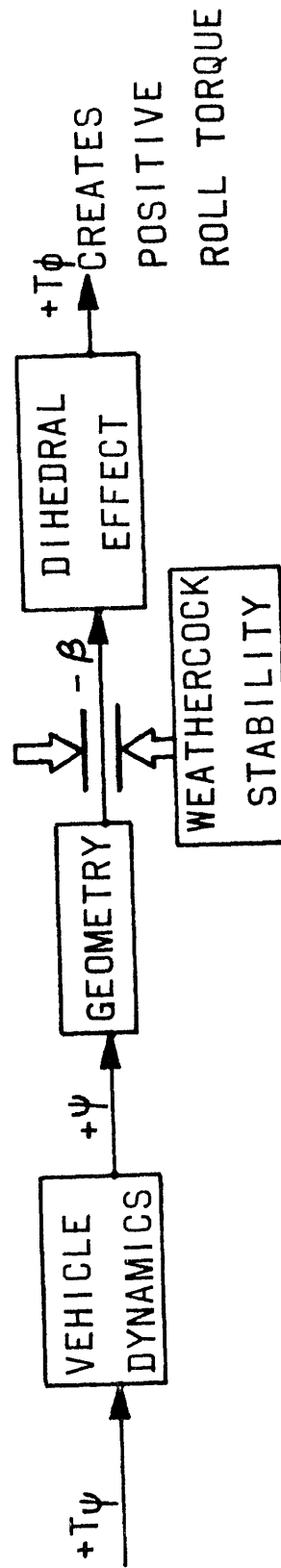
Figure 4-24. Roll and Yaw Torque Control.
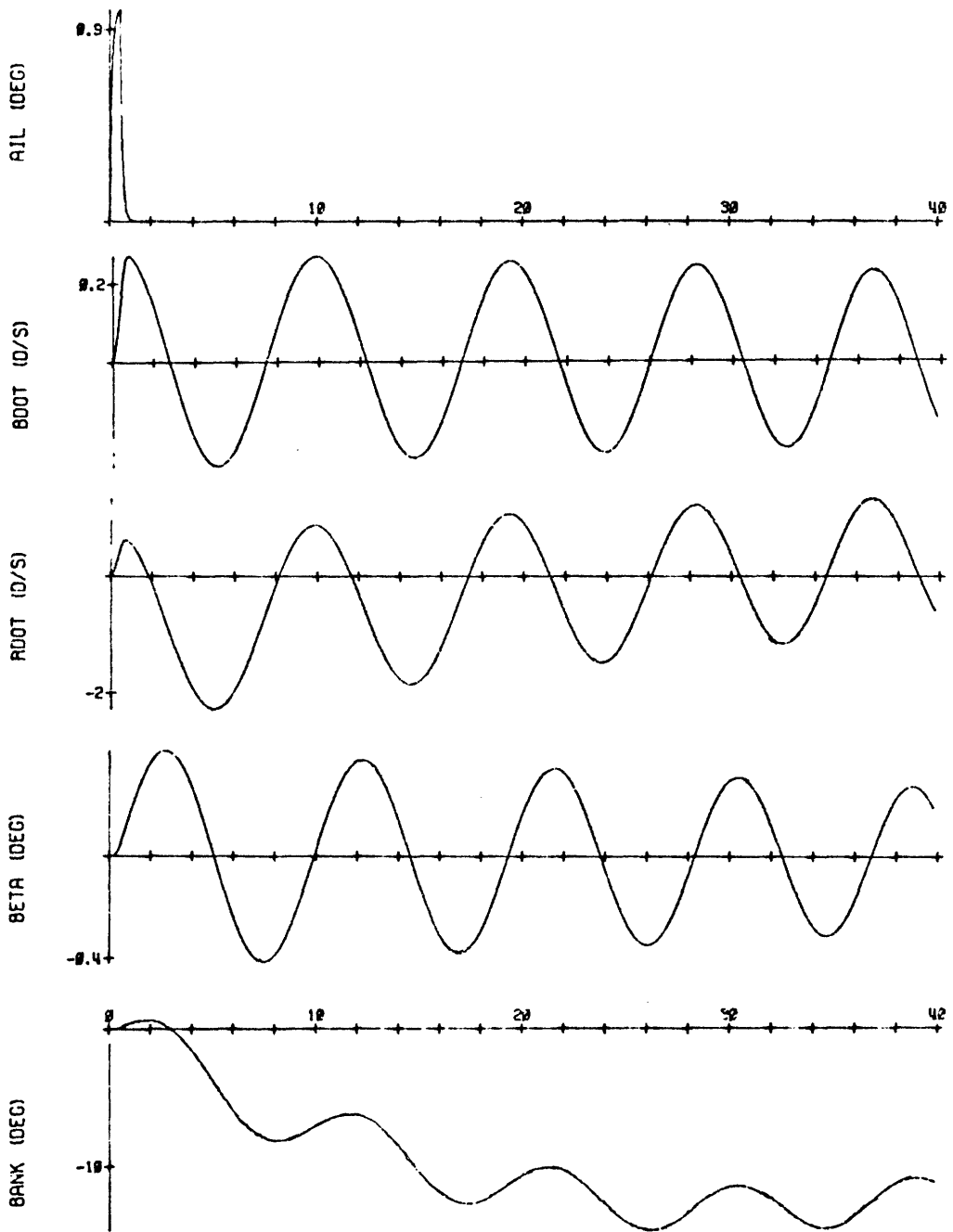
Figure 4-25. Aileron Pulse at $\mathcal{M}$ = 5, $\bar{q}$ = 155 lbf/ft^2, α_T = 20°.

the positive aileron pulse initiates positive rates in both sideslip and bank, as expected, since both $K_{\beta \delta_a}$ and $K_{\phi \delta_a}$ are positive. With the lateral dynamics thus excited, the sideslip history exhibits the characteristic lowly damped oscillations predicted by ω_β and ζ_β. More important, however, is the coupling effect evidenced in the plots. As the sideslip grows positive from its initial zero value, the dihedral coupling term K_β rapidly turns the bank rate around so that the initial effect of the positive aileron pulse is entirely cancelled. Because the sideslip remains positive for half its natural period ($T = 2\pi / \omega_\beta \approx 10$ seconds), the net effect after 5 seconds is a significantly large <u>negative</u> bank rate. This, in turn, gives rise to the reversal effect illustrated by the bank history itself; the oscillations are, of course, due to the sideslip oscillations. It should be clear, then, that the open-loop system exhibits a strong natural tendency to reversal of aileron inputs; the control system design must obviously take this into account.

The characteristics of the vehicle model which have been described above, in conjunction with their implications for control strategy, clearly provide a sound foundation for control system synthesis. As will be seen in the next chapter, the synthesis effort not only draws strongly on the results presented here, but continues this search for simplified models to aid in the analysis of the fundamental dynamics governing the vehicle's short-period rotational motion.

5. Control System Synthesis

This chapter presents a derivation of the entry control logic and consists of both synthesis of several individual control laws and definition of overall control system structure. In addition to the eventual satisfaction of the performance requirements of Chapter 2, three basic goals of any vehicle control system design effort are felt to be especially appropriate here. First, due to the constantly changing characteristics of the vehicle and its intended flight performance, it is most advantageous to maintain as much flexibility as possible in the control law formulation. This immediately suggests an effort to minimize the amount of trial-and-error gain selection that inevitably occurs in design synthesis activities; a more far-reaching implication is that of a stronger dependence on analytic models to better define the dynamics involved, and on a semi-automatic procedure for definition of control system gain selection. The second consideration in the design synthesis effort concerns the type of control laws to be considered as candidates for incorporation in the overall control system. Although linear feedback control clearly provides a degree of aesthetic satisfaction, due to the inherent ease of analysis, an arbitrary restriction on the use of non-linear logics may severely handicap the design effort. The implication here, then, is to avoid a slavish adherence to a linear feedback structure, and, instead use the type of control appropriate to both the vehicle and its performance requirements, regardless of its lack of linearity. The final consideration in the design effort is simplicity. Starting with one or more basic control laws, subsequent modifications made in the name of sophistication can quickly add up to a highly complex system whose dynamic response in a particular situation may be entirely unexpected. Thus, it is most appropriate for the designer to constantly weigh the advantages to be gained from the modification, against the accrued cost in complexity and possible subsequent unpredicted system behavior. This is especially pertinent to digital systems, since the trend toward complexity is so readily facilitated by the ease with which modifications may be implemented.

Before describing the detailed control law synthesis, it is appropriate to consider some aspects of the basic synthesis strategy used in this chapter. One of the major points to note is that, as discussed in Chapter 3, the design is carried out in an iterative manner. Thus, starting with the simplified model of the preceeding chapter, an initial version of a particular control law may be formulated. Both by analytic techniques (e.g., more accurate modelling of the dynamics involved) and from the results of simulation efforts, it may become clear that modifications are required to improve performance. With sophistication versus complexity trades always in mind, the control law may then be expanded to account for particular aspects of the problem which were not present in the initial design formulation. This approach of incorporating more sophisticated control logics only when there is a demonstrated requirement avoids many of the pitfalls associated with an overly general and comprehensive initial problem definition. The presentation format of this chapter is along functional lines, and thus unfortunately does not reveal the true chronological development of the control laws; however, within a particular functional unit (e.g., aileron control), this iterative trend will be apparent in the progressive sophistication of the control law as additional operational requirements are placed on vehicle performance. In fact, it will be seen that this progression is often punctuated by the introduction of new simplified vehicle models to account for a particular aspect of vehicle behavior, and thus provide an analytic basis for control law modifications.

A second point to note in the synthesis procedure is the separation of the overall control problem into smaller subsets that are more easily analyzed and compensated for. Thus, with the motivation of the results of the previous chapter, the separation of the longitudinal and lateral vehicle dynamics immediately suggests an identical separation of control law formulation. This proves to be extremely useful to the synthesis effort, allowing for the control system to be synthesized from two simpler longitudinal and lateral channels. The second type of separation used in the synthesis is that between the ACSS and the ACPS effector subsystems.

Here the motivation for separation is due to the inherently different characteristics of the torque histories produced by the two subsystems: the discrete-level on-off nature of the ACPS torques contrast sharply with the linear characteristics of the ACSS generated torques. This separation is only a temporary convenience however, since the two sub-systems are brought into concert via the blending logic (see Section 5.3) used to make use of both available torque sources in a unified manner.

A final point to consider in the synthesis procedure to follow is the technique used to develop the control laws for the surfaces. Basically what is accomplished by these control laws is closed-loop pole placement in accordance with desired response characteristics, by use of appropriate state feedback gains. Because of the simplicity of the dynamic model of the previous chapter, it is possible to solve analytically for the gains as functions of the model parameters, thus paralleling a root-locus design exercise without the concommitant trial-and-error compensation pole placement. With gains as functions of the (changing) model parameters, it is then fairly straightforward to approximate the important parameters by means of gains scheduled along the trajectory, and thus compensate for the slow changes occurring in the vehicle response characteristics due to changes in dynamic pressure, Mach number, etc. It should be noted that exclusive use is made of the s-plane, or Laplace transformed variables, for the design synthesis of these control laws. Although this failure to make use of the appropriate sampled-data design tools appears inconsistent with the design goal of synthesizing a digital controller, the s-plane, or continuous system representation, is strongly motivated by considerations in two areas.

The first of these is concerned with the ratio of the controller's anticipated sample rate to the vehicle's highest natural frequency. It should be recognized that if, in the future, active control of the vehicle's flexible body dynamics becomes an objective of controller design, a relatively high sample rate will be required, probably between 10 and 50 cps. A comparable minimum rate requirement is imposed by manual

107

control considerations, since loop rates of less than 10 cps result in perceivable and undesirable "stepped" response. Thus, although neither flexible body control nor manual augmentation is addressed directly by this control system study, it would appear that implementation of either would place a relatively high sample rate requirement on the controller. More specifically, it is appropriate to compare an anticipated sample rate imposed by flexible body control requirements ($\gtrsim 10$ cps) with the range of frequencies to be encountered in the rigid body control problem. Referring to Figures 4-7 and 4-12 of the previous chapter, it can be seen that a 10 cps sample rate is approximately 40 times greater than the highest vehicle natural frequency to be encountered during the entry, clearly minimizing the sampled-data aspects of the problem, and, in turn, supporting the validity of a continuous-time, or Laplace transform, design approach. It can be argued, of course, that the high rates imposed by flexible body control (or manual augmentation requirements) need not be reflected in the rigid body control loop, through the judicious use of multi-rate sampling and z-transform analysis. This option was not taken in this study, however, because of the additional complexity required in such an implementation (see below). It may also be argued that a lower sample rate for rigid-body control is in order, simply in view of the anticipated penalty in computer duty cycle associated with high computation rates. This question will remain unresolved here, because of the unavailability of both the flight computer and its associated flight control language; it is expected that future timing studies will evaluate the sensitivity of duty cycle to sample rate, so that the impact of a 10 cps sample rate on computer work-load can be assessed.

The second consideration supporting the use of Laplace transforms over sampled-data techniques is that of simplicity versus complexity, and indirectly, that of the iterative design strategy to be followed in the control law synthesis. Derived in appendix D are the sampled-data versions (i.e., difference equations, z-transforms, and w-transforms) of the vehicle equations of motion of the previous chapter. As can be seen from a quick perusal of the results, the equation base is considerably

more complicated, thus nullifying the advantage of simplicity inherent in the vehicle model of the previous chapter. Coupled with this aspect of complexity is the fact that, to date, there is no evidence of performance degradation due to unmodelled sampling effects.[*] Thus, in keeping with the iterative process of control law sophistication only when there is demonstrated need, the equation base and the synthesis procedure for surface control has been maintained in the Laplace domain of continuous systems.

Because of the somewhat extensive description of the controller synthesis presented in this chapter, a summary system description is provided in Chapter 6, conveniently formatting the results derived here. The remainder of this chapter is devoted to the detail development of the individual control laws comprising the attitude control system, and is divided into five sections. Sections 5.1 and 5.2 are concerned with the synthesis of the longitudinal and lateral control channel logics, respectively, while Section 5.3 defines the blending logic used to integrate the torques produced by both the ACSS and the ACPS. Section 5.4 describes the required signal processing at the interfaces with the other vehicle software modules, and, in particular, discusses stability-axis rate estimation and the ACPS jet selection problem. Finally, Section 5.5 describes the fundamental issues of gain selection; the actual design values are given in the next chapter, along with the system design summary.

5.1 Longitudinal Control

This section derives both the ACPS and the ACSS control laws used to control the vehicle's angle-of-attack in response to commands generated by the guidance system. As noted above, the equation development is strongly dependent on the simplified model of the longitudinal short-period dynamics as given by (4-38) of Chapter 4. Two qualitative aspects of this model are of particular interest. First, it should be recalled that the longitudinal equation specifies the dynamics of angle-of-

---

* See Section 7.2 for additional discussion.

attack deviations from trim, and thus provides no information regarding the relation between trim elevator setting and the associated trim angle-of-attack. This then motivates the introduction of a separate longitudinal trim logic so as to maintain an approximate equilibrium in pitch, and thus provide an environment which ensures the validity of the mistrim model of (4-38). In the derivations which immediately follow, it is assumed that the trim logic is functioning properly and thus only small mistrims need be corrected for; the trim logic itself is discussed at the end of the section. The other qualitative aspect of the model concerns the inputs available to the longitudinal control logic. Recognizing that the model's state variables are angle-of-attack mistrim and mistrim rate, it should be clear that more readily available state variables are in order; i.e., angle-of-attack and angle-of-attack rate. This variable transformation is discussed in greater detail in the subsection describing elevator control; the eventual source of this state information is considered in Section 5.4.

The synthesis effort is split into two separate equation developments, one for the pitch ACPS jets (Section 5.1.1) and the other for the elevator (Section 5.1.2). As mentioned above, the motivation for this separate development stems both from the extremely different torque characteristics of the two effector subsystems and from the simplicity accrued in solving decoupled control problems. Blending between the two control effectors is discussed in Section 5.3. One final remark is appropriate at this point. It must be recognized that both the elevator and pitch jets are abstractions of the actual hardware involved, and thus only exist in a functional sense. The discussion concerning the relation of these control system defined variables to the actual torque producing hardware is to be found in Section 5.4.

5.1.1 Pitch ACPS Control

Recognizing that pitch jet control is required during early entry, due to the lack of aerodynamic control effectiveness, a vehicle dynamic model appropriate to this flight regime must be chosen. As the discussion in Section 4.1.1 points out, all of the aerodynamic dependent

110

model parameters are negligible, so that the vehicle can be viewed as a simple mass with specified inertial properties. Specifically, the longitudinal model of (4-38) reduces to a simple double integrator model of the trim deviation:

$$s^2 \hat{\alpha} = u_y \qquad (5-1)$$

Recognizing that in the absence of aerodynamic torques the trim value for angle-of-attack may be freely specified, it is appropriate to use the guidance commanded value, α_G, to specify the trim value. Thus, letting

$$\epsilon_\alpha \equiv \alpha - \alpha_G \qquad (5-2a)$$

and defining

$$(\epsilon_1, \epsilon_2) \equiv (\epsilon_\alpha, \dot{\epsilon}_\alpha) \qquad (5-2b)$$

then, from (5-1),

$$\dot{\epsilon}_1 = \epsilon_2$$

$$\dot{\epsilon}_2 = u \qquad (5-3)$$

where, in this particular case, the control variable u is taken as the pitch control variable u_y. Assuming that the available pitch acceleration from the ACPS is symmetric* and bounded, then the familiar parabolic phase plane control logic is especially appropriate. Appendix E provides a derivation of the logic which drives ϵ_1 and ϵ_2 to zero, while minimizing a weighted fuel-time cost function (see (E-5)), thus offering a trade between ACPS on-time and total desired response time. In fact, as is shown in the appendix, the variation of a single parameter (σ, see below)

---

* Reference to Table 5-1 of Section 5.5.1 shows that ACPS jets can be chosen such that the difference between "pitch-up" and "pitch-down" acceleration levels is less than 4%.

allows the designer to emphasize the importance of minimizing ACPS fuel expenditures (for a given maneuver) or more heavily favor a fast response time. Figure E-8 of the appendix is repeated below to show the control regions and a typical controlled trajectory in the (ϵ_1, ϵ_2) phase-plane. It should be noted that the control u takes on only one of three values,

$$u = 0, +U, \text{ or } -U \qquad (5-4)$$

where, in this particular case, U is used for the available pitch acceleration level, U_y.

The anticipated control law sample period is on the order of 100 milliseconds; the ACPS minimum impulse time is approximately 20 milliseconds. Thus, if the ACPS acceleration command is maintained between controller samples, the effective minimum jet on-time is the sample period. To ensure practical limit-cycle operation in this situation, it is appropriate to modify the logic of Figure 5-1 to include a deadband region about the origin. In addition, due to the lag induced by the sampling process, overshoot of the switch curves can be anticipated. Thus, to aid trajectory convergence to the desired limit-cycle, the switch curves Γ_- and Γ_+ of Figure 5-1 are shifted away from the origin so as to compensate for the expected overshoot behavior. The resulting phase-plane control logic, with the inclusion of the deadband parameters[*] δ_1 and δ_2, is as shown in Figure 5-2. Also shown is a typical state trajectory illustrating switch curve overshoot and minimum impulse limit cycling. The equations for the switch curves are taken from (E-15) and (E-29) of Appendix E, and are modified to include the deadbands and to simplify the weighting parameter choice:

---

[*] These, and other design parameters to be introduced, are discussed in more detail in Section 5.4.
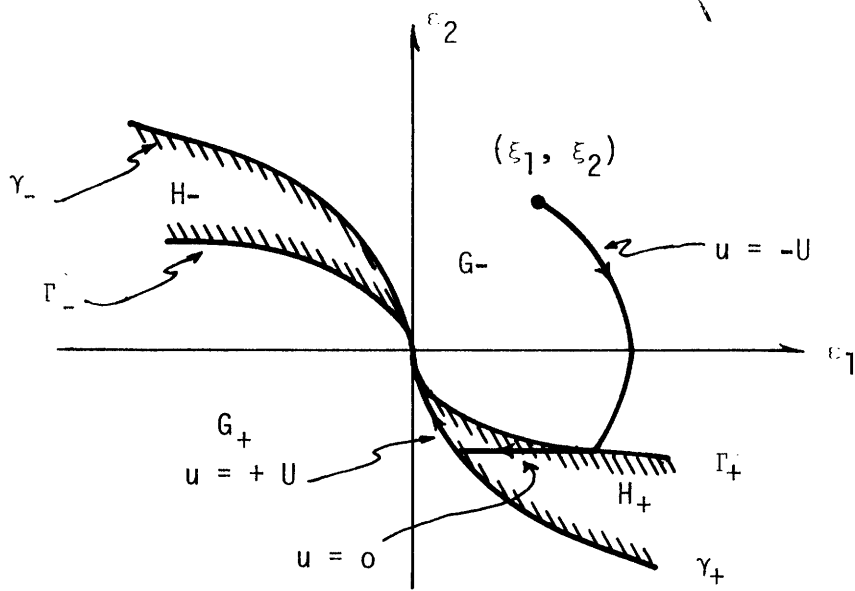
Figure 5-1. Fuel-Time Optimal Phase-Plane Switch Logic.
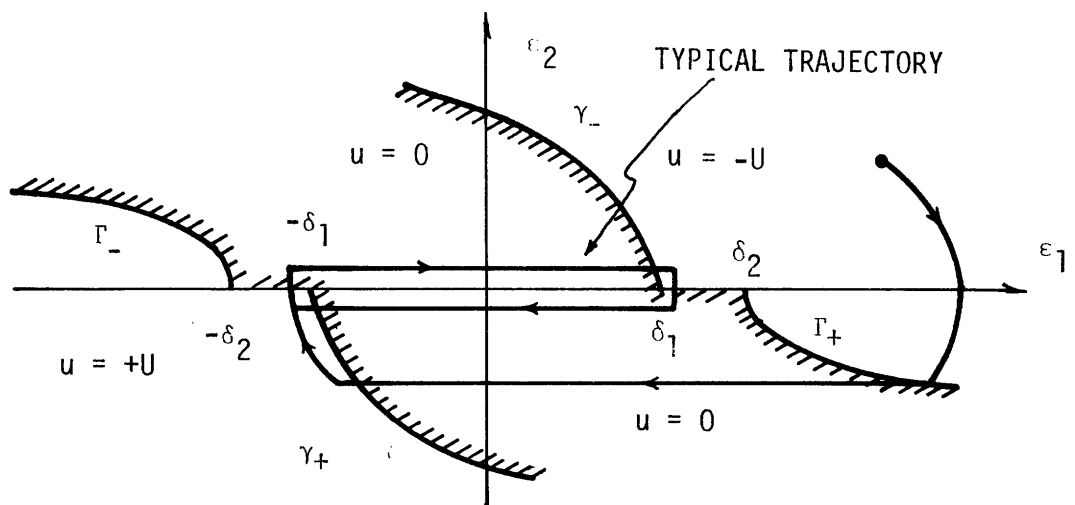
[NOTE: SWITCH CURVES DEFINED BY (5-5)]

Figure 5-2. ACPS Switch Logic.

113

$$\gamma_\pm: \quad \epsilon_1 = \mp (\delta_1 - \frac{1}{2U} \epsilon_2{}^2)$$

$$(5\text{-}5)$$

$$\Gamma_\pm: \quad \epsilon_1 = \pm (\delta_2 + \frac{\sigma}{2U} \epsilon_2{}^2)$$

where, in this case, the deadbands are pitch attitude deadbands, or:

$$(\delta_1, \ \delta_2) = (\delta_{\alpha_1}, \ \delta_{\alpha_2})$$

$$(5\text{-}2c)$$

and where σ is the simplified fuel-time weighting parameter, given for pitch control by:

$$\sigma = \sigma_\alpha$$

$$(5\text{-}2d)$$

and where it should be recalled that

$$(u, \ U) = (u_y, \ U_y)$$

$$(5\text{-}2e)$$

From a comparison of (5-5) with the switch curve definitions of (E-15) and (E-29), it is seen that

$$\sigma = \frac{K/U + 4}{K/U}$$

$$(5\text{-}6)$$

where, from (E-64), it is seen that response time is minimized as $K \to \infty$ ahd that ACPS on-time is minimized as $K \to 0^+$. As a guide to the specification of σ (actually, σ_α in this case), it is seen from (5-6) that response time is minimized as $\sigma \to 1^+$ and that ACPS on-time is minimized as $\sigma \to \infty$. Section E.5 of Appendix E describes additional characteristics of the basic parabolic control law, which, although not central to the design issues at hand, show the great flexibility of this technique, especially in view of the simplicity of digital implementation.

114

5.1.2 Elevator Control

In keeping with the basic separation of the ACPS and ACSS control law synthesis, this section will assume that the elevator provides the entire control torque budget and that no control is obtained through the pitch ACPS jets. Thus, the simplified model defined by (4-38) in Section 4.4 becomes:

$$(s^2 + 2\zeta_\alpha \omega_\alpha s + \omega_\alpha^2)\hat{\alpha} = K_{\delta_e}(\tau_{\delta_e} s + 1)\hat{\delta}_e \qquad (5-7)$$

where the model parameters are defined by (4-34). As was pointed out in Section 4.4.1, neither the damping ratio, ζ_α, nor the time constant, τ_{δ_e}, significantly contribute to the response characteristics of the model, and thus may be conveniently neglected for this synthesis effort. The model defining the longitudinal dynamics is thus a simple undamped oscillator:

$$(s^2 + \omega_\alpha^2)\hat{\alpha} = K_{\delta_e}\hat{\delta}_e \qquad (5-8)$$

It should be noted that the above equation pertains to deviations from trim, and thus provides absolutely no information concerning the required trim elevator deflection, δ_{e_T}, to maintain a trim angle-of-attack, α_T. The techniques for deriving this information are presented in Section 5.1.2.2. It is appropriate to consider control of deviations from trim first, however, and this is done in the section immediately following.

Prior to deriving the elevator control law, it should be noted that the derivations presented here ignore the actuator dynamics, and thus effectively assume: a) very small actuator time constants; and b) no rate-limiting effects. The first assumption is quite easy to justify by comparing the shortest time-constant associated with the longitudinal dynamics, given by $2\pi/(\omega_\alpha)_{max}$, with the actuator time-constant, τ_{act}. Referring to the natural frequency history of 4-7, it is seen that the longitudinal dynamics are approximately 80 times slower than an actuator with a time-constant of 0.1 second. The second point, concerning rate-limiting, is more difficult to justify without further analysis or simulation

results. However, in keeping with the policy of simplicity until there is a demonstrated requirement for additional sophistication, it suffices to note that rate-limiting effects have been, to date, of minor importance in the overall control system performance, and this is demonstrated in Section 7.3.3.

5.1.2.1 Transient Control

The first objective of the elevator control law is to drive the angle-of-attack to a desirable trim value, or, equivalently, drive the trim deviation, $\hat{\alpha}$, to zero. Using standard rate and position feedback of this mis-trim angle, through two control gains c_α and $c_{\dot{\alpha}}$, the closed-loop system may be diagrammed as shown in Figure 5-3.
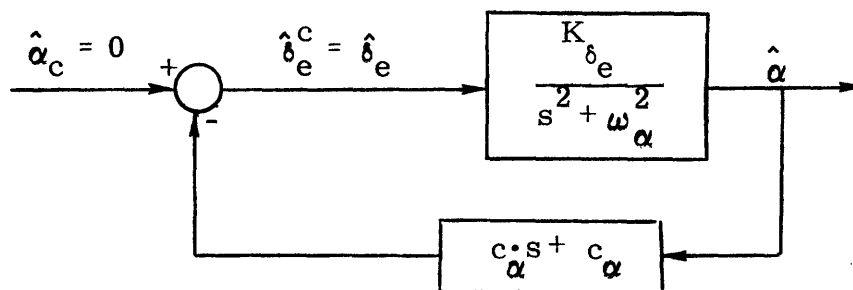
Fig. 5-3: Basic Elevator Control Loop

Ignoring the actuator dynamics, the linear feedback law is then simply given by:

$$\hat{\delta}_e = -(c_{\dot{\alpha}}s + c_\alpha)\hat{\alpha} \qquad (5-9)$$

From the block diagram it is seen that the closed-loop transfer function relating $\hat{\alpha}$ to $\hat{\alpha}_c$ (=0) is given by:

116

$$\frac{\hat{\alpha}}{\hat{\alpha}_c} = \frac{K_{\delta_e}}{s^2 + c_{\dot{\alpha}} K_{\delta_e} s + (\omega_\alpha^2 + c_\alpha K_{\delta_e})} \qquad (5\text{-}10)$$

As mentioned previously, the control law is predicated on closed-loop pole placement. Thus, by requiring that the characteristic equation be given by

$$s^2 + 2\zeta_d \omega_d s + \omega_d^2 = 0 \qquad (5\text{-}11)$$

where ζ_d and ω_d are design-fixed parameters specifying desired pole locations, then from (5-10), the feedback gains are given by:

$$c_\alpha = \frac{1}{K_{\delta_e}} (\omega_d^2 - \omega_\alpha^2) \qquad \text{(a)}$$

$$\qquad (5\text{-}12)$$

$$c_{\dot{\alpha}} = 2\zeta_d \omega_d / K_{\delta_e} \qquad \text{(b)}$$

However, from the model parameter definitions given by (4-34), it follows that

$$K_{\delta_e} = \xi_1 \bar{q} \quad ; \quad \omega_\alpha^2 = \xi_2 \bar{q} \qquad (5\text{-}13)$$

where the dynamic pressure dependence is isolated by the definition of the ξ_i :

$$\xi_1 \equiv \frac{Sc}{I_{yy}} C_{M_{\delta_e}} \quad ; \quad \xi_2 \equiv -\frac{Sc}{I_{yy}} C_{M_\alpha} \qquad (5\text{-}14)$$

The feedback gains may thus be specified in the following form:

$$c_\alpha = \omega_d^2 / \bar{q} \xi_1 - \xi_2 / \xi_1 \qquad \text{(a)}$$

$$\qquad (5\text{-}15)$$

$$c_{\dot{\alpha}} = 2\zeta_d \omega_d / \bar{q} \xi_1 \qquad \text{(b)}$$

Thus, the elevator control law specifying deflections from trim is found from (5-9) and (5-15) to be:

$$\hat{\delta}_e = -\frac{1}{\xi_1}\left\{\frac{\omega_d^2}{\bar{q}}\left[\hat{\alpha} + \frac{2\zeta_d}{\omega_d}\dot{\hat{\alpha}}\right] - \xi_2\hat{\alpha}\right\} \qquad (5\text{-}16)$$

It should be noted that the above equation is a reversion to the time domain, with the inclusion of the mistrim rate, $\dot{\hat{\alpha}}$. In fact, it is appropriate to consider the relations of the mistrim states $\hat{\alpha}$ and $\dot{\hat{\alpha}}$ to the more familiar longitudinal variables. It is convenient to define the angle-of-attack error as the difference between the attitude commanded by guidance, α_G, and the attitude of the vehicle, α (note that the tilda used in Chapter 4 is omitted here for clarity):

$$\alpha_e \equiv \alpha_G - \alpha \qquad (5\text{-}17)$$

If it is assumed that the control system is operating properly so that the trim angle-of-attack is at the commanded guidance value, then from (5-17) and the definition of the mistrim angle, $\hat{\alpha}$, given in (4-22), it follows that:

$$\hat{\alpha} = \alpha - \alpha_T = -\alpha_e \qquad (5\text{-}18a)$$

It then follows from the definition of trim $(\dot{\alpha}_T = 0)$ that

$$\dot{\hat{\alpha}} = \dot{\alpha} \qquad (5\text{-}18b)$$

Thus, (5-18) may be used to redefine the elevator control (5-16) in terms of the angle-of-attack error and rate:

$$\hat{\delta}_e = \frac{1}{\xi_1}\left\{\frac{\omega_d^2}{\bar{q}}\left[\alpha_e - \frac{2\zeta_d}{\omega_d}\dot{\alpha}\right] - \xi_2\alpha_e\right\} \qquad (5\text{-}19)$$

118

This then defines the elevator control law, specifying deflections from a trim setting, designed to drive angle-of-attack to a guidance specified trim value.

5.1.2.2 Trim Control

As mentioned previously, the elevator deflection, δ_e, may be viewed as a trim setting summed with a deflection from trim, so that

$$\delta_e = \delta_{e_T} + \hat{\delta}_e \qquad (5-20)$$

The problem now is to determine the trim setting appropriate to a given trim angle-of-attack. Because trim implies a moment balance of the aerodynamic forces about the vehicle's center-of-gravity, and the moments depend on the aerodynamic coefficients, the trim elevator is a function of three variables[*]: trim angle-of-attack, Mach number, and center-of-gravity location. Early attempts were made to model this dependence and thus provide an open-loop trim setting as a function of these variables; however, the modelling errors combined with the uncertainties in the independent variables resulted in a trim setting which was never sufficiently accurate for mistrim modelling, and, in turn, adequate closed-loop attitude control. The approach used here is a closed-loop determination of the proper trim setting, dependent on the activity of either the pitch ACPS logic or the transient elevator control law of the previous section.

Early in the entry, when the dynamic pressure is low, the trim setting has little effect on the attitude assumed by the vehicle. This is because the pitch ACPS logic maintains the desired angle-of-attack in the presence of what it views as a disturbance torque

---

[*]Reference to the trim data of Figures 3.2-21 and 3.2-22 of Reference 2 illustrates this dependence.

119

about the pitch axis. To illustrate this behavior, consider a situation in which the (fixed) elevator setting is positive (down) with respect to the desired trim setting. The mistrim torque will then be negative, forcing the vehicle to slowly pitch down. Shown in Figure 5-4 is the pitch ACPS phase-plane logic of Figure 5-2 in which a limit-cycle trajectory is shown consisting of a minimum impulse firing segment, A, and a parabolic disturbance torque "coast" segment, B. Clearly, this behavior requires a higher rate of fuel expenditure than the nominal zero disturbance torque design limit-cycle (with a straight line coast segment E), and thus it is appropriate to modify the elevator setting to better approximate trim.
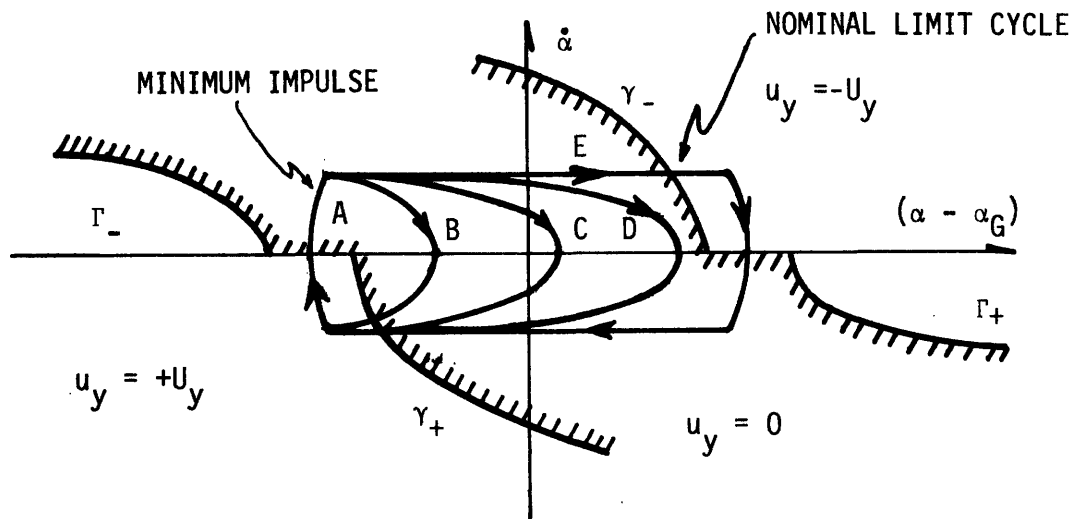
Figure 5-4: Effect of Elevator Mistrim on
Pitch Phase-Plane Trajectories

This is most easily accomplished by first recognizing from Figure 5-4 that as the elevator approaches the proper trim setting, the disturbance torque trajectories more closely approximate (trajectories B, C, and D) the design limit cycle, thus progressing

from an asymmetric jet firing history to the nominal two impulse limit cycle. This asymmetry in percentage on-time can then be used to trim the vehicle in the following manner: simply drive the elevator at a low rate proportional to the average pitch torque commanded by the phase-plane logic. In a sampled-data form, this is most readily accomplished by the following trim control law[*]:

$$\delta_{e_T} = (\delta_{e_T})_{old} + K_{\alpha_1} T \tilde{u}_y \qquad (\overline{q} \leq \overline{q}_1^*) \qquad (5-21)$$

where K_{α_1} is a design specified (negative) gain, T is the control law sample period, and $\tilde{u}_y$ is the normalized pitch ACPS command:

$$\tilde{u}_y \equiv u_y / U_y \qquad (5-22)$$

It should also be noted that (5-21) confines the trim law's region of applicability to low dynamic pressure operation, by introduction of the design specified parameter $\overline{q}_1^*$.

As the dynamic pressure increases and use is made of the elevator effectiveness by means of the transient control law of the previous section, the trim law may be tied more closely to the elevator deflection history. This is most readily accomplished by again slowly driving the elevator, this time at a rate proportional to the angle-of-attack error:

$$\dot{\delta}_{e_T} = \frac{K_{\alpha_2} \omega_d^2}{\overline{q} \xi_1} \alpha_e \qquad (5-23)$$

---

[*]Note that there is no explicit dependence on angle-of-attack mistrim; instead, the mistrim information is implicitly supplied through the activity of the pitch jets.

121

where K_{α_2} is a design specified (positive) gain. The choice of the gain structure for this trim law becomes clear by substitution of (5-19) and the Laplace transformed version of (5-23) into the expression specifying the elevator deflection (5-20), to yield:

$$\delta_e = \frac{1}{\xi_1}\left\{\frac{\omega_d^2}{\bar{q}}\left[\left(1+\frac{K_{\alpha_2}}{s}\right)\alpha_e - \frac{2\zeta_d}{\omega_d}\dot{\alpha}\right] - \xi_2\alpha_e\right\} \qquad (5-24)$$

Thus, the trim law of (5-23) is no more than the conventional parallel channel trim integrator acting on the attitude error. The simplest sampled-data approximation of (5-23) is given by:

$$\delta_{e_T} = (\delta_{e_T})_{old} + \frac{K_{\alpha_2}T\omega_d^2}{\bar{q}\xi_1}\alpha_e \qquad (\bar{q}>\bar{q}_1^*) \qquad (5-25)$$

and, as noted parenthetically, this is the elevator trim logic appropriate to the higher dynamic pressure regimes.

The elevator trim control law, specified by (5-21) and (5-25) may be conveniently summarized in block diagram form as shown in Figure 5-5. It should be noted that the digital integrator is "clamped" so as to preclude violation of the physical deflection limits by the trim elevator command.
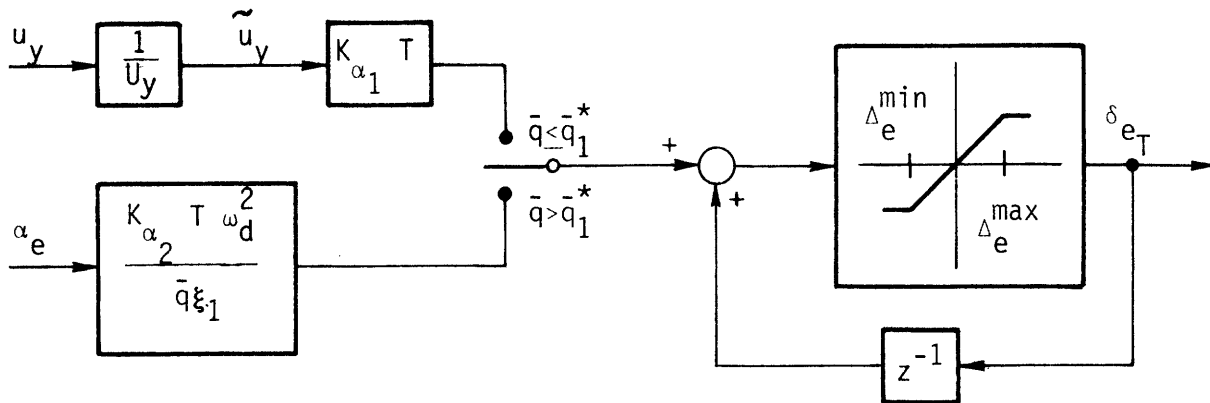
Figure 5-5: Elevator Trim Control

122

5.2 Lateral Control

This section derives both the ACPS and the ACSS control laws
used to control the vehicle's bank angle in response to commands
generated by the guidance system. In addition, inner-loop control
(i.e., inaccessible to guidance requests) is maintained over
sideslip deviations so as to provide the necessary lateral stability
required for lateral attitude control. As in the case of the longi-
tudinal controller synthesis, the lateral control law development is
strongly dependent on the simplified model of the short-period
dynamics described by (4-49) and (4-51) of Chapter 4. There are
three characteristics of this model especially pertinent to the
control synthesis effort. First, because of the relatively large
nominal angles-of-attack maintained by the longitudinal controller,
there is a considerable coupling of the sideslip and bank dynamics
due to the firing of either a roll or yaw ACPS jet. More important
to recognize, however, is that this dynamic coupling must eventually
be reflected by the lateral ACPS logic, and is, in the coupled
development of the roll and yaw control channels presented below.
The second point of interest concerns the somewhat peculiar lateral
aerodynamic characteristics of the vehicle. As discussed in the
previous chapter, a strong dihedral effect induces roll-reversal
tendencies when conventional bank control is attempted (as
illustrated in Figure 4-25); aggravating this situation is the lack of
rudder effectiveness throughout a large portion of the entry envelope.
The design trade is obvious: provide additional control authority
through the use of the ACPS or find a different (i.e., unconventional)
method of lateral control with a single surface. The latter choice is
illustrated by the aileron control law synthesis presented below.
The original motivation for this decision was the desire to minimize
ACPS fuel expenditures; even stronger support now comes from the
apparent uncertainty of ACPS utilization at high dynamic pressures
(see Reference 22). Both the uncertainty in the torques produced by

123

the ACPS at high dynamic pressures, and the possibility of adverse coupling between ACPS exhaust plumes and vehicle aerodynamic flow fields, strongly suggest caution in ACPS utilization during "atmospheric" flight. Insistence on jet activity in this regime may require extensive wind-tunnel testing to verify the feasibility of such a controls approach. The final point of interest concerning the lateral model is that of recognizing the lack of information regarding the relations between trim surface settings and the lateral trim of the vehicle. This is due to the assumption, early in the model development, of a lateral plane of symmetry, a condition readily violated by a small lateral displacement of the vehicle's center-of-gravity. This motivates the introduction of a lateral trim model in Section 5.2, upon which is based a surface trim law providing closed-loop compensation for center-of-gravity asymmetries.

The synthesis effort is split into separate equation set developments, one set for the roll and yaw ACPS jets (Section 5.2.1), and the other for the rudder and aileron (Section 5.2.2). Motivation for this separation is the same as in the longitudinal development: differing torque characteristics and simplicity of synthesis. Blending between the ACSS and ACPS control effectors is discussed in Section 5.3. Finally, as in the longitudinal channel, it must be noted that the aileron is simply an abstraction of the actual hardware involved, as are the roll and yaw jets. The discussion relating these control system defined variables to the actual torque producing effectors is to be found in Section 5.4.

5.2.1 Lateral ACPS Control

As mentioned earlier, the early entry environment precludes the effective use of the ACSS effectors for attitude control, thus implying a requirement for ACPS control, and, in turn, a vehicle dynamic model appropriate to this flight regime. As the discussion in Section 4.4.2 points out, all of the aerodynamic parameters of

the lateral model are negligible here, so that the vehicle can be viewed as a simple mass with specified inertial properties. Specifically, the model defined by (4-49) and (4-51) reduces to two control-coupled double integrator models:

$$s^2 \beta = u_x \sin\alpha_T - u_z \cos\alpha_T \qquad \text{(a)}$$

$$s^2 \phi_s = u_x \cos\alpha_T + u_z \sin\alpha_T \qquad \text{(b)}$$

(5-26)

The problem is now one of defining the control logic to specify u_x and u_z so as to drive the vehicle to a guidance specified bank attitude, ϕ_G, while maintaining a small sideslip to coordinate the turn. First, it should be mentioned that the above equation format is somewhat misleading in that it fails to emphasize the four-dimensional nature of the system. In fact, a very direct method of control law synthesis would be to solve the fuel-time optimal control problem, as was done for the pitch ACPS, but this time in the four-dimensional phase-space of the lateral attitude errors and rates. Two particular difficulties with this approach are worth noting. The obvious problem, of course, is the lack of visualization of the control law switch surfaces and their effects on the phase-space trajectory families; thus, the design advantage afforded by the two-dimensional phase-plane (as used in the pitch ACPS logic) is lost. A more subtle problem is associated with the increasing aerodynamic effects as the vehicle enters the atmosphere. It may be recalled that the aerodynamic induced disturbance torque seen by the pitch ACPS logic (due to elevator mistrim) is readily understood in the context of altered phase-plane trajectories; the lack of visualization in the phase-space clearly makes this a more difficult compensation exercise. More important to recognize, however, is the increased complexity of the lateral model as the aerodynamic effects become larger: disregarding surface

125

effectiveness, it should be recognized that not only does (5-26a) lose its double integrator character (due to a growing ω_β^2), but (5-26b) becomes strongly coupled into the sideslip dynamics (due to a growing K_β).

Instead of a four-dimensional control logic, the approach to be followed will use two coupled phase-plane logics, one specifying one ACPS channel to control bank, and the other specifying the remaining ACPS channel to control sideslip. The question then remains as to which ACPS channel, roll or yaw, is to be used for bank control. Clearly, the choice makes little difference for operation outside of the atmosphere, since whichever ACPS channel is chosen for bank control, the other can readily maintain small sideslips by coordinated firings as indicated by (5-26a). The control problem here is symmetric and provides no motivation for an ACPS channel assignment. For operation within the atmosphere, however, it is appropriate to recall the discussion of dihedral induced bank accelerations given in Section 4.4.3. By attempting to bank the vehicle via the roll jets, the geometrically produced sideslip, combined with the dihedral effect, work to produce an aerodynamically induced adverse roll torque, opposing the initial impulse. In contrast, as shown in Figure 4-24, by assigning the yaw channel to bank control, an inherent tendency towards turn coordination (i.e., maintenance of small sideslips) is provided for by the dihedral induced roll torque. Thus, the channel assignment to be used in the lateral ACPS control law syntheses to follow is: yaw jet control of bank attitude and roll jet control of sideslip.

5.2.1.1 Yaw ACPS Control

As mentioned above, the roll and yaw ACPS control laws are coupled. In particular, for this derivation it is assumed that the roll logic maintains small sideslip accelerations, so that from (5-26a),

$$\dot{\beta} = u_x \sin\alpha_T - u_z \cos\alpha_T \approx 0 \qquad (5\text{-}27)$$

The approximate equality is in recognition of the fact that the yaw-to-roll acceleration ratio (U_z/U_x) will not normally equal the tangent of the trim angle-of-attack, and, in fact, (5-27) should be viewed more as a specification of the average roll and yaw ACPS torques required to maintain a small sideslip acceleration. Substitution of this relation into the simplified bank dynamics model of (5-26b) then allows for the elimination of the roll jet torque contribution:

$$\ddot{\phi}_S \sin\alpha_T = u_z \qquad (5\text{-}28a)$$

Now, if in addition to the satisfaction of (5-27), it is assumed that the sideslip rate, $\dot{\beta}$, is maintained near zero, through the action of the roll jets, then it can be seen from either the appropriately simplified version of (4-39a) or from the definition of $\dot{\phi}_S$ given in Figure 4-6, that:

$$\dot{\phi}_S \sin\alpha_T = r \qquad (5\text{-}28b)$$

where it may be recalled that r is the vehicle's body yaw rate. Thus, letting

$$\epsilon_\phi \equiv (\phi_S - \phi_G)\sin\alpha_T \qquad (5\text{-}29a)$$

where ϕ_G is the guidance commanded bank angle, and defining

$$(\epsilon_1, \epsilon_2) \equiv (\epsilon_\phi, r) \qquad (5\text{-}29b)$$

then, from (5-28) it is seen that the previously defined double integrator dynamics of (5-3) are applicable, where, in this particular case the control variable u is taken as the yaw control variable u_z, which is symmetrically bounded by the available ACPS acceleration, U_z.

127

Thus, the phase-plane logic of Figure 5-2, used previously for the pitch jets, may be applied to the yaw ACPS control problem, with the appropriate redefinition of the switch curve parameters:

$$(u, U) \equiv (u_z, U_z) \qquad \text{(c)}$$

$$(\delta_1, \delta_2) \equiv (\delta_{\phi 1}, \delta_{\phi 2}) \qquad \text{(d)} \qquad (5\text{-}29)$$

$$\sigma \equiv \sigma_\phi \qquad \text{(e)}$$

As before, it should be noted that deadband size and fuel-time weighting are specified through the choice of the design parameters $(\delta_{\phi 1}, \delta_{\phi 2})$ and σ_ϕ, respectively.

5.2.1.2 Roll ACPS Control

The above yaw jet logic requires that the roll jets maintain sideslip acceleration and rate near zero; to accomplish this effectively, it is necessary to account for the coupling torque due to yaw jet activity, as modelled by (5-26a). Consider first the situation in which the yaw jets are firing ($u_z \neq 0$). Shown in Figure 5-6 are the two phase-plane trajectory "families" which result when the yaw jet command is positive ($u_z = U_z$) and when the roll control variable u_x is either zero or at its maximum positive value ($u_x = U_x$). The derivation of these curves is entirely parallel to that given in Appendix E; the equations defining these curves follow directly from the specified dynamics of (5-26a):

$$\left. \begin{aligned} \beta &= \beta_0 - \frac{1}{2U_1} \dot{\beta}^2 \quad (u_x = 0) \\[2em] \beta &= \beta_0 + \frac{1}{2U_2} \dot{\beta}^2 \quad (u_x = U_x) \end{aligned} \right\} \quad (u_z = U_z) \qquad (5\text{-}30)$$

where β_0 is arbitrary and where the effective ACPS accelerations U_1 and U_2 are defined by:
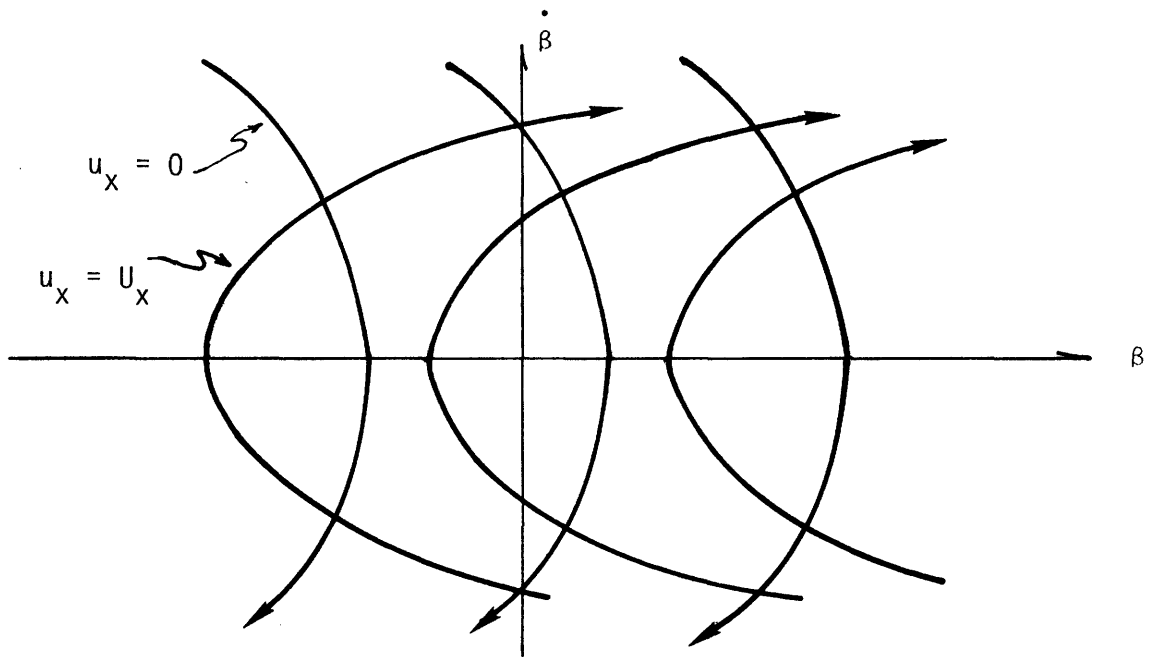
Figure 5-6. Sideslip Phase-Plane Trajectories when $u_z = U_z$.
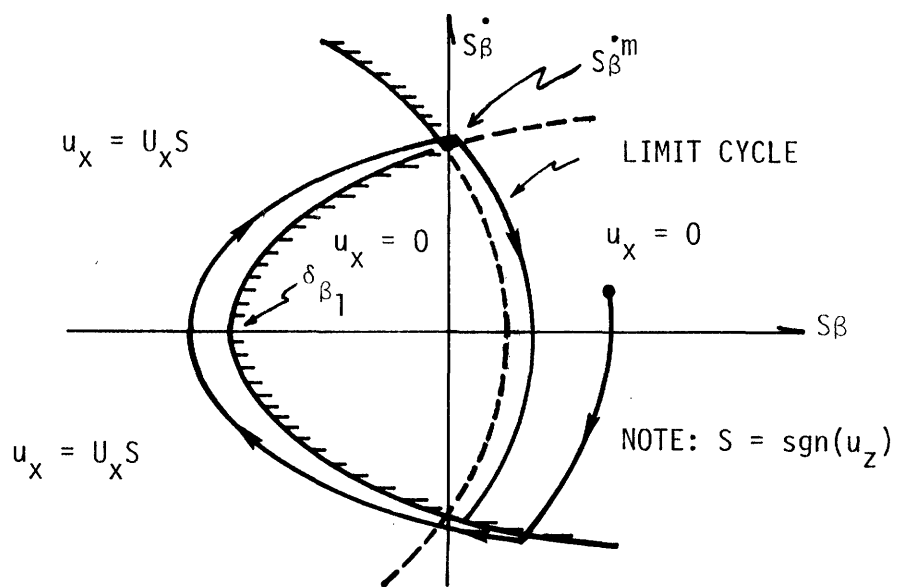
Figure 5-7. Roll ACPS Control Logic when $u_z \neq 0$.

$$U_1 \equiv U_z \cos\alpha_T$$

$$U_2 \equiv U_x \sin\alpha_T - U_z \cos\alpha_T$$

(5-31a)

It should be noted that basic controllability considerations require that U_2 be positive (i.e., that the roll acceleration U_x is large enough to coordinate a yaw jet induced bank maneuver); this is the case during the early portion of the entry, as may be seen from the nominal angle-of-attack history of Figure 2-4 and the relative magnitudes of the available roll and yaw ACPS acceleration levels (see Table 2-5 of Chapter 2)[*].

It may be noted from Figure 5-6 that a stable limit cycle trajectory, during which u_x is alternately positive and zero, may be constructed by choosing any two complementary curves and performing the appropriate roll jet switching at their two intersections. In fact, a control logic may be readily constructed to drive the vehicle state to this limit cycle by defining a switch curve composed of segments of these two trajectory curves. This phase-plane logic defining u_x when $u_z = U_z$ is shown in Figure 5-7 (note that S = 1), along with a typical controlled trajectory exhibiting switch curve overshoot due to sampling. By defining the following variable,

$$S \equiv \text{sgn}(u_z)$$

(5-31b)

then this phase plane logic of Figure 5-7 is also applicable to the situation in which the yaw jet command is negative, or $u_z = -U_z$. The definition of the switch curve μ follows directly from (5-30) and is given by:

---

[*]This is also clear from the acceleration levels of thruster "groups" given later in this chapter in Table 5-1.

$$\mu : S\beta \doteq \frac{1}{2U_1}[(\dot{\beta}^m)^2 - \dot{\beta}^2] \text{ if } S\dot{\beta} > \dot{\beta}^m$$

$$(5\text{-}31c)$$

$$= -\frac{1}{2U_2}[(\dot{\beta}^m)^2 - \dot{\beta}^2] \text{ if } S\dot{\beta} \le \dot{\beta}^m$$

where the maximum maneuver rate $\dot{\beta}^m$ is given by

$$\dot{\beta}^m \equiv \sqrt{2U_2 {}^\delta\beta_1} \qquad\qquad (5\text{-}31d)$$

where the deadband parameter δ_{β_1} is used to couple this logic with the logic to be introduced presently.

It is now appropriate to consider the case when the yaw ACPS is inactive. With no yaw jet commands then $u_x = 0$, and the sideslip dynamics of (5-26a) simplify to the single control input double integrator model previously introduced by (5-3), with the following definitions:

$$(\epsilon_1, \epsilon_2) \equiv (\beta, \dot{\beta}) \qquad\qquad (5\text{-}32a)$$

$$(u, U) \equiv (u_x, U_x \sin\alpha_T) \qquad\qquad (5\text{-}32b)$$

Thus, the parabolic phase-plane logic of Figure 5-2 is once again appropriate, where the switch curve parameters are given by:

$$(\delta_1, \delta_2) \equiv ({}^\delta\beta_1, {}^\delta\beta_2) \qquad\qquad (5\text{-}32c)$$

$$\sigma \equiv \sigma_\beta \qquad\qquad (5\text{-}32d)$$

As before, it should be noted that deadband size and fuel-time weighting are specified through the use of the design parameters $({}^\delta\beta_1, {}^\delta\beta_2)$ and σ_β, respectively.

As the dynamic pressure increases during the entry, it is appropriate to take advantage of the aerodynamic influence on sideslip behavior. As noted in Section 4.4.3, dynamic stability in sideslip is provided for by the dynamic derivative C'_{n_β}, and, as illustrated in Figure 4-22, the sideslip dynamics may be modelled as a simple undamped oscillator. Assuming no yaw jet activity and no surface control effectiveness, the simplified sideslip dynamic model of (4-49) thus reduces to:

$$(s^2 + \omega_\beta^2)\beta = u_x \sin\alpha_T \qquad (5\text{-}33)$$

Thus, rather than attempt to provide direct control over sideslip attitude, it is more economical to simply rate damp the sideslip oscillations by the proper phasing of the roll jet firings. This is most easily accomplished by the deadbanded relay logic of Figure 5-8, where the use of the deadband parameter $\dot{\beta}^m$ assures consistency with the above described control laws, and the dynamic pressure condition $(\bar{q} \geq \bar{q}_3)$ is specified to ensure adequate aerodynamic stability. This abdication of attitude control in the sideslip channel will be discussed further in Section 5.2.2, during the derivation of the lateral trim law.

Fig. 5-8   Roll ACPS Control Logic when $\bar{q} \geq \bar{q}_3$ and $u_z = 0$
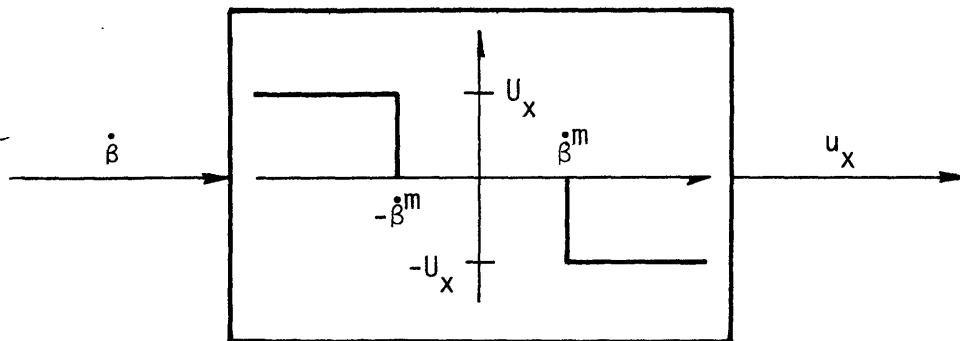
To summarize the three-mode roll jet logic, then, it may be noted that the first mode is used during yaw jet firings ($u_z \neq 0$) and is defined by Figure 5-7 and (5-31). The second mode is used when there is no yaw jet activity and the dynamic pressure is below $\bar{q}_3$, and is defined by Figure 5-2 and (5-32). The third mode is used when there is no yaw jet activity and the dynamic pressure equals or exceeds $\bar{q}_3$, and is defined by Figure 5-8 .

5.2.2 Lateral ACSS Control

In keeping with the separation of the ACPS and ACSS control law synthesis, this section assumes that the aileron and rudder provide all of the control authority for the lateral channel, and that no control is obtained through the use of the roll and yaw ACPS jets. Thus, the simplified model of the lateral dynamics defined by (4-49) and (4-51) in Section 4.4 reduces to:

$$(s^2 + 2\zeta_\beta \omega_\beta s + \omega_\beta^2)\beta + K_\phi s\phi_s = K_{\beta_{\delta_r}} \hat{\delta}_r + K_{\beta_{\delta_a}} \hat{\delta}_a \quad \text{(a)}$$

$$\text{(5-34)}$$

$$K_\beta \beta + (s + 1/\tau_\phi)s\phi_s = K_{\phi_{\delta_r}} \hat{\delta}_r + K_{\phi_{\delta_a}} \hat{\delta}_a \quad \text{(b)}$$

where the model parameters are defined by (4-50) and (4-52). As discussed in Section 4.4.2 both the sideslip damping ratio, ζ_β, and the bank-into-sideslip coupling term, K_ϕ, may be neglected for synthesis purposes, due to their negligible effect on the vehicle's sideslip response characteristics; the sideslip dynamics are thus modelled by a simple control coupled undamped oscillator. As further discussed in the same section, the bank dynamics may be similarly simplified by neglecting the relatively long bank time-constant τ_ϕ ; the bank dynamics are thus modelled by a control coupled double integrator with strong sideslip coupling. The resulting lateral model is shown in block diagram form in Figure 4-22, and the equation base of (5-34) is reduced to the following:

133

$$(s^2 + \omega_\beta^2)\beta = K_{\beta_{\delta_r}} \hat{\delta}_r + K_{\beta_{\delta_a}} \hat{\delta}_a \qquad \text{(a)}$$

$$K_\beta \beta + s^2 \phi_s = K_{\phi_{\delta_r}} \hat{\delta}_r + K_{\phi_{\delta_a}} \hat{\delta}_a \qquad \text{(b)}$$

(5-35)

As in the case of the longitudinal model, it should be noted that the above equation set provides no information concerning the required trim surface deflections to maintain a given lateral trim attitude induced by vehicle asymmetries. This aspect of the control problem thus motivates the introduction of a lateral trim model in Section 5.2.2.2 and the subsequent derivation of an appropriate aileron trim control law.

An additional feature in common with the longitudinal control law synthesis is the neglect of the actuator dynamics in the derivations presented here. As may be seen from the natural frequency history of Figure 4-12, the sideslip dynamics are approximately 40 times slower than an actuator with a time-constant of 0.1 second (compare $2\pi/(\omega_\beta)_{max}$ with τ_{act}), thus justifying, from a frequency separation point of view, this simplified view. However, the rate-limiting characteristics of the actuators are not so easy to ignore, since they clearly show their presence by their effect on the lateral control system performance during the latter part of the entry (see discussions in Sections 5.2.2.1 and 7.3.3). Rather than attempt to introduce a model of this non-linear rate limit into the simplified dynamics of (5-35), the approach taken below is one of providing a compensation logic to lower the rates at which the surfaces are driven, thus minimizing the opportunities for the rate limits to take effect. This then maintains the validity of the linear model of (5-35), where the surface deflections are taken as the commanded deflections, for the lateral control law synthesis.

134

As discussed in Section 4.4.2, the rudder is not effective until relatively late in the entry, thus motivating an "aileron-alone" design philosophy for lateral control at sufficiently high dynamic pressures. As will be seen, this is in contrast to the situation during the latter part of the entry, when the aileron begins to lose its effectiveness in controlling the lateral dynamics, while the rudder gains in its capability of providing control authority for maintenance of desired sideslip and bank attitude. This then motivates the sequence of the design synthesis presented below. Section 5.2.2.1 considers the general problem of vehicle controllability with the lateral surfaces and provides the motivation for the introduction of the rudder as it becomes effective. Section 5.2.2.2 then derives the aileron control law appropriate to the assumption of no rudder effectiveness, but in a format compatible with the eventual introduction of the rudder as a control effector. Finally, Section 5.2.2.3 defines the rudder control law to be used in conjunction with the aileron.

5.2.2.1 Lateral Controllability

Prior to the derivation of the surface control laws, it is appropriate to consider some of the aspects and implications of lateral control with the aileron and rudder, with the particular goal of providing a workable control strategy for their proper utilization. As discussed earlier, the low dynamic pressures of early entry preclude the effective use of the surfaces; however, with the eventual increase of dynamic pressure, the aileron clearly displays a fair amount of control authority, and as the Mach number decreases, the rudder does also. This section will investigate the controllability properties during this "aerodynamic" regime.

This analysis is based on the formal definition of (Kalman) controllability of a linear time-invariant system. Briefly, given the following such system of order n:

$$\dot{\underline{x}} = F\underline{x} + G\underline{u} \qquad\qquad (5\text{-}36)$$

then the system is said to be controllable (i.g., loosely speaking, can be driven by an unbounded control $\underline{u}$ from a state $\underline{x}_o$ to some other state $\underline{x}_1$, where the initial and final states are arbitrary, as is the (positive) travel time) if and only if the rank of the following matrix equals the dimension, n, of the state:

$$C = \left[G, FG, F^2G, \ldots, F^{n-1}G \right] \qquad\qquad (5\text{-}37)$$

It should be noted that this definition provides no information concerning system behavior between states, and thus no implications are made on the finer aspects of performance. What is clear, however, is that if the system is uncontrollable by the above definition, then none of the conventional performance requirements (e.g., step response, frequency response, etc.) will be met.

The particular system of interest is the simplified lateral model of (5-35) in which only the aileron and rudder provide the control torques. By rewriting this equation set in a format compatible with (5-36), the properties of the control matrix C of (5-37) may be examined so as to determine the controllability of the lateral dynamics. The derivation details are the subject of Appendix F; only the pertinent results are presented here. Specifically, it is shown that the lateral dynamics are controllable with the surfaces if and only if at least one of the following three conditions (from (F-19)) are met:

$$\pi_o \neq 0, \text{ or} \qquad\qquad \text{(a)}$$

$$C'_{n_{\delta_a}} \neq 0 \text{ and } \pi_1 \neq 0, \text{ or} \qquad\qquad \text{(b)} \qquad (5\text{-}38)$$

$$C'_{n_{\delta_r}} \neq 0 \text{ and } \pi_2 \neq 0 \qquad\qquad \text{(c)}$$

136

where the dynamic derivatives $C'_{n_{\delta_a}}$ and $C'_{n_{\delta_r}}$ have been introduced earlier and the controllability coefficients π_i are defined (from (F-20)) as functions of the aerodynamic coefficients:

$$\pi_0 = C_{n_{\delta_r}} C_{\ell_{\delta_a}} - C_{\ell_{\delta_r}} C_{n_{\delta_a}} \qquad \text{(a)}$$

$$\pi_1 = C_{n_\beta} C_{\ell_{\delta_a}} - C_{\ell_\beta} C_{n_{\delta_a}} \qquad \text{(b)} \qquad \text{(5-39)}$$

$$\pi_2 = C_{n_\beta} C_{\ell_{\delta_r}} - C_{\ell_\beta} C_{n_{\delta_r}} \qquad \text{(c)}$$

There are three important aspects of these conditions which should be noted. First, from the structure of (5-38) the controllability conditions can be very neatly correlated with available surface control authority. The first condition, $\pi_0 \neq 0$, implies that the surfaces must provide independent body-axis authority in a non-degenerate manner. This is seen by recognizing that the "control matrix" of (5-35), given by:

$$\begin{bmatrix} K_{\beta \delta_r} & K_{\beta \delta_a} \\ K_{\phi \delta_r} & K_{\phi \delta_a} \end{bmatrix}$$

has a non-zero determinant only if $\pi_0 \neq 0$ (see model parameter definition of (4-50) and (4-52)). It is appropriate to mention at this point that the non-degeneracy of the two-axis control authority is the basis for "conventional" lateral control, in which the aileron controls bank and the rudder controls sideslip. Thus, if one of the surfaces is ineffective in both body axes, then π_0 will be zero, violating condition (5-38a). In this situation the implication is, of course, that either of the controllability conditions (5-38b) or (5-38c) must be met for successful control of the lateral dynamics. The correlation of these two conditions should

137

also be clear from the vehicle model: (5-38b) and (5-38c) respectively indicate a capability of "aileron-alone" and "rudder-alone" control of the vehicle. For example, in the "aileron-alone" case, the first condition of (5-38b) implies that the dynamic derivative $C'_{n_{\delta a}}$ be non-zero, in turn implying that the aileron effectiveness in sideslip, $K_{\beta_{\delta a}}$, be non-zero (see definition given in (4-50)). By referring to the model dynamics of (5-35a), it is seen that, in the absence of rudder utilization, the only means of "accessing" the sideslip channel is through $K_{\beta_{\delta a}}$; clearly, then if $C'_{n_{\delta a}}$ is zero, sideslip is uncontrollable. The necessity of the second condition of (5-38b) is readily seen when the transfer function between bank angle and aileron deflection is examined. In the absence of rudder utilization, the lateral model of (5-35) may be used to obtain the desired transfer function relation:

$$\frac{\phi_s}{\hat{\delta}_a} = \frac{K_{\phi_{\delta a}}(s^2 - \omega_\phi^2)}{s^2(s^2 + \omega_\beta^2)} \tag{5-40}$$

where the non-minimum phase nature of the system is determined by the following (normally positive) defined model parameter:

$$\omega_\phi^2 \equiv K_\beta \left(\frac{K_{\beta_{\delta a}}}{K_{\phi_{\delta a}}}\right) - \omega_\beta^2 \qquad (K_{\phi_{\delta a}} \neq 0) \tag{5-41}$$

From the model parameter definitions given in (4-50) and (4-52), and the above definition of π_1, it is seen that ω_ϕ^2 is zero if π_1 is. This, in turn, implies through (5-40), a degeneration of the bank dynamics to a simple oscillator identical (except for steady-state gain) to that of the sideslip channel. Thus, the bank attitude becomes an unchangeable (by control means) linear function of the sideslip. In other words, for the system to be non-degenerate and

138

allow independent control in both bank and sideslip, π_1 must be non-zero. Thus, for "aileron-alone" control, both conditions of (5-38b) must be met; an entirely analogous argument may be made for the "rudder-alone" condition given by (5-38c).

The second aspect of the above controllability conditions pertains directly to their utility in control system design. Shown in Appendix F are contour plots of the controllability coefficients of (5-38); Figure 5-9 through 5-11 repeat three of these figures showing the two-dimensional dependence of π_o, π_1, and $C'_{n_{\delta a}}$ on Mach number and trim angle-of-attack. One of the obvious points to be noted is the distinct lack of zero value contours, implying, by (5-38), that the vehicle is completely controllable aerodynamically during the latter part of the entry (below Mach 10). What must be recalled, however, is that the original definition of controllability allowed for unbounded control magnitudes, clearly in contradiction to the actual situation. To see how this affects the interpretation of the controllability criteria, consider the limiting behavior of $C'_{n_{\delta a}}$ shown in Figure 5-10. As the vehicle approaches the low Mach number regime, the magnitude of $C'_{n_{\delta a}}$ gradually approaches zero, indicating a diminishing amount of aileron effectiveness in the sideslip channel. In order to maintain closed-loop system responsiveness, any control system using aileron for sideslip control will naturally have larger feedback gains to compensate for this loss of effectiveness. However, the direct implication of larger gains is a greater tendency to violate the rate and position limits of the actuators responding to the aileron deflection commands, thus introducing some very fundamental non-linear effects into the overall system dynamics. Recognizing that the controllability criteria are based on the assumption of system linearity, the absolute significance of the null value of $C'_{n_{\delta a}}$ becomes questionable. This argument can be made, of course, for the other controllability coefficients; the point is, however, that the precise controllability
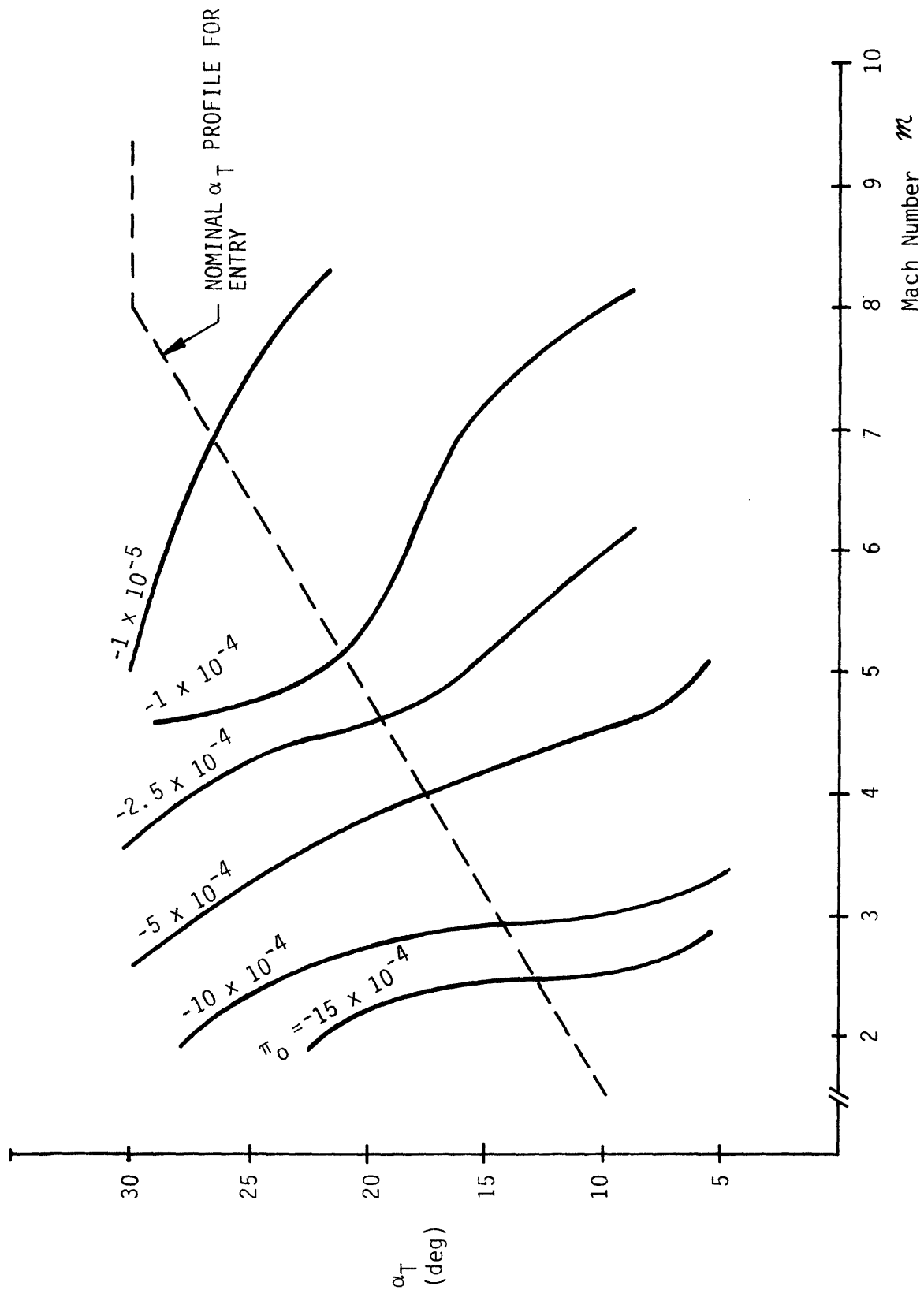
139

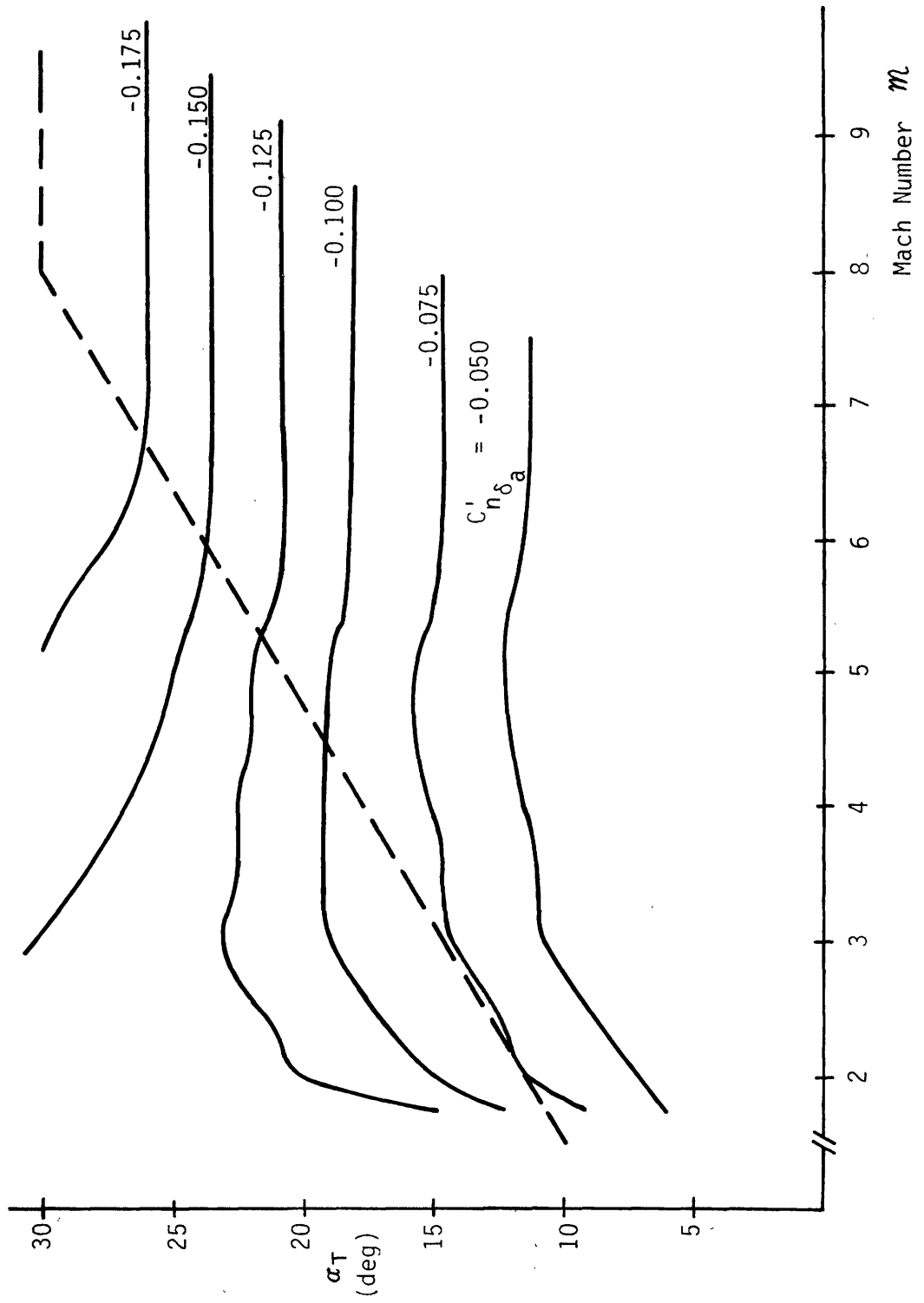Figure 5-9. Contour Plot for π_0 ("conventional" control).

140

Figure 5-10. Contour Plot for $C'_{n_{\delta_a}}$ ("aileron-alone" control).

141
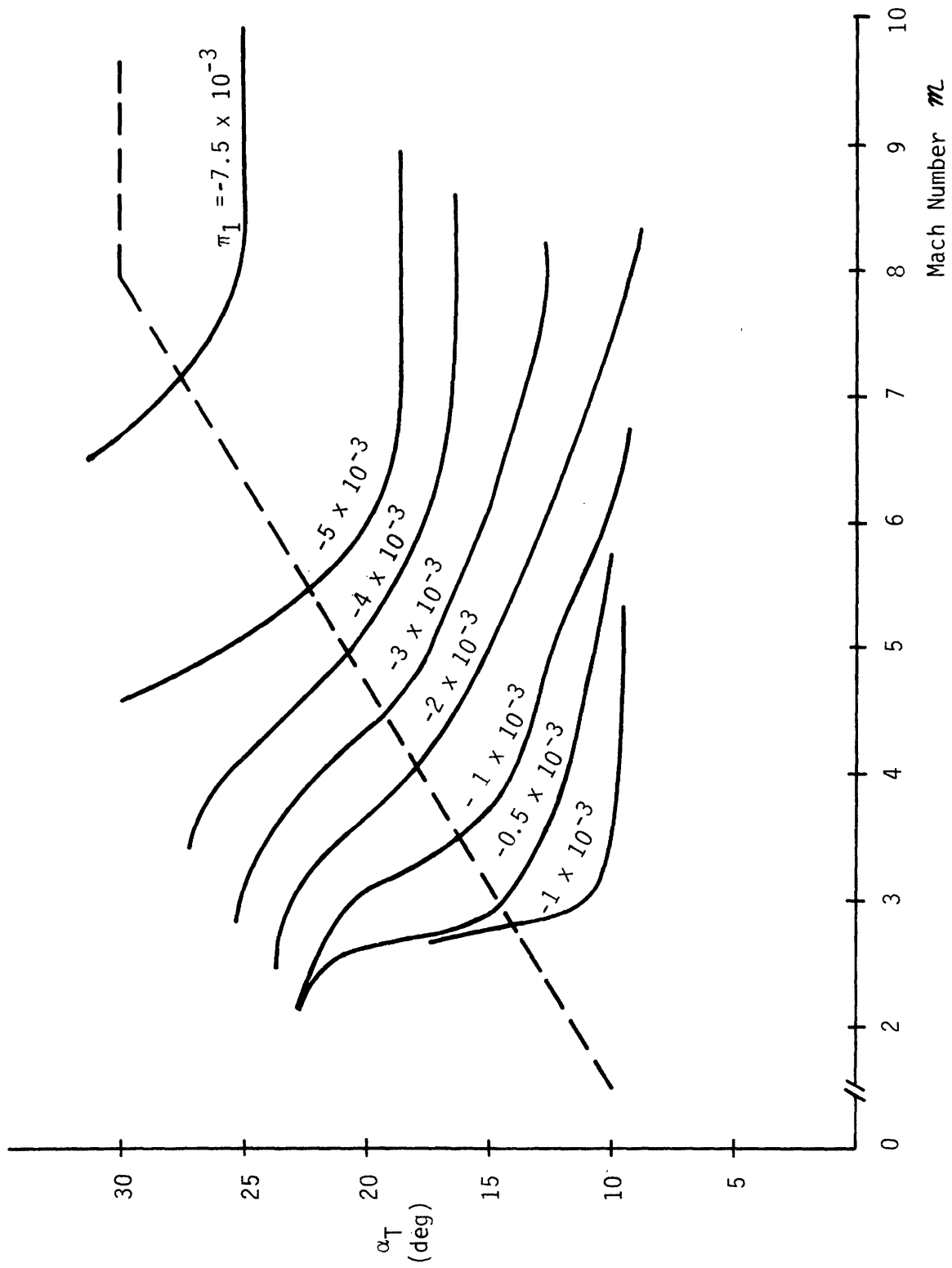
Figure 5-11. Contour Plot for π_1 ("aileron-alone" control).

142

specifications of (5-38) must not be taken literally, and instead should be viewed as limits, which when approached, will result in a loss of controllability. The question immediately raised then is: how near to the zero value contour must the vehicle be for loss of control to occur? Unfortunately, due to the surface non-linearities, this becomes an input/initial condition dependent problem, since the magnitudes of the commanded deflections depend not only on the control law gains, but on the error signals input to the control law. Thus, the question cannot be answered in general as was done for the linear system, since non-linear controllability is clearly a more broad-based issue.

The above discussion is not meant to imply the uselessness of (5-38) and the associated control contour plots. On the contrary, the plots provide fundamental information on controllability trends, especially if (5-38) is interpreted more loosely as the following strategy: avoid control configurations (i.e., aileron/rudder, aileron-alone, and rudder-alone) whose associated controllability coefficients have small magnitudes*. The control contours then provide a spatial aspect to the problem, indicating where in the Mach/alpha envelope a particular control configuration is most appropriate. Thus, referring to the three contour plots presented here, it should be quite evident that rudder/aileron or "conventional" control (Figure 5-9) strongly complements aileron-alone control (Figures 5-10 and 5-11). As the vehicle progresses down the nominal α_T-profile, both $C'_{n_{\delta_a}}$ and π_1 approach zero, indicating the increasing inappropriateness of attempting to control the vehicle with only the aileron. Simultaneously, however, the trajectory intersects contours of increasing (in magnitude) π_o, thus strongly favoring a combined rudder/aileron strategy (i.e., conventional control). Thus, assuming that both techniques are capable of

---

*An attempt at quantitatively defining "small" is deferred until the simulation results of Section 7.2.2 are discussed.

meeting the performance specifications. the linear controllability criteria strongly support aileron-alone control during early entry, with a switch into conventional control at some later point down the trajectory. Before discussing one of the design (as opposed to performance) implications of this switching, it should be noted that the rudder-only controllability criteria ($C'_{n_{\delta r}}$ and π_2) have been ignored in the above discussion. Referring to the appropriate contour plots shown in Figures F-4 and F-5, it is seen that the contour gradients generally parallel those of Figure 5-9, associated with the conventional controllability coefficient π_o. Clearly, the indications are that rudder-only control is also feasible at the low end of the entry; however, given the choice between rudder-alone control and rudder/aileron control, the capability for conventional performance derived from the latter system clearly favors that approach. Thus, the discussion to follow will center on aileron-alone and conventional control only.

It is now appropriate to consider one of the design implications of switching between aileron-alone control and conventional rudder/aileron control. From the above discussion concerning actuator non-linearities, it should be clear that loss of control while using a particular technique will occur at some point prior to reaching the associated zero-contour; it is hypothesized here that given the same initial conditions and guidance commands to the control system, then loss of control will occur along one special non-zero value controllability contour. This situation is illustrated in Figure 5-12, with three contours, one chosen from each of the three preceeding figures. If it is supposed that for successful rudder/aileron control that π_o have a magnitude greater than some π_o^* (here illustrated by $\pi_o^* = -0.001$), then rudder/aileron control
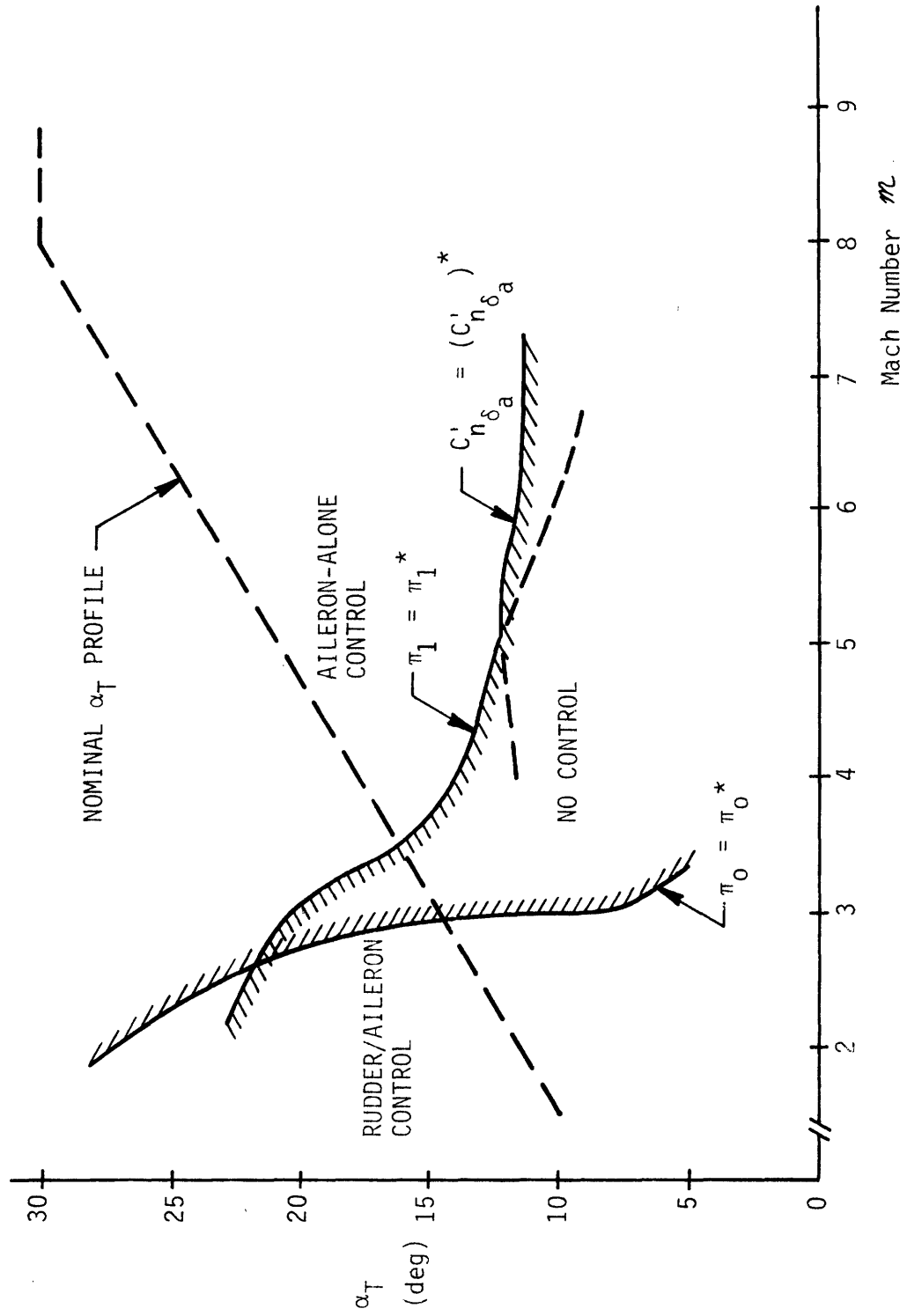
Figure 5-12. Illustrative Example of Possible Controllability Regions.

will be restricted to the region of the Mach-alpha plane to the left

of the π_o^* contour shown.* Similarly, requiring $C'_{n_{\delta a}}$ and π_1 to have

respective magnitudes greater than $(C'_{n_{\delta a}})^*$ and π_1^* (here illustrated

by $(C'_{n_{\delta a}})^* = -0.050$ and $\pi_1^* = -0.001$), then aileron-alone control

will be restricted to the region of the Mach-alpha plane above the

composite contour shown. No inferences are to be made concerning

the particular contour values chosen; what should be most evident,

however, is the possible existence of a region, through which the

vehicle must pass, and throughout which neither control technique

is feasible.

Clearly it is premature at this point to suggest that there will

exist a requirement for ACPS augmentation along some portion of

the late entry trajectory (as implied by Figure 5-12); however, the

possibility of such a situation provides strong motivation for examining

means of ensuring the existence of an overlap region in the Mach-

alpha plane in which both control approaches are feasible. The

control law synthesis presented later will not be concerned with

providing conventional rudder/aileron control, as this design

exercise is felt to be in the domain of the cruise phase autopilot

designer, concerned with subsonic and low supersonic flight regimes.

Thus, no attempt will be made to "shift" the rudder/aileron control-

lability contours, through suitable augmentation, in the direction

which maximizes the overlap with the aileron-alone region. Instead,

the effort will be focused on providing aileron augmentation which

tends to increase the region of aileron-alone control feasibility.

The most obvious choice of effector for aileron augmentation,

from the results presented in Appendix F and the discussion above,

is the rudder. Rather than attempt to use the rudder as an

independent state controller, as is often done in conventional designs

(e. g., a yaw damper loop), it is appropriate to consider the implica-

tions of a much more mundane technique: constant crossfeed drive

*R. Goss of CSDL is currently investigating the correlation between
π_o contours and the upper boundary of conventional control, in an
attempt to properly specify π_o^*.

from the aileron to the rudder, expressed simply by

$$\hat{\delta}_r = C_r \hat{\delta}_a \qquad (5\text{-}42)$$

It should be recognized that this is a degenerate case of rudder/ aileron control, but the distinction between this and conventional independent channel control should be clear, especially when the simplified lateral model is considered. By defining the augmented aileron effectiveness parameters as follows,

$$\tilde{K}_{\beta_{\delta_a}} = K_{\beta_{\delta_a}} + C_r K_{\beta_{\delta_r}} \qquad (a)$$

$$\qquad (5\text{-}43)$$

$$\tilde{K}_{\phi_{\delta_a}} = K_{\phi_{\delta_a}} + C_r K_{\phi_{\delta_r}} \qquad (b)$$

then, the use of (5-40) transforms the lateral model of (5-35) into the following single control input system:

$$(s^2 + \omega_\beta^2)\beta = \tilde{K}_{\beta_{\delta_a}} \hat{\delta}_a \qquad (a)$$

$$\qquad (5\text{-}44)$$

$$K_\beta \beta + s^2 \phi_s = \tilde{K}_{\phi_{\delta_a}} \hat{\delta}_a \qquad (b)$$

It is now of interest to see what effect the rudder crossfeed has on controllability. As discussed in the appendix, this lateral model is simply a special case of the one considered previously; the controllability conditions are accordingly specialized. Thus, from (F-24), the formal controllability requirements specify that an aileron with rudder augment control configuration will maintain vehicle control (in the atmosphere) if and only if the following condition is met:

147

$$\widetilde{C}'_{n_{\delta_a}} \neq 0 \quad \underline{\text{and}} \quad \widetilde{\pi}_1 \neq 0 \tag{5-45}$$

where the use of the tilda continues to indicate augmentation in the following supporting definitions repeated from (F-25) and (F-26):

$$\widetilde{\pi}_1 \equiv C_{n_\beta} \widetilde{C}_{\ell_{\delta_a}} - C_{\ell_\beta} \widetilde{C}_{n_{\delta_a}} \tag{5-46}$$

$$\widetilde{C}'_{n_{\delta_a}} \equiv C'_{n_{\delta_a}} + C_r C'_{n_{\delta_r}} \tag{a}$$

$$\widetilde{C}_{\ell_{\delta_a}} \equiv C_{\ell_{\delta_a}} + C_r C_{\ell_{\delta_r}} \tag{b} \qquad (5\text{-}47)$$

$$\widetilde{C}_{n_{\delta_a}} \equiv C_{n_{\delta_a}} + C_r C_{n_{\delta_r}} \tag{c}$$

It should be recognized that the above condition can be directly correlated with the aileron-alone condition of (5-38b) given above, with the proper substitution of augmented coefficients. Also, as before, the actuator induced non-linearities must be considered in a realistic controllability assessment, so that the condition expressed by (5-45) should be viewed as one to avoid approaching, where "nearness", unfortunately, is not well-defined.[*]

Presented in Figures 5-13 and 5-14 are contour plots of the controllability coefficients $\widetilde{C}'_{n_{\delta_a}}$ and $\widetilde{\pi}_1$, repeated from the figures

---

[*]Some insight into a definition of the "critical" contours is given by the discussion of simulation results in Section 7.2.2.
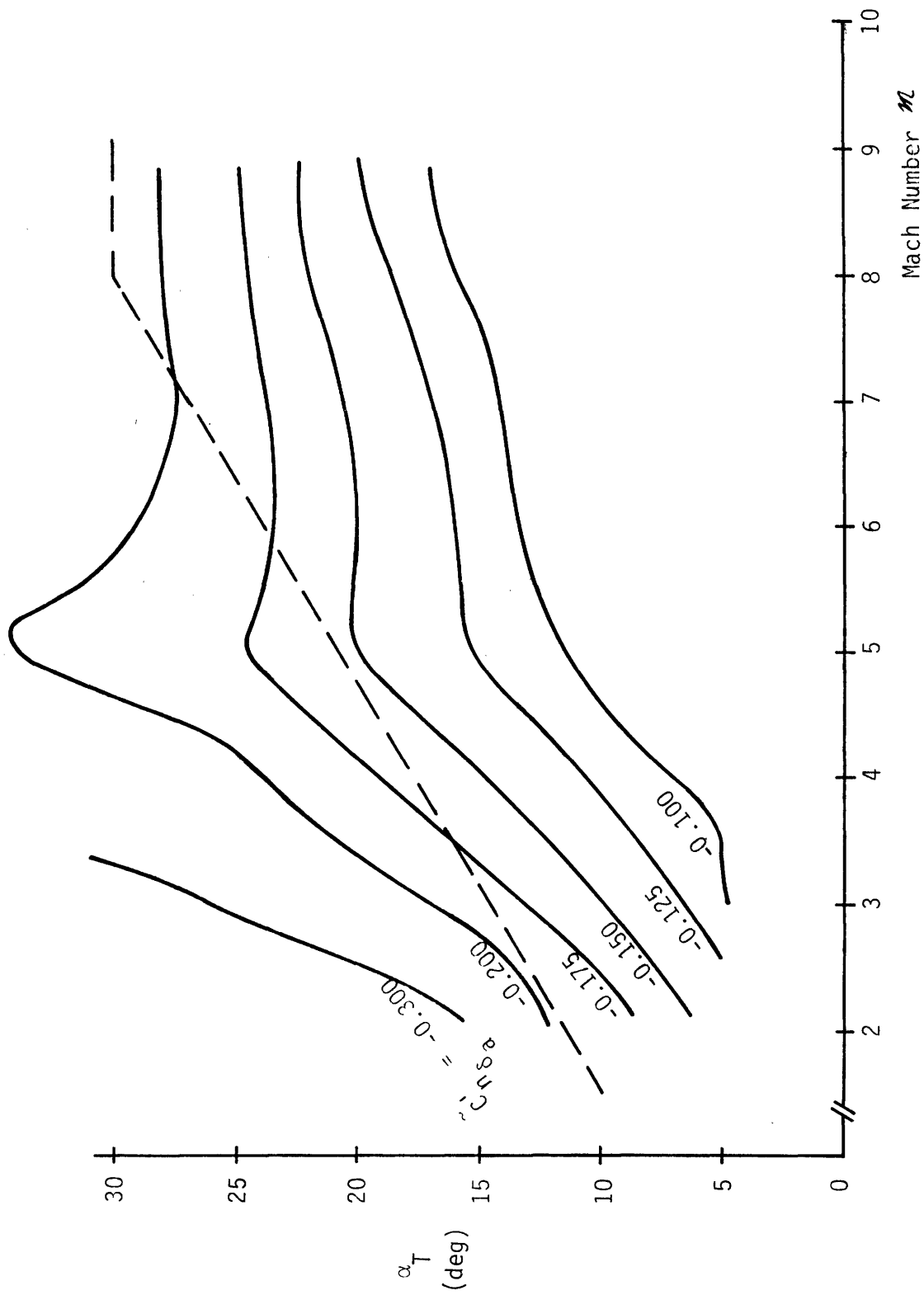
Figure 5-13. Contour Plot for $\tilde{C}'_{n_{\delta_a}}$ (aileron with rudder augment; $C_r = 2$)
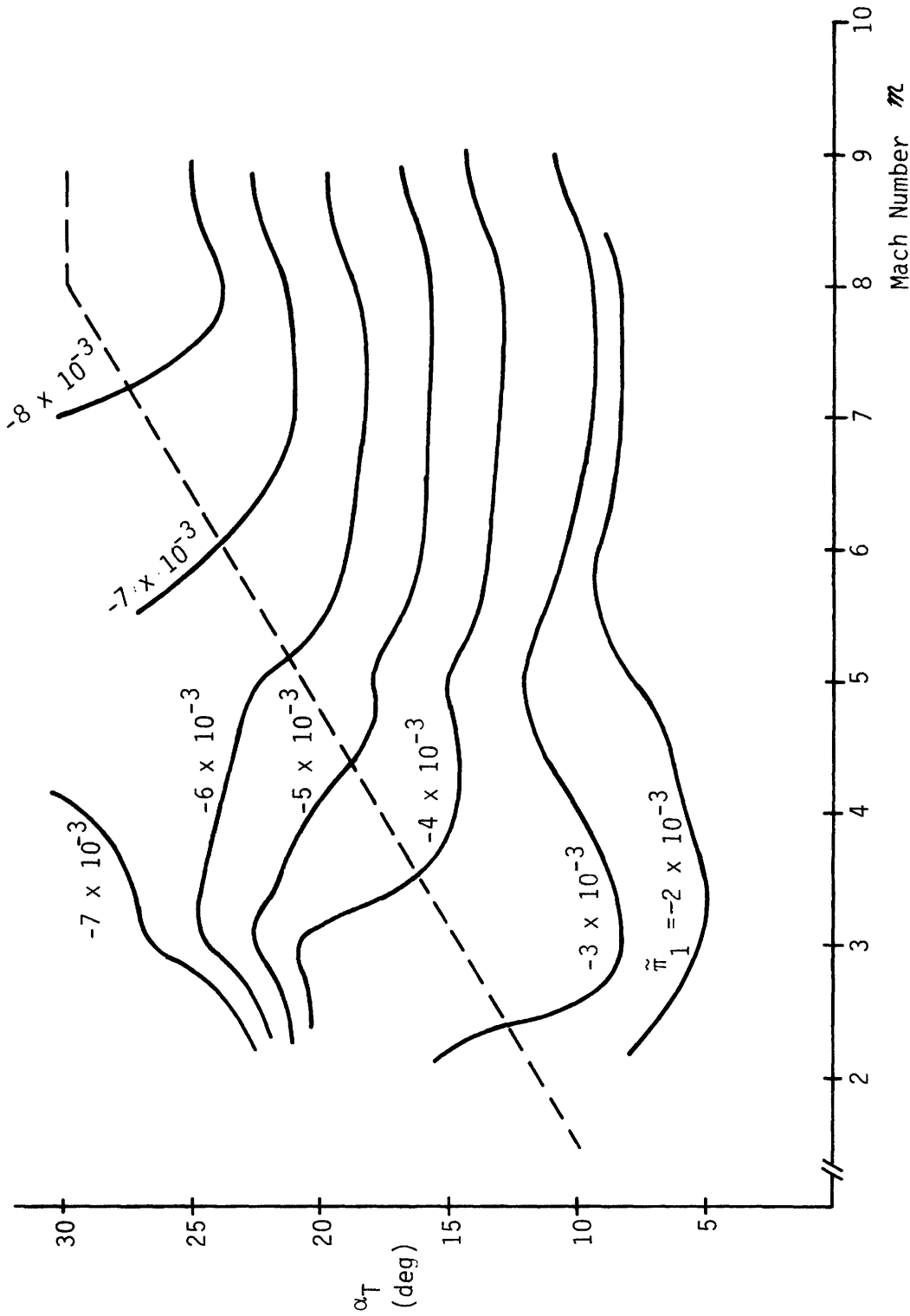
Figure 5-14. Contour Plot for $\tilde{\pi}_1$ (aileron with rudder augment; $C_r = 2$).

150

in Appendix F. To illustrate the effect of aileron augmentation with the rudder, a specific crossfeed gain of 2 was chosen for the value of C_r; the implicit dependence of the contour plots shown on this parameter should be recognized. Comparing these figures with the aileron-alone coefficient plots of Figures 5-10 and 5-11, the dramatic "downward" shift of the contours should be evident, due, of course, to the increased rudder effectiveness at the lower Mach numbers. A more striking comparison is obtained by considering the hypothetical controllability regions presented previously in Figure 5-12. Suppose, for example, that due to the actuator induced non-linear effects, the aileron with rudder augment control technique requires its associated controllability coefficients to have magnitudes greater than twice those used in construction of the control boundaries of Figure 5-12. Shown in Figure 5-15 is the composite control contour generated by requiring $\tilde{C}_{n'_{\delta a}}$ and $\tilde{\pi}_1$ to have magnitudes greater than $2(C_{n_{\delta a}})^*$ and $2\pi_1^*$, respectively; also shown is the same conventional rudder/aileron (hypothetical) control boundary, specified by π_o^*. Simply stated, the downward shift of the composite control contour eliminates the "no control" segment from the nominal entry profile, even with the conservative 100% increase in required controllability coefficient magnitudes.

In spite of the fact that the above discussion is only hypothetically based, the advantage of rudder augmentation of the aileron should be clear: a possible significant extension of aileron control down into the late entry/early cruise regime. Thus, strong motivation is provided for rudder utilization as soon as it becomes effective. Further, from the numerical indications, the proportional crossfeed of (5-42) would appear to be a likely candidate for rudder control law synthesis, and is further discussed in Section 5.2.2.3. The next section proceeds with the aileron control law synthesis.
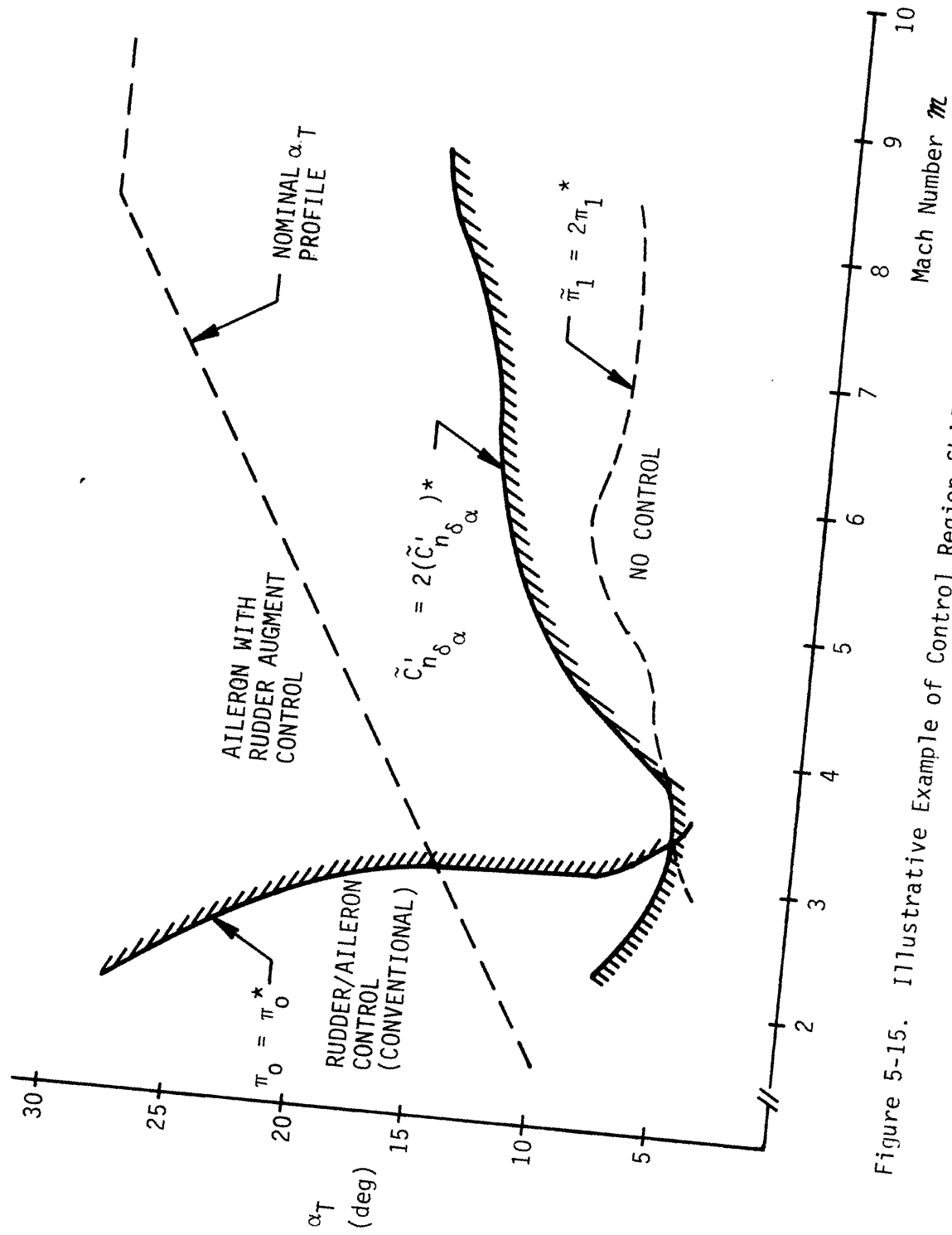
Figure 5-15. Illustrative Example of Control Region Shift (Compare with Fig. 5-12).

5.2.2.2 Aileron Control

It was noted previously that during a considerable portion of the early entry, after the dynamic pressure is sufficiently high, that the significant effectiveness of the aileron is not paralled by a similar rudder effectiveness[*]. This would then motivate, for the aileron control law synthesis of this section, a simplified approach of no rudder utilization, and the consequent simplification of the dynamic model of (5-35). However, because of the crossfeed rudder control law of the previous section, given by (5-42), and the recognition of the eventual introduction of the rudder for control purposes, a slightly more general approach is suggested for this section: the rudder deflection (from trim) may be considered as being driven by the crossfeed control law of (5-42), with a constant crossfeed gain of zero:

$$\hat{\delta}_r = C_r \hat{\delta}_a \quad ; \quad C_r = 0 \qquad (5\text{-}48)$$

The utility of this seemingly wasteful relation will become clearer in the sections to follow. For now, however, (5-48) will be carried through the aileron control law synthesis, with the understanding that C_r is zero, and thus, what is being synthesized is an "aileron-alone" control law. As noted in the previous section, (5-48) may be used to transform the simplified lateral dynamic model of (5-35) into the system defined by (5-44):

$$(s^2 + \omega_\beta^2)\beta = \tilde{K}_{\beta \delta_a} \hat{\delta}_a \qquad \text{(a)}$$

$$(5\text{-}44)$$

$$K_\beta \beta + s^2 \phi_s = \tilde{K}_{\phi \delta_a} \hat{\delta}_a \qquad \text{(b)}$$

---

[*]This is in contrast to the situation during the later portion of the entry discussed in the preceeding section.

where the augmented aileron coefficients are defined by (5-43). It should be recognized that the model above provides no information concerning the required trim aileron deflection δ_{a_T}, to maintain a given trim sideslip[*], β_T. Section 5.2.2.3 introduces a model to explain the effect of a lateral center-of-gravity offset on the vehicle's trim attitude, and, in turn, defines the trim aileron control law to compensate for such a disturbance. However, it is appropriate to consider control of deviations from trim first, and this is the subject of the section following.

5.2.2.2.1 Transient Control

The first objective of the aileron control law is to drive the bank angle to a desired guidance specified value, ϕ_G , while maintaining control over the sideslip excursions. By defining the bank attitude error ϕ_e by

$$\phi_e \equiv \phi_s - \phi_G \qquad (5-49)$$

and by assuming that the guidance value does not change during the control interval (i.e., $\dot{\phi}_G = \ddot{\phi}_G = 0$), then (5-44) may be recast in the following Laplace transform format:

$$A\underline{x} = \underline{b}\,\hat{\delta}_a \qquad (5-50)$$

where the state vector is given by

$$\underline{x} = \begin{bmatrix} \beta \\ \phi_e \end{bmatrix} \qquad (5-51)$$

---

[*]It should also be noted that, because of the non-dependence of aerodynamic torques on bank attitude, there is no "trim" bank attitude. This is discussed at greater length in Section 5.2.2.2.3.

and where the system parameters are given by:

$$A \equiv \begin{bmatrix} (s^2 + \omega_\beta^2) & 0 \\ K_\beta & s^2 \end{bmatrix} \quad ; \quad \underline{b} \equiv \begin{bmatrix} \tilde{K}_{\beta_{\delta_a}} \\ \tilde{K}_{\phi_{\delta_a}} \end{bmatrix} \qquad (5\text{-}52)$$

Thus, the control problem may be restated quite simply: maintain $\underline{x}$ near zero. Perhaps the simplest way of accomplishing this is to use standard rate and position feedback of the following form:

$$\hat{\delta}_a = -\underline{c}'\underline{x} \qquad (5\text{-}53)$$

where the control vector $\underline{c}$ is defined by:

$$\underline{c} \equiv \begin{bmatrix} c_{\dot\beta}\, s + c_\beta \\ c_{\dot\phi}\, s + c_\phi \end{bmatrix} \qquad (5\text{-}54)$$

In order to specify the gains c_β, $c_{\dot\beta}$, c_ϕ, and $c_{\dot\phi}$, the same approach is used as in the elevator control synthesis: analytic closed-loop pole placement. To accomplish this, it is seen that substitution of (5-53) into (5-50) yields the closed-loop system transfer matrix relating the output state $\underline{x}$ to the input command (zero):

$$(A + \underline{b}\,\underline{c}')\underline{x} = \underline{0} \qquad (5\text{-}55)$$

The characteristics of this closed-loop transfer matrix become evident upon substitution of (5-52) and (5-54) to yield the following expansion:

$$(A + \underline{bc}') = \begin{bmatrix} \left[s^2 + c_{\dot{\beta}} \tilde{K}_{\beta_{\delta_a}} s + \left(\omega_{\beta}^2 + c_{\beta} \tilde{K}_{\beta_{\delta_a}} \right) \right] & \left[c_{\dot{\phi}} \tilde{K}_{\beta_{\delta_a}} s + c_{\phi} \tilde{K}_{\beta_{\delta_a}} \right] \\[2ex] \left[c_{\dot{\beta}} \tilde{K}_{\phi_{\delta_a}} s + \left(K_{\beta} + c_{\beta} \tilde{K}_{\phi_{\delta_a}} \right) \right] & \left[s^2 + c_{\dot{\phi}} \tilde{K}_{\phi_{\delta_a}} s + c_{\phi} \tilde{K}_{\phi_{\delta_a}} \right] \end{bmatrix} \qquad (5\text{-}56)$$

The restriction imposed by "aileron-alone" control now becomes obvious: the elements of the closed-loop transfer matrix of (5-55) cannot, in general, be independently specified by the use of only four state feedback gains. To see this, consider the two damping terms in the first column of the matrix, $c_{\dot{\beta}} \tilde{K}_{\beta_{\delta_a}}$ and $c_{\dot{\beta}} \tilde{K}_{\phi_{\delta_a}}$. To be able to set them to arbitrary values, say ζ_{11} and ζ_{21}, then implies that:

$$c_{\dot{\beta}} \begin{bmatrix} \tilde{K}_{\beta_{\delta_a}} \\[1ex] \tilde{K}_{\phi_{\delta_a}} \end{bmatrix} = \begin{bmatrix} \zeta_{11} \\[1ex] \zeta_{21} \end{bmatrix}$$

If either ζ_{11} or ζ_{21} is non-zero, the above vectors must be co-linear, so that their cross-product implies the following constraint:

$$\zeta_{21} \tilde{K}_{\beta_{\delta_a}} - \zeta_{11} \tilde{K}_{\phi_{\delta_a}} = 0$$

Clearly this is a degenerate case involving particular values of the model parameters. Similar arguments may be used for the remaining elements of the transfer matrix; the conclusion is that the use of only four feedback gains does not allow the independent specification of the eight non-unity components of the closed-loop transfer matrix of (5-56).

The approach taken, then, it to simply specify the lateral closed-loop poles, or, equivalently, the coefficients of the characteristic equation defined by:

$$|A + \underline{b}\,\underline{c}'| = 0 \qquad (5\text{-}57)$$

Specifically, it is desired to match (5-57), term by term, with the following fourth-order characteristic equation:

$$(s^2 + 2\zeta_1\omega_1 s + \omega_1^2)(s^2 + 2\zeta_2\omega_2 s + \omega_2^2) = 0 \qquad (5\text{-}58)$$

where ζ_i and ω_i are design specified parameters. Use of (5-56) to expand (5-57), combined with a term by term match with (5-58) then yields the following four relations defining the feedback gains as functions of the model parameters and the desired closed-loop pole locations:

$$c_\phi = -a_1/(\tilde{K}_{\beta\delta_a}\rho^2) \qquad (a)$$

$$c_{\dot{\phi}} = -a_1 a_2/(\tilde{K}_{\beta\delta_a}\rho^2) \qquad (b)$$

$$(5\text{-}59)$$

$$c_\beta = \frac{1}{\tilde{K}_{\beta\delta_a}}\left[a_4 - \omega_\beta^2 + \left(\frac{\tilde{K}_{\phi\delta_a}}{\tilde{K}_{\beta\delta_a}}\right)\left(\frac{a_1}{\rho^2}\right)\right] \qquad (c)$$

$$c_{\dot{\beta}} = \frac{1}{\tilde{K}_{\beta\delta_a}}\left[a_3 + \left(\frac{\tilde{K}_{\phi\delta_a}}{\tilde{K}_{\beta\delta_a}}\right)\left(\frac{a_1 a_2}{\rho^2}\right)\right] \qquad (d)$$

where the model dependent parameter ρ^2 is defined by[*]:

---

[*] Note that this is simply the negative of $\tilde{\eta}$ defined by Eq. (F-23) in Appendix F.

157

$$\rho^2 \equiv K_\beta - \left(\frac{\tilde{K}_{\phi \delta_a}}{\tilde{K}_{\beta \delta_a}}\right) \omega_\beta^2 \qquad (5\text{-}60)$$

and where, for compactness of notation, the a_i are defined by:

$$a_1 \equiv \omega_1^2 \omega_2^2 \qquad \text{(a)}$$

$$a_2 \equiv 2(\zeta_1 \omega_2 + \zeta_2 \omega_1)/\omega_1 \omega_2 \qquad \text{(b)}$$

$$a_3 \equiv 2(\zeta_1 \omega_1 + \zeta_2 \omega_2) \qquad \text{(c)}$$

$$a_4 \equiv \omega_1^2 + \omega_2^2 + 4\zeta_1 \zeta_2 \omega_1 \omega_2 \qquad \text{(d)}$$

(5-61)

Use of (5-59) and (5-54) then allows the control law of (5-53) to be expressed in the following (time domain) form:

$$\hat{\delta}_a = -\frac{1}{\tilde{K}_{\beta \delta_a}} \left\{ (a_3 \dot{\beta} + a_4 \beta) - \frac{a_1}{\rho^2} \left[(\dot{\phi}_e + a_2 \ddot{\phi}_e) - \left(\frac{\tilde{K}_{\phi \delta_a}}{\tilde{K}_{\beta \delta_a}}\right)(\beta + a_2 \dot{\beta}) \right] \right\}$$

$$+ \frac{\omega_\beta^2}{\tilde{K}_{\beta \delta_a}} \beta \qquad (5\text{-}62)$$

where it should be noted that the bank rate $\dot{\phi}_s$ may be used to replace the bank error rate $\dot{\phi}_e$ ($= \dot{\phi}_s - \dot{\phi}_G$), since it is assumed that the guidance commanded bank attitude remains constant during the control interval. The above expression may readily be put in a form which more explicitly defines the dependence on the modelled aerodynamics. Specifically, use of the intermediate model parameter definitions given in (5-60) and (5-43), combined with the basic parameter definitions given in (4-50) and (4-52) of Section 4.3, then allows for the following expression of the aileron control law:

$$\hat{\delta}_a = \frac{\xi_4}{\bar{q}} \left\{ \left(\frac{a_1 \xi_5}{\bar{q}}\right) \left[-\dot{\phi}_e - a_2 \ddot{\phi}_e + \xi_6(\beta + a_2 \dot{\beta}) \right] + (a_3 \dot{\beta} + a_4 \beta) \right\} - \xi_3 \beta$$

$$(5\text{-}63)$$

where, in a manner similar to that used in the longitudinal derivation, the vehicle dependent gains, ξ_i, are defined, so as to isolate the dynamic pressure dependence, as follows:

$$\xi_3 \equiv C'_{n_\beta} / \widetilde{C}'_{n_{\delta_a}} \tag{a}$$

$$\xi_4 \equiv \left(\frac{I_{zz}}{Sb}\right) \frac{1}{\widetilde{C}'_{n_{\delta_a}}} \tag{b}$$

$$\text{(5-64)}$$

$$\xi_5 \equiv \left(\frac{I_{xx}}{Sb}\right) \frac{C'_{n_{\delta_a}}}{C_{n_\beta}\widetilde{C}_{l_{\delta_a}} - C_{l_\beta}\widetilde{C}_{n_{\delta_a}}} \tag{c}$$

$$\xi_6 \equiv -\left(\frac{I_{zz}}{I_{xx}}\right) \left(\frac{\widetilde{C}'_{l_{\delta_a}}}{\widetilde{C}'_{n_{\delta_a}}}\right) \tag{d}$$

It should be noted that this set of gains makes use of the "augmented" aileron coefficients previously defined by (5-47) during the discussion of lateral controllability[*]:

$$\widetilde{C}'_{n_{\delta_a}} \equiv C'_{n_{\delta_a}} + C_r C'_{n_{\delta_r}} \tag{a}$$

$$\widetilde{C}'_{l_{\delta_a}} \equiv C'_{l_{\delta_a}} + C_r C'_{l_{\delta_r}} \tag{b}$$

$$\text{(5-65)}$$

$$\widetilde{C}_{n_{\delta_a}} \equiv C_{n_{\delta_a}} + C_r C_{n_{\delta_r}} \tag{c}$$

$$\widetilde{C}_{l_{\delta_a}} \equiv C_{l_{\delta_a}} + C_r C_{l_{\delta_r}} \tag{d}$$

where the rudder crossfeed gain C_r is taken to be zero for the aileron-alone configuration, and the dynamic derivatives are those introduced in Section 4.3 by (4-43) and (4-47). It is appropriate at this point to

---

[*] The definition of $\widetilde{C}'_{l_{\delta_a}}$ is added here for completeness.

159

comment on the gain structure of (5-64), in light of the lateral control-lability requirements. First, it is clear from the definitions of three of the gains, that $\widetilde{C}'_{n\delta a}$ must be non-zero, or, with $C_r = 0$ and the defin-ition of (5-65a), $C'_{n\delta a}$ must be non-zero. Similarly, from the definition of ξ_5 given by (5-64c), the quantity $(C_{n\beta}\widetilde{C}_{\ell\delta a} - C_{\ell\beta}\widetilde{C}_{n\delta a})$ must be non-zero, or, with $C_r = 0$ and the definition of (5-65c) and (5-65d), the quantity $(C_{n\beta}C_{\ell\delta a} - C_{\ell\beta}C_{n\delta a})$ must be non-zero. It is reassuring to note that these requirements correspond precisely with the aileron controllability requirements given in the previous section by (5-45) and (5-38b), for the respective cases in which $C_r \neq 0$ and $C_r = 0$. Thus, the formal definition of the gains of (5-64) is tied directly to the control-lability of the vehicle, implying that if the vehicle is controllable, then the control law of (5-63) is a feasible approach. This inverse depend-ence of the gains on the controllability coefficients also implies an in-crease in gain magnitudes as the vehicle intersects controllability co-efficient contours of decreasing magnitude, as illustrated by Figures (5-10), (5-11), (5-13), and (5-14) of the preceeding section. Thus, the continued use of the aileron control law may lead to an eventual viola-tion of the actuator rate limits, depending, of course, on vehicle state and guidance commands. This input dependent controllability clearly suggests conservatism in the definition of the region of applicability of (5-63).

To summarize the development at this point, it may be noted that the aileron control law of (5-63) is designed to maintain the desired guidance commanded bank attitude, while keeping the sideslip deviations small. The feedback gains, defined by (5-61), (5-64), and (5-65), are chosen so as to maintain the poles of the lateral transfer function(s) at locations that are design specified. Additional comments on this gain configuration and its effect on the closed-loop response characteristics are to be found in Section 7.2.1.

5.2.2.2.2 Maneuver Logic

As discussed in Section 2.3, there may exist a minimum bank maneuver rate requirement imposed by the guidance system specifications, applicable to large attitude maneuvers (e.g., bank reversals) performed at relatively high dynamic pressures. Because the logic of the previous section does not provide a capability for explicit control of the maneuver rate, it is appropriate to consider a modification which allows the control law to maintain a desired maneuver rate during large attitude transients.

Perhaps the most direct means of providing this capability, while taking advantage of the established gain structure of the previous section, is to simply inhibit the bank attitude feedback while in a maneuver situation and simultaneously bias the bank rate feedback consistent with the desired attitude maneuver. A logic which generates this bias, effectively a bank rate command, $\dot{\phi}_c$, is shown in block diagram form in Figure 5-16. The non-linear portion of the logic generates a desired maneuver rate proportional to the attitude error, with a design specified maximum maneuver rate, $\dot{\phi}_{max}$, for all attitude errors greater than the design specified limit, ϕ_{max}. In addition, a deadband, specified by ϕ_{min}, is used to stop the maneuver (by generating a zero bank rate command) when the attitude error is small, thus allowing a smooth transition into the aileron control mode described in the previous section. The linear portion of this logic is simply a first-order digital filter, with a design specified time constant, τ, used to smooth the rate command history. This is the compensation mentioned earlier used to maintain the linearity of the actuator model; smoothing of the rate command signal blinds the aileron control law to instantaneous steps in the bank attitude error, thus avoiding large transients in the commands to the actuators. Thus, in the presence of large changes in the commanded bank rate, the filter logic allows only gradual changes in the commanded bank rate, which, in turn, drives the aileron at more moderate rates, avoiding the actuator rate limits.
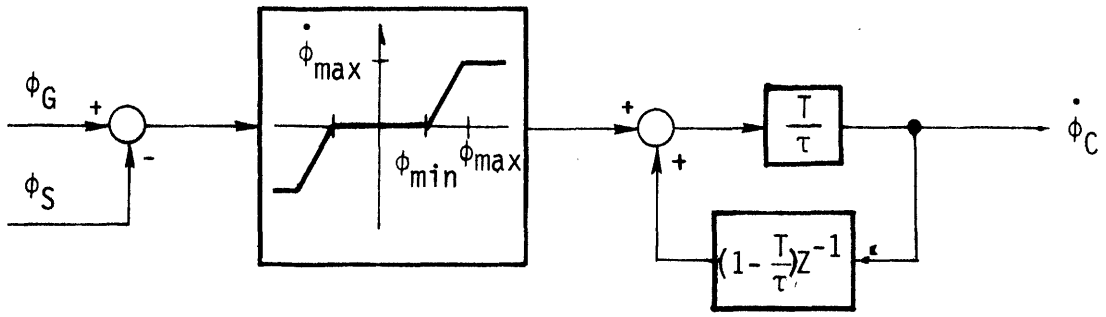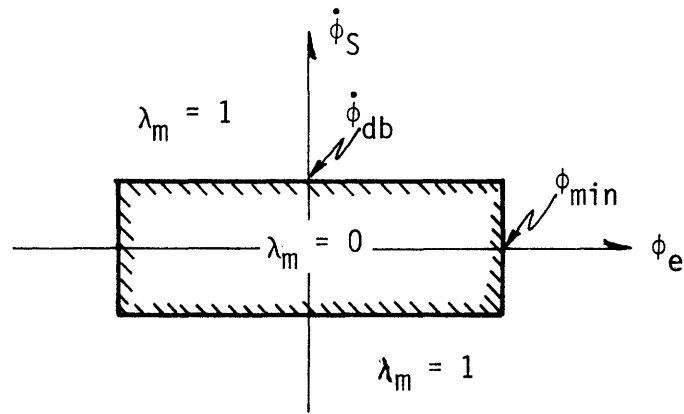
Figure 5-16.   Basic Rate Command Logic.

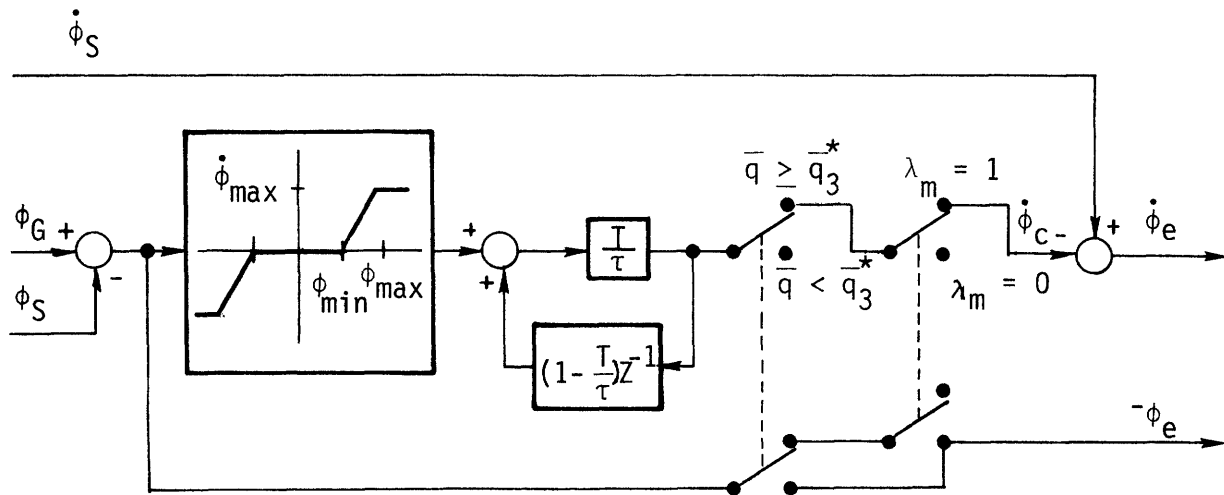Figure 5-17.   Phase-Plane Logic for Rate Command Flag.

Figure 5-18.   Bank Maneuver Logic.

162

A very crude phase-plane logic, shown in Figure 5-17, may be used to determine whether or not use of the above rate command logic is appropriate. The design parameters ϕ_{min} and $\dot{\phi}_{db}$ allow for a specification of the deadband region in which the maneuver flag, λ_m, is set to zero, indicating that the rate command logic is to be inoperative. As mentioned above, the bank attitude feedback loop is broken while in the rate command mode; with this definition of λ_m, the maneuver logic may be summarized in block diagram form as shown in Figure 5-18. Two points should be noted regarding this logic. First, the biasing of the bank rate is performed by a simple subtraction of the commanded rate; thus the outputs are consistent with the bank error and bank rate error, ϕ_e and $\dot{\phi}_e$, used in the aileron control law of (5-63) of the previous section. Second, since the guidance requirement for this maneuver capability only accurs at relatively high dynamic pressures, this rate command logic is entirely bypassed when the dynamic pressure is below a design specified value, $\bar{q}_3^*$.

This logic thus provides the capability of maneuvering at a desired bank rate so as to drive a large guidance induced bank attitude error to zero. Its compatibility with the previously defined linear control law, through the proper selection of the design specified parameters, is demonstrated in Section 7.2.1.6.

5.2.2.2.3 Trim Control

As was mentioned in the introduction of this section, the simplified lateral dynamic model provides no information concerning the required trim surface deflections to maintain an equilibrium trim attitude in the presence of disturbance torques induced by vehicle asymmetries. The purpose of this section, then, is to briefly examine the effects of vehicle asymmetry, specifically those due to a lateral center-of-gravity displacement from the nominal plane of symmetry, and then propose two compensatory trim laws, each appropriate to a particular flight regime.

Derived in Appendix G are the equations which specify the effects of a lateral center-of-gravity offset on the vehicle's dynamics. Figure 5-19 is repeated from Figure G-1 to show the induced body-axis disturbance torques due to a shift ℓ of the center-of-gravity out of the vehicle's
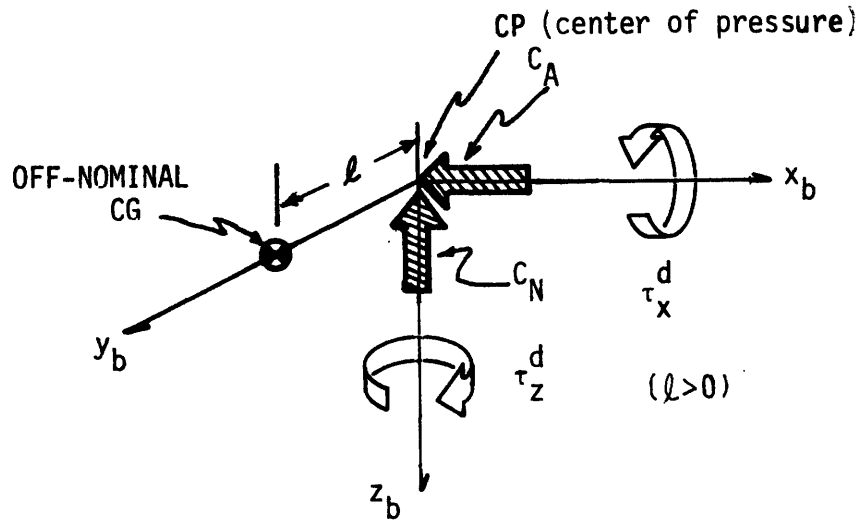
Figure 5-19. Positive y-axis CG Offset Effects.

plane of symmetry (indicated by the x_b-z_b plane). As shown by (G-8) in the appendix, if the surfaces are not used in a trim capacity, then the offset ℓ gives rise to an "open-loop" (i.e., uncompensated) trim sideslip attitude and a concommitant bank acceleration:

$$\beta_T^{OL} = \left(\frac{\ell}{b}\right)\left(\frac{I_{zz}}{I_{xx}}\right)\left(\frac{C_N}{C_{n_\beta}'}\right) \sin \alpha_T \qquad \text{(a)}$$

$$\ddot{\phi}_s^{OL} = \left(\frac{\bar{q}S\ell}{I_{xx}}\right)\left(\frac{C_{n_\beta}}{C_{n_\beta}'}\right) C_N \qquad \text{(b)}$$

$$(5\text{-}66)$$

where, it should be noted that C_N is the normal force coefficient. The above equations thus show that, if, in the presence of a lateral CG

offset, sideslip rate damping is provided by the control system, then the vehicle will "trim" at a non-zero sideslip angle. More important, however, is the fact that there is no equilibrium bank attitude, and, in fact, there exists a disturbance acceleration (proportional to dynamic pressure) about the bank axis, implying rapid bank attitude divergence in the absence of control compensation.

This disturbance acceleration takes on added significance when the lateral control loop is taken into account. The impact of a lateral CG displacement on ACPS performance should be obvious in light of the previous discussion concerning pitch trim. For example, consider the situation in which the vehicle is in the hypersonic regime at an angle-of-attack of approximately 30 degrees. Using (5-66) and the appropriate vehicle parameter values, it is seen that

$$\beta_T^{OL} \approx 0.6°/\text{inch CG offset}$$

$$\ddot{\phi}_S^{OL}/\bar{q} \approx -0.006°/\text{sec}^2/\text{inch CG offset}$$

Thus, even at the relatively low dynamic pressure of 20 lbf/ft^2, it is seen that a two-inch offset can result in a bank acceleration of approximately 0.24 deg/sec^2, a not insignificant fraction of the available ACPS control accelerations (see Table 2-5 of Section 2.2.1), thus implying large duty cycles simply to maintain attitude in the face of the offset induced disturbance torque. An order-of-magnitude increase in the dynamic pressure, to 200 lbf/ft^2, clearly indicates control authority problems if the ACPS were to be used as the primary control effector during high dynamic pressure operation.

This is not meant to suggest that the CG offset problem disappears when surface control is initiated; on the contrary, the aileron logic of the previous section is based on a symmetric vehicle model, and the lateral offset clearly violates the validity of this model. Specifically, it may be seen from the aileron control law of (5-63) that, in the presence of an offset induced trim sideslip, the aileron need not

165

-necessarily drive the bank attitude error to zero, since the following equilibrium (i. e., $\dot{\phi}_s = \dot{\beta} = 0$) situation can exist:

$$\hat{\delta}_a = -\frac{a_1\xi_4\xi_5}{\bar{q}^2}\phi_e + \left[\frac{a_1\xi_4\xi_5\xi_6}{\bar{q}^2} + \frac{a_4\xi_4}{\bar{q}} - \xi_3\right]\beta_T \qquad (5\text{-}67)$$

thus allowing for a steady-state non-zero bank attitude error in combination with a non-zero aileron deflection. Clearly a trim logic is required in this situation so as to drive the bank error to zero while maintaining a trim sideslip with a properly chosen trim aileron deflection.

Both the increased ACPS fuel expenditures and the possibility of steady-state attitude errors during aileron control thus motivate the introduction of a surface trim law to compensate for disturbance torques induced by vehicle asymmetries. As is shown in Appendix G, an equilibrium may be maintained with the proper choice of aileron deflection, so that the steady-state vehicle attitude is specified by a "closed-loop" (i. e., compensated) trim sideslip angle β_T^{CL}, and the desired bank attitude (i. e., there is no bank angle acceleration). This trim situation, as a function of the lateral CG offset l, is specified by (G-13) in the appendix, which defines the following trim (β_T^{CL}, δ_{a_T}) pair:

$$\beta_T^{CL} = \left(\frac{\mathit{l}}{b}\right)\frac{C_N\widetilde{C}_{n\delta_a}}{C_{n\beta}\widetilde{C}_{\mathit{l}\delta_a} - C_{\mathit{l}\beta}\widetilde{C}_{n\delta_a}} \qquad (a)$$

$$\qquad (5\text{-}68)$$

$$\delta_{a_T} = -\left(\frac{\mathit{l}}{b}\right)\frac{C_N C_{n\beta}}{C_{n\beta}\widetilde{C}_{\mathit{l}\delta_a} - C_{\mathit{l}\beta}\widetilde{C}_{n\delta_a}} \qquad (b)$$

where $\widetilde{C}_{n\delta_a}$ and $\widetilde{C}_{\mathit{l}\delta_a}$ are the augmented coefficients previously introduced by (5-65). It should be recalled that these coefficients collapse to the aileron effectiveness coefficients, $C_{n\delta_a}$ and $C_{\mathit{l}\delta_a}$, respectively, when the rudder crossfeed gain C_r is zero. The important point,

however, is that a trim solution exists and is given by (5-68); furthermore, the term in the denominator is the controllability parameter $\tilde{\pi}_1$, so that the region of applicability of this trim solution corresponds precisely to the region of applicability of aileron control discussed in Section 5.2.2.1.

With the trim condition thus defined, it is appropriate to consider a trim logic implementation. Because of the expected uncertainties in the aerodynamic coefficients and the fact that the center-of-gravity offset ℓ will not be known, a direct implementation of (5-68b) to determine the required trim aileron is clearly inappropriate; instead, less direct methods are necessary. As was done for the elevator trim logic, the aileron trim logic may be broken into an ACPS phase and a conventional trim integrator phase.

Early in the entry, when the dynamic pressure is low, a positive lateral CG offset ($\ell > 0$) will result in an open-loop trim sideslip which is positive. This follows from the fact that the trim sideslip is given by (5-66a) and that both C_N and C'_{n_β} are positive. However, the roll jet logic of Section 5.2.1.2 will attempt to maintain sideslip and sideslip rate near zero, thus constantly opposing the offset induced disturbance torque with negative roll jet firings. This asymmetry in roll jet firings can thus be used to trim the vehicle in a manner entirely analogous to that used in the pitch channel: simply drive the aileron at a low rate proportional to the average roll torque commanded by the roll ACPS logic. In a sampled-data format, this is most readily accomplished by the following trim control law:

$$\delta_{a_T} = (\delta_{a_T})_{old} + K_{\phi_1} T \tilde{u}_x \qquad (\overline{q} \leq \overline{q}_2^*; \, u_z = 0)$$

(5-69)

where T is the control law sample period, $\tilde{u}_x$ is the normalized roll ACPS command:

$$\tilde{u}_x \equiv u_x / U_x \qquad (5\text{-}70)$$

and $K_{\emptyset_1}$ is a design specified (positive) gain to ensure convergence toward the required negative trim aileron setting specified by (5-68b)[*]. It should be noted that (5-69) confines the trim law's region of applicability to low dynamic pressure operation by introduction of the design specified dynamic pressure parameter, $\bar{q}_2^*$. Further, to avoid misinterpreting roll jet firings which occur during a maneuver ($u_z \neq 0$) as CG offset induced correction torques, trim accumulation is inhibited when the yaw jets are firing; this is shown as the $u_z = 0$ condition in (5-69).

As the dynamic pressure increases and use is made of the aileron effectiveness by means of the control law of the previous two sections, the trim law may be tied more closely to the aileron deflection history. This is most readily accomplished by recognizing from (5-66b) that a positive offset results in a negative bank acceleration, which, in a non-maneuver situation, results in a negative bank rate. Thus, by slowly driving the aileron at a rate proportional to this disturbance induced bank rate, the desired negative trim aileron setting of (5-68b) may be obtained. Stated formally, the trim aileron rate may be defined as follows:

$$\dot{\delta}_{a_T} = -K_{\emptyset_2} \frac{a_1 a_2 \xi_4 \xi_5}{\bar{q}^2} \dot{\emptyset}_s \qquad (5\text{-}71)$$

where $K_{\emptyset_2}$ is a design specified (positive) gain. The choice of the gain structure for this trim law becomes clear by recalling that the aileron deflection, δ_a, may be viewed as a trim setting summed with a deflection from trim, so that

$$\delta_a = \delta_{a_T} + \hat{\delta}_a \qquad (5\text{-}72)$$

Thus, substituting the control law of (5-63) and the Laplace transformed version of (5-71) into the above expression, there results the following:

---

[*] Note that the denominator is negative, as is C_{n_β}.

$$\delta_a = \frac{\xi_4}{\bar{q}} \left\{ \left(\frac{a_1 \xi_5}{\bar{q}} \right) \left[-\phi_e - a_2 \left(1 + \frac{K_{\phi 2}}{s} \right) \dot{\phi}_e + \xi_6 (\beta + a_2 \dot{\beta}) \right] + (a_3 \dot{\beta} + a_4 \beta) \right\}$$

$$- \xi_3 \beta \qquad\qquad\qquad (5\text{-}73)$$

Thus, the trim law of (5-71) is no more than a parallel channel integrator placed in the bank rate loop. The simplest sampled-data approximation of (5-71) is given by:

$$\delta_{a_T} = (\delta_{a_T})_{old} - K_{\phi 2} T \frac{a_1 a_2 \xi_4 \xi_5}{\bar{q}^2} \dot{\phi}_s \qquad (\bar{q} > \bar{q}_2^*; \ \lambda_m = 0)$$

$$(5\text{-}74)$$

where, as before, T is the sample period. As noted parenthetically in the above formulation, the use of the logic is inhibited during the higher dynamic pressure regime and when no maneuvers are being conducted (recall the λ_m flag definition of the previous section).

The aileron trim control law, specified by (5-69) and (5-74), may be conveniently summarized in block diagram form as shown in Figure 5-20. It should be noted that the digital integrator is "clamped" so as to preclude violation of the aileron deflection limits (to be introduced in Section 5.3).

5.2.2.3 Rudder Control

From the discussion of lateral controllability in Section 5.2.2.1, it is clearly advantageous to utilize the rudder as soon as its effectiveness becomes significant. The question is, of course, how it can be used to advantage to maintain or improve the overall system performance, in light of the decreasing aileron effectiveness discussed above. One possible approach is to implement a conventional rudder control logic which maintains tight control over sideslip and/or yaw rate so as to provide stability augmentation about one vehicle axis. What this requires, however, is an aileron control law compatible with this approach, and the one described above is not.
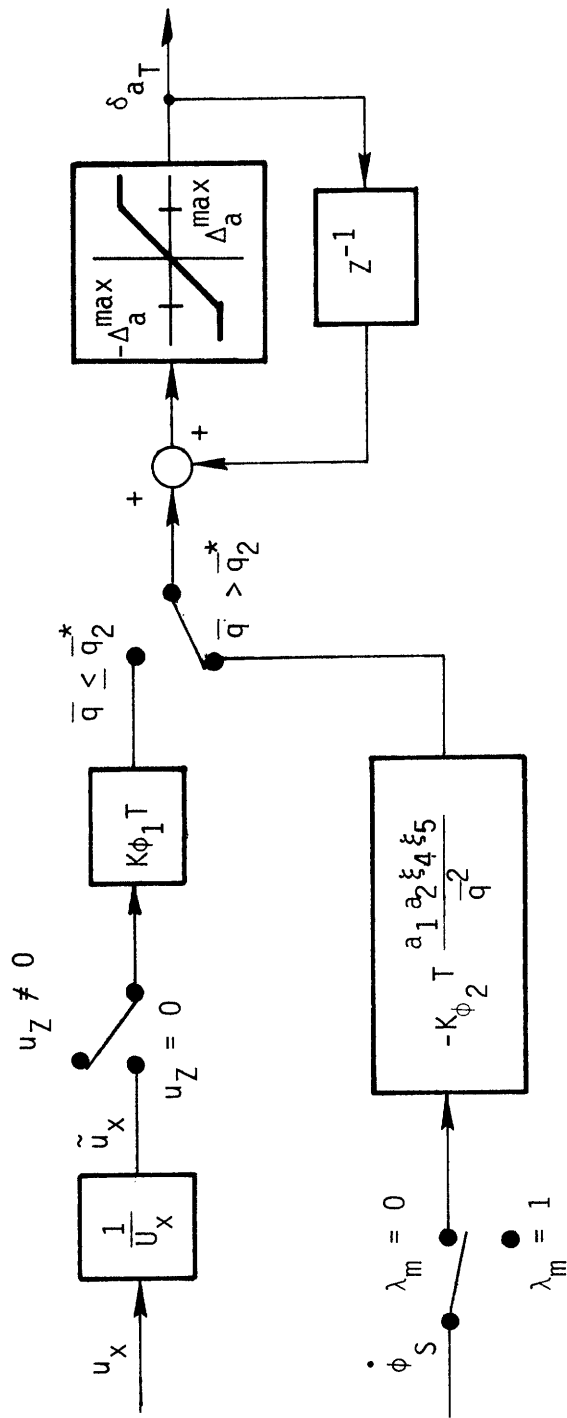
Figure 5-20. Aileron Trim Control.

To see this incompatibility it suffices to describe one basic characteristic of the aileron control law of (5-63), relevant to the question of rudder utilization, and based on the fundamental lateral dynamics described in Section 4.4.3. Described there is the noticeable effect of sideslip induced bank acceleration due to the large coupling constant K_β; also described is the effect of a positive roll torque (for example, caused by a positive aileron deflection) inducing an adverse roll torque due to the geometrically generated sideslip (recall Figure 4-24). The implication, of course, is that conventional use of the ailerons may not be desirable due to roll reversal tendencies. As will be seen from the performance histories of Section 7.2.1.8, the aileron control law described by (5-63) is not conventional, and, in fact, takes advantage of the dihedral effect to bank the vehicle; it does this by using the ailerons to generate a small sideslip which, in turn, banks the vehicle as desired. Thus, any use of another effector which tends to clamp sideslip and/or yaw rate will be an antagonist to the above proposed use of the aileron. This then motivates a cautious appraisal of any proposed conventional control role for the rudder, and, in fact, has led to the elimination from consideration any technique which would oppose the basic operational goals of the aileron.

An alternative, of course, is to change the aileron control law upon introduction of a conventionally controlled rudder. The objections here are twofold. First, from the trends of the conventional controllability contours of Figure 5-9, it may be necessary to delay the introduction of the rudder (and the concommitant aileron control law switch) significantly past the point at which the rudder becomes "effective". This, in turn, implies the possibility of a controllability "gap", a situation in which aileron-alone control is not capable of maintaining vehicle control late enough into the entry so that conventional control may be utilized. The second objection is less serious, and is concerned with the additional complexity involved due to the requirement of a second basic aileron control law. Although the extra lines of coding will not strain the digital system, the design verification process becomes more involved.

171

Discussion of the selected rudder control technique is somewhat anticlimactic, since the control law has already been introduced by the constant crossfeed law of (5-42) in Section 5.2.2.1. The advantages of this approach should be clear at this point. First, by comparing the aileron-alone controllability contour plots of Figures 5-10 and 5-11 with those associated with the aileron with rudder augment technique, given in Figures 5-13 and 5-14, there is seen a significant extension of aileron controllability late into the entry. Second, because of the derivation format of Section 5.2.2.2, the linear crossfeed law of (5-42) is clearly compatible with, and, in fact, enhances, the aileron control law of (5-63). Finally, the extreme simplicity of the rudder crossfeed ensures a minimum implementation and validation effort. This quality of simplicity, in fact, argues against the consideration of similar but more sophisticated approaches (i.e., incorporation of a rate dependent crossfeed term) until there is a demonstrated need for performance improvement.

From previous discussions, and as illustrated in the control authority histories of Figures 4-18 and 4-20, it is recognized that the rudder becomes effective only during the late portion of the entry regime; thus, it is appropriate to maintain the crossfeed gain C_r at zero until the rudder can contribute a non-negligible torque. Recognizing that rudder turn-on is not critical, since there is no discrete control law switch for the aileron, an entirely adequate gain strategy for the rudder logic is to simply switch the crossfeed gain from its zero value to some design specified value at an appropriate low Mach number, here designated by the design specified parameter $\mathcal{M}_1$. Due to the non-monotonicity of Mach number, illustrated by its rise from zero at the beginning of the entry, it is appropriate to specify a dynamic pressure regime so as to ensure that the Mach number switching condition is recognized only during the late entry portion of the trajectory. Thus, the crossfeed gain may be defined as follows:

$$C_r = C_{rud} \quad \text{for } \mathcal{M} \leq \mathcal{M}_1 \text{ and } \bar{q} \geq \bar{q}_3^*$$

$$= 0 \quad \text{otherwise} \tag{5-75}$$

where C_{rud} and $\mathcal{M}_1$ are design specified, and $\bar{q}_3^*$ is chosen from the bank maneuver logic of Section 5.2.2.2.2 so as to provide an indication of late entry operation.

One point should be recognized concerning the constant crossfeed law of (5-42): as formulated, it is concerned only with rudder deflections from trim. However, it should be recalled from the discussion of the previous section (and the derivation given in Appendix G), that the crossfeed law also governs rudder trim, so that:

$$\delta_{r_T} = C_r \delta_{a_T} \tag{5-76}$$

As was done for both elevator and aileron, the rudder deflection, δ_r, may be viewed as a trim setting summed with a deflection from trim, so that

$$\delta_r = \delta_{r_T} + \hat{\delta}_r \tag{5-77}$$

Thus, combining (5-76) with (5-42) and (5-72), an extremely simple rudder control law results:

$$\delta_r = C_r \delta_a \tag{5-78}$$

This section completes the lateral ACSS control law synthesis description, and thus completes Section 5.2, describing the lateral control logic synthesis.

5.3 Blending Logic

This section presents a rationale for a blending logic which integrates the control effector commands issued by the ACPS and ACSS control logics of the previous two sections. As discussed earlier, the design synthesis procedure has been one of separate control law

173

derivations for the two effector subsystems; the purpose of this section is to provide a logic which ensures their cooperation in providing vehicle control torques. Actually, it should be noted that the fundamental basis for mutualism between the two subsystems lies in both the use of a common vehicle model for control law synthesis and in the design goal of attaining the same basic vehicle response characteristics, irrespective of the particular control effector subsystem being used. Thus, rather than guarantee smooth cooperation between the two subsystems, the blending logic should be viewed more as a means of enhancing the natural tendency of common operation.

This section is broken into two subsections. Section 5.3.1 discusses the longitudinal design problem by a simple examination of vehicle environment changes which occur as the entry progresses. As will be seen, the basis for the non-linear blending logic presented in this section rests strongly on the closed-loop pole placement technique used in the elevator control law synthesis of Section 5.1. Section 5.3.2 then presents the lateral blending logic, which, it will be seen, is virtually identical to that used in the longitudinal channel; the basis for this is, of course, the similarity of the design problem of ACPS and ACSS control torque allocation.

5.3.1 Longitudinal Blending Logic

As was noted in Section 5.1, the very low dynamic pressures encountered at the beginning of the entry result in an elevator control authority which is too low for effective angle-of-attack control, but may be large enough so that mistrim induced disturbance torques result in excessive pitch ACPS fuel consumption. Thus, the first objective of the blending logic is to maintain the use of the ACPS for attitude control while providing the proper elevator command necessary for pitch trim. As the dynamic pressure increases, the elevator effectiveness does likewise, and it is clearly advantageous to minimize ACPS fuel expenditures by utilizing the control laws of (5-19) and (5-20) to maintain

174

attitude instead of firing the pitch jets. An abrupt "turn-on" of this elevator control law, say at $\bar{q} = \bar{q}_1$, where $\bar{q}_1$ is design specified, will almost certainly lead to large transients in the elevator history. The reason for this is the combined effect of fair-sized attitude errors allowed by the ACPS deadband (see Figure 5-2) along with relatively large elevator control law gains due to their inverse dependence on dynamic pressure (see (5-19)). Clearly, there are several feasible techniques which can be used to avoid this situation. If the switch point $\bar{q}_1$ is made large enough, the elevator gains will be relatively small, and thus, so will the transients; however, this implies considerably more dependence on the ACPS for attitude control, with consequently large fuel expenditures. Alternatively, the ACPS deadband may be "shrunk" with increasing dynamic pressure, thus decreasing the attitude error magnitudes feeding the elevator control law at its eventual turn-on; this, of course, has the same drawback as the previous technique. Finally, the gains which are not dependent on dynamic pressure (e.g., ω_d, ξ_1, etc.) may be scheduled so as to counteract the large gain effect induced by a small dynamic pressure; the result of this is a shift in the desired closed-loop pole location originally specified. Even if this is acceptable, there is a more fundamental objection, as will be seen below.

The approach taken here will be to use the control law of (5-19), unmodified by gain shaping, with a "turn-on" at $\bar{q} = \bar{q}_1$, and a deflection limiter logic incorporating limits which gradually grow with dynamic pressure:

$$\delta_e^{max} = (1 - K_e)\delta_{e_T} + K_e\Delta_e^{max} \qquad \text{(a)}$$

$$\tag{5-79}$$

$$\delta_e^{min} = (1 - K_e)\delta_{e_T} + K_e\Delta_e^{min} \qquad \text{(b)}$$

where δ_{e_T} is defined by the trim logic of (5-21), Δ_e^{min} and Δ_e^{max} are chosen to equal the physical deflection limits of the elevons[*], and K_e

---

[*] See Section 5.4.2 for further discussion.

is a dynamic pressure dependent parameter shown in Figure 5-21. Shown in Figure 5-22 is a block diagram of this portion of the blending logic (a superscript c is used to indicate a commanded deflection), including the use of the elevator for trim-only operation when the dynamic pressure is less than $\bar{q}_1$. It should be recognized from (5-79) that the deflection limits δ_e^{min} and δ_e^{max} "float" about the trim value, and, as dynamic pressure increases from $\bar{q}_1$ to $\bar{q}_1^*$ (also design specified), the behavior of K_e causes the deflection limits to grow from zero (about trim) to the physical deflection limits of the elevator. It should be clear that, with the proper selection of $\bar{q}_1$ and $\bar{q}_1^*$, the elevator may be used for attitude control fairly early in the trajectory, with the "turn-on" transients well clamped. The major disadvantage is, of course, the non-linearity introduced into the elevator logic; its effects on performance are minimal and are discussed in Section 7.2.1.5.
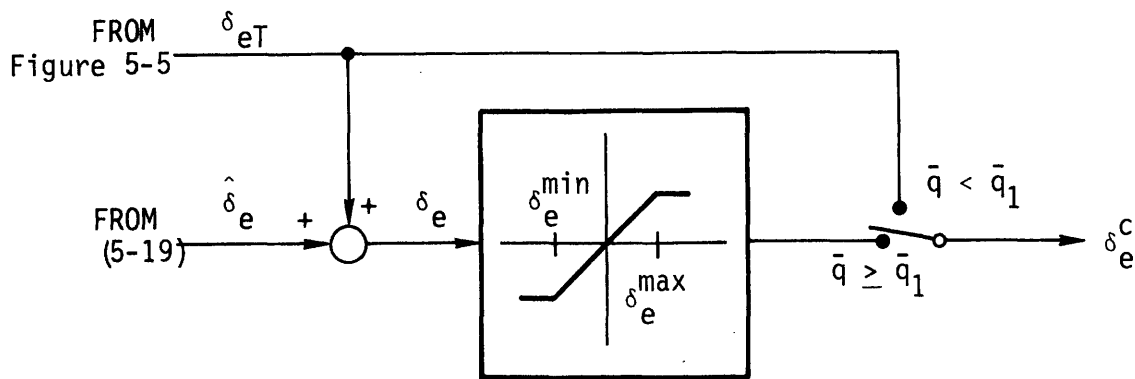

Figure 5-21. Blending Logic for Elevator Turn-on.
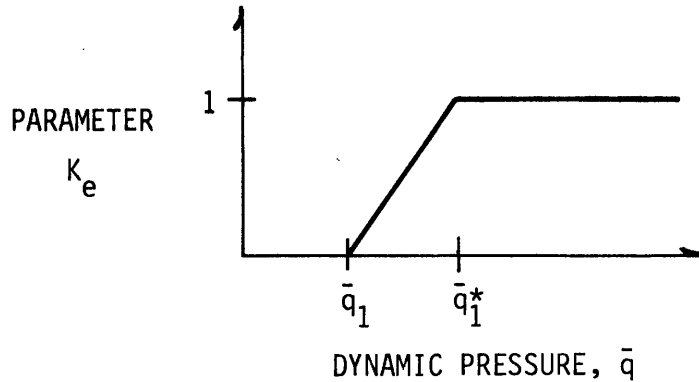
PARAMETER
K_e

DYNAMIC PRESSURE, $\bar{q}$

Figure 5-22. Elevator Blending Logic Parameter.

In conjunction with this gradual "blending in" of elevator authority, it is appropriate to consider an analogous method of ACPS inhibition, so as to save unneeded pitch ACPS fuel expenditures. One approach is to simply inhibit all commands after a certain dynamic pressure is reached or exceeded, the switch point chosen so as to ensure adequate control authority from the elevator. The choice of such an open-loop switch point is, however, strongly dependent on the vehicle's aerodynamic co-efficients, the nominal trim angle-of-attack, and on the anticipated mag-nitude of the guidance steps. A conservatively chosen switch point only wastes ACPS fuel. A more fundamental approach than that of using a fixed switch point is to provide a logic which somehow "measures" the elevator's capability to perform a desired maneuver, and then deter-mines whether or not ACPS assistance is required. As it so happens, the elevator control law of (5-19) is precisely suited to a logic of this type, because of the closed-loop pole placement synthesis procedure used in its development. Requiring the elevator to provide a fixed re-sponse regardless of the flight condition implies the use of compensatory gains; e. g., the large gain tendency of (5-19) at low dynamic pressures. Since large deflection commands only occur when the elevator has low authority (low $\bar{q}$) and/or the state errors (i. e., α_e, $\dot{\alpha}$) are large, it is then a direct matter to simply compare the commanded deflection with the maximum allowed by physical constraints. The closer the deflection

is to this maximum, the stronger is the indication for pitch ACPS augmentation. A simple logic which takes advantage of this property is the threshold discriminator shown in Figure 5-23, a summary block diagram of the overall longitudinal blending logic. The threshold function "floats" about the elevator trim value by using the following deflection magnitude parameters:

$$r_1 = (\delta_e^{min} - \delta_{e_T})f_1 + \delta_{e_T} \qquad \text{(a)}$$

$$r_2 = (\delta_e^{min} - \delta_{e_T})f_2 + \delta_{e_T} \qquad \text{(b)}$$

$$r_3 = (\delta_e^{max} - \delta_{e_T})f_2 + \delta_{e_T} \qquad \text{(c)}$$

$$r_4 = (\delta_e^{max} - \delta_{e_T})f_1 + \delta_{e_T} \qquad \text{(d)}$$

(5-80)

where the design specified parameters f_1 and f_2 are chosen such that

$$0 < f_2 < f_1 < 1 \qquad (5\text{-}81)$$

and δ_e^{min} and δ_e^{max} are obtained from (5-79). The variables r_i are chosen to provide a measure of elevator deflection from trim: for example, with f_1 set at, say, 0.8, then, from (5-80a), r_1 specifies a deflection magnitude near the minimum setting, specifically within 20% of the range between the minimum setting and the current trim value. Thus, from the block diagram, the logic effectively recognizes a "small" elevator deflection (i.e., $r_2 < \delta_e < r_3$) as an indication of sufficient elevator effectiveness, so that no ACPS augmentation is required, and thus the pitch jet command may be inhibited through the zero value taken on by the blending variable λ_e. The converse occurs with large deflections (i.e., $\delta_e < r_1$ or $\delta_e > r_4$), although the actual existence of a command to fire the pitch jet will depend on the pitch ACPS phase-plane logic output. The hysterisis path is included in the logic to prevent possible elevator chatter and high-frequency ACPS activity due to unanticipated cross-coupling effects. One last point should be noted concerning this logic: the dynamic pressure switch precludes jet inhibition when the dynamic pressure is below $\bar{q}_1$, when the elevator is used solely for trim.
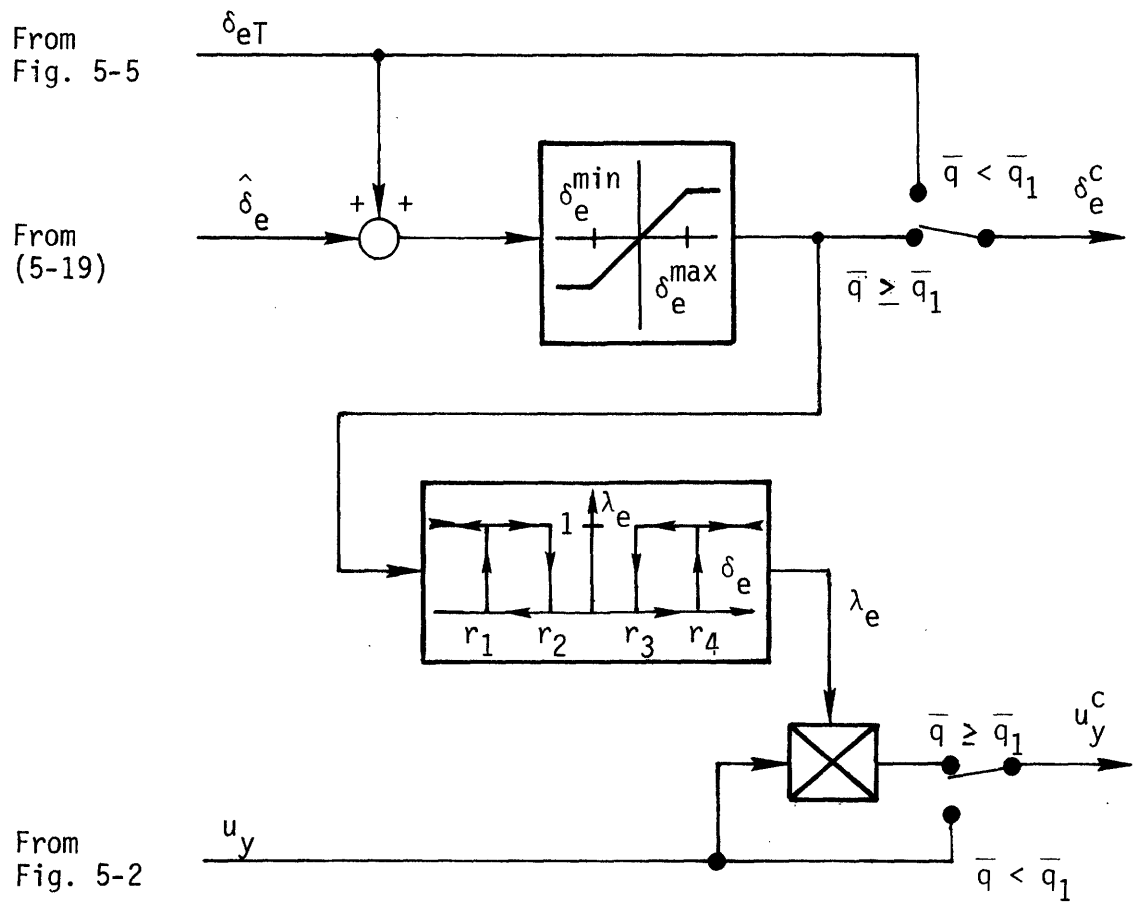
178

Figure 5-23.   Longitudinal Blending Logic.

5.3.2 Lateral Blending Logic

Initiation of rudder control poses no particular problems because of both the relatively high dynamic pressure and the small attitude errors maintained by the aileron. Thus, at present there appears to be no requirement for a gradual blending in of rudder control, although at some point in the future it may be necessary. Also, since the rudder command is linearly related to the aileron command, no basic control surface effectiveness information can be obtained by "measuring" rudder commands, over and above the information obtained from an examination of aileron commands. Thus, rudder deflection need play no part in the lateral blending logic.

The lateral channel design problem is almost identical to that of the longitudinal channel; consequently, the same blending techniques may be used. Recognizing aileron control is ineffective during the beginning of the entry, but that a trim setting is required to minimize lateral ACPS fuel expenditures, the same approach for aileron "turn-on" may be used as for the elevator: when the dynamic pressure is below a design specified value, given by $\bar{q}_2$, the aileron is used only for trim; when the dynamic pressure reaches and exceeds $\bar{q}_2$, the aileron is gradually blended in to full authority by use of the control law of (5-63) and the following limits on aileron deflection:

$$\delta_a^{max} = (1 - K_a)\delta_{a_T} + K_a\Delta_a^{max} \qquad \text{(a)}$$

$$\tag{5-82}$$

$$\delta_a^{min} = (1 - K_a)\delta_{a_T} - K_a\Delta_a^{max} \qquad \text{(b)}$$

where δ_{a_T} is defined by the trim logic of Figure 5-20, Δ_a^{max} is the design specified (symmetric) maximum aileron deflection*, and K_a is a dynamic pressure dependent parameter shown in Figure 5-24.

---

* See Section 5.4.2 for further discussion of this limit.
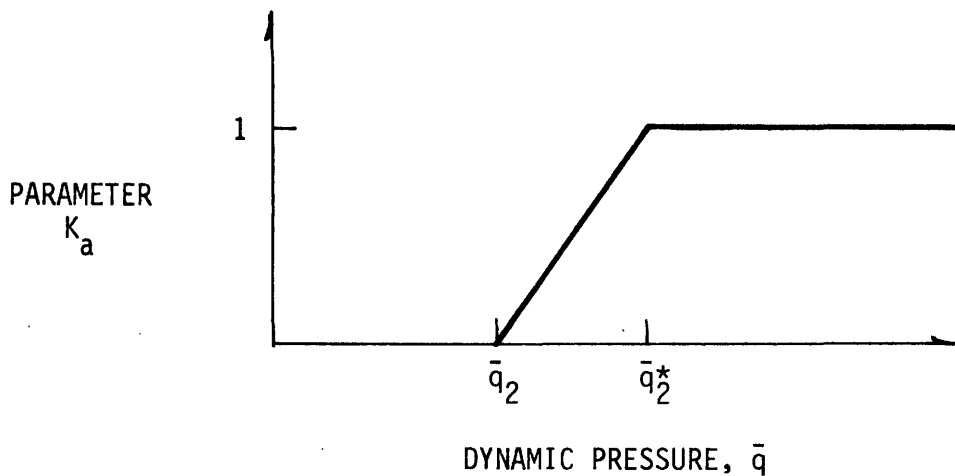
Figure 5-24. Aileron Blending Logic Parameter.

The lateral ACPS firings may be phased out with the same type of logic used for the pitch ACPS jets: a threshold logic which "measures" aileron effectiveness by comparing deflection commands with the limits specified by (5-82). Again, the closed loop pole placement synthesis used in the aileron control law development provides the basis for the use of this type of logic to ascertain the requirement for ACPS augmentation. This logic, along with the "turn-on" logic described above, is shown in Figure 5-25. In precisely the same manner as was done in the longitudinal channel, the threshold function "floats" about the aileron trim value, by using the following deflection magnitude parameters:

$$r_5 = (\delta_a^{min} - \delta_{a_T})f_3 + \delta_{a_T} \qquad \text{(a)}$$

$$r_6 = (\delta_a^{min} - \delta_{a_T})f_4 + \delta_{a_T} \qquad \text{(b)}$$

$$r_7 = (\delta_a^{max} - \delta_{a_T})f_4 + \delta_{a_T} \qquad \text{(c)}$$

$$r_8 = (\delta_a^{max} - \delta_{a_T})f_3 + \delta_{a_T} \qquad \text{(d)}$$

(5-83)

where the design specified parameters f_3 and f_4 are chosen such that:

$$0 < f_4 < f_3 < 1 \qquad \text{(5-84)}$$

181

Figure 5-25. Lateral Blending Logic.

and δ_a^{min} and δ_a^{max} are obtained from (5-82). As before, the hysterisis is used to prevent possible aileron 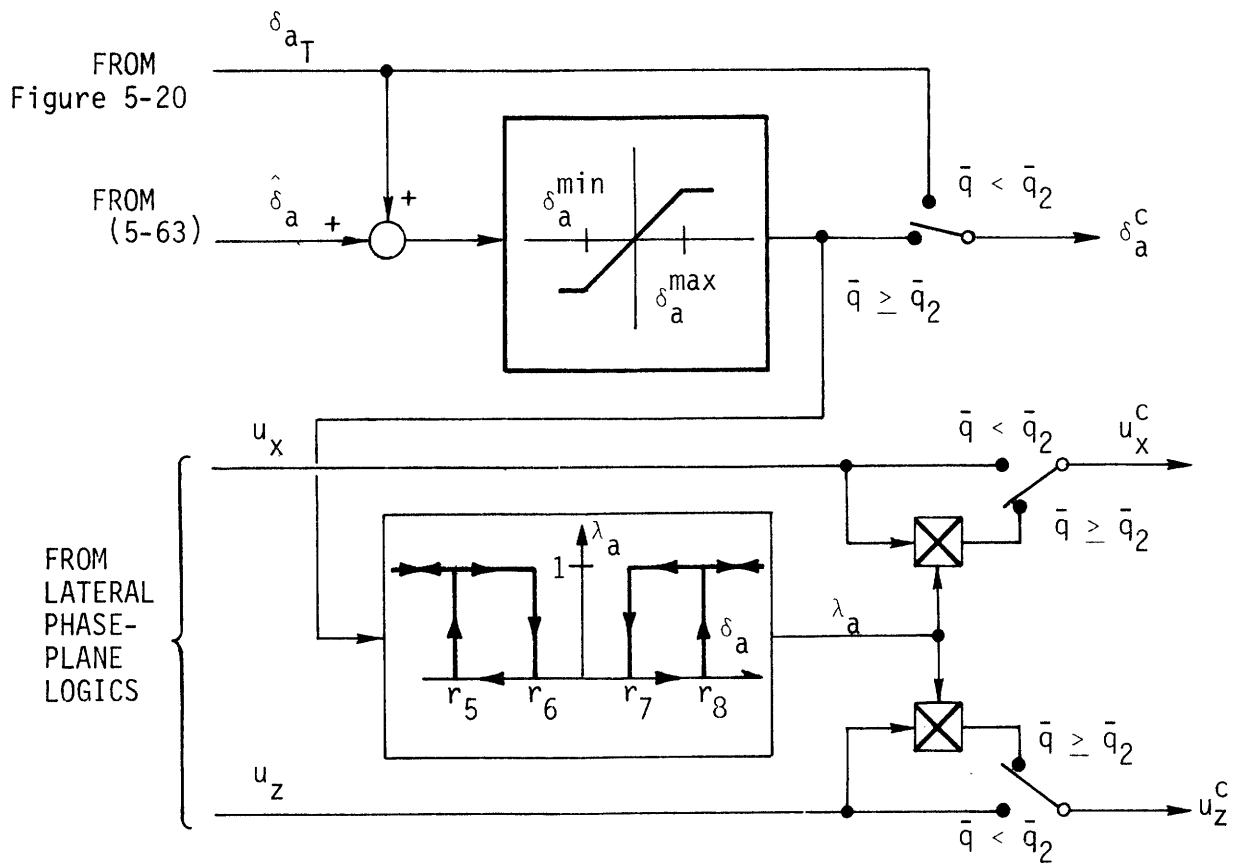chatter, and the additional dynamic pressure switch precludes jet inhibition when the dynamic pressure is below $\bar{q}_2$, when the aileron is used solely for trim.

5.4 Input/Output Processing

Although the interfaces between the control system and its working environment are not well-defined, this section will describe the input/output signal processing necessary for practical implementation of the control laws derived above. Because of this lack of firm demarcation between controller and environment (e. g., sensors, actuators, etc.) the final configuration of I/O processing will be subsystem dependent, and it is not in the scope of this study to attempt to define an overall avionics system for attitude control. Thus, what follows will be one view of the interface problem and possible solutions to the processing requirements. The bulk of the solutions presented here are not, however, included in the design summary of the next chapter, so as to allow for greater interface flexibility with configuration dependent state estimator and control effector logics.

Section 5.4.1 is concerned with the inputs to the control laws, including the guidance generated and measured/estimated state variables, along with the more slowly varying trajectory state variables. Section 5.4.2 discusses the output signal processing, concentrating on the surface actuator logic and the ACPS jet selection logic.

5.4.1 Inputs

As was noted earlier in the development, the design presented here is basically a stability-axis state controller; thus, input processing is primarily concerned with generating this state information from conventional sensors which generally provide other types of state information. This section will thus provide a simple rationale for the necessary transformations between the state spaces, and discuss some

183

of the alternative means for deriving the same necessary information. What will not be covered here, however, is the practical problem of estimation in the presence of errors, as this is thoroughly developed in References 14, 16, and 17.

5.4.1.1 Stability-Axis Attitude

Two of the three stability-axis attitude angles, α and β, are defined by Figure 4-5 of Chapter 4 which is repeated below in Figure 5-26 in slightly modified form[*]. Knowing (U, V, W), it is then a direct matter to specify these angles:

$$\alpha = \tan^{-1}(W/U) \qquad \text{(a)}$$

$$\beta = \sin^{-1}(V/V_T) \approx V/V_T \qquad \text{(b)}$$

(5-85)

where the approximation is made since $\beta \ll 1$ normally. It should be noted that the velocity vector $\underline{v}$, coordinatized in the body frame as (U, V, W), represents the vehicle's velocity with respect to the atmosphere. The bank angle ϕ_S may be similarly specified, if the "down" direction is known. Shown in Figure 5-27 is the velocity vector in relation to the local horizontal frame and the "down" unit vector $\underline{u}_D$. By normalizing the velocity vector, the following triad may be formed:

$$\underline{u}_V = \underline{v}/|\underline{v}| \qquad \text{(a)}$$

$$\underline{u}_H = \underline{u}_D \times \underline{u}_V \qquad \text{(b)} \quad \text{(5-86)}$$

$$\underline{u}_N = \underline{u}_H \times \underline{u}_V \qquad \text{(c)}$$

Now, if $\underline{u}_{y_B}$ is the unit vector along the y_B axis of the vehicle, then the bank "pointer", $\underline{u}_p$, may be defined as follows:

$$\underline{u}_p = \underline{u}_{y_B} \times \underline{u}_V \qquad \text{(5-86d)}$$

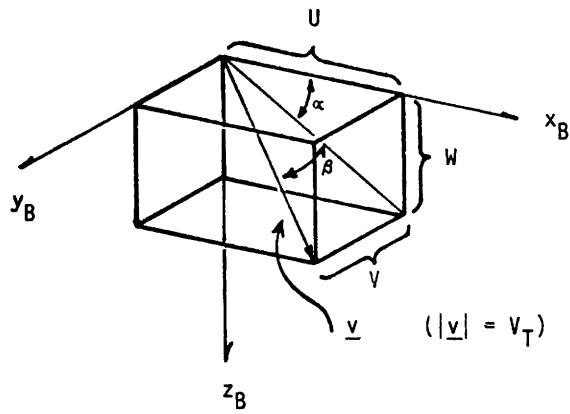[*] The tildas are omitted as was done earlier in the development of this chapter.
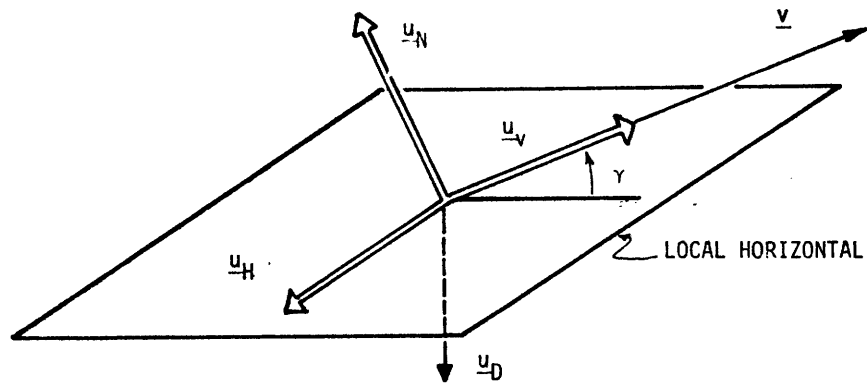
Figure 5-26. Definition of α and β

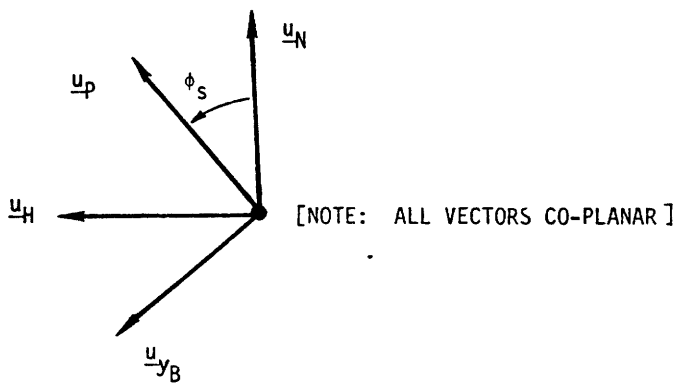Figure 5-27. Velocity Frame Triad

[NOTE: ALL VECTORS CO-PLANAR]

Figure 5-28. Bank Pointer Definition.

185

Shown in Figure 5-28 is a view down the velocity vector, relating the various unit vectors for a given bank angle, ϕ_s. It should be clear then that:

$$\underline{u}_p \cdot \underline{u}_N = \cos \phi_s$$

$$\underline{u}_p \cdot \underline{u}_H = \sin \phi_s$$

so that

$$\phi_s = \tan^{-1}[(\underline{u}_p \cdot \underline{u}_H)/(\underline{u}_p \cdot \underline{u}_N)] \qquad (5\text{-}85c)$$

Thus, given the vehicle's air relative velocity and a down reference, the stability-axis angles may be calculated from (5-85). It may be assumed that a down reference is available (or computable from outputs) from the inertial measurement unit (IMU); the question is the source of the velocity information. Available (or computable from outputs) from the IMU will be earth relative velocity, coordinatized in the body-axis frame. Required in the above formulation, however, is vehicle velocity with respect to the atmosphere, so that the presence or absence of winds clearly affects the accuracy of the velocity information derived from the IMU. Although this subject is discussed at greater length in Reference 14, it is appropriate to note the type of estimator solution implied by wind "noise". Since the earth relative velocities are large at the beginning of entry, small wind perturbations do not seriously affect the accuracy of inertially derived estimates of the stability-axis angles. As the velocity decreases the converse is true; however, by this time the dynamic pressure is sufficiently high so that body mounted accelerometer information may be put to good use. For example, if it is assumed that the only aerodynamic side force (i. e., in the y_B direction) on the vehicle is due to sideslip, then from (A-14) of Appendix A, it is seen that the following approximate expression holds[*]:

---

[*] A more exact expression, accounting for a velocity magnitude variation, is given in Reference 14.

186

$$\overline{q}SC_{y_\beta}\beta = m\,a_y$$

where a_y is the specific force sensed by a lateral accelerometer mounted at the center of gravity. Thus, an alternate estimate of β, valid at sufficiently high dynamic pressures, is obtained from:

$$\beta = \frac{m}{\overline{q}S}\frac{1}{C_{y_\beta}}a_y \qquad (5\text{-}87)$$

The aerodynamic model dependence of this estimate should be abundantly clear. The point is made in Reference 14 that a judicious mixing of the estimates of (5-85b) and (5-87) can provide a means of obtaining "good" sideslip estimates; the same arguments can be made for angle-of-attack and bank angle estimates. For the block diagrams and flow charts of the next chapter, it is assumed that α, β, and ϕ_s are provided by an estimator logic which performs the appropriate geometric transformations and sensor blending necessary for "good" estimates. Simulation results with a particular estimator logic are discussed in Sections 7.2 and 7.3.

5.4.1.2 Stability-Axis Rates

In order to define the stability-axis rates, $\dot{\alpha}$, $\dot{\beta}$, and $\dot{\phi}_s$, in terms of the conventional body rates p, q, and r, the appropriate results of the modelling exercise of Chapter 4 may be used. However, it is more straightforward to simply consider the geometric transformation between the two body rate sets without regard to the aerodynamic effects on the vehicle's rotational dynamics. This is possible because the vehicle's total angular velocity, $\underline{\omega}_b$, may be considered as composed of an angular velocity with respect to the stability-axis frame, $\underline{\omega}_s$, combined with the angular velocity of the stability-axis frame itself, $\underline{\omega}_v$. Rather than introduce the several frames necessary for a formal definition of these relationships, and the corresponding transformation matrices, it suffices for the purpose here to repeat the following relation derived in Appendix C of Reference 15:

$$\underline{\omega}_b = T\underline{\omega}_s + C\underline{\omega}_v \qquad (5\text{-}88)$$

where the transformation matrices T and C are simplified by assuming that $\beta \ll 1$, so that:

$$T \equiv \begin{bmatrix} \cos\alpha & 0 & \sin\alpha \\ \beta & 1 & 0 \\ \sin\alpha & 0 & -\cos\alpha \end{bmatrix} \qquad (5\text{-}89a)$$

$$C \equiv \begin{bmatrix} \cos\alpha & (\sin\alpha\sin\phi_s - \beta\cos\alpha\cos\phi_s) & (-\sin\alpha\cos\phi_s - \beta\cos\alpha\sin\phi_s) \\ \beta & \cos\phi_s & \sin\phi_s \\ \sin\alpha & (-\cos\alpha\sin\phi_s - \beta\sin\alpha\sin\phi_s) & (\cos\alpha\cos\phi_s - \beta\sin\alpha\sin\phi_s) \end{bmatrix}$$

$$(5\text{-}89b)$$

The total angular velocity of the vehicle, $\underline{\omega}_b$, coordinatized in the body frame, and the stability-axis angular velocity, $\underline{\omega}_s$, coordinatized in the stability-axis frame, are defined by:

$$\underline{\omega}_b \equiv \begin{bmatrix} p \\ q \\ r \end{bmatrix} \quad ; \quad \underline{\omega}_s \equiv \begin{bmatrix} \dot{\phi}_s \\ \dot{\alpha} \\ \dot{\beta} \end{bmatrix} \qquad (5\text{-}90a)$$

The angular velocity of the stability-axis frame itself, $\underline{\omega}_v$, is defined in terms of the rotation rates of the vehicle velocity vector:

$$\underline{\omega}_v \equiv \begin{bmatrix} -\dot{\psi}\sin\gamma \\ \dot{\gamma} \\ \dot{\psi}\cos\gamma \end{bmatrix} \qquad (5\text{-}90b)$$

where γ is, as before, the flight path angle, and ψ is the vehicle's heading angle. As will be seen in a review of Appendix B, it is precisely this angular velocity which is ignored in the simplified equation development; and justifiably so, since it is basically a slow "gravity turn"

effect acting on the velocity vector, which, in turn, defines the stability-axis variables. It is clearly inappropriate to include this low turn rate in a simplified model of the short-term rotational dynamics. For the purposes here, however, model simplification is not so strong an issue; thus, the stability-axis rates may be solved for from (5-88) rather directly:

$$\underline{\omega}_s = \underline{\omega}_1 + \underline{\omega}_2 \qquad (5\text{-}91)$$

where $\underline{\omega}_1$ and $\underline{\omega}_2$ are the "fast" and "slow" angular velocity components of $\underline{\omega}_s$, given by

$$\underline{\omega}_1 = \begin{bmatrix} (p \cos \alpha + r \sin \alpha) \\ q - \beta(p \cos \alpha + r \sin \alpha) \\ (p \sin \alpha - r \cos \alpha) \end{bmatrix} \qquad (a)$$

$$(5\text{-}92)$$

$$\underline{\omega}_2 = \begin{bmatrix} -\dot{\psi} \sin \gamma \\ \dot{\gamma} \cos \phi_s + \dot{\psi} \cos \gamma \sin \phi_s \\ \dot{\gamma} \sin \phi_s - \dot{\psi} \cos \gamma \cos \phi_s \end{bmatrix} \qquad (b)$$

It should be noted that in deriving these expressions, terms containing $\dot{\psi}\beta$ and $\dot{\gamma}\beta$ were dropped due to their second-order contributions. Thus, given the body rates (p, q, r), the attitude (ϕ_s, α, β), the flight path angle and rate (γ, $\dot{\gamma}$), and the heading rate $\dot{\psi}$, the stability-axis attitude rates ($\dot{\phi}_s$, $\dot{\alpha}$, $\dot{\beta}$) can be found from (5-91) and (5-92). A simpler approach is to recognize that the flight path angle rate and heading rate are defined by (from Reference 15):

$$\dot{\psi} = \frac{\overline{q}S}{mV_T} C_{\mathcal{L}} \sin \phi_s \sec \gamma \qquad (a)$$

$$(5\text{-}93)$$

$$\dot{\gamma} = -\frac{g}{V} \cos \gamma + \frac{\overline{q}S}{mV_T} C_{\mathcal{L}} \cos \phi_s \qquad (b)$$

189

Recognizing that $\gamma \ll 1$, then (5-91), (5-92) and (5-93) may be used to define the following relation between the stability-axis rates and the body-rates:

$$\dot{\phi}_S = p\cos\alpha_T + r\sin\alpha_T + \frac{a_{\mathcal{L}}}{V_T}\gamma\sin\phi_S \qquad \text{(a)}$$

$$\dot{\alpha} = q - \beta\dot{\phi}_S + \frac{1}{V_T}(g\cos\phi_S - a_{\mathcal{L}}) \qquad \text{(b)} \quad \text{(5-94)}$$

$$\dot{\beta} = p\sin\alpha_T - r\cos\alpha_T + \frac{g}{V_T}\sin\phi_S \qquad \text{(c)}$$

where the lift acceleration $a_{\mathcal{L}}$ is defined by:

$$a_{\mathcal{L}} \equiv \frac{\bar{q}SC_{\mathcal{L}}}{m} \qquad \text{(5-94d)}$$

and where it should be noted that the trim angle-of-attack α_T is used to approximate the instantaneous angle-of-attack, α. Thus, from the simple form of the (approximate) transformation from body-axis rates, whose source is assumed to be either the IMU or body mounted rate gyros, to stability-axis rates, it should be clear that digital implementation is fairly straightforward. By approximating the lift coefficient $C_{\mathcal{L}}$ as a simply scheduled gain, then $a_{\mathcal{L}}$ is simply proportional to dynamic pressure, similar in structure to other gains of the control law derived earlier. The alternative, of course, is to use axial and normal body mounted accelerometer information to provide a closed-loop estimate of the lift acceleration, less subject to vehicle aerodynamic modelling errors.

It should be noted that in the derivation of (5-94) that no consideration was given to error sources and their effect on the accuracy of the (derived) stability-axis angular velocity vector. Because of this reason and because the ultimate sources of the basic rotational information are as yet undefined, the signal processing implied by (5-94) will not be formalized as an additional "module" to the overall controller defined in Sections 5.1 through 5.3. Thus, in concert with the treatment of

190

the attitude estimation problem addressed in the previous section, it will be assumed that $\dot{\alpha}$, $\dot{\beta}$, and $\dot{\phi}_s$ are provided by an estimator which performs the appropriate transformations and blending of sensor outputs necessary for "good" rate estimates. Simulation results with a particular estimator logic are discussed in Sections 7.2 and 7.3.

5.4.1.3 Guidance Commands

In contrast with the situation just described, the identity of the guidance commands with the controlled state variables of angle-of-attack and bank angle makes it unnecessary to provide for transformations in the input signal processing. It is, however, appropriate at this point to introduce a simple modification to the logics presented earlier due to its proximity to the input interface. Shown in figure 5-29 is the inclusion of limiters in the attitude error signal paths of both the longitudinal and lateral control logics. This is done for three reasons. First, by limiting the input magnitude, cooperative effort between the ACPS and ACSS control logics is enhanced, since their operational characteristics become more nearly alike as the vehicle approaches a commanded equilibrium state. Second, variation of the magnitude of the limiter provides a convenient, if not precise, means of adjusting the maximum closed-loop maneuver rate in response to a large commanded step input. Finally, the limiter provides some protection against large transients in the guidance commands. It should be noted that in the lateral channel ϕ_{max} is the same design specified parameter as is used in the maneuver logic described in Section 4.2.2.2, so as to preserve consistency in the limits.
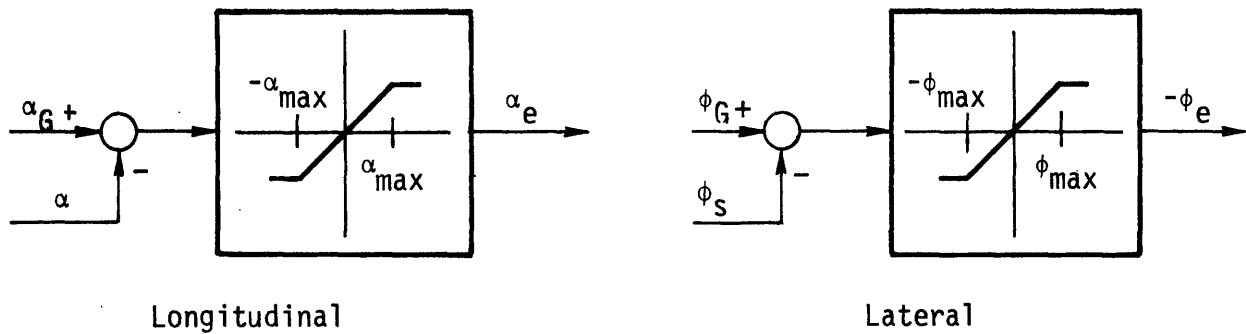
Longitudinal   Lateral

Figure 5-29. Attitude Error Limiters.

5.4.1.4 Trajectory State Variables

The final set of input variables required by the control system are three of the variables which define the trajectory envelope: Mach number, $\mathcal{M}$, dynamic pressure $\bar{q}$, and trim angle-of-attack, α_T. It is assumed for this study that these variables are estimated and/or measured by an air data system, so that, except for α_T, this section will not be concerned with their derived relations with more fundamental environmental parameters (e.g., temperature, density, etc.). Instead, it is appropriate to consider the update rates at which these variables are supplied to the control system.

As may be recalled, Mach number is used to determine the start of rudder utilization, and, as is noted in the next section, gain scheduling will be performed by using $\mathcal{M}$ as the independent variable. In a similar fashion, dynamic pressure is used both to determine the beginning and end of various control modes, and as a gain parameter in the surface control laws. Thus both $\mathcal{M}$ and $\bar{q}$ are used for mode switching and gain determination, implying a relatively low update

192

rate requirement, since mode switching is not critical and gain changes should occur at the slow rates characteristic of the trajectory parameter variations (see Appendix C). An appropriate sample rate for these two variables would appear to be that of the relatively slow guidance cycle.

The trim angle-of-attack is used both as a gain parameter in the lateral ACPS logic, and, as should be clear from (5-94), is used in estimating the stability-axis rates. In this latter capacity it is more closely tied to the "fast" control loop dynamics, and thus the frequency characteristics of α_T are of importance. Rather than attempt a slow update rate which may incur relatively large step changes (and, subsequently, high frequency disturbance inputs to the control loop) it is advisable to use a fast update rate coupled with a long time-constant linear filter. In this manner the high-frequency components of the instantaneous α measurement can be filtered out so as to provide an α_T estimate which changes very little at any given control law sample instant. The implementation details of such an estimator are not given here, as they are the province of the air data system.

5.4.2 Outputs

As was noted earlier in the chapter, the elevator, aileron, and ACPS accelerations are merely convenient abstractions of the actual torque producing hardware, and although this type of treatment facilitates control law development, it also imposes an output processing requirement: that of transforming the control law output commands to realizable control effector subsystem input commands. In particular, it may be recalled from the description given in Section 2.2 that the elevator and aileron "deflections" are, in actuality, due to left and right elevon deflections, while the ACPS control accelerations, modelled as an uncoupled body-axis triad, are, in actuality, due to the separate firings of 24 ACPS jets whose torque

193

vectors are not necessarily co-linear with any one body axis. Thus, this section will discuss some of the problems in transforming these idealized commands into realizable commands, and suggest appropriate solution techniques. As with the input processing, however, these techniques will not be incorporated into the control system design summary of the next chapter, so as to maintain some degree of configuration independence.

5.4.2.1 ACSS Commands

It should be recalled from Figure 2-6 of Section 2.2 that the elevator and aileron "deflections" are defined in terms of the left and right elevon deflections as follows:

$$\delta_e \equiv \frac{1}{2}(\delta_{E_L} + \delta_{E_R}) \qquad \text{(a)}$$

$$(5-95)$$

$$\delta_a \equiv \frac{1}{2}(\delta_{E_L} - \delta_{E_R}) \qquad \text{(b)}$$

where the elevons are physically limited as follows:

$$\Delta_{min} \le \delta_{E_L} \le \Delta_{max} \qquad \text{(a)}$$

$$(5-96)$$

$$\Delta_{min} \le \delta_{E_R} \le \Delta_{max} \qquad \text{(b)}$$

Thus, given the elevator and aileron commands generated by the appropriate control laws, then (5-95) may be solved for the corresponding elevon commands:*

$$\delta_{E_L}^c = \delta_e^c + \delta_a^c \qquad \text{(a)}$$

$$(5-97)$$

$$\delta_{E_R}^c = \delta_e^c - \delta_a^c \qquad \text{(b)}$$

---

*In the notation that follows, a superscript c is used to distinguish commands from deflections.

so that this is an extremely simple transformation logic, taking in the fictitious surface commands and outputting commands which can be implemented by the surface actuators. It is, however, appropriate to examine one of the effects of this control effector "sharing", namely, elevon allocation in the presence of simultaneous elevator and aileron commands which are inconsistent with the physically attainable deflection limits of (5-96).

Suppose that the following commands, <u>limited</u> by the appropriate surface logic, are issued by the controller:

$$(\delta_e^c, \delta_a^c) = (-40°, +10°) \qquad (5\text{-}98)$$

The elevon deflections necessary to satisfy this command pair is found from (5-97) to be:

$$(\delta_{E_L}^c, \delta_{E_R}^c) = (-30°, -50°) \qquad (5\text{-}99)$$

which is unrealizable when

$$(\Delta_{min}, \Delta_{max}) = (-40°, +15°)$$

and the constraints of (5-96) are imposed. If the elevons are driven independently to attempt to reach the command given by (5-98) then the right elevon will limit, resulting in the following deflection pair:

$$(\delta_{E_L}, \delta_{E_R}) = (-30°, -40°) \qquad (5\text{-}100)$$

Substitution of these deflections back into (5-95) gives the effective elevator and aileron deflections:

$$(\delta_e, \delta_a) = (-35°, +5°) \qquad (5\text{-}101)$$

195

so that the command given by (5-98) is satisfied for neither δ_e nor δ_a. The errors between command and actual deflections, due to limiting at the elevon level, thus allow for an undesired control induced lateral and longitudinal cross-coupling. This, it should be noted, is even in the presence of individual elevator and aileron limiting by the control logic (see Section 5.3). Clearly these design specified limits can be reduced to a level that precludes any elevon limiting effects, but is done at the expense of reduced total control power. Another approach is to augment the lacking elevator and/or aileron torque by use of appropriate ACPS firings. Not only does this approach have the disadvantage of requiring a logic to determine the torque compensation required (a non-trivial task due to the large variations in surface effectiveness during entry), but it also encourages jet activity during periods of high surface activity, a somewhat questionable approach due to the previously-mentioned possibility of flow interaction. Appendix H presents a third alternate in the form of a simple algorithm which, when faced with an unattainable elevator/aileron command pair attempts to satisfy whichever command is emphasized by the control logic. Thus, the controller may set a flag so that the allocation algorithm always attempts to satisfy the elevator command, even in the presence of a conflicting aileron command; or, the flag may be oppositely set to satisfy aileron commands at the expense of meeting elevator commands. More details are given in the appendix. The solution is a rather convenient one, and, via the setting of the allocation flag by the control logic, places the elevon allocation problem in the hands of the designer, rather than at the mercy of the elevon limiter properties.

Although the logic presented in the appendix ameliorates the steady-state elevon allocation problem, difficulties still remain due to the effective "sharing", by the elevator and aileron, of elevon rate limits. Clearly, an argument analogous to that summarized by (5-95) through (5-101), can be made for the rate limitng properties

of the elevons, and it is felt that a solution to the rate limiting problem would be similarly congruent. The effectiveness of such a technique has not been investigated in this study.

Whether or not an elevon allocation logic is used to interface with the commanded surface deflections generated by the ACSS control laws, the blending logic of Section 5.3 provides for limiting of the elevator and aileron commands. It is appropriate at this point to introduce a simple modification to the rudder logic of Section 5.2.2, due to its proximity to the output interface. Shown in Figure 5-30 is the use of a limiter operating on the rudder command (defined by (5-78)); as discussed in Section 5.3.2, a constant unscheduled limit, δ_r^{max}, is adequate for the rudder channel. In contrast with material presented in the remainder of this section, this logic is included in the design summary of the next chapter.
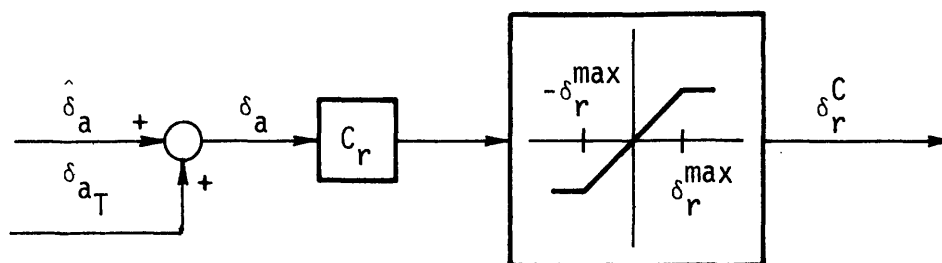

Figure 5-30. Rudder Limit Logic.

5.4.2.2 ACPS Commands

The acceleration commands generated by the ACPS control logic pose a similar problem in transformation from the idealized single-axis acceleration commands to the individual jet firing commands. Here, however, the problem is more difficult because of three reasons: the nature of the commands generated by the control logic, the discrete firings characterizing jet activity, and the large number of thrusters whose axes are not conveniently aligned for attitude control. The interface logic between the control law and the individual jet commands is normally referred to as the jet select logic (JSL), and it is the purpose of this section to note the performance implications of the control law combined with the JSL, for a particular jet configuration.

Conventional ACPS control laws, such as those used in the Apollo design, (see Reference 27) generate a "ΔV-command" (or "request" depending on the designer's point of view) which specifies a change in rotational and translational velocities to be effected by the proper combination of jets and their firng times, this command being transformed by the JSL into commands which can be implemented by the hardware. Such a command normally allows sufficient time for the JSL to satisfy the request by blending together the discrete (both in space and time) jet torques by using firing time as the modulating influence. As should be recognized from the ACPS control law development presented here, the outputs of the controller are rotational <u>acceleration</u> requests (translation being both unnecessary and ineffective), and, in fact, are sent to the JSL at the relatively high sample rate of the control cycle. Thus, the control law does not allow a selection logic the freedom to choose its own maneuver time in which to satisfy the ΔV-commands, and furthermore adds the constraint of reaching a commanded acceleration level within the control law sample period. To expect reasonable operation from a selection logic it is thus imperative that the control

law take a realistic view of the acceleration levels attainable by a particular jet configuration. This configuration dependence is, however, only reflected in the choice of the acceleration parameters U_x, U_y, and U_z used in the ACPS logics of Sections 5.1 and 5.2; thus, with acceleration level realizability a strong consideration, the control law may remain essentially independent of the JSL it is eventually interfaced with. This gain selection is discussed further in Section 5.5.

Two basic JSL techniques have been used to account for acceleration command inputs (and are described in Reference 25): table look-up and modified ΔV. The first approach basically correlates anticipated requested acceleration levels with a group of jets (one or more) which can provide an angular acceleration of approximately the same magnitude, about the appropriate body axis, and with minimum coupling into the other two axes. Additional compensation is provided for instances of strong coupling. Thus, given a specific command from the control logic, a particular group of jets is fired, the group determined from a table look-up procedure. The modified ΔV approach interprets the acceleration commands as ΔV requests to be satisfied within the control law sample period (thus $\Delta \omega_x = U_x T$), so that compensation is added to scale the normal ΔV response time to the controller cycle time. This approach thus allows for a greater flexibility in jet selection, since the transformed ΔV request can be "solved" in any appropriate manner; a fuel minimization approach is discussed in the JSL description given in reference 25.

Even with the proper choice of acceleration levels used in the control logic, the high sample rate of the requests sent to the JSL may make it difficult for uncoupled torque production, resulting in a control induced coupling between the body axes. This is due, of course, to the jet configuration; as can be seen from Table 2-5, there does not exist a single thruster which produces a torque vector closely paralleling a body axis. In fact, some of the thrusters,

199

notably the "yaw" thrusters (numbers 17 through 24) produce highly coupled body-axis torques. This would not necessarily be a disadvantage since stability-axis control implies a requirement for strong roll/yaw coupling in order to maintain small sideslips during a bank maneuver. However, it can be seen from Figure 2-5 that the location of the "yaw" cluster above the vehicle CG implies that the use of these jets will always miscoordinate any attempted maneuver (i.e., the vehicle will sideslip out of a bank). The basic responsibility for compensating for this behavior lies with the JSL; any residual cross-coupling will be viewed by the ACPS control logic as a disturbance torque, and appropriate action will be taken (perhaps in the form of an additional acceleration command to the JSL).

Thus, successful ACPS control demands attention to the thruster configuration, even though the JSL is the primary translator of the control commands. Operation of the control law with a particular jet select logic is demonstrated in Section 7.2.

5.5 Gain and Parameter Selection

Although the operational objectives of the control law described in the previous four sections should be clear by the functional description given, the selection of the "design specified" gains and parameters clearly plays an important role in the overall system performance. This section thus provides the rationale for assigning numerical values to the gains and parameters of the control laws, by examining some of the fundamental issues of the design problem. Those particularly relevant to this exercise are the closed-loop performance requirements, the subsystem constraints and specifications, and the accuracy of the model base used in synthesis. Clearly all three of these areas should motivate particular numerical assignments, and do, as is evidenced by the individual discussions below. It should be noted, however, that this type of "open-loop" gain and parameter specification only serves to approximate the

optimum numerical choices present in a "tuned" system; thus, as with all practical design efforts, recourse must eventually be made to a realistic simulation of the dynamic environment surrounding the control system. The objective of this section is thus not one of attempting to justify the particular numerical values presented in the next chapter; nor is it one of attempting to justify particular numerical values to be inferred by consideration of performance requirements, vehicle parameters, etc. Instead, what is presented below are the various design issues influencing parameter selection, and the trades to be made at arriving at an eventual compromise value.

This section is broken into two subsections. Section 5.5.1 discusses the fixed gain and parameter selection problem, in which the satisfaction of vehicle configuration constraints and performance requirements play a large part. Section 5.5.2 then introduces the "scheduled" gains necessary for control law implementation, and describes a technique for their specification, in which model accuracy is a strong consideration.

5.5.1 Fixed Parmeters

Because of the similar considerations involved in the numerical assignment of different control law parameters, it is appropriate to group the parameters along functional lines differing from those of their original introduction. Thus, consideration is given to parameters closely associated with: a) the ACPS control laws; b) the ACSS control laws; c) the blending logic; and d) mode switching. As noted above, this section will only attempt to discuss the basic trades involved in gain selection; an illustrative example of how this type of information may be used to arrive at particular numerical values is given in the discussion below concerning the ACPS control acceleration level assignment. The remainder of the section is purposefully more general so as to provide a basic guide which is relatively configuration independent.

5.5.1.1 ACPS Control Laws

Selection of the ACPS acceleration levels, U_x, U_y, and U_z, involves three basic considerations: compatibility with the jet select logic and the jet configuration; maneuver rate requirements; and a desire to minimize switch curve chatter. As discussed in Section 5.4.2, it is required that the acceleration commands approximate the torque levels which can be generated by firing a "reasonable" number of thrusters in the short span of a control cycle allowed for satisfaction of the acceleration requests. This translates to a requirement that the basic body-axis torque be provided by a small number of appropriate jets so that correction torques to account for cross-coupling are minimal. Shown in Table 5-1 is a rearrangement of some of the angular acceleration data given in Table 2-5; the grouping of jets helps identify thrusters appropriate to a particular control law command acceleration. Since the "roll" and "yaw" accelerations are symmetric, only those jets providing positive torques are shown.

From this form of data presentation, it is fairly straightforward to estimate appropriate values for the ACPS acceleration levels to be used in the control logic. Since the "roll" jets provide a strong pitch acceleration, it is appropriate to use couples as indicated in the table. The residual pitch and yaw accelerations should prove to be of no difficulty for jet select logic (JSL) compensation. Although three couples are available for roll acceleration, a desire for minimum fuel and small minimum impulse limit cycles motivates the use of a single couple, so that a reasonable roll acceleration figure is 1.43 deg/sec^2. The "yaw" jets provide a very strong (miscoordinating) roll acceleration and no simple jet combinations are available to compensate for this. Thus, the greater number of "yaw" jets that are used, the more difficult will be the task of the JSL. This, coupled with a desire to minimize the total minimum impulse, suggests a yaw acceleration figure of approximately 0.5 deg/sec^2. It should be recognized that the "pitch" jets are also "roll" jets, so that use of

202

Table 5-1: Acceleration Groups of ACPS Thrusters

Jet Number	Angular Acceleration ($°/sec^2$)			Grouping
	a_x	a_y	a_z	
26	.74	.56	.01	Positive Roll (u_x)
35	.69	-.54	.03	
28	.74	.57	.01	
31	.69	-.52	.03	grouped to cancel pitch coupling
30	.74	.58	.01	
33	.69	-.53	.03	
18	-.46	0.0	.53	
20	-.53	0.0	.53	
22	-.60	0.0	.53	Positive Yaw (u_z)
24	-.69	0.0	.53	
25	-.74	.56	-.01	Positive Pitch (u_y)
26	.74	.56	.01	
27	-.74	.57	-.01	
28	.74	.57	.01	grouped to cancel roll coupling
29	-.74	.58	-.01	
30	.74	.58	.01	
31	.69	-.52	.03	Negative Pitch (u_y)
32	-.69	-.52	-.03	
33	.69	-.53	.03	
34	-.69	-.53	-.03	grouped to cancel roll coupling
35	.69	-.54	.03	
36	-.69	-.54	-.03	

couples (as indicated) is mandatory to prevent pitch-into-roll coupling. Again, a desire to minimize fuel suggests the use of only one couple, implying an acceleration magnitude of approximately 1.0 deg/sec^2. It should be noted that the maximum magnitude <u>difference</u> between a positive and negative acceleration amounts to 10% of the average of their magnitudes, so that the assumption made in Section 5.1.1 of symmetric pitch torques is fairly accurate. Thus, the choice of $(U_x, U_y, U_z) \approx (1.4, 1.0, 0.5)$ deg/sec^2 appears justified from jet configuration and fuel consumption considerations.

Acceleration levels during maneuvers is another important consideration, however, and "snappy" performance, from a manual point of view, motivates the use of acceleration levels (i.e., a greater number of thrusters in a group) considerably higher than those above. Since there is no performance specification on maneuver acceleration, however, light weight is given here to the satisfaction of a qualitative performance requirement. This, of course, must be balanced with the requirement of achieving satisfactory maneuver rates within an appropriate control interval, a question best answered by simulation experience.

A final consideration in selecting values for the acceleration level parameters is that of ensuring a minimum of switch curve "chatter". This is illustrated in the phase plane trajectory of Figure 5-31, in which the acceleration level used in the definition of the γ-switch curve (see (5-5)) is too low with respect to the actual acceleration being delivered by the JSL and ACPS configuration. The simple solution, of course, is to raise the value of the acceleration level constant in the control law; the more general implication is to use a value for the acceleration level constant (U_x, U_y, or U_z) which is slightly greater than the maximum anticipated value delivered by the JSL. Thus, this consideration, along with more qualitative performance considerations, suggests that the levels derived above (compatible with the JSL and the jet configuration) be considered as minimum values, the required increases being determined from simulator experience.
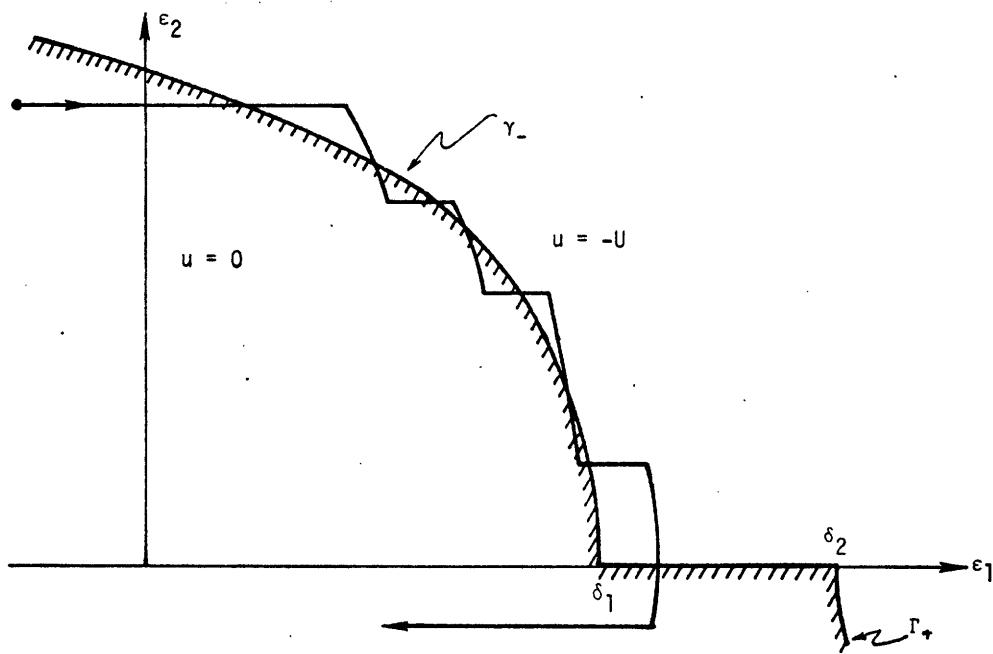
Figure 5-31。 Switch Curve Chatter.

Selection of the deadband parameters for the ACPS logics is considerably less configuration dependent, so that a more general discussion is appropriate here. Selection of the larger of the two deadbands for each channel $(\delta_{\alpha_2}, \delta_{\phi_2}, \delta_{\beta_2})$ is based both on attitude accuracy requirements, and on limit cycle fuel consumption, so that a compromise value is clearly indicated. The attitude accuracy requirements for angle-of-attack and bank angle are, in turn, specified by guidance requirements for attitude hold operation, while the sideslip accuracy requirement is basically configuration dependent. This latter dependence on vehicle aerodynamic properties is due to the requirement for well-coordinated bank maneuvers, so as to minimize disturbances to the bank channel due to adverse sideslip-induced dihedral torques. This accuracy requirement is naturally at odds with the minimum fuel motivation of large deadbands. The smaller deadband set $(\delta_{\alpha_1}, \delta_{\phi_1}, \delta_{\beta_1})$ is readily obtained from the

larger set by assuming a maximum switch curve overshoot equal to the product of a typical maneuver rate and the sample time. This attitude error may then be subtracted from the larger deadband parameter to obtain the smaller. It should be noted that there is no "nominal" maneuver rate, so that some judgement is also called for in assigning values to this latter set of parameters.

The final group of parameters used in the ACPS logics are the fuel-time weighting coefficients, $(\sigma_\alpha, \sigma_\phi, \sigma_\beta)$, and they are precisely what their names imply. As may be recalled from (5-6), σ is a non-linear function of the weighting parameter K used in the linear cost function of Appendix E. Thus, rather than attempt to specify the cost function, it is more convenient to directly specify, σ, recalling that as $\sigma \rightarrow 1^+$ response time is minimized, while as $\sigma \rightarrow +\infty$, the ACPS fuel required to perform a maneuver is minimized. This weighting is best determined in the simulator environment. Since the choice of σ directly affects the maneuver rate for a given attitude step command input, it should be clear that the choice of numerical values assigned to both σ_α and σ_ϕ is strongly dependent on the maneuver rate requirements imposed on the controller. Conversely, σ_β is relatively independent of external performance requirements; its choice is motivated by the requirement of tight sideslip control, enhanced by the deadband choice described above. Maintenance of small attitude errors implies fast response time, so that σ_β should be chosen accordingly. Of course, in the selection of all three weighting parameters, fuel expenditure trades must be taken into account.

5.5.1.2 ACSS Control Laws

Selection of the longitudinal and lateral pole placement parameters, $(\zeta_1, \omega_1, \zeta_2, \omega_2)$, respectively, basically involves attempting to satisfy closed-loop dynamic response specifications within the constraints imposed by the large variations in the entry environment. During the latter half of the entry, when the dynamic pressure is relatively high,

considerable control authority is available from the surfaces. It is thus appropriate to specify a large natural frequency ω (consistent with the subsystem constraints mentioned below), so that this capability for good maneuverability may be taken advantage of. What this implies, of course, is very high surface gains at the beginning of entry, since the dynamic pressure is low and the control law gains are inversely proportional to the dynamic pressure. Rate limiting thus becomes a dominant factor in the control surface deflection dynamics, with subsequent destabilizing effects on the overall controlled vehicle loop. The numerical value assigned to the natural frequency is thus a compromise between the very low values needed at the beginning of entry and the relatively large desirable values appropriate to the latter portion of entry. Appropriate scheduling of the natural frequencies is a non-compromise approach, but it should be recognized that the blending logic parameter specification also couples into this gain specification problem. That is, flexibility in specifying surface "turn-on" with the appropriate blending logic parameter alleviates the high gain problem at low dynamic pressures. This discussion is thus continued in Section 5.5.1.3. Specification of the damping ratios involves different considerations for the two axes. The longitudinal damping ratio, ζ_d, is chosen conventionally: an even compromise between fast response time and small overshoot. The choice of the lateral damping ratios, ζ_1 and ζ_2, is slightly more complicated due to the sideslip-bank coupling. Recognizing that the bank response is heavily dependent on the sideslip history, it should be clear that a high-frequency lowly-damped oscillation in sideslip will appear as a "ripple" in the bank response during a large attitude maneuver commanded by the guidance. Thus, good bank response implies a well-damped sideslip mode, which, in turn, is obtained by choosing a relatively large value for one of the damping ratios. The remaining damping ratio can then be chosen with the conventional considerations of response time and overshoot.

Selection of the longitudinal and lateral trim gains, $(K_{\alpha_1}, K_{\alpha_2})$ and (K_{ϕ_1}, K_{ϕ_2}), respectively, primarily involves a trade between fast trim operation and non-interference with the transient control laws already specified. Thus, early in the entry, when the dynamic pressure is low, the choice of K_{α_1} and K_{ϕ_1} effectively specify the surface trim <u>rates</u>, since, from (5-21) and (5-69), it may be recalled that:

$$\delta_{e_T} = \left(\delta_{e_T}\right)_{old} + K_{\alpha_1} T \tilde{u}_y \qquad (5\text{-}21)$$

$$\delta_{a_T} = \left(\delta_{a_T}\right)_{old} + K_{\phi_1} T \tilde{u}_x \qquad (5\text{-}69)$$

Recognizing that $\tilde{u}_x$ and $\tilde{u}_y$ are normalized jet commands, the effective trim rate magnitudes are thus given by:

$$\dot{\delta}_{e_T} = \pm K_{\alpha_1} \quad ; \quad \dot{\delta}_{a_T} = \pm K_{\phi_1} \qquad (5\text{-}102)$$

The choice of the magnitudes of K_{α_1} and K_{ϕ_1} is consequently a compromise, since the rates specified by (5-102) must be sufficiently high to ensure practical convergence on an appropriate trim value, and yet not so high as to interfere with the ACPS phase-plane logics attempting to control the vehicle's "fast" variations in attitude.

It was noted earlier that the algebraic signs on K_{α_1} and K_{ϕ_1}, are, respectively, negative and positive; the following argument may help explain these choices. For the longitudinal case, consider the situation in which the vehicle is operating in a low dynamic pressure regime and the elevator is incorrectly trimmed too far up (i.e., displacement is too negative). The (small) aerodynamic disturbance torque will tend to pitch the vehicle up, and the pitch ACPS logic will thus call for negative pitch jet firings to maintain the desired attitude. By choosing K_{α_1} to be negative, then $K_{\alpha_1} \tilde{u}_y$ will be positive, thus

incrementing the elevator in a positive sense: down. This lower
trim elevator position more closely approximates the desired trim
setting, thus reducing the disturbance torque seen by the pitch ACPS
logic. Iterations of this sequence will result in a proper trim setting
and an insignificantly low pitch disturbance acceleration. Operation
of the lateral trim logic is similar. In a low dynamic pressure
regime and with a positive lateral CG offset, the vehicle will attempt
to trim with a positive sideslip (see (5-66a); the roll ACPS will naturally
oppose this tendency with a sequence of negative roll jet firings. By
choosing K_{ϕ_1} to be positive, then $K_{\phi_1} \tilde{u}_x$ will be negative, thus decre-
menting the aileron in a negative sense. This negative aileron more
closely approximates the desired negative trim setting (see (5-68b)),
thus reducing the disturbance torque seen by the roll ACPS logic.
Iterations of this sort allow for a convergence to the proper trim setting.

Choice of the trim gains K_{α_2} and K_{ϕ_2}, appropriate to higher
dynamic pressure operation, is dictated by the requirement of suffi-
ciently fast trim operation within the constraints imposed by the
"transient" surface control laws. Thus, the gains must be chosen
large enough so that trim operation is responsive to changes in
center of gravity location and/or changes in desired trim attitude,
and yet small enough so as not to compromise the stability of the
transient loops. This latter point should be clear by recognizing that
introduction of a parallel channel integrator will add phase lag to
the control signal, generally a destabilizing contribution. As shown in
Figure 5-32, the larger the trim gain, the greater the lag at a given
operational frequency. Thus, an upper limit on trim gain magnitude
is specified by the transient loop stability characteristics.

Specification of the surface deflection limits is motivated by
the available deflections of the control surfaces. The rudder deflection
limit, δ_r^{max}, may be simply set to the physical limits of the corre-
sponding actuator. Selection of the elevator and aileron limits,
$(\Delta_e^{max}, \Delta_e^{min})$ and Δ_a^{max}, is less straightforward due to the elevon

$$1 + \frac{K_i}{s} = \frac{s + K_i}{s}$$
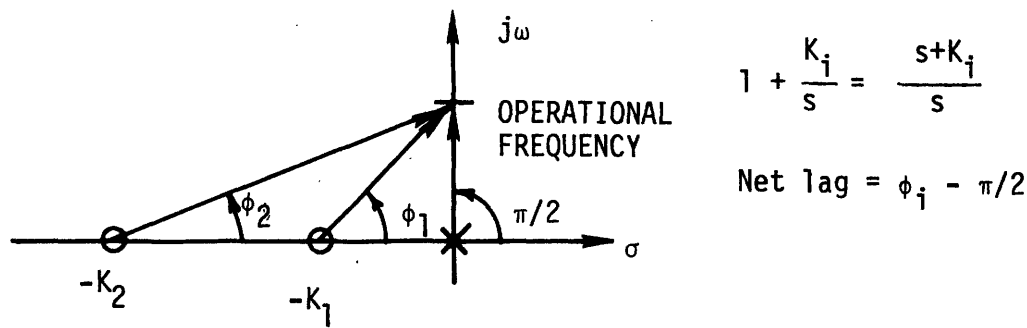
Net lag $= \phi_i - \pi/2$

Figure 5-32. Trim Gain Frequency Effects.

allocation problem discussed in Section 5.4.2. As noted there, the design specified limits may be set low enough to ensure that there are no allocation problems; this is, of course at the expense of reducing the vehicle's available control authority. Without the allocation logic described in Appendix H, the choice is thus between the possibility of occasional violation of the elevon limits (and subsequent cross-coupling) and smaller allowed maximum deflections (with subsequently less available authority). As is seen in the next chapter, the former approach is taken, based on simplicity of implementation: set Δ_e^{max} and Δ_e^{min} to the elevon limit values, and choose Δ_a^{max} to compromise between elevon allocation constraints and required aileron travel.

The final parameter group to discuss in the ACSS logic is that composed of the bank maneuver parameters, $(\dot{\phi}_{max}, \phi_{max}, \phi_{min}, \dot{\phi}_{db}, \tau)$, used in the aileron control logic. Since this modification to the basic control law is motivated by guidance bank rate requirements, a lower limit on $\dot{\phi}_{max}$ is set by the minimum bank rate required specified by the particular guidance system interfacing with the controller. The upper limit is set by control authority and actuator rate limit effects, and is best determined from simulation efforts. Specification of ϕ_{max} is more readily accomplished by viewing it as a parameter which provides "lead" to the maneuver

logic; that is, if the attitude error is large and the vehicle is maneuvering at $\dot{\phi}^{max}$ approaching the target attitude, then ϕ_{max} signifies the point at which deceleration should begin to terminate the maneuver. With ϕ^{max} too small, there is insufficient lead and considerable overshoot. With ϕ^{max} too large, the desired large attitude maneuver rate $\dot{\phi}_{max}$ is never reached, since the attitude error is small with respect to ϕ_{max}. This type of compromise must also consider the logic introduced by the filter parameter τ (see below). Specification of the maneuver logic deadband parameters, ϕ_{min} and $\dot{\phi}_{db}$, is a balance between ensuring that the maneuver logic "completes" a maneuver, and providing sufficient state separation between this logic and the nominal transient aileron control law. Thus, with small deadband parameters, the maneuver logic targets for very small attitude and rate errors, the qualities of a successful maneuver. However, a small deadband implies high-frequency switching between the transient and the maneuver logics, obviously undesirable for the operation of either. Large deadbands avoid this problem, but imply that the transient control law is to be used for large attitude errors, clearly a maneuver situation. The resulting compromise value should also take into account the inevitable switching transients which will occur between logics, and this is best done by examining simulated maneuvers. Finally, the filter time constant, τ, should be chosen large enough so that an instantaneous logic step command from the guidance results in a not unreasonably large rate command; choosing τ too large, of course, results in sluggish response.

The final ACSS parameter to consider is the magnitude of the rudder crossfeed gain, C_{rud}. It should be clear from the controllability discussion of Section 5.2.2, and the controllability contours of Appendix F, that the larger C_{rud} is, the greater is the (theoretical) rudder augmentation of the aileron effectiveness, in turn implying a larger flight envelope in which aileron control may be used. This, of course, is counterbalanced by both the specified limits on rudder

deflection and the fact that a high crossfeed gain will result in a noisy rudder deflection history due to small (digitized) step changes in the aileron deflection command. This latter situation is somewhat ameliorated by the fact that a large value for C_{rud} implies small gains for the aileron (see (5-64) and (5-65)), but the noise content of the rudder signal can only be increased with an increase in the crossfeed gain. Specification of C_{rud} is thus based on a choice between increased controllability and increased high-frequency content of the rudder signal.

5.5.1.3 Blending Logic

Assigning values to the dynamic pressure blending parameters, $(\bar{q}_1, \bar{q}_1^*, \bar{q}_2, \bar{q}_2^*)$, is equivalent to specifying when and how quickly the surface "turn-on" is to occur. Favoring the early use of the surfaces is the consideration of ACPS fuel expenditures and the recognition of the more desirable control characteristics of smoothness and accuracy attainable with surface control. Favoring a delayed introduction of ACSS control is the early entry low surface effectiveness. As noted above, this low effectiveness plays a large part in the compromise used to determine the design specified natural frequency for closed-loop pole placement. Because of the inverse dependence of the gains on dynamic pressure, delaying surface turn-on allows for generally higher gains, which are more appropriate to later operation in the denser atmosphere. A second advantage to delaying surface control is that the ACPS logics have sufficient operating time at not insignificant dynamic pressures so as to provide accurate surface trim settings to offset the long-term average disturbance torques. Thus, selection of the surface turn-on parameters $\bar{q}_1$ and $\bar{q}_2$ must be made with the above trades in mind. Specification of $\bar{q}_1^*$ and $\bar{q}_2^*$ must also take the above considerations into account, in addition to recognizing that if the $\Delta\bar{q}$ (i.e., $\bar{q}_i^* - \bar{q}_i$) is too small, then not enough clamping of turn-on transients is provided, while if it is too large the full surface authority is being wasted.

212

The hysterisis logic parameters, f_1 through f_4, can be chosen to emphasize either high or low degrees of surface augmentation by the ACPS, and clearly the same arguments of the preceeding paragraphs can be applied here. The basic difference is that these parameters provide a finer capability for "tuning" the blending logic, especially with regard to transient operation. It should be recognized that the f_i parameter selection should proceed simultaneously with the dynamic pressure parameter specification, since the two groups are well-coupled in their effects on performance.

5.5.1.4 Mode Switches

The final group of parameters to be considered are those to do with control mode switching, $(\bar{q}_3, \bar{q}_3^*, \mathcal{M}_1)$, a highly configuration-dependent parameter set. Choice of $\bar{q}_3$ is dependent on the vehicle's dynamic derivative in sideslip, C_{n_β}', since roll jet mode switching from attitude hold to rate damping presumes a sufficiently high sideslip natural frequency. This, in turn, is due to the dynamic behavior of sideslip; recalling from (4-53) the simple oscillator model

$$\ddot{\beta} = -\omega_\beta^2 \beta \qquad (4-53)$$

it should be noted that for the deadband rate damping logic of the roll channel to work, ω_β^2 must be sufficiently high to produce a non-negligible sideslip rate due to a sideslip mistrim. Otherwise, low drift rates will go uncorrected by the logic and the attitude will diverge. In contrast, favoring an early switch to rate damping are the dynamic pressure dependent aerodynamic torques, which are viewed by the sideslip phase-plane logic as distrubance torques. Thus, early switching reduces ACPS fuel consumption, so that $\bar{q}_3$ should be chosen as low as possible, consistent with the requirement that ω_β^2 be large enough for rate damping to be effective in maintaining small sideslip deviations.

The dynamic pressure parameter $\bar{q}_3^*$ specifies at which point in the trajectory the aileron meneuver logic is available for initiating large attitude maneuvers. If there exists a guidance requirement for the high rates produced by this logic, then it will occur at relatively high g-loads (see reference 13), implying high dynamic pressure operation. It is thus appropriate to restrict the operation of this mode to this regime, since low dynamic pressures result in low surface effectiveness, which, in turn, will result in a high degree of surface activity if fast maneuvers are attempted. Whether or not a compromise value of $\bar{q}_3^*$ is necessary depends on vehicle configuration; at present it appears that it can be set sufficiently low so as to satisfy the guidance maneuver requirements, and yet not incur unduly high aileron activity.

The final mode switch parameter, $\mathcal{M}_1$, is used to determine rudder "turn-on", and its choice, though configuration dependent, is not critical. It is simply required that $\mathcal{M}_1$ be large enough to ensure that the control system enjoys the full benefits of rudder augmentation, but not so large as to allow rudder activity when its effectiveness is insignificant.

This then completes the discussion of the fixed gain parameter selection problem, and the associated trades in arriving at appropriate values. As noted earlier, these considerations must always be tempered with realistic simulator results, since the subtleties of control law cross-coupling are not always evident from an "open-loop" inspection of the system. The values chosen for the above-described parameters, appropriate to the vehicle configuration described in Chapter 2, are summarized in the next chapter.

5.5.2 Scheduled Gains

It is the purpose of this section to introduce the "scheduled" gains which are necessary for a practical implementation of the control laws described in Sections 5.1 and 5.2. In particular, it may be recalled from the pole-placement techniques used in elevator and aileron control law synthesis that the following gains were defined

as functions of the vehicle's nominal aerodynamic, mass, and geometric properties:

$$\xi_1 \equiv \left(\frac{Sc}{I_{yy}}\right) C_{M\delta_e} \quad ; \quad \xi_2 \equiv -\left(\frac{Sc}{I_{yy}}\right) C_{M_\alpha} \qquad (5\text{-}14)$$

$$\xi_3 \equiv C'_{n_\beta} / \tilde{C}'_{n\delta_a} \qquad (a)$$

$$\xi_4 \equiv \left(\frac{I_{zz}}{Sb}\right) \frac{1}{\tilde{C}'_{n\delta_a}} \qquad (b)$$

$$(5\text{-}64)$$

$$\xi_5 \equiv \left(\frac{I_{xx}}{Sb}\right) \frac{\tilde{C}'_{n\delta a}}{C_{n_\beta} \tilde{C}_{\ell\delta_a} - C_{\ell_\beta} \tilde{C}_{n\delta_a}} \qquad (c)$$

$$\xi_6 \equiv -\left(\frac{I_{zz}}{I_{xx}}\right)\left(\frac{\tilde{C}'_{\ell\delta a}}{\tilde{C}'_{n\delta_a}}\right) \qquad (d)$$

where the aerodynamic coefficients used in these expressions are functions of the trim angle-of-attack and Mach number (and implicitly of the inertia ratios). It is thus clear that an implementation of these gains requires a knowledge of the aerodynamic coefficients, the technique of implementation dependent both on the gain accuracy required and the degree of accuracy to which the aerodynamic coefficients are known.

It should be clear that a stringent requirement for precision and accuracy in these gains is impossible to meet because of the uncertainty which characterizes the coefficients upon which the gains are based. It should be recognized from the derivation of the control laws that gain variation will result in displacement of the desired closed-loop poles from their design specified locations. Thus, the question of sensitivity of pole location to

gain variation (and, ultimately, to aerodynamic coefficient variations) becomes important, and this is an additional factor which must be considered in the selection of the fixed closed-loop pole location parameters.

Thus, the accuracy with which these gains are implemented must take into account both design sensitivity and the accuracy of the source information. It is clearly futile to attempt, for example, a least squares fit of an n-th order two-dimensional polynomial surface to one of the aerodynamic coefficients whose sign may not be known with confidence. The approach taken here is slightly more pedestrian: attempt a piecewise-linear fit to the gain histories as they change with the progress of the entry. This may be accomplished in the following manner. First, using (5-14) and (5-64), the "ideal" gains are computed from the nominal values taken on by the aerodynamic coefficients, which, in turn, are specified by the nominal entry profile in the Mach/alpha plane (note that there is no dependence on dynamic pressure). With a particular gain history plotted verses Mach number, a piecewise-linear curve fit (for simplicity in digital table look-up procedures) may then be used to approximate the history with the following considerations in mind: accuracy of representation, number of segments, and range of variation of the associated aerodynamic coefficients. It should be recognized that a two-dimensional fit, over both Mach number and trim angle-of attack, would avoid the dependence on nominal entry profile, and thus provide a more accurate set of gain values for off-nominal trajectory situations. This gain in accuracy must, of course, be assessed in light of the accuracy of the aerodynamic coefficient information, and of the additional complexity involved. This course has not been found necessary in the studies to date.

Given in the next chapter are the gain "schedules" for the ξ_i, appropriate to the vehicle described in Chapter 2 and generated by the piecewise-linear fit procedure described above. Thus, the six gains are scheduled verses Mach number so as to maintain the closed-loop poles in the neighborhoods of the specified pole locations, with due consideration given to the anticipated aerodynamic uncertainties, and the sensitivity of pole location to gain variation. Performance of this system in a realistic aerodynamic environment is discussed in Section 7.3.2.

6.0 Summary Design Description

This chapter provides a summary description of the complete attitude control system, in a format which integrates the results of the previous chapter's design synthesis descriptions. Both the structure of the controller and the various levels of interaction between the separate control laws are not adequately illustrated in the previous chapter because of the control law development details; it is the purpose of this chapter to make clear the system structure. In addition, it is convenient to describe the controller design in a "user oriented" manner, so that a complete familiarity with the discussions of the previous chapter is unnecessary for an understanding of the controller design. Thus, some of the material presented here is somewhat repetitious; however, it is felt that this allows some degree of independence from the previous chapter, so that the description given below is a convenient self-contained reference.

This chapter is organized into four sections. Section 6.1 provides an overview of the entry controller organization and operational characteristics, while Section 6.2 is a detailed description of the control system, in terms of both organization and function. Section 6.3 then summarizes the gain and parameter values used in the design, appropriate to the vehicle description given in Chapter 2. Finally, Section 6.4 presents a flow chart summary of the control law as presently implemented on the FORTRAN simulator used for design verification.

6.1 Overview

Figure 6-1 provides an overview of the control logic structure. It is assumed for this discussion that a state estimator, an air data system, and an input interface logic are present to provide the necessary control system inputs. Specifically, the purpose of the state estimator is to provide stability-axis attitude and rate information, while the purpose of the air data system is to provide estimates of the dynamic pressure, Mach number, and trim angle-of-attack (see Section 5.4.1).
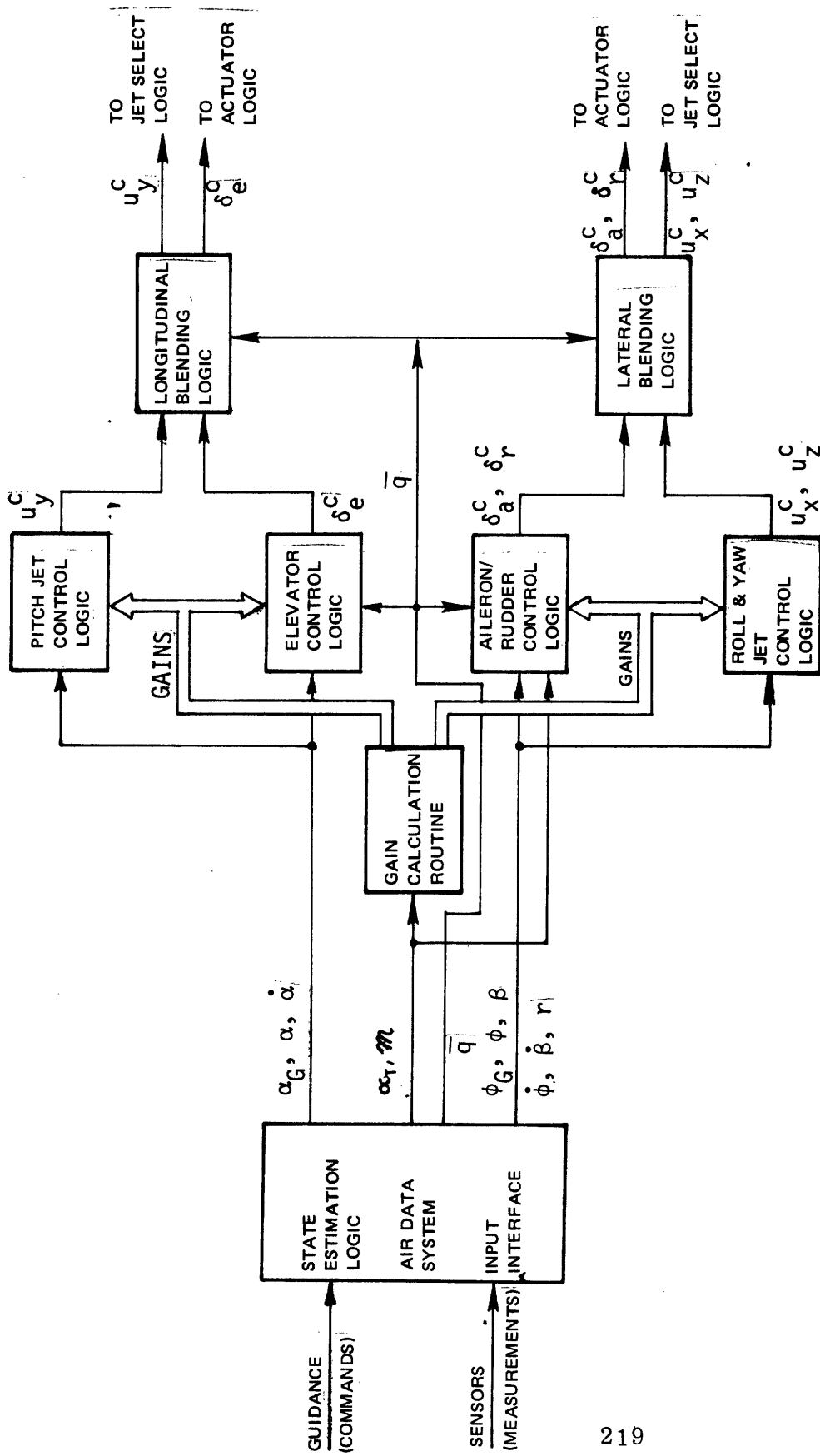
218

Figure 6-1.   Control System Overview.

219

Finally, the input interface transmits this information to the control system, along with the control commands generated by the guidance system.

Longitudinal control of angle-of-attack and pitch rate is provided by elevator (tandem elevon) deflections and pitch ACPS jet firings. The elevator logic uses conventional rate and position feedback (with feedforward trim integration) through scheduled gains to maintain relatively constant closed-loop pitch dynamics, while the ACPS logic uses phase-plane control to maintain a desired limit-cycle operation.

Lateral control of sideslip and bank angle is provided by aileron (differential elevon) and rudder deflections, and roll and yaw ACPS firings. The aileron/rudder logic uses rate and position feedback of the lateral variables (with feedforward trim integration for center-of-gravity offset compensation) to provide attitude and rate control of both sideslip and bank. The ACPS logic uses phase-plane control to maintain a desired limit-cycle operation when there is low dynamic pressure, and sideslip rate damping to maintain lateral stability when there is high dynamic pressure.

In both the lateral and longitudinal channels, blending of control by the surfaces and the ACPS is provided through a logic which determines ACPS inhibition on the basis of the magnitude of the current surface command and determines surface utilization on the basis of the dynamic pressure level.

6.2   Control System Description

This section presents a detailed summary description of the control system functional block diagrams and equations defining the complete logic derived in the previous chapter. Little justification for the design choice is given here, and it is suggested that the interested reader refer to the appropriate section of the previous chapter for questions of design synthesis. To help understand the gross operational

characteristics of the system, descriptive histories are given of typical entry operation through the use of different modes provided for by the control design. This section is broken into two subsections, longitudinal and lateral control.

6.2.1 Longitudinal Control

Longitudinal control uses both elevator (tandem elevon) and pitch ACPS jets to maintain the commanded angle-of-attack. As shown in Fig. 6-2, which illustrates a typical sequence of control activity during entry, there are two control modes for the elevator and one for the pitch jets.

Early in the entry, when the dynamic pressure is low, the elevator is used strictly for trim, so as to minimize pitch disturbance torques and thus fuel usage. The trim control law operates in a closed-loop fashion by slowly driving the elevator in the direction which nulls the pitch disturbance. The estimate of the disturbance torque is obtained by observing the pitch ACPS firing history. During this flight regime, the pitch ACPS jets, controlled by an angle-of-attack attitude/rate phase-plane logic, provide attitude and rate control in response to guidance commands. There is no jet inhibition in this regime.

When the dynamic pressure gets high enough, $(\bar{q}_1)$, the elevator is used for both trim and transient control. Trim is initially maintained through the use of the trim logic of the previous mode. At a slightly higher dynamic pressure, $(\bar{q}_1^*)$, trim is maintained through the use of an integrator acting upon the angle-of-attack error; the initialization value of the integrator is obtained from the value generated by the previous trim logic. Elevator control of transient errors is maintained through feedback of angle-of-attack and angle-of-attack rate, with appropriate gains. During this flight regime, pitch jet control identical to that of the previous regime may be utilized together with the elevator, or control with the jets may be inhibited. This is done by the blending
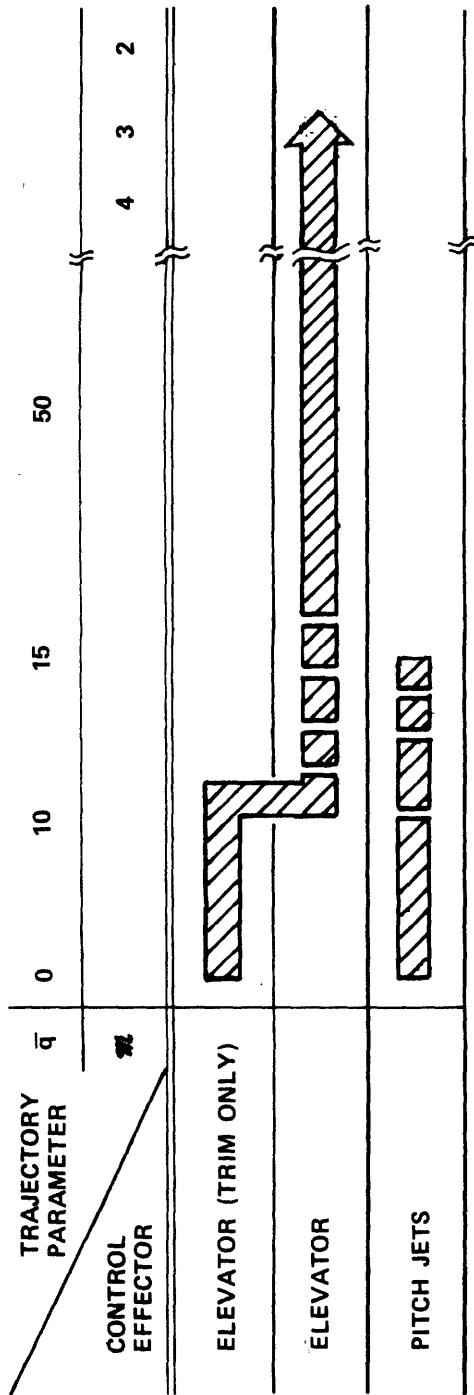
221

Figure 6-2. Controller Activity during Entry (Longitudinal).

logic which is essentially a two-sided deadbanded relay with hysteresis. The commanded elevator deflection is compared with preset fractions of its maximum and minimum values; should the command be "small", it is assumed that the elevator has sufficient control authority, and thus the pitch jets are not required. Conversely, should the elevator command be "large", the pitch jet control is not inhibited, but is allowed to assist the elevator in controlling the vehicle. This blended control continues throughout the rest of the entry, so that the pitch jets are always available for control assistance.

The logic provides for a gradual turn-on of the elevator control so as to avoid a switching transient when the second control mode is entered.

The remainder of this section describes the longitudinal control laws in detail. The block diagrams and equations defining the control logic for the elevator and pitch jets are given in Sections 6.2.1.1 and 6.2.1.2.

6.2.1.1 Elevator Control

Figure 6-3a is a block diagram of the elevator control loop, showing the two control modes, with switching determined by $\bar{q}_1$.

When the dynamic pressure is less than $\bar{q}_1$, only an elevator trim setting is sent to the actuator logic. This trim setting is determined by integrating the pitch ACPS commands (u_y^c), or, equivalently, by slowly driving the elevator so as to null the longitudinal disturbance torques.

When the dynamic pressure reaches $\bar{q}_1$, closed-loop control of the angle-of-attack is provided by conventional position (α) and rate $(\dot{\alpha})$ feedback through a network which attempts to maintain a constant transient response throughout the flight envelope. Specifically, the desired closed-loop transfer function is chosen to be a well-damped second-order system, or

Note: $\bar{q}_1 < \bar{q}_1^*$

Nonlinearities: (1) Limiter: unity slope: $\delta_e^{max} = (1 - K_e)\delta e_T + K_e\Delta_e^{max}$

$\delta_e^{min} = (1 - K_e)\delta e_T + K_e\Delta_e^{min}$

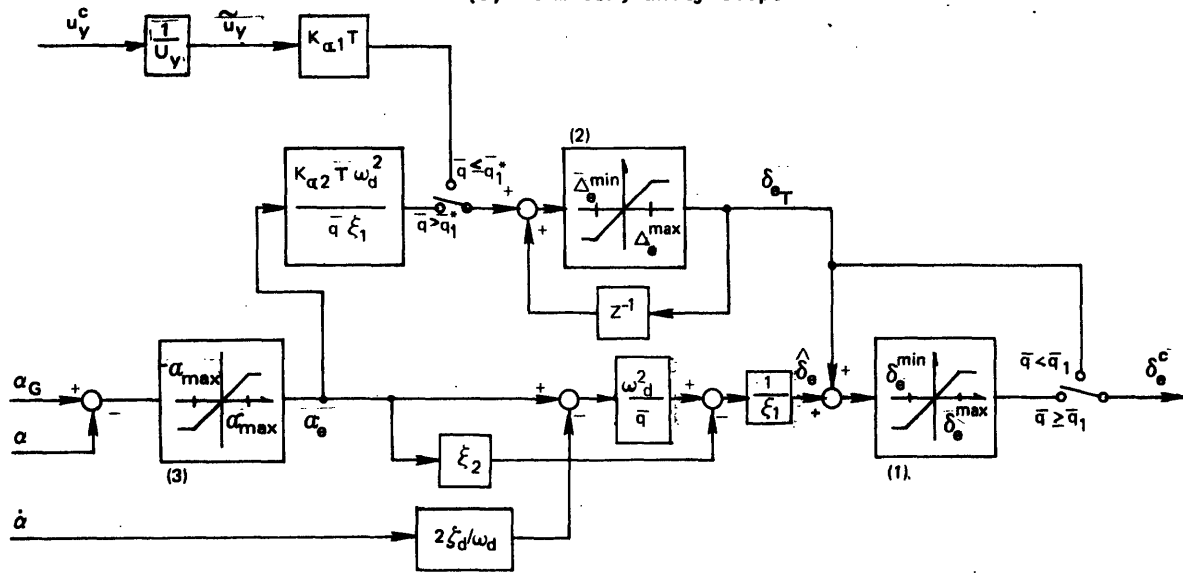(2) Clamped integrator; unity slope

(3) Limiter; unity slope
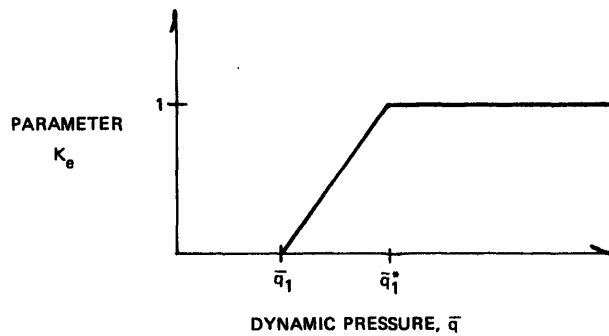

Figure 6-3a. Elevator Control Block Diagram.

Figure 6-3b. Elevator Deflection Limit Parameter.

224

$$\left[\frac{\alpha}{\alpha_G}\right]_{desired} = \frac{k_\alpha}{s^2 + 2\zeta_d\omega_d s + \omega_d^2} \tag{6-1}$$

where (ζ_d, ω_d) are specified for acceptable performance (k_α is not explicitly specified). The gains shown in the diagram may be separated into one of three types: (1) prespecified by the desired closed-loop characteristics; (2) dynamic pressure dependent $(1/\bar{q})$; or (3) scheduled gains which are functions of the aerodynamic flight regime (e.g., ξ_1). Trim control is accomplished in this mode either by the trim logic of the previous mode (if $\bar{q} \leq \bar{q}_1^*$) or by a conventional clamped trim integrator acting on the angle-of-attack error, thus providing a steady-state trim elevator command in the absence of transient angle-of-attack errors.

As can be seen from Fig. 6-3a and 6-3b, in order to allow a gradual blending in of active elevator control, the elevator command limits are functions of dynamic pressure which gradually open up from the trim setting to the physical deflection limits.

6.2.1.2 Pitch ACPS Control

Shown in Fig. 6-4 is the ACPS phase-plane switch logic representation used for control of the pitch jets. For longitudinal control, the phase-plane coordinates are angle-of-attack error and angle-of-attack rate, or

$$(\epsilon_1, \epsilon_2) = (\alpha - \alpha_G, \dot{\alpha}) \tag{6-2a}$$

The phase-plane is separated into three regions (by the switch curves), in which the commanded jet firing is either positive ($u = +U$), negative ($u = -U$) or zero ($u = 0$). Thus, for the particular application of pitch jet control
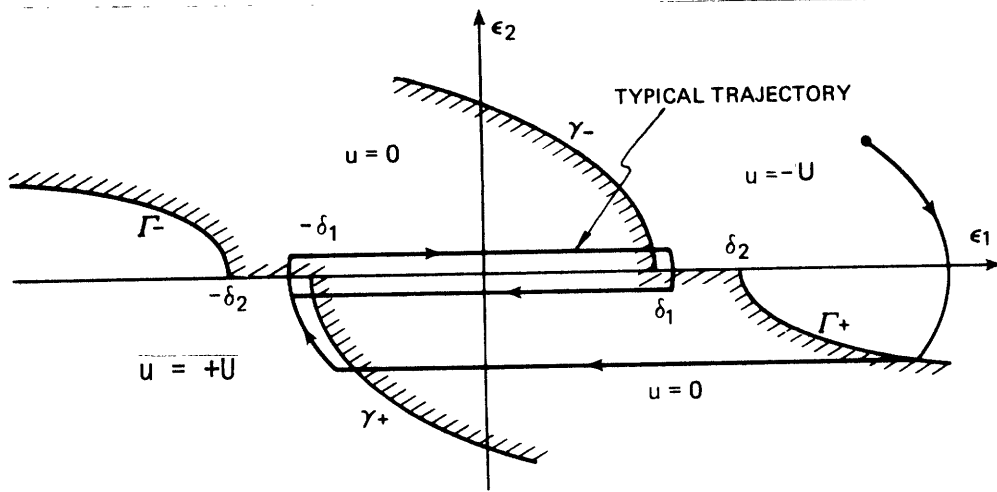
$$(u, U) = (u_y, U_y) \tag{6-2b}$$
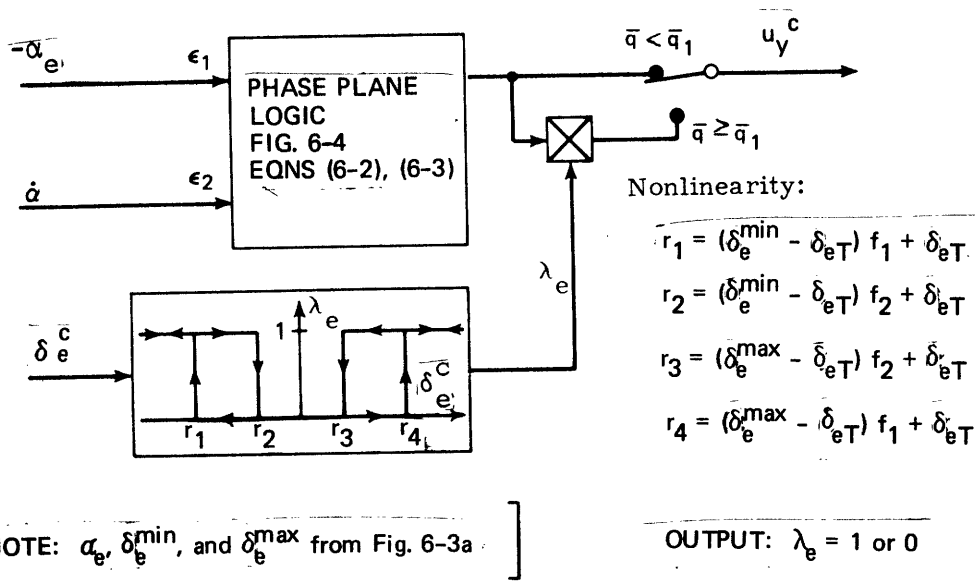
225

Figure 6-4. ACPS Switch Logic.

$$r_1 = (\delta_e^{min} - \delta_{eT}) f_1 + \delta_{eT}$$

$$r_2 = (\delta_e^{min} - \delta_{eT}) f_2 + \delta_{eT}$$

$$r_3 = (\delta_e^{max} - \delta_{eT}) f_2 + \delta_{eT}$$

$$r_4 = (\delta_e^{max} - \delta_{eT}) f_1 + \delta_{eT}$$

'NOTE: α_e, δ_e^{min}, and δ_e^{max} from Fig. 6-3a

OUTPUT: $\lambda_e = 1$ or 0

Figure 6-5. Pitch ACPS Control Block Diagram.

where u_y and U_y symbolize the jet command and the available acceleration level, respectively.

The equations for the switch curves themselves are based on the fuel-time optimal solution to the double integrator control problem and are modified by deadband incorporation to ensure practical limit-cycle convergence (see typical trajectory of Fig. 6-4). The switch curves are defined by:

$$\gamma\pm: \quad \epsilon_1 = \mp(\delta_1 - \frac{1}{2U} \epsilon_2^2)$$

$$(6-3)$$

$$\Gamma\pm: \quad \epsilon_1 = \pm(\delta_2 + \frac{\sigma}{2U} \epsilon_2^2)$$

where, in this case, the deadbands are pitch attitude deadbands, or:

$$(\delta_1, \delta_2) = (\delta_{\alpha 1}, \delta_{\alpha 2}) \tag{6-2c}$$

and σ is a fuel-time weighting constant, greater than unity, given for pitch control by:

$$\sigma = \sigma_\alpha \tag{6-2d}$$

The interface (or blending) logic between commanded pitch jet firings and the commanded elevator deflections is shown in Fig. 6-5. The approach taken is to inhibit firing when there is "sufficient" pitch control acceleration from the elevator. This measure of sufficiency is obtained by comparing commanded elevator (δ_e^c shown in Fig. 6-3a) with threshold values to determine whether or not "excessive" elevator deflection is being called for. The hysteresis path included in the blending interface avoids chatter in elevator and ACPS activity due to cross-coupling effects. Note that this design includes an additional switch to preclude jet inhibition when the dynamic pressure is low and the elevator is used solely for trim.

6.2.2 Lateral Control

Lateral control uses both aileron (differential elevons) and rudder, and roll and yaw ACPS jets to maintain small sideslip angles and follow commanded bank maneuvers. As shown in Fig. 6-6, which illustrates a typical sequence of control activity during entry, there are three control modes for the aerodynamic control surfaces, one for the yaw jets, and three for the roll jets.

Early in the entry, when the dynamic pressure is low, the rudder command is zero while the aileron is used strictly for trim, so as to minimize roll and yaw disturbance torques, and thus fuel usage. The trim control operates in a closed-loop fashion by slowly driving the aileron in the direction which nulls the disturbance, by integrating the roll jet pulse history. During this regime, the yaw jets, controlled by a bank angle/yaw-rate phase-plane logic, provide attitude and rate control of the bank angle in response to guidance commands. The roll jets are controlled by one of two logics, depending on the yaw jet activity. When there are no yaw commands, the roll jets, controlled by a sideslip/ sideslip-rate phase-plane logic, maintain small sideslip attitudes and rates. When the yaw jets are commanded to maneuver the vehicle, the roll jets are controlled by a sideslip/sideslip-rate phase-plane logic, which is similar to the first mode except that compensation for yaw jet torques is included. Again, the purpose of this logic is to maintain small sideslip attitudes and rates. There is no jet inhibition in this flight regime.

Later in the entry, when the dynamic pressure reaches a certain prespecified value ($q = \bar{q}_3$), the rudder command is still zero, and the aileron continues to be used only for trim, maintained by the logic of the previous mode. The yaw jets are controlled by the same logic as in the previous regime. The roll jets are controlled by one of two logics, again depending on yaw jet activity. When there are no yaw jet commands, the roll jets are commanded by a deadbanded relay logic which simply provides rate damping in sideslip. When the yaw jets are commanded to maneuver the vehicle, the roll jets are commanded by the same corresponding roll jet logic of the previous regime. There is no jet inhibition in this flight regime.
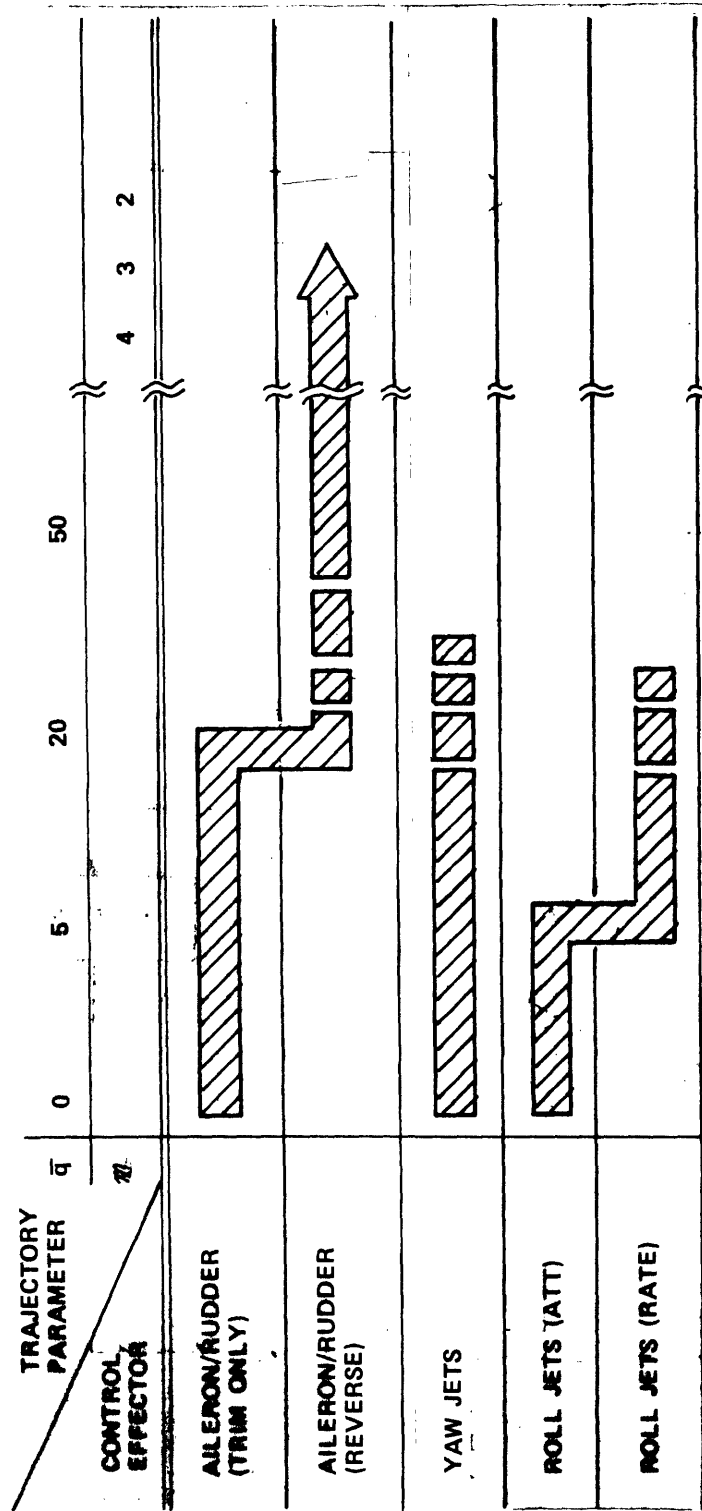
228

Figure 6-6.   Controller Activity during Entry (Lateral).

Still later in the entry, when the dynamic pressure is higher ($\overline{q} \geq \overline{q}_2$), the aileron is used for both trim and transient control. Trim is initially maintained through the use of the trim logic of the previous mode. At a slightly higher dynamic pressure ($\overline{q}_2^*$), trim is maintained through the use of an integrator acting upon the "steady-state" bank rate; the initialization value of the integrator is obtained from the value generated by the previous trim logic. Aileron control of transient errors is maintained through feedback of bank and sideslip attitudes and rates with appropriate gains. During this regime, the rudder command is null until the Mach number reaches a certain level ($\mathcal{M}_1$), after which it is proportional to the commanded aileron deflection. The proportionality variable is a constant. Also during this regime, roll and yaw jet control identical to that of the previous regime may be utilized together with the aileron and rudder, or control with the jets may be inhibited. This is done with the same type of blending logic used longitudinally; here, the commanded aileron deflection determines jet inhibition. Also as in the longitudinal case, there is a gradual turn-on of the allowed aerodynamic control authority.

The remainder of this section describes the lateral control laws in detail. The block diagrams and equations defining the control logic for the aileron and rudder are given in Section 6.2.2.1 , while those for the yaw and roll jets are given in Section 6.2.2.2.

6.2.2.1 Aileron/Rudder Control

Figure 6-7a is a block diagram of the basic aileron control loop including the rudder augmentation logic provided by a channel crossfeed.

When the dynamic pressure is less than $\overline{q}_2$, only an aileron trim setting is sent to the actuator logic. This trim setting is determined by integrating the roll ACPS commands (u_x^c), or, equivalently, by slowly driving the aileron so as to null the lateral disturbance torques (in both roll and yaw). Integration is inhibited when the yaw jets fire, as they would during a maneuver (see yaw jet logic below). The rudder command

230

Figure 6-7a. Aileron/Rudder Control Block Diagram.
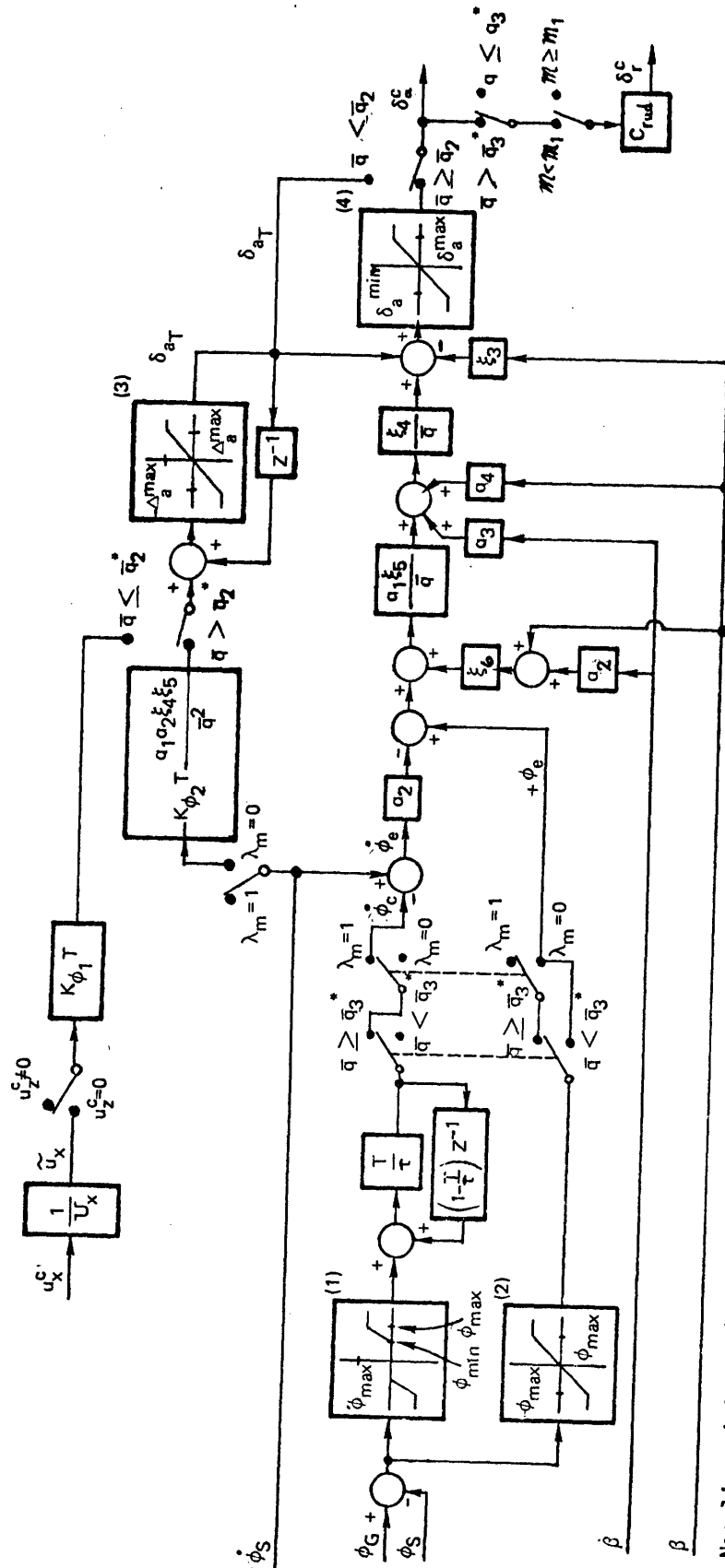
Non-linearities: (1) Limiter with deadband (symmetric)
(2) Limiter; unity slope
(3) Limiter; unity slope
(4) Limiter; unity slope; $\delta_a^{max} = (1 - K_a)\delta_{a_T} + K_a\Delta_a^{max}$
$\delta_a^{min} = (1 - K_a)\delta_{a_T} - K_a\Delta_a^{max}$

Note: 1) $\bar{q}_2 < \bar{q}_2^* < \bar{q}_3^*$

2) λ_m defined by figure 6-7c.

231

is maintained at zero during this interval.

When the dynamic pressure reaches $\bar{q}_2$, closed-loop control of bank and sideslip (by the aileron alone) is provided by position (β, ϕ) and rate ($\dot{\beta}$, $\dot{\phi}$) feedback of the lateral state variables, through a network which attempts to maintain a constant response throughout the trajectory. Specifically, the desired closed-loop transfer function for bank angle response is chosen to have four specified poles*, or:

$$\left[\frac{\phi}{\phi_G}\right]_{desired} = \frac{K_\phi(\tau_\phi s + 1)(s^2 - \omega_\phi^2)}{(s^2 + 2\zeta_1\omega_1 s + \omega_1^2)(s^2 + 2\zeta_2\omega_2 s + \omega_2^2)} \quad (6\text{-}4)$$

where the (ζ_i, ω_i) are chosen for acceptable transient response, K_ϕ and ω_ϕ are functions of the airframe parameters, and τ_ϕ is design specified. This response is obtained, in the absence of rudder effectiveness, by making use of sideslip mistrims to bank the vehicle.

As with the longitudinal controller, the gains of Fig. 6-7a may be separated into one of three types: (1) prespecified by the desired closed-loop characteristics (e. g., a_1); (2) dynamic pressure dependent; or (3) scheduled gains which are functions of the aerodynamic flight regime (e. g., ξ_3). For convenient reference, the gains of the first category are defined in terms of desired response characteristics with the following equation set:

$$a_1 = \omega_1^2 \omega_2^2$$

$$a_2 = 2(\zeta_1\omega_2 + \zeta_2\omega_1)/(\omega_1\omega_2)$$

$$a_3 = 2(\zeta_1\omega_1 + \zeta_2\omega_2)$$

$$a_4 = \omega_1^2 + \omega_2^2 + 4\zeta_1\zeta_2\omega_1\omega_2$$

(6-5)

---

* This transfer function is derived in Appendix I, based on the synthesis approach of Section 5.2.2.2.

232

where, as noted above, the (ζ_i, ω_i) are chosen for acceptable roll response.

When the dynamic pressure reaches $\bar{q}_2^*$, aileron trim is determined through the use of a clamped trim integrator in the bank rate channel. This allows the vehicle to trim to a non-zero sideslip angle (by commanding a non-zero trim aileron deflection) in the presence of body-axis roll disturbance torques due to lateral displacements in the vehicle's center-of-gravity. To avoid interpreting large transients (such as occur during a bank reversal) as lateral cg-offset induced mistrims, integration of large magnitude rates is inhibited by the λ_m switch (see discussion below). The gradual expansion of the aileron command limits during this mode as dynamic pressure increases is shown in Figs. 6-7a and 6-7b.
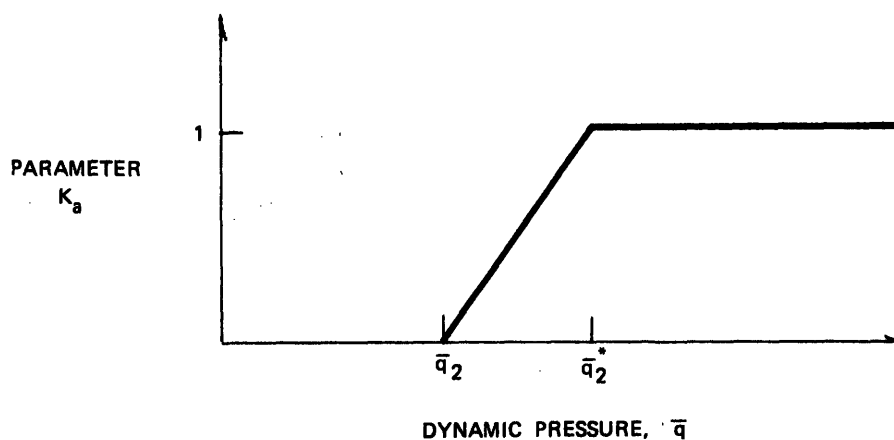

Figure 6-7b. Aileron Deflection Limit Parameter.

When the dynamic pressure reaches $\bar{q}_3^*$, a rate command loop becomes effective when large attitude errors are detected (as in a bank reversal). As shown in Fig. 6-7c, when the attitude error is greater than ϕ_{min} or the bank rate is greater than $\dot{\phi}_{db}$, the maneuver flag λ_m is set to

1, indicating that the controller need no longer be concerned with maintaining a bank attitude; instead, the logic is configured to drive the vehicle to a desired bank rate, normally higher than what would be obtained with the attitude control loop providing the feedback.

Finally, when the Mach number drops below M_1, the rudder is switched in to augment the aileron effectiveness, with a constant aileron to rudder crossfeed gain. An additional dynamic pressure switch is included to preclude early entry utilization of the rudder. The aileron-to-rudder crossfeed gain is a (positive) constant.
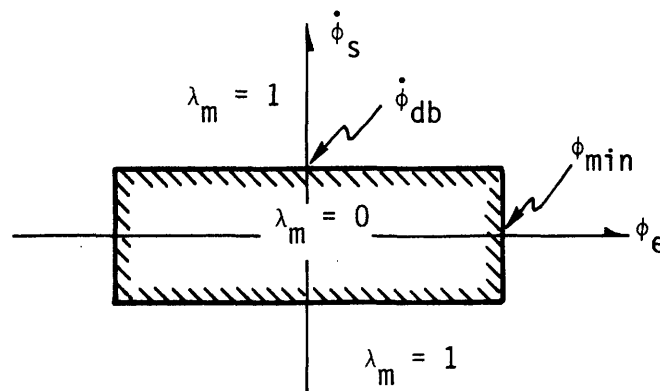

Figure 6-7c. Definition of Maneuver Flag.

6.2.2.2 Yaw and Roll ACPS Control

Yaw jet ACPS control synthesis is based on double integrator modeling of the bank angle dynamics, so that the switch logic presented for pitch ACPS control may be used. The roll jet logic consists of three modes, one based on double integrator modeling of the sideslip dynamics, a second based on oscillator modeling, and a third which accounts for control axis cross-coupling.

234

6.2.2.2.1 Yaw Jet Control

A double integrator model of the bank angle dynamics, combined with the assumption of turn coordination provided by the roll jets, allows for the use of the ACPS pitch jet control logic, with the appropriate redefinition of control parameters. Specifically, yaw jet control is defined by the phase-plane switch logic of Fig. 6-4 and (6-3), where the coordinates are given by:

$$(\epsilon_1, \ \epsilon_2) \ = \ \left[-\phi_e \sin \alpha_T, \ r \right] \tag{6-6a}$$

and the switch curve parameters are given by:

$$(u, \ U) \ = \ (u_z, \ U_z) \tag{6-6b}$$

$$(\delta_1, \ \delta_2) \ = \ (\delta_{\phi 1}, \ \delta_{\phi 2}) \tag{6-6c}$$

$$\sigma \ = \ \sigma_\phi \tag{6-6d}$$

The blending interface logic is discussed below.

6.2.2.2.2 Roll Jet Control

Roll jet control of vehicle sideslip is accomplished by the use of three control modes. Two of these use a double integrator model for sideslip; the remaining one uses an oscillator model.

The purpose of the first mode is to provide turn coordination when the yaw jets are firing ($u_z \neq 0$). This is accomplished by the phase-plane logic of Fig. 6-8, which is a generalized (β, $\dot{\beta}$) plane. The figure illustrates a typical state trajectory and the resultant limit cycle (with switch curve overshoots). The equations for the switch curve μ are:

$$\mu: \ S\beta \ = \ \frac{1}{2U_1} \left[(\dot{\beta}^m)^2 - \dot{\beta}^2 \right] \ \text{if} \ S\dot{\beta} > \dot{\beta}^m$$

$$\tag{6-7a}$$

$$= \ - \frac{1}{2U_2} \left[(\dot{\beta}^m)^2 - \dot{\beta}^2 \right] \ \text{if} \ S\dot{\beta} \leq \dot{\beta}^m$$

where

$$U_1 = U_z \cos \alpha_T$$

$$U_2 = U_x \sin \alpha_T - U_z \cos \alpha_T$$

$$S = \text{sgn}(u_z)$$ \hfill (6-7b)

$$\dot{\beta}^m = \sqrt{2 U_2 \delta_1}$$

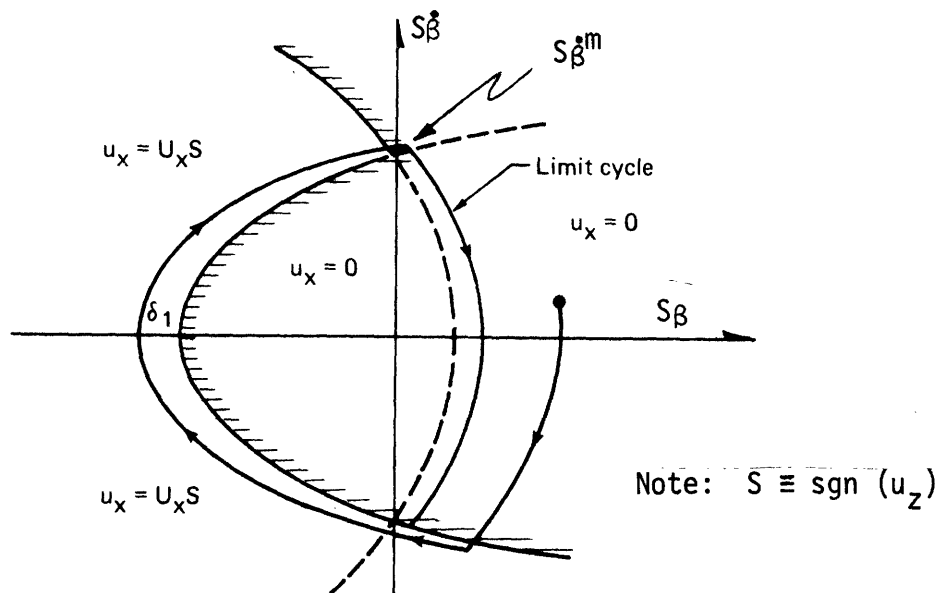and where δ_1 is defined below in (6-8).

Figure 6-8. Roll Jet Control when $\dot{u}_z \neq 0$.

The purpose of the second mode is to provide direct control over sideslip when the yaw jets are inactive ($u_z = 0$) and when the dynamic pressure is low. With double integrator modeling, the phase-plane logic of Fig. 6-4 and (6-3) may be used, where the coordinates are given by:

$$(\epsilon_1, \epsilon_2) = (\beta, \dot{\beta}) \hfill (6-8a)$$

and the switch curve parameters are given by:

$$(u, \ U) \ = \ (u_x, \ U_x \sin \alpha_T) \qquad (6\text{-}8b)$$

$$(\delta_1, \ \delta_2) \ = \ (\delta_{\beta 1}, \ \delta_{\beta 2}) \qquad (6\text{-}8c)$$

$$\sigma \ = \ \sigma_\beta \qquad (6\text{-}8d)$$

It is convenient to label this control mode (used at low $\bar{q}$ and when $u_z = 0$) as attitude hold, since both rate and attitude error are driven toward zero.

The third control mode takes advantage of the vehicle's dynamic stability in sideslip, which becomes significant once the dynamic pressure becomes sufficiently high. What is required is simply rate damping of the sideslip angular velocity as shown in Fig. 6-9, where $\dot{\beta}^m$ is given by (6-7b).
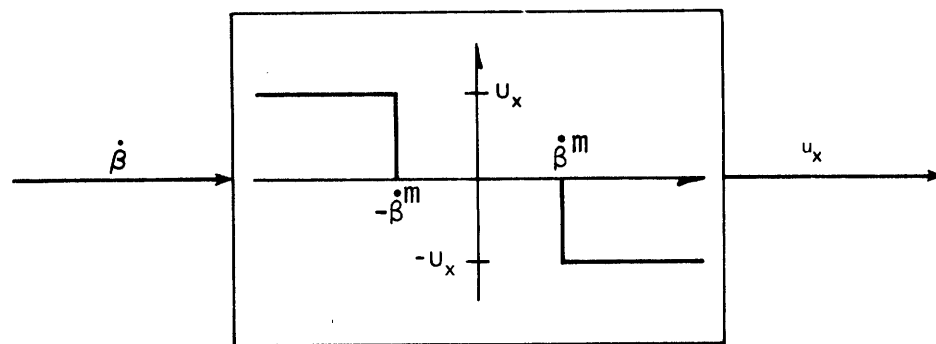

Figure 6-9. Roll Jet Control when $u_z = 0$ $(\bar{q} \geq \bar{q}_3)$.

The control modes described above, defining lateral control with yaw and roll jets, are summarized in block diagram form in Fig. 6-10. Several points should be noted. First, the mode select block which defines the roll jet control mode to be used is defined by:

$$\text{If } u_z \neq 0 \qquad \text{then Mode } = \text{ I}$$
$$u_z = 0, \; \bar{q} < \bar{q}_3 \qquad\qquad \text{II} \qquad\qquad (6-9)$$
$$u_z = 0, \; \bar{q} \geq \bar{q}_3 \qquad\qquad \text{III}$$

where the modes are coordination, attitude hold, and rate damping, respectively. The three roll control blocks correspond with the above modes. A second point to note is the gating by the blending parameter λ_a, which is defined by logic that is identical to that of the pitch channel. Finally, it may be noted that the logic disallows ACPS inhibition during aileron trim-only operation.

6.3 Gain and Parameter Specification

All parameters and gains used in the control law computations are either fixed constants or are schedules on the basis of Mach number. The particular values are chosen from the considerations given in the previous chapter and in light of performance results obtained in a simulator environment. The values are appropriate to the 89B vehicle configuration description given in Section 2.1 (and described in reference 2). Table 6-1 tabulates all fixed control parameters. In an initialization pass through the control logic, several parameters which are functions of these fixed constants are calculated and stored for future use. This is illustrated in flow chart form in Fig. 6-11. The scheduled control gains ξ_1 through ξ_6 are tabulated functions of Mach number, as shown in Figs. 6-12 through 6-17; a linear interpolation routine is assumed available for their computation.
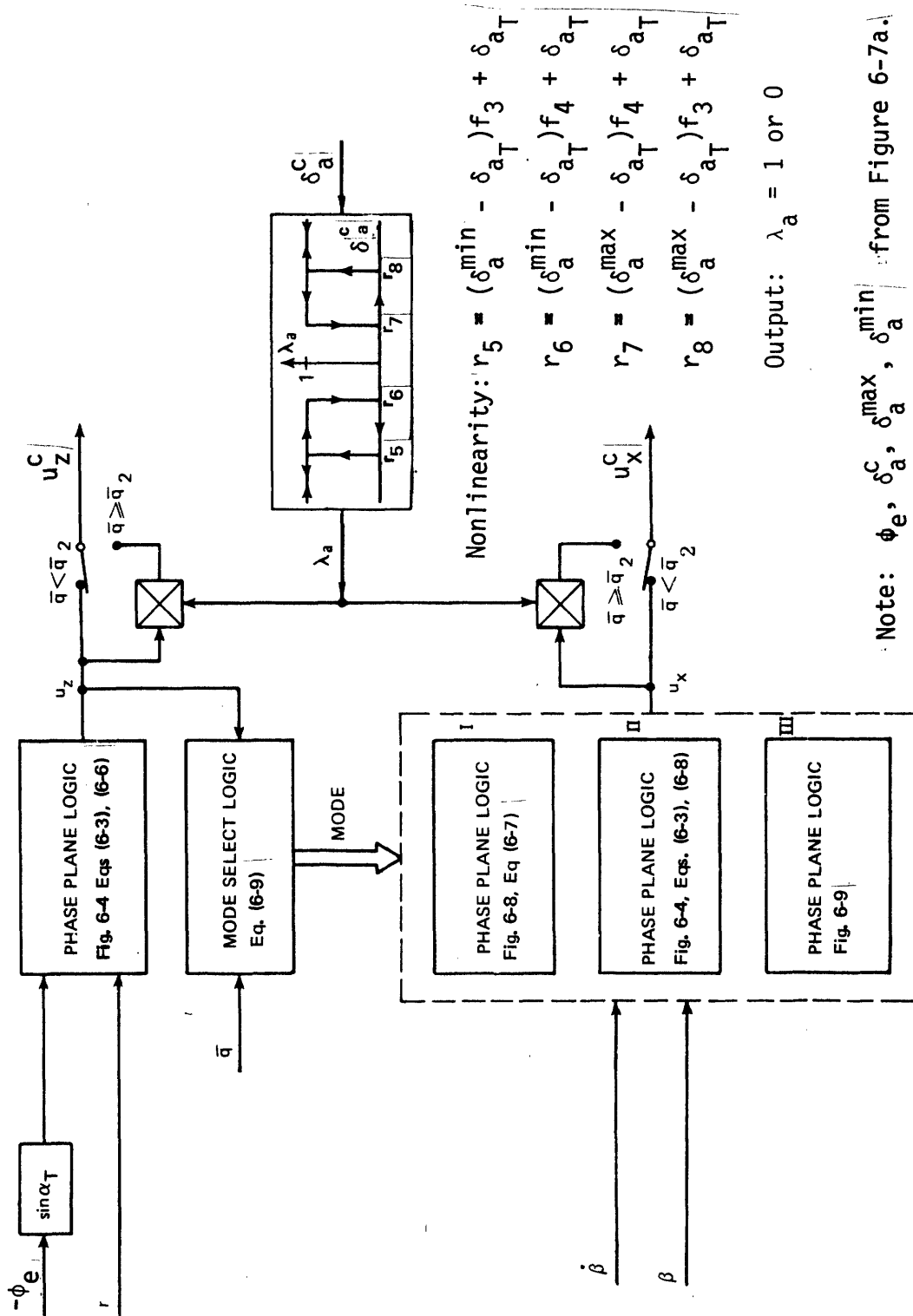
Figure 6-10. Yaw and Roll ACPS Control Block Diagram.

Nonlinearity: $r_5 = (\delta_a^{min} - \delta_{a_T})f_3 + \delta_{a_T}$

$r_6 = (\delta_a^{min} - \delta_{a_T})f_4 + \delta_{a_T}$

$r_7 = (\delta_a^{max} - \delta_{a_T})f_4 + \delta_{a_T}$

$r_8 = (\delta_a^{max} - \delta_{a_T})f_3 + \delta_{a_T}$

Output: $\lambda_a = 1$ or 0

Note: ϕ_e, δ_a^c, δ_a^{max}, δ_a^{min} from Figure 6-7a.

Table 6-1: Fixed Gains and Parameters (89B Vehicle)

Symbol	Value	Dimension	
$\bar{q}_1$	10	lbf/ft^2	Mode switching parameters
$\bar{q}_2$	20	lbf/ft^2	
$\bar{q}_3$	5	lbf/ft^2	
$\bar{q}_1^*$	20	lbf/ft^2	
$\bar{q}_2^*$	30	lbf/ft^2	
$\bar{q}_3^*$	80	lbf/ft^2	
$\mathscr{M}_1$	6	-	
K_{α_1}	-1.0	deg/sec	Aerodynamic control parameters and gains
K_{α_2}	0.2	sec^{-1}	
K_{ϕ_1}	0.6	deg/sec	
K_{ϕ_2}	0.1	sec^{-1}	
ω_d	0.7	sec^{-1}	
ζ_d	0.7	-	
ω_1	0.7	sec^{-1}	
ω_2	0.7	sec^{-1}	
ζ_1	1.4	-	
ζ_2	0.7	-	
α_{max}	5	deg	
ϕ_{max}	35	deg	
ϕ_{min}	5	deg	
$\dot{\phi}_{max}$	8	deg/sec	

Table 6-1: Fixed Gains and Parameters (89B Vehicle) (cont.)

Symbol	Value	Dimension	
$\dot{\phi}_{db}$	1	deg/sec	
τ	0.5	sec	
C_{rud}	2	–	
Δ_e^{max}	15	deg	
Δ_e^{min}	–45	deg	
Δ_a^{max}	20	deg	
δ_r^{max}	15	deg	
U_x	1.65	deg/sec^2	ACPS control parameters
U_y	1.32	deg/sec^2	
U_z	0.66	deg/sec^2	
δ_{α_1}	0.75	deg	
δ_{α_2}	1.0	deg	
δ_{β_1}	0.2	deg	
δ_{β_2}	0.4	deg	
δ_{ϕ_1}	0.75	deg	
δ_{ϕ_2}	1.5	deg	
σ_α	5	–	
σ_β	2	–	
σ_ϕ	5	–	
f_1	0.8	–	
f_2	0.6	–	
f_3	0.8	–	
f_4	0.6	–	
T	0.1	sec	Sample period
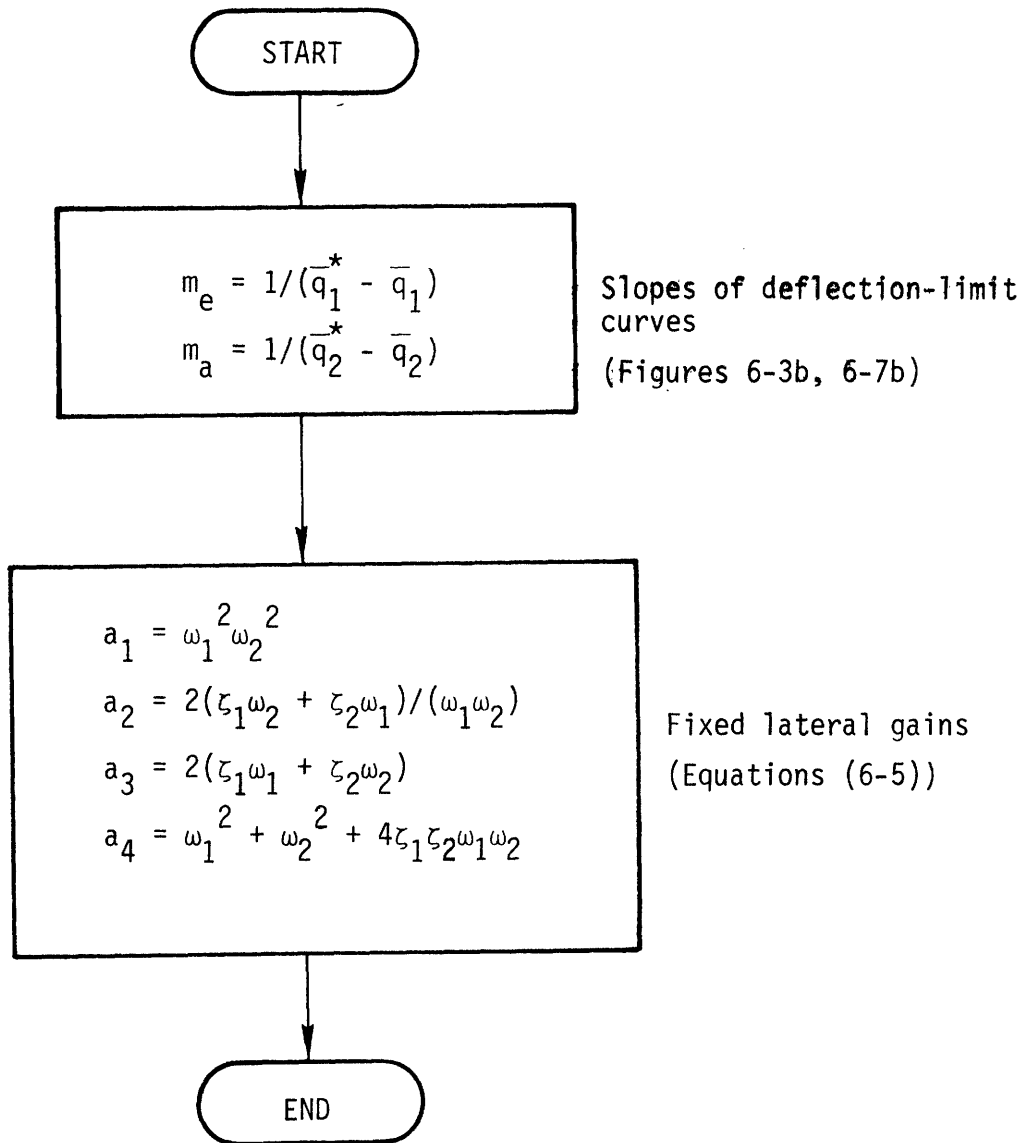
Figure 6-11. Parameter Initialization.

In the flowchart:

START

$$m_e = 1/(\overline{q}_1^* - \overline{q}_1)$$

$$m_a = 1/(\overline{q}_2^* - \overline{q}_2)$$

Slopes of deflection-limit curves

(Figures 6-3b, 6-7b)

$$a_1 = \omega_1^2 \omega_2^2$$

$$a_2 = 2(\zeta_1\omega_2 + \zeta_2\omega_1)/(\omega_1\omega_2)$$

$$a_3 = 2(\zeta_1\omega_1 + \zeta_2\omega_2)$$

$$a_4 = \omega_1^2 + \omega_2^2 + 4\zeta_1\zeta_2\omega_1\omega_2$$

Fixed lateral gains

(Equations (6-5))

END
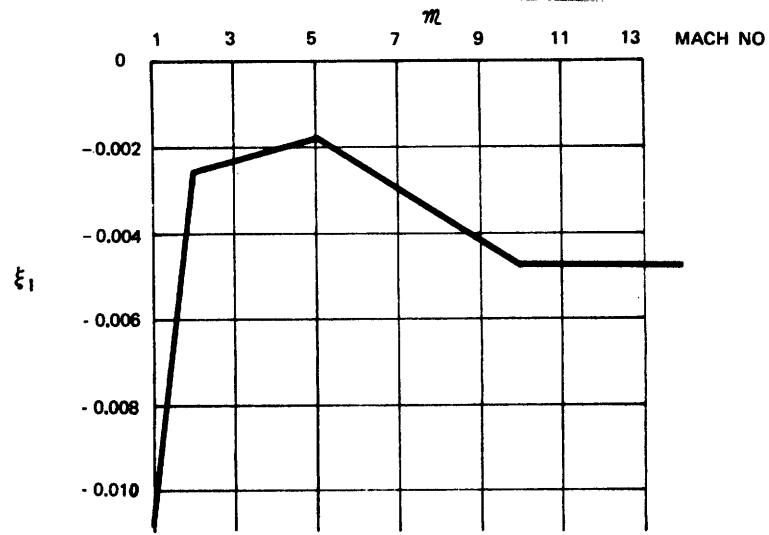
Figure 6-12. Gain Schedule for ξ_1 (89 B vehicle)
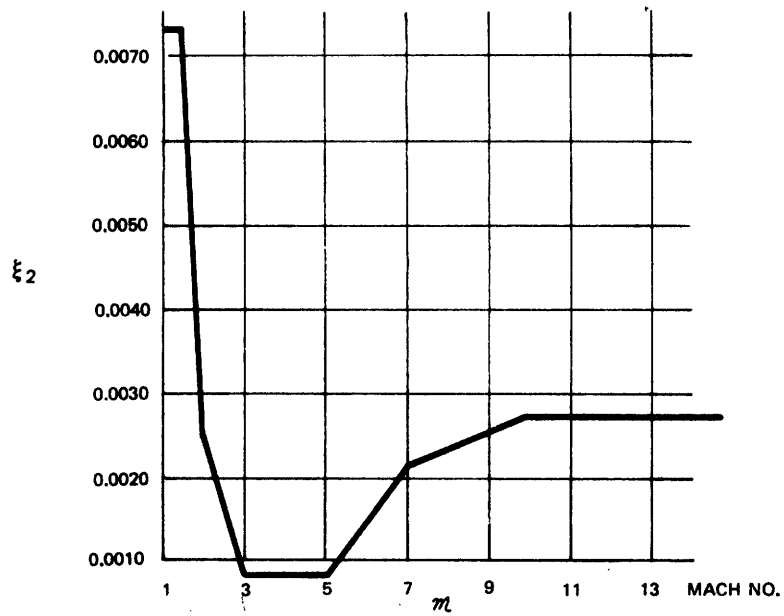
Figure 6-13. Gain Schedule for ξ_2 (89 B vehicle)

243
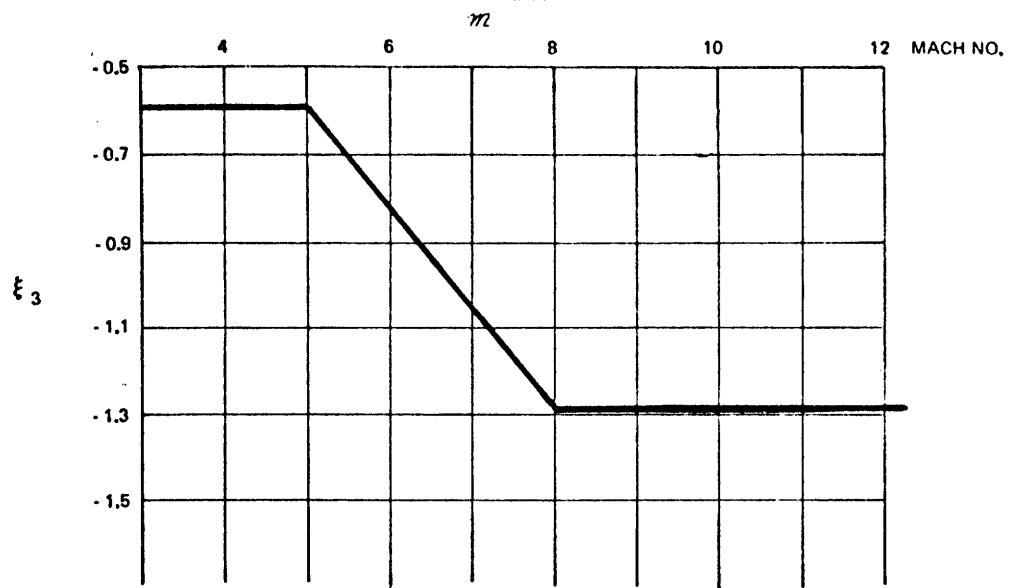
Figure 6-14. Gain Schedule for ξ_3. (89 B vehicle)
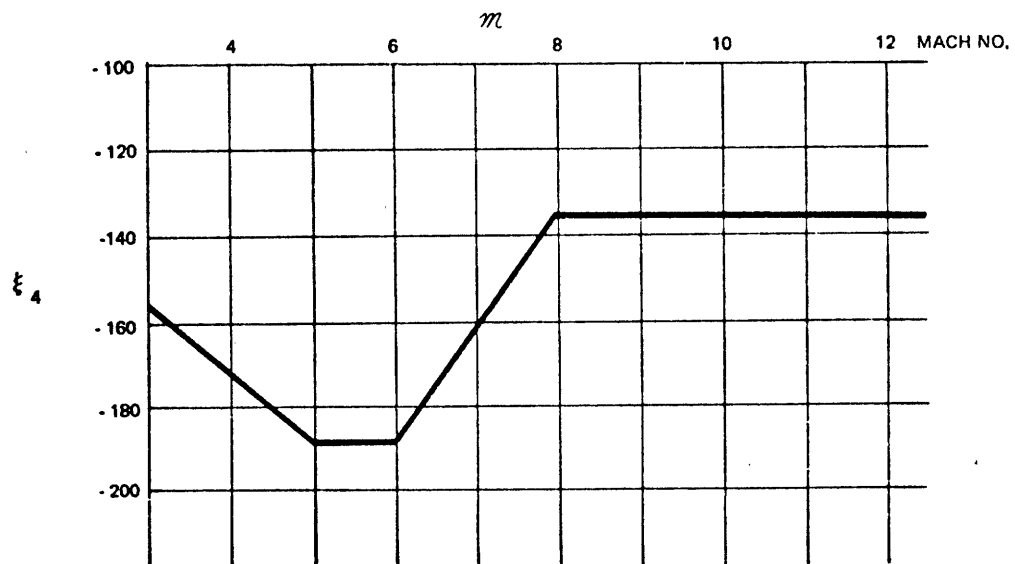
Figure 6-15. Gain Schedule for ξ_4. (89 B vehicle)
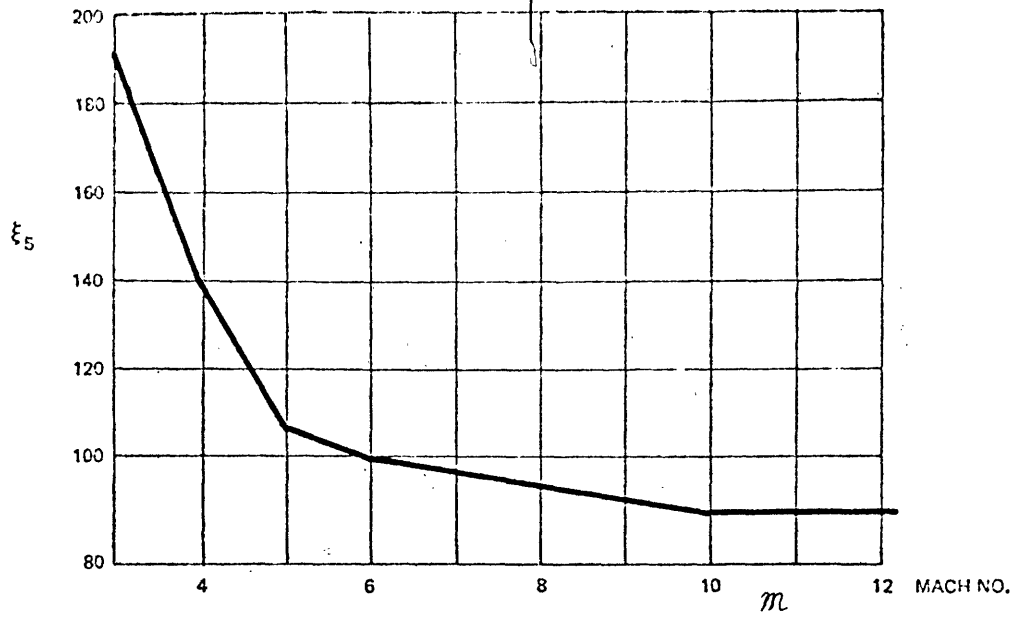
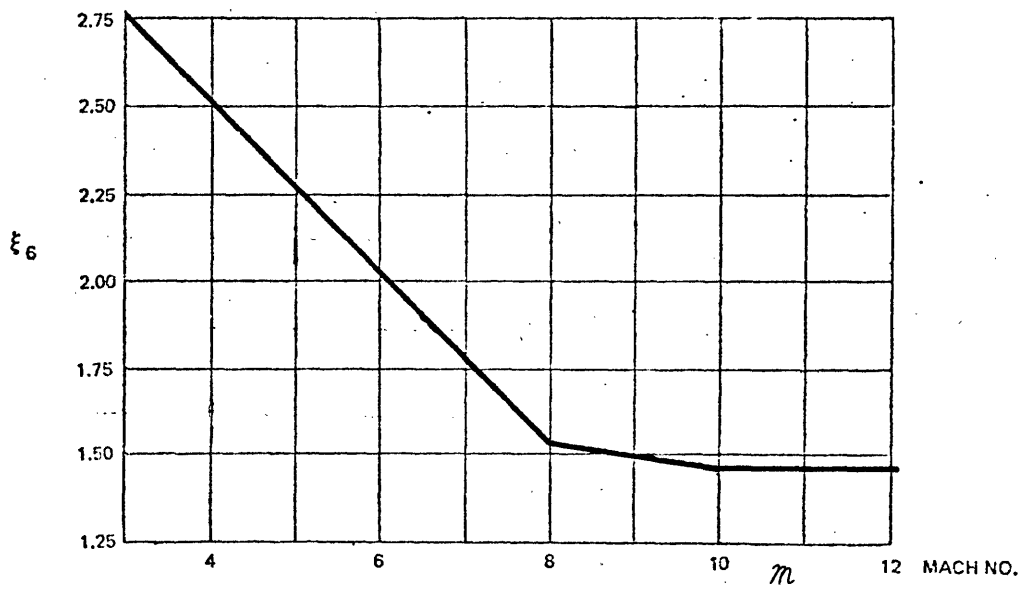Figure 6-16: Gain Schedule for ξ_5 (89B vehicle)

Figure 6-17: Gain Schedule for ξ_6 (89B vehicle)

6.4 Digital Implementation

The entry control system just described is presently implemented as part of the Digital Flight Control System (DFCS) currently under development by the Control and Flight Dynamics Division of the Charles Stark Draper Laboratory, Inc. The DFCS as implemented on the Space Shuttle Functional Simulator (SSFS) is a FORTRAN program which provides a unified structure for control algorithms appropriate to different mission phases; details of its definition and its relation to the entry design presented here are to be found in reference 25. It suffices to note here that the DFCS structure provides for scheduling of appropriate peripheral subroutines necessary to control system operation (e. g., state estimation, initialization, jet selection, etc.); accordingly, Appendix J describes only the core control law calculations presented above, in a flow chart format of the FORTRAN program. It will be noted from a perusal of the appendix that many of the logical functions and control law calculations, which appear to be reasonably complicated in the functional block diagrams presented above, often take on an elegant simplicity when expressed in a user-oriented computer language such as FORTRAN or HAL. Indeed, the occasional lack of precise correspondence between functional block diagram and flow chart descriptions is motivated by programming efficiency considerations, so as to take advantage of digital implementation.

7. Performance Evaluation

This chapter attempts to give some measure of the closed-loop vehicle performance, throughout the flight envelope and under varying nominal and off-nominal conditions, by describing simulation results obtained in testing the control system. The results presented here are primarily for the purpose of design verification and evaluation, although it should be recalled from the discussion given in Chapter 3 that design simulation is an integral part of the design process; thus these results also provide the motivation for further design modifications to either improve performance or meet new requirements placed on the overall controlled vehicle. In fact, as these results are being documented, the design effort is continuing with a new vehicle and new performance constraints, naturally drawing heavily on the experience gained from the simulation results presented here.

In addition to design evaluation, there are two secondary and closely related objectives of this chapter. First, the results presented here present an implicit evaluation of the validity of the entire design approach, starting with the simplified vehicle modelling of Chapter 4, through the separate control law synthesis of Chapter 5, and ending with the integrated design summary of Chapter 6. Clearly, any major misstep in this path will show up as unanticipated dynamic response characteristics in a simulation, and, if not pinpoint the source of the problem, at least indicate the necessity for a reevaluation of the techniques used. The second objective of this chapter is to familiarize the reader with the fundamental operational characteristics of the control system. Some understanding of the important vehicle dynamics should have been gained by the discussion in Section 4.4; likewise, some clear inferences can be made on anticipated closed-loop behavior from the designs of Chapter 5; knowledge in both of these areas, however, is insufficient to fully describe the operational characteristics of the control system working in the non-linear, time-varying environment. Thus, the discussion accompanying some of the simulation results will attempt to explain more fully the system's behavior, and how it relates

to the design choices made earlier.

In contrast to the frequency domain approach used in some of the control law syntheses of Chapter 5, practically all of the closed-loop system evaluation has been conducted in the time domain, by inspection of simulated responses to various inputs and under differing test conditions. The motivation for this approach comes from three areas. First, the fundamental performance specifications are stated as time domain response characteristics (e.g., maneuver rates, steady state error, etc.), so that response histories provide the most direct evaluation of acceptable performance. Even though there obviously exist many direct correlations between a system's frequency characteristics and its time response under various conditions, a detailed evaluation of the closed-loop system in the frequency domain leads immediately to the second argument for time domain evaluation: the non-linearity and non-stationarity of both the vehicle and the control system. Non-linear analysis is so limited in its range of applicability that it is questionable that any useful indicator of performance could be applied to this particularly complex problem; the results of classic linear systems analysis would, of course, always be shadowed by the question of their validity. The inapplicability of both approaches is compounded by the fact that the system dynamics change radically during the course of the entry, suggesting a greater complexity in non-stationary analysis. The final motivation for time domain evaluation, and perhaps the strongest of the three, is that of evaluating the dynamics of subsystem interaction. Thus, the control system should be viewed as one part of a larger system, the latter encompassing such diverse areas as the jet selection logic, the state estimator, the executive sequencer, and the guidance routines. Predicting the subtle interplay of these various subsystems with the controller and the vehicle would appear to be impossible without the use of a simulator. It should also be clear that as subsystem designs mature, a greater emphasis will be placed on the dynamics of subsystem interactions; unfortunately, the results presented here only skim the surface of this problem.

The results presented here are necessarily only a sampling of the simulation output, and, perhaps more restrictively, of the output of a single simulator. Efforts are presently being made to extend the breadth of the simulator base by developing simulators specifically oriented to examine particular aspects of the entry controls problem (e.g., manual control modes). For the design verification and evaluation effort required here, however, the all-digital, non-real-time simulator (described below), used in generating the closed-loop vehicle response histories, provides a more than adequate test of the control system.

This chapter is organized into three sections. Section 7.1 gives a very brief description of the simulator itself, describing both the software "environment" of the control logic and the various modules making up the vehicle/environment package. Section 7.2 then describes some of the operational characteristics of the simulated system, in a "nominal" entry environment, so as to verify the basic design choices made in the earlier chapters. Here, also, is a basic evaluation of controller performance in such an environment and a summary flight envelope delineating the system's limitations. Finally, Section 7.3 describes the system's performance under off-nominal conditions, so as to give some indication of design sensitivity to anticipated (realistic) variations in the entry environment.

7.1 Simulator Description

The simulator used for the design verification effort is a modified version of the Space Shuttle Functional Simulator (SSFS), an all-digital, non-real-time FORTRAN program originally developed by Lockheed Electronics Corporation (LEC). This modified version closely follows the original, the major changes being centered on machine compatibility as opposed to functional representation of the desired "environment". Thus, the extensive documentation series[*] supported by LEC provides

---

[*] See reference 5 for a complete system description.

a comprehensive description of the simulator details, and no effort is made here to duplicate that information. It is, however, appropriate to mention some of the basic features of the SSFS relating to representation of the fundamental vehicle model characteristics.

The SSFS is modularly programmed, so that, for example, the equations of motion are implemented independently of the particular forces and torques which drive the vehicle, which, in turn, are independent of the particular actuator model chosen to represent control surface dynamics. Thus, several modules may be collected together to represent a particular vehicle/environment/control system combination, with a fair degree of interchangeability so as to allow investigation of alternate configurations. The particular configuration chosen for this study involved a full six degree-of-freedom rigid-body dynamic model complete with accurate gravity and atmosphere models appropriate to the entry regime (see references 4, 10 and 26). The aerodynamic module (see reference 9) models the complete non-linear aerodynamic forces and torques, excluding aeroelastic effects, and is based on the data of reference 2; the mass properties module is also consistent with this data source as are both the ACPS and ACSS modules; the former models all 40 jets, complete with cross-coupling effects and finite firing dynamics, while the latter is a non-linear model of the actuator dynamics including signal limiting. The point to recognize from this descriptive summary is that the simulator is a considerably more complex model of the vehicle dynamics than that developed in Chapter 4; thus, successful simulator operation is one means of implicitly verifying the validity of the simplifications used in the derivations of that chapter. Of course, it is also the means of verifying the appropriateness of the design choices made in Chapter 5.

As noted in the previous chapter, the entry control logic is implemented in the Digital Flight Control System (DFCS), a FORTRAN program which provides a unified programming structure for the various mission phases. The detailed description of the DFCS is given in reference 25; it is appropriate here to note some of the features of

direct concern to the controls problem. Shown in Figure 7-1 is the logical flow of the DFCS executive (repeated from reference 25), giving an overview of the operational environment of the control logic coding.

For perspective, the bold arrow indicates the control logic coding as implemented in the overall structure; the amount of "buffering" by other routines should be clear from the diagram. Disregarding the initialization loops, the basic flow can be described as follows. The filter subroutine incorporates measurements derived from the sensors into vehicle state variables desired by the control logic (A in the diagram). In the case of entry, these are the stability-axis attitude angles and rates. One technique of conversion from sensor information to the desired state information has already been discussed in Section 5.4.1; an alternate approach is discussed in reference 16. The control algorithm is then entered (B), and this is fundamentally the set of control equations as described in Appendix J. The control output subroutine (C) then processes the control law commands to generate signals compatible with the (simulated) effector hardware interfaces. It is at this point that the elevator and aileron surface commands are appropriately mixed to provide left and right elevon commands; here also is where the jet select logic (JSL) converts the control logic generated torque commands into realizable jet firing times to effect the desired acceleration maneuver. Having sent out the effector commands, the control loop then enters the second portion of the filter equations (D) so as to minimize lag time for the next measurement incorporation. Parameter estimation (e.g., scheduled gain computation) then occurs last (E), completing the loop.

Two points should be noted regarding the above implementation. First, the logic used to transform from sensor information to vehicle state in the stability-axis system is essentially that given by (5-85) and (5-94) in Section 5.4.1. As presently implemented, the DFCS provides an option for filtering of the data (as described in reference 25) in the presence of a realistically modelled noisy sensor environment. For most of the simulation results presented here, a noise-free sensor
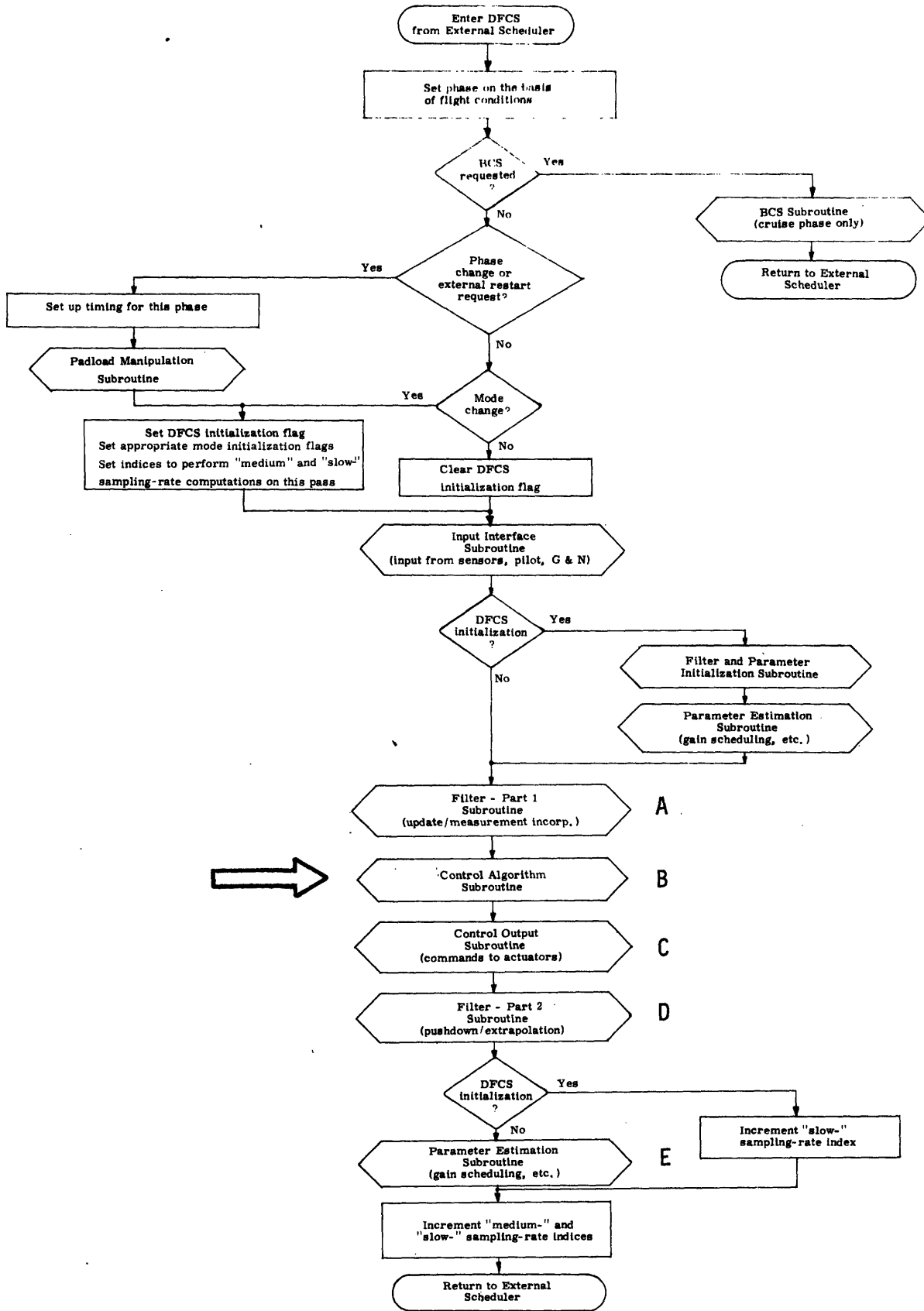
Figure 7-1. Logic Flow of DFCS Executive.

environment was assumed, so that filtering was neither needed nor used. Filter operation in a noisy environment is discussed, however, in Section 7.3. The second point to note regards the jet firing command process logic, specifically the jet select logic (JSL). Rather than simulate the ACPS as a system of controllable ideal torque sources, and thus eliminate the requirement for a JSL, it was decided to use the full 40-jet ACPS model in conjunction with an appropriate JSL. This logic is described in reference 25; functionally, the logic provides the transformation from torque commands to jet on-time commands. Thus, even though the vehicle model is more realistic and complex, the use of the JSL allows greater configuration independence and greater applicability of the design results presented below.

It should be recognized that the above simulator description is quite cursory and a much more comprehensive description can be found in the previously mentioned references. A qualitative statement is perhaps appropriate here: the SSFS provides a very realistic environment and vehicle model, particularly suited to the design verification tasks required in control law development. Thus, the performance results presented here provide an implicit measure of the modelling accuracy and design validity of the material presented in the previous chapters.

7.2 Performance in a Nominal Environment

As noted earlier, the objective of this section is to provide a basis for design verification and evaluation, while familiarizing the reader with the typical nominal operating characteristics of the system. To be completely convincing, such a presentation should be exhaustive in its consideration of nominal vehicle configurations, flight conditions within the nominal envelope, and nominal mission profiles; this is not done here, simply because of the quantity of data involved. Instead, what will be described here are sample runs, illustrative of the many simulations made throught the course of testing the control system.

For the purpose of verification, some means must be found for testing the control system over a densely packed set of flight condition "points" within the nominal entry envelope. A convenient approach has been to use the simulator to generate various entry trajectories which span the flight envelope. By testing the controlled vehicle response at points along these trajectories, fair coverage of the entire envelope has been effected. To illustrate this, Figure 7-2 shows the nominal altitude/ velocity corridor introduced in Chapter 2; also shown is the profile of a moderate crossrange entry trajectory* typical of guided entry operation. Although the indicated set of flight condition points is a rather sparse sampling of the entire envelope, a greater test density may be obtained by evaluating system response at more points along the illustrated trajectory and by the use of flight conditions appropriate to other trajectories. Both of these courses have been taken, so that there exists a high sampling density throughout (and, in some cases, beyond) the nominal flight envelope. For the purpose of the present discussion, many of the performance results illustrated later will use the flight condition points defined by Figure 7-2. It is felt that the trajectory is a representative sample of those several flown throughout the envelope, and the point selection along the trajectory adequately illustrates controller performance under a variety of conditions.

The nominal vehicle parameters used in the studies reported on in this section are as described in Chapter 2. Briefly, it may be noted that testing was done for the vehicle's center-of-gravity located forward and in the (assumed) plane of symmetry; aft center-of-gravity and lateral offset cases are treated in Section 7.3. The control surfaces are limited to deflection rates of 15°/sec, and the ACPS acceleration levels are as described by Table 2-5. The sample period used for the control loop cycle time is 0.10 seconds, with a gain schedule update period of 2 seconds. Finally, it is assumed that there is no sensor noise corrupting the control system input.

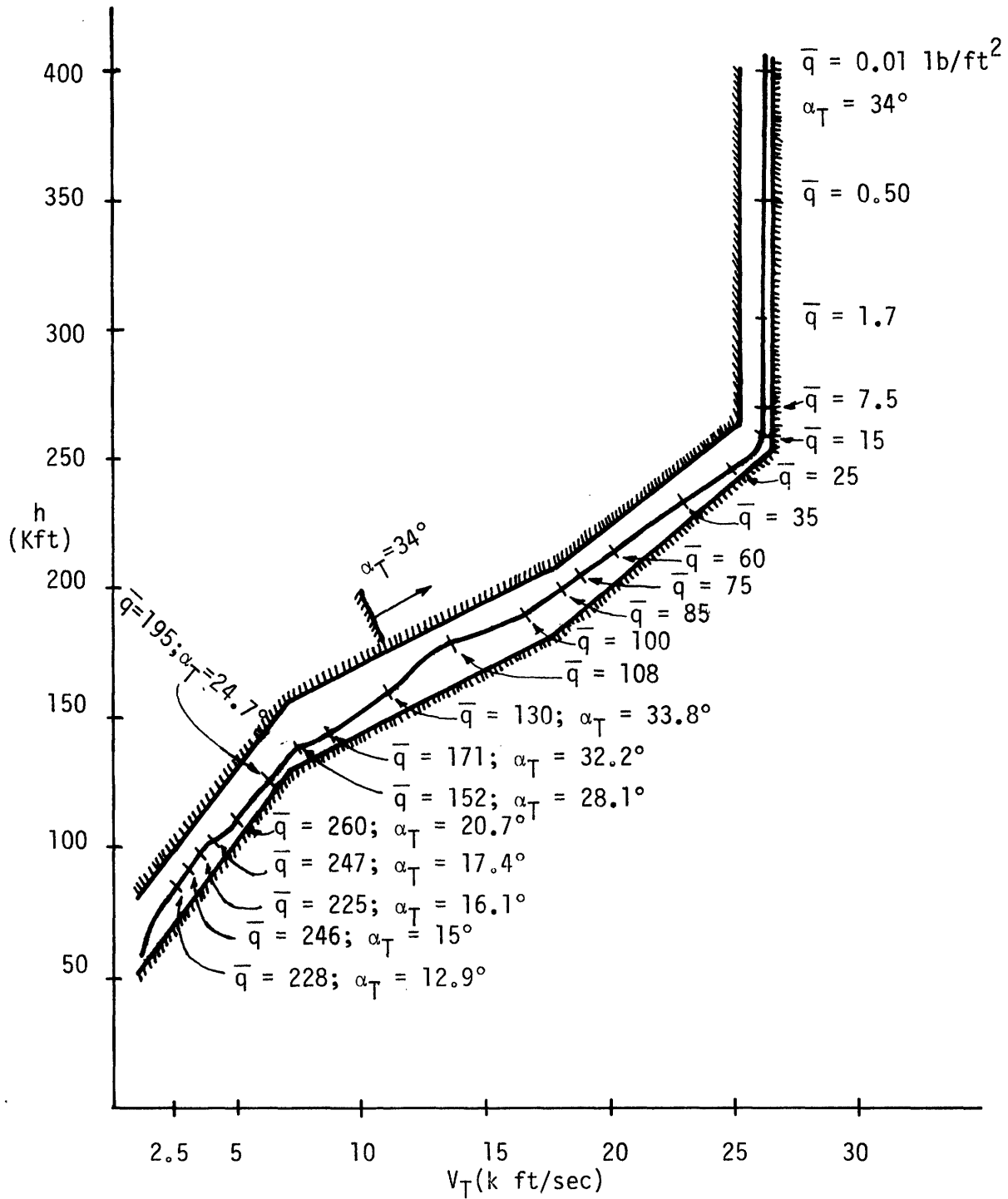* For a description of the trajectory, see Section 7.2.3.

Figure 7-2. Sample Trajectory Points.

For convenience of discussion, this section is divided into three subsections. Section 7.2.1 discusses the vehicle's transient response at various flight conditions, relating the observed performance to the desired performance. Section 7.2.2 then examines the operational bounds at the lower end of the flight envelope, so as to indicate the region of applicability of the entry control system. Section 7.2.3 then discusses system operation with the associated software routines of . guidance, state estimator, control system executive, and jet select logic. Finally, Section 7.2.4 provides a brief summary of system operation in a nominal environment.

7.2.1 Transient Response

This section presents simulation results showing closed-loop transient response to various system inputs, in an effort to describe and evaluate controller performance. Since it is anticipated that the guidance system eventually decided upon will issue constant-level commands at two- to four-second intervals, the most appropriate transient test is that of the system's step response; consequently, most of the results presented here consist of relatively short (40 to 60 seconds, primarily) runs, showing a response to a guidance commanded step within the interval. Also presented are some simple attitude-hold cases, in which no maneuver is called for. Finally, to gain some "feel" for the closed-loop frequency characteristics, sinusoidal test commands are used to drive the control logic.

The data is presented here in approximately chronological fashion down the sample trajectory of Figure 7-2. In this way, the initial conditions of the simulation runs may be taken from the flight envelope points of the figure, and the flight condition being described can be readily related to the progress of the overall trajectory. Another advantage in this approach is that the slowly changing operational characteristics of the controller can be better integrated with the changing flight conditions and the progress of the entry mission phase. The remainder of this section will be concerned with a detailed description of the simulation results.

Shown in Table 7-1 are the English literals used to identify plotted variables in the simulation histories to follow. It is also appropriate to note at this time two peculiar features of the plotting routine used to display the output. First, the physical dimensions of the plots are held constant, independent of the plot variable magnitude. Thus, the ordinate scaling will vary from plot to plot, depending on the magnitude range of the variable in question. Second, the time-axis does not necessarily indicate a zero value for the plotted variable, since the axis is constructed through the initial value of the plotted variable (which may not be zero). This latter feature allows for a greater emphasis on perturbations from initial conditions.

7.2.1.1 Operation at Entry Interface

The first three simulation runs to be discussed illustrate entry control operation at the entry interface (defined by the altitude of 400,000 ft) when the dynamic pressure is extremely low. They show, respectively, angle-of-attack and bank maneuver response, and long-term hold operation.

Shown in Figure 7-3a are time histories from a simulation run at entry interface, where $\bar{q}$= 0.01 lbf/ft^2 and the Mach number is 19, illustrating the closed-loop response to a step command in angle-of-attack. As can be seen, the command step, from $30°$ to $35°$, occurring at t=4 seconds, initiates the familiar bang-coast-bang pitch jet history, so that a maneuver rate of approximately $1.25°$/sec is generated, and then nulled once the desired attitude is approached. A correction pulse at t = 19 sec is applied to finalize the limit cycle operation. This time history may be related to the control law by the phase-plane trajectory plot of Figure 7-3b, showing the same maneuver, along with the switch curves defined by the longitudinal logic of (5-5) and the parameter values of Table 6-1. Note that because of the unusually large magnitude of the step command, a larger than anticipated maneuver rate is called for, which, in turn, results in an overshoot of the notched region between the γ_- and Γ_+ switch curves. The correction pulse at t = 19 seconds is the net result of this overshoot.

Table 7-1: Plot Variables

Variable	Mnemonic	Dimensions
α	ALPHA	deg
$\dot{\alpha}$	ADOT	deg/sec
ϕ	BANK	deg
$\dot{\phi}$	BANKDOT	deg/sec
β	BETA	deg
$\dot{\beta}$	BETADOT	deg/sec
p	P	deg/sec
q	Q	deg/sec
r	R	deg/sec
δ_e	ELEV	deg
δ_a	AIL	deg
δ_r	RUD	deg
u_x	UX	-
u_y	UY	-
u_z	UZ	-
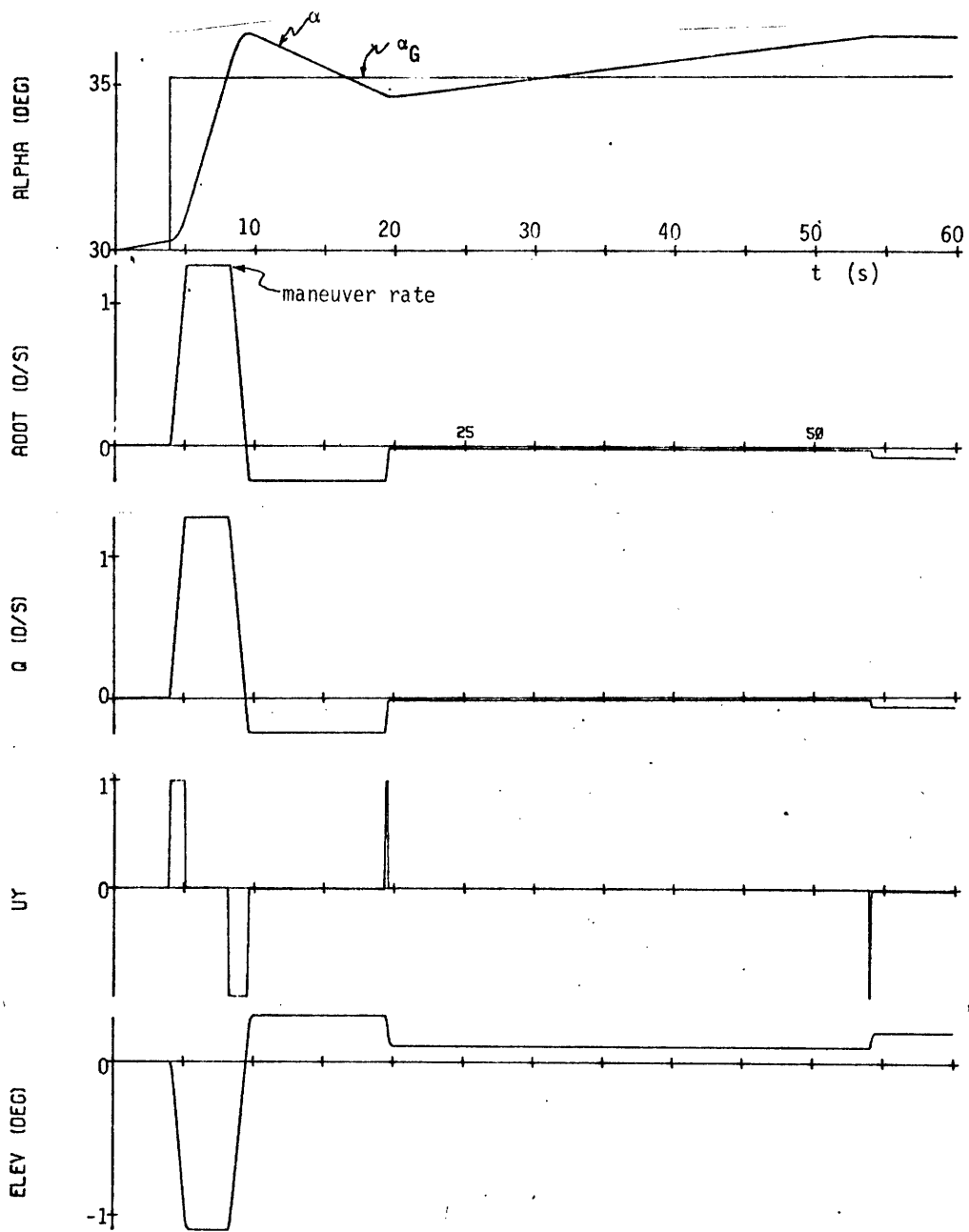
Figure 7-3a. Step Response to α_G ($\bar{q} = 0.01$).
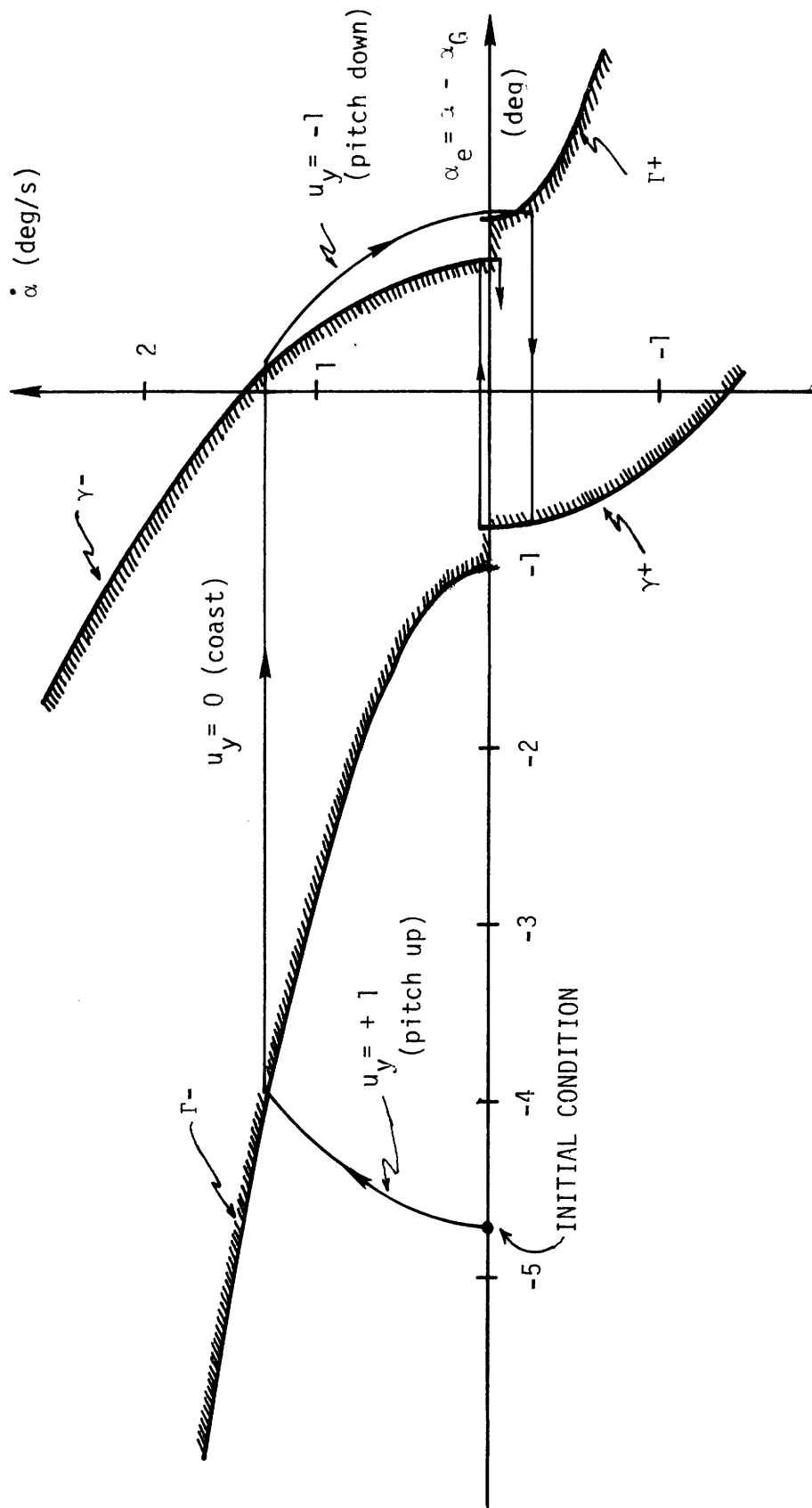
Figure 7-3b. Step Response to α_G ($\bar{q} = 0.01$), Showing Phase-Plane Trajectory.

Some additional points should be made regarding this response history. It may be recalled from the requirements discussed in Chapter 2 that no minimum maneuver rate was specified, although it would appear from present guidance requirements that $\dot{\alpha}_{min} \sim 0.2$ deg/sec[*]. This is clearly satisfied here, as is the steady state attitude error requirement of $\alpha_e^{max} \lesssim 1°$. The approximate jet on-time was 2.8 seconds (for two pitch jets), resulting in a fuel expenditure of 23.8 lbs for the 5° maneuver, clearly a low figure considering the anticipated budget ($\sim$700 lbs) and the large maneuver magnitude.

Some non-performance-oriented aspects of the maneuver may also be noted. In particular:

a) The double integrator model of the pitch dynamics (at low $\bar{q}$), derived in Chapter 4 and used as a synthesis base in Chapter 5, is clearly adequate here. The discrepancy between the model's continuity and the sampled-data nature of the system shows up only as small switch curve overshoots, as seen in Figure 7-3b. Note that the worst overshoot occurs at the highest rate, so that the error incurred is less than $(1.25°/sec)(0.1$ sec$) = 1.25°$.

b) With the low dynamic pressure environment, the elevator is commanded by the trim mode logic, integrating the pitch jet commands. However, since the dynamic pressure is at such an extremely low level, the elevator deflection of Figure 7-3a has essentially no effect on the pitch dynamics.

c) For this maneuver, the lateral dynamics were unaffected, because of vehicle geometry and jet thruster symmetry; thus, attitude hold in bank and sideslip is maintained throughout the pitch up.

Two final points of general applicability to both this run and the remainder of the simulation runs should be noted. As was mentioned earlier in the chapter, the control logic, as implemented on the SSFS, is embedded in the DFCS executive logic structure (recall Figure 7-1),

---

[*] From informal discussions with those working in the entry guidance area.

which provides the timing and sequencing necessary for successful execution. Rather than go into the details of the program operation, it suffices to say that this run and others demonstrate the compatibility between the executive structure and the control logic coding. To date, no problems have been found with this interface, since the executive and the control logic constitute a well-integrated functional structure. The second point to note is that the jet select logic (JSL) was used in this run (and the others to follow) to interface between the torque commands issued by the control logic (here, u_y) and the jet firing commands sent to the ACPS. The simplest measure of JSL efficiency and compatibility is evidenced by the fact that the vehicle behaves as if commanded by ideal torque sources, as is clear from the maneuver trajectory of Figure 7-3b. This type of performance allows for a high degree of confidence in the functional compatibility between the JSL and the control logic coding, and, of course, provides a considerable degree of simplification in control logic design and verification (recall discussion of Section 5.4.2.2).

The remainder of the simulation results to be discussed here primarily exercise the lateral control channel, since the pitch dynamics are fairly mundane. The performance of the longitudinal channel can be monitored, however, by recognizing that the angle-of-attack hold mode used for the bank maneuvers to follow provides an implicit measure of longitudinal channel operation.

Shown in Figures 7-4a, b, and c are time histories from a simulation at the same flight condition as in the previous run ($\bar{q} = 0.01$ lbf/ft^2, $\mathcal{M} = 19$), illustrating the closed-loop response to a step command in bank, with a constant angle-of-attack command of 34°. As can be seen from Figure 7-4b, the bank command step, from -45° to +45°, occurring at t = 4 seconds, initiates the bang-coast-bang yaw jet history (u_z) shown, so that a maneuver rate of approximately 4°/sec is generated, and then nulled once the desired attitude is approached.

An understanding of the operation of the lateral ACPS logic is facilitated by a somewhat more detailed description of this maneuver.
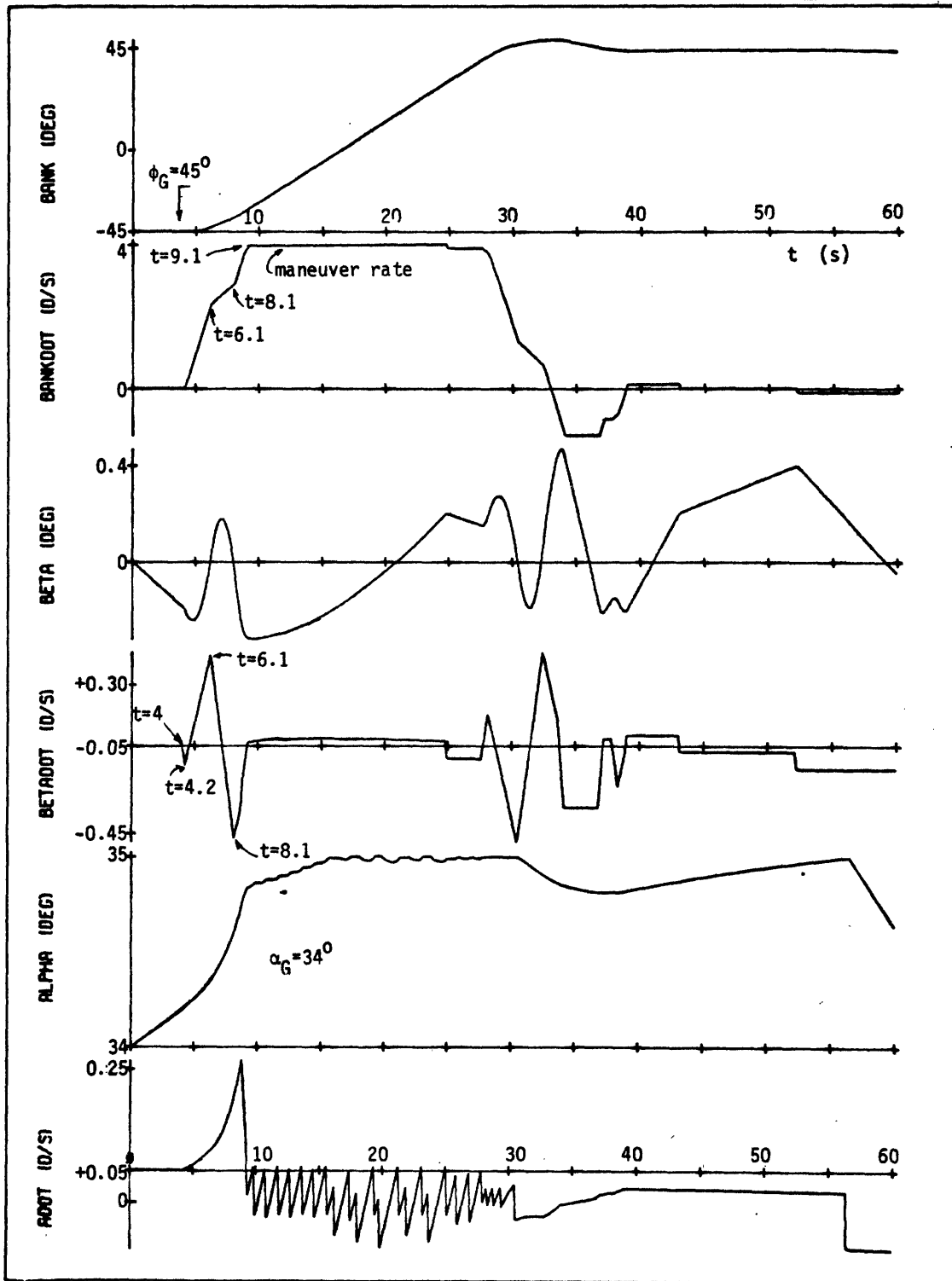
262

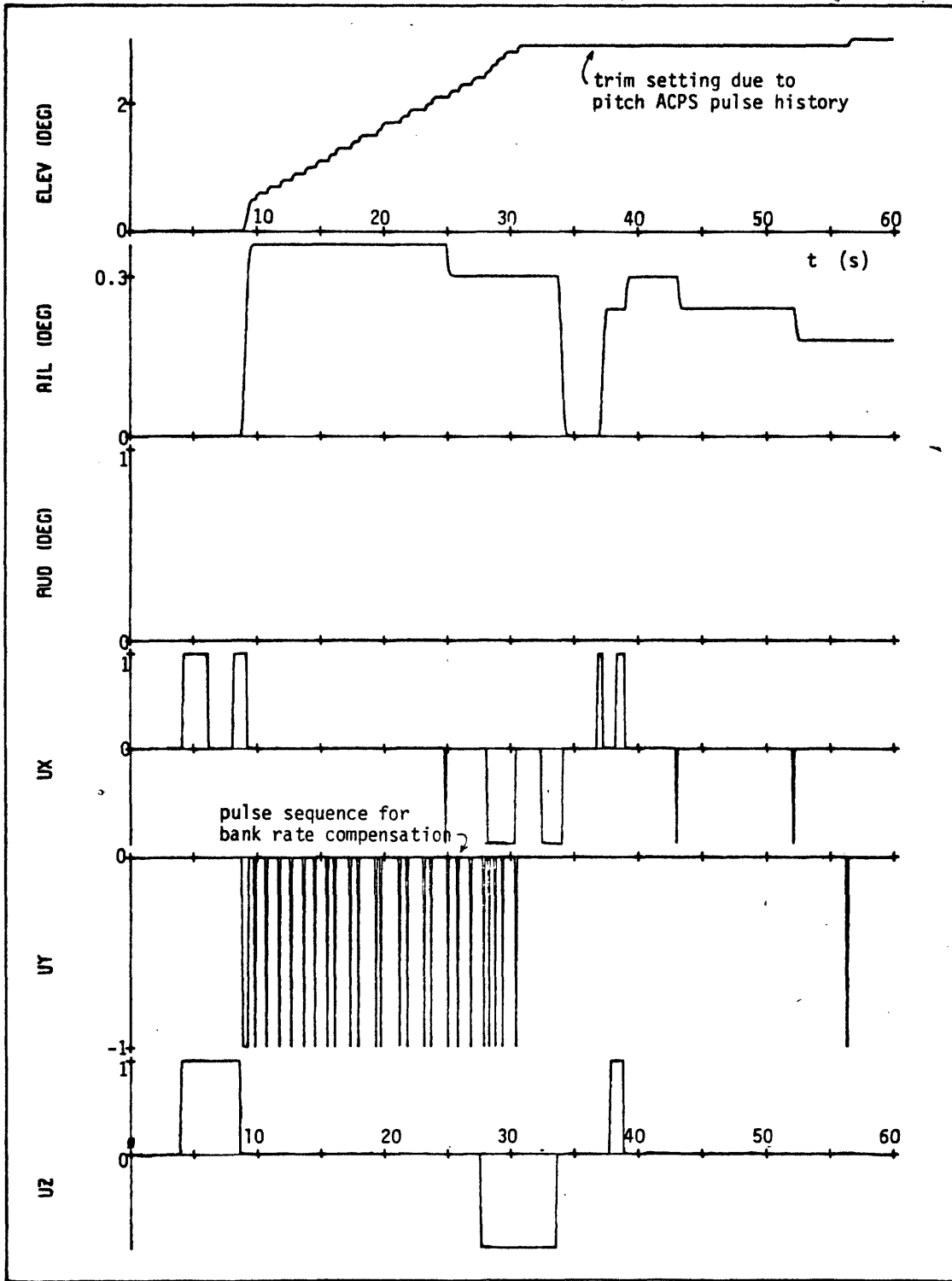Figure 7-4a. Step Response to ϕ_G ($\bar{q}=0.01$).

Figure 7-4b. Step Response to ϕ_G ($\bar{q}$ = 0.01).
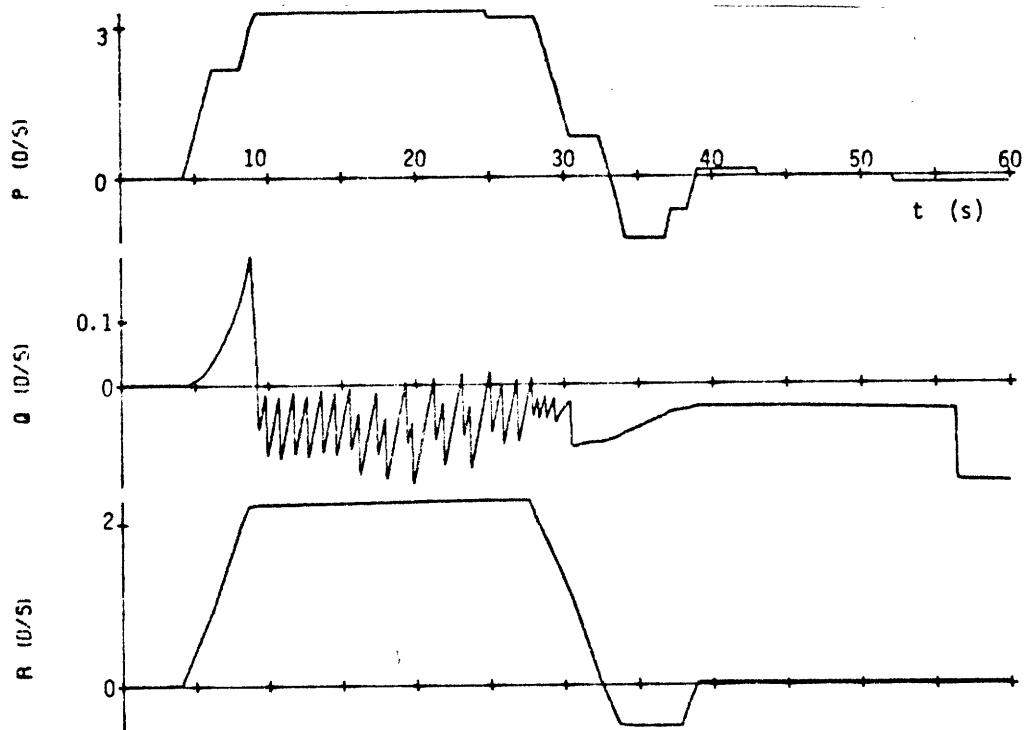
Figure 7-4c. Step Response to ϕ_G ($\bar{q}$=0.01).

At t = 4.0, the bank step command gives rise to a large negative attitude error in the bank angle/yaw rate phase-plane controlling yaw jet firings. As shown in Figure 7-4b, the yaw jets fire positively, causing an increase in the yaw rate, and, perhaps more significantly, cause a negative sideslip rate (recall the geometric discussion in Section 4.4.3 or simply recognize that $\dot{\beta} \approx -u_z \cos \alpha_T$ under these conditions). This eventually leads to a violation of the sideslip deadbands, resulting in a positive corrective roll jet command at t = 4.2 (see Figure 7-4a). From this point until t = 6.1, both yaw and roll jets fire, resulting in a bank angle acceleration of:

$$\ddot{\phi}_s = U_x \cos \alpha_T + U_z \sin \alpha_T \approx 1.1°/\sec^2$$

At t = 6.1, the sideslip deadbands are no longer violated, so that roll jet firing ceases, giving rise to the slope discontinuity in the bank rate history of Figure 7-4a. At t = 8.1, the sideslip deadbands are once again violated, initiating roll jet firings until the end of the acceleration maneuver at t = 9.1. The vehicle then "coasts" through the bank maneuver, until a similar sequence drives the rate to zero as the proper bank attitude is attained. As in the case of the previously described pitch maneuver, overshoot at the terminal end causes a slight asymmetry in the jet on-times (see Figure 7-4b), a direct result of the relatively high maneuver rate.

It may be recalled from the performance requirements discussion of Chapter 2 that a bank maneuver rate of approximately 5°/sec was called for; here, it can be seen that the performance is on the low side. What should be clear, however, is that the guidance requirement for relatively high bank rates is only applicable at high dynamic pressures, when a change in bank angle can substantially change the trajectory through the rotation of the aerodynamic lift force vector. This is certainly not the case here, and the maneuver rate appears to be adequate to satisfy early entry guidance requirements. At the completion of the maneuver, the limit cycle magnitudes are less than 3° and 0.4° for bank

angle error and sideslip, respectively, and thus within the specified limits given in Chapter 2. To gain some idea of what such maneuvers cost in terms of ACPS fuel, it may be noted that the jet on-times were approximately 8.5, 2.9, and 11.7 seconds, for roll, pitch, and yaw jet firings, respectively; the fuel expended was 121 lbm from roll and yaw jet firings, and 25 lbm for the pitch channel, resulting in a 146 lbm expenditure for the $90°$ maneuver. Although accomplished at a cost within 20% of the theoretical minimum, the maneuver is nonetheless an expensive one; an increased maneuver rate could only increase fuel costs.

At this point, it is appropriate to note some other aspects of the maneuver which are not so directly tied to the performance requirements. The first point to note is that the double integrator models of the bank and sideslip dynamics (at low $\bar{q}$), derived in Chapter 4 and used in the control design synthesis, are clearly adequate as demonstrated by the results. As in the longitudinal maneuver, the discrepancy between the model's continuity and the discreteness of the actual system shows up as switch curve overshoots due to the sampling lag. Again, the worst overshoot occurs after the high maneuver rate trajectory intersects the "braking" switch curve. What should be clear from the roll and yaw jet histories, however, is that the pulse sequences are extremely clean, with no chatter and only an occasional spike for limit cycle maintenance.

This is clearly not the case in the longitudinal channel, in which a relatively high-frequency string of pitch jet pulses (see Figure 7-4b) is attempting to maintain the (constant) commanded angle-of-attack during the bank maneuver. It should be recalled that in both the model development of Chapter 4 and the controller synthesis of Chapter 5, the longitudinal and lateral channels were treated as being uncoupled from one another. At first glance, the apparent cross-coupling shown in the longitudinal state and control variables would indicate a discrepancy in system operation; that this is not the case can be seen from a quick review of the pertinent equations. In the simplified vehicle model development of Chapter 4, the non-linear equations of motion were

linearized about specified equilibrium attitudes and rates, given by (4-7):

$$p_0 = q_0 = r_\theta = 0 \qquad \text{(a)}$$

$$v_0 = 0 \qquad \text{(b)} \qquad \qquad \text{(4-7)}$$

$$\dot{\phi}_0 = 0 \qquad \text{(c)}$$

Although all of these conditions are violated depending on the time-scale over which "trim" is defined, the condition most obviously not satisfied <u>during</u> the maneuver is the first one, since, on the average,

$$p_0 = \dot{\phi}_s \cos\alpha_T; \quad r_0 = \dot{\phi}_s \sin\alpha_T \qquad (7-1)$$

where $\dot{\phi}_s$ is the bank maneuver rate ($\sim 4°$/sec, in this example). It is thus appropriate to recall the pitch torque equation of (4-2), in its non-linearized form:

$$I_{yy}\dot{Q} + (I_{xx}-I_{zz})PR + I_{xz}(P^2-R^2) - M = \hat{M} \qquad (4-2)$$

where M and $\hat{M}$ are the aerodynamic and pitch ACPS torques, respectively. In the absence of aerodynamic forces (as is the case here), and with no pitch ACPS compensation, use of (7-1) in the above equation allows for the following prediction concerning steady-state pitch acceleration due to a constant bank maneuver rate:

$$\dot{q}_0 / \dot{\phi}_s^2 = \frac{1}{2}\left(\frac{I_{zz}-I_{xx}}{I_{yy}}\right)\sin 2\alpha_T - \frac{I_{xz}}{I_{yy}}\cos 2\alpha_T \qquad (7-2)$$

With a trim angle-of-attack value of approximately 35°, and the inertia values given by Table B-1 of Appendix B, the above equation indicates that a bank rate of 4°/sec will induce a pitch acceleration, or $\dot{q}_0$, of 0.12°/sec^2. This value is within a few percent of the observed value

268

illustrated in the pitch rate history of Figure 7-4c. Clearly then, what is being observed is inertial cross-coupling of the steady state lateral body rates into the pitch dynamics.

As seen by the pitch ACPS phase-plane logic, this bank rate effect is viewed as a pitch disturbance torque (see Section 5.1.2.2 for a more complete discussion) and thus the jets are fired to provide a compensatory torque. As shown in Figure 7-4b, the elevator simply integrates the pitch jet pulses, since it is being commanded by the trim mode logic. However, since the dynamic pressure is at such an extremely low level, no compensatory torques are provided by the elevator, and the pitch jet pulse train simply continues throughout the maneuver. What should be recognized is that the pitch jet firings cannot be avoided, since they must supply, on the average, a pitch acceleration to null $\dot{q}_0$ of (7-2). Of course, the frequency of the firings could be reduced in a maneuver situation such as this, by providing a mode switch to force the use of pulses of longer duration; this additional complication has not been deemed necessary, and this characteristic pitch jet activity during a bank maneuver will be seen in several of the simulation histories to follow.

One final point should be made regarding the aileron history. As may be recalled, the aileron trim logic appropriate to this low dynamic pressure situation commands a deflection proportional to the integral of the roll jet commands, and only when the yaw jets are not firing. As can be seen, this latter qualification prevents the trim logic from integrating most of the roll jet pulses, and yet allows for a sufficiently high integrator gain to compensate for lateral mistrims (see Section 7.3.1.2). Of course, in this particular situation, the aileron is ineffective in providing a compensatory control torque, due to the low dynamic pressure.

Shown in Figures 7-5a and 7-5b are time histories from a simulation initiated at the same flight condition as in the two previous cases ($\overline{q}$= 0.01, h = 400,000 ft, $\mathcal{M}$ = 19), illustrating limit cycle operation over a longer time span. Over this 200-second interval, the vehicle
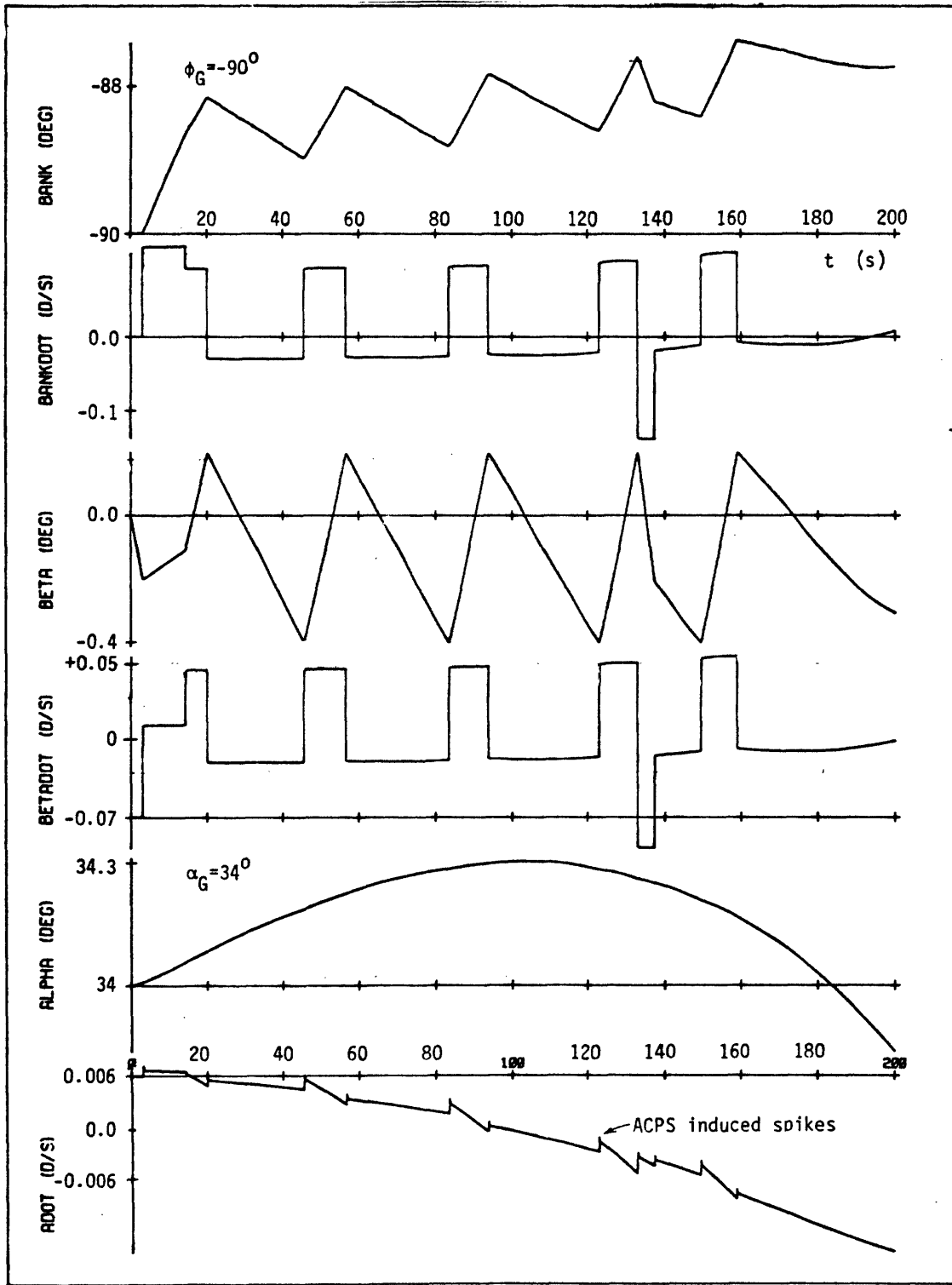
269

Figure 7-5a. Early Entry Limit Cycle Operation
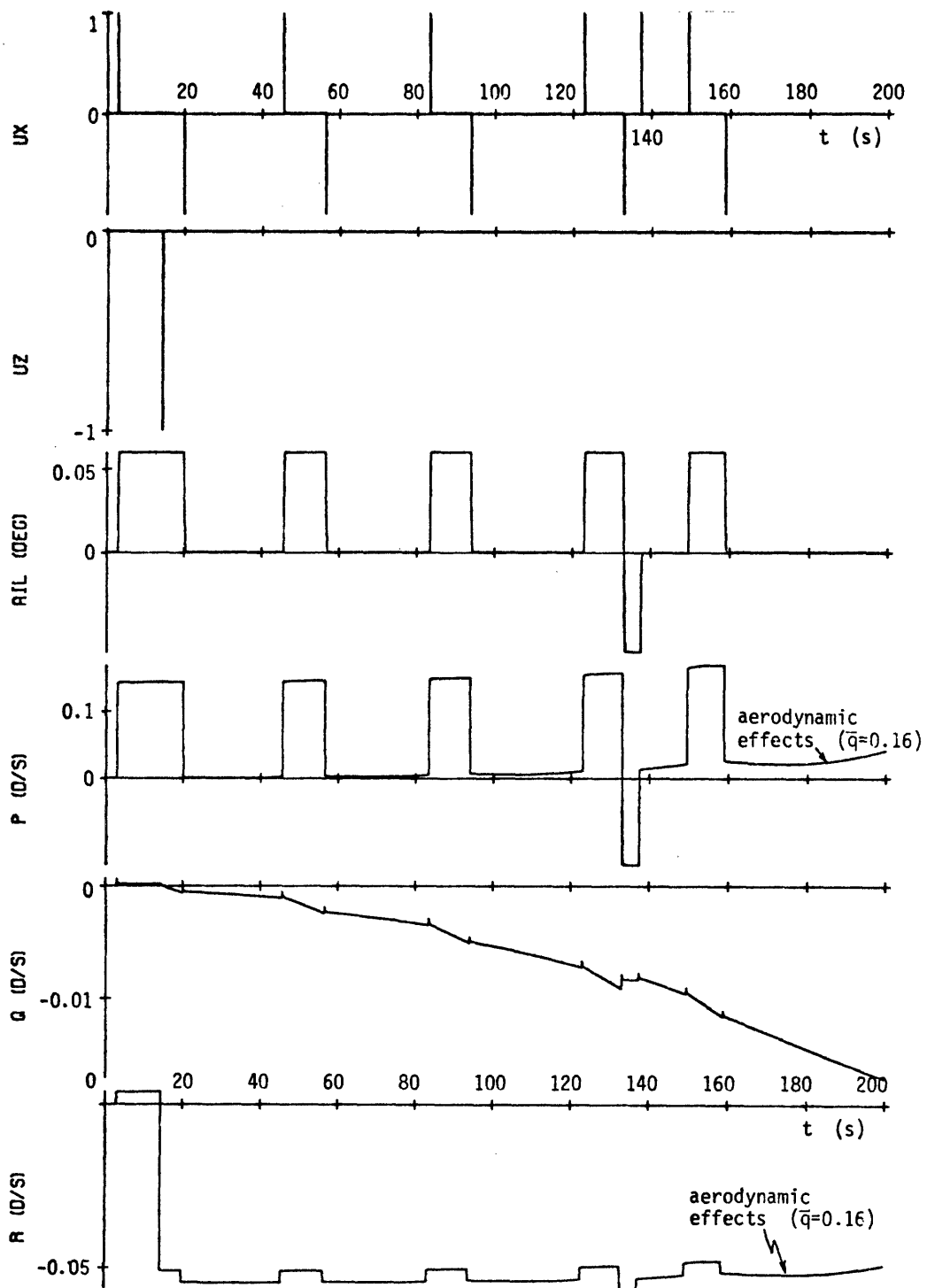$(\bar{q}_{init} = 0.01 \ \ell \, bf/ft^2)$.

270

Figure 7-5b. Early Entry Limit Cycle Operation ($\bar{q}_{init}$ = 0.01 lbf/ft^2).

velocity remains approximately 26,000 ft/sec while altitude drops from 400,000 ft to 340,000 ft, resulting in a Mach number increase from 19.4 to 26.1 and a dynamic pressure increase from 0.01 lbf/ft^2 to 0.17 lbf/ft^2. Angle-of-attack is maintained at approximately 34° while a full-left bank attitude of -90° is held so as to effect the vehicle "drop" into the atmosphere. As should be clear from Figure 7-5a, bank, sideslip, and angle-of-attack are all maintained within their desired limit cycle deadbands, with only occasional pulses from the ACPS jets (see Figure 7-5b). The total ACPS fuel use for this interval was slightly over 11 lbm, less than 10% of the cost of the above-discussed bank maneuver.

Several additional points regarding this simulation run are worth noting. For the longitudinal channel no control authority was required to maintain vehicle attitude within the desired deadbands; thus, neither the pitch jet history nor the elevator history is shown, since no jets were fired and the elevator was maintained at zero deflection. The small spikes in both the $\dot{\alpha}$ and pitch rate histories are due to roll jet firings (see Figure 7-5b) in which pitch rate residuals were not immediately compensated for by the JSL; clearly these have little effect on the overall histories. Of more interest is the presence, again, of a pitch acceleration (see Figure 7-5b); this time of quite low level and relatively constant throughout the run. The source of the acceleration is the same as before, however, as can be ascertained by correlating changes in the bank rate level with changes in the pitch rate and angle-of-attack rate histories; thus, (7-2) is applicable here also.

Operation in the lateral channel is also fairly straightforward. It should be clear from Figure 7-5a that the bank angle tends to "hang" on one side of the deadband, so that the desired symmetric limit cycle behavior is not observed. What is occurring, in fact, is an almost total absence of yaw jet control over bank angle (see Figure 7-5b); instead, the roll jets, in maintaining a small sideslip attitude, are providing sufficient torque at appropriate times for simultaneous and effective control of bank attitude. That they do not provide for symmetric limit cycle operation in a cross-channel is thus not surprising. The body

rates, p and r of Figure 7-5b, provide a good illustration of the increasing effect of dynamic pressure as the mission progresses. For the first half of the time interval, the rates are simply the integrals of the roll and yaw jet pulses; near the end, however, the curved deviations from a simple rectangular integration of jet pulses belies the presence of aerodynamic forces at work, in turn due to the dynamic pressure approaching 0.2 lbf/ft^2 near the end. Finally, it is interesting to note that the relatively constant yaw rate of -0.05°/sec is consistent with zero sideslip operation at -90° bank. To see this, it may be noted that the local horizontal rotates at approximately V_T/R_e rad/sec, where R_e is the earth's radius. Since the flight path angle remained relatively constant during the run ($\gamma_0 \approx -0.85°$), this implies a velocity vector pitch down rate of approximately 0.062°/sec (= V_T/R_e). Shown in Figure 7-6 is a view looking "down" at the vehicle, along the gravity vector. For the vehicle to maintain the velocity vector in the body plane of symmetry, a steady-state yaw rate, r_{ss}, must be present, given by:

$$r_{ss} \approx -\frac{V_T}{R_e} \cos \alpha_T \qquad (\phi_s = -90°) \qquad (7-3)$$

Substituting in the appropriate values yields a value of 0.051°/sec for r_{ss}, in close agreement with the history of Figure 7-5b.
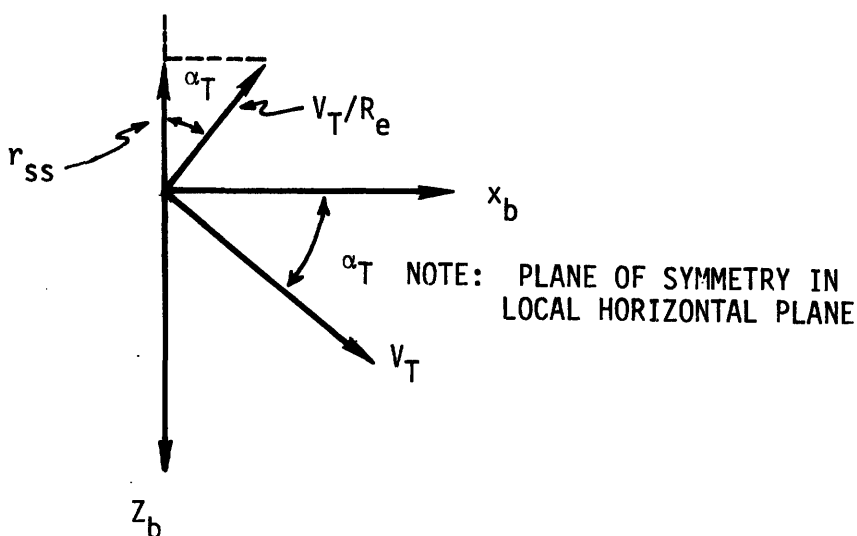

Figure 7-6. Required Yaw Rate for Zero Sideslip Flight (ϕ = 90°, $\gamma \approx 0°$).

It should be recognized that the simulation results presented above are appropriate to the vehicle center-of-gravity in the forward position and in the vehicle plane-of-symmetry. Deviations from this situation are treated in Section 7.3.1. This completes the discussion of the first three simulation runs conducted at entry interface.

7.2.1.2 Operation at Early Stage of Dynamic Pressure Growth

The next two simulation runs illustrate the subtle effect of increasing dynamic pressure early in the entry; as will be seen, the effect is primarily in the longitudinal channel.

Shown in Figures 7-7a and b are time histories of a bank maneuver performed at an initial altitude of 320,000 ft and Mach number of 27.9; during the 60-second interval shown, the altitude drops approximately 20,000 ft and the dynamic pressure grows from an initial value of 0.5 lbf/ft^2 to 1.6 lbf/ft^2. By comparison with the previous bank maneuver performed at the entry interface (see Figures 7-4a and b), it can be seen that the state variable histories are quite similar. The major difference in the lateral channel is evidenced by the slight curvature in the sideslip rate history of Figure 7-7a, implying the presence of aerodynamic forces influencing the dynamics, in turn caused by the tripling of the dynamic pressure through the course of the run. As can be seen, however, it has little effect on lateral channel operation.

This is not the case with the longitudinal channel, as can be seen by comparing the angle-of-attack histories of Figures 7-4a and 7-7a. As before, negative pitch jet firings are required to cancel the inertially induced pitch acceleration caused by the non-zero bank maneuver rate; and, as before, the elevator trim logic integrates these firings to produce an elevator deflection history as shown in Figure 7-7b. What is interesting to note, however, is that in the previous low dynamic pressure situation ($\bar{q}$= 0.01 lbf/ft^2), the elevator setting of Figure 7-4b remained at the setting reached by the end of the bank maneuver (at t $\approx$ 32 seconds). The elevator history shown in Figure 7-7b is not quite the
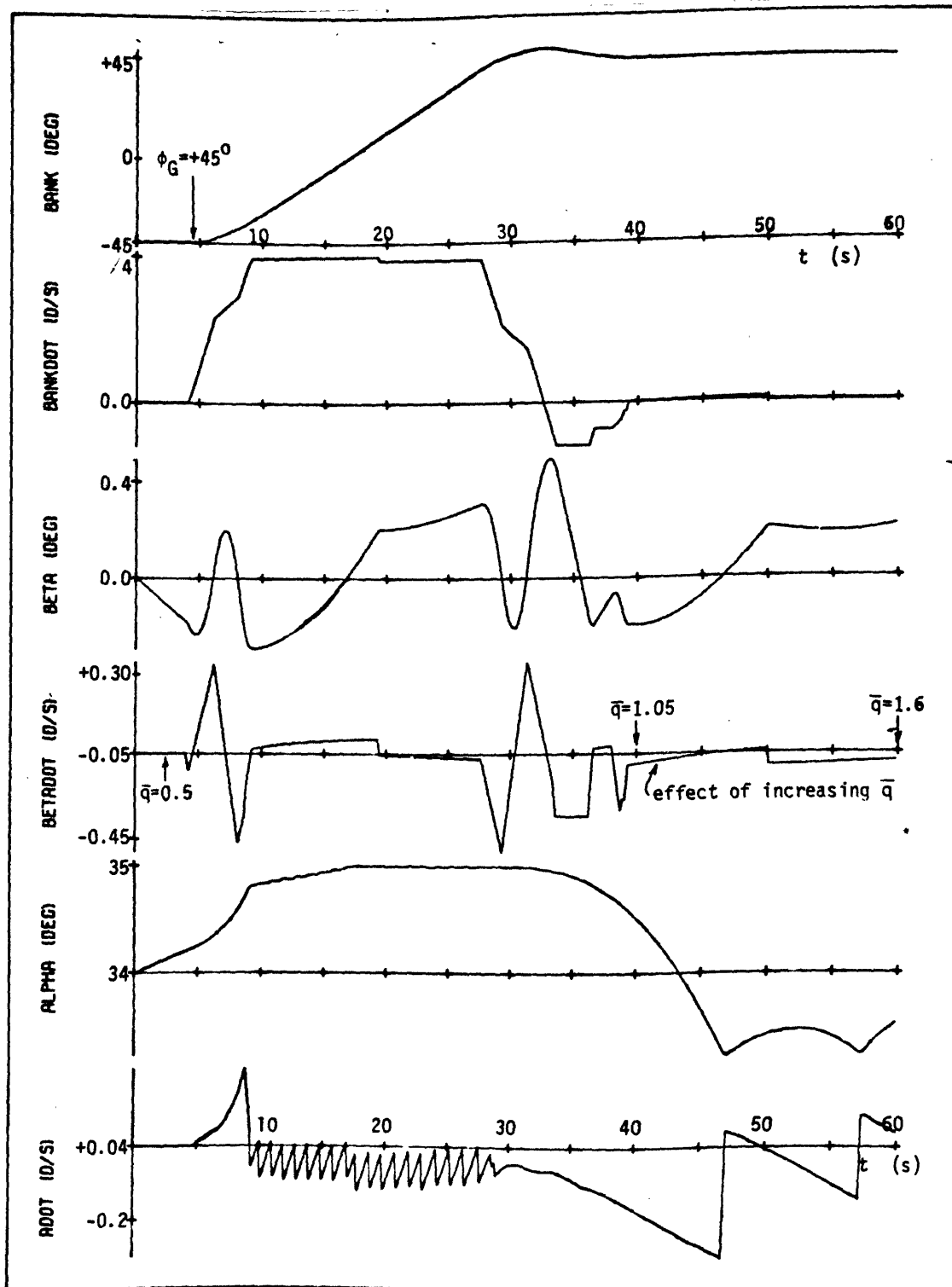
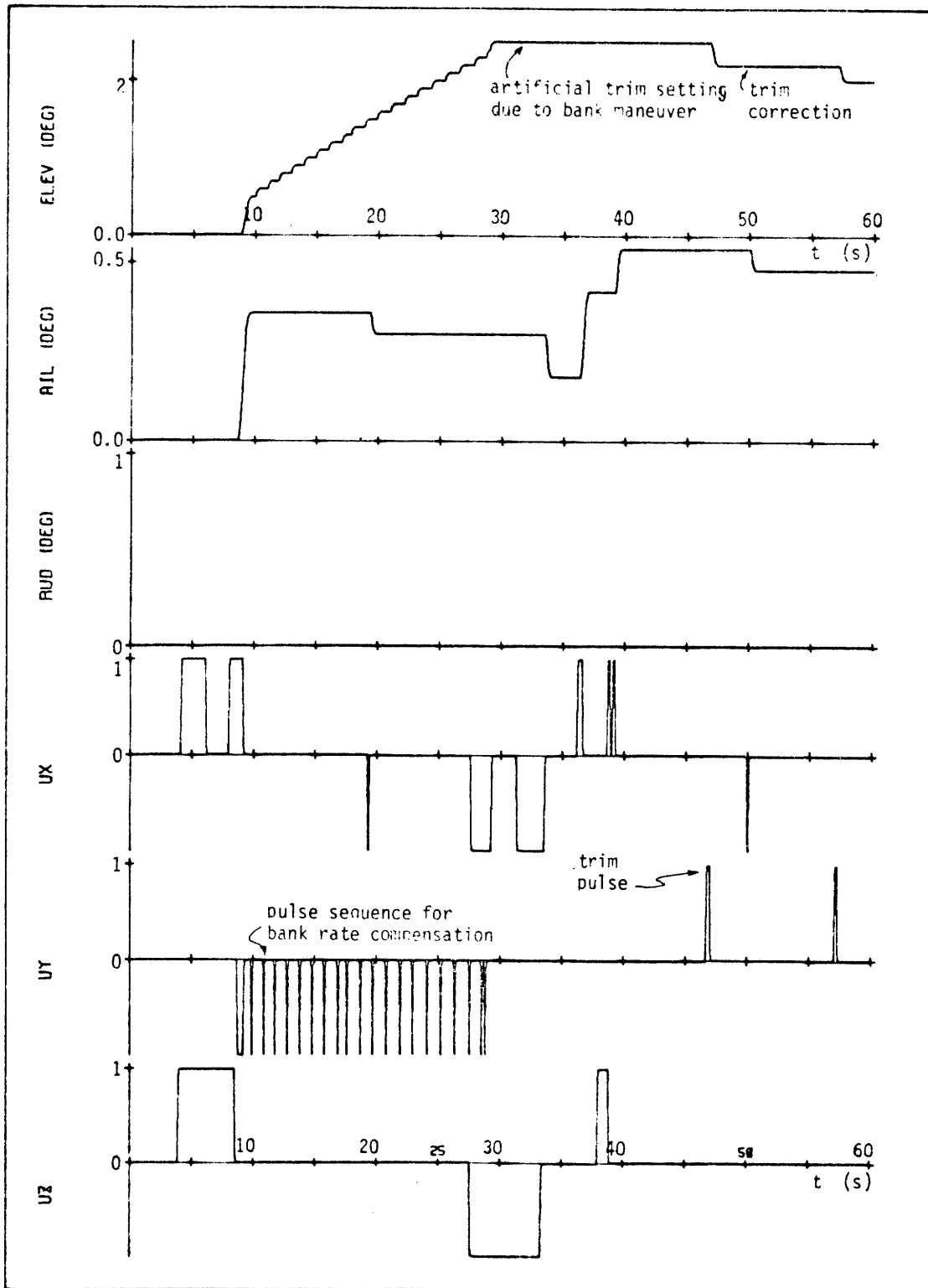Figure 7-7a. Step Response to ϕ_G ($\bar{q}$=0.5 → 1.6).

Figure 7-7b. Step Response to ϕ_G $(\bar{q}=0.5 \longrightarrow 1.6)$.

276

same, since the trim setting reached at the end of the bank maneuver (here at t ≈ 30 seconds) is being slowly decremented back towards its original zero setting. What has happened here is that the artificially derived trim setting of some 2.5° down elevator causes the vehicle to pitch down once the bank maneuver is concluded. Thus, the angle-of-attack history of Figure 7-7a violates the pitch ACPS deadbands, initiating compensatory positive pitch ACPS firing (the two pulses seen at t ≈ 47 seconds and t ≈ 57 seconds). Of course the cause of this elevator induced mistrim is the increased dynamic pressure level, and is why this behavior was not observed in the run at $\bar{q}$ = 0.01 lbf/ft^2.

Naturally, this effect is even more pronounced at higher dynamic pressure levels. Shown in Figures 7-8a and b are time histories of a bank maneuver performed still later in the entry: the initial altitude was 300,000 ft and the Mach number was 29.3. During the 60 seconds shown, altitude dropped 22,000 ft and the dynamic pressure increased from an initial value of 1.7 lbf/ft^2 to 5.4 lbf/ft^2. As in the previous cases, the angle-of-attack is maintained near 34° while a 90° bank maneuver is effected. The overall maneuver is, of course, basically the same as the one just described (at $\bar{q}$ = 0.5 lbf/ft^2) and the one performed at the entry interface ($\bar{q}$ = 0.01 lbf). The trends with increasing dynamic pressure are also quite clear, as can be seen by reviewing all three sets of data. In particular, Figure 7-8a shows the beginnings of aerodynamic effects in the bank channel, by the slight curvature evidenced in the bank rate history near the end of the run. A similar, although more marked, effect is seen in the sideslip channel, by the effect on the rate history. In fact, the beginnings of oscillatory behavior in sideslip, as predicted by the model of (4-53) of Chapter 4, can be seen in this trace. This behavior will be more obvious in the next simulation run to be discussed.

The trends in the longitudinal channel with increasing dynamic pressure should also be clear from this simulation run. The pitch ACPS pulses again induce a trim elevator setting appropriate to the bank rate magnitude (but not as large as before), and then correct this setting for attitude hold operation (at a rate faster than before). Table 7-2
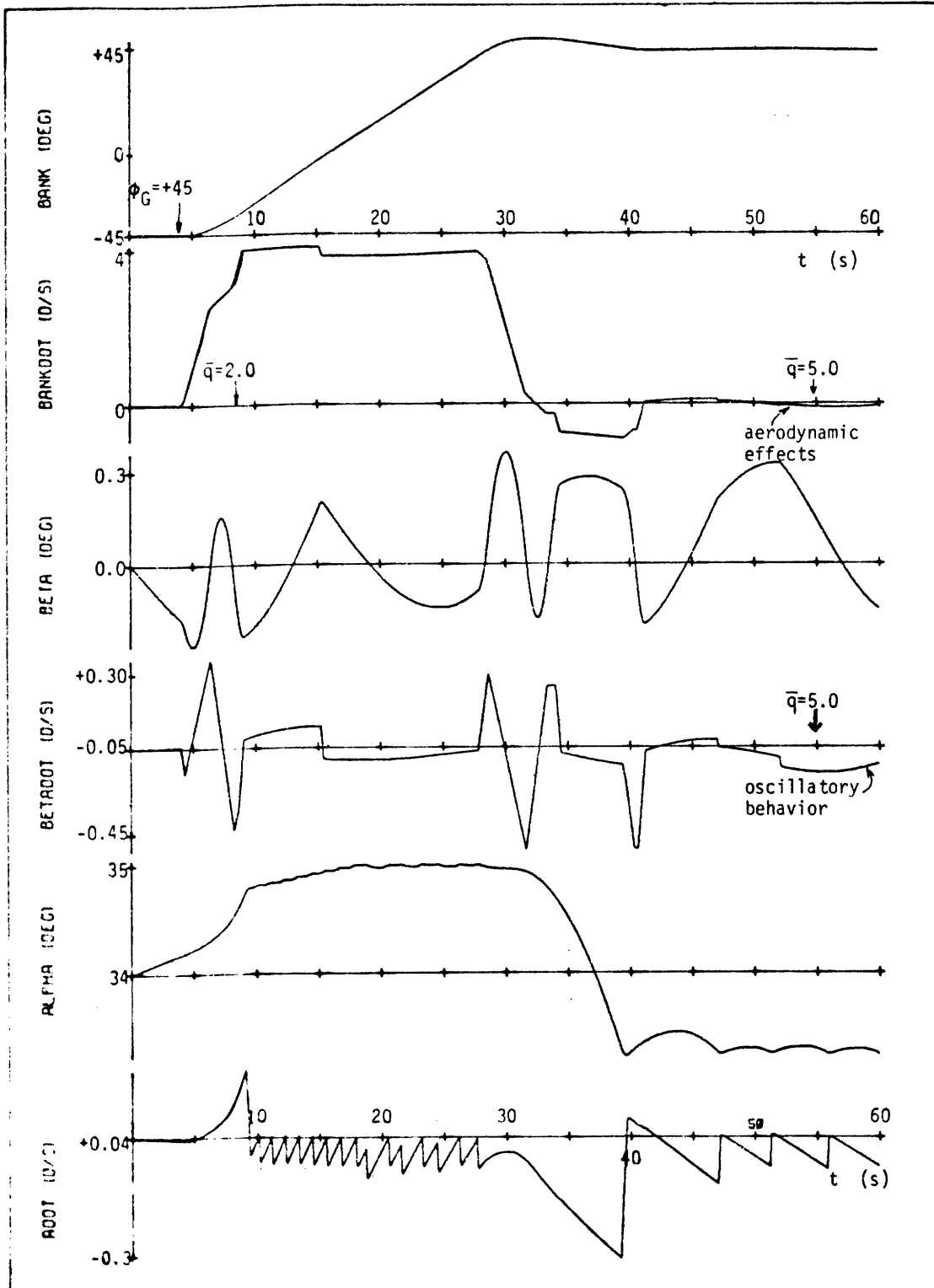
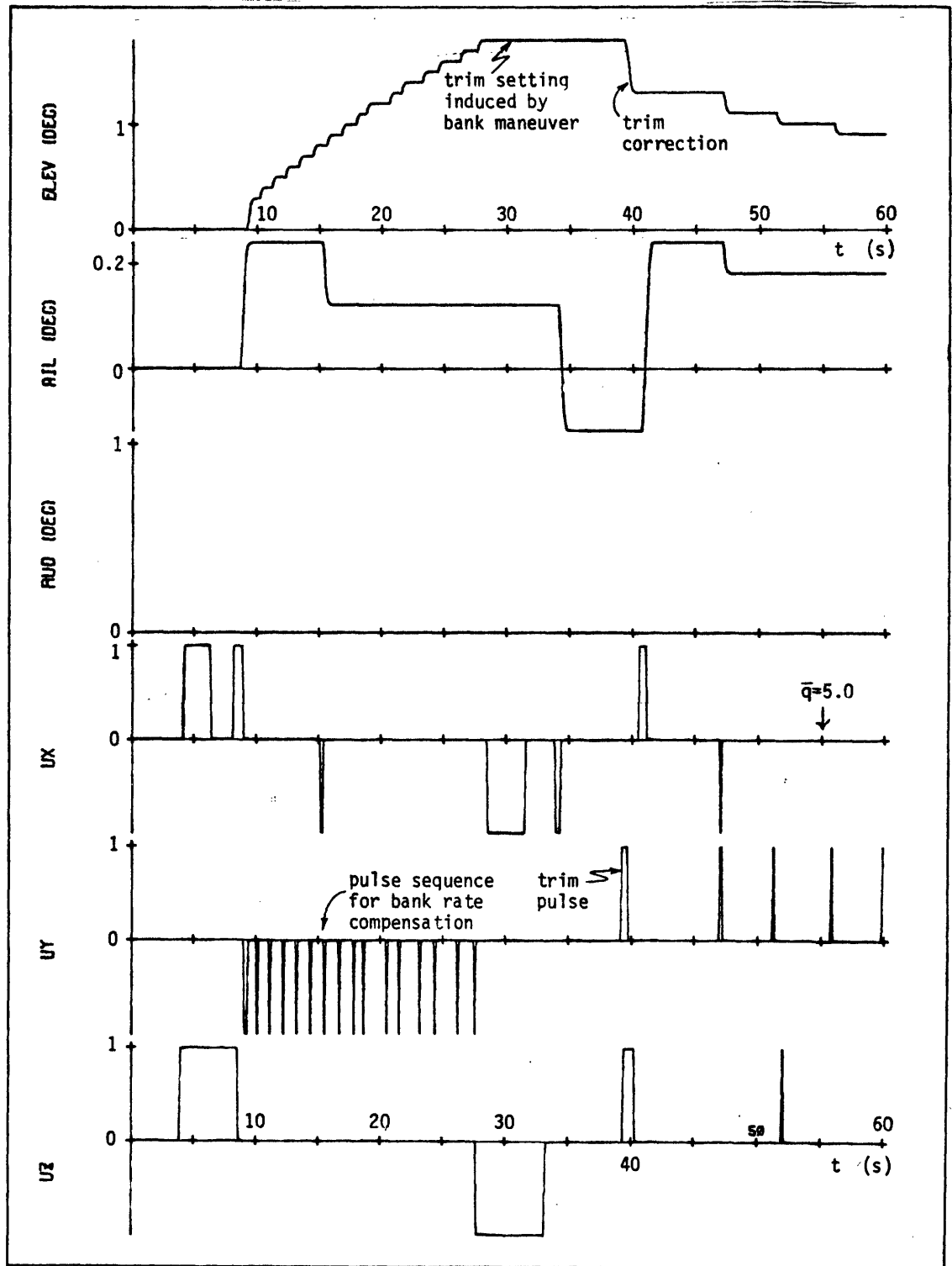Figure 7-8a. Step Response to ϕ_G ($\bar{q}$=1.7⟶5.4).

278

Figure 7-8b. Step Response to ϕ_G ($\overline{q} \approx 1.7 \rightarrow 5.4$).

summarizes these trends with dynamic pressure: the label T_1 indicates the pitch jet on-time during the bank maneuver, T_2 indicates the jet on-time for trim correction after the maneuver, and δ_e^{max} and δ_e^f indicate the maximum and final elevator deflection settings, respectively. Two points should be clear: first, with increased dynamic pressure, the elevator provides some of the pitch torque compensation required during the bank maneuver, thus reducing the jet on-time (T_1); and second, increased dynamic pressure also forces a more rapid correction of post-maneuver elevator trim setting (T_2), since elevator effectiveness has increased. Note that the total on-time $(T_1 + T_2)$ is approximately the same for all three situations.

Table 7-2: Dynamic Pressure Trends in the Longitudinal Channel

$\bar{q}$(lbf/ft^2)	T_1(sec)	T_2(sec)	(T_1+T_2)(sec)	δ_e^{max}(deg)	δ_e^f(deg)
0.01	2.9	0.0	2.9	2.9	3.0
0.50→1.6	2.5	0.5	3.0	2.5	2.0
1.7→5.4	1.8	1.0	2.8	1.8	0.9

One final note should be made regarding this run. A mode switch from attitude hold to sideslip rate damping was made in the roll jet logic at $t \approx 55$ seconds, when $\bar{q}$ exceeded 5 lbf/ft^2. Of course, the objective in this mode switch, as has already been stated, is to take advantage of the oscillatory sideslip dynamics; what is appropriate to note is that there were no switching induced transients, thanks to the digital struc-ture of the controller.

7.2.1.3 Elevator Turn-On

The next two simulation runs illustrate operation during the first major mode switch later in the entry: elevator turn-on at $\bar{q} = \bar{q}_1$ (= 10 lbf/ft^2). As will be seen, the turn-on transients are relatively minor.

Shown in Figure 7-9 are time histories of attitude hold operation, in which the commanded angle-of-attack and bank angle are 34° and -45°, respectively. The initial altitude is 272,000 ft at a Mach number of 29.5; during the run the altitude drops 15,000 feet and the dynamic pressure increases from an initial value of 7.5 lbf/ft^2 to a final value of 16.9 lbf/ft^2. In terms of performance, it may be noted that all three stability-axis attitude angles are maintained within their specified deadbands, with only a single yaw jet pulse (neither pitch nor roll jets are fired) needed for an early correction of the bank attitude drift. The particular nature of the time histories shown for bank and sideslip will be discussed shortly.

As can be seen from Figure 7-9, elevator turn-on (to the "transient" control mode) at this flight condition occurs rather dramatically and over a fairly short time interval. What initiates this activity is the fact that the dynamic pressure reaches 10 lbf/ft^2 at t ≈ 16.7 seconds into the run. Because of the timing structure of the DFCS, parameter updating occurs at a relatively slow rate of every two seconds; thus, the control logic does not "read" a new dynamic pressure level until some time later, at t ≈ 17.9 seconds. Thus, for t < 17.9 seconds, the transient control mode is bypassed and a zero trim elevator command is issued; at t = 17.9 seconds, the dynamic pressure threshold is exceeded, the transient control coding is entered, and a non-zero elevator command is issued. Since the control law gains are inversely proportional to dynamic pressure and thus relatively large, and since the attitude and rate errors tolerated by the pitch ACPS phase-plane logic appear relatively large to the linear logic of the elevator control law, a large elevator deflection is called for by the transient control law. This is limited, however, by the blending logic (see Section 5.3.1) which schedules the deflection limits as a function of dynamic pressure; in particular, the lower limit is given by:

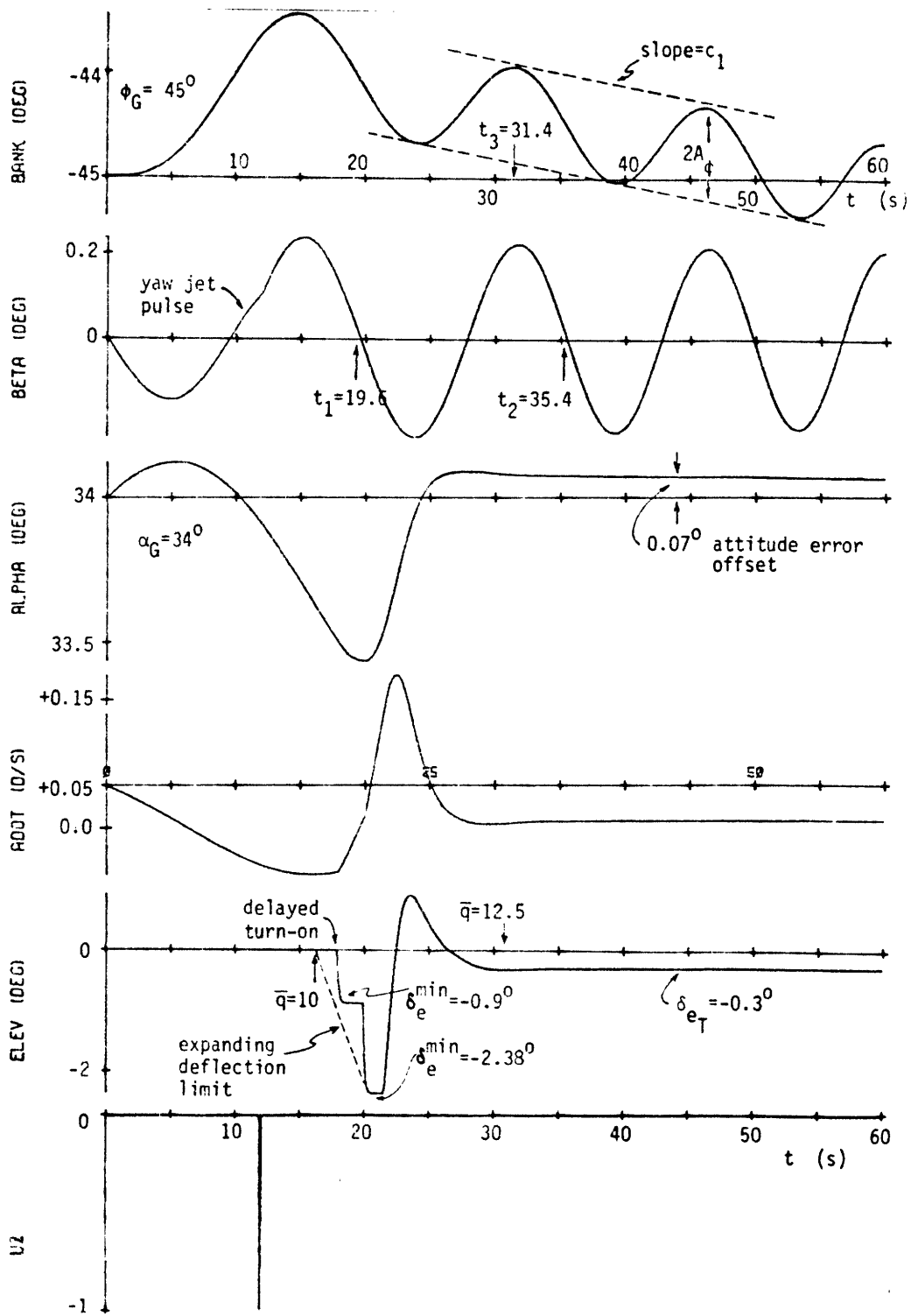$$\delta_e^{min} = (1-K_e)\delta_{e_T} + K_e \Delta_e^{min} \qquad (5-79b)$$

Figure 7-9.   Elevator Turn-on During Attitude

Hold ($\overline{q}$=7.5⟶16.9).

where, from Table 6-1, $\Delta_e^{min} = -45°$ and where the blending parameter K_e is defined by Figure 5-22, and is equivalently defined by

$$K_e = \frac{\bar{q} - \bar{q}_1}{\bar{q}_1^* - \bar{q}_1} \qquad (\bar{q}_1 \leq \bar{q} \leq \bar{q}_1^*) \qquad (7-4)$$

where $\bar{q}_1 = 10$ lbf/ft^2 and $\bar{q}_1^* = 20$ lbf/ft^2 from Table 6-1. Now, at t = 17.9 seconds, $\bar{q} = 10.2$ lbf/ft^2 and $\delta_{e_T} = 0$. Thus, from the two relations above, $\delta_e^{min} = -0.9°$, which, as can be seen from the elevator history, is precisely where the elevator limits. This setting is then held for two seconds until the next dynamic pressure update at t = 19.9 seconds, where $\bar{q} = 10.53$ lbf/ft^2; the commanded deflection is again limited according to (5-79b), at $\delta_e^{min} = -2.38°$. This setting is then held for slightly less than two seconds, at which time the cumulative effects of the elevator deflections have reduced the attitude errors to relatively small magnitudes; thus, the elevator commands are no longer large, and limiting effects thereafter are consequently not present in the elevator trace.

What should be clear from this discussion is that the blending logic prohibits the full exercise of the linear transient elevator control logic, thus violating the linearity assumptions upon which the elevator control design was based. To fully test the stability of this non-linear system requires a large number of simulations with differing longitudinal states at elevator turn-on, since system stability, in general, is initial condition dependent. In this manner, an envelope of acceptable initial conditions for elevator turn-on, as is illustrated in Figure 7-10, could be defined so as to guarantee convergence to the final desired state. This has not been done for three reasons. First, the stability contour of the figure is also a function of the angle-of-attack (not simply the attitude error), the blending parameters K_e, $\bar{q}_1$ and $\bar{q}_1^*$, and the rate of change of dynamic pressure $\dot{\bar{q}}$; thus, what is actually involved is the definition of a stability hypersurface in a high order parameter/state space. Second, even if it were possible to empirically define (via
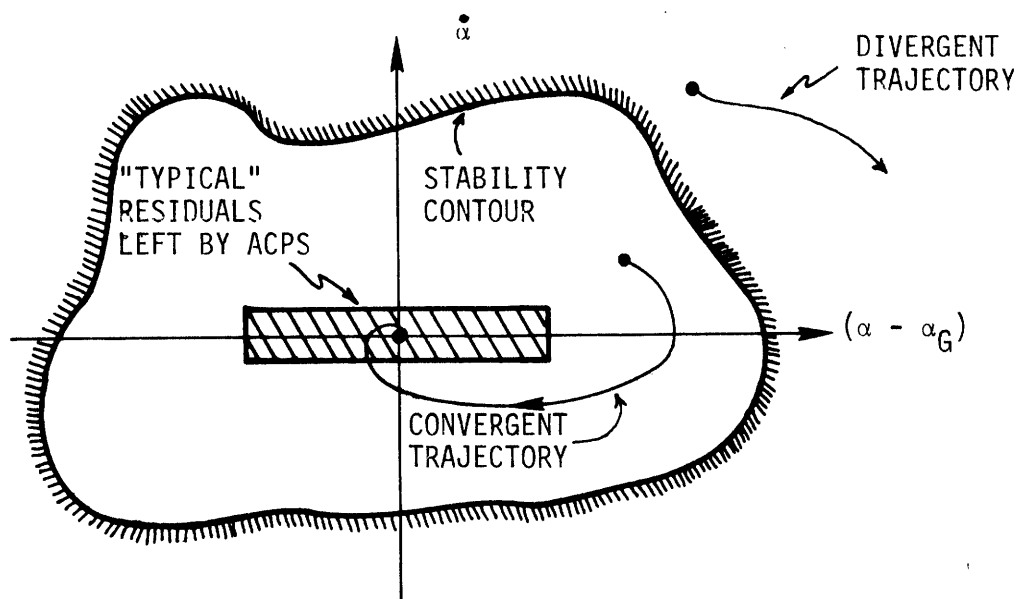
Figure 7-10. Hypothetical Stability Envelope for Elevator Turn-on.

simulation results) such a surface, little can be inferred concerning overall system performance beyond simple stability. The final reason is that some testing to define the contour(s) has been done, and although the data is insufficient to properly specify a controllable region about the state space origin, all indications are that the region of "anticipated" initial conditions lies well within the boundary defining "allowable" initial conditions. In fact, with the many runs made in the course of testing, there has never been any indication of any behavior other than convergence. This is illustrated in the above figure by the small rectangle representing the region of anticipated initial conditions at elevator turn-on, due to the tolerant deadbands of the ACPS phase-plane logic. Thus, in spite of the non-linear nature of the initial elevator transients, there exists a high degree of confidence in the consistency of simultaneous operation of both the transient control logic and the blending limiter logic.

One final point regarding the elevator deflection history should be noted. After the elevator turn-on transients have subsided, an apparent

284

trim situation has been attained through the use of a slightly negative elevator setting; unfortunately, the attitude is offset from the guidance commanded steady state value by $0.07°$. The cause of this is the fact that during this regime ($\bar{q} < \bar{q}_1^* = 20$ lbf/ft^2) the elevator trim setting is determined by integrating the pitch jet firings, as in the maneuvers described above. Since there are no such firings, the elevator trim setting (δ_{e_T}) is zero and thus the proper trim setting must be provided by the transient control law logic, or, from (5-20) and (5-19),

$$\delta_e^c = \frac{1}{\xi_1} \left\{ \left(\frac{\omega_d^2}{\bar{q}} - \xi_2 \right) \alpha_e - \frac{2\zeta_d \omega_d}{\bar{q}} \dot{\alpha} \right\} \qquad (7-5)$$

For the vehicle to trim at the guidance commanded value, both α_e and $\dot{\alpha}$ must be zero; but this implies a zero elevator trim setting by the above equation, a situation which may not be compatible with the vehicle's trim characteristics. This is certainly the case here, since the vehicle will not trim at exactly $34°$ angle-of-attack with zero elevator. What has happened in this case is that the control system, being constrained to satisfy (7-5), has not, in actuality, trimmed the vehicle, but instead, has arrived at a "triplet" (δ_e^c, α_e, $\dot{\alpha}$) which satisfactorily approximates the desired trim state. Because of the initial accuracy of the trim setting provided by the ACPS logic (here, zero deflection), this temporary attitude error is small and quite acceptable. Also, it should be recognized that the integrator trim logic will cut short this type of operation once the dynamic pressure exceeds $\bar{q}_1^*$, so that this small error is also short-lived.

As was noted above, the oscillations seen in the bank and sideslip histories of Figure 7-9 are of particular interest since they are so distinct from the previous traces obtained at low dynamic pressures. Clearly, the aerodynamic effects are becoming more noticeable at this point in the flight envelope, and it is appropriate to see how well this observed behavior correlates with that predicted by the simplified model developed in Chapter 4. With no control torque inputs (neither ACPS

285

nor ACSS), it may be recalled that the fundamental open-loop bank and sideslip dynamics can be specified in the following form[*]:

$$\ddot{\beta} + \omega_\beta^2 \beta = 0 \qquad \text{(a)}$$

$$K_\beta \beta + \ddot{\phi}_s = 0 \qquad \text{(b)} \qquad (7\text{-}6)$$

where the two parameters ω_β and K_β are defined by:

$$\omega_\beta^2 \equiv \left(\frac{\bar{q}Sb}{I_{zz}} \right) C'_{n_\beta} \qquad (4\text{-}50a)$$

$$K_\beta \equiv -\left(\frac{\bar{q}Sb}{I_{xx}} \right) C'_{\ell_\beta} \qquad (4\text{-}52a)$$

The above differential equations may be Laplace transformed to yield:

$$\beta(s) = \frac{s}{s^2 + \omega_\beta^2} \beta_0 + \frac{1}{s^2 + \omega_\beta^2} \dot{\beta}_0 \qquad \text{(a)}$$

$$(7\text{-}7)$$

$$\phi_s(s) = \frac{1}{s} \phi_0 + \frac{1}{s^2} \dot{\phi}_0 - \frac{K_\beta}{s^2} \beta(s) \qquad \text{(b)}$$

where (β_0, ϕ_0) and $(\dot{\beta}_0, \dot{\phi}_0)$ are the attitudes and rates at the beginning of the time interval of interest. By retransforming into the time domain, the bank and sideslip histories can be expressed in the following manner:

$$\beta(t) = A_\beta \cos(\omega_\beta t + \psi) \qquad \text{(a)}$$

$$(7\text{-}8)$$

$$\phi(t) = A_\phi \cos(\omega_\beta t + \psi) + c_1 t + c_0 \qquad \text{(b)}$$

where the parameters are defined by:

---

[*]See, for example, Figure 4-22.

$$A_\beta \equiv \left[\beta_0^2 + (\dot{\beta}_0/\omega_\beta)^2 \right]^{\frac{1}{2}} \qquad \text{(a)}$$

$$\psi \equiv \tan^{-1}(-\dot{\beta}_0/\omega_\beta \beta_0) \qquad \text{(b)}$$

$$A_\phi \equiv \frac{K_\beta}{\omega_\beta^2} A_\beta \qquad \text{(c)} \qquad \text{(7-9)}$$

$$c_1 \equiv (\dot{\phi}_0 - \frac{K_\beta}{\omega_\beta^2} \dot{\beta}_0) \qquad \text{(d)}$$

$$c_0 \equiv (\phi_0 - \frac{K_\beta}{\omega_\beta^2} \beta_0) \qquad \text{(e)}$$

Now, from (7-8a) it is clear that the simplified dynamic equations model sideslip as an undamped oscillator, in strong agreement with the history of Figure 7-9. The natural frequency observed in the simulation may be found from the first free oscillation after the yaw jet pulse, and is calculated to be:

$$\omega_\beta^{obs} = 2\pi/(t_2 - t_1) = 0.398 \text{ sec}^{-1} \qquad \text{(7-10a)}$$

whereas the natural frequency of (7-8a) may be calculated from the definition of (4-50a), the data base of Appendix B, and the dynamic pressure value occurring in the middle of the observation interval $(\bar{q} = 11.88 \text{ lbf/ft}^2)$, so that the following is obtained:

$$\omega_\beta^{pred} = 0.396 \text{ sec}^{-1} \qquad \text{(7-10b)}$$

clearly an excellent correlation with the observed oscillation frequency. In like manner, K_β may be cross-checked. From (7-8b) it is seen that the bank history should consist of a constant added to a linear time-varying term superimposed on a sinusoid identical in form to the side-slip history. This also is clearly in agreement with the bank history shown in Figure 7-9. From the parameter definitions given in (7-9), it

287

is seen that there are two means by which K_{β} can be readily calculated from observed quantities in the simulation histories:

$$(K_{\beta})_1^{obs} = \omega_{\beta}^2 (A_{\phi}/A_{\beta}) \qquad \text{(a)}$$

$$(K_{\beta})_2^{obs} = \frac{\omega_{\beta}^2}{\dot{\beta}_0} (\dot{\phi}_0 - c_1) \qquad \text{(b)}$$

(7-11)

As shown in the figure, the bank history can be approximately bounded by the two lines shown, so that half their vertical spacing specifies A_{ϕ}. With A_{β} directly measured from the sideslip history and the observed value of ω_{β}, use of (7-11a) yields:

$$(K_{\beta})_1^{obs} = 0.345 \text{ sec}^{-2} \qquad (7\text{-}12a)$$

The slope of the envelope lines is, of course, c_1 in (7-8b); measured from the figure, $c_1 = -0.0280°/\text{sec}$. Choosing the initial time to be t_3 as shown, then $(\dot{\beta}_0, \dot{\phi}_0) = (0.125°, 0.0°)$, so that use of (7-11b) yields:

$$(K_{\beta})_2^{obs} = 0.355 \text{ sec}^{-2} \qquad (7\text{-}12b)$$

which is in fairly close agreement with the value above. Now, the predicted sideslip coupling constant can be computed from (4-52a), the data base of Appendix B, and the dynamic pressure level at t_3 ($\overline{q} = 12.52 \text{ lbf/ft}^2$), to yield the following:

$$K_{\beta}^{pred} = 0.351 \text{ sec}^{-2} \qquad (7\text{-}12c)$$

again in excellent agreement with the observed dynamics. Thus the lateral dynamic model of Chapter 4 provides an accurate prediction of vehicle behavior, at least for this dynamic pressure regime and small magnitude attitude rates and errors. It has been found from studies similar to those above and conducted at other flight regimes later in the entry that the simplified model provides a very accurate prediction of

the open-loop dynamics. Such studies will not be presented here, but model verification will follow implicitly by the demonstrated successful working of the control system upon which it is based. Specific discussion of model validity will be resumed in the description of simulation runs conducted very late in the entry.

The results of a second simulation illustrating elevator turn-on are shown in Figures 7-10a and b. The initial flight conditions are the same as in the previously described run (h_0 = 272,000 ft, $\mathcal{M}_0$ = 29.5, $\bar{q}_0$ = 7.5 lbf/ft^2), but here the vehicle is in the midst of a bank maneuver when the elevator is used for the first time for transient control. What is occurring here can be briefly stated as follows. At t = 4 seconds the guidance commands a bank reversal and the vehicle quickly generates (via the yaw jets) a maneuver rate to satisfy the command. As in the previous runs, the pitch jets must supply a negative torque to counteract the induced pitch disturbance acceleration, causing the elevator to trim down to a setting of 0.7°. In the middle of the bank maneuver, at t = 17.9 seconds, the dynamic pressure exceeds the elevator mode switch threshold ($\bar{q}_1$ = 10 lbf/ft^2) and the elevator is used for transient control for the first time. As with the previous simulation, the blending logic limits the allowable elevator excursions, and with the 2-second update rate for dynamic pressure, the elevator trace exhibits the previously encountered stairstep behavior. Still during the bank maneuver, the linear logic eventually "catches" the longitudinal dynamics (at t $\approx$ 25 seconds) and maintains the desired small attitude errors without further limiting by the blending logic. Two points are worth noting: first, there is no evidence of any elevator/pitch jet interaction during this automatic changeover to elevator control; and second, no pitch jet firings are issued after entering the transient elevator control mode. This behavior is, of course, due to the fact that the blending logic provides a measure of elevator effectiveness and inhibits jet firings accordingly; in this instance there was clearly sufficient elevator authority to maintain pitch attitude in the face of a bank rate induced disturbance acceleration.
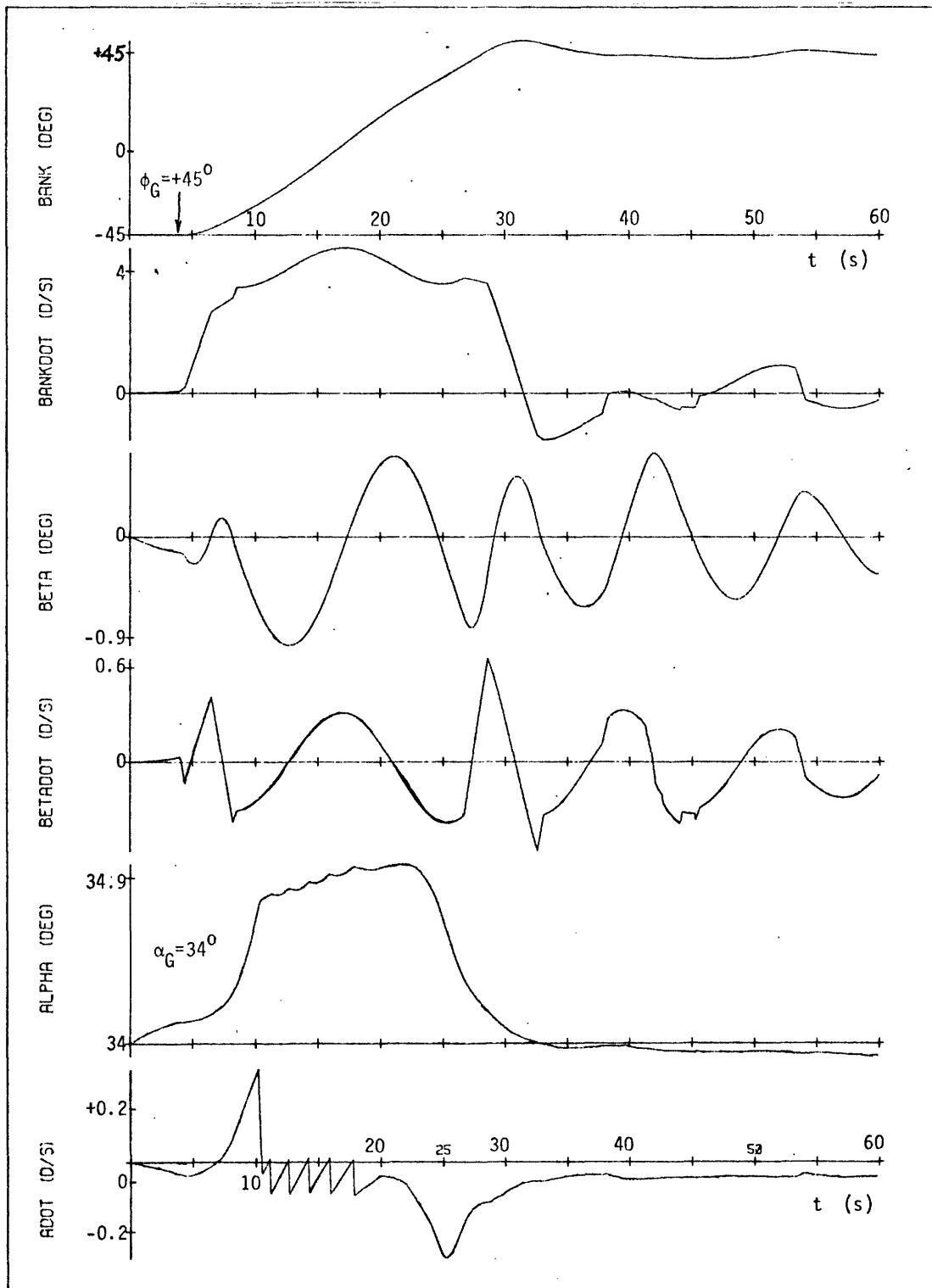
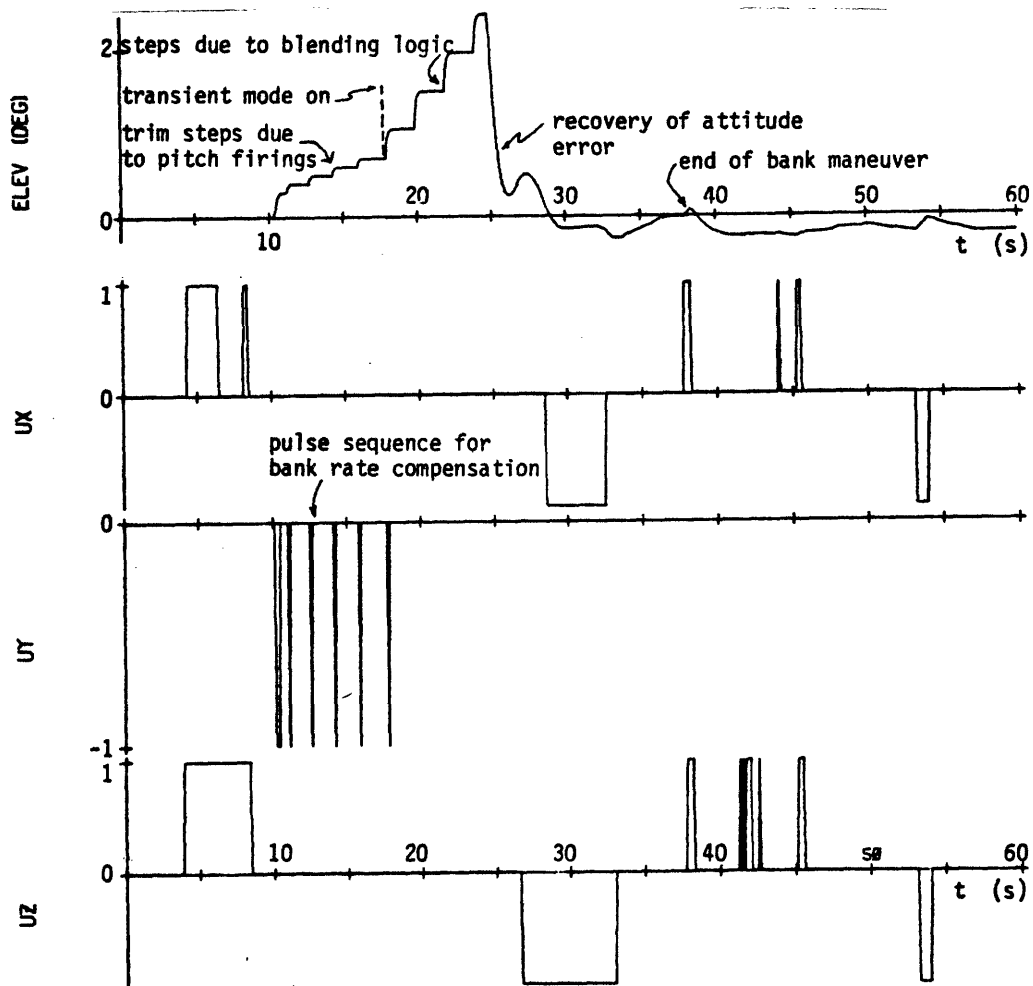Figure 7-10a. Elevator Turn-on During Bank Maneuver ($\bar{q}$=7.5→16.4).

290

Figure 7-10b. Elevator turn-on During
Bank Maneuver ($\bar{q}$=7.5 → 16.4).

7.2.1.4 Aileron Turn-on

The next two simulation runs illustrate the trend with increasing dynamic pressure of less reliance on the ACPS and greater utilization of the increasingly effective surface authority. As will be seen, the switchover is gradual and automatic, the entire process determined by the blending logic and the requirement for ACPS augmentation.

Shown in Figures 7-11a and b are time histories of a 90° bank reversal initiated at an altitude of 260,000 ft and a Mach number of 29.1; during the run the altitude drops only 4,000 ft, while the dynamic pressure grows from an initial value of 15.0 lbf/ft^2 to a final value of 17.6 lbf/ft^2. The salient features of the run can be summarized quite briefly:

1) The dynamic pressure is sufficiently high to preclude the necessity of pitch jet firings. Thus, during the bank maneuver, the elevator, whose history is shown in Figure 7-11b, is sufficiently effective to provide the entire pitch torque authority required to counteract the induced disturbance acceleration.

2) The lateral channel, however, is still controlled entirely by the roll and yaw jets, as seen from the control histories (aileron and rudder histories are not shown, since they remain at zero throughout the run). Because the dynamic pressure exceeds the 5 lbf/ft^2 mode switch level of the roll jet ACPS logic, the sideslip is controlled by simple rate damping, when the yaw jets are not firing. As it happens here, all of the roll jet firings occur simply to ensure coordinated bank maneuvers when the yaw jets are used to control bank; thus, the control over sideslip is relatively loose, taking advantage of the natural spring force provided by the dynamic derivative C'_{n_β}.

3) The large sideslip oscillation initiated by the bank maneuver shows up quite clearly in the bank rate trace (recall $\ddot{\phi}_s = -K_\beta \beta$), due to the increasing magnitude of the coupling constant K_β, here approximately 0.5 sec^{-2}. As will be seen, this effect becomes very prominent in the next two simulation runs to be discussed.
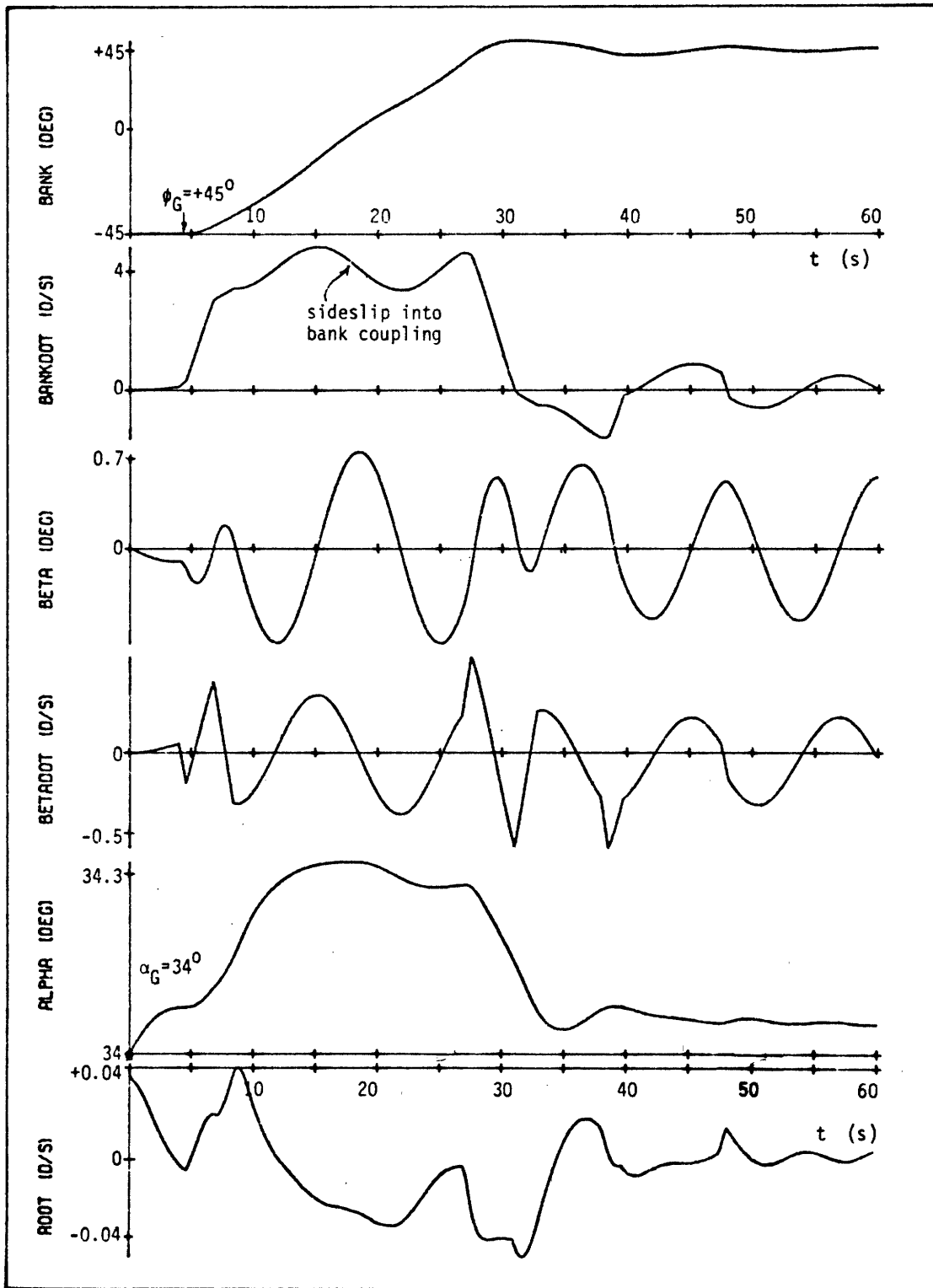
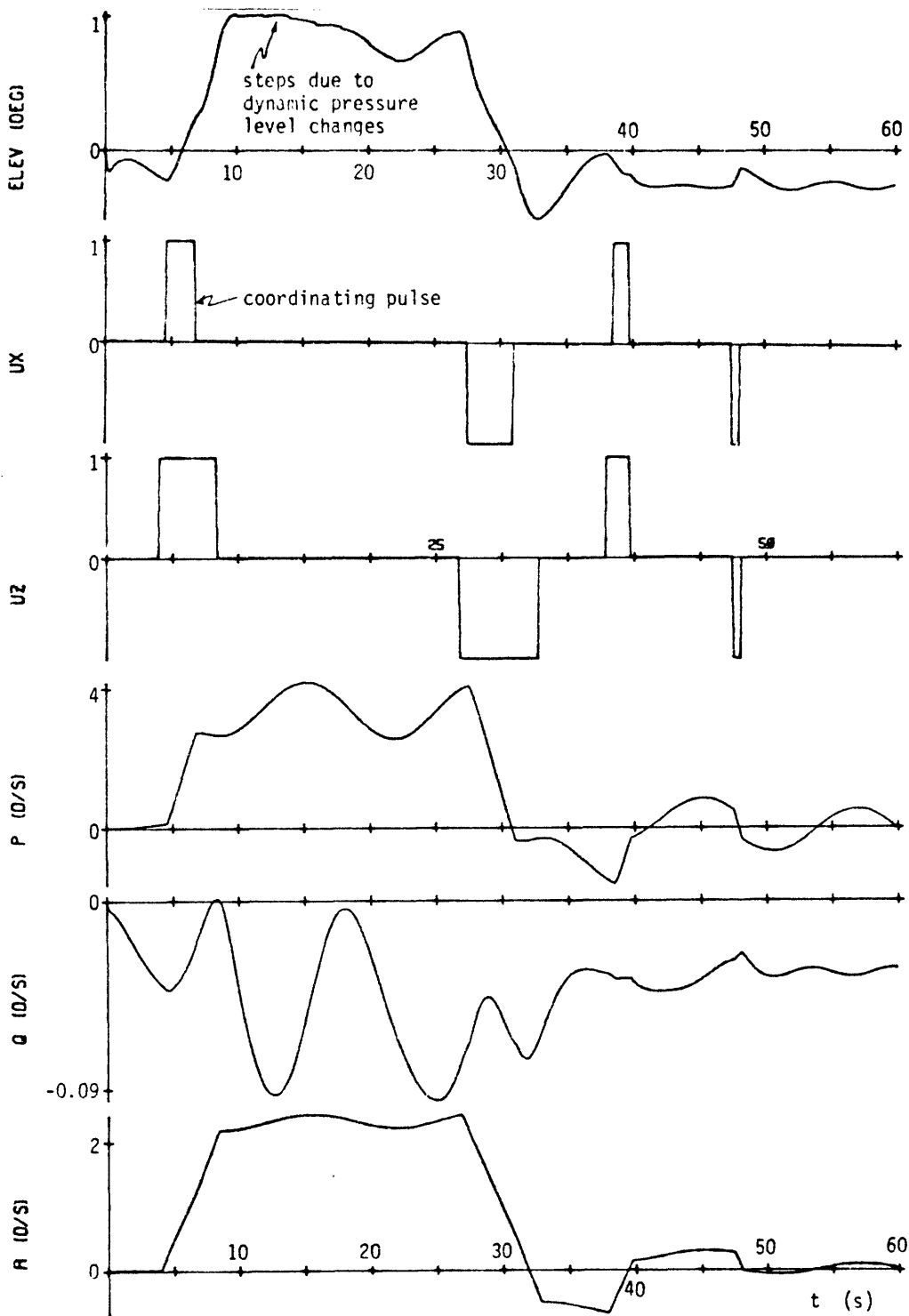Figure 7-11a. Step Response to ϕ_G ($\bar{q}$=15.0 →17.6).

Figure 7-11b. Step Response to ϕ_G ($\bar{q}$=15.0 → 17.6).

4) The effect of the two-second update frequency of dynamic pressure can be seen in the elevator trace during the 20-second time interval of the maneuver. The slight changes in dynamic pressure levels propagate through the system via the gain multipliers, resulting in very small but discernable steps in the elevator deflection history.

The time histories for the second simulation run in this set are shown in Figures 7-12a and b, where a -45° to -90° bank maneuver is accomplished, while the dynamic pressure increases from a level of 25.0 lbf/ft^2 to one of 30.1 lbf/ft^2. Here, the initial altitude is 247,000 ft at a Mach number of 26.8; during the run, the altitude drops 5,000 ft. As in the previous runs, the bank maneuver is initiated by the yaw jet pulse shown, but because the dynamic pressure exceeds the threshold level for transient aileron control ($\bar{q}_2$ = 20 lbf/ft^2), the aileron is simultaneously deflected to provide an appropriate control torque. A detailed description of how aileron control is used to actually perform a bank maneuver will be given in a simulation description below; the important features to note here are the following:

1) Because of the relatively low dynamic pressure, the transient control gains for the aileron channel are large, and the aileron deflection to the bank command rapidly limits against the maximum deflection level specified by the lateral blending logic (see Figure 7-12b). Upon reversal of the aileron deflection, a negative limit of approximately -11° is attained and held for a short period of time; thereafter the aileron works within its (blending logic imposed) deflection limits and successfully maneuvers the vehicle to the target attitude.

2) The familiar bang-coast-bang yaw jet history is no longer present, since the aileron is being utilized for control. The initial pulse is of course required, due to the finite response time of the aileron; its effect is to aid the aileron in generating a positive sideslip so as to bank the vehicle via the dynamic dihedral aerodynamic coupling (see discussion below).
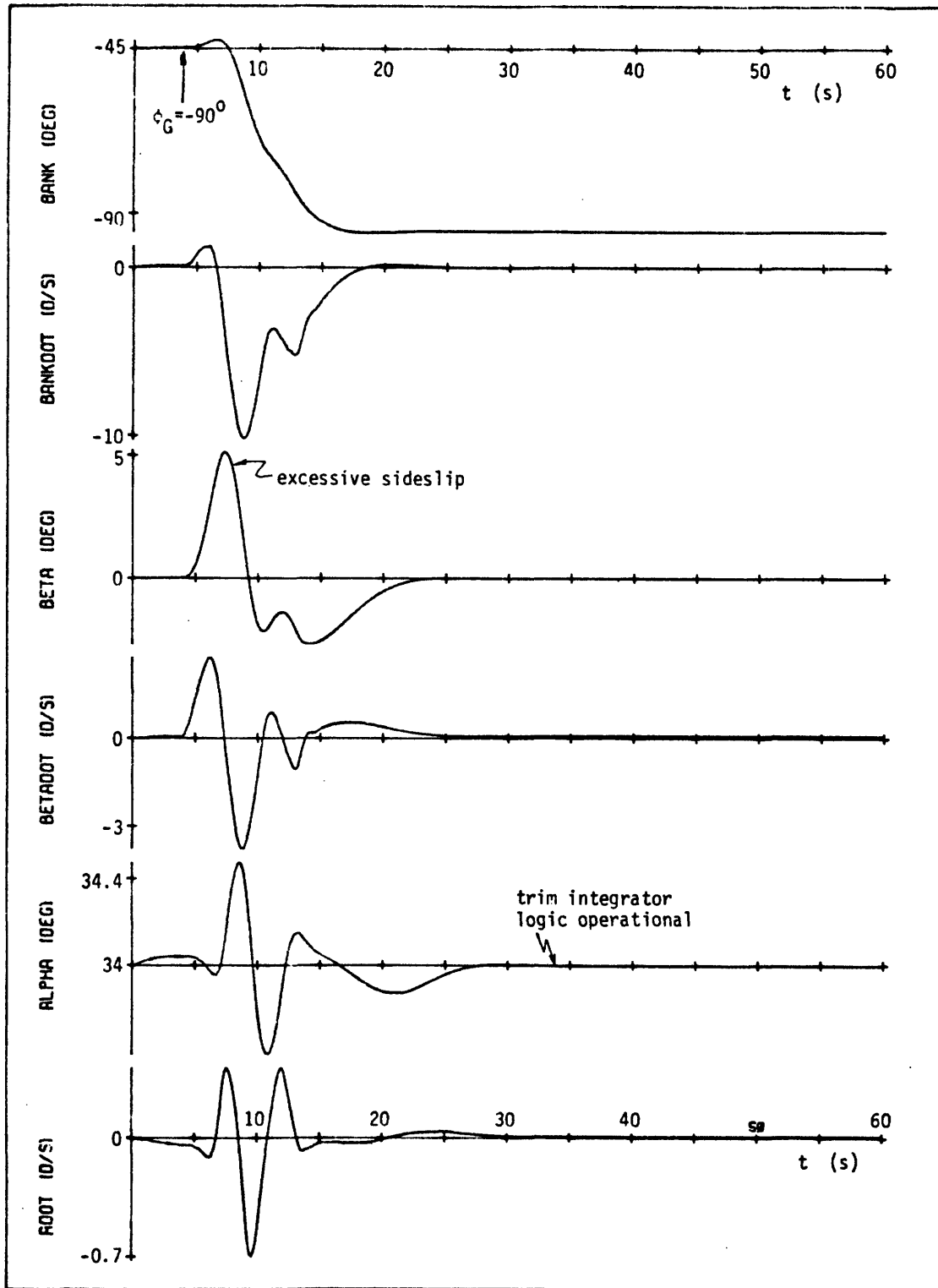
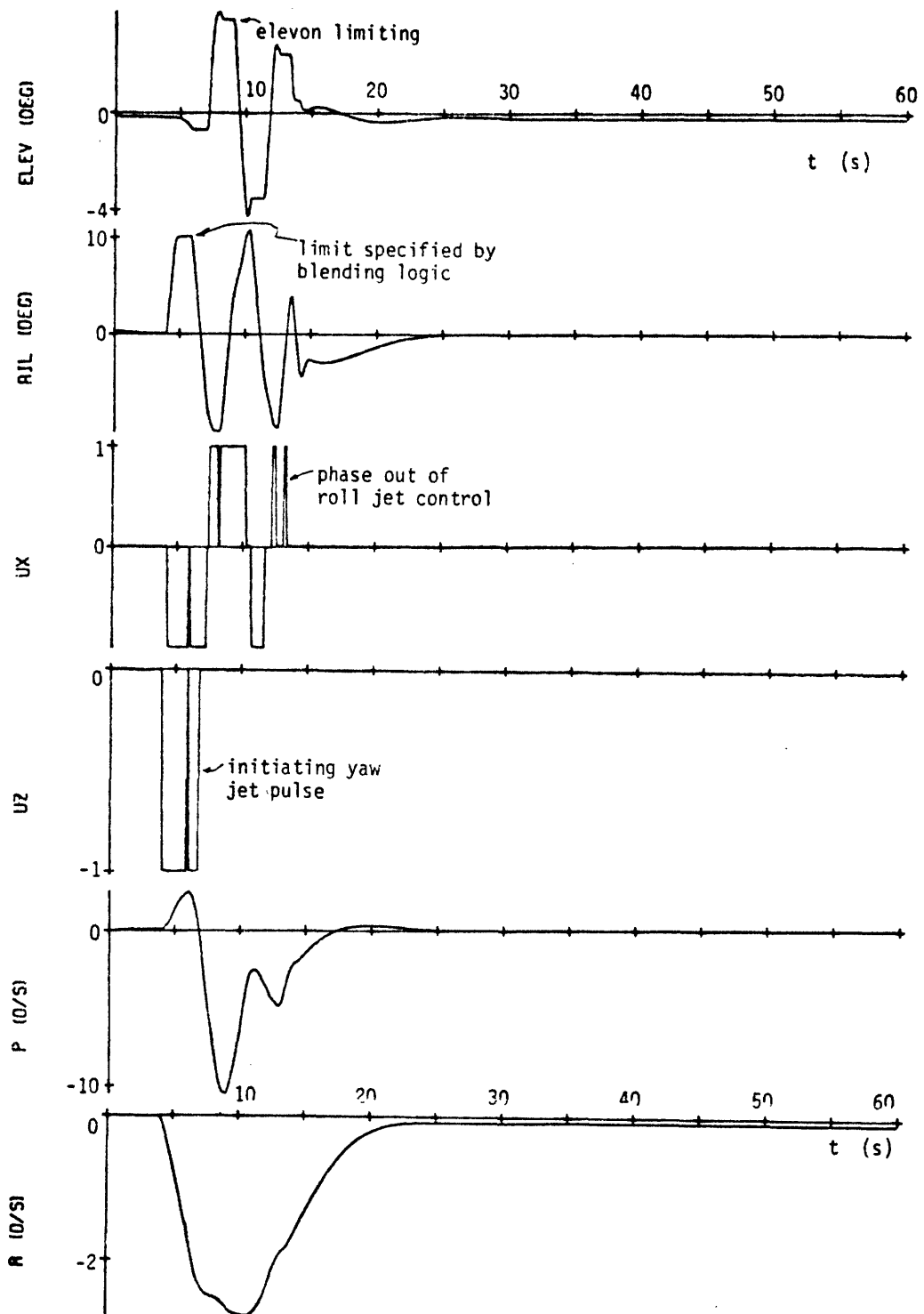Figure 7-12a. Step Response to ϕ_G ($\bar{q}$=25.0→29.9).

Figure 7-12b. Step Response to ϕ_G ($\bar{q}$=25 ⟶ 29.9).

3) Neither the bank rate nor the sideslip is particularly well-behaved during this maneuver, the former because of the evident "ripples" which result in a non-ideal bank step response, and the latter because of the maximum sideslip incurred during the bank rate build-up. Corrections to this behavior are presently under consideration; it suffices to note here that the response is both acceptable and amenable to improvement.

4) The elevator history shown is a natural response to the high bank rates generated by the lateral logic; the limiting apparent in the history is due to the fact that the elevons are shared by both the longitudinal and lateral channels, and, in this case, the aileron command is relatively large ($\delta_a \approx -11°$ at $t \approx 7.5$ sec). Review of the discussion given in Section 5.4.2.1 will show that the right elevon is position limited at $t \approx 7.5$ sec, giving rise to the short period of steady-state elevator occurring at that time. A second point to note here is that the linear trim integrator in the elevator logic is operational at this point (since $\bar{q} > \bar{q}_1^* = 20$ lbf/ft^2), so that the trim angle-of-attack is readily maintained by the proper trim elevator setting (compare this with the slight trim discrepancy of the previous run).

7.2.1.5 Early Entry Mode Switching

A relatively smooth transition from all ACPS to all ACSS control is clearly evident in the simulation histories of runs conducted at gradually increasing levels of dynamic pressure as the entry progresses. This behavior has already been discussed completely for the longitudinal channel; lateral channel operation is similar, although staggered in time, due to the differing surface effectiveness. It is appropriate at this point to review some of the basic operational features of this transition, by way of discussion of a simulation conducted over a relatively long time span during the early entry portion of the mission. Shown in Figures 7-13a and b are time histories of a simulation of attitude hold operation ($\phi_G = -90°$, $\alpha_G = 34°$) initiated at a dynamic pressure of 0.5 lbf/ft^2, and altitude of 320,000 ft, and a Mach number of 27.9.

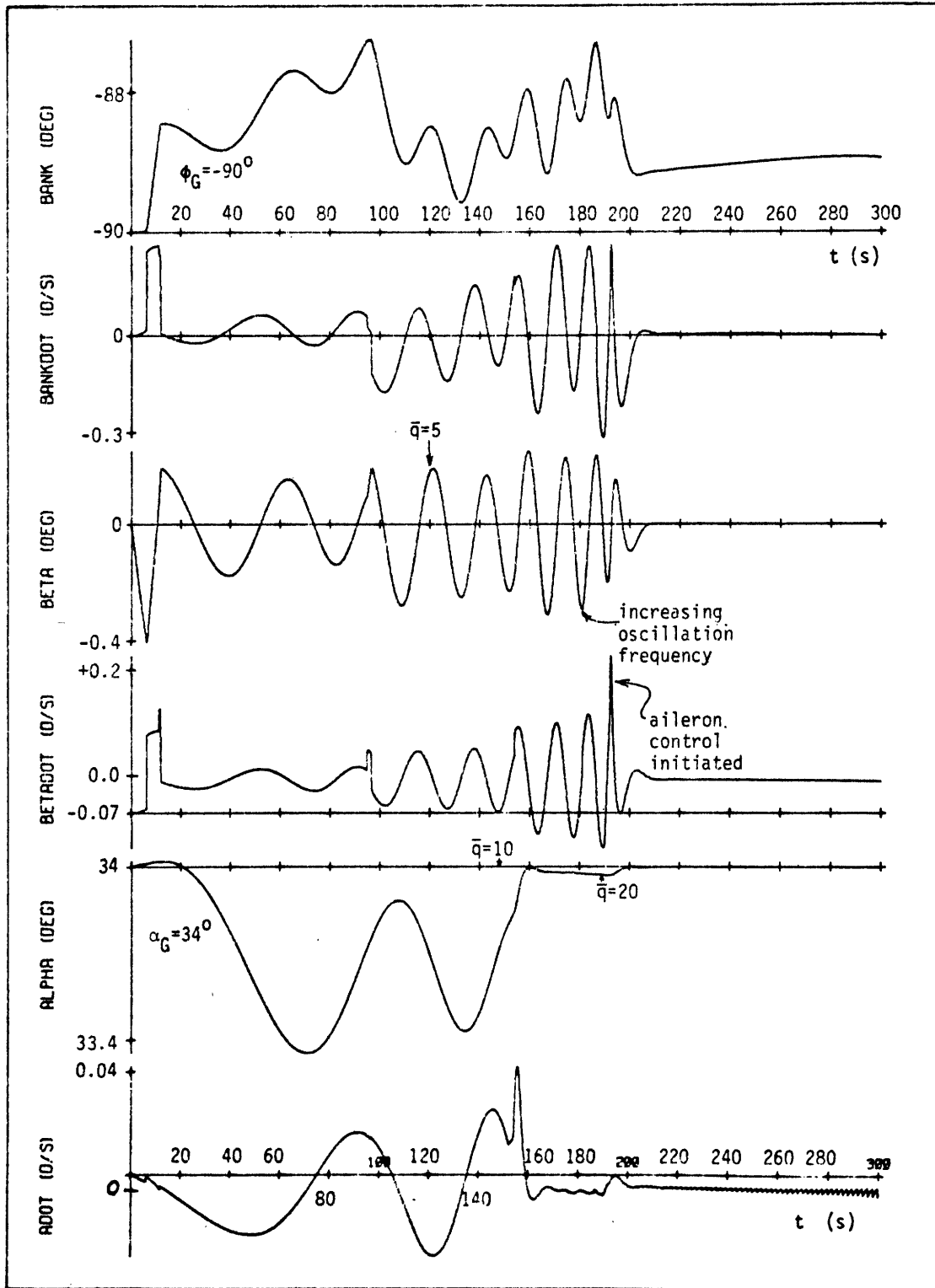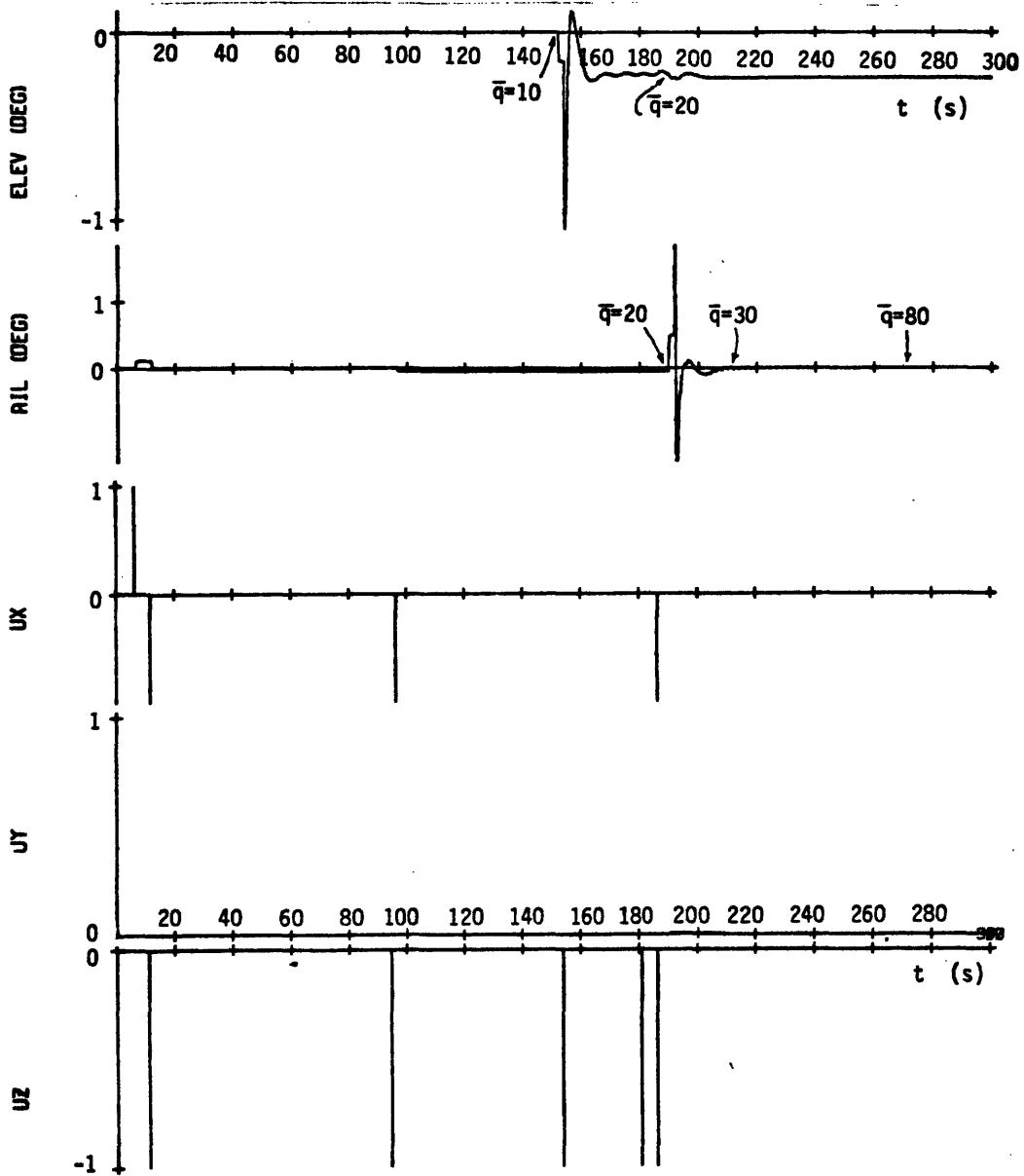Figure 7-13a. Attitude Hold during mode switching ($\bar{q}$ = 0.5÷128).

Figure 7-13b. Attitude Hold Operation During
Mode Switching ($\bar{q}$=0.5 → 128).

During the 300-second run, the altitude drops to 205,000 ft, the Mach number lowers to 23.3, and the dynamic pressure increases to 128 lbf/ft^2, thus clearly establishing the vehicle in a high dynamic pressure flight regime by the end of the run. As can be seen from the traces, the attitude hold performance requirements of Chapter 2 are well-satisfied throughout the run; the total ACPS fuel use amounted to 8.4 lbm. Several points regarding this run should be noted:

1. Because of the initial trim conditions, and the non-zero dynamic pressure levels during the first half of the simulation, no pitch jets are fired. As was done earlier for the lateral dynamics, the oscillatory behavior of the angle-of-attack can be quite readily predicted by the simplified vehicle model natural frequency, ω_α. It is, of course, this longitudinal spring force (proportional to C_{M_α} and $\bar{q}$) which maintains the angle-of-attack near the commanded value, and thus inside the pitch ACPS phase-plane deadband.

2. Elevator turn-on occurs at approximately t = 150 sec, when the dynamic pressure exceeds the 10 lbf/ft^2 threshold level. The observed one-degree transient is sufficient to null the longitudinal channel residual errors allowed by the ACPS logic, so that within 15 seconds, the elevator is quite close to its desired trim value. Note that the dynamic pressure does not reach 20 lbf/ft^2 until t $\approx$ 190 sec, so that the elevator must work about the zero trim setting determined by the early elevator trim logic. The resultant attitude error (for the time interval during which $10 \leq \bar{q} \leq 20$) is quickly cancelled out, however, once the second threshold is reached ($\bar{q} \geq \bar{q}_1^* = 20$), and the linear trim integrator logic is exercised.

3. In the lateral channel, the effect of dynamic pressure growth shows up quite clearly in the increased sideslip oscillation frequency; this stability, of course, allows for the successful application of roll jet rate damping control of sideslip, once the dynamic pressure is large enough ($\bar{q} \geq \bar{q}_3 = 5$ lbf/ft^2 at t $\approx$ 115 sec). As described earlier, the sideslip oscillations show up in the bank history, and become more

301

prominent as the dynamic pressure increases and the coupling parameter, K_β, grows accordingly. A few yaw jet pulses, however, readily maintain bank attitude near the commanded value.

4. Aileron turn-on occurs at approximately $t \approx 190$, when the dynamic pressure exceeds the 20 lbf/ft^2 threshold level. As with the elevator, a transient deflection of a few degrees (limited by the lateral blending logic) rapidly damps out as the aileron takes over the lateral attitude hold function. Note that the oscillations tolerated by the ACPS logic rapidly damp out, as the aileron maintains linear control over the state variables, and inhibits any further jet firings. Although no further activity is shown in the aileron history, two other additional dynamic pressure switch points are passed through during the run: one at $t \approx$ 215 sec when the dynamic pressure exceeds 30 lbf/ft^2, allowing full aileron authority, and one at $t \approx 270$ seconds, when the dynamic pressure exceeds 80 lbf/ft^2, allowing a maneuver mode switch capability.

7.2.1.6 Maneuvering during Mid-Entry

To examine the effect of this maneuver logic (recall Section 5.2.2.2.2) on the vehicle's bank response, the next two simulations to be discussed will show vehicle response with and without the maneuver rate coding exercised.

Figures 7-14a and b are from a simulated maneuver conducted later in the entry than all of the above-described maneuver histories; here, a bank reversal is executed at an initial altitude of 206,000 ft, a Mach number of 18.2 and a velocity (earth-relative) of approximately 18,800 ft/sec. Because of the lift force acting on the vehicle during the maneuver, the vehicle's altitude is only 1000 ft lower at the end of the 60-second interval illustrated; the velocity, however, decreases to 17,600 ft/sec. The net effect is a decrease in the dynamic pressure in the course of the run, from an initial value of 75 lbf/ft^2 to a final value of 68 lbf/ft^2, with a peak value encountered at approximately $t = 16$ sec, where a 78 lbf/ft^2 level was reached. The point to note is that throughout
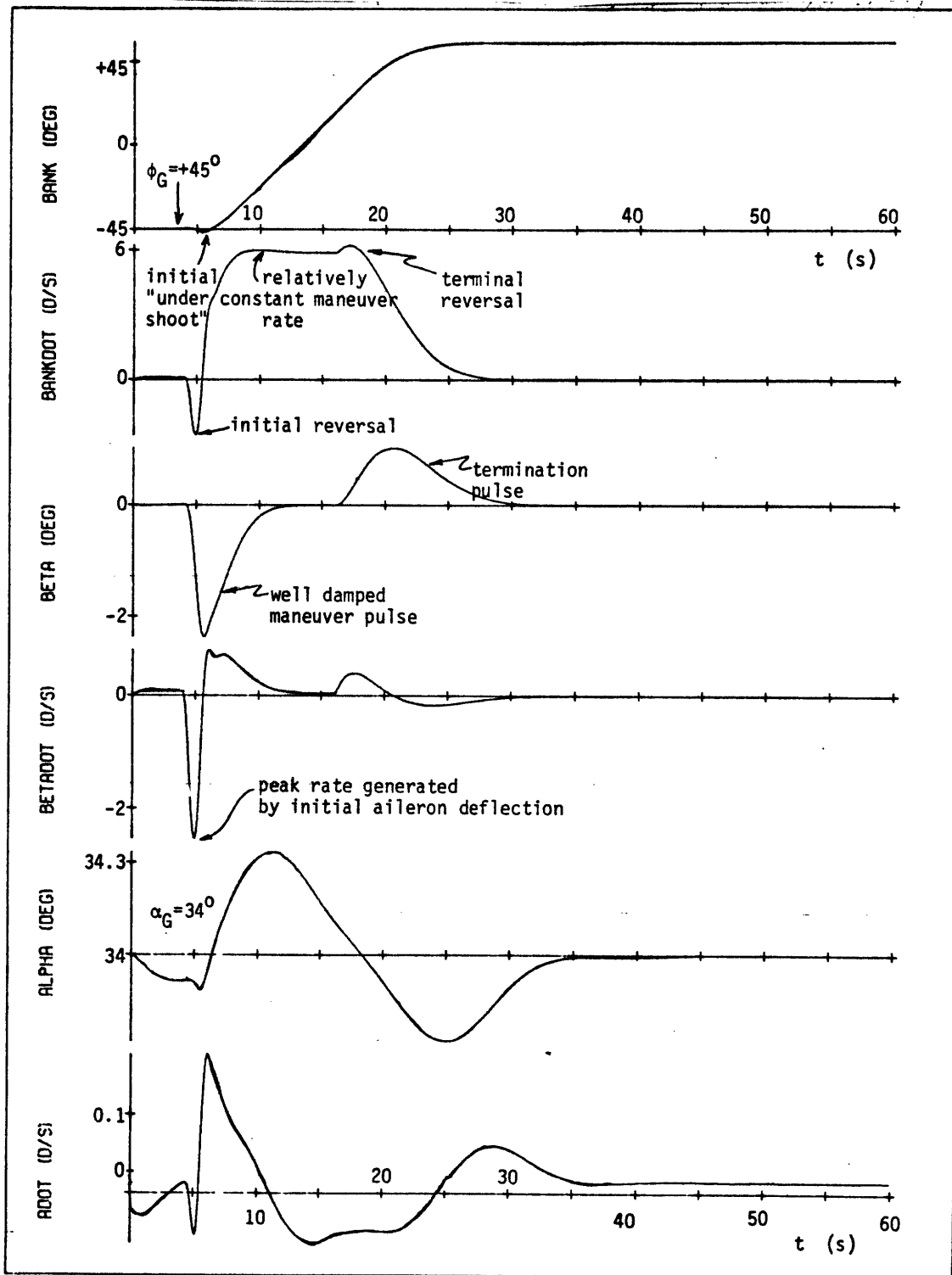
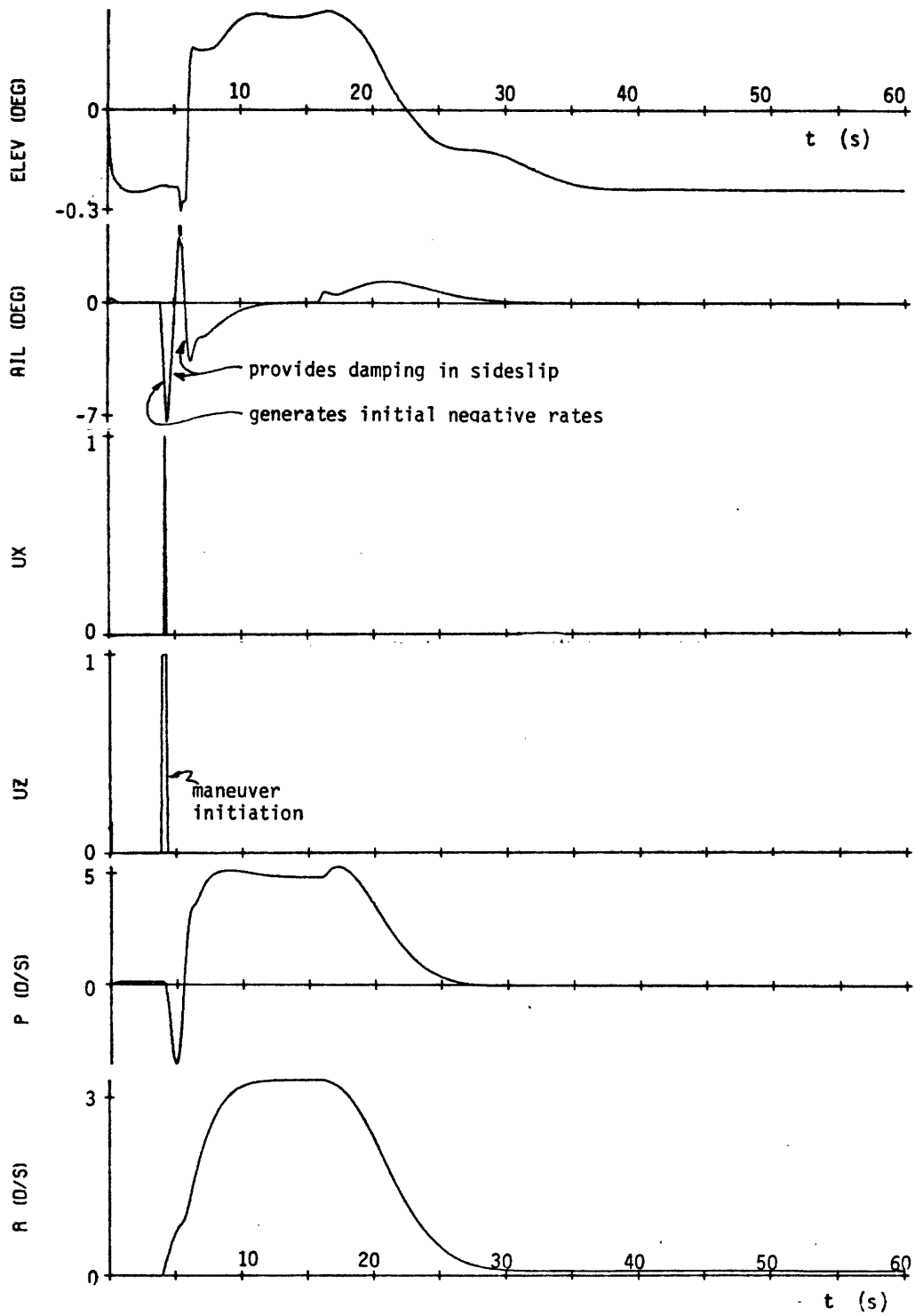Figure 7-14a. Bank Maneuver with Attitude Control Loop ($\bar{q}$=75 $\rightarrow$ 68).

303

Figure 7-14b. Bank Maneuver with Attitude
Control Loop ($\bar{q}$=75 → 68).

the run the dynamic pressure never reaches the 80 lbf/ft^2 mode switch threshold (= $\bar{q}_3^*$) which allows for maneuver rate control of the bank angle.

As in the previous cases, the bank maneuver is initiated at t = 4 sec, by a positive yaw jet pulse, and a short coordinating roll jet pulse (see Figure 7-14b); because of the dynamic pressure regime, the aileron is also used, in parallel with the ACPS pulses. What is important to note is that, unlike conventional control in a positive bank situation, the aileron is quickly driven in a negative direction, by the attitude control loop of the lateral logic. This of course results in a negative sideslip rate and a negative bank rate as shown in the histories, eventually peaking at the maximum negative values 0.9 second after the start of the maneuver. Prior to this point, however, the aileron reverses direction (at t = 4.5 sec), with the primary result of damping out the sideslip rate. The net effect of the initial aileron activity, then, is the generation of a well-damped negative sideslip "pulse", with a side effect of an initially misdirected bank rate. It is at this point that the vehicle's dihedral comes into play, since the negative sideslip buildup results in a strong positive bank torque (recall $\ddot{\phi}_s$ = $-K_\beta \beta$, where $K_\beta > 0$), thus reversing the initially induced bank rate and providing for a quick acceleration to a well-maintained bank maneuver rate as shown in the history. This maneuver rate, generated by the attitude control loop of the transient aileron control logic, is approximately $4.8°/sec$, and is held until the bank attitude begins to approach the guidance commanded target attitude, at which point a reverse sequence takes place: the aileron is deflected positively giving rise to a positive sideslip pulse, which, in turn, provides negative bank acceleration, thus nulling the maneuver rate. Although not as dramatic as the maneuver initiation, the maneuver termination is also characterized by a bank rate reversal (i.e., a more positive rate) prior to the gradual reduction of the maneuver rate. As can be seen, the entire sequence is quite well-behaved, with two well-damped sideslip maneuvers providing for a very smooth bank attitude history.

The type of vehicle response seen in the histories is of course clearly supported by the simplified lateral model used in the design synthesis of Chapter 5. For example, the bank dynamics may be recalled from (5-44) of Section 5.2.2.1:

$$K_\beta \beta + \ddot{\phi}_s = K_{\phi \delta_a} \delta_a \qquad (7\text{-}13)$$

As shown in the bank rate trace, the bank acceleration is zero at $t = 4.9$ sec, so that this relation may be solved for $K_{\phi \delta_a}$ in the following manner:

$$K_{\phi \delta_a} = K_\beta \frac{\beta(4.9)}{\delta_a(4.9)} \qquad (7\text{-}14)$$

where, from the simulation histories, the sideslip at $t = 4.9$ sec is $-1.09°$ and the aileron deflection is $-2.63°$. Using methods similar to those used earlier in the verification of the model parameters, the coupling parameter K_β is found to have a value of 2.13 sec^{-2}. Thus, the observed aileron effectiveness in bank is found from the above relation to be:

$$K_{\phi \delta_a}^{obs} = 0.884 \text{ sec}^{-2} \qquad (7\text{-}15a)$$

However, from the definition of this parameter in (4-52d),

$$K_{\phi \delta_a} \equiv \left(\frac{\bar{q} S b}{I_{xx}} \right) C'_{\ell \delta_a} \qquad (7\text{-}16)$$

so that substitution of the appropriate parameters yields a model predicted aileron effectiveness coefficient of:

$$K_{\phi \delta_a}^{pred} = 0.854 \text{ sec}^{-2} \qquad (7\text{-}15b)$$

clearly in close agreement with the observed effectiveness. This
type of model verification can be used for the other model parameters
with similar results: the predicted values all correlate very closely
with the observed or inferred values, lending support to the general
applicability of the model throughout the entry flight regime.

Two additional points regarding this simulation run should be
noted. It may be recalled in the design development of Section 5.1
that there was some concern for the possible deleterious effects of
surface rate limiting, based on the fact that the rate limits violate
the linearity of the controlled system. However, as can be seen in
figure 7-14b, the rate limiting evidenced in the initial portion of the
aileron trace appears to have little effect on the overall operation
of the control system. Clearly without the rate limiting, system
response would be faster; the induced lag however does not appear
to hinder the basic maneuver objectives. System sensitivity to a
lower actuator rate limit will be discussed in Section 7.3.3; it
suffices to note here that the nominal surface rates of $15^{\circ}/$sec
appear entirely adequate for vehicle control during the atmospheric
phase of the entry. The second point with regard to this run is that
the elevator logic performs quite well throughout the bank maneuver,
maintaining the angle-of-attack within a few tenths of a degree of
the commanded value. The simulation was deliberately initialized
in a mistrim, so that it was necessary for the elevator to seek its
own trim during the first five seconds of the run, and also after the
bank maneuver was completed. As will be seen, this is typical of the
simulations to follow.

The simulation histories shown in Figures 7-15a and b are
quite similar to those just described, with one major difference:
the bank maneuver rate is slightly in excess of $8^{\circ}/$sec. This dif-
ference is caused by the fact that this run begins later in the entry,
at an altitude of 200,000 ft, a Mach number of 17.3, and an initial
dynamic pressure of 85 lbf/ft^2. As before, the dynamic pressure

307

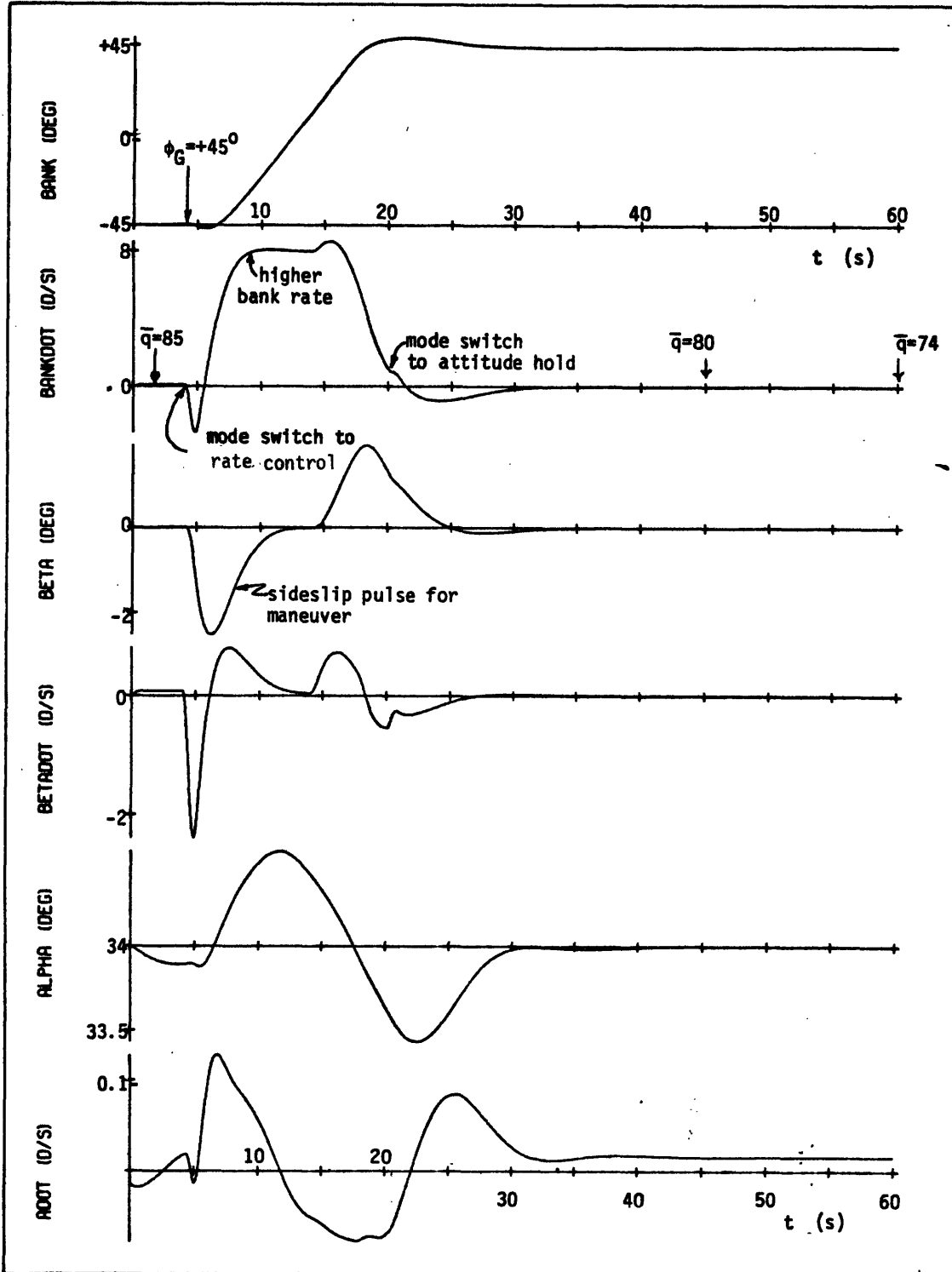Figure 7-15a. Bank Maneuver with Rate Control Loop
(q̄≈85→74)
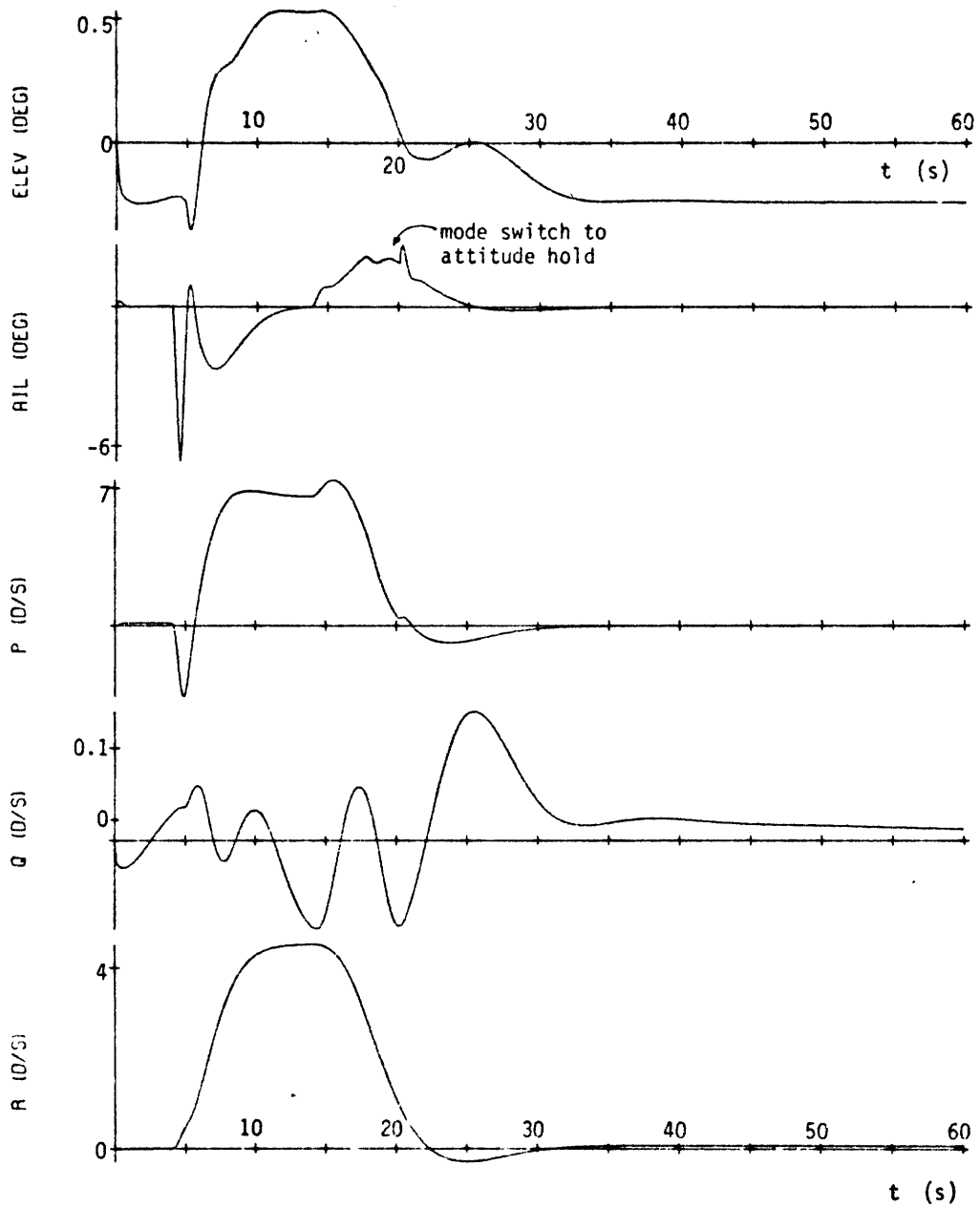
Figure 7-15b. Bank Maneuver with rate control loop ($\bar{q}$=85 →74).

decreases slightly during the 60-second interval shown, but the level remains above 80 lbf/ft^2 during the entire maneuver (t $\leq$ 40 seconds), thus allowing the use of the rate maneuver mode of the aileron control logic. Briefly, the sequence is as follows: 1) the bank angle command at t= 4 sec gives rise to a large attitude error; 2) since the dynamic pressure is greater than the mode switch value (= $\bar{q}_3^*$ = 80 lbf/ft^2), the aileron control logic temporarily terminates direct attitude control and simply attempts to drive the vehicle to a bank rate consistent with the desired target attitude (recall the logic of Figure 5-18); 3) this results in aileron, sideslip rate, and bank rate histories qualitatively similar to the previous run, except that a slightly larger sideslip is induced, resulting in more bank acceleration and a resultant bank rate higher than before; 4) the sideslip is damped out and the maneuver rate maintained until the target attitude is approached, at which time the reverse sequence occurs; 5) as the bank and bank rate approach the commanded value and zero, respectively, the maneuver logic is switched out, and the attitude hold loop completes the maneuver.

Thus, the maneuver logic considerably enhances vehicle response to large attitude maneuvers; its compatibility with the linear attitude hold loop is clearly illustrated by the relatively smooth switch between the two modes, as illustrated by the aileron history of Figure 7-15b. It is also appropriate to note that because of the slightly higher dynamic pressure levels encountered here, and because of less initial aileron activity, the blending logic completely inhibits any ACPS firing, in contrast to the small pulses exhibited in the previous run. Thus, the bank maneuver is performed entirely by the aileron, with no ACPS augmentation.

7.2.1.7 Pre-Transition Operation

Figures 7-16 through 7-18 illustrate histories of three simulated bank maneuvers conducted still further down the entry trajectory.
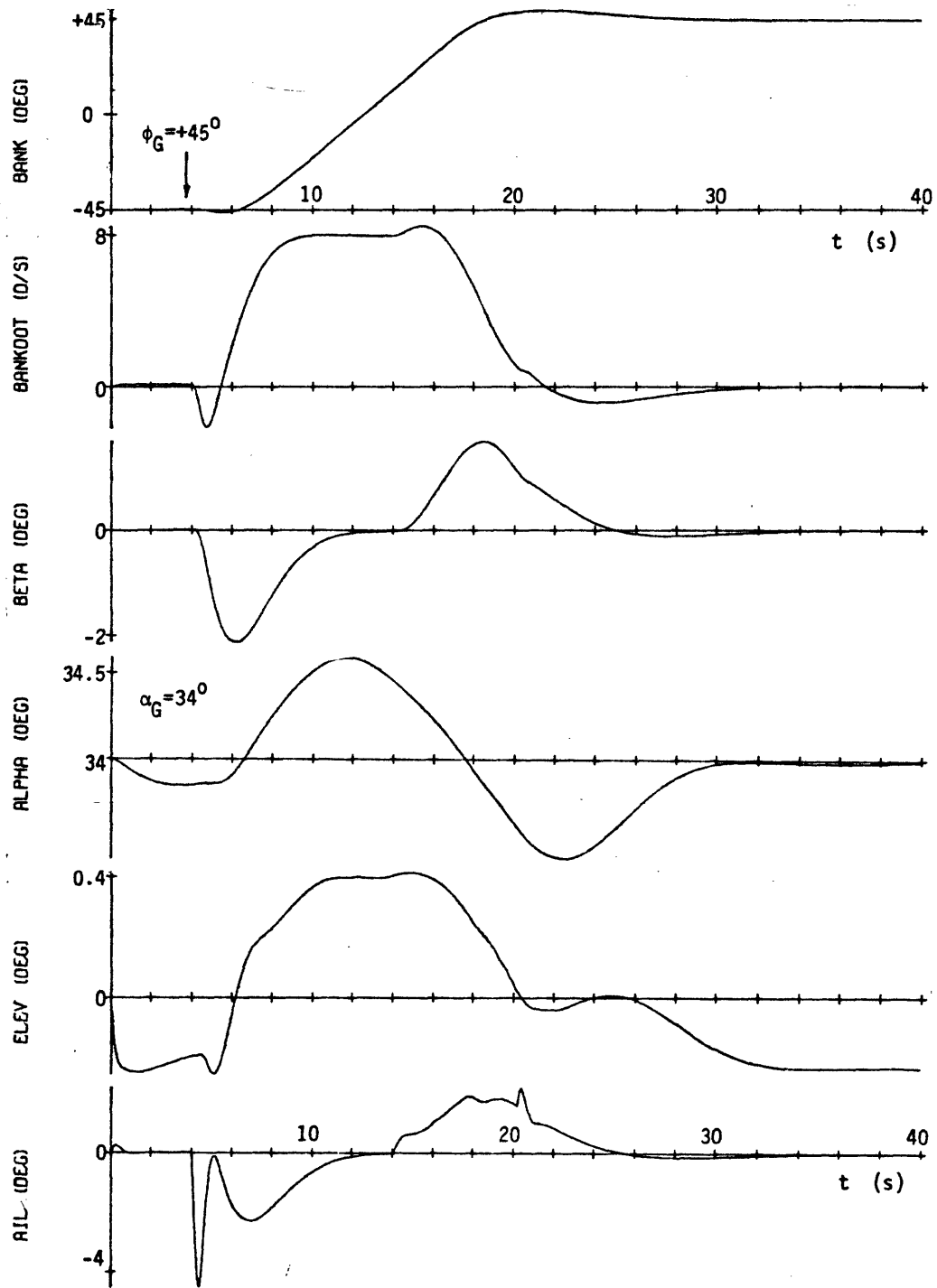
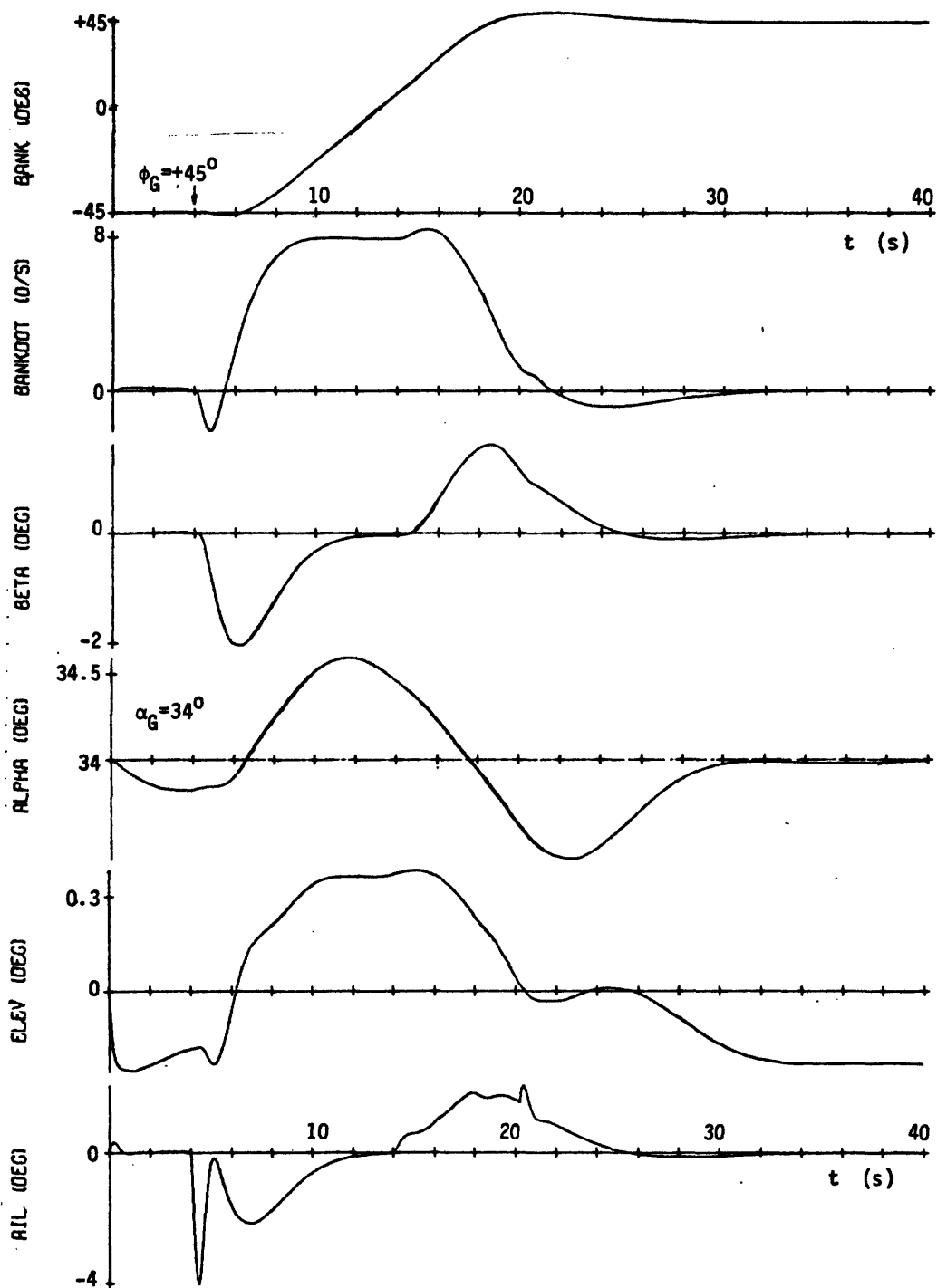Figure 7-16. Bank Maneuver at $m=15$ ($\bar{q}=102 \rightarrow 88$).

311

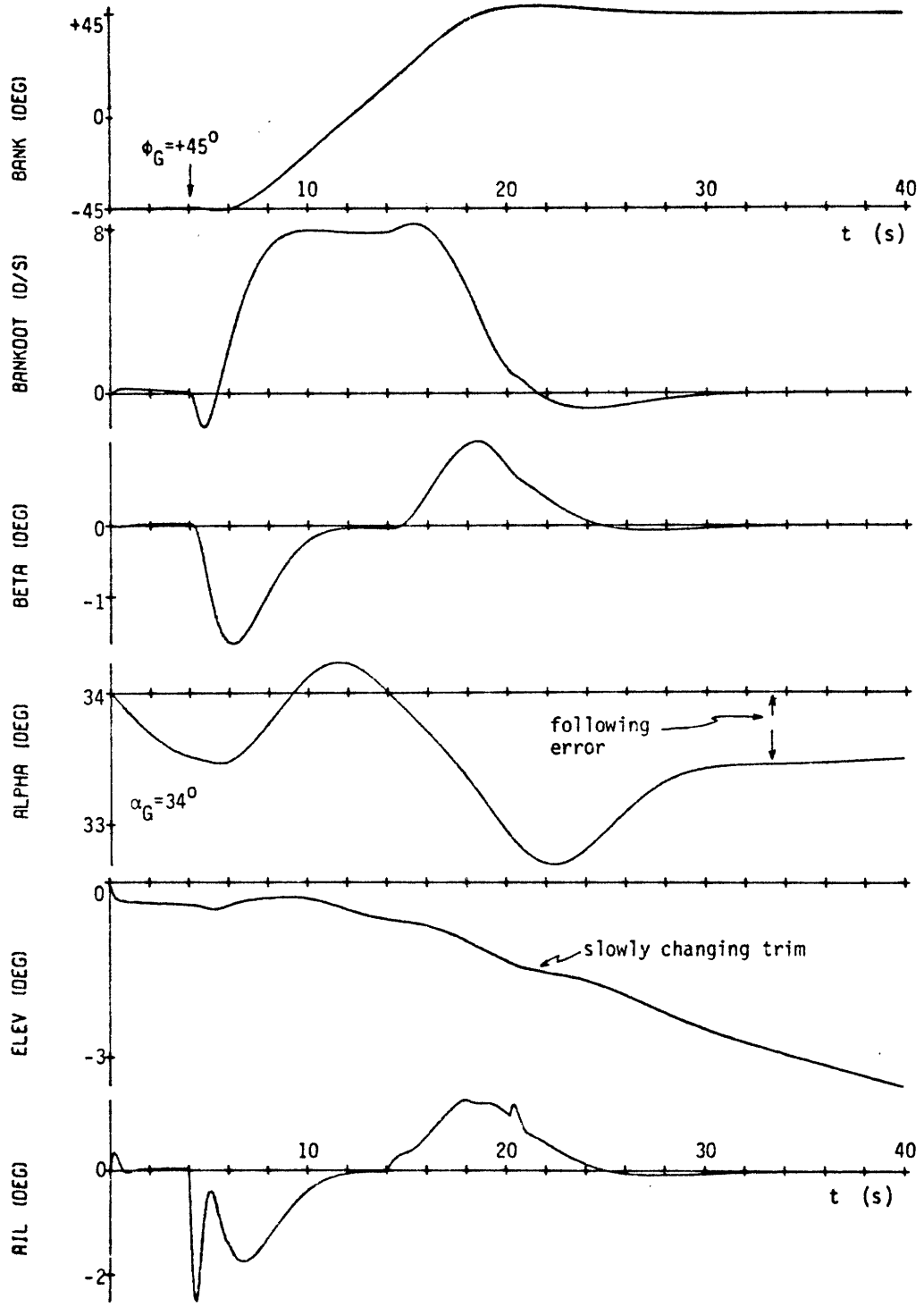Figure 7-17. Bank Maneuver at $\mathcal{M}$=12.5 ($\bar{q}$=108 →93).

Figure 7-18. Bank Maneuver at m=10 ($\bar{q}$=130 → 134).

As can be seen from Table 7-3, the dynamic pressures encountered are all relatively near 100 lbf/ft^2, the altitude change during each run is modest, and the Mach number range extends from 15 to 8.7. As in

Table 7-3: Trajectory Parameters for Three Simulated Bank Reversals

Figure	$\mathcal{M}_i$	$\mathcal{M}_f$	h_i(kft)	h_f(kft)	$\bar{q}_i$(lbf/ft^2)	$\bar{q}_f$(lbf/ft^2)
7-16	15.0	14.0	189	189	102	88
7-17	12.5	11.5	178	177	108	93
7-18	10.0	8.7	161	153	130	134

the run discussed previously, the vehicle is well into the atmospheric portion of the entry, and the three runs shown here depend entirely on aerodynamic surface control for the maneuver. By a comparison of the figures, it should also be clear that almost identical vehicle response is obtained in each case; the major difference is seen in the angle-of-attack history in the run initiated at Mach 10 (see Figure 7-18). In this case, the slowly changing Mach number results in a slowly changing pitch moment coefficient, which, in turn, results in a variable trim situation as the run progresses. The angle-of-attack offset seen in the figure is responsible for driving the trim integrator in the elevator logic, resulting in the monotonic up elevator history shown. This type of "following" error will continue as long as the pitch charactersitics of the vehicle continue to vary. The point to recognize, however, is that the bank maneuver remains relatively independent of this longitudinal behavior, so that all three runs exhibit very similar behavior in the lateral channel; this, of course, is not surprising, considering the similarity in dynamic pressure levels, and the fact that approximately the same trim angle-of-attack is maintained throughout the three simulations.[*]

[*] Recall that the aerodynamic coefficients are insensitive to changes in Mach number above (approximately) Mach 10.

Because the responses shown are typical of a large number of bank maneuvers conducted during the entry, it is appropriate to mention one facet of the aileron control logic which has not been covered in the previously described simulations: the validity of digital implementation of a control law derived for a continuous system application. Clearly, from the histories shown, the design synthesis is successful in its objective of attitude control; the basis for this must be that the continuous system design synthesis (i.e., s-plane pole placement) is a sufficiently accurate approximation to the actual sampled-data system dynamics involved. To see that this is so, it is only necessary to examine the longitudinal and lateral natural frequencies encountered during a run; for example, for the simulation illustrated by Figure 7-17, the model parameters can be calculated from their definitions in (4-34a) and (4-50a), so that:

$$\omega_\alpha \approx 0.51 \text{ sec}^{-1}$$

$$\omega_\beta \approx 1.19 \text{ sec}^{-1}$$

(7-16a)

The sampling frequency, however, is defined by the 0.10-second sample period, so that:

$$\omega_s = 2\pi/T = 62.8 \text{ sec}^{-1}$$

(7-16b)

clearly a much higher frequency than that encountered in the rigid-body dynamics. Thus, the lags introduced by the sample-and-hold operation of the digital program are insignificant, and loop design by continuous system analysis is quite appropriate here.

7.2.1.8 Operation Along Transition Profile

The remaining simulation runs to be discussed in this section illustrate controlled vehicle response along the "transition" portion of the entry trajectory; that is, during the latter portion of the entry

315

when the angle-of-attack is gradually lowered from its early entry value to a low level compatible with subsonic operation. Shown in Figure 7-19 is the nominal transition profile of Chapter 2, plotted in the Mach number/angle-of-attack plane; also shown is the sample trajectory from which were taken the initial flight conditions for the simulations to be described below (note that these initial conditions correspond with these shown in Figure 7-2, the altitude/velocity profile). The ranges of the test cases are indicated by the horizontal line segments, showing the commanded angle-of-attack and the Mach number span. The evident bias shown toward the "up" side of the nominal profile need not be of concern here, since this transition region is explored in more detail in the next subsection; the purpose of the runs discussed here is to illustrate typical operation of the controlled vehicle down into the late entry portion of the trajectory.

Figure 7-20 shows the history of a simulated bank maneuver initiated at an altitude of 143,000 ft, a Mach number of 8, and a dynamic pressure of 170 lbf/ft^2. As in some of the previous runs, the vehicle lift strongly affects the trajectory flown in this 40-second interval; in this case, the vehicle climbs 2,000 ft in altitude during the course of the run, so that with the lower velocity at the end of the run, the dynamic pressure drops to 107 lbf/ft^2. The point to recognize, however, is that the vehicle response is quite similar to the Mach 10 case just described: the bank maneuver is performed smoothly at approximately 8°/sec while the angle-of-attack history exhibits a following error due to the constantly changing pitch trim with the decreasing Mach number. This pitch trim behavior is, of course, induced by the attempt to maintain an artificially held constant angle-of-attack as the Mach number decreases; it should be clear from Figure 7-19 that this type of forced behavior would be mitigated by a more realistic constantly decreasing angle-of-attack profile. It should be noted that the major difference between this
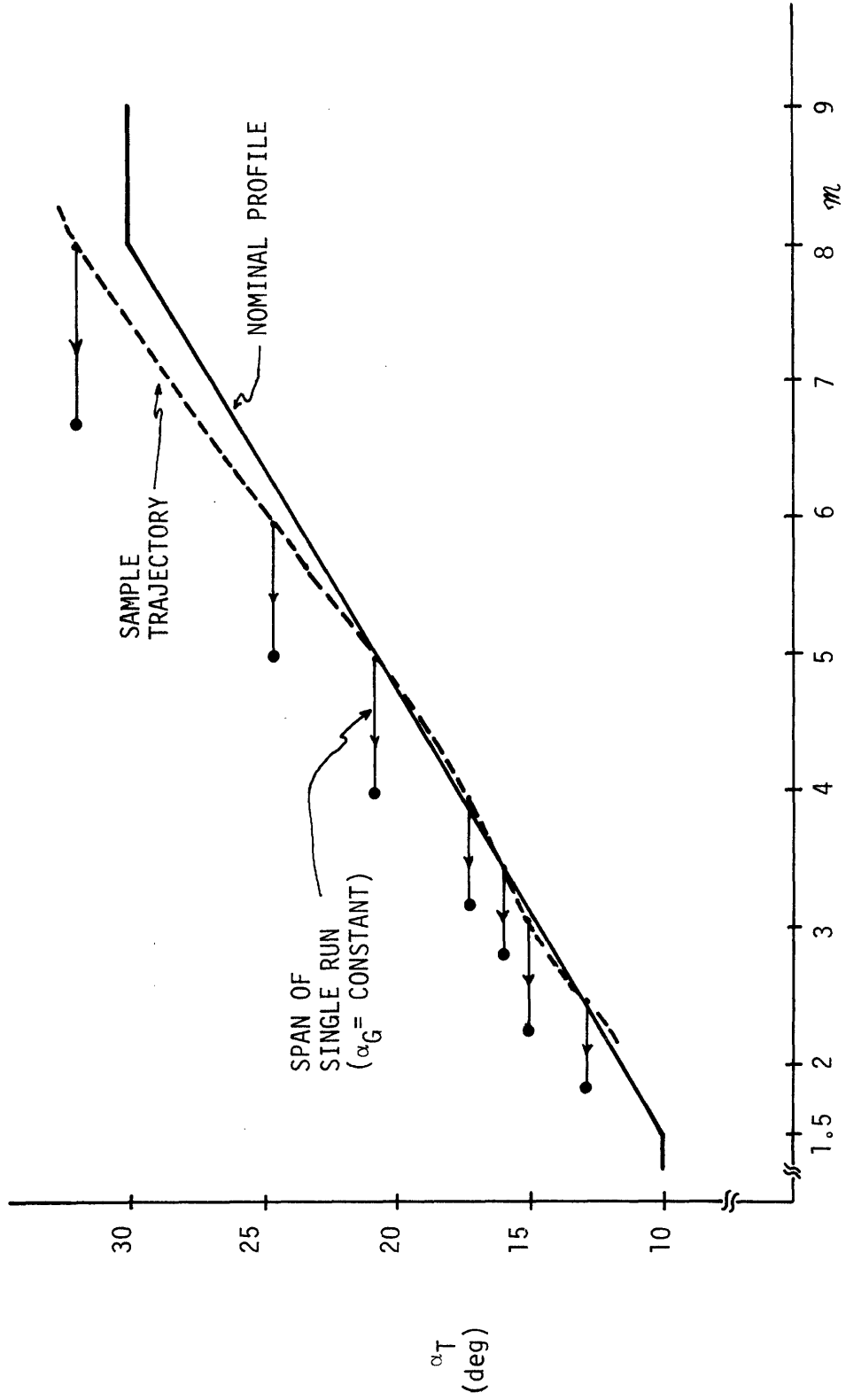
316

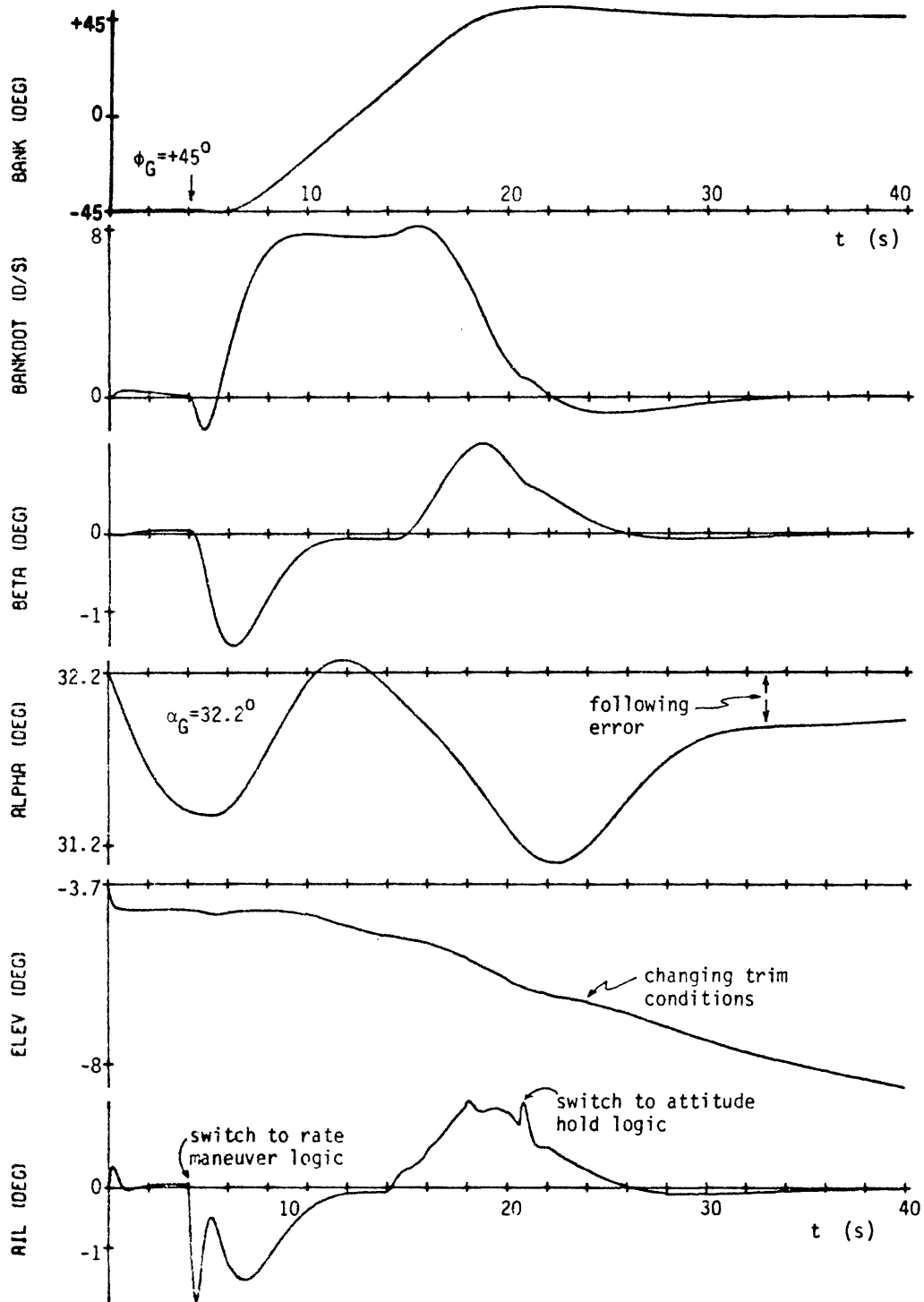Figure 7-19. Relation of Test Cases to Nominal Transition Profile.

Figure 7-20. Bank Maneuver at $\mathcal{M}=8$, $\alpha_G=32.2^o$ ($\bar{q}=170 \longrightarrow 107$).

run and the one conducted at Mach 10 is in the amplitudes of the aileron deflections and the sideslip pulses. The smaller peak amplitudes encountered here are due to both the higher dynamic pressure levels and the concommitant inverse scheduling of the aileron gains with respect to these higher levels (recall the $1/\bar{q}$ gains in the aileron control block diagram of Figure 6-7a). Thus, the bank response is maintained relatively independent of the dynamic pressures encountered, at least for this neighborhood of the flight envelope.

Shown in Figures 7-21a and b are histories from a similar maneuver conducted at an initial Mach number of 6 at an altitude of 125,000 ft; here the angle-of-attack is dropped $10°$ from the early entry value, held near the nominal transition value of approximately $25°$. It should be noted that this lower Mach number results in the activation of the rudder, in accordance with the threshold logic and constant crossfeed gain control already described in Section 5.2.2.3. Because of the low surface authority at these Mach numbers and angles-of-attack, the rudder is not particularly effective and thus the vehicle response is quite similar to the aileron-alone control of the previously described runs. The point to recognize from the surface histories, however, is that the rudder is used in a "cross-control" sense, in that it is not used in the conventional manner as a sideslip or yaw rate damper. Rather, it is used in the opposite sense, so as to deliberately miscoordinate the initial portion of the bank maneuver, thus aiding the aileron in its task of quickly building up a negative sideslip so as to accelerate the vehicle to the desired positive bank rate[*]. The basis for this technique is of course the fact that rudder augmentation of this sort extends the flight envelope over which the basic "reverse" aileron control technique is successful in maneuvering the vehicle; it may be recalled

_____
[*]From the manual control definitions given in Reference 2, it may be recognized that an equivalent manual sequence for a positive bank would be an initial left stick and right rudder, resulting in an uncoordinated left roll, clearly at odds with normal piloting techniques. Stopping the maneuver also follows a sequence opposite to normal operation.

319
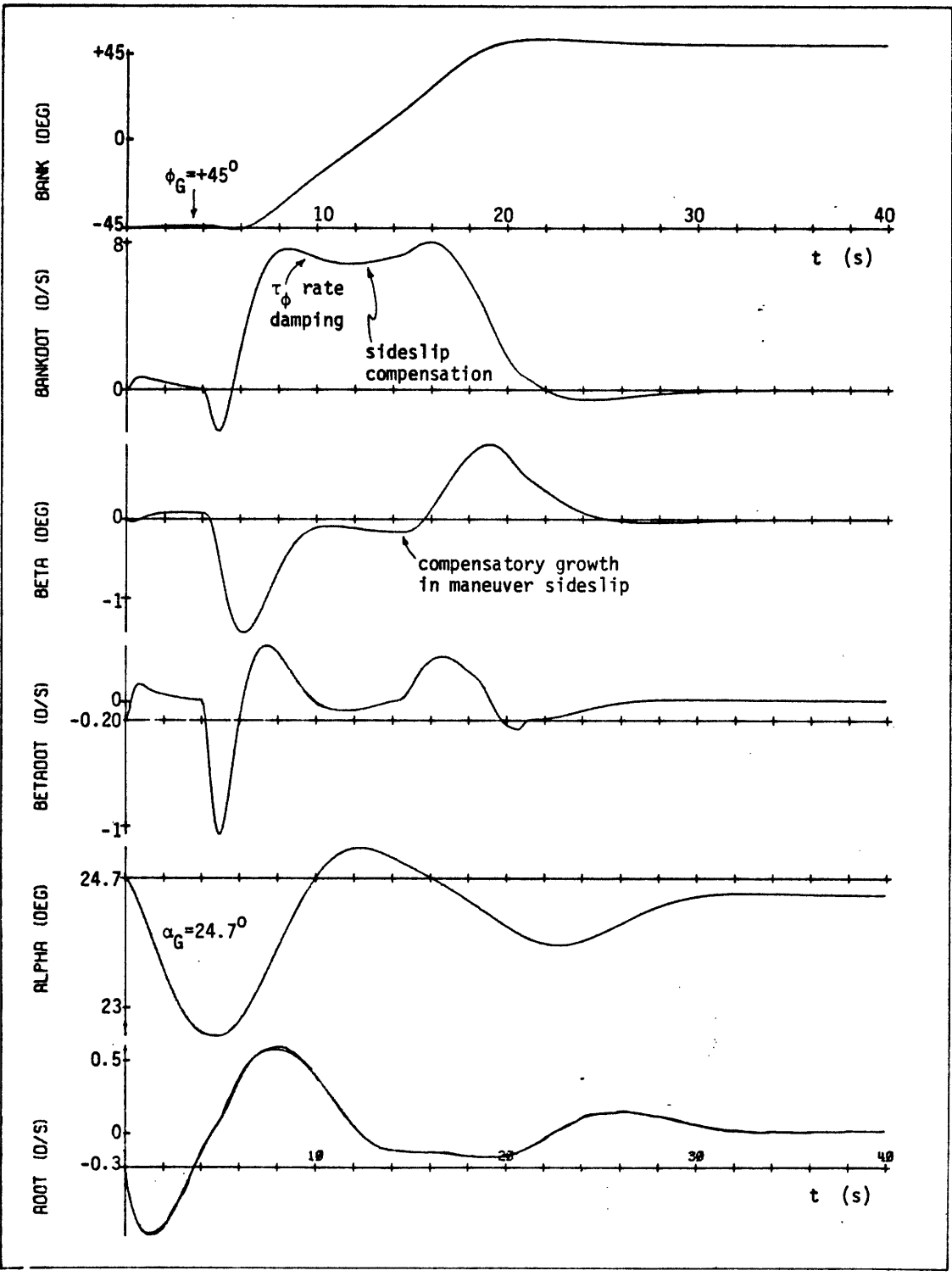
Figure 7-21a. Bank Maneuver at m=6, α_G=24.7^O ($\bar{q}$=195 ➔ 154).

ELEV (DEG)

-3

10   20   30   40
                    t (s)

bank maneuver

changing trim
characteristics

initial trim
found by trim logic

-8

AIL (DEG)

0

-2

RUD (DEG)

0

constant crossfeed
rudder history

-4

P (D/S)

7

0

initial left roll

Q (D/S)

0.6

$q_{ss}=0.20^{\circ}/s$

0

R (D/S)

3

$r_{ss}=0.23^{\circ}/s$

10   20   30   40

0

t (s)

Figure 7-21b.   Bank Maneuver at m =6, α_G=24.7° ($\bar{q}$=195 ⟶ 154).

321

that Section 5.2.2.1 formalizes this concept by describing the induced shift in the vehicle's controllability contours, due to constant crossfeed rudder augmentation. It should be recognized that the use of the rudder in a conventional sense can only hinder control of the vehicle here, since the aileron is attempting to generate a non-zero sideslip to bank the vehicle, and sideslip damping would be at cross purposes.

Several other points regarding this run should be noted:

1. The initial $2°$ swing in the angle-of-attack of Figure 7-21a is caused by both the initial rate value, which is negative, and the fact that the elevator is initially mistrimmed down by more than $2°$, resulting in a sizeable downward pitch acceleration. Correction of the resulting attitude error is then interrupted by the compensation that must be provided for, due to the bank maneuver.

2. Compared with Figure 7-20, the bank rate history of Figure 7-21a shows signs of damping toward a value lower than the desired $8°$/sec specified by the bank rate logic. It may be recalled from the simplified model of (4-51), that the bank dynamics can be approximated as follows:

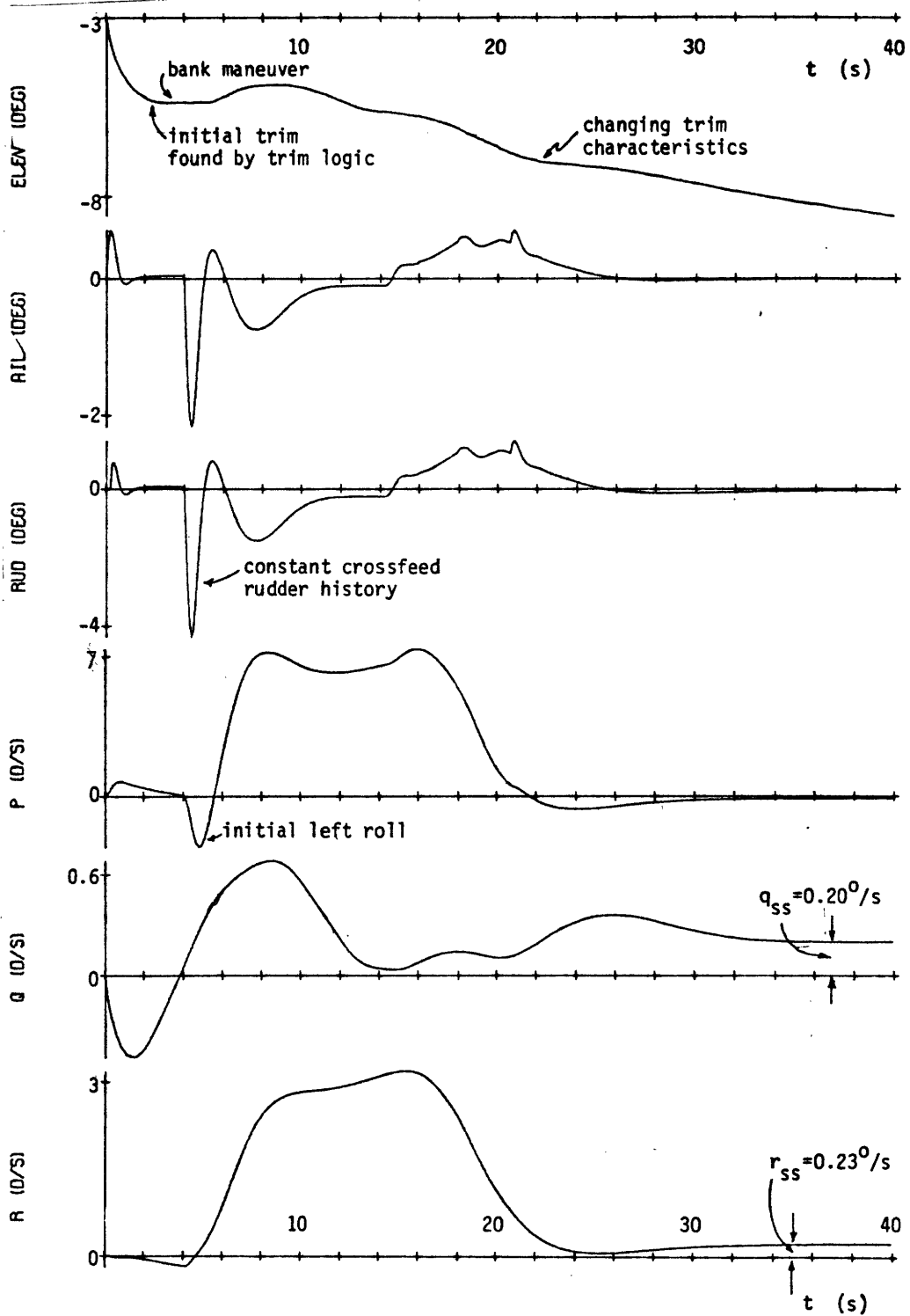$$K_\beta \beta + (s + 1/\tau_\phi) s\phi_s = K_{\phi_{\delta_r}} \delta_r + K_{\phi_{\delta_a}} \delta_a \qquad (7-17)$$

where τ_ϕ is a function of gravity coupling terms and aerodynamic rate derivative coefficients. Its value can be calculated for this flight condition (at t = 10 sec) from the definition given in (4-52b); the value taken on by τ_ϕ is thus found to be approximately 50 sec. Thus, from the above relation, a maneuver rate, $\dot\phi_s$, of approximately $8°$/sec results in a damping acceleration of $0.16°$/sec^2, resulting in the deviation from constant bank rate operation shown. It should also be noted that the control logic compensates for this effect somewhat, by gradually increasing the sideslip during the middle of the maneuver, so that, from (7-17),

322

$$K_\beta \beta + \frac{1}{\tau_\phi} \dot{\phi}_s \approx 0$$

As will be seen in maneuvers performed still later in the entry, this effect becomes more pronounced, resulting in greater deviations from a constant rate maneuver.

3. The non-zero steady-state pitch and yaw rates shown in Figure 7-21b are due to the slow turn rate of the vehicle, caused by the 45° right bank being held. These are readily predicted from the relations derived in Section 5.4.1.2, given by (5-94):

$$\dot{\phi}_s = p\cos\alpha_T + r\sin\alpha_T + \frac{a_\mathscr{L}}{V_T} \gamma \sin\phi_s \qquad \text{(a)}$$

$$\dot{\alpha} = q - \beta\dot{\phi}_s + \frac{1}{V_T}(g\cos\phi_s - a_\mathscr{L}) \qquad \text{(b)} \qquad \text{(5-94)}$$

$$\dot{\beta} = p\sin\alpha_T - r\cos\alpha_T + \frac{g}{V_T}\sin\phi_s \qquad \text{(c)}$$

Assuming zero rates about the stability axes, and with the flight path angle practically zero for this flight condition ($\gamma \approx -1°$), the above set may be solved for the steady-state body rates in the pitch and yaw axes:

$$q_{ss} = \frac{\bar{q}SC_\mathscr{L}}{mV_T} - \frac{g}{V_T}\cos\phi_s \qquad \text{(a)}$$

$$\text{(7-18)}$$

$$r_{ss} = -\frac{g}{V_T}\sin\phi_s \cos\alpha_T \qquad \text{(b)}$$

where (5-94d) was used for the definition of $a_{\mathcal{L}}$. These rates are
precisely those observed in the histories. The point to recognize
from this is that the use of stability axis rates in the control logic
is very similar to the more conventional approach of using body rates
processed through "wash-out" filters in an analog design. These
filters high-pass the rate signals so that steady-state turn rates are
not seen by the control system; in the digital design here, the filter
dynamics are entirely eliminated by the direct computation of the
stability-axis rates, according to (5-94). Thus, the steady-state
body rates of Figure 7-21b are not reflected in the stability-axis
rate histories of Figure 7-21a.

Table 7-4 summarizes the initial and final flight conditions for
five other simulations performed during the late entry portion of the
mission; the time histories for the simulated bank reversals are
shown in Figures 7-22 through 7-26. As should be clear from a
perusal of the bank and sideslip histories, the maneuvers are all
completed in approximately the same fashion, being quite similar
to the simulated reversals already described. This, of course, is
due to the gain structure already described, in which the scheduled

Table 7-4: Trajectory Parameters for Five Simulated
Bank Reversals (late entry)

Figure	$\mathcal{M}_i$	$\mathcal{M}_f$	α_G(deg)	$\overline{q}_i$(lbf/ft^2)	$\overline{q}_f$(lbf/ft^2)	h_i(kft)	h_f(kft)
7-22	5	4	20.7	259	190	110	106
7-23	4	3.2	17.4	247	160	101	101
7-24	3.5	2.8	16.1	225	206	98	89
7-25	3	2.3	15.0	246	198	89	81
7-26a,b	2.5	1.8	12.9	228	186	83	74

gains compensate for the changing open-loop dynamics, so that the closed-
loop response remains roughly constant down the trajectory, as specified by

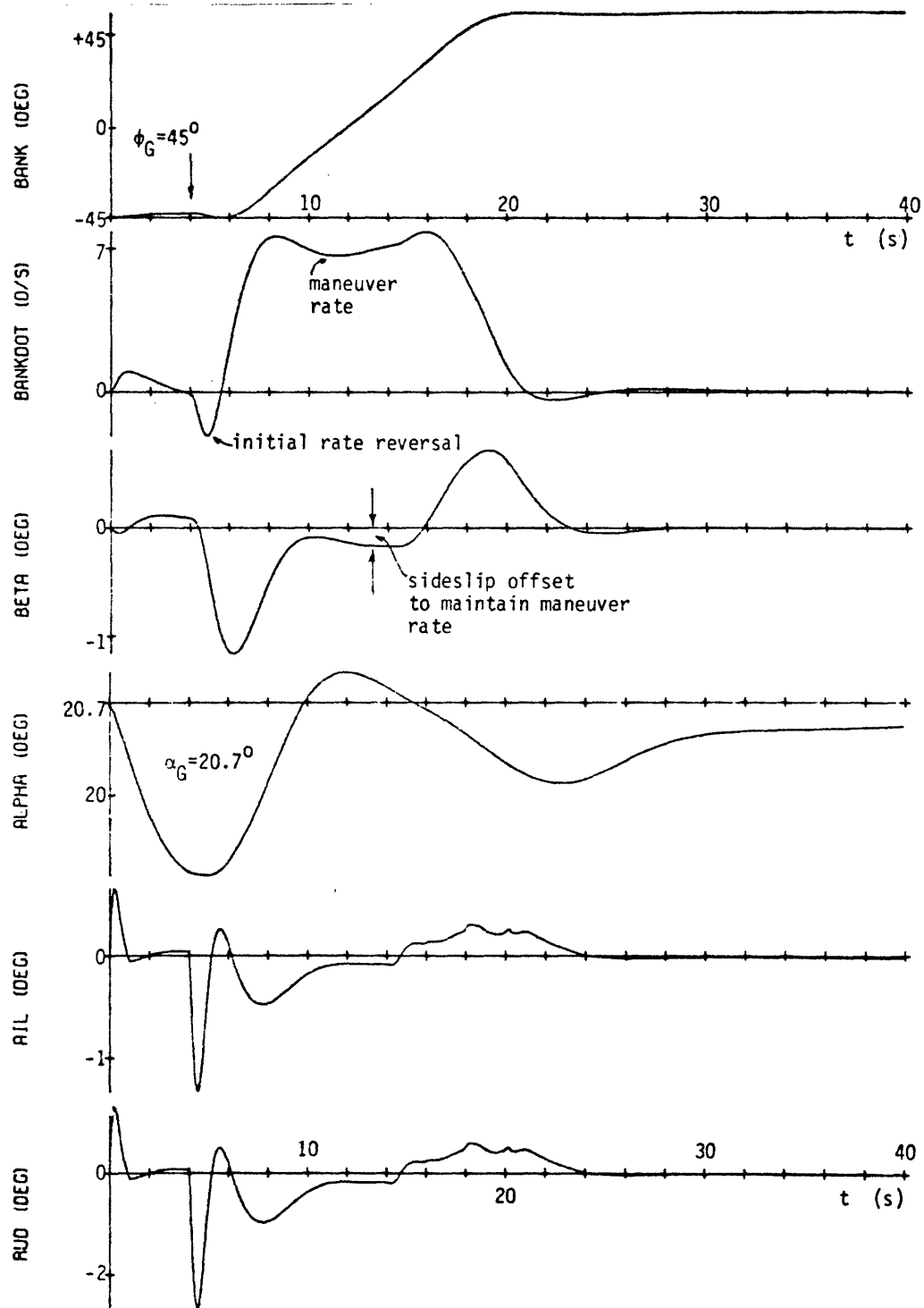Figure 7-22. Bank Maneuver at m =5, α_G=20.7°.
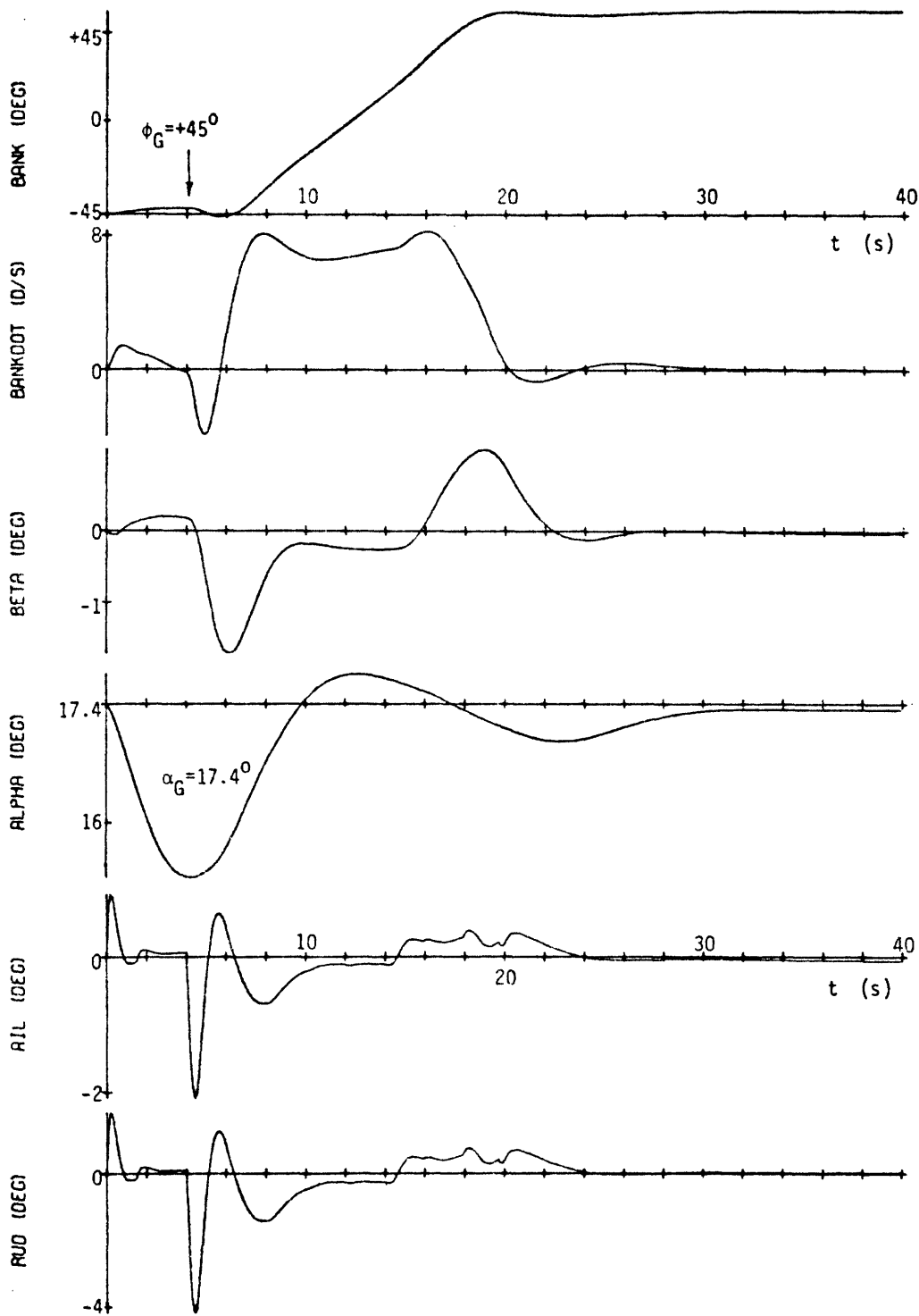
Figure 7-23. Bank Maneuver at $\mathcal{m}=4$, $\alpha_G=17.4°$.
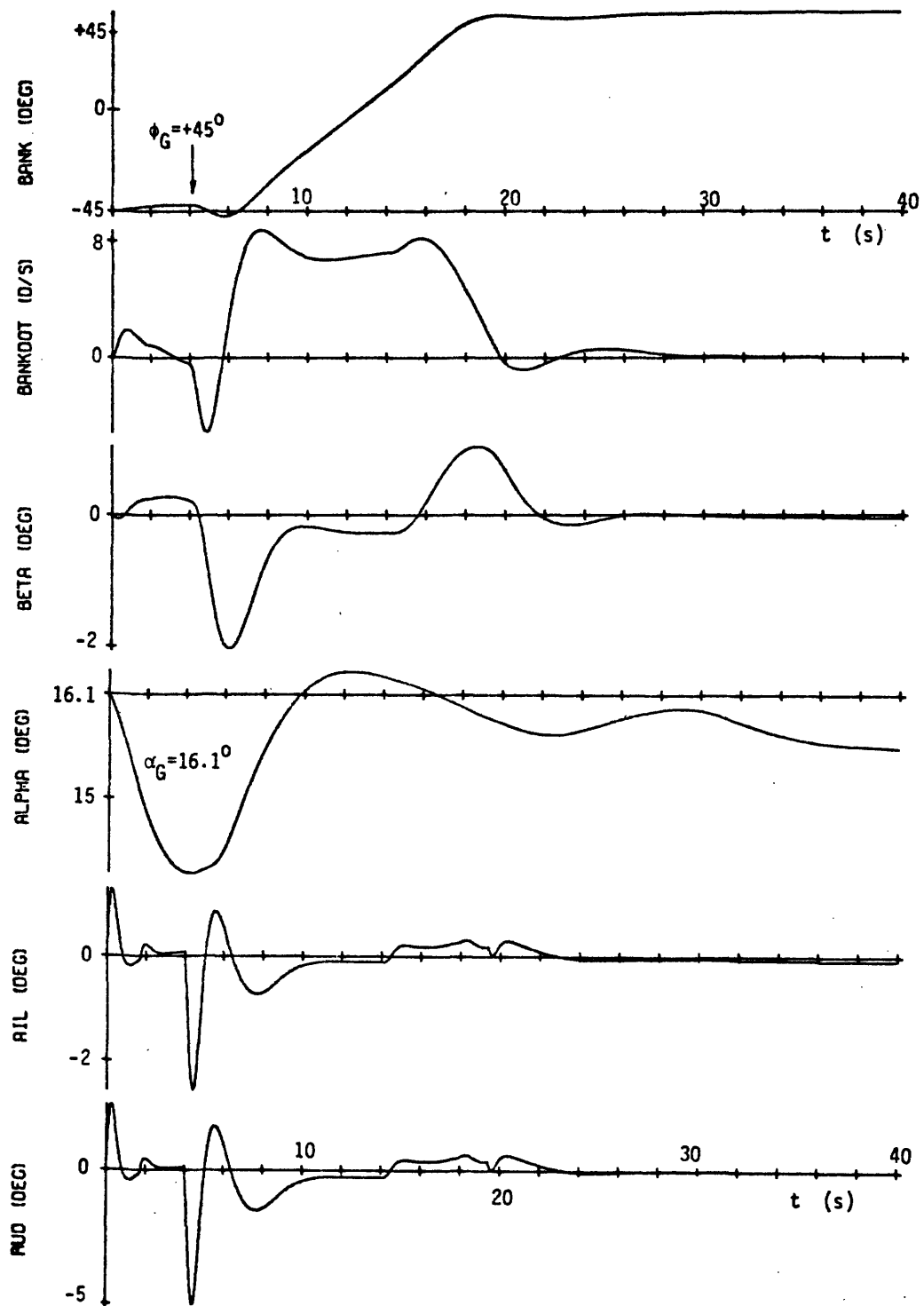
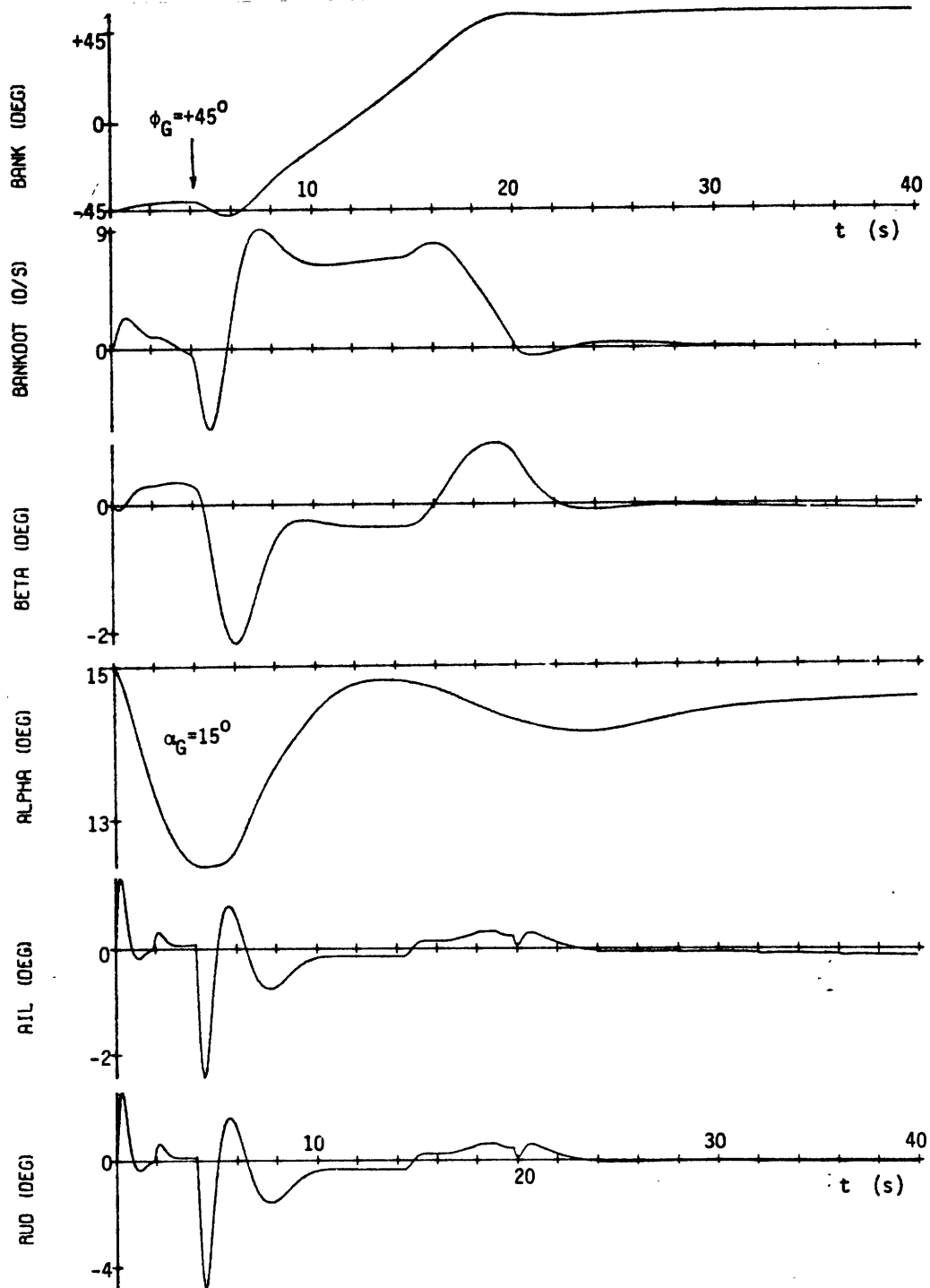Figure 7-24. Bank Maneuver at $\mathcal{M}$=3.5, α_G=16.1^0.

Figure 7-25. Bank Maneuver at $\mathcal{M}=3.0$, $\alpha_G=15.0^O$.
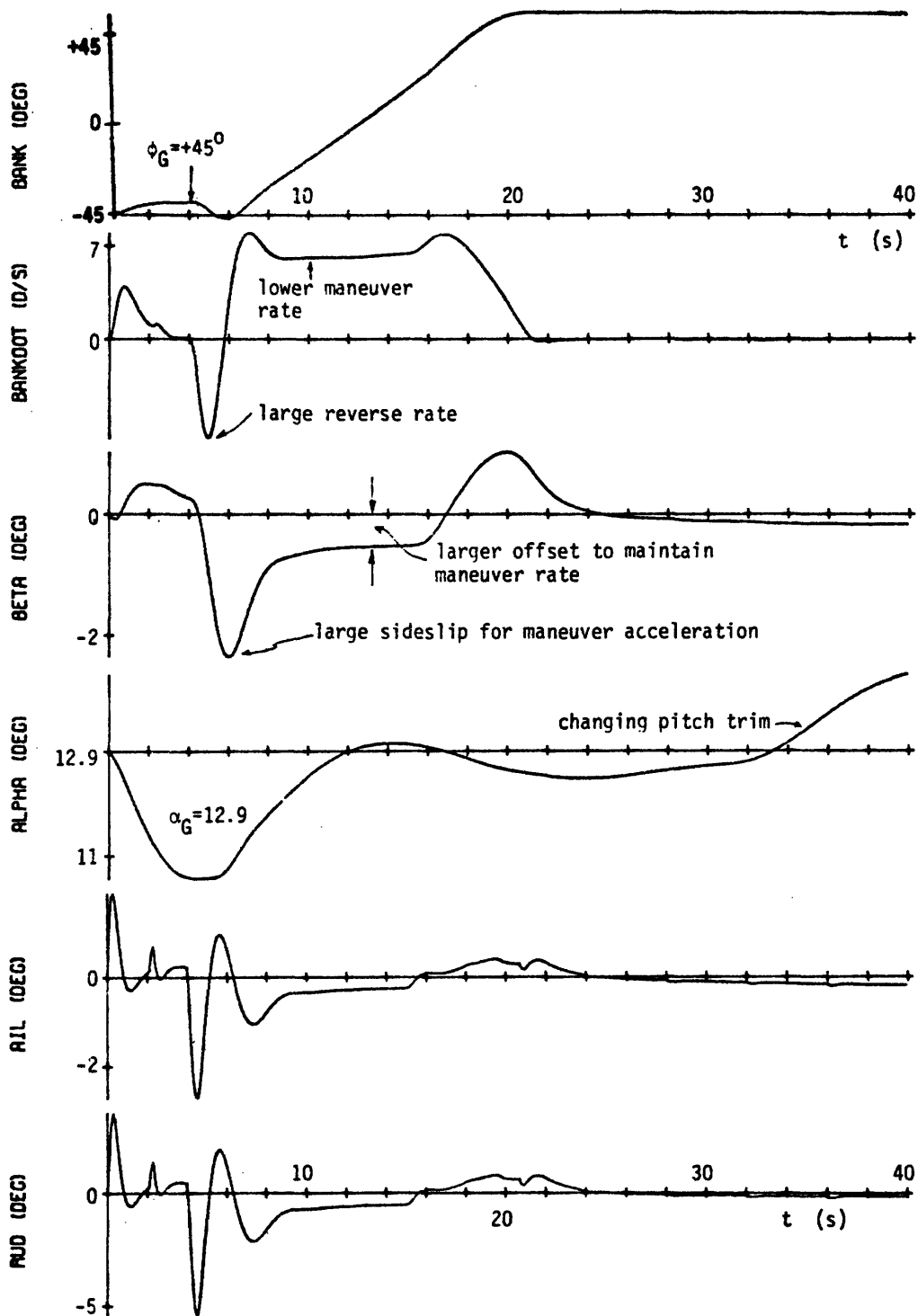
328

Figure 7-26a. Bank Maneuver at m =2.5, α_G =12.9°.
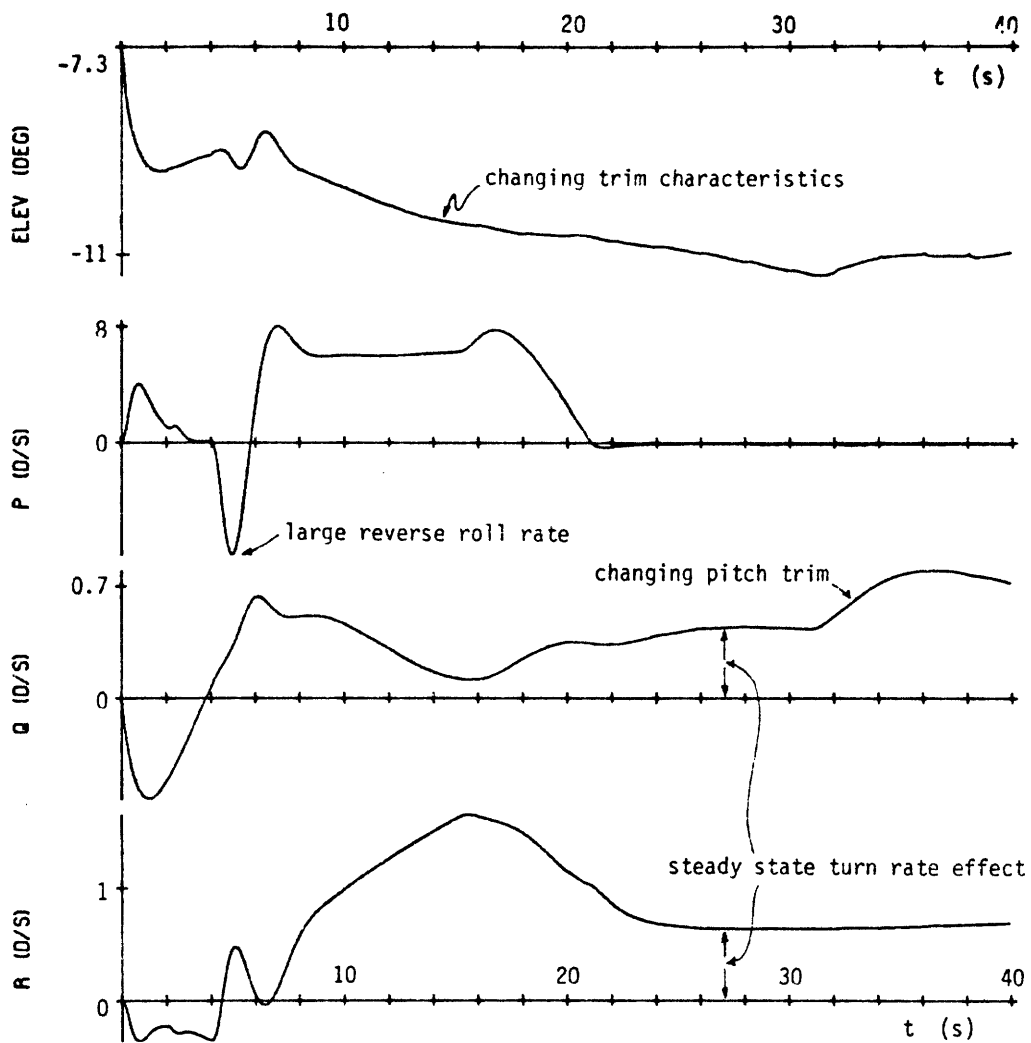
Figure 7-26b. Bank Maneuver at $\mathcal{M}$ =2.5, α_G=12.9°.

the pole placement parameters used in the aileron control logic (see Section 5.2.2.2.1). An example of this type of compensation can be seen from the variation in surface effectiveness between the Mach 5 flight condition and the Mach 2 flight condition: between these two extremes, the aileron effectiveness in sideslip ($K_{\beta\delta_a}$) decreases, while the rudder effectiveness in sideslip ($K_{\beta\delta_r}$) increases. Using the two controls in tandem thus provides a measure of self-compensation, and the further use of gain scheduling provides an additional means of response equalization throughout this late entry mission segment.[*] Perhaps of more interest, however, are some of the basic trends shown in this sequence of bank reversals. First, the initial surface deflections required to initiate a maneuver gradually increase in magnitude as the vehicle progresses down the transition profile. This is due to both the decreasing trend in the dynamic pressure levels encountered, and the fact that the bank effectiveness for both aileron and rudder ($K_{\phi\delta_a}$ and $K_{\phi\delta_r}$) take on increasingly greater values. This latter characteristic adversely affects response since the generation of an initial sideslip entails an initial bank acceleration in the direction opposite to that ultimately desired. Thus, the initial bank reversal becomes more pronounced as the surface bank effectiveness increases; that this is another trend in the maneuvers can be seen by a comparison of the bank rate histories. The net result then, is a trend toward larger surface deflections which provide larger sideslip magnitudes, so as to cancel the increasing bank effectiveness of the surfaces. Yet another trend

---

[*]This self-compensating feature of direct coupled aileron and rudder has previously been noted in another context in the controllability analysis of Section 5.2.2.1. Reference to Figure 5-13, showing the sideslip controllability contours, indicates that the vehicle's transition profile is approximately parallel to a late transition contour. Thus, the control system "sees" a similar sideslip response to a given commanded deflection pair throughout the Mach 5 to Mach 2 pitch-down.

is seen in the approximately steady-state sideslip offset required to hold the maneuver rate at a somewhat constant level. As discussed earlier, this is due to the damping effect of the vehicle parameter τ_ϕ: in this sequence of maneuvers, τ_ϕ decreases from a value of 35 seconds at Mach 5 to a value of 11 seconds at Mach 2, clearly a significant contributor to the bank dynamics. The fact that it was unmodelled in the design synthesis (recall the development of Section 5.2.2.2.1) results in the decreasing trend in maneuver rates, although the system does maintain the rate adequately to complete the reversal satisfactorily.

It should be clear then, from these five simulated maneuvers, that the trend is towards larger incurred sideslip angles and greater initial bank rate reversals, as the vehicle progresses down the late transition portion of the entry trajectory. This type of behavior was anticipated by the discussion on lateral controllability in Chapter 5, and will be the basis for flight envelope definition in the next subsection. Thus, even though the bank maneuver is accomplished properly, the trend toward less desirable initial transients suggests a lower bound in the flight envelope for utilization of the reverse aileron approach.

This then completes the discussion of sample simulations of step response and attitude hold performance under nominal conditions. It should be recognized that the cases discussed above represent only a small fraction of the simulations performed for design verification and evaluation; however, they are felt to be representative of controller operation throughout the entry flight regime and thus should provide some insight into the basic dynamic characteristics of the vehicle/controller system. Before summarizing the observations made above, it is appropriate at this point to consider one more view of controller performance: closed-loop frequency response.

7.2.1.9 Frequency Response Testing

Although it has been emphasized earlier that the system under study is decidedly non-linear and time-varying, some feeling for the response characteristics of the controlled vehicle can be obtained by investigating the frequency response to conventional sinusoidal inputs. Under flight conditions which allow a reasonable approximation to linear system operation (i.e., high dynamic pressure, no ACPS firings), the closed-loop response to such a signal can yield additional performance information. The approach used here is to generate a sinusoidal guidance command and have the control system sample it every control loop pass (every 0.1 second), so that the guidance command is continually changing. Since the sampling frequency $(\omega_s = 2\pi/T \approx 63 \text{ sec}^{-1})$ is much larger than the frequency band of the sinusoidal test signals used $(0.1 \text{ sec}^{-1} \leq \omega \leq 1.0 \text{ sec}^{-1})$, the sampled-data effects need be of little concern.

Shown in Figures 7-27a and b are time histories from such a test, conducted while the Mach number decreases from 5 to 4.2, the altitude drops from 122,000 ft to 117,000 ft, and the dynamic pressure decreases from 154 lbf/ft^2 to 132 lbf/ft^2. The angle-of-attack is commanded to a constant $20°$ while the bank angle is commanded sinusoidally, with an amplitude of $15°$ and a test frequency, ω_T of 0.45 sec^{-1}. After approximately 25 seconds from the start of the run, the start-up transients have died out and the system displays the fundamental frequency of the command signal, along with harmonics generated by the non-linear logic of the aileron channel (see Figure 7-27b; also note the coupling into the elevator channel due to the inertial bank rate effects discussed previously). The amplitude ratio (AR) is readily calculated from the peak amplitudes of the bank command and bank histories, while the phase lag (Φ) is obtained from the lag time (T_{lag}) between the two signals:
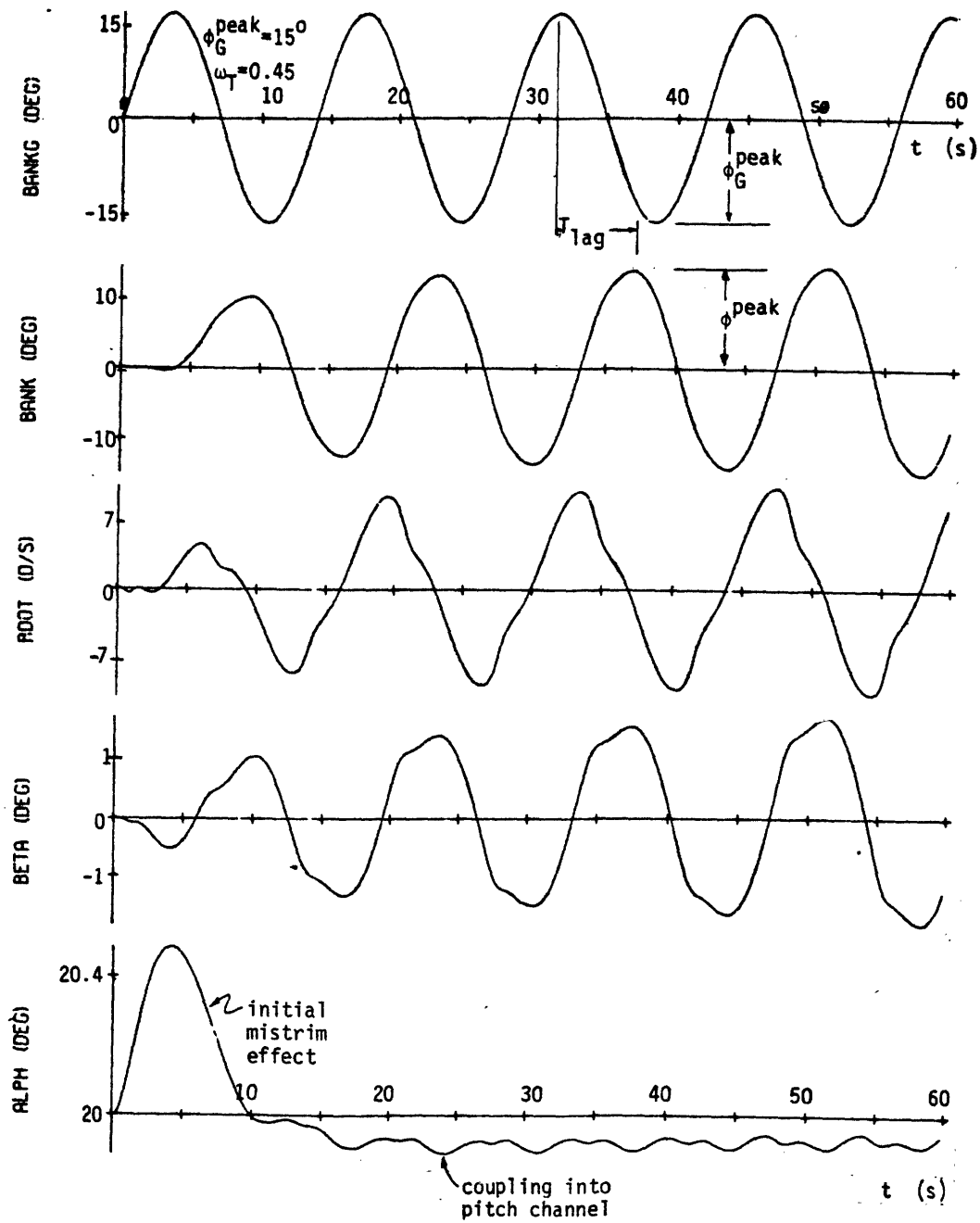
Figure 7-27a. Response to Sinusoidal Bank

Command at m =5 $(\alpha_G = 20^0)$.
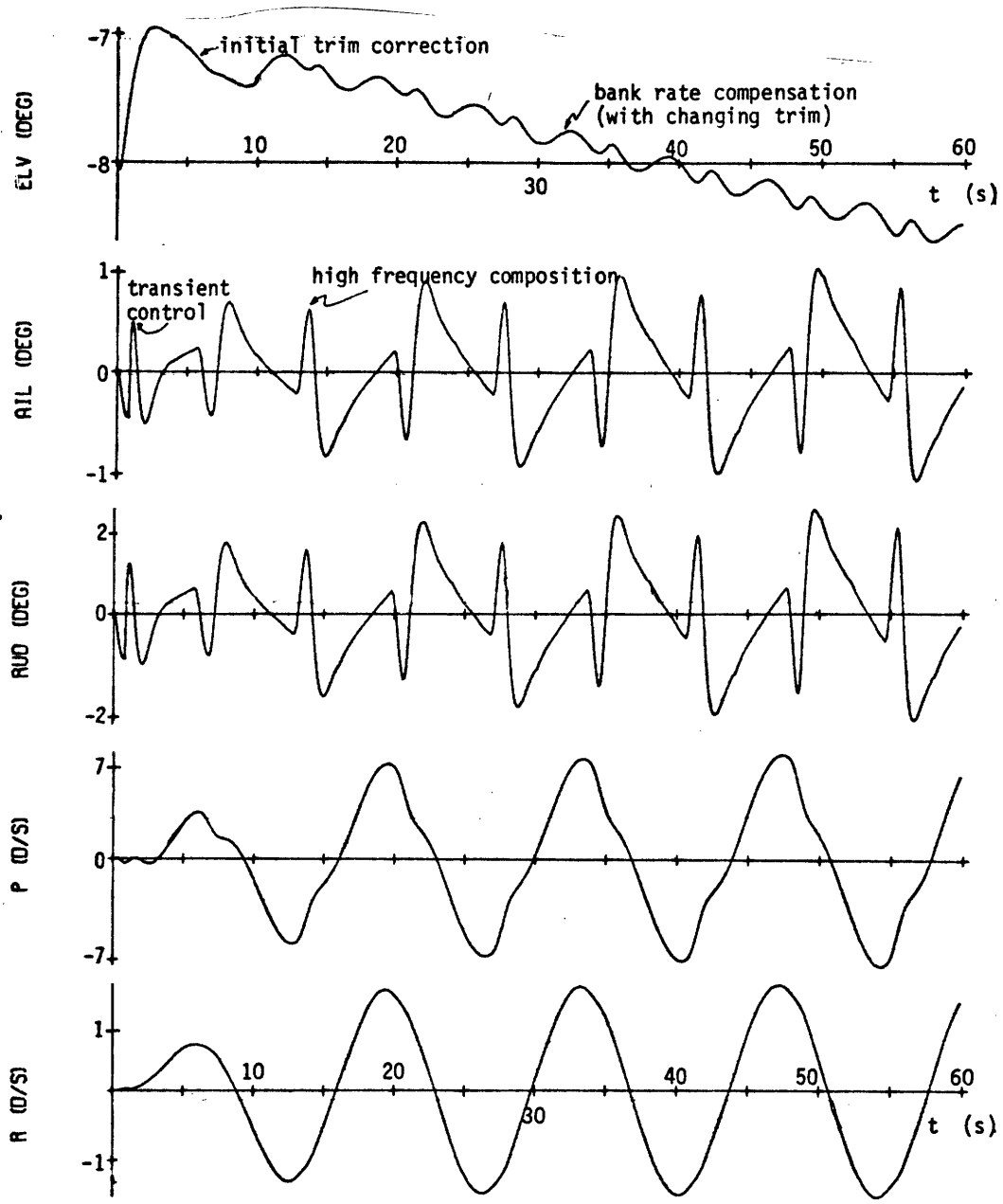
Figure 7-27b. Response to Sinusoidal Bank Command at $\mathscr{m}$=5 (α_G=20°).

$$AR = 20 \log (\phi^{peak}/\phi_G^{peak}) \qquad \text{(a)}$$

$$\Phi = -\omega_T \, T_{lag} \qquad \text{(b)}$$

(7-19)

For the particular case illustrated here, the amplitude ratio is
-0.8, while the phase lag is -130°. Thus, by varying the test
frequency, conventional Bode plots may be made of the system's
frequency response over the range of interest. Shown in Figures
7-28a and b are such plots, for the flight condition just described,
and for two others on the transition segment of the entry profile.
The obvious conclusions to be drawn from this data are: first,
the break frequency increases with decreasing Mach number, and
second, the phase lag at all three flight conditions is quite sizeable.
Both of these observations qualitatively agree with the observed
transient behavior already described: as the vehicle progresses
down the transition profile both rudder and aileron effectiveness
increase, allowing for more rapid maneuvering and better responsive-
ness to input commands (until the late transition portion, when con-
trollability decreases and the system again becomes less responsive);
the phase lag is of course due to the reversal tendencies of the con-
troller, and must ultimately be traced back to the non-minimum
phase nature of the lateral vehicle dynamics. Although this data
clearly reinforces some of the qualitative observations made
earlier, one point should be made here regarding system performance
in a dynamic interacting environment: the guidance and control
interface. Clearly, this much lag introduced by the controller is
cause for concern, due to the possible effects on guidance performance,
and the eventual interaction of the two subsystems. That this has
been shown to be no handicap during a nominal guided entry will be
discussed in Section 7.2.3. However, this type of frequency response
has stronger implications for possible manual adaptation of the
control loop: direct replacement of the commanded bank angle by
a stick generated signal is clearly inappropriate, due to both the

336
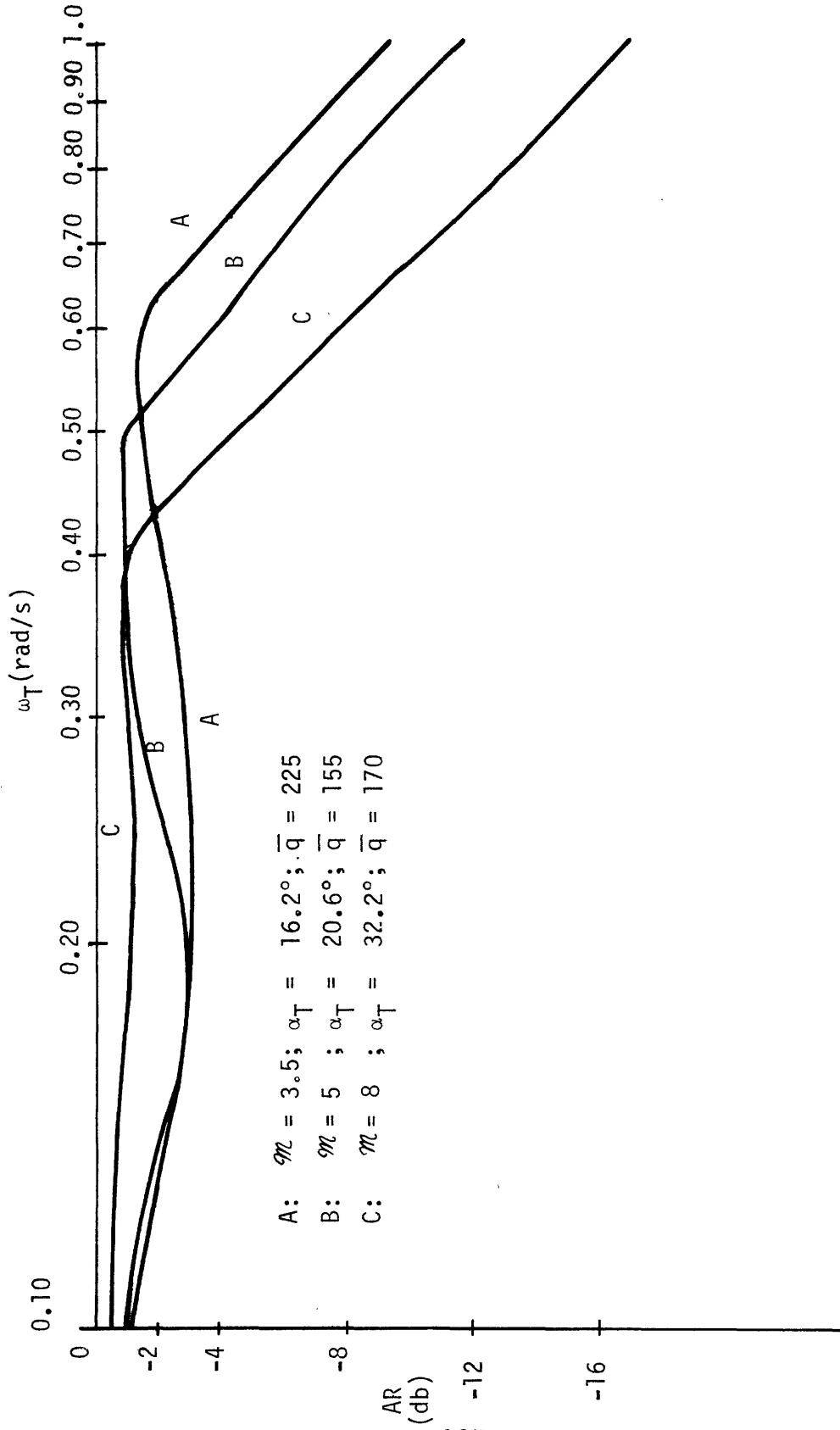
Figure 7-28a. Closed-Loop Amplitude Ratio Characteristics.

A: $\mathcal{M} = 3.5$; $\alpha_T = 16.2°$; $\bar{q} = 225$
B: $\mathcal{M} = 5$; $\alpha_T = 20.6°$; $\bar{q} = 155$
C: $\mathcal{M} = 8$; $\alpha_T = 32.2°$; $\bar{q} = 170$

337
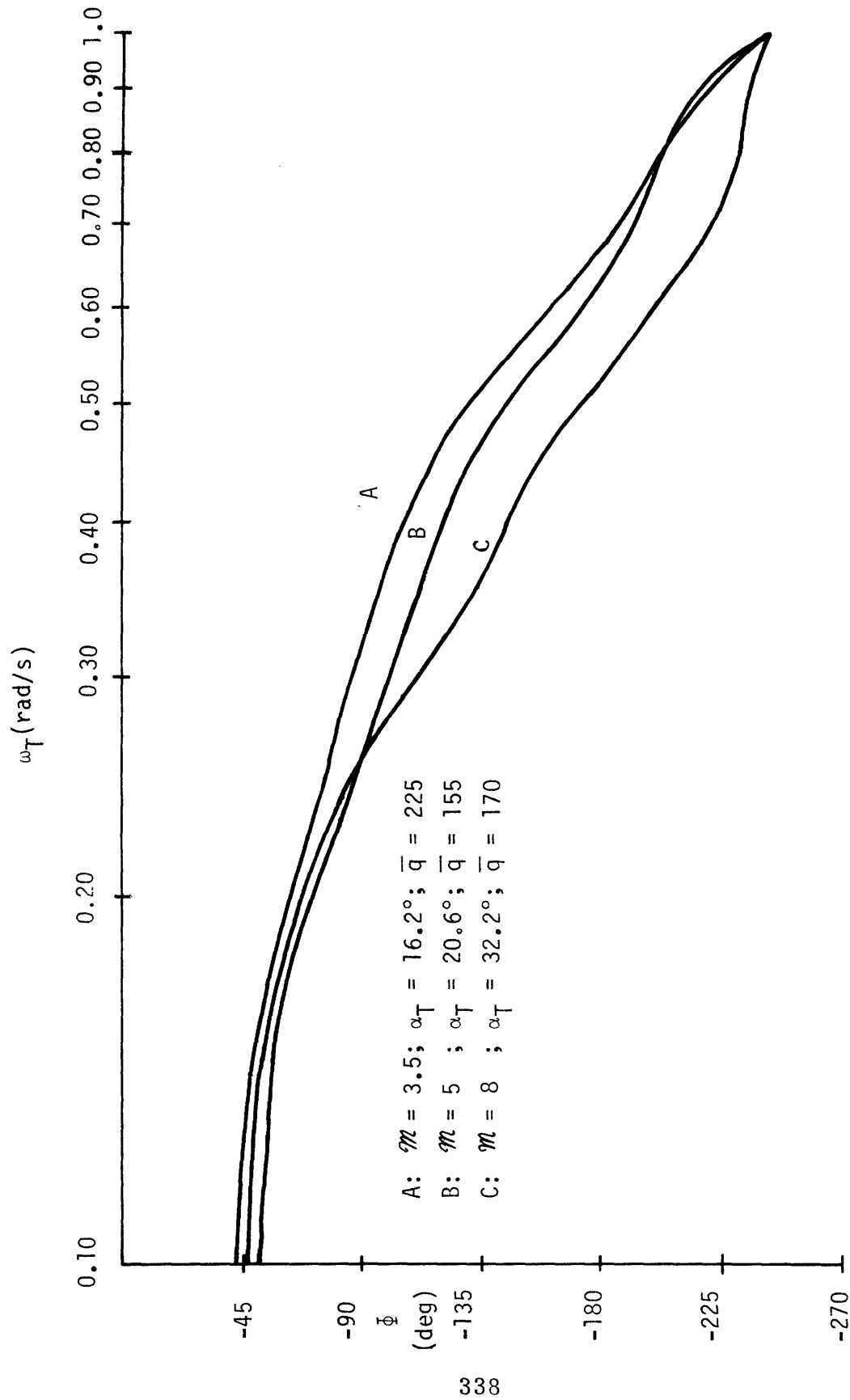
Figure 7-28b. Closed-Loop Phase Lag Characteristics.

338

low system bandpass and the inherent lag of the system. A less direct approach is obviously called for, and may require elimination of the attitude loops in favor of a rate command system; the rate reversal problem will still be present however, and thus additional modification to the logic may be necessary.

It is appropriate to make one last comment on this frequency response data, regarding its relation to the predicted vehicle response obtained from the simplified vehicle. It may be recalled that the lateral closed-loop transfer functions were derived in Appendix J, assuming linear system operation and ideal gain scheduling (i.e., perfect knowledge of the vehicle's aerodynamic coefficients. The Bode plot break frequencies can thus be predicted for the various flight conditions of interest and compared with the empirically derived curves of Figures 7-28a and b. It suffices to note that there is fair agreement in the frequency range of interest, although deviations between the two occur throughout the band, primarily due to the effects of the non-linear control logic, the gain scheduling approximations used (recall Section 6.3), and the system's non-stationarity during a test run. There is clearly more work required in this area for a more precise interpretation of the system's frequency response.

7.2.1.10 Summary of Transient Response Testing

Before proceeding with the next section and a discussion of the system's flight envelope, it is appropriate to briefly summarize here some of the basic observations made above, during simulated nominal operation. First, from the observed vehicle response on the SSFS, a non-linear, time-varying six degree-of-freedom simulator, it appears that the simplified linear quasi-static vehicle model derived in Chapter 4 does an entirely adequate job of predicting vehicle dynamic response. The unmodelled bank rate into pitch torque coupling is the only observed significant deviation from simplified model-predicted performance; the closed-loop operation of the

339

control system, however, provides adequate compensation for this mismatch, and thus the effect of this coupling is minimized. The second point to note is that the simulations above provide strong support for the validity of the several design techniques used in Chapter 5. As expected, the sampling effects are relatively minor, and the Laplace-transform approach used in the ACSS control logic synthesis appears entirely appropriate to this design environment. Similarly, the surface non-linearities and slowly varying vehicle dynamics appear to require no more than the proper choice of fixed gain values in concert with properly designed gain schedules. Similarly, the ACPS control logic synthesis based on double integrator modelling and parabolic phase-plane switch curves performs the attitude control function as expected. The third and final point to note is that the system satisfies the primary performance requirements of Chapter 2 throughout the entry. The ACPS logic provides a compromise between fuel use and maneuver rate, while the ACSS logic operates so as to minimize jet activity once sufficiently high dynamic pressure levels are encountered. As anticipated, the "reverse" characteristics of the aileron control logic take advantage of the vehicle's natural dynamics, at the expense of a fair amount of lag as evidenced in the frequency response data. The implications of this for operation with guidance are noted in Section 7.2.3.

7.2.2 Operational Flight Envelope

The nominal entry flight envelope has already been discussed in Chapter 2; the purpose of this section is to delineate the operational bounds of the trajectory space within which the controlled vehicle performance can be considered satisfactory. Because of the relatively uncomplicated and fairly predictable dynamics involved during early entry, the material presented here is centered on vehicle performance during the late entry or "transition" portion of the mission. It is here that the vehicle dynamics change most dramatically and have continued to be cause for concern throughout the vehicle development program.

It may be recalled that the controllability considerations of Section 5.2.2.1 showed a tendency toward "uncontrollability" (in the formal sense) in the lateral channel as the vehicle progressed down the nominal Mach number/angle-of-attack profile, and into the regime where conventional lateral surface control is clearly appropriate. Similar indications are seen in the last few simulated maneuvers discussed; here, controllability is not at issue, but rather a trend towards undesirable response during bank maneuver initiation. It should be clear from previous discussions that such response can be traced back to the changing dynamics of the vehicle, making the aileron control law more inappropriate as the cruise phase is approached. The dynamics are, in turn, basically functions of the vehicle's aerodynamic coefficients and the dynamic pressure (recall the simplified model definitions of Section 4.4); since Mach number and angle-of-attack specify the coefficient values, the most appropriate trajectory space for envelope definition is thus the three-space of $(\mathcal{M}, \alpha_T, \bar{q})$. For a first approximation, however, this is not necessary, since the dynamic pressure effectively divides out of most stability and control performance indicies and thus the $\mathcal{M}/\alpha_T$ plane provides a good tool for envelope definition. Thus, what is presented here is a constraint curve in this plane, defining the lower operational bounds of successful system performance.

The most direct method for the definition of such a boundary is to simply simulate vehicle performance at different Mach numbers and angles-of-attack, so as to provide a "grid" of test points in the $\mathcal{M}/\alpha_T$ plane. A test point may then be deemed "successful" or "unseccessful" depending on the observed performance, and a contour then drawn so as to separate the two sets of data points. A second method is to simply "fly" the vehicle down some arbitrary $\mathcal{M}/\alpha_T$ profile, performing maneuvers along the way to test system operation, and then simply noting the point at which the last maneuver was

performed adequately. A set of such points will thus similarly define the operational contour. Both of these techniques have been used for this task; typical simulation results obtained with the latter approach are worth noting here.

Shown in Figure 7-29 is a typical commanded angle-of-attack profile programmed against Mach number, and generated by a pseudo-guidance module in the SSFS; this particular profile corresponds with that of the nominal trajectory. Also shown is the ϕ^{max} profile used to limit the magnitude of the bank angle command, in keeping with the type of limiting used by the guidance logic described in Reference 19 (used in order to control sonic boom overpressures). The actual bank command sent to the control system during a simulation was simply $\pm\phi^{max}$, with the sign alternating every 16 guidance cycles, so that a bank reversal was commanded every 32 seconds. Shown in Figures 7-30a and b are simulation histories which were generated using this type of command logic: the bank command history is a sequence of reversals of decreasing magnitude, while the angle-of-attack command gradually steps down along the profile just described. The run was initialized at Mach 5 at an altitude of 110,000 ft; over the two-hundred second span of the run, the vehicle slowed down to Mach 1.6 at an altitude of 73,000 ft, so that the dynamic pressure dropped from an initial value of 259 lbf/ft^2 to a final value of 152 lbf/ft^2. Several points should be noted:

1. As usual, the initial longitudinal mistrim results in quick corrective action by the elevator, although not fast enough to prevent a transient in the angle-of-attack history. The sawtooth signal seen in the elevator trace is due to the stair-step angle-of-attack command history, and gradually dies out as the steps become smaller near the end of the run. Also evident is the pitch rate compensation which must be provided every time the controller executes a reversal, seen as occasional humps in the elevator history. Naturally, these transients are eventually reflected in the angle-of-attack history.
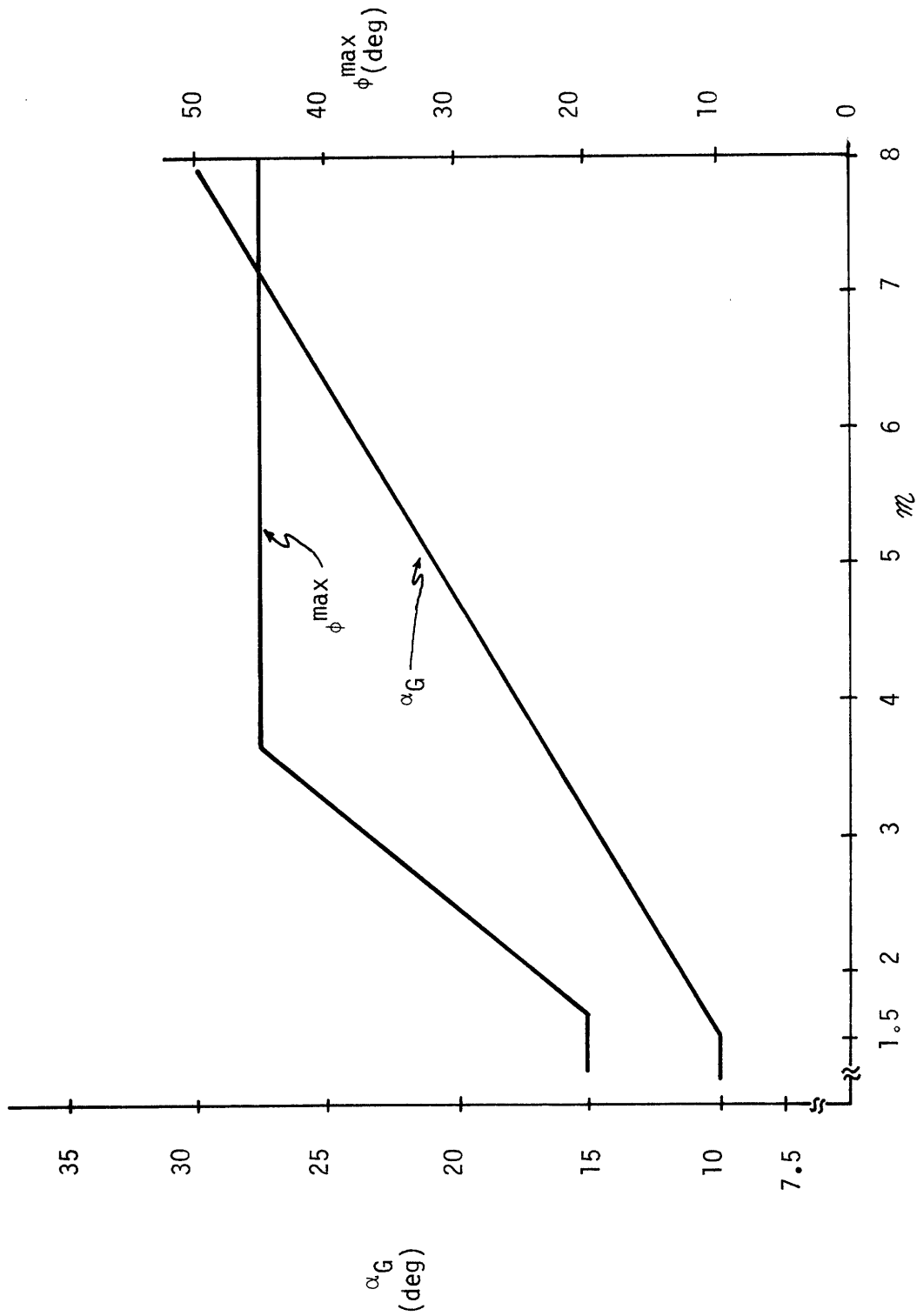
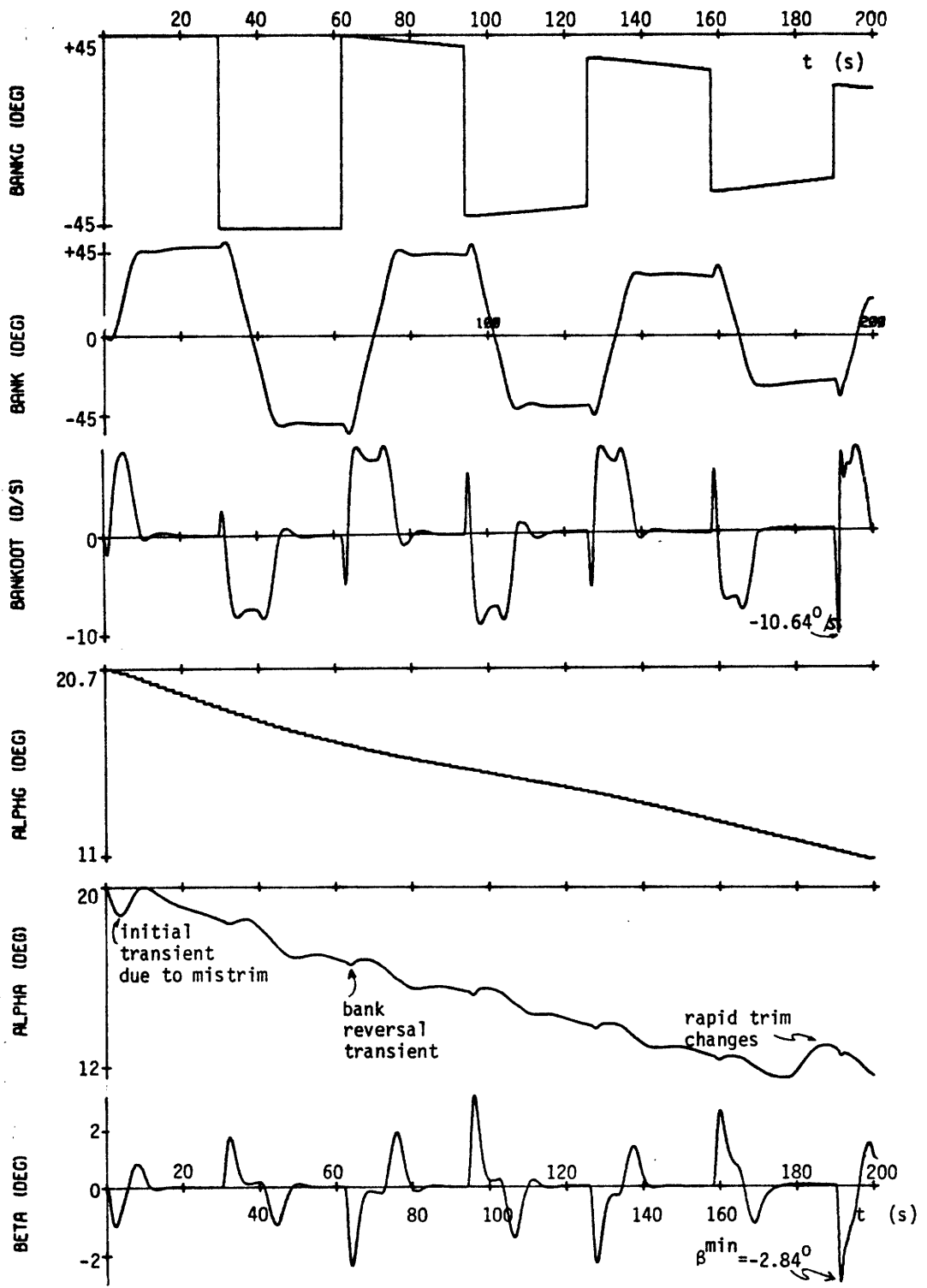Figure 7-29. Guidance Command Profiles Used for Late Entry Testing.

Figure 7-30a. Response Along Nominal Transition
Profile ($\mathcal{m}_i$=5, $\bar{q}_i$=259 lbf/ft^2).

344
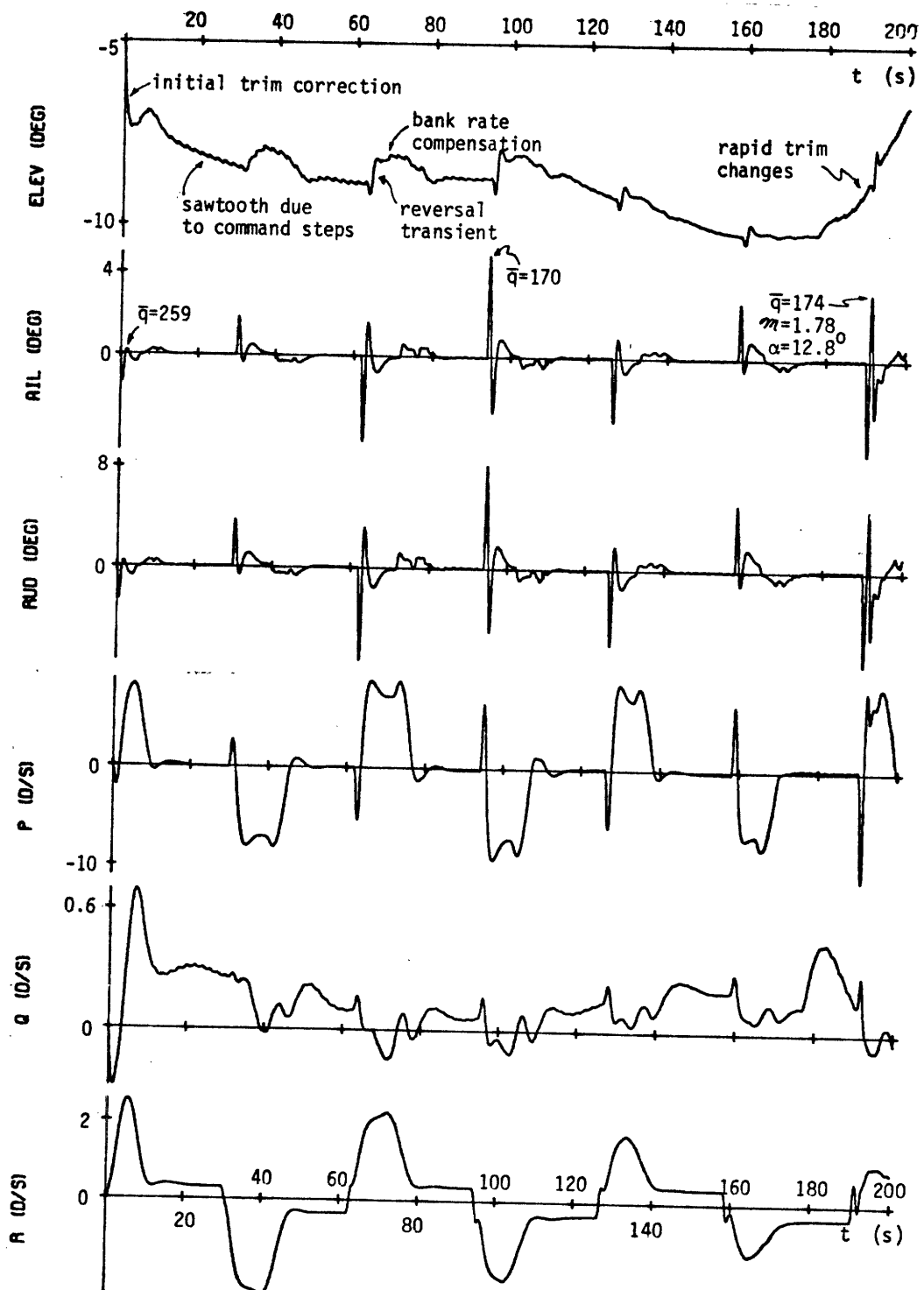
Figure 7-30b. Response Along Nominal Transition Profile (m_i=5, $\overline{q}_i$=259 lbf/ft^2).

2. The control system response to the bank reversals is typical of similar regime step response runs already described. Note that because of the relatively high dynamic pressure at the start of the run ($\bar{q}_i$ = 259 lbf/ft^2), the control logic provides automatic compensation and calls for relatively small surface deflections to execute a maneuver. In contrast, the maneuver conducted at t= 94 seconds, with the dynamic pressure down to 170 lbf/ft^2, requires the larger surface deflections shown, so as to compensate for the relative loss in authority.

3. The most interesting controller activity occurs during the last 20 seconds of the run. Here the pitch trim is changing quite fast (due to the decreasing Mach number) and the elevator trim logic is attempting to compensate; unfortunately, it is not fast enough and the controller incurrs a two-degree error between desired and actual angle-of-attack, at t= 190 seconds. At this point, at a Mach number of 1.78 and an angle-of-attack of 12.8°, the guidance commands a reversal, resulting in the sharp rate-limited doublets seen in the aileron and rudder traces. The resulting sideslip is a healthy -2.84° and the initial bank rate reversal reaches a peak of -10.64° before it is nulled by the negative slip. This type of response is clearly deviating from the original design goals, and is caused by both the relatively rapid changes in trim elevator setting, changing the aileron effectiveness, and by changes in the other aerodynamic coefficients, in the direction which drives the two appropriate controllability coefficients toward zero (recall the behavior of $\tilde{C}_{n\delta_a}'$ and $\tilde{\pi}_1$ as discussed in Section 5.2.2.1). The net result of this simulation, then, is the definition of a (M, α) pair which specifies a point at which controlled vehicle behavior diverges from the desired response.

Several simulations of this type may be made, so as to span the area of interest in the M/α plane; combined with additional short-interval step response runs, the observed terminal (M, α) points can

then be used to generate a contour as shown in Figure 7-31. Shown here is the nominal transition profile along with that of the run just described, and two other command profiles that are typical of those used for contour definition. This contour is thus a constraint curve, setting a lower boundary on control system operation under nominal vehicle and trajectory conditions. The practical implications are quite straightforward: first, the region is quite large and thus sizeable variations about the nominal pitch profile can be handled by the system (larger variations may be possible with modifications to the gain schedules; recall that the gains are scheduled along the nominal profile); and second, there clearly must be a mode switch to a conventional lateral control logic prior to intersecting the constraint curve. This latter point will be discussed shortly; it is appropriate here, however, to discuss two additional aspects of the data presented in Figure 7-31.

Two contours (repeated from Figures 5-13 and 5-14) for the controllability coefficients $\tilde{C}'_{n\delta_a}$ and $\tilde{\pi}_1$ are shown in the figure to provide some motivation for the general shape of the flight envelope contour. It may be recalled from the discussion of Section 5.2.2.1 that lateral controllability requires that both coefficients be non-zero, and in the realistic non-linear environment, be sufficiently far from zero so as to preclude instability due to ACSS rate-limiting effects (among others). With the contour gradients indicated by the bold arrows, it is thus not unreasonable to see that the empirically defined envelope boundary is "above" both contours, and in a loose sense, takes on the shape of the union of the two contours (that is, the curve labelled ABC). No justification is given for the particular controllability coefficient values, except that their associated contours help explain the shape of the flight envelope lower boundary.

The second point to note is that the contour drawn in the figure is weakly dependent on dynamic pressure; a more precise specification of the flight envelope would involve sets of contours

347
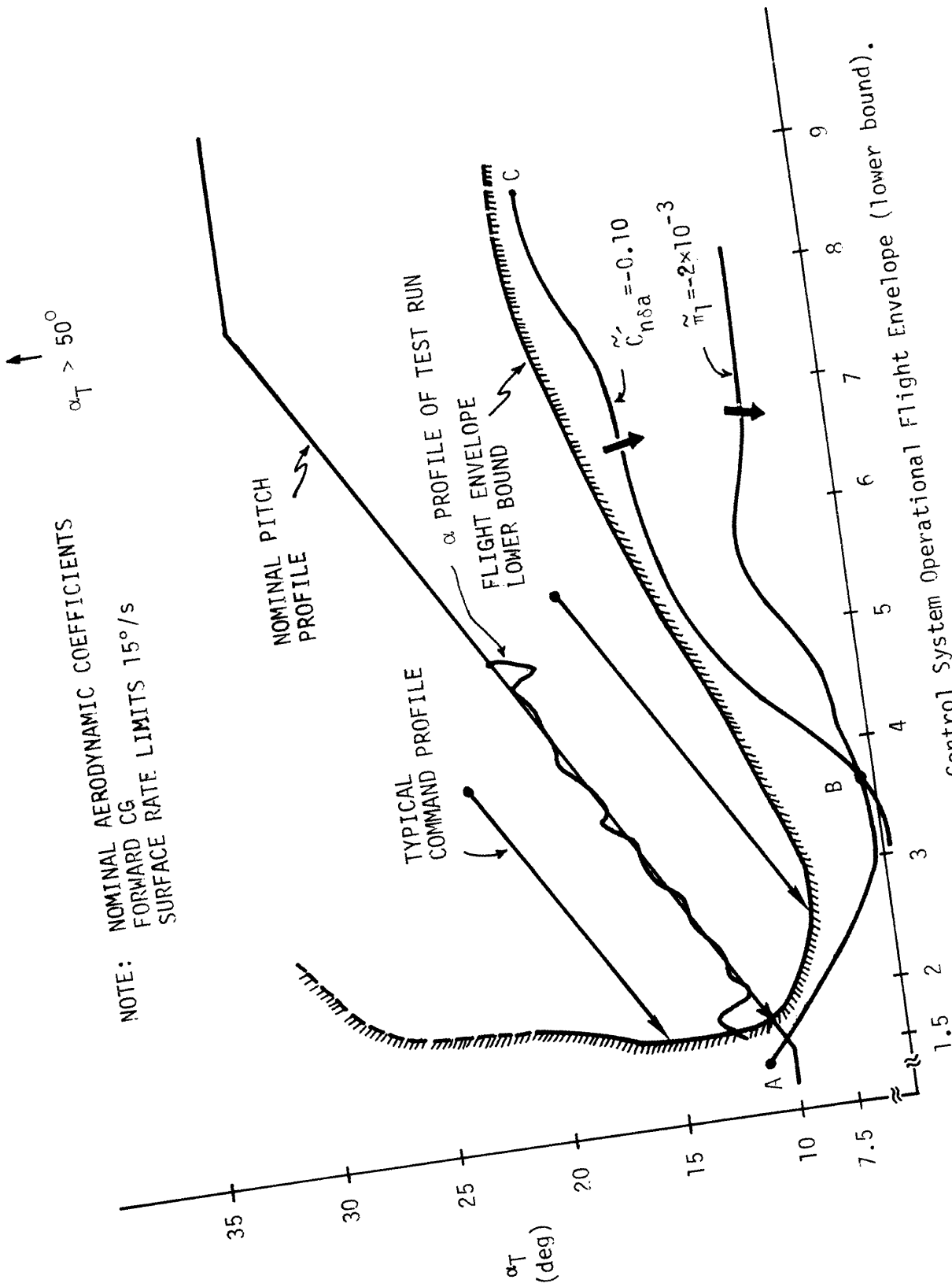
Figure 7-31. Control System Operational Flight Envelope (lower bound).

NOTE: NOMINAL AERODYNAMIC COEFFICIENTS
FORWARD CG
SURFACE RATE LIMITS 15°/s

$\alpha_T > 50^{\circ}$

NOMINAL PITCH PROFILE

TYPICAL COMMAND PROFILE

α PROFILE OF TEST RUN

FLIGHT ENVELOPE LOWER BOUND

$\tilde{C}'_{n\delta a} = -0.10$

$\tilde{\pi}_{\eta} = -2 \times 10^{-3}$

α_T (deg)

A
B
C

parameterized against dynamic pressure. For practical purposes, however, the contour shown is quite insensitive to dynamic pressure variations, provided the variations are within the bounds specified by the altitude/velocity profile of Figure 2-2 of Chapter 2. That this is the case can be illustrated by a simulation similar to the last, except for the starting altitude: shown in Figures 7-32a and b are histories from such a run starting at Mach 5 at an altitude of 122,000 ft, thus 12,000 ft higher than the previous run. The initial dynamic pressure is thus only 155 lbf/ft^2, although it grows to 180 lbf/ft^2 by the end of the run. The point to note is that the histories are quite similar (for example, compare the aileron traces of Figures 7-30b and 7-32b) and that the terminal $(\mathcal{M}, \alpha)$ points are in close agreement. Several runs of this type have been conducted and the results all indicate a very weak dependence of the envelope boundary on dynamic pressure variations; the variations of the aerodynamic coefficients are clearly the dominant factors in envelope definition.

Returning to the point raised earlier concerning the necessity for control mode switching into conventional control, it is appropriate to consider how much "margin" exists for such a switch. Figure 7-33 repeats the contour of Figure 7-31 and also shows a similarly derived contour for a conventional lateral control system developed at the CSDL[*]. Here, of course, the contour is an upper bound on the flight envelope, so that within the "overlap" region it is thus possible to use either technique; clearly the mode switching must be done somewhere along the entry trajectory segment contained in this region. It would appear that no mode switching problems are likely to be caused by a lack of operational envelope overlap. It should be recognized, however, that variations in the vehicle and trajectory conditions, especially undesirable variations in the aerodynamic coefficient values, may tend to "shrink" the overlap region and thus place greater constraints on the mode switch logic. This problem is addressed in Section 7.3, in evaluating the vehicle's performance in off-nominal situations.

[*]For motivation of such a contour, see the text accompanying Figure 5-15 of Chapter 5.
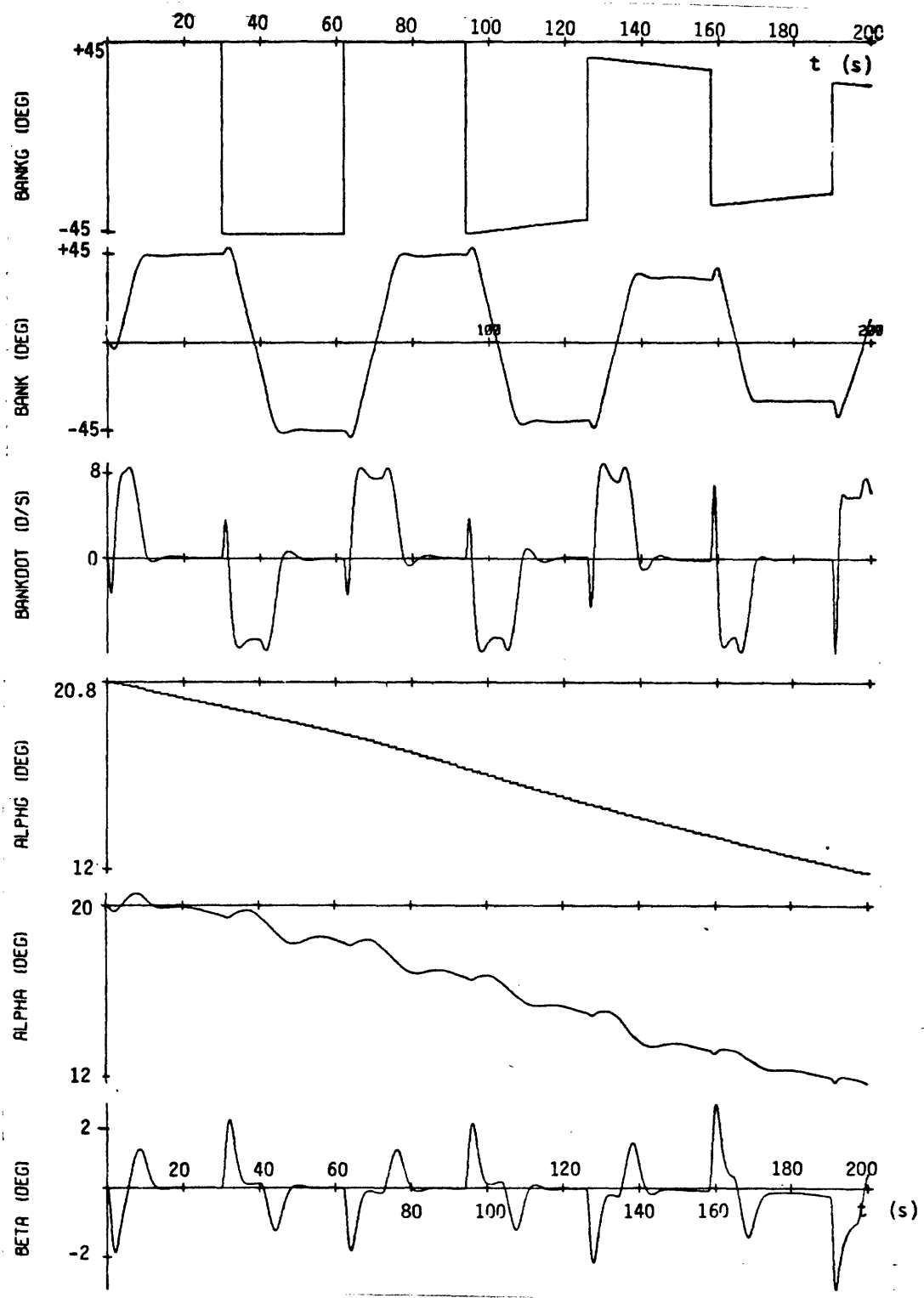
Figure 7-32a.   Response Along Nominal Transition Profile
$(\mathcal{m}_i=5,\ \bar{q}_i=155\ \text{lbf/ft}^2)$.

350
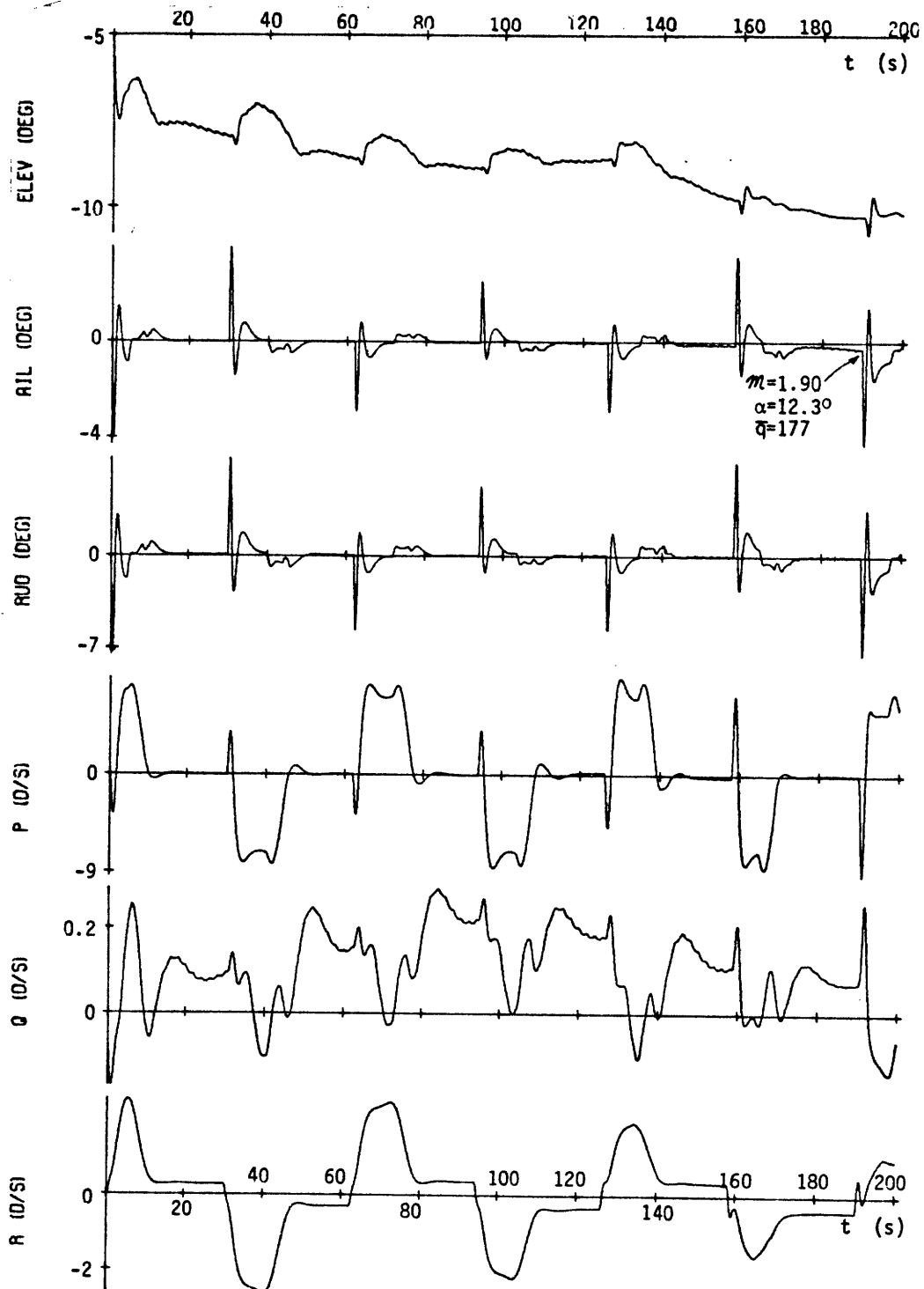
Figure 7-32b. Response Along Nominal Transition Profile
$(m_i=5, \bar{q}_i=155 \text{ lbf/ft}^2)$.

351
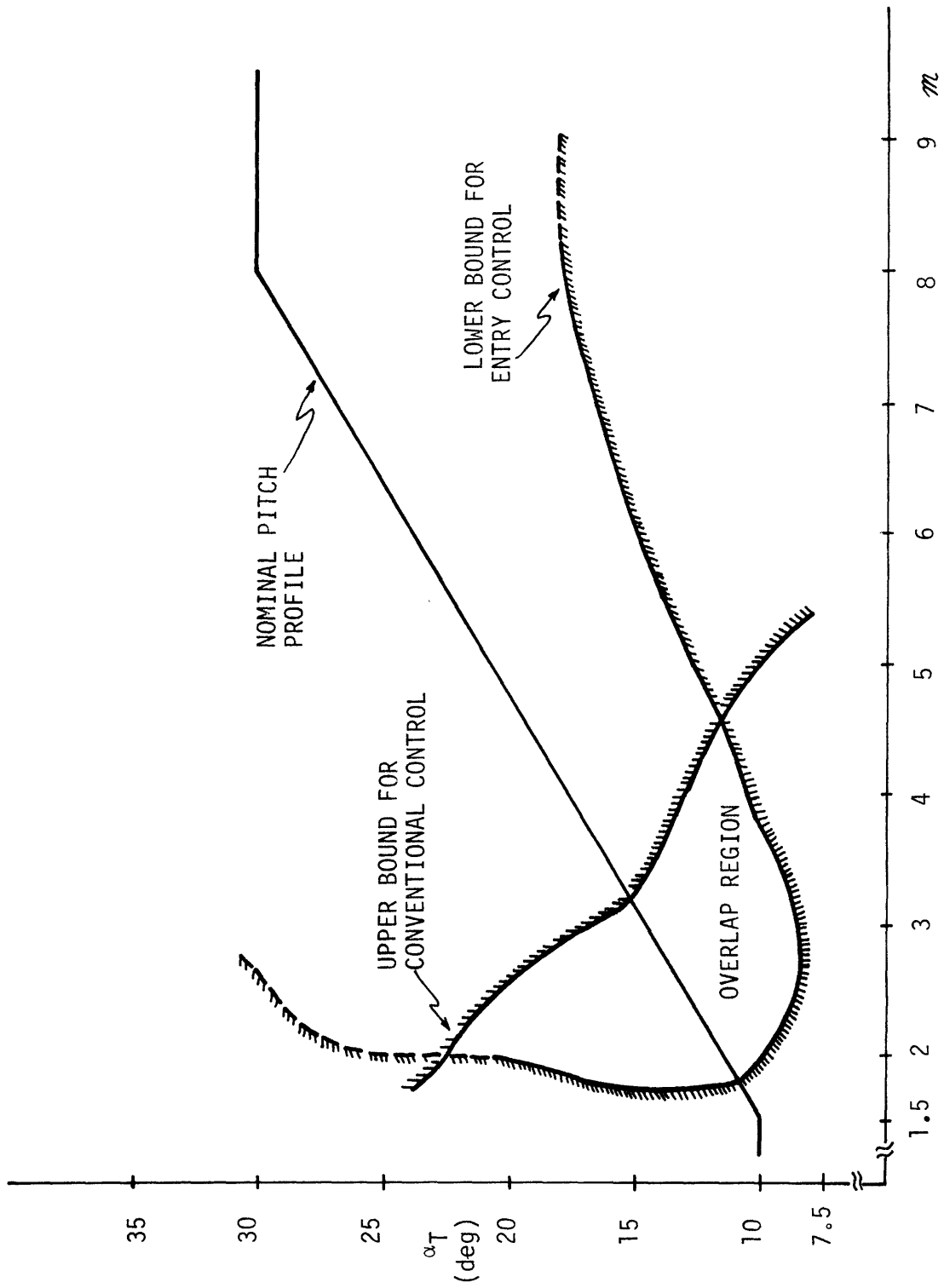
Figure 7-33. Overlap Regions for Mode Switch to Conventional Control.

352

7.2.3 Systems Integration

The previous two sections have concentrated on transient performance and flight envelope definition; this section is less directly related to maneuver performance in that it attempts to briefly describe system operation with regard to the interfaces with other flight software routines. Specifically, it is of interest to discuss operation with the closely associated routines of the DFCS executive, the jet selection logic, the state estimator, and the guidance package. Although the control logic is fundamentally independent of these particular routines, any integrated simulation which extends beyond the scope of simple control system testing must take into account the modes of interaction between these routines. Given below are short descriptive summaries of such findings to date, along with simulation results illustrating a preliminary attempt at functional integration.

The relation of both the DFCS executive and the jet select logic to the control logic "module" has already been discussed in Section 7.1. It suffices to note here that the simulations described in the previous two sections took full advantage of both the DFCS structure and the JSL interface computations. That is, system initialization, scheduling for execution of the control logic coding, periodic updates of the scheduled gains, and input/output processing, were all handled by the DFCS executive program. From the performance evidenced in the simulations, it would appear that not only does the DFCS perform these "peripheral" functions adequately, but that both the DFCS structure and the objectives of the control logic are quite compatible. In fact, during the process of control logic coding and modification, the DFCS structure has proven to be a more than adequate vehicle for control law implementation, and it is anticipated that this relationship will continue throughout the future anticipated modifications to the entry control logic. Similarly, the previous simulations show the high degree of compatibility between the JSL

353

and the entry control logic. The computations performed by the former effectively free the latter from jet configuration dependence; that this is successfully accomplished is illustrated in the simulation histories by the relation between commanded and resultant body-axis accelerations. They are clearly in close agreement, and this is due to both the compatibility of the two logic modules and (primarily) to the successful transformations performed by the JSL (from body-axis acceleration commands to individual jet-on-time commands). It should be noted here that configuration independence has been well-demonstrated in the past, by the natural process of vehicle design changes throughout the program; it is anticipated that further changes will be similarly isolated from the control logic by the JSL.

The state estimator logic, which is part of the DFCS and is documented in Reference 25 was not utilized in the previously discussed simulations, although considerable interface testing with the entry control logic has been accomplished. This is reported on in Reference 16, which considers system operation in both noisy and noise-free environments. Some results appropriate to the latter case are commented on in Section 7.3.5; for nominal operation in a noise-free environment, it suffices to note that system operation with the estimator is practically indistinguishable from operation without it (see Reference 16). That is, not only are the two routines (estimator and controller) compatible in terms of their interfaces, but the lag introduced by the estimator calculations have essentially no effect on controller performance. In a noisy environment, performance improvement is possible through the utilization of the estimator, and this is noted in Section 7.3.5.

Performance evaluation of the control system coupled with a guidance logic requires simulations of longer time spans than described above. To this end, some preliminary simulations of the entire entry flight have been conducted, two of which will be described here. The guidance logic used is a FORTRAN version of the CSDL design documented in Reference 19, modified for SSFS implementation. A complete description of the guidance logic is given in this reference;

354

it should be noted here the system uses both angle-of-attack and bank angle modulation to satisfy the ranging, heating, and g-load constraints, and that no other commands are issued to the control logic. As before, the two simulations described below also implicity test the DFCS structure and the JSL computations; the state estimator is not incorporated here. Because of the flight envelope considerations of the previous section, switching of control logics (by the DFCS executive) is performed near the end of the entry, so as to leave the entry control logic and enter a late entry, pre-cruise logic which is somewhat similar to the conventional control logic of the DFCS used subsonically. A description of this logic is given in Reference 25.

Histories from the first entry simulation are shown in Figures 7-34a through e. Run initialization occurred after deorbit burn, from an orbit of 104° inclination, at an altitude of 402,900 ft, an earth-relative velocity of 26,056 ft/sec, and an inertial flight path angle of -0.83 degree. During the run, the guidance targetted for a point 5250 miles downrange and 1045 miles crossrange. The first two figures (7-34a and b) illustrate the trends in the trajectory parameters: altitude, Mach number, velocity, and dynamic pressure, while the third Figure (7-34c) illustrates the trajectory in the altitude/velocity plane. The remaining figures illustrate the histories of the variables more directly related to controller performance.

In general, the entry can be considered to have been conducted fairly successfully; the miss distance of approximately 5 miles at 71,000 ft (when t $\approx$ 1815 seconds, $V_T \approx$ 1500 ft/sec) is partially attributable to the low performance of the conventional controller, which was utilized for demonstration purposes when the Mach number fell below 3 (recall the contour plots of Figure 7-33). Its failure to adequately follow the relatively high frequency bank commands issued by the guidance contributed to a trajectory deviation, and a resulting target error. Prior to control system switchover at
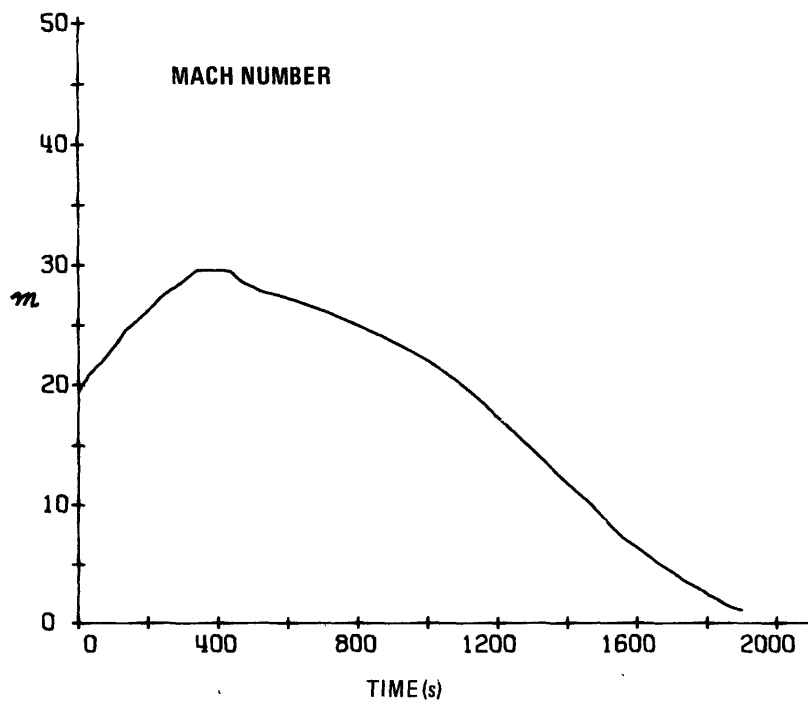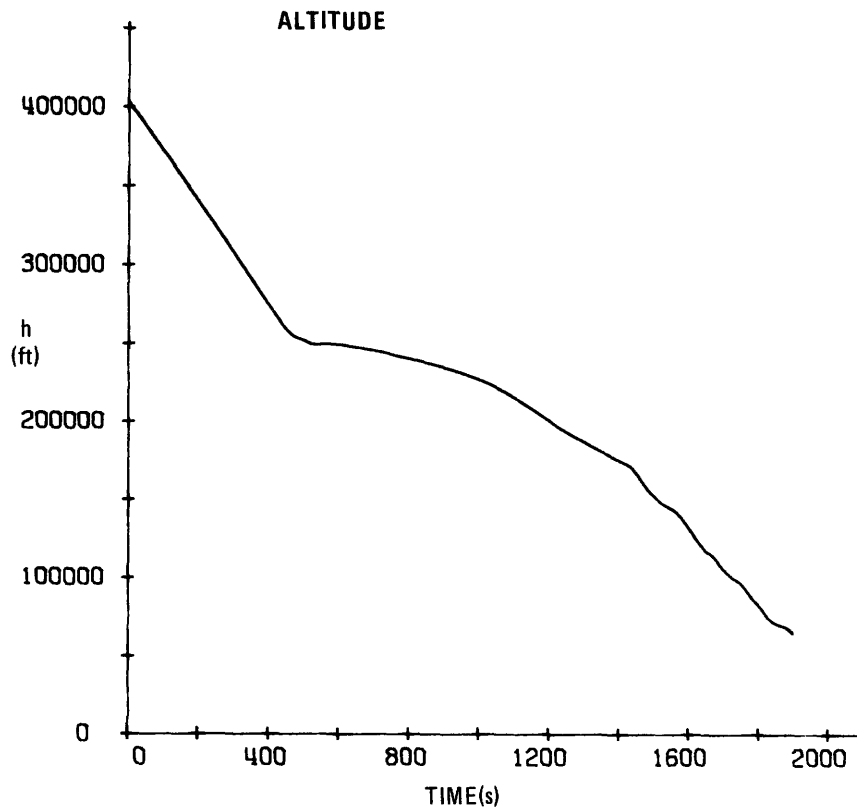
Figure 7-34a. Altitude and Mach Number Histories
for High-Cross Range Entry.
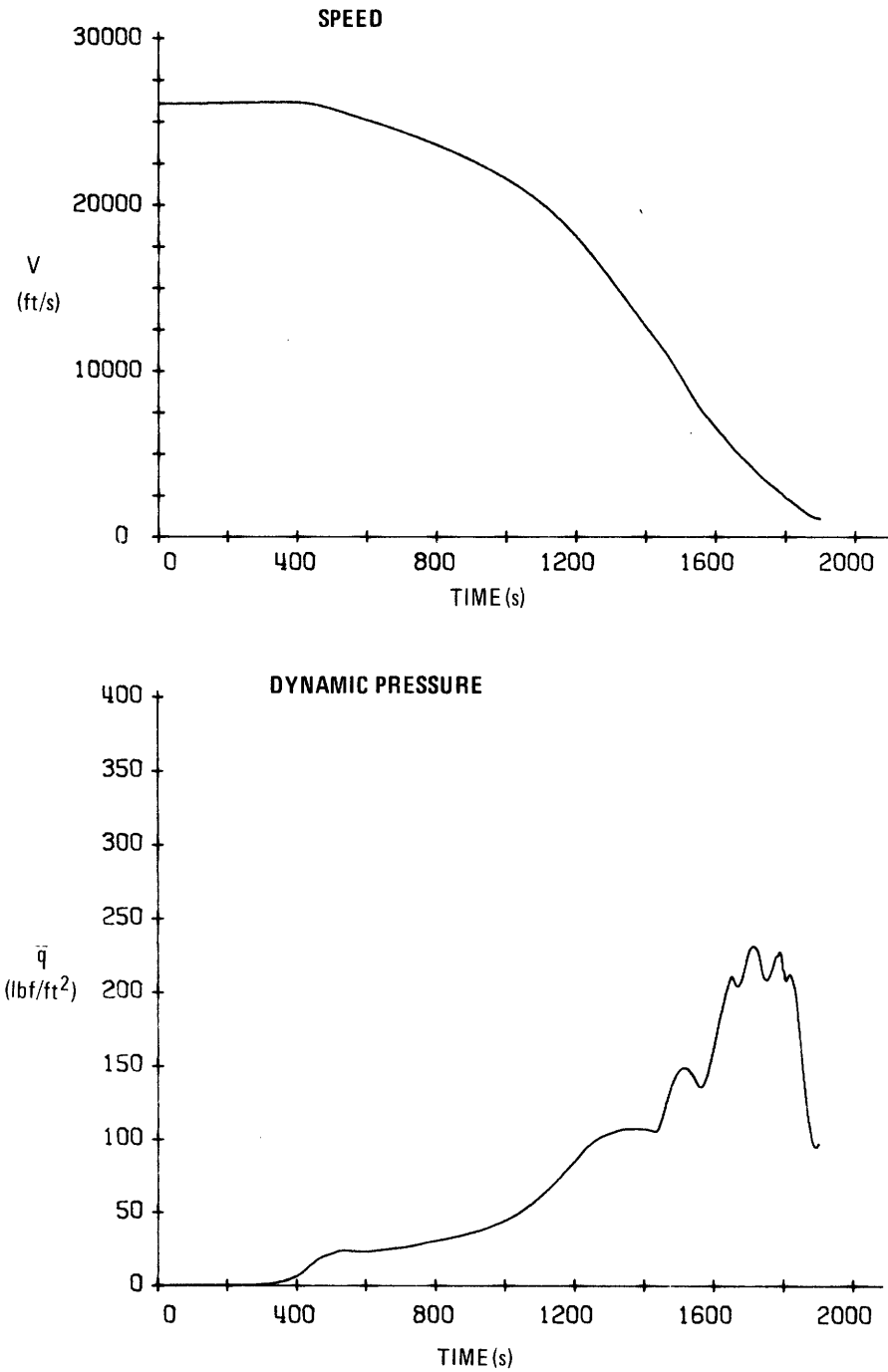
Figure 7-34b. Velocity and Dynamic Pressure Histories for High Cross-Range Entry.
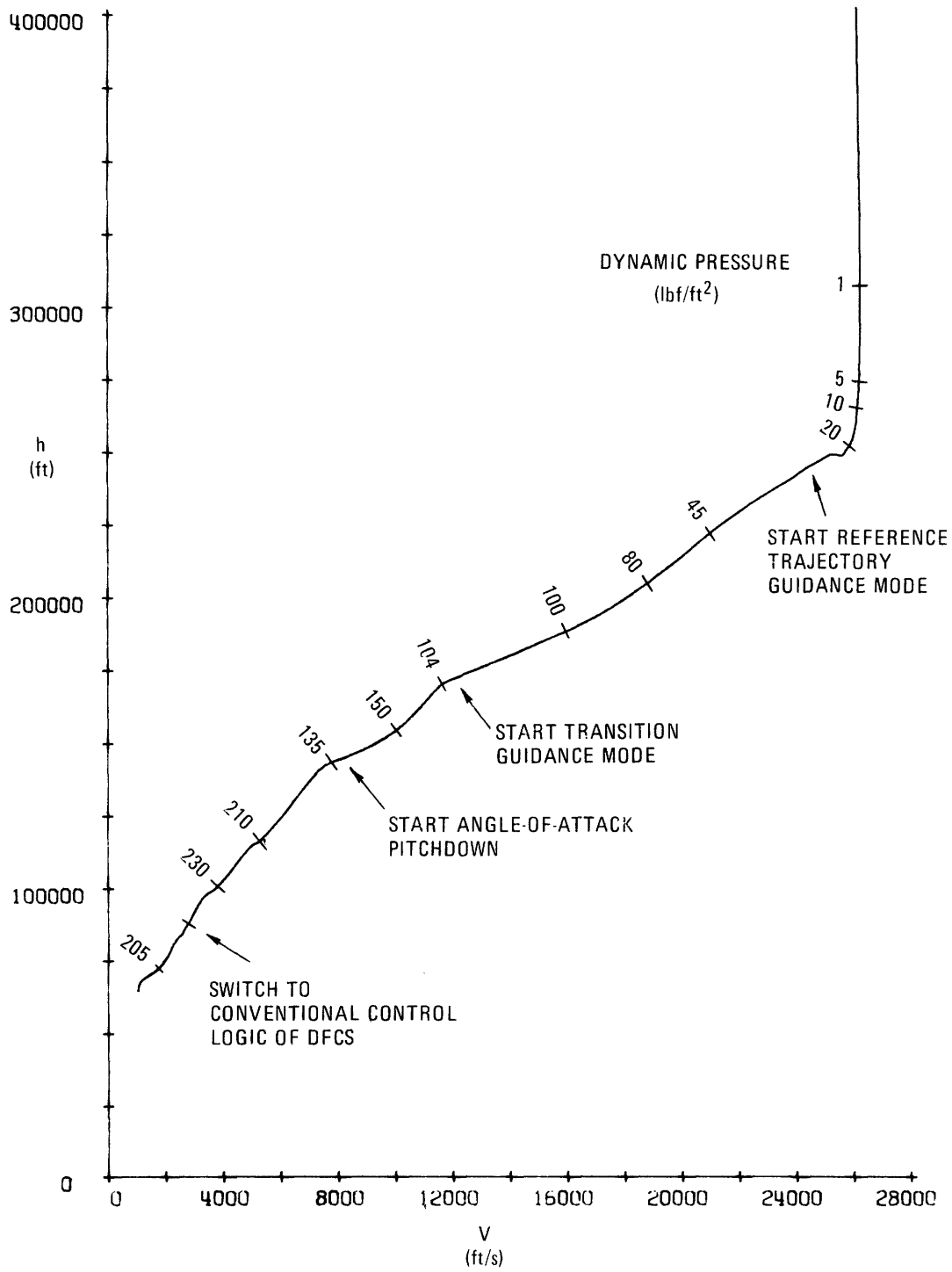
Figure 7-34c. Altitude/Velocity Profile for
High Cross-Range Entry.
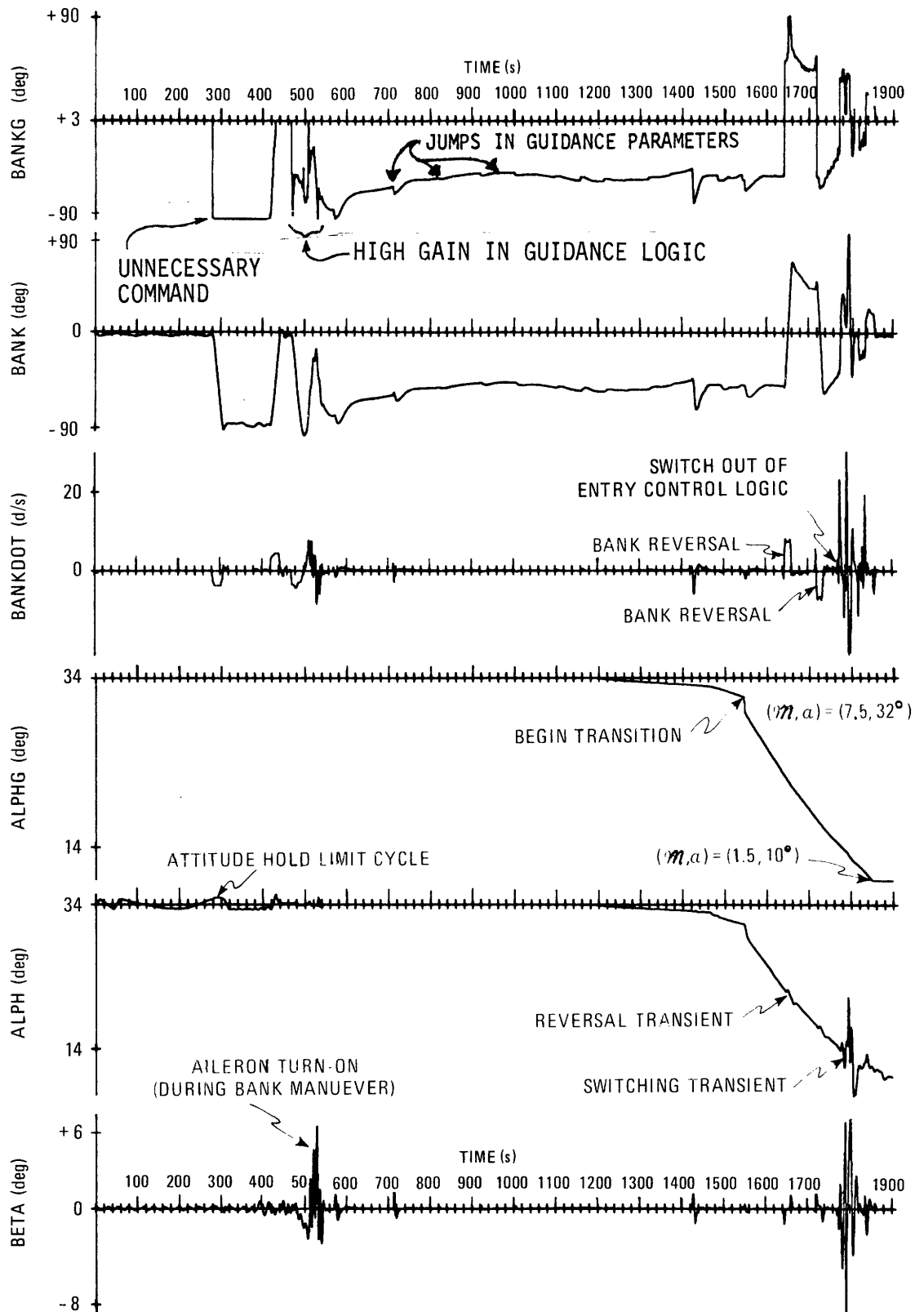
Figure 7-34d. Attitude Histories for
High Cross-Range Entry.

359
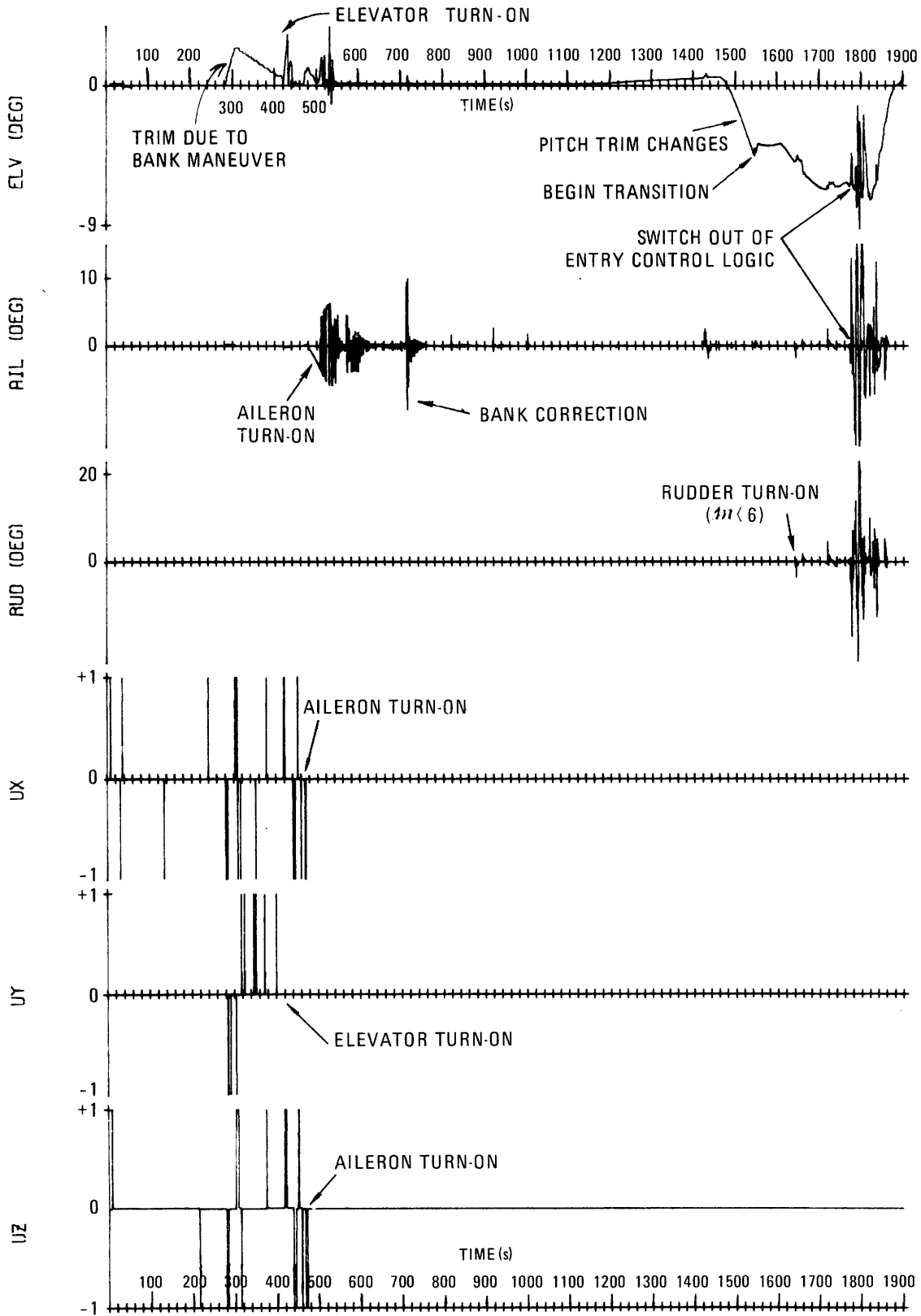
Figure 7-34e. Control Effector Histories
for High Cross-Range Entry.

360

t = 1775 seconds, however, the entry control logic performs quite well, maintaining tolerably small attitude errors and providing sufficient maneuverability to satisfy guidance requests. It is appropriate to comment on some of the features seen in the histories:

1. The first bank maneuver (at t = 280) is performed when the dynamic pressure is below $10\,\mathrm{lbf/ft}^2$, so that the pitch jets must provide the compensatory pitch torques required during the maneuver. The elevator trim logic interprets the resulting pitch jet pulses as a mistrim, and thus the elevator is slowly stepped up between t = 280 sec and t = 300 sec (see Figure 7-34e). Of course, this trim is incorrect once the vehicle stops the bank maneuver; correspondingly, the pitch jet logic senses the induced mistrim, commands the appropriate pitch jet firings, and the elevator trim steps down gradually to its proper setting (see trace).

2. Elevator turn-on occurs at approximately t = 420 seconds; the three-degree transient is due partially to the fact that turn-on occurs as the second bank maneuver is being terminated (see Figure 7-34d), thus driving the linear logic with a fairly sizeable pitch rate error. Note that there are no pitch jet firings after this point.

3. Since the angle-of-attack command is relatively constant at 34 degrees, the remaining portion of the elevator history is fairly smooth (peaks occur during large bank maneuvers). At t = 1460 seconds, the vehicle slows down below Mach 10, so that the changing pitch trim characteristics become apparent in the elevator trace. The pitch transition maneuver is accomplished satisfactorily by the longitudinal logic, until $\mathcal{M} < 3$, when switching into the conventional control system introduces large transients in the lateral channel, which are eventually reflected in the angle-of-attack pitch down profile.

4. Lateral channel activity is somewhat more interesting because of the higher frequency of the bank commands issued by the guidance logic. The first bank maneuver is accomplished entirely by the roll and yaw jets, at a cost of approximately 140 lbm. During the interval t= 400 seconds to t≈540 seconds, the guidance logic appears to be suffering from a high gain in its lateral channel (to date, the source of the error has not been pinpointed) resulting in much unnecessary bank command activity, and, specifically, in a second bank maneuver called for at t= 420 seconds; the fuel cost here is also approximately 140 lbm. It is also appropriate to note the filtering action of the control system on the command history, due, of course, to the relatively low maneuver rates.

5. Aileron turn-on occurs during this period of high frequency guidance activity, at t= 480 seconds, when the dynamic pressure exceeds 20 lbf/ft^2. The gradual limit expansion allowed by the blending logic is clear from the aileron trace (Figure 7-34e). Note that although the bank command is followed relatively well (at least its low frequency component), sideslip exceeds 5 degrees during this period, clearly outside of the performance limits. The implications for phasing of control mode switching with guidance activity should be clear.

6. There are no ACPS firings for the remainder of the entry after aileron turn-on. The total fuel use is 402 lbm, of which at least 140 are due to a malfunction in the guidance logic. This, it would appear that slightly in excess of 260 lbm would be required for this type of entry; other types of entries should not be significantly different, since all jet activity ceases prior to the initiation of characteristically different maneuver sequences.

7. There is little lateral channel activity after aileron turn-on until after the transition maneuver is initiated. The two bank reversals accomplished by the controller (at t= 1640 at t= 1720 seconds) are quite similar to those already illustrated in the previous section. Note the filtering action once again, provided by the low break frequency of the closed-loop controller/vehicle system (recall Figure 7-28).

362

8. At t = 1780, when $\underset{\sim}{M} \leq 3$, the DFCS switches the entry logic out and switches in another control logic to take over the attitude control functions. There are considerable transients evident in all of the histories, although it is unclear as to how much is due to the switching itself, and how much is due to the fact that the switching was performed during a bank maneuver. After a short period, however, the system recovers and the guidance commands are followed quite well thereafter.

Some histories from a second simulation are shown in Figure 7-35; here the target is at a moderately low cross-range of 746 miles, necessitating an earlier initiation of bank reversal commands used by the guidance to correct for cross-range targetting errors. The trajectory parameter histories are similar to those of the run just described, and many of the features shown in the histories of Figure 7-35 have already been discussed. What is interesting to note, is that after the entry control logic performs four well-executed bank reversals, the conventional control logic is switched in during a pause between reversals. A comparison of the traces of Figure 7-35 with those of Figure 7-34e shows an improvement in the switching transients (although subsequent controller activity is still quite high). It should be noted that the entry control law performance in this run is quite similar to that just discussed in the previous run; the ACPS fuel use for the two runs was within 2% of one another, again attesting to the early turn-off of the jets. It is also appropriate to note that the altitude/velocity profile of Figure 7-2 was taken from this particular simulation, as were the individual test points for the step response evaluations discussed in Section 7.2.1.

Some general points regarding both simulations should be made here. First, no attempt was made to "tune" either the guidance logic or either of the two control system logics, so as to provide a more compatible series of commands and responses. This should be evident by some of the transients already discussed. Second, the

363
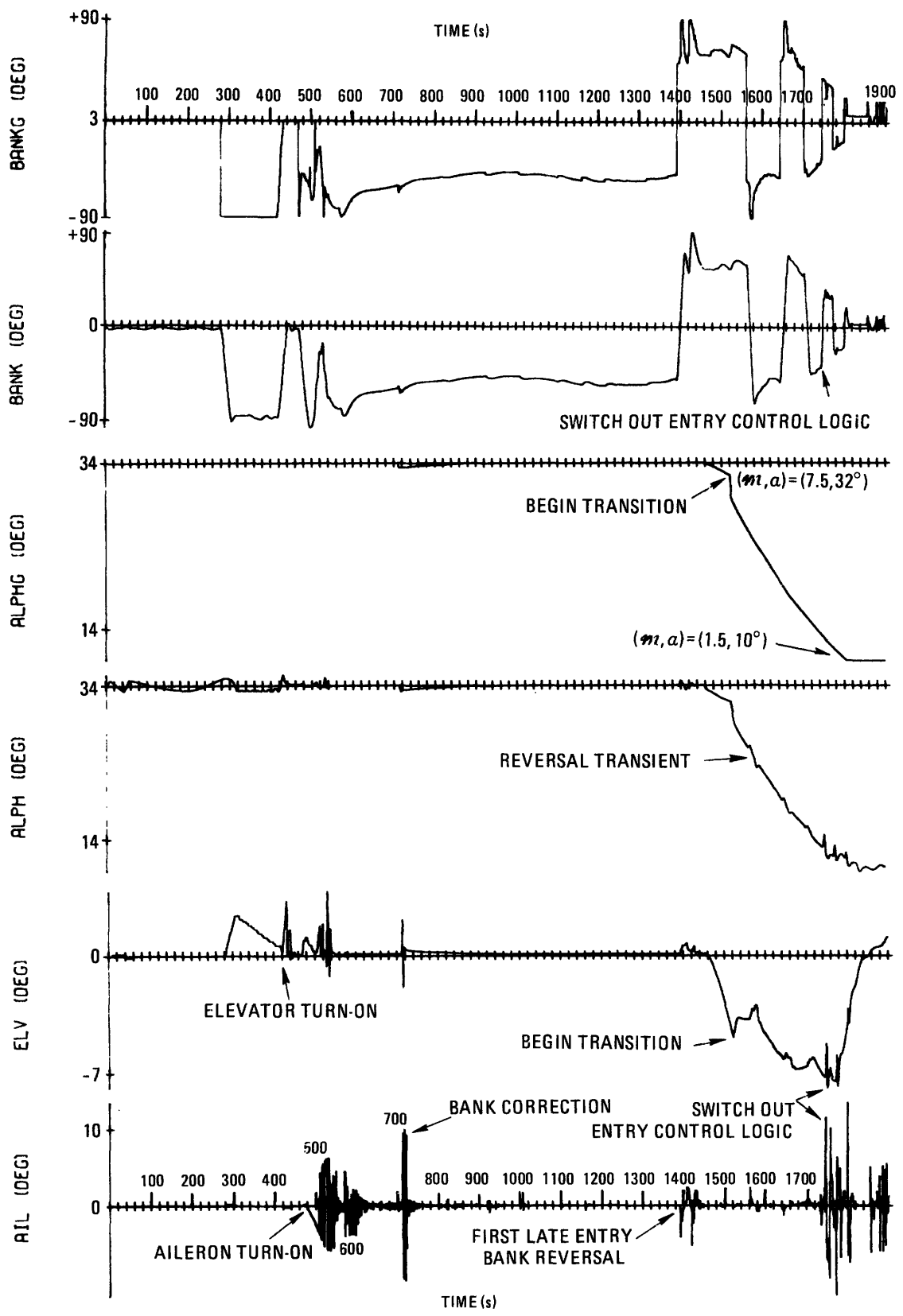
Figure 7-35. Attitude and Control Effector Histories
for Low Cross-Range Entry.

guidance logic, as implemented on the SSFS for these simulations, has not been completely validated; that there are still problems with this implementation are quite clear in some of the anomalies in the bank command history. Finally, the conventional control logic used in the simulation has likewise not been fully verified, let alone "tuned", for late entry operation. This factor is probably the largest contribution to the late entry switching transients, although there may be some subtleties in control mode switching, as yet undetected, responsible for some of the behavior seen. Nevertheless, such a simulation has shown a good functional interplay between the entry guidance and control systems. The basic guidance functions appear to be satisfied by the controller's performance, and there would appear to be no subtle interactions leading to performance degradation or instability. This is especially important, in view of the implications of the Bode plots of Section 7.2.1.9; apparently, the guidance system can tolerate both the low bandpass and the relatively large lags imposed by the control system. If there exist situations in which these factors could lead to performance problems, they have yet to be discovered in future simulation studies.

7.2.4 Summary of Performance in a Nominal Environment

As noted earlier, the simulation results just described represent a small fraction of the total testing involved in the system's design verification and evaluation; nevertheless, it is felt that these results are sufficiently representative so as to provide a convincing demonstration of system performance in the design environment. Specifically, discussed were the basic issues of the controller's maneuver performance and attitude hold capability, and its closed-loop frequency response, operational flight envelope, and related system compatibility. Some of the findings, based on the simulator results described here, may be summarized as follows:

365

1. Both attitude hold and maneuver capability meet the primary performance requirements identified in Chapter 2, and in the face of the large range of flight conditions encountered during the course of a typical entry. This, of course, is accomplished through the system's mode switching and gain scheduling features, which, in turn, owe their success to the demonstrated accuracy of the simplified vehicle model derived in Chapter 4. Automatic blending in of surface control allows for the early utilization of the ACSS for attitude control, thus avoiding high ACPS fuel expenditures and the uncertainties involved in firing jets in a high dynamic pressure environment. Surface-alone control is, of course, made possible by the unconventional aileron logic used in the lateral channel.

2. Many of the simulated maneuvers illustrate a relatively slow response in the bank channel, compounded by an initial reversal tendency when full aerodynamic control is utilized. These findings are supported by the sample frequency response data described here, which show a low bandpass and a relatively large phase lag through the frequency band of interest. Although the conclusions from such linear analyses must be treated with caution, due to the inherent system non-linearities, the indications are that a straightforward implementation of a manual control loop may be entirely inadequate, and, in fact, may require considerable design revision.

3. The late entry flight envelope, derived here through both analytic predictions and results of multiple simulations, provides a large margin for operation away from the nominal pitch down profile used to approach the nominal cruise attitudes. Taken together with a conservative upper bound defining the flight envelope for conventional lateral surface control, there would appear to be sufficient "overlap" of regions of mutual controllability which allows for non-critical switching from entry control to conventional control.

4. Discussed here were the results of a simulated entry, demonstrating a successful (preliminary) integration of guidance and

control systems, along with their attendant interface and "peripheral" routines. Apparently, the lags introduced by the controller are entirely tolerable to the guidance system dynamics. Also, the results obtained from the step response testing provide an accurate prediction of control system response when driven by an operational guidance logic; unanticipated, however, were periods in which the guidance exhibited a high degree of activity, when the control system was simultaneously attempting to effect a mode switch. The resultant interaction clearly motivates further study, with the possible solution of a phasing protocol agreeable to the operation of both systems.

In general, it may be noted that the simulation results demonstrate that the basic design objectives of the controller have been met, over an extremely wide range of flight conditions. Studies to better define the nature of the guidance and control system dynamic interactions are clearly in order here, as is controller operation in a non-designed-for environment. This latter area is treated in more detail in the next section.

7.3 Performance in an Off-Nominal Environment

As noted earlier, the objective of this section is to describe the control system's performance under selected off-nominal conditions, so as to gain some insight into anticipated performance in an environment characterized by uncertainties. The scope of this study is limited to investigating the effects of only a few of the most obvious off-nominal conditions, and thus is only a preliminary analysis of system sensitivity to environmental variations. As was seen in the previous section, even the nominal condition system evaluation is formidable due to the large flight envelope of the vehicle; the few off-nominal situations considered here only serve to expand the dimension of the parameter space in which testing must be conducted. Thus what will be presented here are primarily illustrative simulations so as to indicate the general performance characteristics which can be expected during off-nominal operation.

367

The approach taken in this section is similar to that used in the (nominal condition) performance studies of the previous section: examine the system's simulated transient response at a number of flight conditions (taken from the set of points on the illustrative altitude/velocity profile of Figure 7-2), and evaluating the performance in terms of the design objectives. Here, of course, the testing seeks to evaluate response to perturbations in the control system's working environment. Some of the possible perturbations have already been discussed in Section 2.4; those examined here can be categorized as either variations in the vehicle parameters or as errors in the software environment. In the former category are center-of-gravity displacements away from nominal, variations in the aerodynamic coefficient values, and variations in the actuator rate limits. In the latter category are errors in estimating the trajectory parameters necessary for gain scheduling and errors in the vehicle's attitude and attitude rate. At first glance, this choice of parameters for study may seem somewhat arbitrary, and it is, in the sense that the primary motivation comes from both past experience with similar systems (e. g. , the X-15) and from concern generated by various agencies throughout the many design phases of this program. It suffices to note that these are the parameters under study presently by other workers in this area, and there exists a general consensus as to their importance to vehicle performance. Of course, as designs mature, this preliminary set will expand to cover the more subtle aspects of uncertainties in vehicle configuration and errors in system software.

Accordingly, this section is divided into six subsections. Sections 7.3.1, 7.3.2, and 7.3.3 examine vehicle operation in the presence of center-of-gravity offsets, aerodynamic coefficient variations, and actuator rate limit variations, respectively. Sections 7.3.4 and 7.3.5 then discuss the software problems of errors in both trajectory parameter and vehicle attitude estimation.

Finally, Section 7.3.6 concludes with a brief summary of control system performance in the presence of off-nominal conditions.

7.3.1 Center-of-Gravity Displacements

In all of the above-discussed simulations, the center-of-gravity of the vehicle was located in the longitudinal plane of symmetry and at the "forward" location. Here, both the "aft" center-of-gravity configuration and the lateral asymmetry are investigated as to their effects on vehicle operation.

7.3.1.1 Longitudinal Center-of-Gravity Displacement

The forward center-of-gravity location, used in all of the previous simulations, is associated with the 25,000 lb payload configuration, and commonly referred to as the 66% body length location.[*] Here, the no payload case is simulated, and is associated with an "aft" center-of-gravity location 26 inches behind the forward location, at the 68% body length location. It should be clear that the primary effect of such a rearward CG shift will be to cause a pitch up moment once the dynamic pressure reaches a sufficiently high level, when the aerodynamic effects become significant. However, the body flap (recall its schedule given in Figure 2-6b) is used to provide a compensatory torque via downward deflection, and thus emulate forward CG operation; i.e., the elevator trim location is not significantly changed by the CG shift except late in the entry (this is discussed below). The direct effects on control system operation are illustrated in the next two simulations to be discussed.

Shown in Figure 7-36 are histories of a pitch trim correction performed for the aft CG location, during attitude hold operation ($\alpha_G = 34°$, $\phi_G = 0°$) in the early portion of the entry. During the run,

---

[*]This refers to the relation between longitudinal CG position x_{CG} and the reference length ℓ_B: $x_{CG}^{fwd} = x_o + 0.66\ell_B$, where for this vehicle $x_o = 200''$ and $\ell_B = 1328''$.
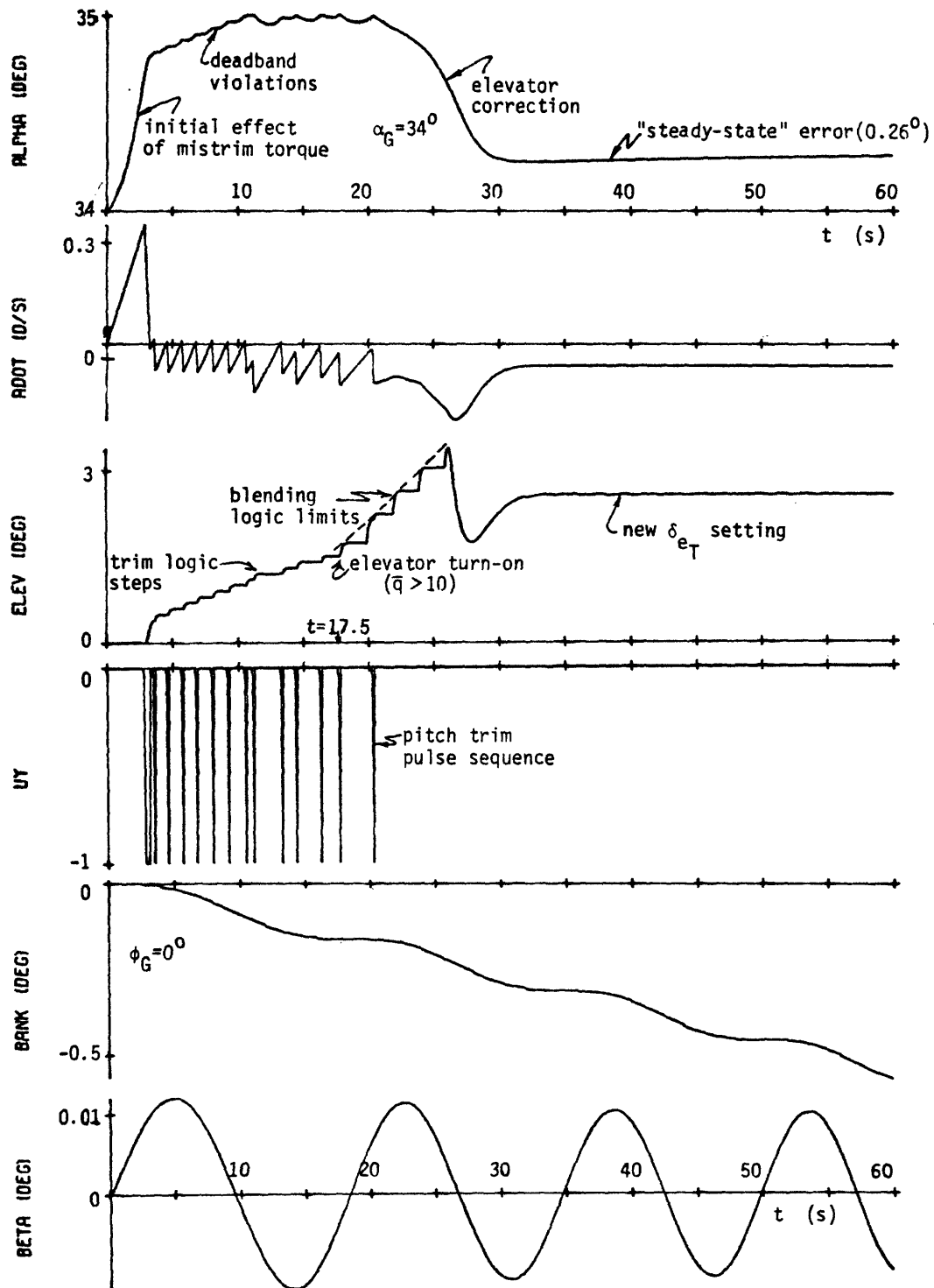
Figure 7-36. Early Entry Trim Correction for AFT CG ($\bar{q}$=7.5→15).

the dynamic pressure increases from 7.5 lbf/ft^2 to 15 lbf/ft^2, so that the initial portion of the run ($\bar{q} < 10$ lbf/ft^2 and t < 17.5 seconds) is characterized by pitch jet firings attempting to trim the vehicle by driving the elevator stepwise to a (down) trim setting appropriate to the aft CG location. Because the run initialization is so close to the 10 lbf/ft^2 mode switch, the proper trim setting is not reached by the time the blending logic begins to allow transient control with the elevator (at t= 17.5 sec). However, the elevator rapidly reduces the angle-of-attack error and simultaneously eliminates the need for any further pitch jet firings. It can be seen that the trim attitude maintained by the elevator is in error by $0.26°$: this, of course is due to the fact that the linear control logic is working about an incorrect trim setting provided by the earlier integration of the pitch jet firings. As seen earlier, this type of steady-state offset will be nulled once the dynamic pressure reaches 20lbf/ft^2, at which point the trim integrator logic of the elevator channel can be activated to correct the trim setting.

Shown in Figures 7-37a and b are histories from a simulation in which an extremely severe pitch mistrim is corrected by the control logic, while executing a bank reversal. Needless to say, the initial mistrim conditions are unrealistic, but serve to illustrate some of the effects of an aft CG location. The initial flight conditions are the same as the previously described Mach 5 run (see text accompanying Figure 7-22): the initial Mach number is 5, the dynamic pressure is 259 lbf/ft^2, and the altitude is 110,000 ft. The initial elevator setting is deliberately mistrimmed by setting it to a value appropriate to forward CG operation at a $20°$ angle-of-attack; the resultant mistrim acceleration due to the actual aft CG location is readily calculated from the following relation:[*]

---

[*] This equation is entirely analogous to (G-2) of Appendix G, relating a lateral CG offset to roll and yaw disturbance accelerations.
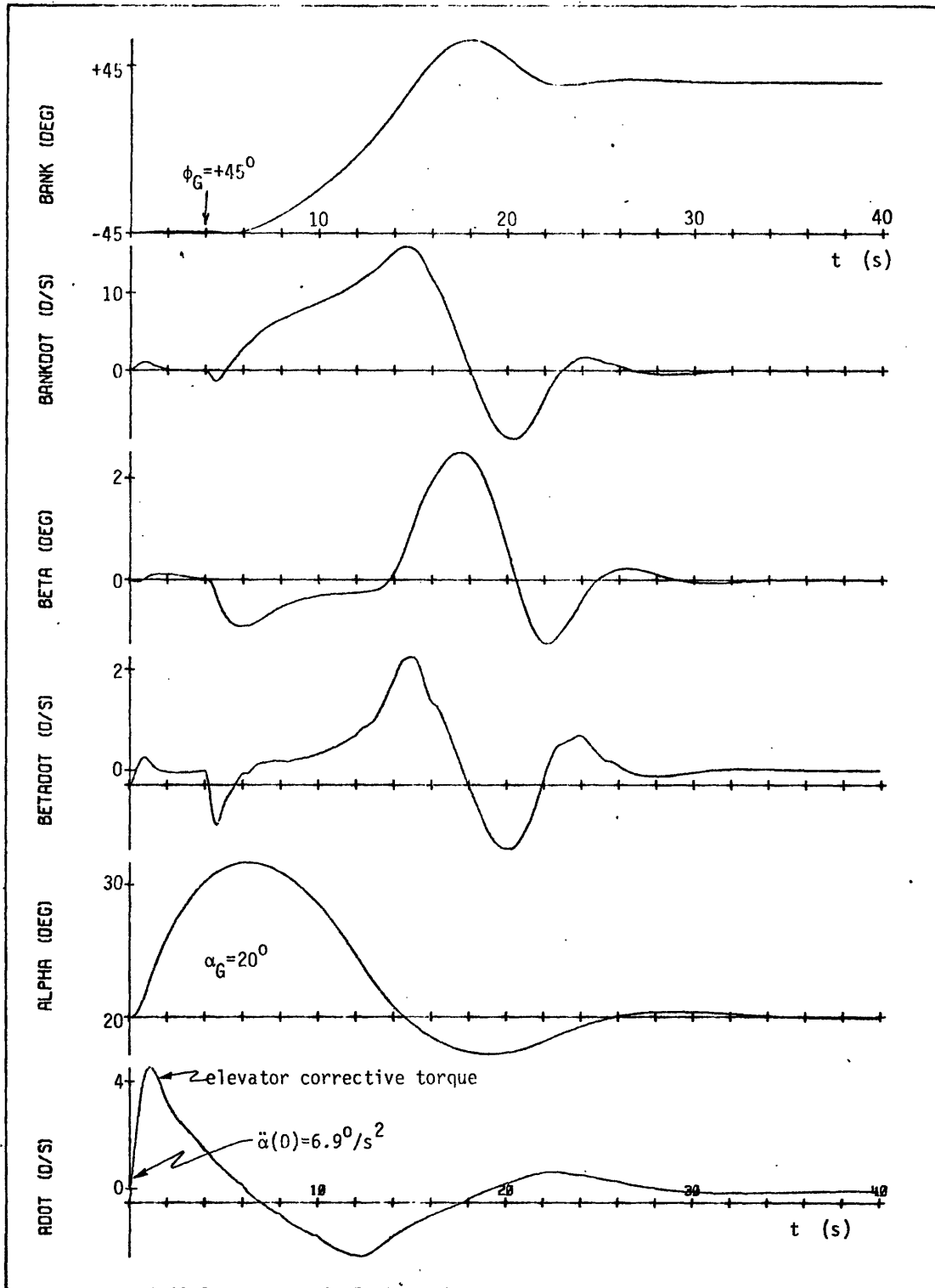
Figure 7-37a. Late Entry Bank Maneuver with Trim Correction for AFT CG (m_i=5, α_G=20°).
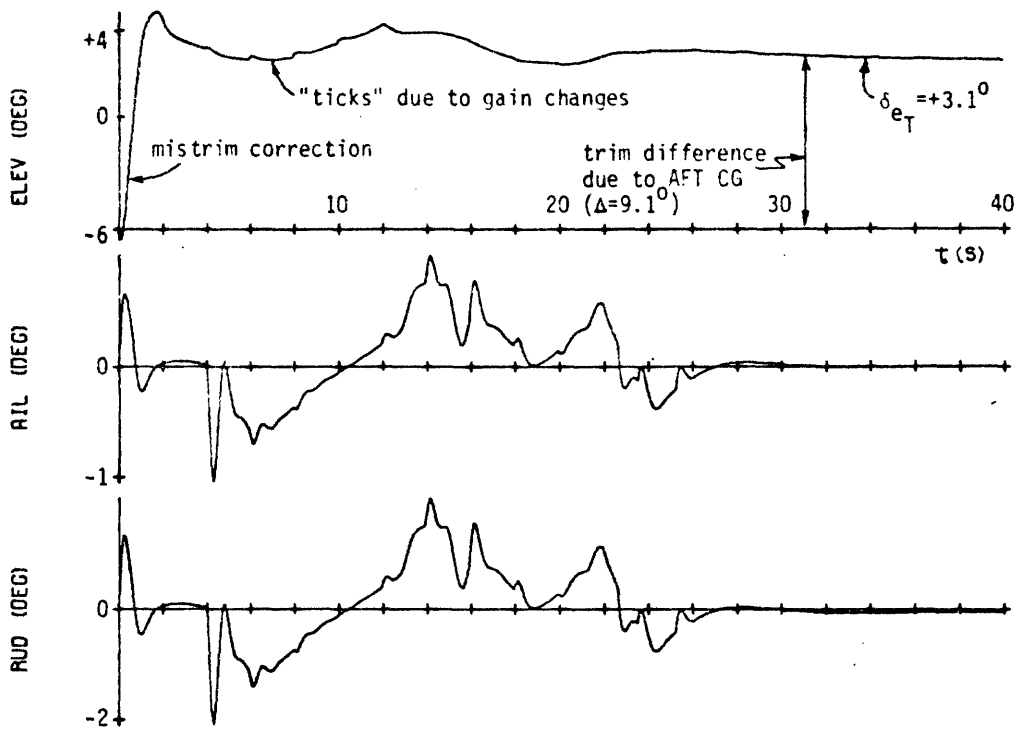
Figure 7-37b. Late Entry Bank Maneuver with Trim. Correction for AFT CG ($m_i=5$, $\alpha_G=20^0$).

$$\ddot{q}_{CG} = \frac{\overline{q} S \ell}{I_{yy}} C_N \qquad (7\text{-}20)$$

where ℓ is the 26-inch moment arm and C_N is the normal force coefficient. Thus, the initial pitch up acceleration is approximately $6.9°/\sec^2$, a sizeable disturbance which elicits a rapid corrective elevator transient. The trim integrator then slowly correct the residual angle-of-attack error, which is quite sizeable due to the initial severe mistrim conditions. It should be recognized that the final trim setting reached by the elevator (actually, a slowly changing "trim" due to the slowly decreasing Mach number) is approximately 9 degrees down from the setting appropriate to the forward CG location. The reason for this deviation can be seen in the schedule of Figure 2-7: the body flap schedule below Mach 6 is the same for both forward and aft CG operation, and thus differences in CG locations must be compensated for entirely by trim elevator setting. The implications of down elevator (for the aft CG configuration) on lateral controllability will be noted shortly.

While the longitudinal logic is attempting to recover from the initial mistrim, the lateral logic receives a reversal command at t= 4 seconds, initiating the familiar sequence of initial reverse aileron followed by compensation to damp the generated sideslip. In this case, however, the bank rate fails to level off as in previous runs (at approximately 8 deg/sec) but continues to grow until the control logic provides the commands to stop the maneuver at the target attitude. Naturally, because of the large bank rate, the control system must generate a large sideslip to provide an opposing bank torque, adding to the overshoot seen in the bank rate history. The cause of this entire sequence is, of course, the large variation in the angle-of-attack while the bank maneuver is being conducted, strongly compromising the accuracy of the lateral model used in the design synthesis. It should be clear that this type of bank maneuver

performance is atypical of aft CG operation, and is due solely to the artificially induced pitch mistrim. In fact, the several simulations which have been conducted with a properly trimmed aft CG show lateral performance to be very similar to that already extensively discussed in the previous section, with the forward CG configuration.

It is appropriate here to comment on the effect the aft CG location has on the flight envelope lower bound, the contour having already been defined for the forward CG case in Figure 7-31. It was noted above that the aft CG location induces a corrective down elevator trim setting, with respect to that required for forward CG operation. This, in turn, provides for greater aileron effectiveness (see, for example, the dependence of aileron roll effectiveness on elevator trim setting as given by the aerodynamic data of Reference 2), which contributes to the lateral controllability of the vehicle at a given Mach number and angle-of-attack (recall the controllability coefficient definitions of Section 5.2.2.1). Thus aft CG operation should provide a greater region of controllability in the $\mathcal{M}/\alpha$ plane, by pushing the envelope contour further in the direction of low Mach number and low angle-of-attack operation. Although extensive testing, comparable to that associated with the forward CG location, has not been conducted for the aft CG configuration, several "spot-check" simulations have verified that an increased regime of controllability is indeed the situation. Of course, the associated contour is irrelevant to flight envelope definition, since the limiting case is clearly associated with the forward CG location. The point of this, however, is that the dual control overlap region defined in Figure 7-33 is not subject to "shrinkage" due to an aft CG location[*].

7.3.1.2 Lateral Center-of-Gravity Displacement

In the simulations discussed previously, the center-of-gravity was always located in the vehicle's plane of symmetry; here, the

---

[*]This, of course, assumes that the conventional control boundary is unaffected by CG location. More work is clearly required in this area.

375

simulations to be discussed will be concerned with the effect of a two-inch positive lateral offset (i.e., out the right wing), and the required corrections provided by the control system. It may be recalled from the discussion given earlier in Section 5.2.2.2.3 that the primary effect of such a lateral CG offset shows up as an asymmetric lateral trim, so that the vehicle is held at a non-zero sideslip by a non-zero aileron deflection. This is, of course, assuming that the control system can "find" the proper trim setting. The simulations described below all illustrate system operation in the presence of a two-inch positive offset[*]:   two during early entry, and two later in the transition profile.

The histories from the first early entry run, illustrating attitude hold operation, are shown in Figures 7-38a and b, with initial flight conditions identical to the run described earlier and illustrated in Figures 7-5a and b; it suffices to recall that the dynamic pressure is quite low, initially 0.01 lbf/ft^2 and slowly increasing to 0.16 lbf/ft^2. Here, of course, the lateral CG offset makes its presence known by the increasing slope of the sideslip rate profile, indicating a non-zero sideslip acceleration, which, in turn, is due to the mass asymmetry (compare with the rate history given in 7-5a). Since this acceleration is proportional to dynamic pressure, the effects of the asymmetry are small, and the time histories are dominated by the characteristic limit cycle operation of the roll jet logic (see Figure 7-38b). Although the pulse history appears to be similar to the symmetric firings seen in the no offset case (see Figure 7-5b), the aileron history uncovers the basic difference: asymmetric firings and a trim aileron setting tending to some non-zero value (recall that the aileron trim logic during this regime merely integrates the roll jet firings to determine the commanded deflection). To see

---

[*]As noted in Chapter 2, this value is the current estimate of the maximum CG asymmetry anticipated. Also, it should be noted that the CG is located forward.
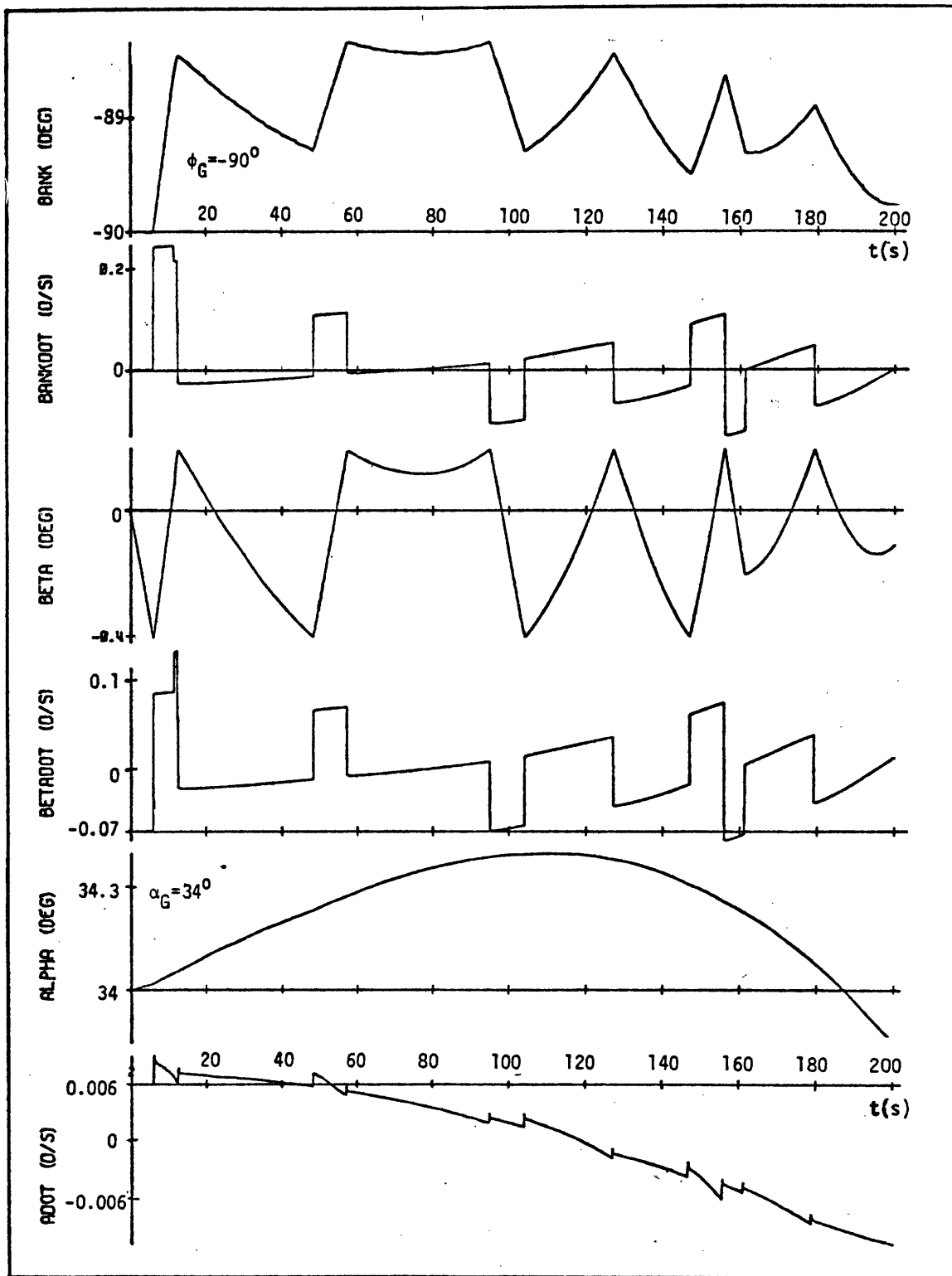
Figure 7-38a. Early Entry Lateral Trim Operation with $\ell=2"$ ($\bar{q}=0.01\rightarrow0.16$).
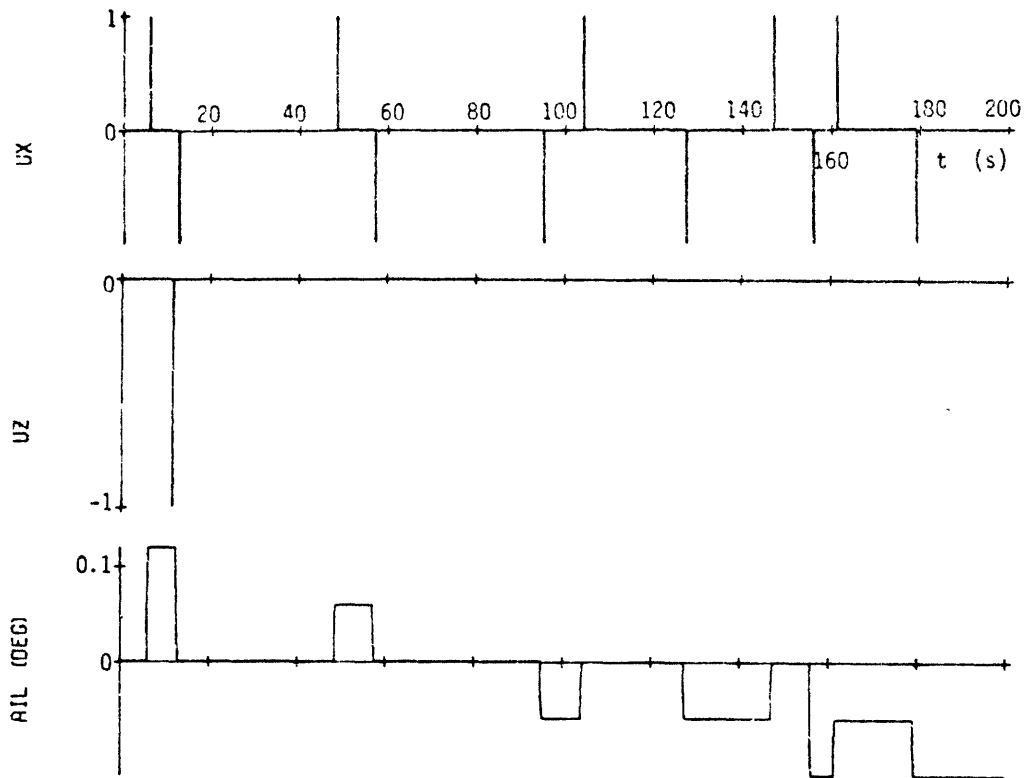
Figure 7-38b.   Early Entry Lateral Trim Operation with $\ell=2"$
($\bar{q} = 0.01 \longrightarrow 0.16$)

that the trim logic is converging on the proper trim setting for the two-inch offset, it is necessary to observe operation at slightly higher dynamic pressures.

Shown in Figures 7-39a and b are histories from a second early entry simulation, again illustrating attitude hold in the presence of a two-inch lateral offset. The initial flight conditions are identical to the run described earlier and illustrated in Figures 7-13a and b. It may be noted here that the dynamic pressure grows from an initial value of 0.5 lbf/ft^2 to greater than the maneuver mode switch value of 80 lbf/ft^2; thus, the early control mode switches are all present in this simulation. Many features of this simulation have already been discussed, so that only those aspects related to lateral control of the CG asymmetry need be of concern here. Specifically, it can be seen that the early sideslip rate history is characterized by a sawtooth waveform, the up slopes due to the offset induced body torques and the down slopes due to corrective pulses furnished by roll jet firings (see Figure 7-39b). In effect, the attitude hold mode of the roll jet logic (effective below $\bar{q} = 5$ lbf/ft^2) is preventing the vehicle from trimming to its preferred non-zero sideslip, given by (5-66a) of Chapter 5:

$$\beta_T^{OL} = \left(\frac{\ell}{b}\right)\left(\frac{I_{zz}}{I_{xx}}\right)\left(\frac{C_N}{C'_{n_\beta}}\right) \sin \alpha_T \qquad (5-66a)$$

where, here, both coefficients are positive, so that the positive offset results in the trim tendency seen in the sideslip history. The resultant roll jet pulse sequence causes the aileron to gradually approach a negative trim setting, appropriate to the predicted negative value given by (5-68b) of Chapter 5:

$$\delta_{a_T} = -\left(\frac{\ell}{b}\right) \frac{C_N C_{n_\beta}}{C_{n_\beta} C_{\ell_{\delta_a}} - C_{\ell_\beta} C_{n_{\delta_a}}} \qquad (5-68b)$$

379
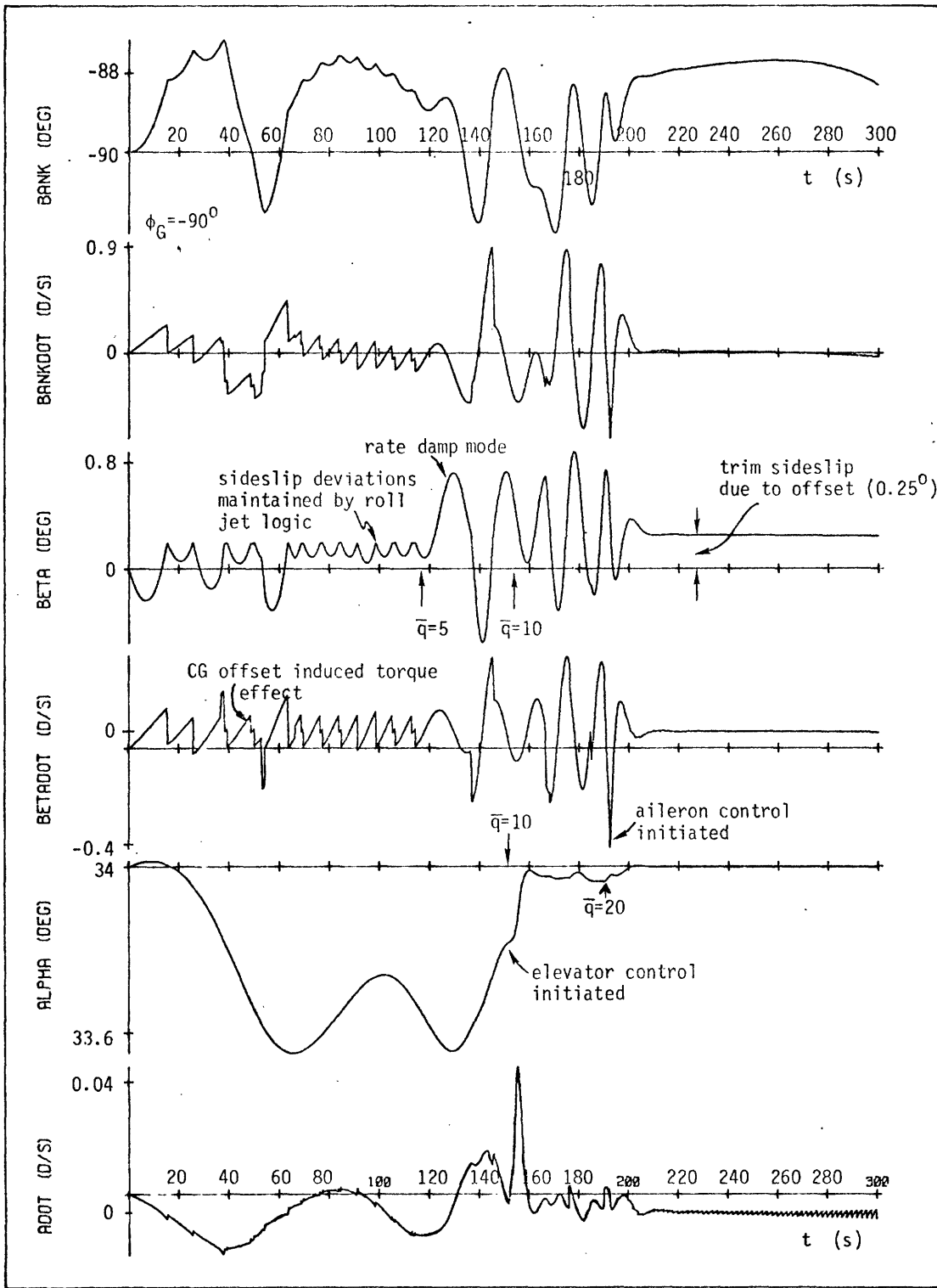
Figure 7-39a. Mode Switching and Lateral Trim Operation
with ℓ=2" (q̄=0.5 → 128).

380
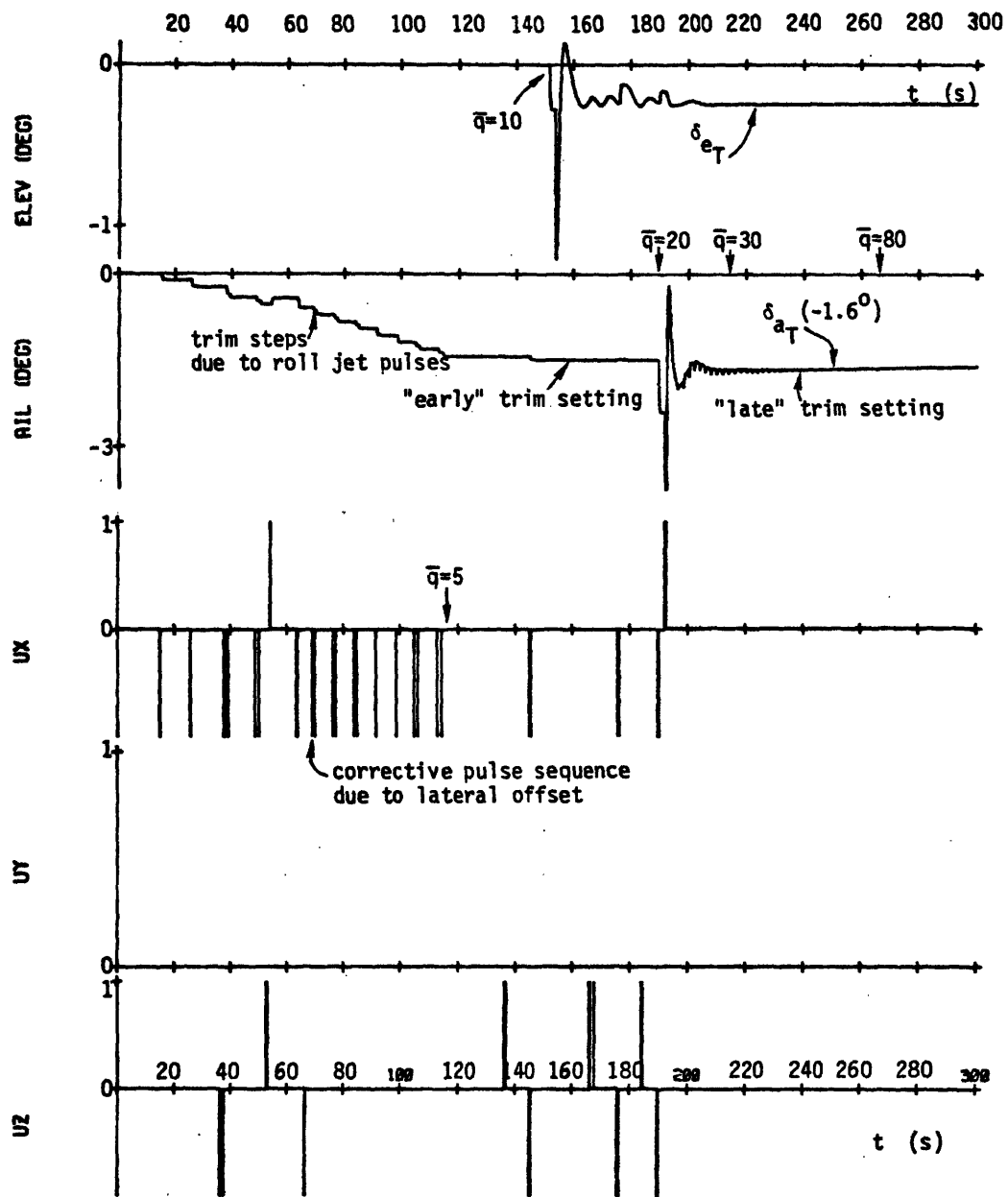
Figure 7-39b. Mode Switching and Lateral Trim Operation with ℓ=2" (q̄=0.5 ÷ 128).

where the fractional coefficient term is positive. Before this setting is reached, however, the dynamic pressure crosses the $5\,\text{lbf/ft}^2$ mode switch threshold, so that the roll jet logic no longer attempts to maintain attitude but simply rate damps the sideslip oscillations. This of course allows the vehicle to oscillate about the CG induced non-zero trim sideslip, while dramatically reducing the roll jet pulse frequency. When the dynamic pressure exceeds the second lateral mode switch point at $20\,\text{lbf/ft}^2$, the aileron is turned on and rapidly damps out the oscillations tolerated by the ACPS deadband logic, eventually arriving at a trim setting slightly different from the "early" setting obtained by integrating the roll jet pulses. This difference accounts for the small "bumps" in the aileron history shortly after turn-on; once the dynamic pressure exceeds $30\,\text{lbf/ft}^2$ the trim integrator logic corrects the trim setting discrepancy and this type of aileron activity disappear shortly thereafter. It should be noted that the trim aileron/sideslip pair of $(-1.6°, 0.25°)$, arrived at by the lateral logic, allows the bank attitude to "hang" approximately one degree away from the commanded attitude; this, of course, is a consequence of the bank rate being used in the trim integrator logic, as opposed to a conventional integration of attitude error.

The next two simulations to be discussed illustrate CG offset trim correction considerably later in the entry. The first set of histories are shown in Figure 7-40 which illustrates a maneuver sequence conducted at an initial Mach number of 5, dynamic pressure of $259\,\text{lbf/ft}^2$, and angle-of-attack of $20.7°$ (see text accompanying Figure 7-22 for the description of a comparable nominal run). Here it can be seen that the aileron initially responds quickly to the CG offset induced sideslip deviation thus approximating the required trim setting at the expense of tolerating some drift in the bank axis. This would have eventually been corrected for by the trim integrator logic, but at t = 4 seconds a reversal is commanded, resulting in the
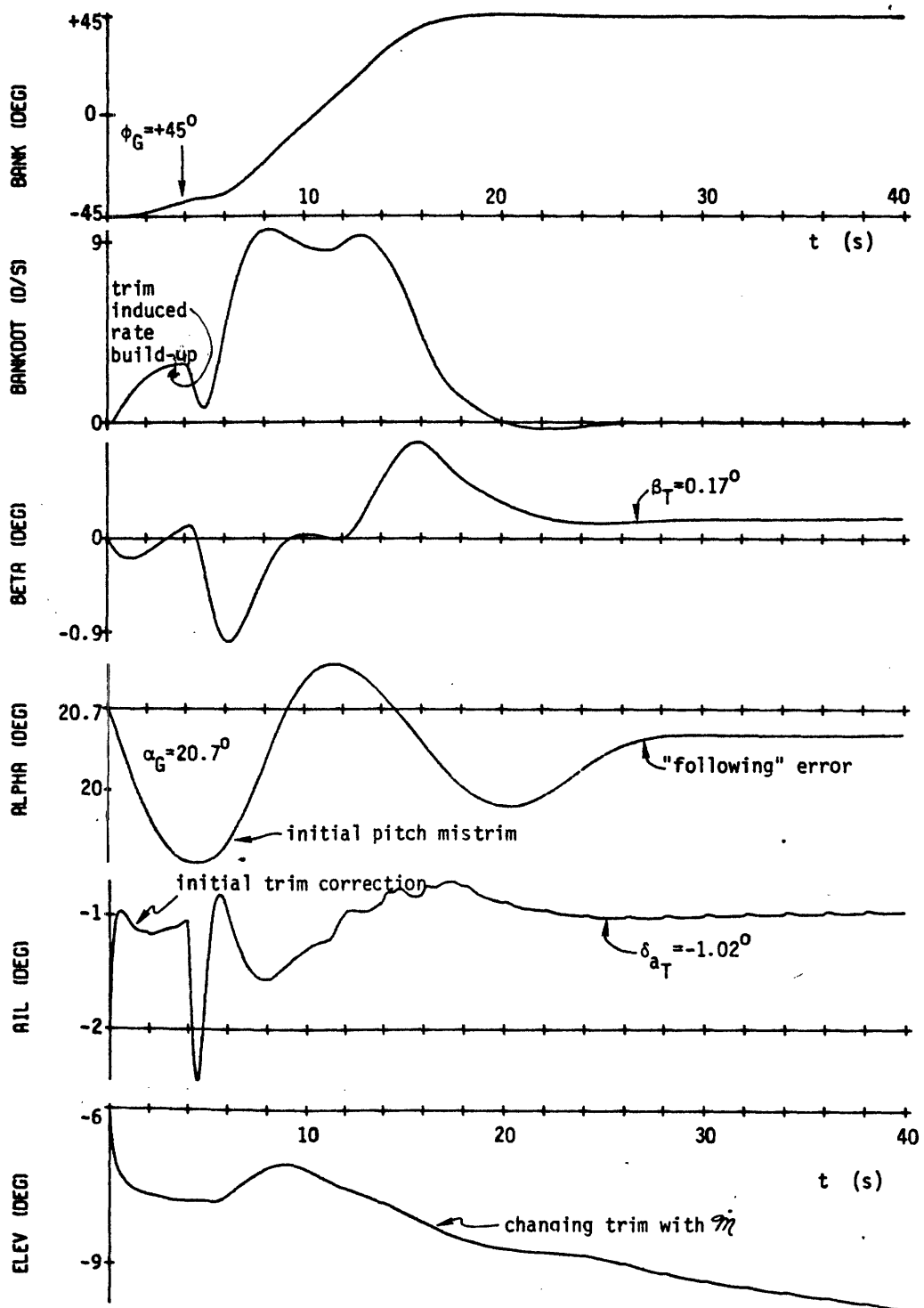
Figure. 7-40. Bank Maneuver at $\mathcal{M}=5$, $\alpha_G=20.7°$, with Lateral Offset, $\ell=2"$.

aileron transient necessary to initiate the maneuver. A comparison
with the same simulation with no offset (histories shown in Figure
7-22) shows that the maneuver bank rate reached here is almost 30%
higher (9.5°/sec peak rate verses 7.5°/sec peak rate), clearly a
direct effect of the mistrim torque adding in the direction of the
desired maneuver, and due to the fact that insufficient time was allowed
for the trim logic to attain the desired trim setting. After completion
of the maneuver, a trim state is attained with less than 0.2° sideslip
and 1° aileron (the rudder setting, not shown, is simply twice that
of the aileron due to the constant crossfeed gain). Thus, except
for the higher bank rate due to the inadequate interval alotted for
trim correction, the maneuver is performed in a manner quite
similar to that seen in the no offset case.

This similarity in performance between offset and no offset
cases is typical of operation throughout this transition portion of
the entry. It should be recognized that any tendencies toward an
inability to trim out the offset closely parallels a tendency towards
uncontrollability in the lateral channel. That this should be so can
be seen by combining the equation defining the required trim aileron,
(5-68b), with the equation defining the controllability coefficient
$\tilde{\pi}_1$, (5-46), so that:

$$\delta_{a_T} = - \left(\frac{\iota}{b} \right) \frac{C_N C_{n_\beta}}{\tilde{\pi}_1} \tag{7-21}$$

Thus, as the controllability approaches zero (as it does as seen by
the contour gradients of Figure 5-14), the required trim deflection
grows larger and eventually exceeds the surface limits. That the
converse is true is more difficult to show, but simulator experience
has shown that when the vehicle is maneuvered in the "controllable"
region of the $\mathcal{M}/\alpha$ plane (recall Figure 7-33) then the required trim
deflection is well within the allowable travel of the aileron (and
rudder). An example of this behavior is seen in the histories of

Figure 7-41, in which a simulated reversal sequence is conducted down the nominal transition profile, with a two-inch CG offset present. As in the simulation just described, the initial Mach number is 5 and the dynamic pressure is 259 lbf/ft^2, and as with the case in which nominal operation was simulated (recall text accompanying Figures 7-30a and b), the angle-of-attack command is stepped to follow the nominal profile, while the bank command is periodically reversed to test maneuver operation. Two observations are particularly appropriate here. First, the change in the trim sideslip and corresponding trim aileron deflection is relatively slow, and thus there is little difference in the trim settings between the initial and final flight conditions ($\Delta \delta_{a_T} = 0.70°$)[*]. Second, the rapid changes in the aerodynamic coefficients occuring in the last 20 seconds of the run quickly degrade the controller's performance, in a manner almost identical to that observed in the no offset case (compare the aileron history with that shown in Figure 7-30b). Thus, because of both the small trim aileron deflections required and the eventual loss of adequate maneuver performance independent of the trim situation, it should be clear that the presence of the lateral offset has no significant effect on the determination of the ($\mathcal{M}, \alpha$) point at which performance is no longer satisfactory. Although extensive testing has not been conducted, it would appear that a similar situation occurs for other profiles "flown" through the lower portion of the flight envelope. Thus, the lower bound of the flight envelope, given in Figure 7-33, appears to be relatively insensitive to the presence or absence of reasonably-sized lateral CG offsets.

7.3.2 Variations in Aerodynamic Coefficient Values

The purpose of this section is to provide some insight into system operation in the presence of off-nominal variations in the

---

[*]Note that the trim aileron requirements decrease in this case, primarily because C_{n_β} approaches zero and cancels the effect of π_1, also approaching zero (recall the relation given by (7-21)).
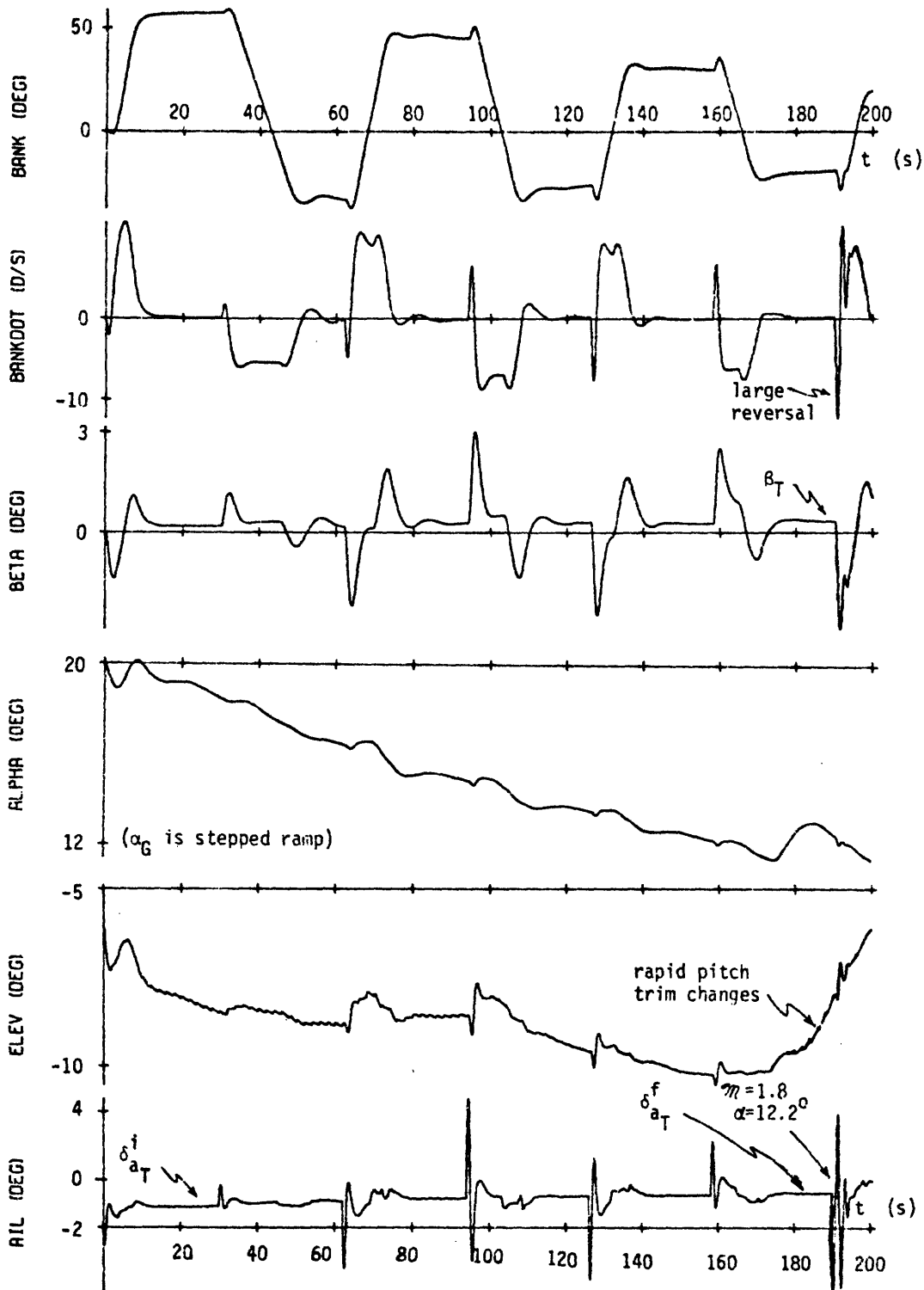
Figure 7-41.　Response Along Nominal Transition Profile with 2" Lateral Offset $(\mathcal{M}_i=5,\ \bar{q}_i=259\ \mathrm{lbf/ft}^2$.

vehicle's aerodynamic coefficient values. The material presented here addresses only a very small portion of the overall problem of aerodynamic variations, simply because of the magnitude of the effort required for a definitive analysis. To gain some appreciation of the problems involved, consider the table of variations given in Table 2-7 of Chapter 2. As has already been noted, there are two basic types of variations: a "known" possible variation from the present data book values to those values associated with the final design, reflecting design changes, and an "unknown" possible variation (an uncertainty) due to inaccuracies in predicting the actual coefficients of the vehicle. Both are given in terms of percentages of the nominal coefficient values, and an additional "delta" is specified for the type of variation due to design changes. With 13 coefficients in the table, an unsophisticated parameter study is thus 39-dimensional. This, of course, is for one flight condition, hypersonic at a 30° angle-of-attack; the multiplicity clearly becomes enormous if different variational data is specified for other flight conditions (as it is for several of the coefficients at Mach 2). It should also be recognized that because of the uncertainty in the accuracy of these variational estimates, any such parameter study is subject to constant changes in the search space, due to continuing revisions of the estimates. Finally, even if the coefficients should become well-defined, with a high degree of confidence attached to the values, it is not at all obvious how the variations should be "stacked". A "worst-case" combination is most likely too conservative, since the coefficients are clearly coupled through the vehicle's fundamental mass and geometric properties; however, the uncertainties involved in defining the coupling relationships would no doubt cast suspicions on the conclusions drawn from any "non-worst-case" stacking of the variations.

Clearly, a definitive treatment of this problem will not be attempted here. Instead, a simplified approach will be used, by greatly restricting the dimension of the parameter space, in the following manner. First, only uncertainties in the coefficient values will be considered, and these taken about the nominal coefficient values documented in reference 2.

If variations due to design changes were to be considered, it would be necessary to change the control law gain schedules accordingly, since the only fair test of the system would be to take advantage of these "known" variations. Gain schedule variations naturally act to increase the parameter test space, and this is not desired. Second, only those uncertainties associated with torque coefficients will be considered, and of these, uncertainties in the pitch moment coefficient will be neglected. The omission of the translational coefficient uncertainties ($\Delta C_{\mathscr{L}}$, ΔC_D, etc.) is justified by recognizing, from the simplified model of Chapter 4, that the important rotational model parameters are independent of the translational coefficients. The omission of the pitch moment coefficient uncertainty (ΔC_{M_0}) is justified by the observation that the effect of such an uncertainty can be approximated by a longitudinal center-of-gravity shift, and the sensitivity of system operation to such a shift has already been described in the previous section. To see this, it may be recognized that an axial CG displacement gives rise to a change in the pitch moment according to the following relation:

$$\Delta C_M = \frac{\Delta x_{CG}}{\bar{c}} C_N \tag{7-22}$$

where ΔC_M is positive if Δx_{CG} is in the aft direction (negative in the body-axis frame). For example, at Mach 5 at an angle-of-attack of 20 degrees, $C_{M_0} \approx -0.016$, so that by the above relation, a 10% variation in C_{M_0} is equivalent to a longitudinal CG shift of less than 2 inches. Clearly, this figure will vary as the vehicle's pitch characteristics change through the entry, but it is felt that the basic sensitivity to pitch moment coefficient uncertainties can be readily inferred from the previous discussion of longitudinal CG displacement effects.

The two restrictions just described limit the parameter set to variations in the sideslip derivatives, C_{n_β} and $C_{\mathscr{L}_\beta}$, the aileron derivatives, $C_{n_{\delta a}}$ and $C_{\mathscr{L}_{\delta a}}$, and the rudder derivatives, $C_{n_{\delta r}}$ and $C_{\mathscr{L}_{\delta r}}$. A third simplification is possible, by making use of the previously described controllability coefficients described in Section 5.2.2.1. Specifically, it

should be recalled from (5-45) that lateral controllability with the surfaces requires that the two coefficients, $\tilde{C}'_{n_{\delta a}}$ and $\tilde{\pi}_1$, be non-zero; more to the point here, it should be recognized that any <u>aerodynamic</u> coefficient change, which drives one or both of these controllability coefficients towards zero, can be identified as a deleterious coefficient variation. Thus, with the objective of further reducing the parameter search space, an approximate "worst-case" stacking of the coefficient variations can be determined by examining the effect on the controllability coefficients. The derivation details are given in Appendix K; a summary of the results of this derivation is given in Table 7-5 which shows the sign of the variation of each aerodynamic coefficient nexessary to drive either one of the two controllability coefficients to zero. It should be noted that this is only a first-order approximation derived for the nominal pitch profile of late entry. Even so, it is complicated by the fact that a variation in an aerodynamic coefficient may not necessarily drive both controllability coefficients to zero, and by the fact that the surface roll derivatives are dependent on Mach number for their effect on $\tilde{\pi}_1$. This has proven to be a useful guide, however, in preliminary simulations of system sensitivity to coefficient uncertainties.

Table 7-5: Required Coefficient Variations to
Degrade Lateral Controllability

Effect / Coefficient	$\tilde{C}'_{n_{\delta a}} \to 0$	$\tilde{\pi}_1 \to 0$
$C_{n_{\delta a}}$	$\Delta > 0$	$\Delta > 0$
$C_{n_{\delta r}}$	$\Delta > 0$	$\Delta > 0$
C_{n_β}	-	$\Delta > 0$
$C_{\ell_{\delta a}}$	$\Delta < 0$	$\Delta < 0 \ (M \gtrsim 2.8)$
		$\Delta > 0 \ (M \lesssim 2.8)$
$C_{\ell_{\delta r}}$	$\Delta < 0$	$\Delta < 0 \ (M \gtrsim 2.8)$
		$\Delta > 0 \ (M \lesssim 2.8)$
C_{ℓ_β}	-	$\Delta > 0$

389

The simulation results to be described below illustrate the effects of such coefficient variations on system performance. In keeping with the percentage error specifications given earlier in Chapter 2, the variations are implemented on the simulator via a fractional perturbation of the nominal aerodynamic coefficient values. With no knowledge of such perturbations, the control system provides no open-loop compensation, such as would be effected by gain schedule adjustments; thus, the simulator variations can be viewed functionally as aerodynamic coefficient uncertainties, and the results indicative of performance in such an environment. Four simulations are described below, all illustrating bank reversal performance down the latter half of the transition profile, with the forward CG vehicle configuration.

Shown in Figure 7-42 are bank, sideslip, and aileron histories from two different simulations: the upper three histories are repeated from the previously described simulation of transition performance under nominal conditions (recall text accompanying Figure 7-30), while the lower three histories illustrate performance when the dihedral coefficient, C_{l_β}, is increased (i.e., made less negative) by 20%, throughout the flight envelope. As may be recalled, initialization is at a Mach number of 5, a dynamic pressure of 259 lbf/ft^2, and an altitude of 110,000 ft; by the end of each run, the Mach number is down to 1.6, the dynamic pressure level is approximately 150 lbf/ft^2, and the altitude is slightly above 73,000 ft. Since the change in C_{l_β} is in the direction to degrade system performance, it would be expected that a comparison of the histories would uncover performance differences; this is not the case here, as can be seen from a close inspection of the traces. This is due to two reasons: first, the last bank maneuver is performed at the same point in each trajectory, so that a possible shift (upward) in the envelope boundary might not be detectable; and second, the closed-loop performance is simply not sensitive to small variations in C_{l_β}.

A second example, this time of enhanced performance, is shown in Figure 7-43. Here, the nominal run is compared with a run in which the <u>sign</u> of $C_{n_{\delta_a}}$ was reversed throughout the entire maneuver sequence.

390
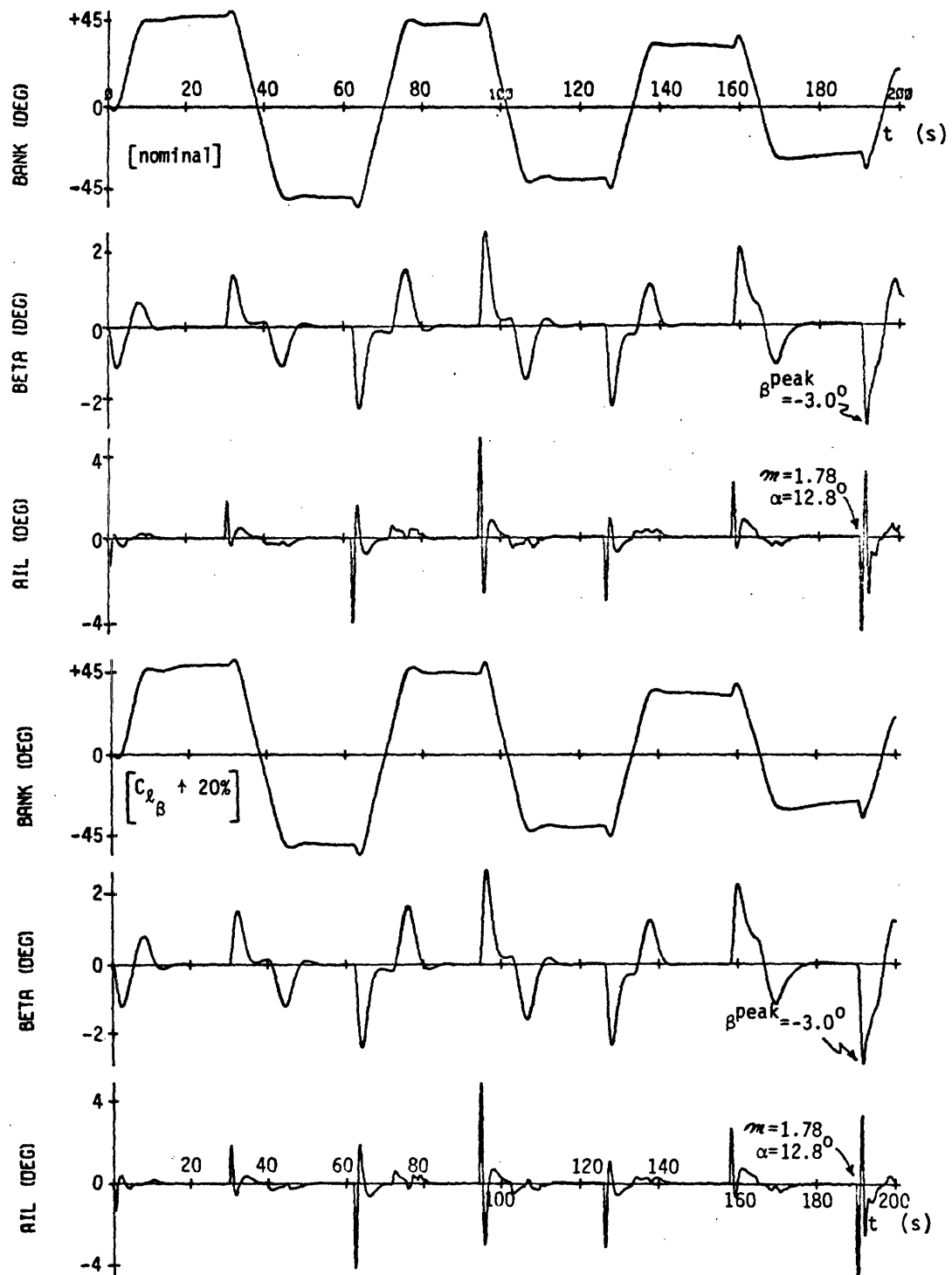
Figure 7-42.   Nominal Transition Performance vs. Performance
with C_{ℓ_β} Increased by 20%
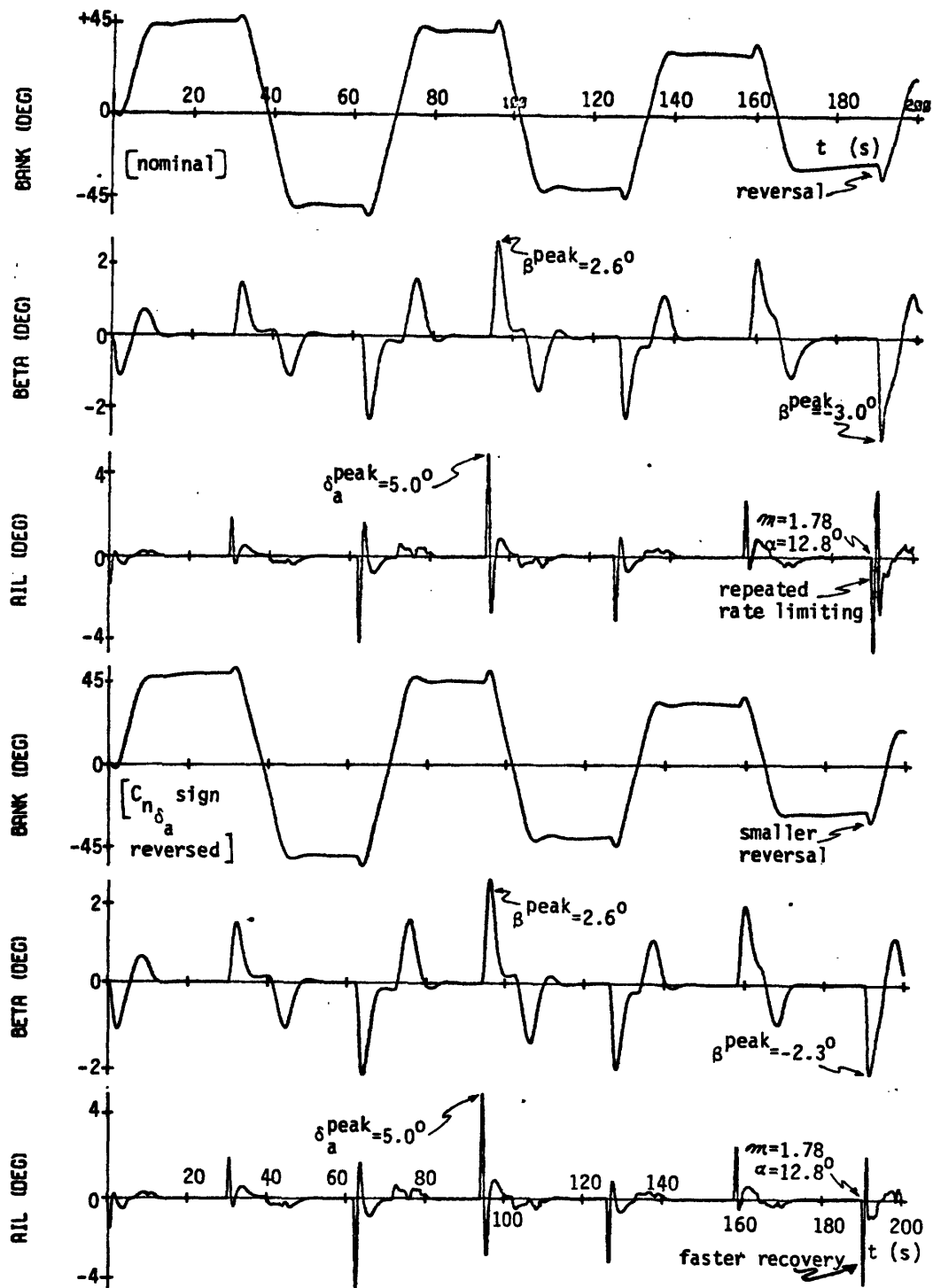
Figure 7-43. Nominal Transition Performance vs Performance with a Sign Reversal in $C_{n_{\delta_a}}$.

392

It may be noted from the aileron coefficient history, given in Figure K-1 of Appendix K, that $C_{n_{\delta_a}}$ is positive for Mach numbers less than 2.8; thus, from Table 7-5 a change of sign will drive both controllability coefficients away from zero, and thus improved performance should result. This is the case here, as can be seen by the successful completion of the final bank maneuver, an unaccomplished task with the nominal adverse aileron coefficient.

A third example is given in Figure 7-44, this time of degraded system performance in the presence of an adverse variation in $C_{n_{\delta_a}}$. Here, the nominal coefficient value is tripled, so that near the end of the run $C_{n_{\delta_a}}$ is quite positive, and thus, by Table 7-5, should result in poorer maneuver performance. This, of course, is the case, but the performance degradation is not quite as dramatic as might be inferred from a first glance comparison of the two simulations. In fact, the only basic effect of the $C_{n_{\delta_a}}$ variation is to make the control system incapable of recovering from the last initiated bank maneuver, a maneuver which was poorly executed under nominal conditions in any case. Thus, if the limits of the flight envelope of Figure 7-33 had been properly observed in these two simulations, the last bank maneuver would not have been attempted, and no discernable differences in the two maneuver histories would have been apparent. Stated slightly differently, the $C_{n_{\delta_a}}$ variation changes the path of system divergence, but not its onset point.

It should be recognized that the two simulations just described illustrated system performance with ±200% uncertainties in the adverse aileron coefficient, and yet the system's maneuver capability was, for practical purposes, unaffected. This is clearly at odds with the oft-stated misconception that the reverse aileron control technique is "dependent on accurate knowledge of yaw due to aileron deflection" (see, for example, reference 6). In fact, the technique is not, and a quick review of the simplified vehicle equations (see (4-49) and (4-50)) will show that this body-axis coefficient only enters into the dynamics through a small inertial coupling term, which greatly attenuates its variational effects. As noted earlier, the control technique is dependent primarily

BANK (DEG)

+45

20 40 60 80 100 120 140 160 180 200

0

t (s)

[nominal]

-45

BETA (DEG)

2

$\beta^{peak}=2.6^o$

0

-2

$\beta^{peak}=-3.0^o$

AIL (DEG)

4

$\delta_a^{peak}=5.0^o$

$m=1.78$
$\alpha=12.8^o$

0

recovery from
rate limiting

-4

BANK (DEG)

45

0

$[C_{n_{\delta_a}}$ tripled$]$

-45

BETA (DEG)

10

$\beta^{peak}=2.6^o$

0

$\beta^{peak}=-3.9^o$

-10

AIL (DEG)

10

$m=1.78$
$\alpha=12.8^o$

$\delta_a^{peak}=5.0^o$

20 40 60 80 100 120 140 180 200

0

160

no recovery
from maneuver

t (s)

-10
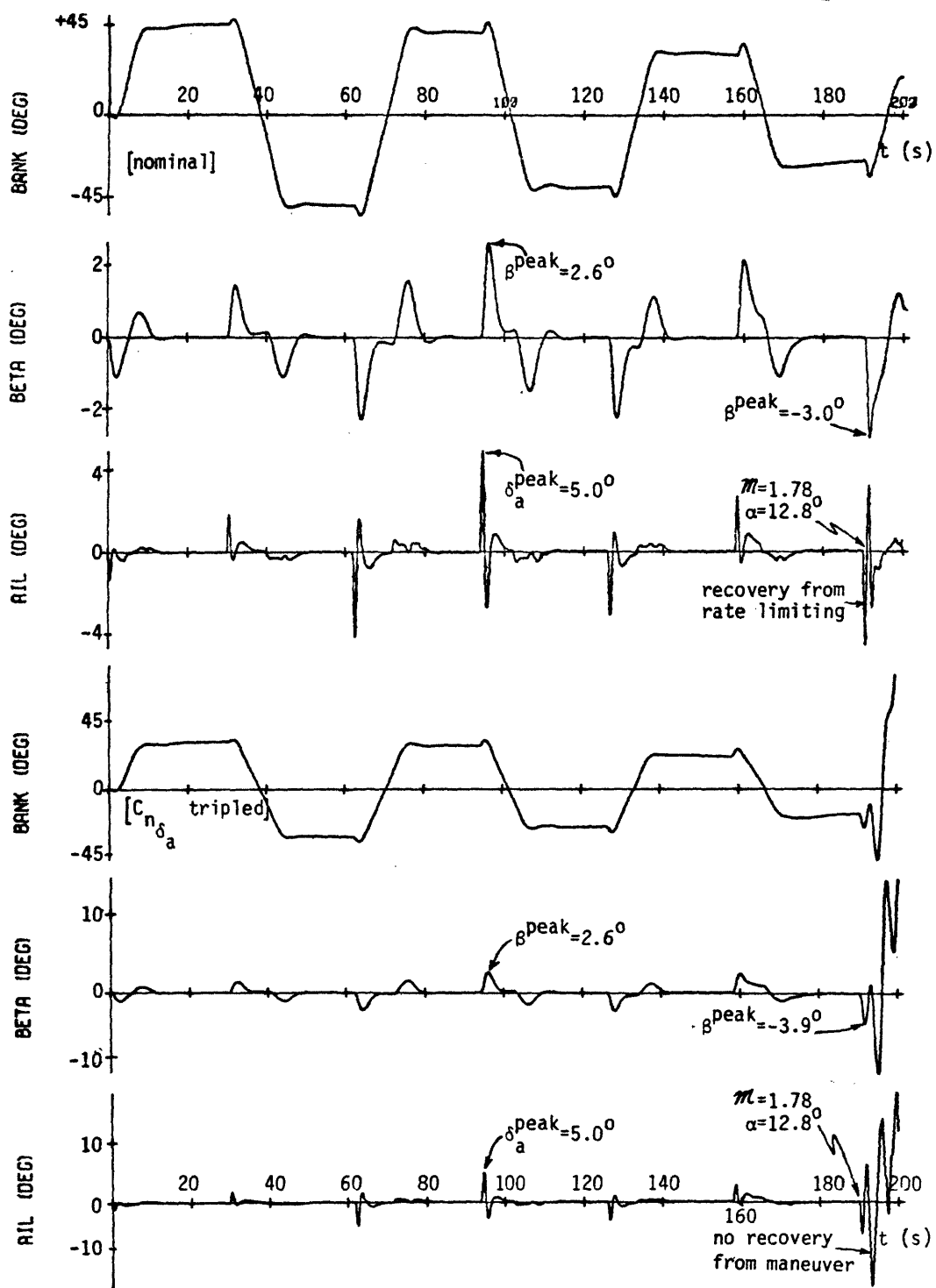
Figure 7-44. Nominal Transition Performance vs. Performance
with $C_{n_{\delta_a}}$ Tripled in Value.

394

on the dihedral coupling of sideslip into bank, and the fundamental in-
sensitivity to values of $C_{n_{\delta_a}}$ is borne out by the above two simulations.

The final simulation results to be discussed illustrate performance
with a "stacked" set of coefficient variations. The histories are given in
Figure 7-45, and again are compared with the nominal case illustrated
in Figure 7-30. In this case, the stacking of the variations was as
follows:

$$C_{n_\beta} + 25\%; \quad C_{\ell_\beta} + 20\%; \quad C_{n_{\delta_a}} + 200\%; \quad C_{\ell_{\delta_a}} + 20\%; \quad C_{n_{\delta_r}} + 20\%; \quad C_{\ell_{\delta_r}} + 20\%$$

$$(7-23)$$

where ↟ indicates a <u>positive</u> increment to the nominal value, and the
percentage indicates the magnitude of the increment with respect to the
coefficient's nominal value (at any given flight condition). As can be
seen by reference to Table 7-5 this is one possible "worst-case" stack-
ing, although others are clearly possible. As with the $C_{n_{\delta_a}}$ variation
case just discussed, the observed performance degradation is not quite
as dramatic as might be inferred from a quick glance at the histories;
again, the primary effect is a failure to recover from a maneuver
initiated at the edge of the nominal flight envelope. In addition, however,
it can be seen that the bank command tracking ability (recall that the
command magnitude is gradually decreasing) begins to degrade at ap-
proximately t = 180 seconds, with a series of high frequency aileron
commands. In keeping with the guidelines used to define the lower
bound of the entry envelope, this "stacked" case clearly indicates a
shift (upward) of the envelope boundary, at least in the neighborhood of
the nominal transition profile. Because of the preliminary nature of
this testing, performance along other $\mathcal{M}/\alpha$ profiles has not been investi-
gated and thus the total contour shift has not been determined; however,
with the perhaps naive assumption that system performance is equally
sensitive to these variations throughout the envelope, then a speculative
envelope boundary may be drawn as shown in Figure 7-46, illustrating
the shift due to this stacked case, and the resultant "shrinkage" of the
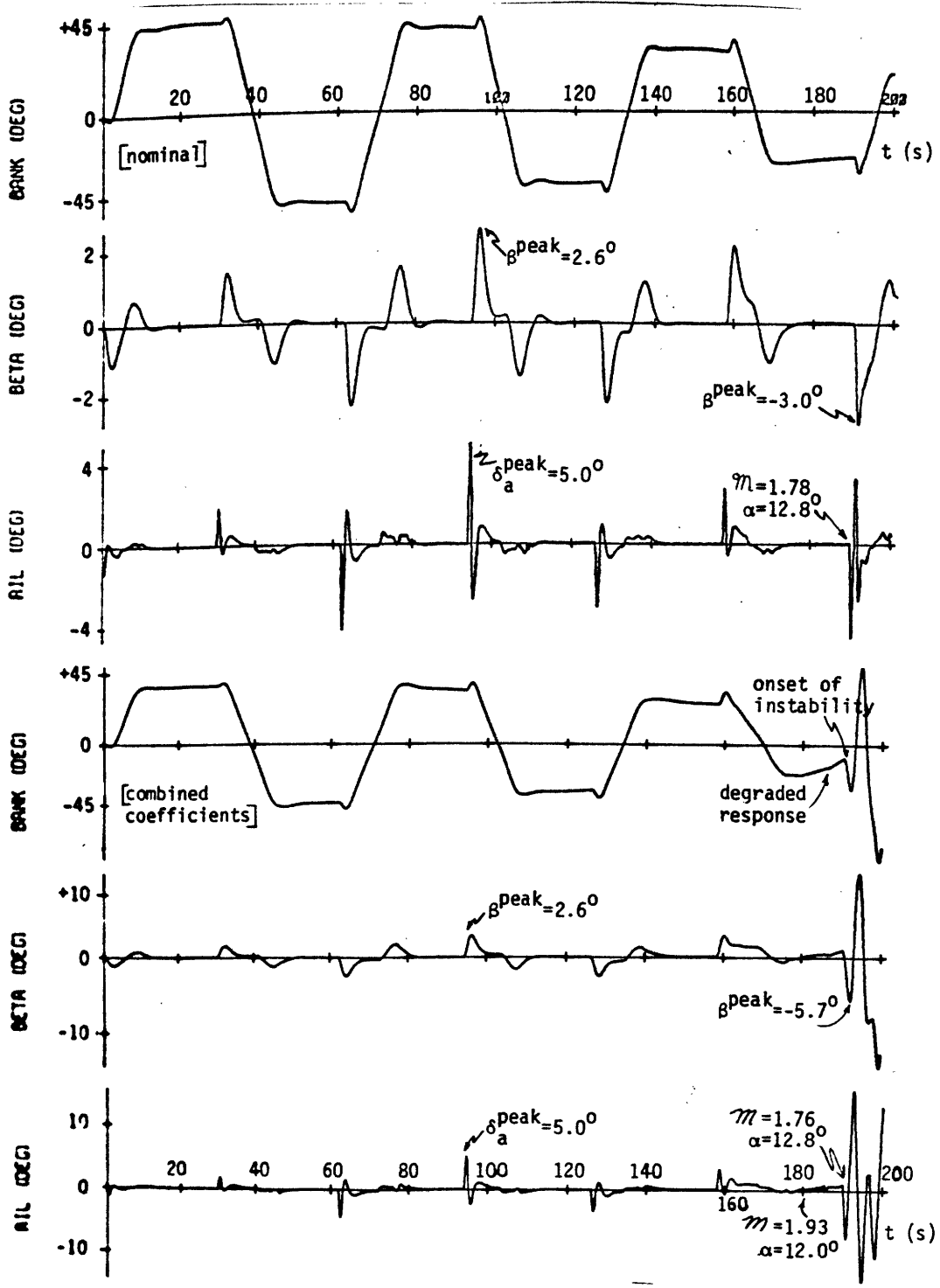
Figure 7-45. Nominal Transition Performance vs Performance
with Combined Coefficient Variations.
(see (7-23)).
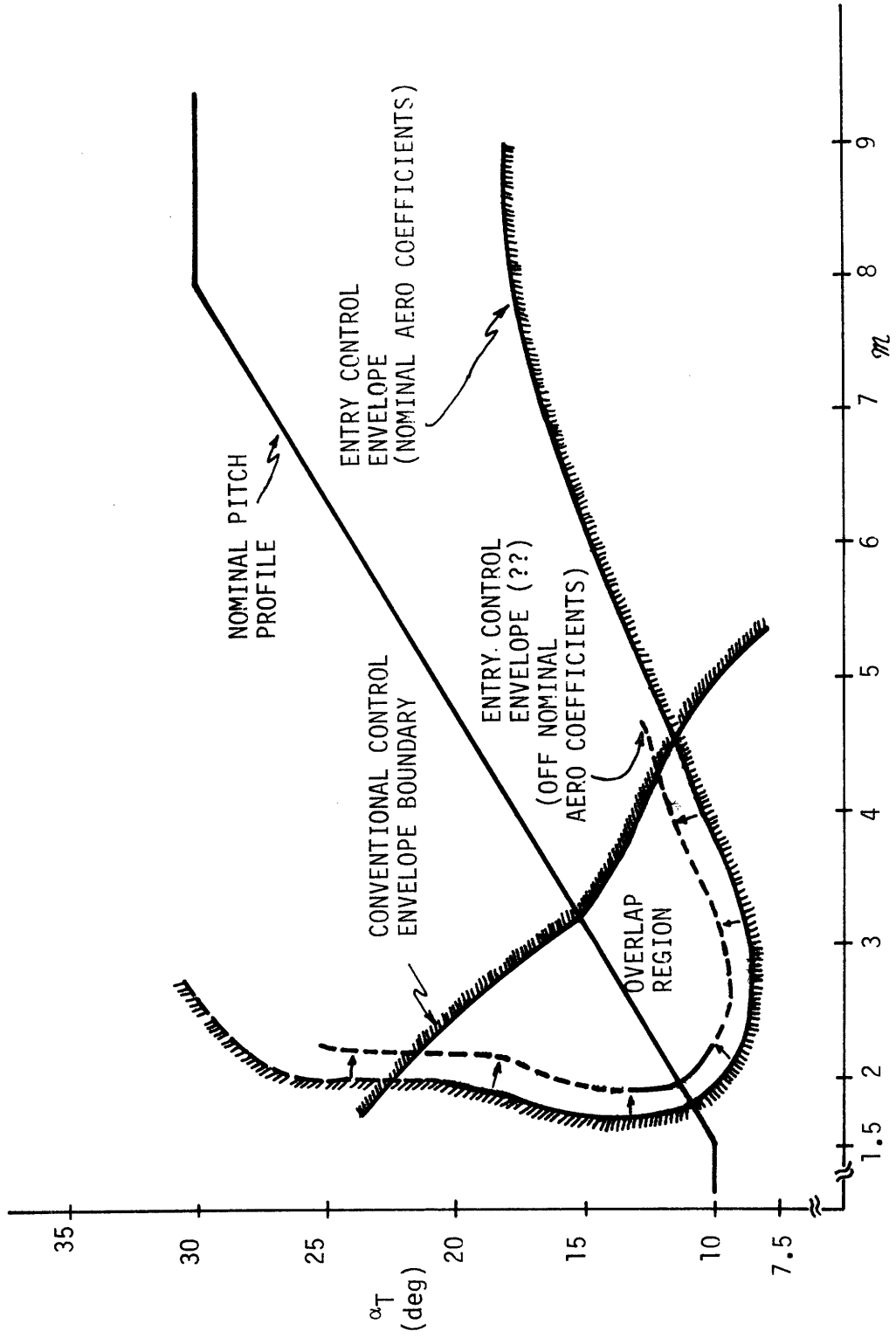
Figure 7-46. Shrinkage of Overlap Region Due to Off-Nominal Aerodynamics

397

overlap region (recall Figure 7-33). It should be recognized that this new boundary is applicable to the particular set of uncertainties specified by (7-23), and any other particular "stacking" may result in different shifts.

7.3.3 Actuator Rate Limits

This section describes the effect of a low actuator rate limit on controller performance, with the objective of indicating system sensitivity to such a constraint. Because of the non-linear nature of the problem, a global sensitivity study is perhaps as challenging a problem as the determination of sensitivity to aerodynamic coefficient variations. This section will simply describe a few simulation results pertaining to the rate limit effect, so as to illustrate performance sensitivity.

It may be recalled that the surface control laws were derived under the assumption of the validity of a linear plant, and any non-linear effects were sufficiently small so as to not significantly effect closed-loop performance. Because of the hard rate and position limits of the actuators, the implication is that the control logic must command small deflections at low rates. However, the gain logic is clearly structured otherwise, for at low dynamic pressures, for example, the surface commands are correspondingly large. A similar response is elicited when a large bank command is issued by the guidance, resulting in large error signals in the linear network. This situation, however, is somewhat ameliorated by the first-order filter in the maneuver logic (when the dynamic pressure exceeds 80 lbf/ft^2; recall the block diagram of Figure 5-18), which lags the input error step and thus reduces the magnitude of the control system's initial response. Whether the gains are large or the system is responding to a large commanded attitude change, however, the effect is the same: rate limiting of the surfaces, followed by position limiting if the maneuver situation allows such rates to persist. Clearly, the rate limiting property of the surfaces becomes more important in cases when the rates are low or the controller issues high frequency commands to the surfaces.

The three simulations to be described below illustrate system performance when the surface rates are lowered to 10°/sec (from their nominal 15°/sec limits) and the control logic is driven by large input errors. It should be noted that the simulations were conducted with the forward CG configuration and the nominal aerodynamic coefficient values.

Figure 7-47 shows the history of a simulated bank maneuver initiated at Mach 5 at a dynamic pressure of 259 lbf/ft^2. The surface rate limit of 10°/sec, for both elevons and rudder (not shown), has absolutely no effect here, since the limit is not violated (due to the maneuver logic lag); a comparison of these histories with those shown in Figure 7-22 shows the identical response for both nominal and low actuator rate limit situations. This is not the case, however, for a comparable maneuver performed at a lower dynamic pressure, as seen from the histories of Figure 7-48. Here, the initial dynamic pressure is 40% lower (due to a higher initialization altitude; this is still within the flight envelope of Figure 7-2, however): 155 lbf/ft^2 at Mach 5. Although the angle-of-attack is lower here, the main difference to be seen between the two simulations is in the aileron trace. This, of course, is due to the lower dynamic pressure, which results in a compensatory gain increase by the control logic (recall the $1/\bar{q}$ gain structure), which, in turn, results in a high actuator drive rate, as evidenced by the limiting seen in the aileron trace of Figure 7-48. The differences in the simulations are not limited to the aileron traces alone, however, as can be seen by a comparison of the initial sideslip peaks and the initial bank rate reversal peaks: clearly, the aileron rate limiting degrades the system's performance. The reason for this can be seen by recognizing that the lower rate limit implies a lower sideslip acceleration to the desired peak value necessary for the bank maneuver; this, of course, prolongs the required time over which the aileron must be deflected negatively, in turn prolonging the initial period of negative bank acceleration. Because the control system is responsive to this undesirable bank rate change, additional compensation is provided in the form of yet a further extension of the time interval of negative aileron rate. This positive feedback operation

399
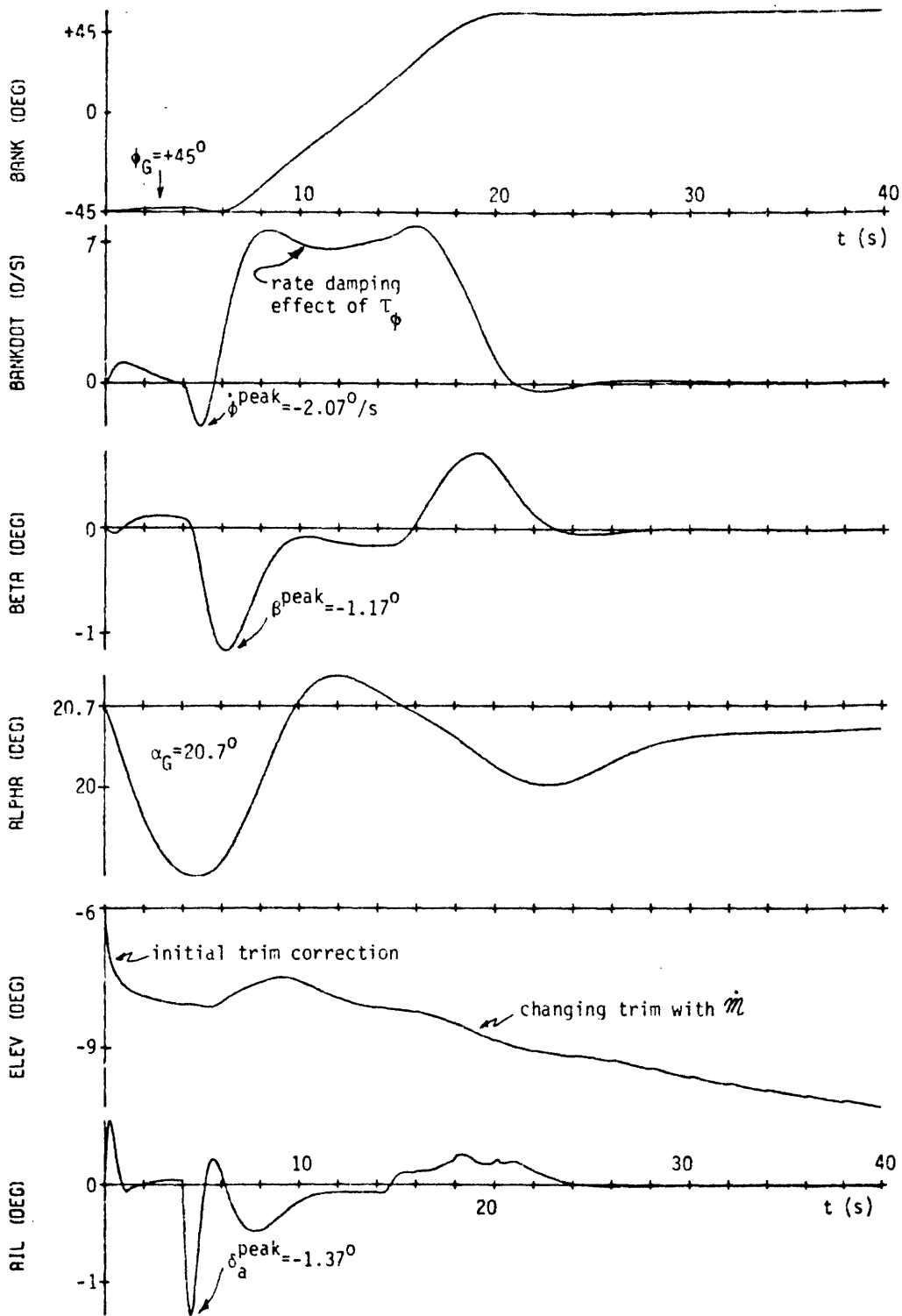
Figure 7-47. Bank Response with Surface Rate Limits
of 10°/s at $\overline{q}$=259 ($\mathcal{M}_i$=5).
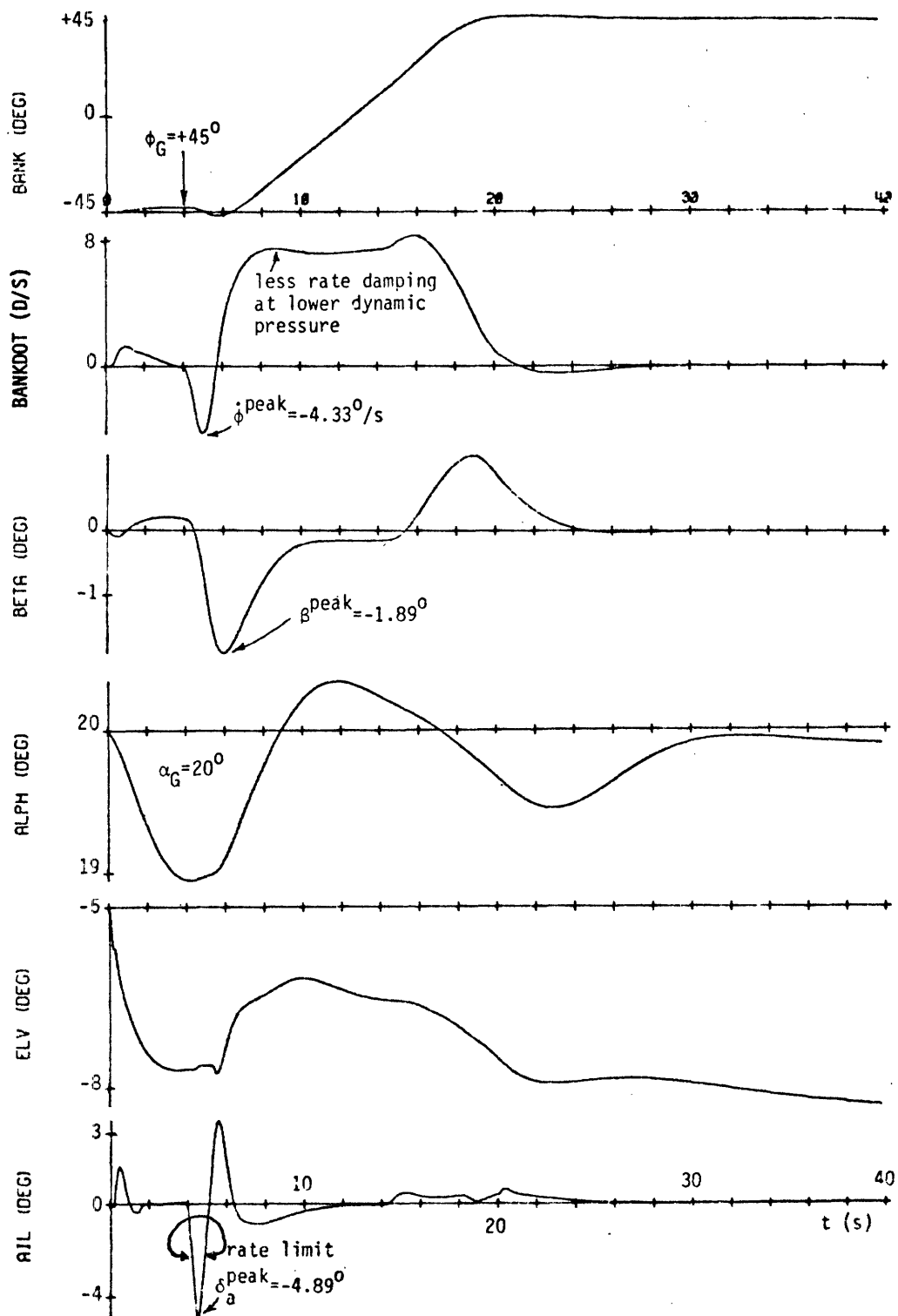
Figure 7-48. Bank Response with Surface Rate Limits of 10°/s at $\bar{q} = 155$ ($\mathcal{M}_i = 5$).

continues until a sufficiently negative sideslip angle has been achieved, at which point the surface reverses its rate so as to damp the pending sideslip oscillations. Needless to say, the maneuver is completed successfully, although the initial transients are clearly of concern.

This actuator rate limit effect is typical of operation with high gain situations in which the system is attempting to respond to a large magnitude input error. Low surface rates naturally aggravate the situation, although, in the case just described, did not significantly affect the overall performance. Because of the additional degree of freedom involved due to the dynamic pressure dependence, no parameter study has been made of the system's performance over the flight envelope as a function of surface rate limits. The next simulation to be described, however, gives some indication of performance along the nominal transition profile.

Figure 7-49 shows histories of a reversal sequence conducted down the nominal $\mathcal{M}/\alpha$ profile, starting at Mach 5 at a dynamic pressure of 259 lbf/ft^2. The dramatic loss of control occurs at Mach 1.8, when the angle-of-attack is slightly over 12 degrees; thus, the effect of the 10°/sec surface rate limit is similar to the other off-nominal cases considered. That is, the $\mathcal{M}/\alpha$ flight envelope does not appear to be especially sensitive to this lower than nominal surface rate limit, although crossing of the previously established nominal controllability boundary results in a catastrophic degradation of performance.

7.3.4 Trajectory Parameter Estimator Errors

Although no specific simulation testing has been conducted to evaluate system performance in the presence of trajectory parameter errors, it is appropriate at this point to briefly discuss the anticipated effects of such errors, by drawing upon the results of past simulation experience. The trajectory parameters of interest, used explicitly in the control logic formulation, are Mach number, $\mathcal{M}$, dynamic pressure, $\bar{q}$, and trim angle-of-attack, α_T. Because it is beyond the scope of this study to suggest
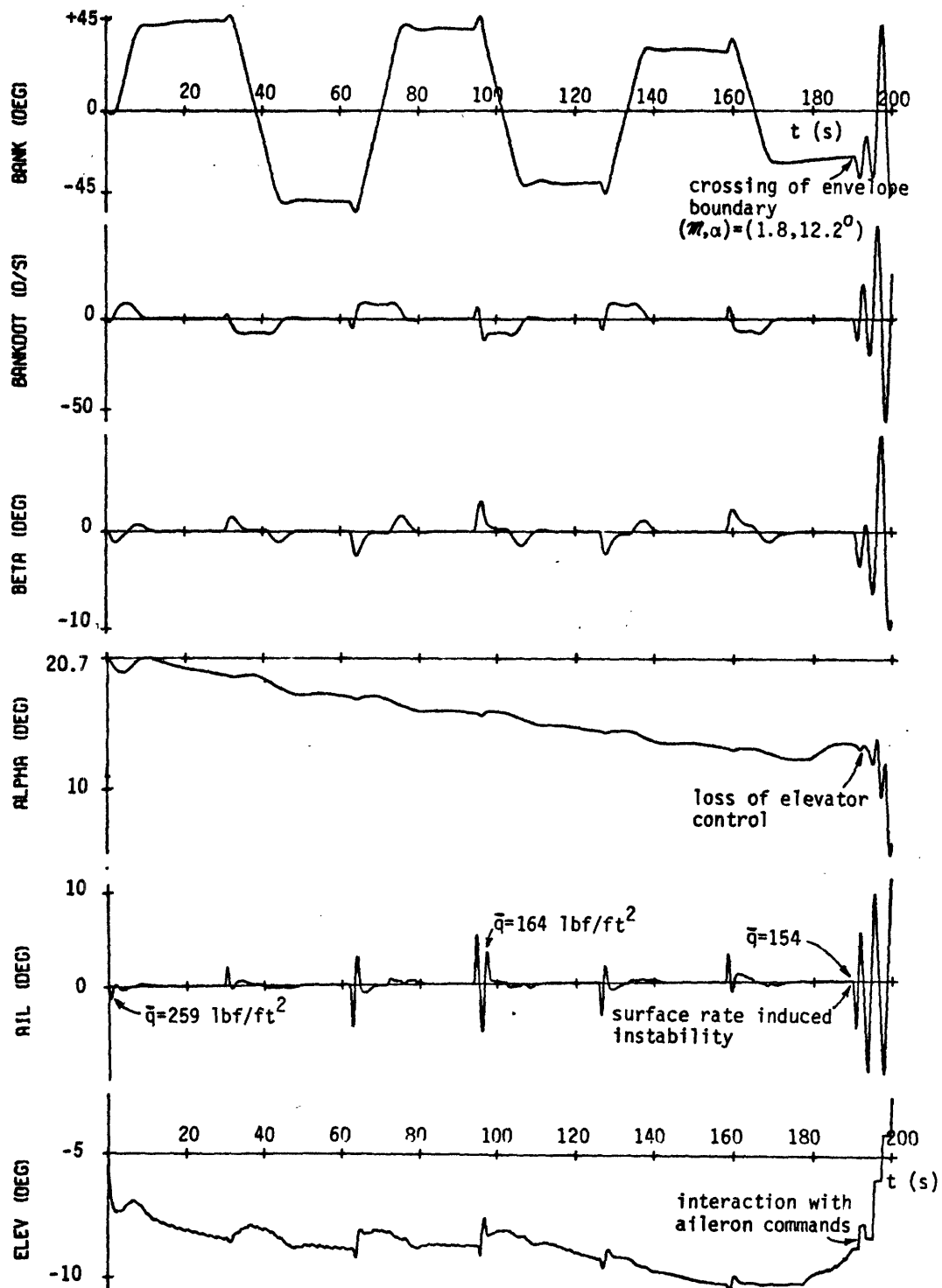
Figure 7-49. Response Along Nominal Transition Profile with 10 °/sec Surface Rate Limits ($\mathcal{m}_i=5$, $\bar{q}_i=259$ lbf/ft²).

403

appropriate estimation techniques for these parameters, the discussion
to follow will be concerned strictly with system sensitivity to estimator
errors. Further, no noise dynamics are considered, since these param-
eters are effectively quasi-stationary as viewed from the fast time scale
of the controller.

As may be recalled from the control logic summary description
given in Chapter 6, the vehicle's Mach number is used for two basically
different functions by the control logic: mode switching and gain schedul-
ing. In the former case, $\mathcal{M}$ is used for rudder turn-on so as to augment
the aileron effectiveness early in the transition profile ($\mathcal{M}$= 6). It should
be obvious that the switchpoint is non-critical because of the low rudder
effectiveness at this point (see, for example, the rudder coefficients
given in Appendix B); thus, earlier turn-on only results in inefficient use
of actuator power, while turn-on at a slightly later point only results in a
slight increase in rudder authority, due to the gradual increase of the
surface's effectiveness. This has, in fact, been borne out by earlier
simulation testing in which the rudder was activated at Mach 5 instead of
Mach 6 as in the present design: there was very little difference in ob-
servable performance. The gain scheduling requirements placed on Mach
number estimation accuracy would not appear to be quite as straightfor-
ward, simply because of the six scheduled gains involved (ξ_1 through ξ_6).
However, two points should be recognized. First, reference to the gain
schedules of Chapter 6 (Figures 6-12 through 6-17) shows that they are
relatively slowly varying functions of $\mathcal{M}$, so that variations in $\mathcal{M}$ tend to
lead to attenuated variations in the gains. Second, and more fundament-
ally, it should be recalled that the schedules themselves were derived
as only approximate fits to the desired theoretical values given in Chap-
ter 5 (see, for example, (5-64)), and solely for the purpose of compensat-
ing for the gross trends in the vehicle's changing aerodynamics through
the entry. The fundamental operation of the controller is closed-loop
attitude control, and no serious attempt is made at predicting open-loop
behavior through stringent requirements on the gain schedule accuracy,
and, in turn, on Mach number. This too is borne out by previous

simulation results, in which different angle-of-attack profiles were flown through the entry (for example, see Figure 7-31). Because of the two-dimensional dependence of the aerodynamic coefficients on Mach number and angle-of-attack, and the one-dimensional gain schedule dependence (on Mach number), a different entry profile translates into a Mach number error, as seen by the linear logic using the computed gain schedules. The large flight envelopes already discussed clearly demonstrate system insensitivity to this effective Mach number error, and the implication is that the system is similarly insensitive to Mach number estimator errors. Although this has yet to be demonstrated exhaustively, all other indirect evidence strongly suggests this non-criticality of Mach number accuracy.

The use of dynamic pressure information by the controller is similar to that just described: as a mode switch parameter and as a gain in the surface control logics. Again, the accuracy requirements imposed by mode switching objectives are modest, since none of the switch points need be precisely executed. During the early entry portion, the blending logic is designed to compensate for early or late switching (from ACPS to ACSS), while later in the entry, the maneuver logic turn-on point is chosen as a matter of convenience to satisfy (possible) guidance maneuver requirements. This type of insensitivity had been observed earlier in the design development simulation effort, and the switch points finally specified were chosen basically as midpoints in a large interval of acceptable switch points. The accuracy requirements imposed by the use of dynamic pressure as a gain in the surface control logics appear to be similarly modest, and for the same type of reason cited above for Mach number insensitivity: the dynamic pressure is used as a normalizing factor to compensate for local variations in the pressure level throughout the entry. Such system insensitivity has yet to be confirmed by direct simulation, but it would appear almost certain that the dynamic pressure accuracy requirements are relatively loose.

The final trajectory parameter to be considered, the trim angle-of-attack, is used in the lateral ACPS logic to aid in coordinated bank

maneuvers. The closed-loop lateral logic provides the ultimate source of maneuver convergence, while knowledge of the proper trim angle-of-attack only aids in the speed of convergence. That the sensitivity to estimator errors is low was demonstrated by a simulation in which the angle-of-attack used by the control logic differed from the (maintained) angle-of-attack by 10 degrees. The performance naturally suffered although the response was marginally acceptable. The implication is that the expected order-of-magnitude (or two) smaller estimation error in trim angle-of-attack will have essentially no effect on controller performance.

Thus, controller performance, in the face of reasonable-magnitude errors in the trajectory parameter estimates, is anticipated to be effectively unchanged from performance in an error-free environment. Future studies clearly need to identify the magnitudes of such acceptable estimator errors, but it would appear that the problem of trajectory parameter sensitivity is not a pacing item in further design development.

7.3.5 Vehicle Attitude Estimation Errors

In all of the simulations described here, it should be recognized that the controller is operating with essentially perfect state information; that is, except for computation errors* involved in an approximate transformation from the (sensed) body-axis states to the (controller input) stability-axis states, the information upon which the controller acts is not corrupted by any type of noise. Clearly, this is an unrealistic environment, and it is appropriate here to provide a brief comment on system performance evaluation under these less than ideal conditions.

In this study, no simulation testing was performed to relate system performance to the noise content of the estimated state variables, for

---

* These are, of course, dependent on the type of transformation used between the two axis systems. Some idea of the possible error sources is gained by a reinspection of the proposed transformation equations of Section 5.4.1, with attention given to both the sensor inputs and the "quasi-static" equation parameters.

three reasons. First, such an analysis is strongly dependent on the "estimator" used to interface between the sensors and the control system input, and it was desired to maintain as much independence as possible from a particular software configuration, when discussing performance results. Second, the sensor instrumentation has yet to be well-defined, let alone the error characteristics of interest. Finally, it should be recognized that this type of sensitivity analysis must be coupled with a realistic appraisal of flexible body dynamic effects, since sensor error dynamics and resonant modes may be closely related because of similar frequency characteristics.

However, some attempt has been made in this area of operation in a noisy environment, and is reported on in reference 16. Presented in this reference is a design description and performance evaluation of the estimator logic mentioned earlier (see Sections 7.1 and 7.2.3), a design closely integrated with the entry controller. Briefly, the rigid body simulation results show that operation with artificially severe measurement noise and environmental disturbances (i.e., "torque noise") substantially degrades controller performance when the estimator is not used, and only moderately degrades performance when the filtering characteristics of the estimator are taken advantage of. Such performance trends should be obvious when it is recognized that absolutely no filtering by the control logic is performed on the control system state inputs; thus, noisy inputs will a priori lead to noisy outputs, with practically no attenuation. Unfortunately, neither the vehicle model, nor the noise model used in this study is appropriate for a realistic appraisal of noise effects on controller performance.

Thus, preliminary results of estimator/controller/vehicle closed-loop performance, in a realistic environment of flexible body dynamics and typical sensor noise statistics, have yet to be obtained. Once satisfactory definitions of the appropriate subsystems and vehicle parameters become available, this should clearly become an area of intensive design evaluation.

7.3.6 Summary of Performance in an Off-Nominal Environment

This section has discussed some aspects of simulated vehicle performance when the environmental conditions differ from the conditions assumed for design synthesis; specifically, the off-nominal concerns discussed were: center-of-gravity offsets, aerodynamic coefficient uncertainties, low actuator rate limits, and trajectory parameter and vehicle attitude estimation errors. The findings, based both on direct simulator studies and implications from observed nominal performance, can be summarized briefly as follows:

1. A longitudinal displacement of the center-of-gravity is automatically compensated for by the elevator trim logic, so that operation with an aft CG is simply one special case of off-nominal CG displacement. Because operation with the aft CG location enhances controllability late in the entry, the envelope boundary of Figure 7-31, derived for forward CG operation, is a conservative estimate of entry control applicability.

2. A lateral displacement of the center-of-gravity is also automatically compensated for, by an asymmetric aileron trim deflection and a coupled trim sideslip attitude. Because the capability to "trim-out" such lateral offsets is directly related to lateral controllability, the late entry envelope boundary noted above would appear to be relatively insensitive to the presence or absence of vehicle mass asymmetries.

3. Uncertainties in the aerodynamic coefficients clearly affect controller performance, but only near the "edge" of the previously defined envelope, and to a much lower degree than originally speculated. A definitive "worst-case" study of combined uncertainties has yet to be accomplished, but the one example discussed shows only a slight reduction in the entry envelope due to such an adverse combination of coefficient variations.

4. Low actuator rate limits similarly effect performance, because of the lag induced by the uncompensated for non-linear effects. Although

the flight envelope does not appear to be significantly reduced by these actuator constraints, the obvious dependence on dynamic pressure suggests the necessity for a more complete three-dimensional (i. e., $\mathcal{M}$, α, and $\bar{q}$) specification of the late entry flight envelope.

5. Errors in estimates in the trajectory parameters used for mode switching and gain scheduling would appear to have little effect on system operation, simply because of the non-criticality of their utilization. The effect of errors in attitude and rate estimates, however, is not well-defined, and meaningful simulation efforts in this area are clearly required. This, of course, involves sensor/estimator subsystem definitions, in addition to inclusion of flexible body dynamic effects, because of the high frequency aspects of the problem.

In general, it may be noted that the off-nominal effects investigated here provided no operational surprises, and, in fact, were quite consistent with the observed nominal performance already discussed. It should be clear that both the controller and vehicle designs have reached sufficient maturity so as to allow more complete and more sophisticated analyses of some of the more subtle effects of off-nominal environmental and software factors; this, of course, is an area of present effort.

8. Summary and Recommendations

The previous chapters have provided fairly extensive coverage of the entry control system design objectives, the techniques used to synthesize a working controller, and the system's performance under a variety of conditions. It is appropriate here to summarize some of the basic findings and suggest further avenues of analysis and design necessary for the evolution of an on-board system.

The performance results of the previous chapter are a culmination of the design effort described in the preceding chapters, starting with the problem definition and constraint identification of Chapter 2. Although the successful simulated performance of the controller, as described in the previous chapter, does not prove the validity of the design approach used, it certainly is a strong indicator that the design techniques and general synthesis approach were appropriate to the problem. Specifically, it suggests that a practical design problem of this nature calls for an amalgamation of synthesis techniques, each tailored to a particular aspect of the overall problem; equivalently, it suggests the inadequacy of a single, albeit sophisticated, design tool. The system's satisfactory performance also supports the use of the simulator as yet another valuable design tool, an integral part of the almost continuous loop of design modification, simulation testing, and subsequent verification or revision. Unfortunately, the presentation format of this study does not fully convey the truly iterative nature of the design process involved in arriving at the final design described in Chapter 6. Perhaps the most important aspect of the design effort, and well-validated by the performance results, is the utilization of a simplified vehicle model to explain the fundamental rotational dynamics of the vehicle. The rigid-body, quasi-static, stability-axis model is simple enough to provide excellent insight into the plant dynamics of interest to the control designer, and yet sophisticated enough to account for practically every observed transient illustrated in the simulation histories of the previous section (bank rate-into-pitch coupling was the exception, although this

was explained easily by recourse to the body-axis equations of motion).
The simplified model also provided the analytic foundation for the pole-
allocation method used in the successful design of the lateral surface
control logic, a non-trivial accomplishment in view of the system con-
straints involved.

Naturally, the most easily identifiable output of this study is the
control system design itself, an all-digital logic providing attitude con-
trol of the vehicle over an exceptionally large flight envelope, and in
the presence of a wide variety of uncertainties and perturbing influences.
As described in Chapter 6, the controller is basically an end product
whose parameter values are strongly vehicle configuration dependent.
This would suggest inflexibility as vehicle designs and/or mission re-
quirements change, but, in actuality, this is not the case. This is
because the more fundamental output of this study is the basic control-
ler logic, derived in Chapter 5, which is relatively configuration in-
dependent. Thus, given a similar vehicle and flight envelope, it is
anticipated that simple gain changes will be all that is required to
modify the controller for a new vehicle application.* Also, because
of the experience gained with this vehicle in the controller's design
development, it is felt that future efforts in this area will proceed at
a much faster pace, the fundamental design work having been com-
pleted.

Because of this anticipated ease of control logic conversion to
operation with a new vehicle design, it is recommended that a "second-
level" of design effort now be initiated, with the goal of answering
some of the questions raised in the previous chapter. Specifically, it
is felt that both the simulator and the controller should be made more
sophisticated: the latter by inclusion of flexible body dynamics and
realistic sensor models with associated noise statistics, and the

---

* This is the case with the current vehicle, the RI 147B. Successful
operation required six gain changes.

411

former by inclusion of resonant mode suppression filters (if required) and input preprocessor filters for noise attenuation. The high frequency signals introduced by this type of system update may require some rethinking of the pole-allocation technique used earlier; specifically, design in the z-plane may be more appropriate than the present design technique utilizing the s-plane. In addition to addressing design problems of this sort, it is also appropriate to continue the performance evaluation studies initiated here, for the purpose of better defining system response as a function of off-nominal operating conditions (i.e., aerodynamic uncertainties, center-of-gravity offsets, etc.). It is felt that a more exhaustive parametric study can only aid the design effort, and, most likely, will lead to design revisions allowing for a greater span of operating conditions tolerated by the controller. Finally, it is recommended that more effort be placed in evaluation of system interactions with the control logic (e.g., guidance, estimator, etc.) so as to guarantee compatible operation between the various flight control software modules.

Appendix A: <u>Stability and Control Derivatives</u>

The purpose of this appendix is to show how the body stability and control derivatives may be related to the more commonly used non-dimensional stability derivatives. The results of this appendix are used directly in the development of the stability-axis dynamic model of Section 4.3, and serve to specify model parameter dependence on the fundamental aerodynamic coefficients. The basic relationships derived here involve both the use of non-dimensionalizing factors (such as dynamic pressure and reference length) and the transformation of forces and torques from the stability axis system to the body axis system.

As an example, the following derivation is taken from Reference 8 to show how X_u may be related to the lift and drag stability derivatives. Assuming that the sideslip velocity v is zero (for symmetric flight), then the body force X results from the resolution of lift and drag along the x_B axis, as shown in Figure A1:
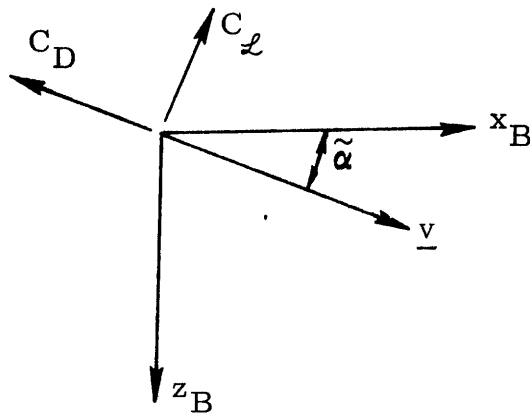
Figure A1

The angle-of-attack is denoted by $\tilde{\alpha}$, so that

$$X = \bar{q}\,S[\,-C_D \cos \tilde{\alpha} + C_{\mathcal{L}} \sin \tilde{\alpha}\,] \qquad (A-1)$$

where $\bar{q}$ is the dynamic pressure and S is the reference area. The following relations are required before differentiating (A-1):

$$\bar{q} = \frac{1}{2}\rho V_T^2 \qquad (A-2)$$

$$\tilde{\alpha} = \tan^{-1}(U/V) \qquad (A-3)$$

$$C_D = C_D(\alpha) \qquad (A-4)$$

$$C_{\mathcal{L}} = C_{\mathcal{L}}(\alpha) \qquad (A-5)$$

where ρ is the (constant) density and V_T, the total velocity, is given by

$$V_T = (U^2 + W^2)^{1/2} \qquad (A-6)$$

and is related to the forward velocity by the following

$$U = V_T \cos \tilde{\alpha} \qquad (A-7)$$

Now, from (A-2), (A-6), and (A-7), it follows that

$$\frac{\partial \bar{q}}{\partial U} = \frac{2\bar{q}}{V_T} \cos \tilde{\alpha} \qquad (A-8)$$

Also, from (A-3) and (A-6), there results

$$\frac{\partial \tilde{\alpha}}{\partial U} = -\frac{\sin \tilde{\alpha}}{V_T} \qquad (A-9)$$

Finally, from (A-4) and (A-5),

$$\frac{\partial C_D}{\partial U} = \left(\frac{\partial C_D}{\partial \tilde{\alpha}}\right)\left(\frac{\partial \tilde{\alpha}}{\partial U}\right) \equiv C_{D_\alpha}\left(\frac{\partial \tilde{\alpha}}{\partial U}\right) \qquad (A-10)$$

414

$$\frac{\partial C_{\mathcal{L}}}{\partial U} = \left(\frac{\partial C_{\mathcal{L}}}{\partial \tilde{\alpha}}\right)\left(\frac{\partial \tilde{\alpha}}{\partial U}\right) \equiv C_{\mathcal{L}_{\alpha}}\left(\frac{\partial \tilde{\alpha}}{\partial U}\right) \qquad \text{(A-11)}$$

Differentiation of (A-1) with respect to U, and substitution of (A-8)- (A-11) yields the following:

$$X_u = \left(\frac{\overline{q}S}{V_T}\right)\left[-2C_D\cos^2\tilde{\alpha} + (C_{D_{\alpha}} + C_{\mathcal{L}})\sin\tilde{\alpha}\cos\tilde{\alpha} - (C_D + C_{\mathcal{L}_{\alpha}})\sin^2\tilde{\alpha}\right]$$

By evaluating the above derivative at the nominal flight condition where $\tilde{\alpha}$ is at its trim value (i.e., $\tilde{\alpha} = \alpha_T$), the desired relationship is obtained:

$$X_u = \left(\frac{\overline{q}S}{V_T}\right)\left[-2 C_D\cos^2\tilde{\alpha}_T + (C_{D_{\alpha}} + C_{\mathcal{L}})\sin\alpha_T\cos\alpha_T - (C_D + C_{\mathcal{L}_{\alpha}})\sin^2\alpha_T\right]$$

$$\text{(A-12)}$$

where the non-dimensional stability derivatives on the right-hand side are evaluated at the nominal flight condition.

An entirely analogous procedure may be carried out for the other body axis stability derivatives requiring a rotational transformation of the form given by (A-1), and the reader is referred to Reference 8 for a more complete treatment. Due to the fact that some non-dimensional derivatives (such as $C_{\mathcal{L}_{\beta}}$ and $C_{n_{\beta}}$) are computed along body axes there is no angular transformation involved, and the associated equations are considerably simplified.

For convenient reference, the 18 body axis stability derivatives are summarized below:

$$X_u = (\overline{q}S/V_T)\left[-2C_D\cos^2\alpha_T + (C_{D_{\alpha}} + C_{\mathcal{L}})\cos\alpha_T\sin\alpha_T - (C_{\mathcal{L}_{\alpha}} + C_D)\sin^2\alpha_T\right]$$

$$X_w = (\overline{q}S/V_T)\left[(-C_{D_{\alpha}} + C_{\mathcal{L}})\cos^2\alpha_T + (C_{\mathcal{L}_{\alpha}} - C_D)\cos\alpha_T\sin\alpha_T + 2C_{\mathcal{L}}\sin^2\alpha_T\right]$$

$$X_q = (\overline{q}S\overline{c}/2V_T)\left[-C_{D_q}\cos\alpha_T + C_{\mathcal{L}_q}\sin\alpha_T\right]$$

$$\text{(A-13)}$$

415

$$Y_v = (\bar{q}S/V_T)[\,C_{y_\beta}\,]$$

$$Y_p = (\bar{q}Sb/2V_T)[\,C_{y_p}\,] \tag{A-14}$$

$$Y_r = (\bar{q}Sb/2V_T)[\,C_{y_r}\,]$$

$$Z_u = (\bar{q}S/V_T)[\,-2C_{\mathcal{L}}\cos^2\alpha_T + (C_{\mathcal{L}_\alpha} - C_D)\cos\alpha_T\sin\alpha_T + (C_{D_\alpha} - C_{\mathcal{L}})\sin^2\alpha_T\,]$$

$$Z_w = (\bar{q}S/V_T)[\,-(C_{\mathcal{L}_\alpha} + C_D)\cos^2\alpha_T - (C_{D_\alpha} + C_{\mathcal{L}})\cos\alpha_T\sin\alpha_T - 2C_D\sin^2\alpha_T\,]$$

$$Z_q = (\bar{q}Sc/2V_T)[\,-C_{\mathcal{L}_q}\cos\alpha_T - C_{D_q}\sin\alpha_T\,] \tag{A-15}$$

$$L_v = (\bar{q}Sb/V_T)[\,C_{\ell_\beta}\,]$$

$$L_p = (\bar{q}Sb^2/2V_T)[\,C_{\ell_p}\,] \tag{A-16}$$

$$L_r = (\bar{q}Sb^2/2V_T)[\,C_{\ell_r}\,]$$

$$M_u = (\bar{q}Sc/V_T)[\,-C_{M_\alpha}\sin\alpha_T\,]$$

$$M_w = (\bar{q}Sc/V_T)[\,C_{M_\alpha}\cos\alpha_T\,] \tag{A-17}$$

$$M_q = (\bar{q}Sc^2/2V_T)[\,C_{M_q}\,]$$

$$N_v = (\bar{q}Sb/V_T)[\,C_{n_\beta}\,]$$

$$N_p = (\bar{q}Sb^2/2V_T)[\,C_{n_p}\,] \tag{A-18}$$

$$N_r = (\bar{q}Sb^2/2V_T)[\,C_{n_r}\,]$$

where $\bar{q}$ = dynamic pressure

S = reference area

b = reference span

c = reference chord

V_T = vehicle airspeed

α_T = trim angle of attack

Similar results may be found for the control derivatives (see
reference 8), and are summarized below:

$$X_{\delta_e} = -(\bar{q}S)\, C_{D\delta_e} \tag{A-19}$$

$$Y_{\delta_a} = (\bar{q}S)\, C_{y\delta_a}$$

$$Y_{\delta_r} = (\bar{q}S)\, C_{y\delta_r} \tag{A-20}$$

$$Z_{\delta_e} = -(\bar{q}S) C_{\mathcal{L}\delta_e} \tag{A-21}$$

$$L_{\delta_a} = (\bar{q}Sb)\, C_{\mathcal{L}\delta_a}$$

$$L_{\delta_r} = (\bar{q}Sb)\, C_{\mathcal{L}\delta_r} \tag{A-22}$$

$$M_{\delta_e} = (\bar{q}Sc)\, C_{M\delta_e} \tag{A-23}$$

$$N_{\delta_a} = (\bar{q}Sb) C_{n\delta_a}$$

$$N_{\delta_r} = (\bar{q}Sb) C_{n\delta_r} \tag{A-24}$$

Appendix B: Numerical Approximations for a Simplified Vehicle Model

The purpose of this appendix is to provide the numerical basis justifying the vehicle model approximations outlined in Section 4.3. In particular, this appendix will consider the relative magnitudes of various vehicle dynamic parameters, and their effective contribution to the overall dynamic response. Shown in Table B-1 are the relevant mass and geometric properties of the vehicle for the forward center-of-gravity, 25K payload configuration; the values are taken from Tables 2-1 and 2-2 of Section 2.1. Table B-2 consists of entry trajectory parameter values, chosen so as to delineate the extremes of the flight envelope under consideration.[*] These parameter extremes, in effect, specify the envelope for which the simplified vehicle dynamic model is appropriate. It should also be noted that the trajectory parameters of Table B-2 do not normally take on the given values simultaneously, so that the approximations made below will be conservative ones.

Table B-1: Mass Property and Geometric Parameter Values

m	5640	slug
I_{xx}	0.805	10^6 slug-ft^2
I_{yy}	5.85	"
I_{zz}	6.07	"
I_{xz}	0.14	"
S	2690	ft^2
b	78.06	ft
c	39.56	ft

This Appendix is organized into two sections: Section B.1 is concerned with the longitudinal equations while Section B.2 is concerned with the lateral equations.

[*] Reference to Figures C-2 through C-4 of Appendix C indicates the typical ranges of these parameters.

Table B-2: Trajectory Parameter Values

$\bar{q}_{max}$	200	lbf/ft^2
$|\gamma_0|_{max}$	10	deg
$(V_T)_{min}$	2000	ft/sec
$(\alpha_T)_{max}$	40	deg
$(\alpha_T)_{min}$	10	deg

B. 1 Longitudinal Paramaters

The objective of this section is to provide the simplifying relations for the approximations used in Section 4.3.1. Shown in Figures B-1 through B-8 are some of the vehicle's longitudinal stability derivatives parametrically plotted over the Mach-alpha regime of interest. Figures B-1, B-4, and B-7 are adapted from reference 2, while the remainder were generated using standard numerical techniques from appropriate data in the same reference. With these plots as the primary data base, the typical and maximum values of the pertinent longitudinal derivatives may be summarized as in Table B-3.

Table B-3: Longitudinal Stability Derivative Values

$C_{\mathcal{L}}$	1.0	(upper bound)
$C_{\mathcal{L}\alpha}$	2.0	(upper bound)
$C_{\mathcal{L}q}$	<1	(conservative upper bound: no value available)
$C_{\mathcal{L}\delta e}$	0.30	(upper bound)
C_D	1.3	(upper bound)
$C_{D\delta_e}$	0.16	(upper bound)
C_{M_α}	-0.10	(typical value)
C_{M_q}	2.0	(upper bound)
$C_{M\delta_e}$	-0.15	(typical value)

419
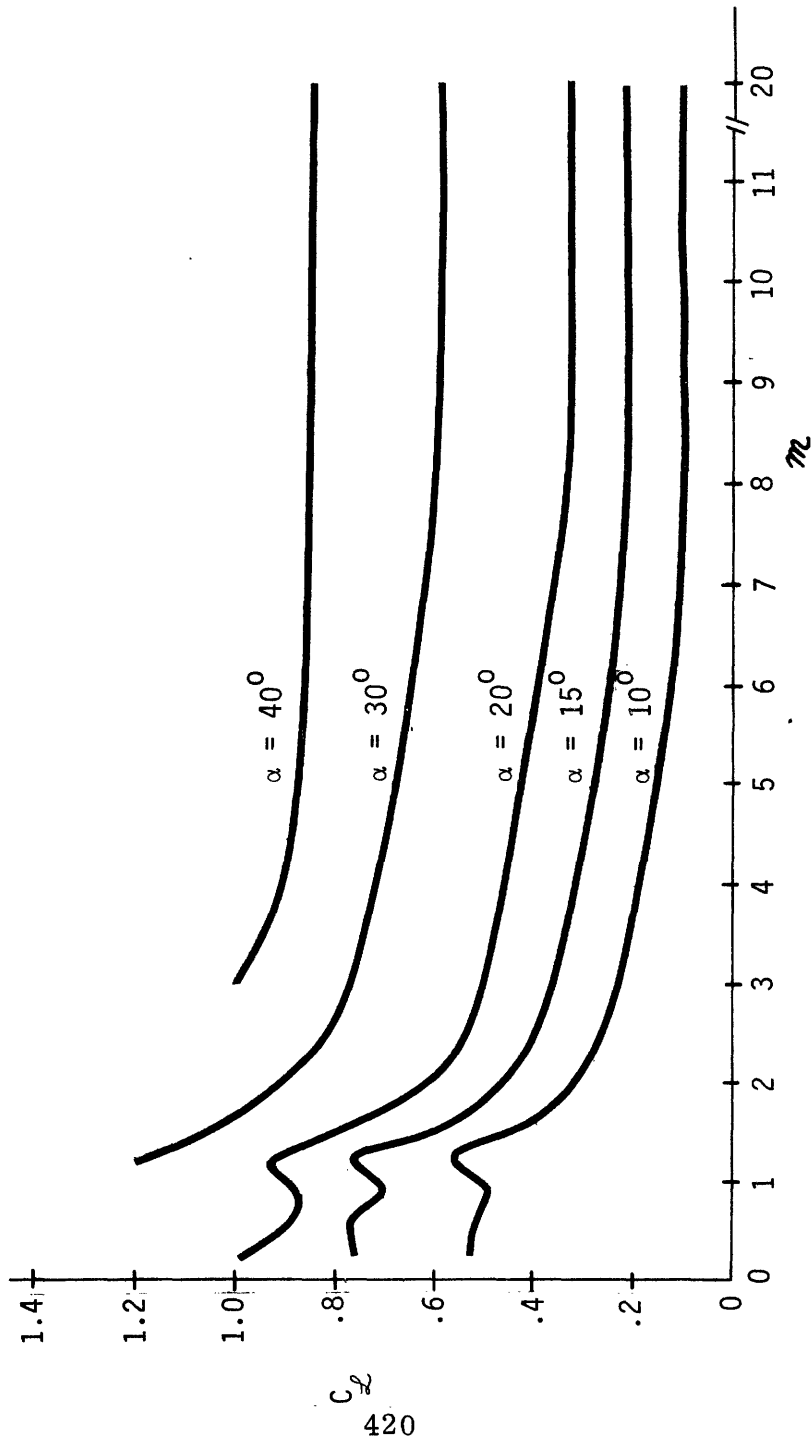
Figure B1. Lift Coefficient (Trimmed).
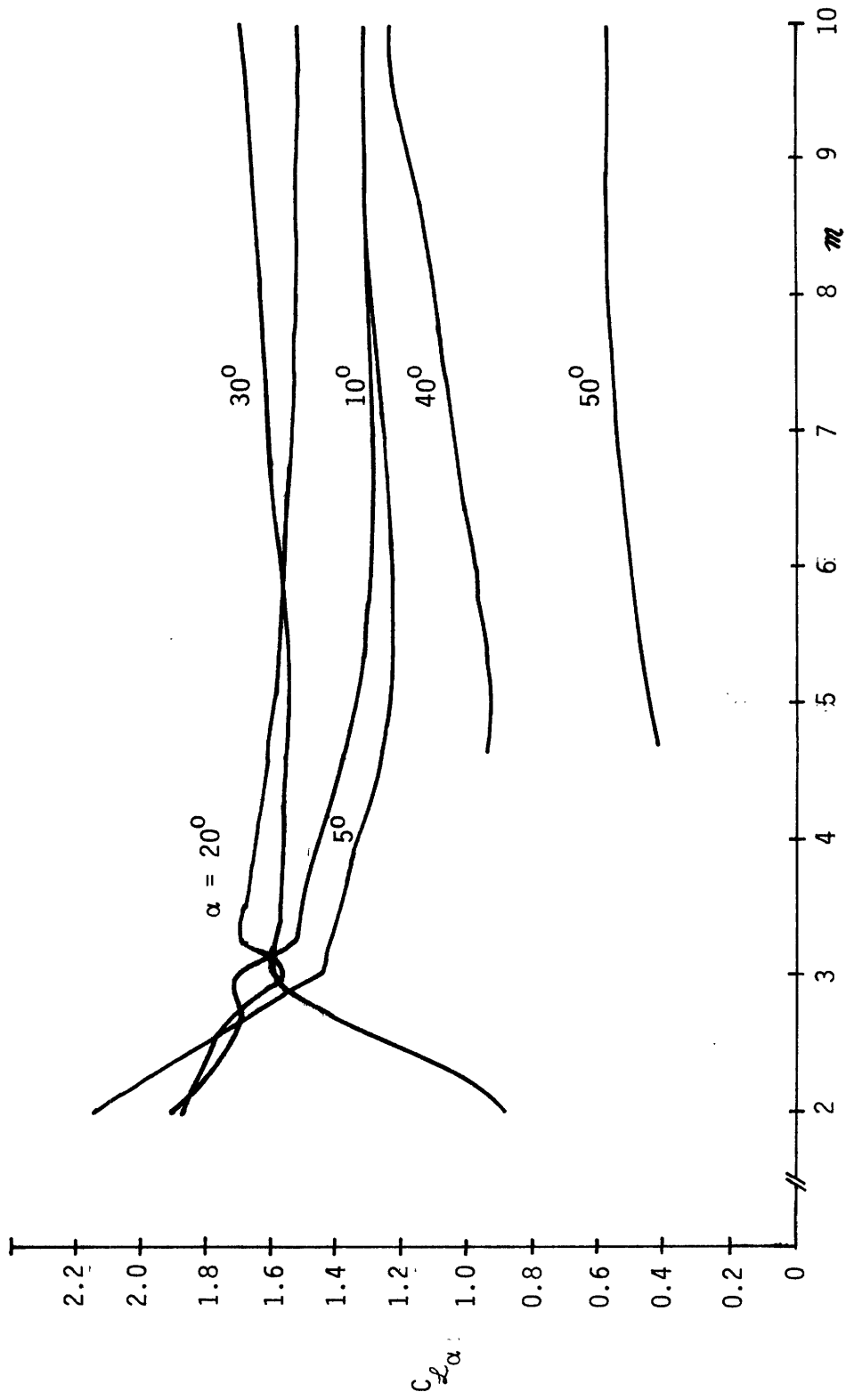
Figure B2. Angle-of-Attack Lift Derivative.

421
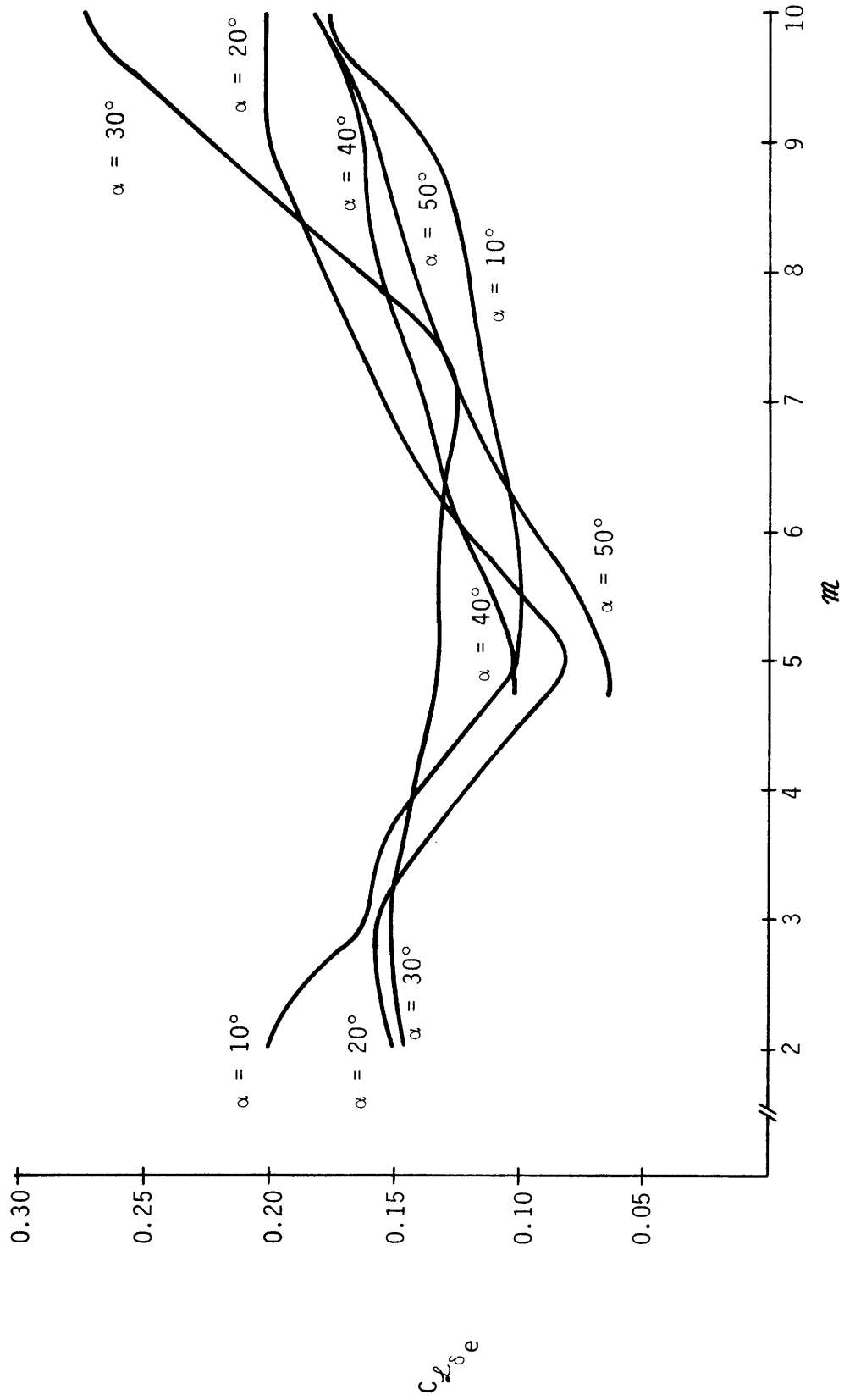
Figure B-3. Elevator Lift Derivative.
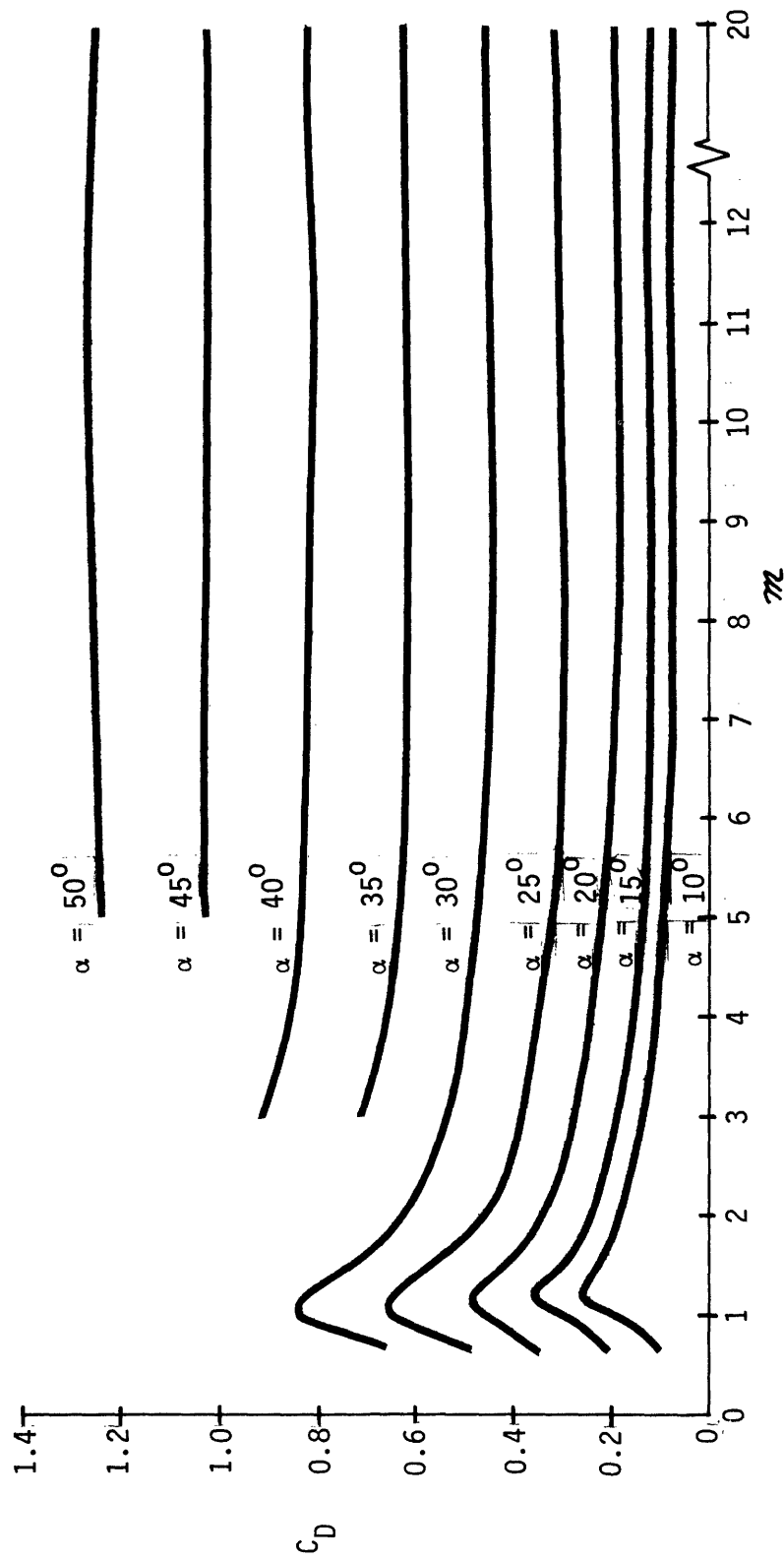
Figure B4. Drag Coefficient (Trimmed).
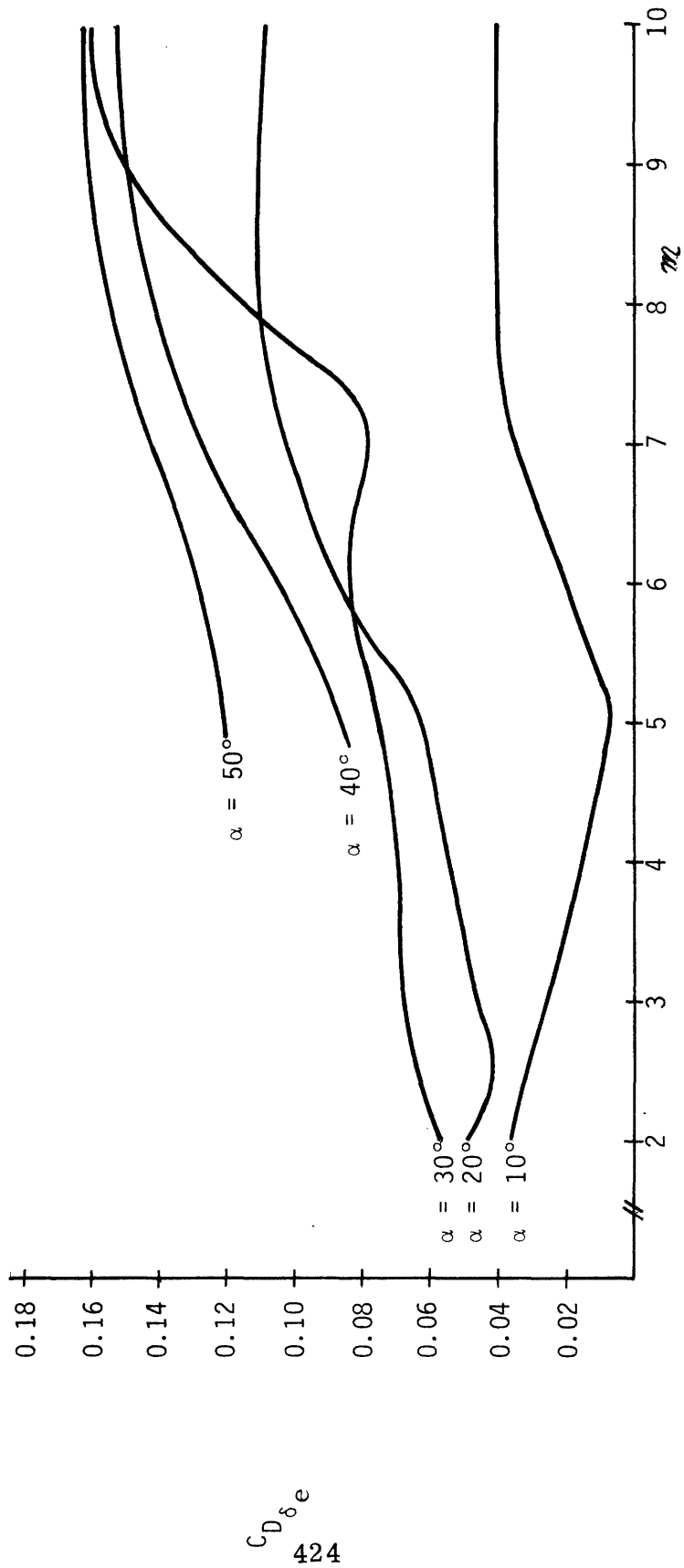
Figure B5. Elevator Drag Derivative.

424
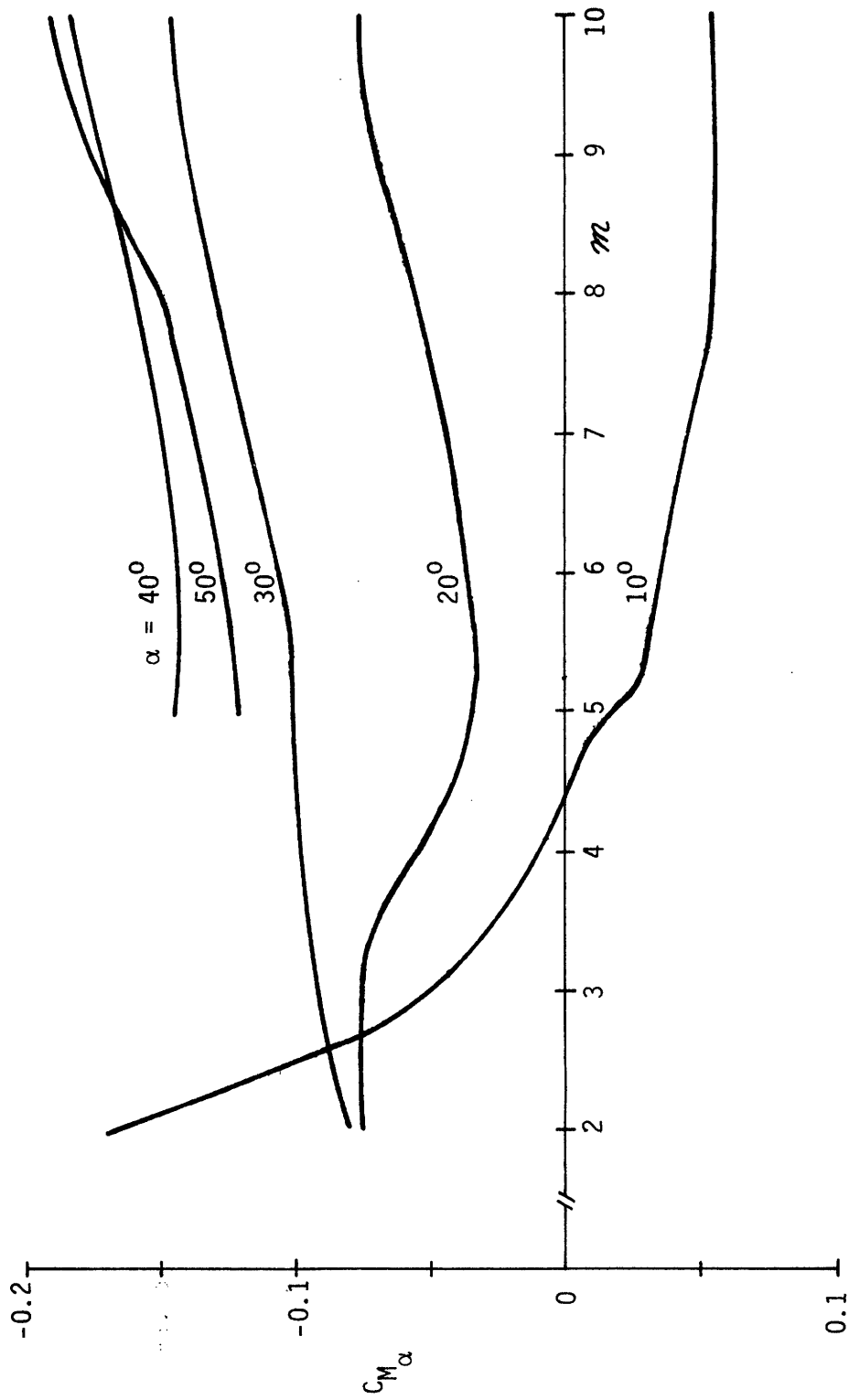
Figure B6.   Angle-of-Attack Pitch Moment Derivative.
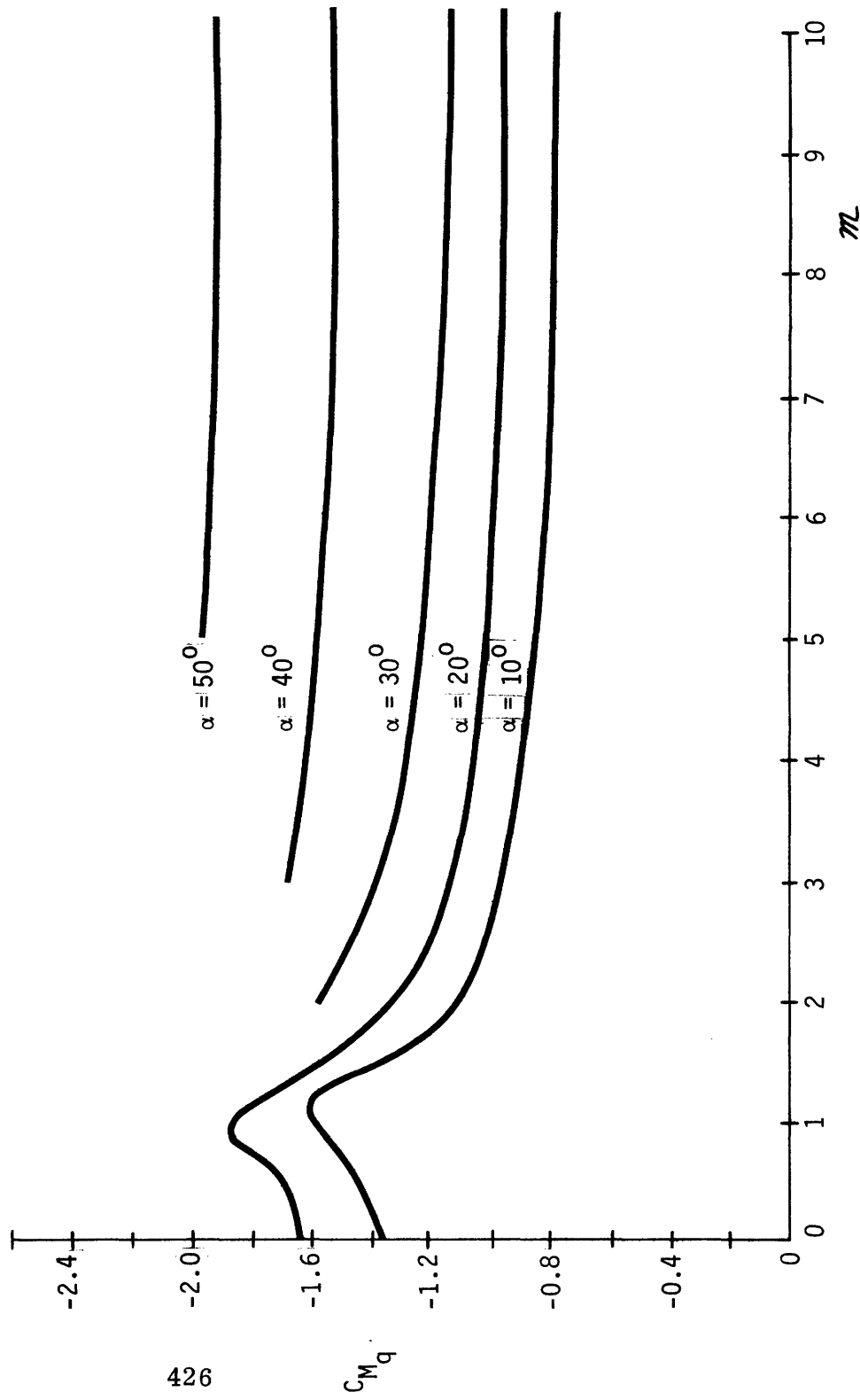
Figure B7. Pitch Rate Pitch Moment Derivative.
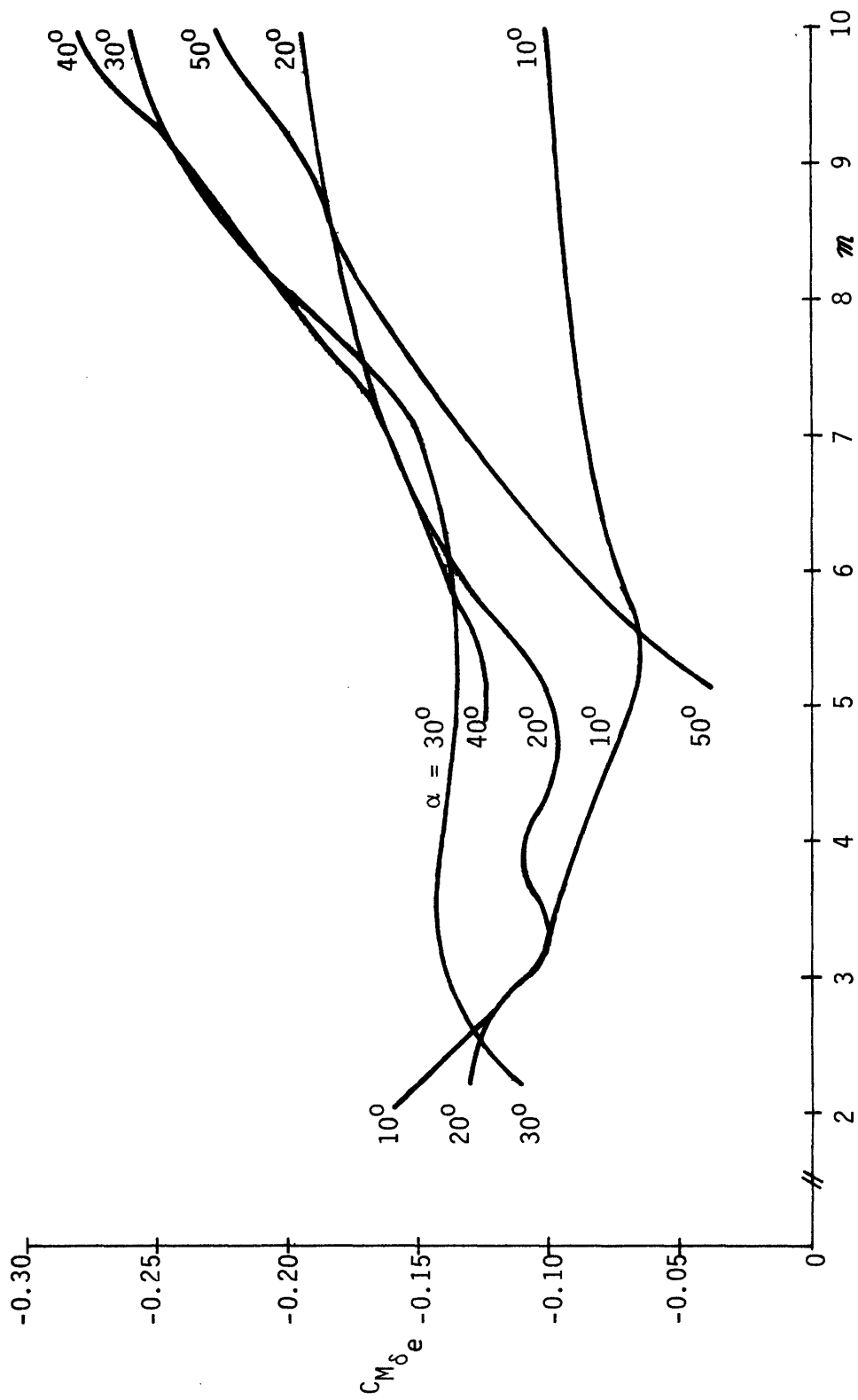
Figure B8. Elevator Pitch Moment Derivative.

The first objective will be to simplify (4-30) so that it may be conveniently solved for the pitch rate q. Recalling the equation,

$$s\,\hat{\alpha} + \left(\frac{\bar{q}\,S}{mV_T}\right)(C_D + C_{\mathscr{L}\alpha})\,\hat{\alpha} + \left(\frac{\bar{q}\,S}{mV_T}\right)(2C_{\mathscr{L}})\,\mu - \left[1 - \left(\frac{\bar{q}\,Sc}{2mV_T^2}\right)C_{\mathscr{L}q}\right.$$

$$\left. + \frac{(g/V_T)\sin\gamma_0}{s}\right]q = -\left(\frac{\bar{q}\,S}{mV_T}\right)\left(C_{\mathscr{L}\delta_e}\cos\alpha_T - C_{D\delta_e}\sin\alpha_T\right)\hat{\delta}_e$$

$$(4\text{-}30)$$

A maximum value for one of the multiplicative constants appearing above is obtained in the following manner:

$$\left(\frac{\bar{q}\,Sc}{mV_T^2}\right)_{max} = \frac{\bar{q}_{max}\,Sc}{m(V_T)^2_{min}}$$

so that, from Tables B-1 and B-2,

$$\left(\frac{\bar{q}\,Sc}{mV_T^2}\right) < 1 \times 10^{-3} \qquad\qquad (B\text{-}1)$$

Thus, from Table B-3,

$$\left|\left(\frac{\bar{q}\,Sc}{2mV_T^2}\right)C_{\mathscr{L}q}\right| < 1 \times 10^{-3} \ll 1 \qquad (B\text{-}2)$$

so that the $C_{\mathscr{L}q}$ term of (4-30) may be conveniently dropped. The gravitational term may be computed from Table B-2 to be:

$$\left|\frac{g}{V_T}\sin\gamma_0\right| < \frac{1}{(V_T)_{min}}\left|g\sin(\gamma_0)_{max}\right| < 2.8 \times 10^{-3} \ll 1 \quad (B\text{-}3)$$

Assuming that the dynamic time period of interest is short (i. e., on the order of seconds) then the integrated gravity term of (4-30)

428

will contribute little to the vehicle response[*]. Thus, dropping this term allows the pitch rate coefficient to be approximated as unity, so that solving for q, (4-30) becomes:

$$q = s\hat{\alpha} + \left(\frac{\bar{q}S}{mV_T}\right)\left(C_D + C_{\mathscr{L}_\alpha}\right)\hat{\alpha} + \left(\frac{\bar{q}S}{mV_T}\right)\left(2C_{\mathscr{L}}\right)\mu$$

$$+ \left(\frac{\bar{q}S}{mV_T}\right)\left(C_{\mathscr{L}\delta_e}\cos\alpha_T - C_{D\delta_e}\sin\alpha_T\right)\hat{\delta}_e \qquad \text{(B-4)}$$

The above equation may thus be used to eliminate pitch rate in the longitudinal dynamic model. Substitution of (B-4) into (4-31) then yields the following:

$$\left\{ s^2 + \left(\frac{\bar{q}S}{V_T}\right)\left[\frac{C_D + C_{\mathscr{L}\alpha}}{m} - \left(\frac{c^2}{2I_{yy}}\right)C_{M_q}\right]s \right.$$

$$\left. - \left(\frac{\bar{q}Sc}{I_{yy}}\right)\left[C_{M_\alpha} + \left(\frac{\bar{q}Sc}{2mV_T^2}\right)C_{M_q}\left(C_D + C_{\mathscr{L}_\alpha}\right)\right] \right\}\hat{\alpha} \qquad \text{(B-5)}$$

$$+ \left\{\left(\frac{2\bar{q}S}{mV_T}\right)C_{\mathscr{L}}\right\}\left\{s - \left(\frac{\bar{q}Sc^2}{2I_{yy}V_T}\right)C_{M_q}\right\}\mu =$$

$$= \left(\frac{\bar{q}Sc}{I_{yy}}\right)\left\{\left(\frac{I_{yy}}{mcV_T}\right)\left(C_{D\delta_e}\sin\alpha_T - C_{\mathscr{L}\delta_e}\cos\alpha_T\right)s \right.$$

$$\left. + \left[C_{M\delta_e} - \left(\frac{\bar{q}Sc}{2mV_T^2}\right)C_{M_q}\left(C_{D\delta_e}\sin\alpha_T - C_{\mathscr{L}\delta_e}\cos\alpha_T\right)\right]\right\}\hat{\delta}_e + u_y$$

Now from (B-1) and Table B-3, it follows that

---

[*]For more discussion of this "gravity turn" effect, see Section 5.4.1.2

$$\left| \left(\frac{\overline{q}Sc}{2mV_T^2} \right) C_{M_q} \left(C_D + C_{\mathcal{L}_\alpha} \right) \right| < 6.6 \times 10^{-3} \ll \left| C_{M_\alpha} \right| \qquad \text{(B-6)}$$

Also, since

$$\left| \left(\frac{\overline{q}Sc}{2mV_T^2} \right) C_{M_q} \left(C_{D\delta_e} \sin\alpha_T - C_{\mathcal{L}\delta_e} \cos\alpha_T \right) \right| <$$

$$\left| \left(\frac{\overline{q}Sc}{2mV_T^2} \right) C_{M_q} \left[\left| C_{D\delta_e} \right| + \left| C_{\mathcal{L}\delta_e} \right| \right] \right|$$

then, from (B-1) and Table B-3, it follows that

$$\left| \left(\frac{\overline{q}Sc}{2mV_T^2} \right) C_{M_q} \left(C_{D\delta_e} \sin\alpha_T - C_{\mathcal{L}\delta_e} \cos\alpha_T \right) \right| < 9.2 \times 10^{-4} \ll \left| C_{M_{\delta_e}} \right|$$

$$\text{(B-7)}$$

Thus, (B-6) and (B-7) may be used to simplify (B-5), yielding the following relation:

$$\left\{ s^2 + \left(\frac{\overline{q}S}{mV_T} \right) \left[\frac{C_D + C_{\mathcal{L}\alpha}}{m} - \left(\frac{c^2}{2I_{yy}} \right) C_{M_q} \right] s - \left(\frac{\overline{q}Sc}{I_{yy}} \right) C_{M\alpha} \right\} \hat{\alpha}$$

$$+ \left\{ \left(\frac{2\overline{q}S}{mV_T} \right) C_{\mathcal{L}} \right\} \left\{ s - \left(\frac{\overline{q}Sc^2}{2I_{yy}V_T} \right) C_{M_q} \right\} \mu$$

$$= \left(\frac{\overline{q}Sc}{I_{yy}} \right) \left\{ \left(\frac{I_{yy}}{mcV_T} \right) \left(C_{D\delta_e} \sin\alpha_T - C_{\mathcal{L}\delta_e} \cos\alpha_T \right) s + C_{M_{\delta_e}} \right\} \hat{\delta}_e + u_y$$

$$\text{(B-8)}$$

This result may then be put in a more convenient notational format, as is done in (4-33). One last simplification of the above relation is possible by noting that from (B-1) and Table B-3 that

$$\left| \left(\frac{\overline{q}Sc}{mV_T^2} \right) C_{M_q} C_{\mathcal{L}} \right| < 2 \times 10^{-3} \ll \left| C_{M\alpha} \right| \qquad \text{(B-9)}$$

The above relation is used to simplify (4-33). This then completes the longitudinal section. 430

B.2 Lateral Parameters

The objective of this section is to provide the simplifying relations for the approximations used in Section 4.3.2. Shown in Figures B-9 through B-24 are some of the vehicle's lateral aerodynamic derivatives parameterically plotted over the Mach-alpha regime of interest. Figures B-9 through B-22 show the dependence of the dynamic derivatives on flight regime, and were calculated from the classical stability derivatives, whose values, in turn, are given in Reference 2. Figures B-9 through B-13 specify the sideslip dynamic derivative values (generated by (4-43)), Figures B-14 through B-18 specify the bank dynamic derivative values (generated by (4-47)), and Figures B-19 through B-22 specify the auxiliary rate derivative coefficients (generated by (4-42) and (4-46)). Finally, Figures B-23 and B-24 specify two side-force derivatives, and are adapted from Reference 2. With these plots as the primary data base, typical and maximum values of the pertinent lateral derivatives may be summarized as in Table B-4.

Table B-4: Lateral Dynamic Derivative Values.

C'_{n_β}	0.3	(typical value)
C'_{n_p}	1.0	(upper bound)
C'_{n_r}	0.5	(upper bound)
C'_{ℓ_β}	-0.10	(typical value)
C'_{ℓ_p}	+0.11	(upper bound on magnitude)
C'_{ℓ_r}	0.05	(upper bound)
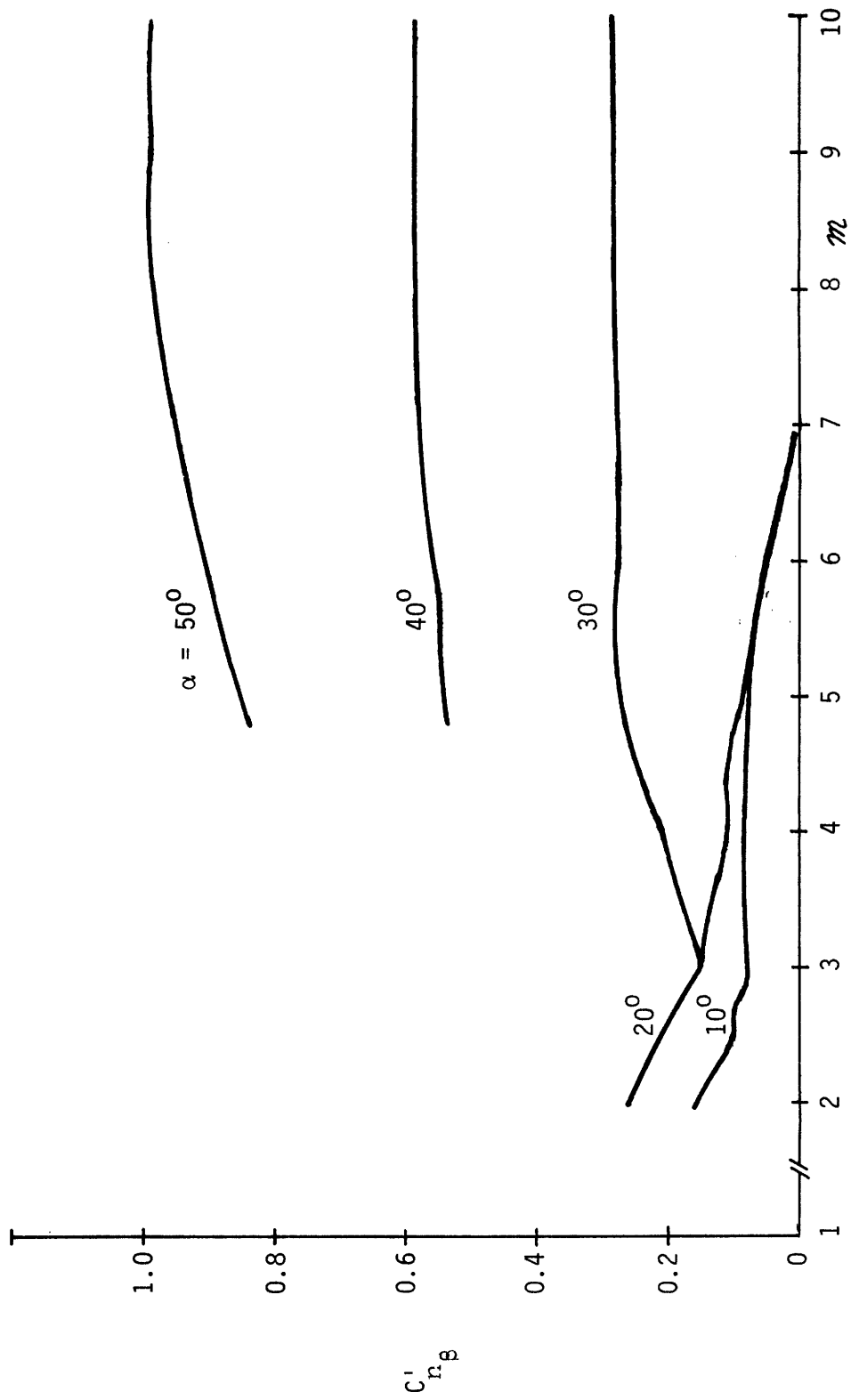
Figure B9. Yaw Due to Sideslip Dynamic Derivative.
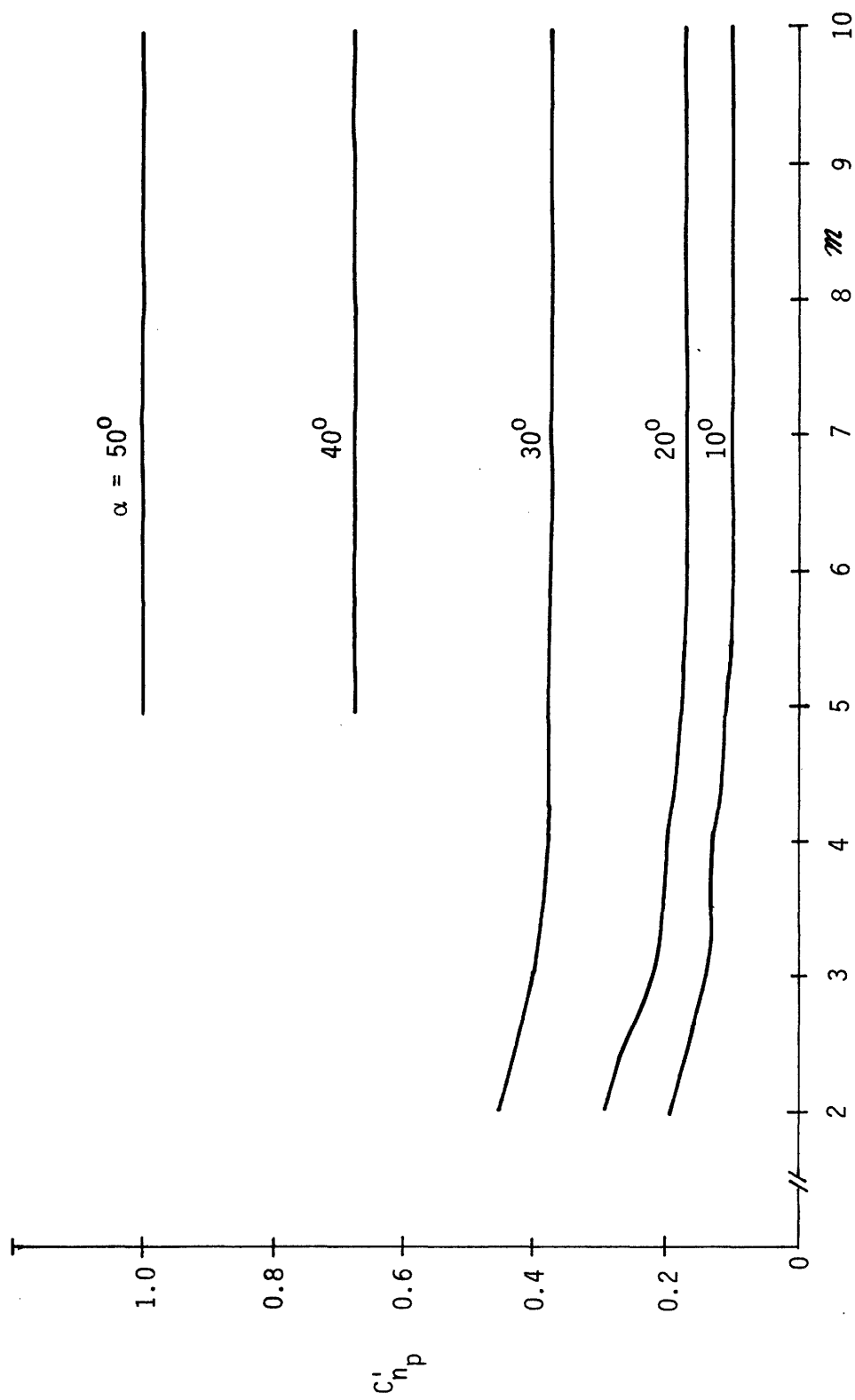
Figure B10. Yaw Due to Roll Rate Dynamic Derivative
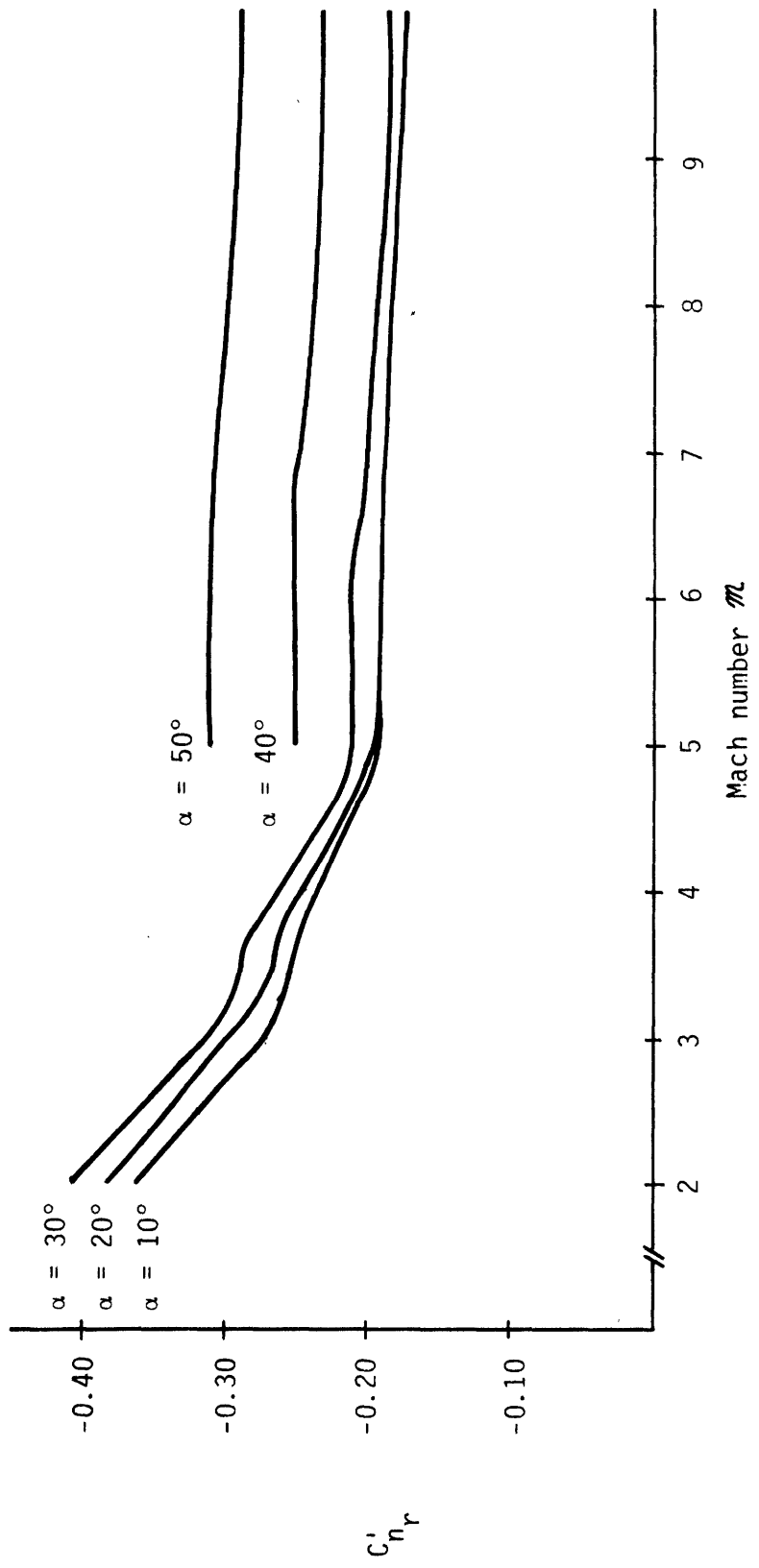
Figure B11. Yaw Due to Yaw Rate Dynamic Derivative.

434
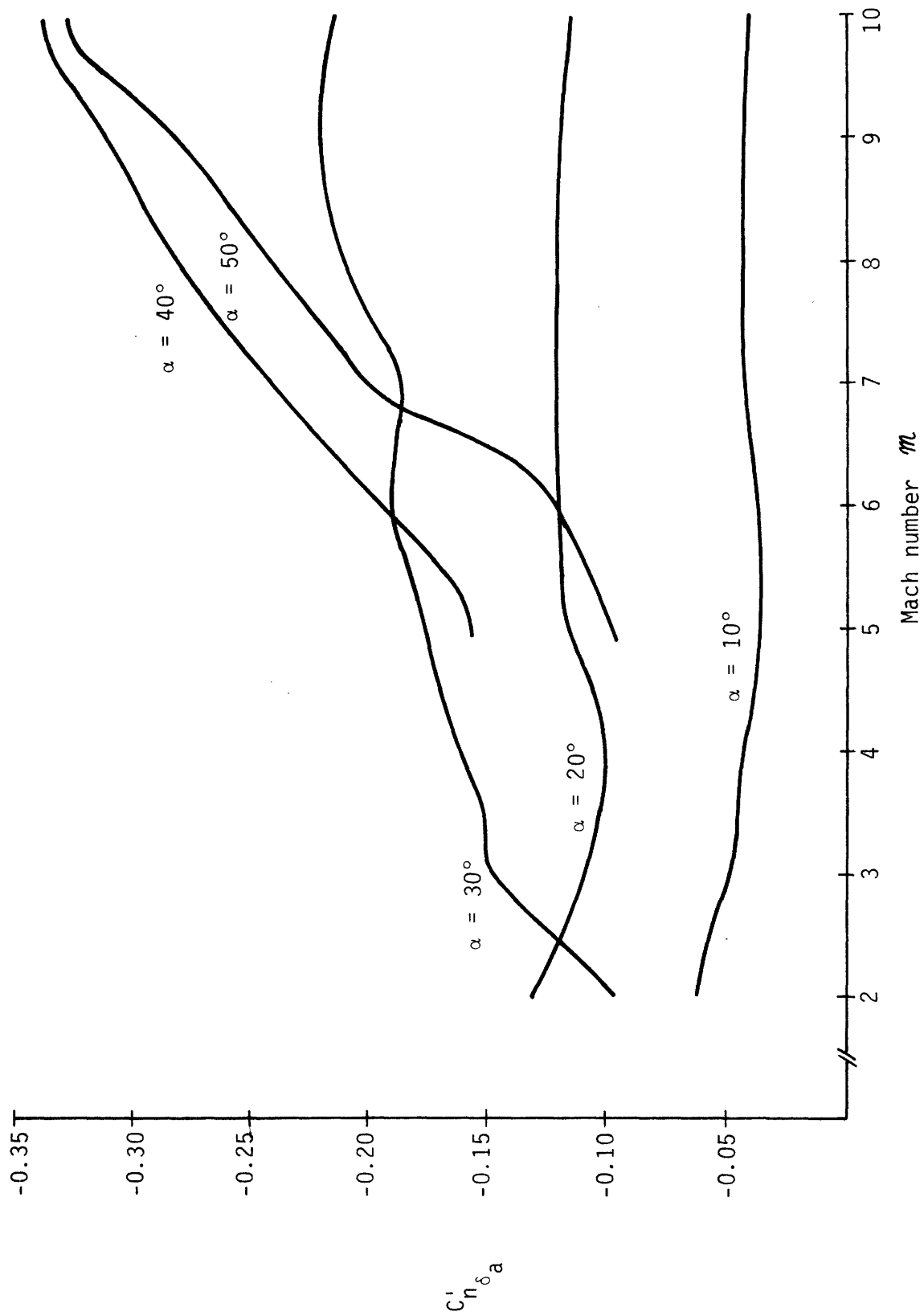
Figure B12. Yaw Due to Aileron Dynamic Derivative.

435
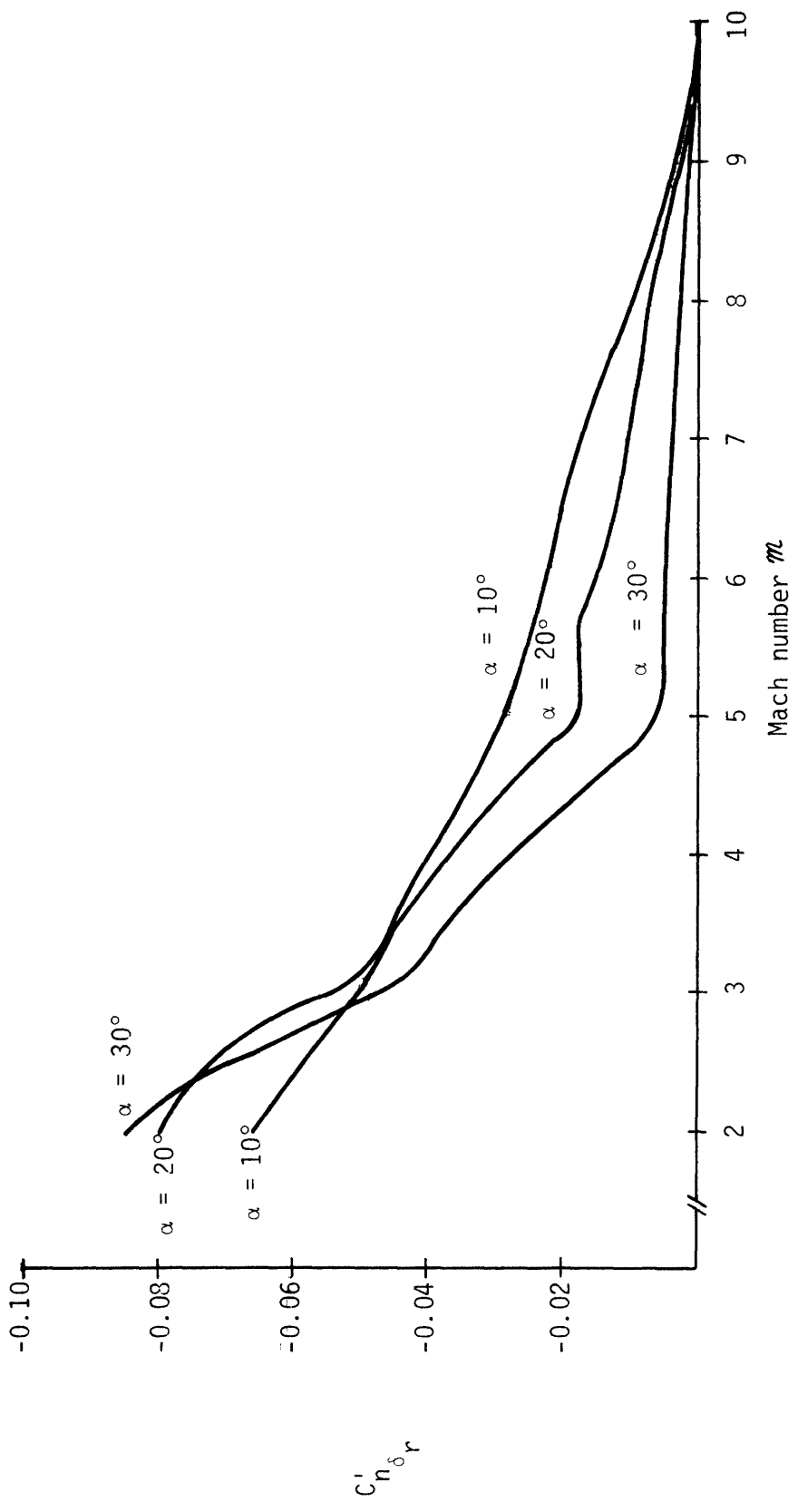
Figure B13. Yaw Due to Rudder Dynamic Derivative.

436
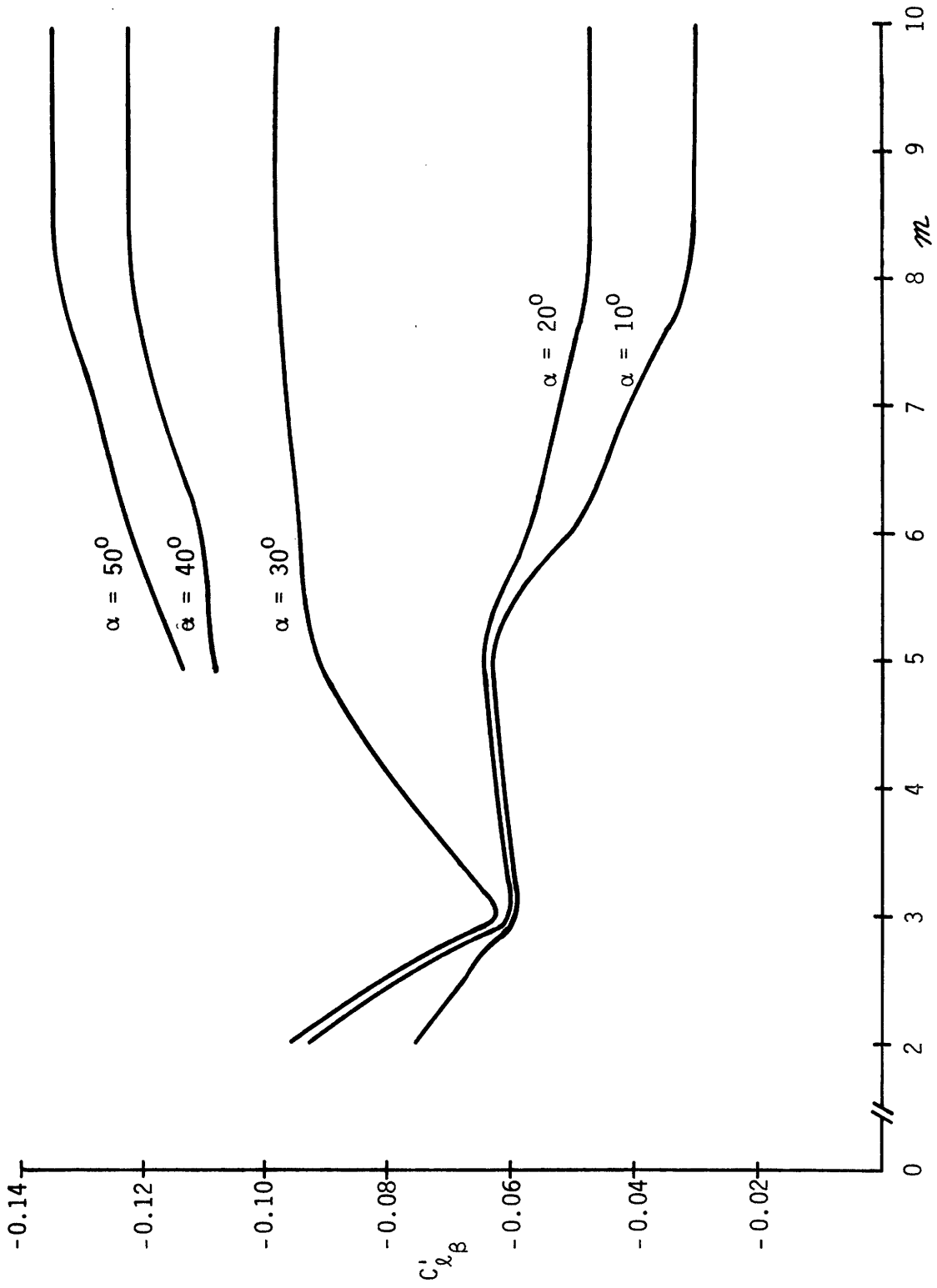
Figure B14. Roll Due to Sideslip Dynamic Derivative.

437
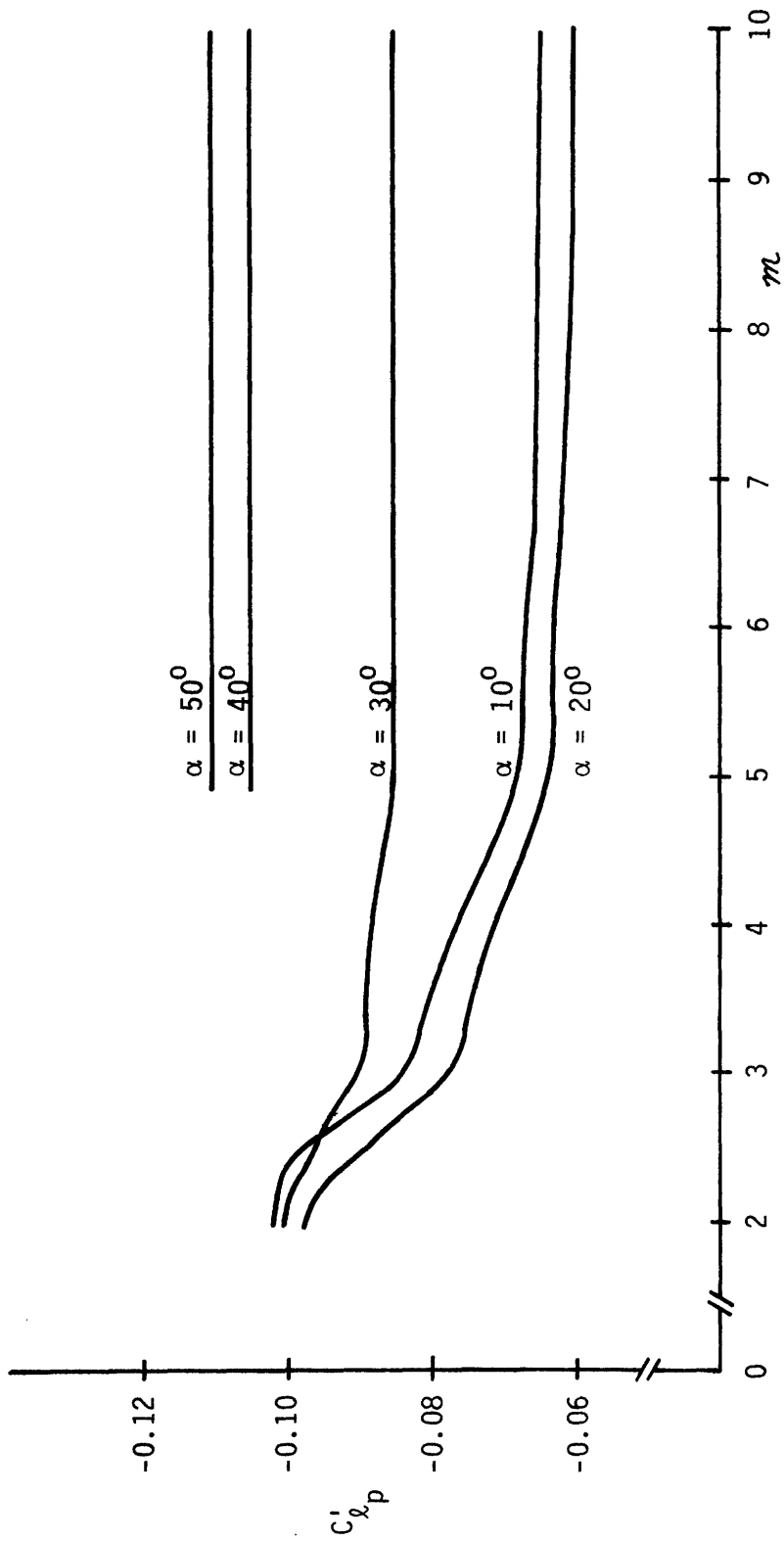
Figure B15. Roll Due to Roll Rate Dynamic Derivative.
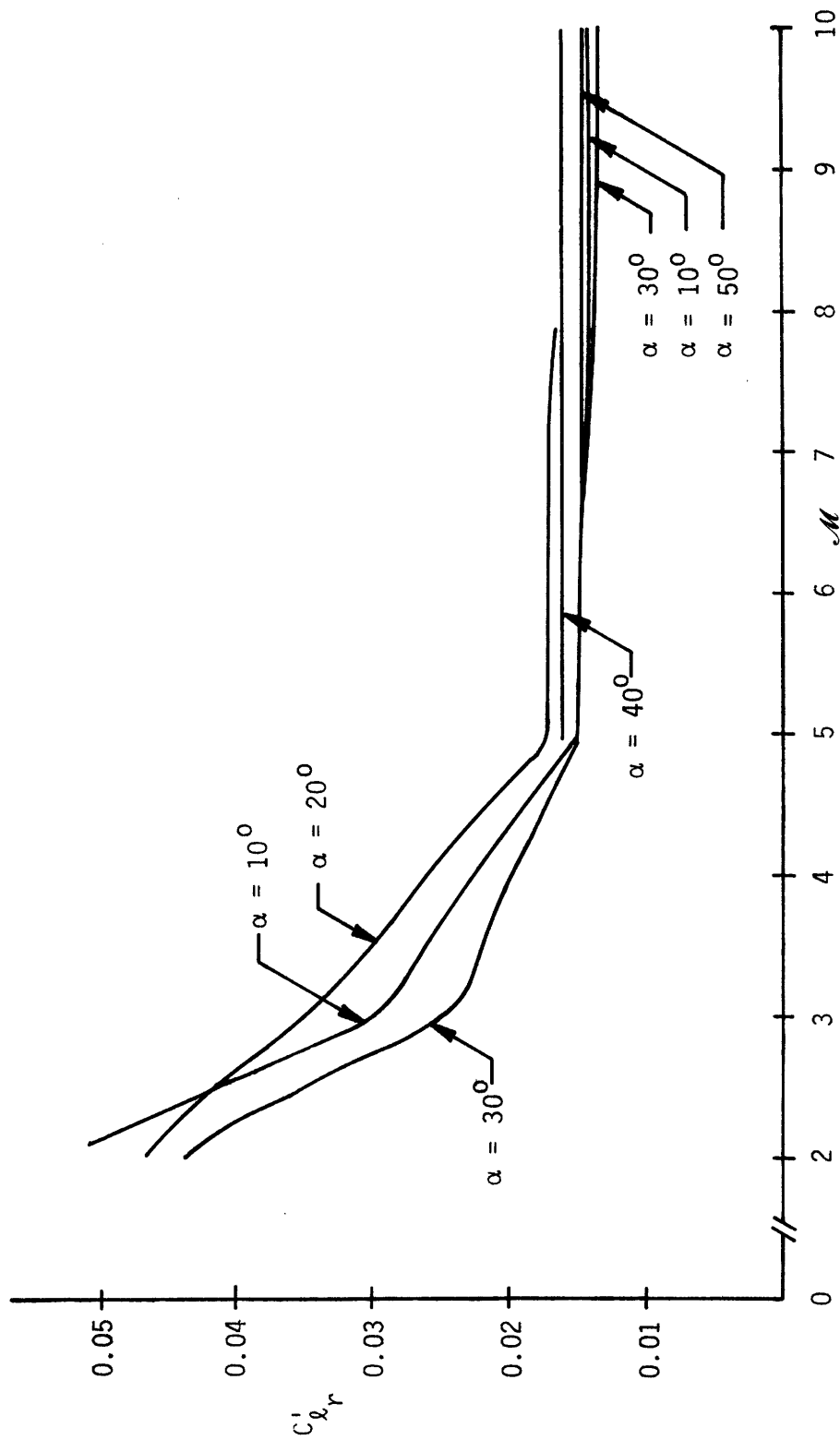
Figure B16. Roll Due to Yaw Rate Dynamic Derivative.

439
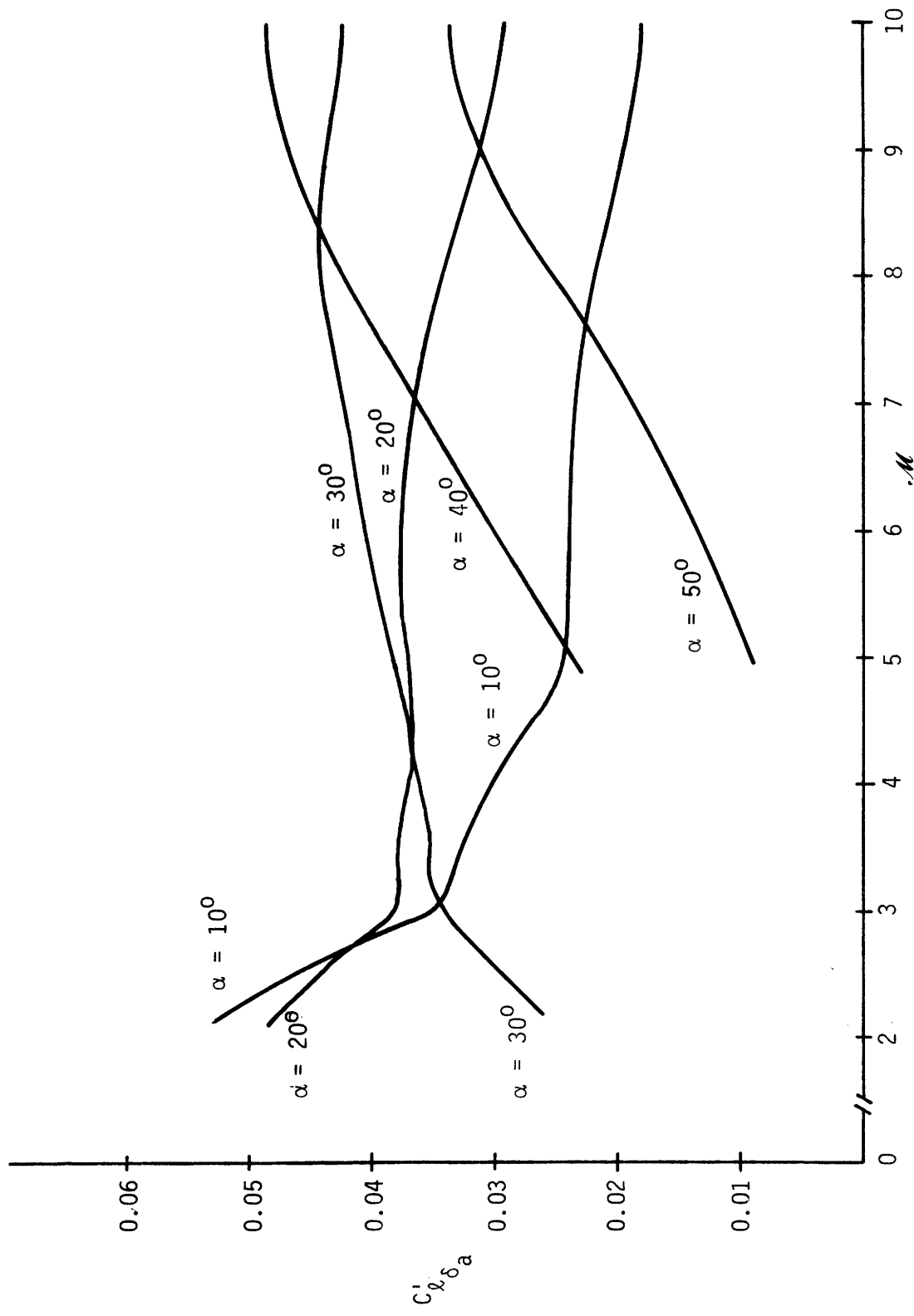
Figure B17. Roll Due to Aileron Dynamic Derivative.

440
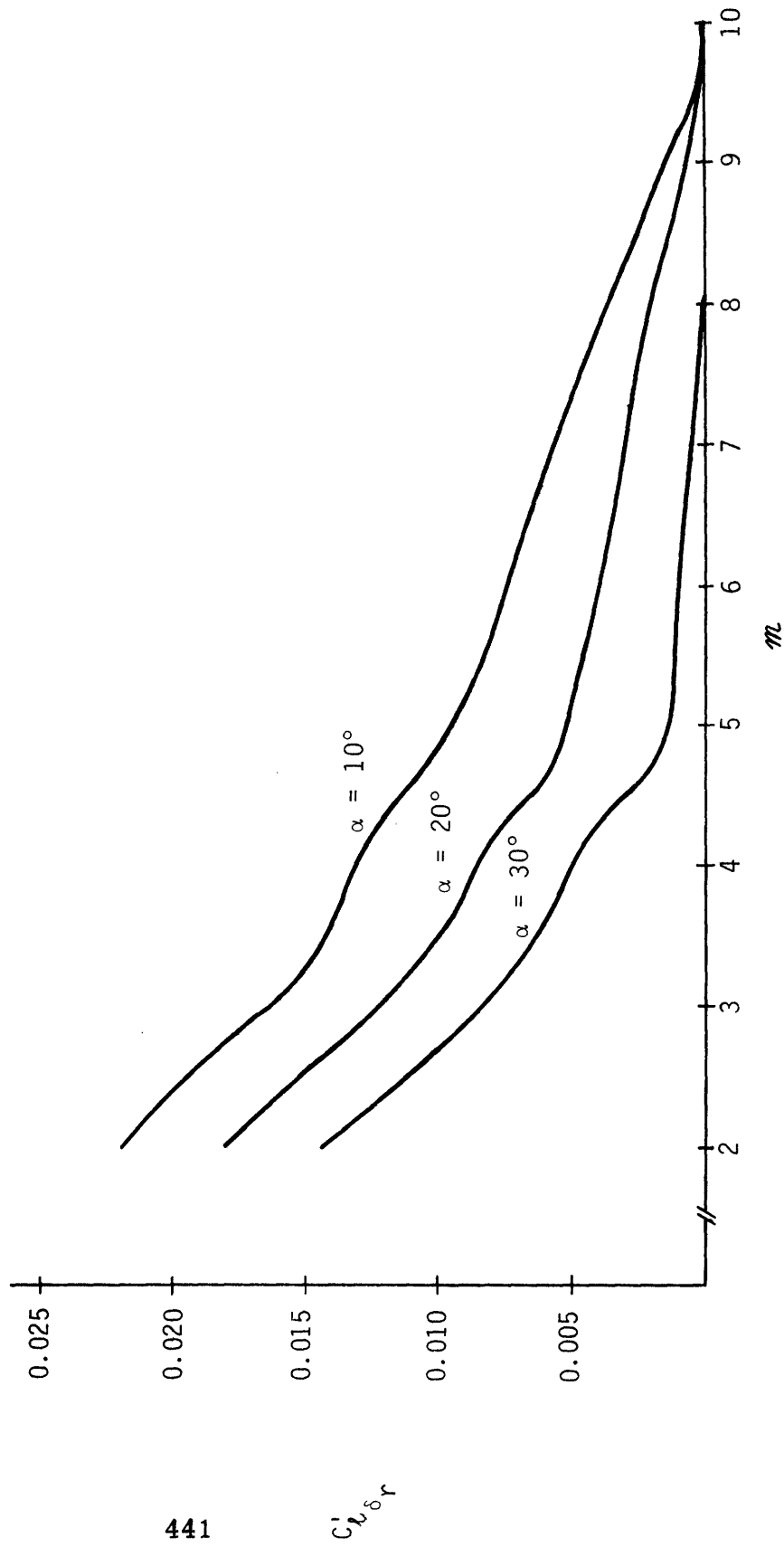
Figure B18. Roll Due to Rudder Dynamic Derivative.
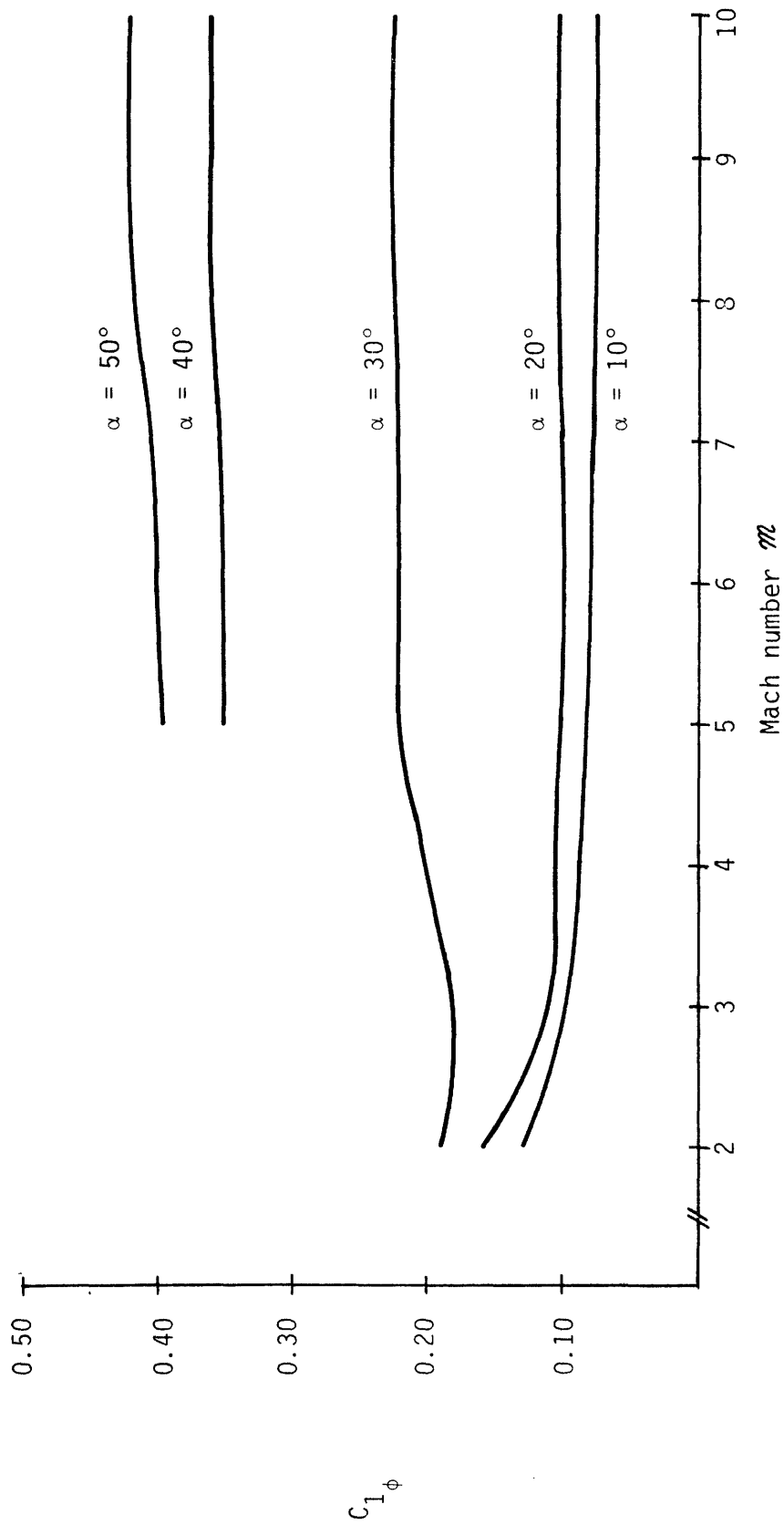
Figure B19. Bank Rate Coefficient.

442
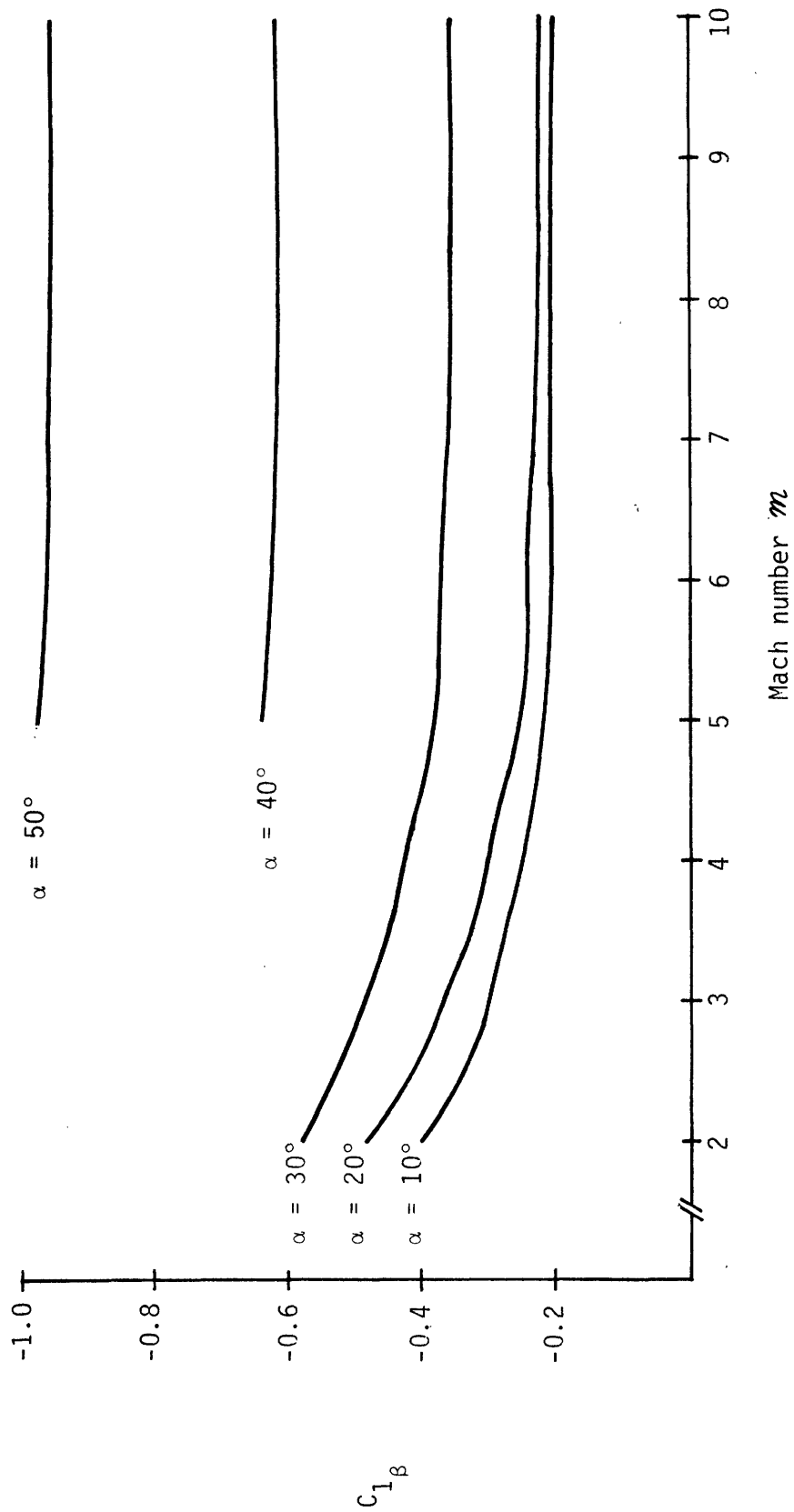
Figure B20.   Sideslip Rate Coefficient.

443
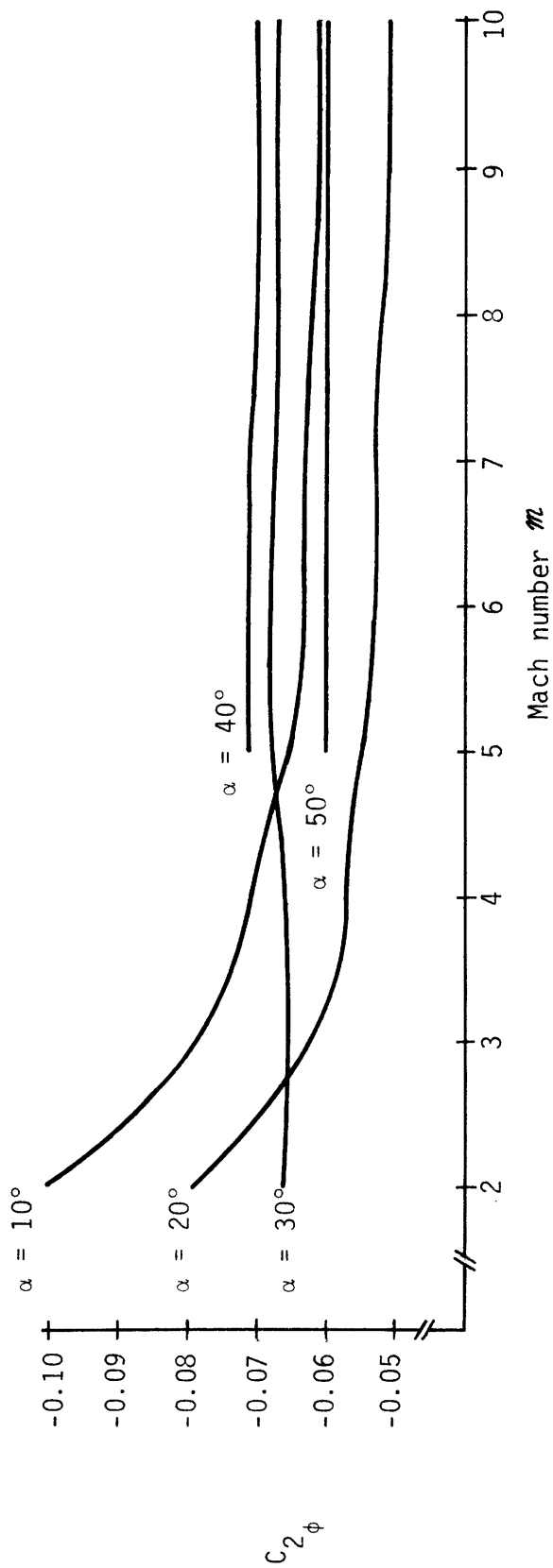
Figure B21. Bank Rate Coefficient.
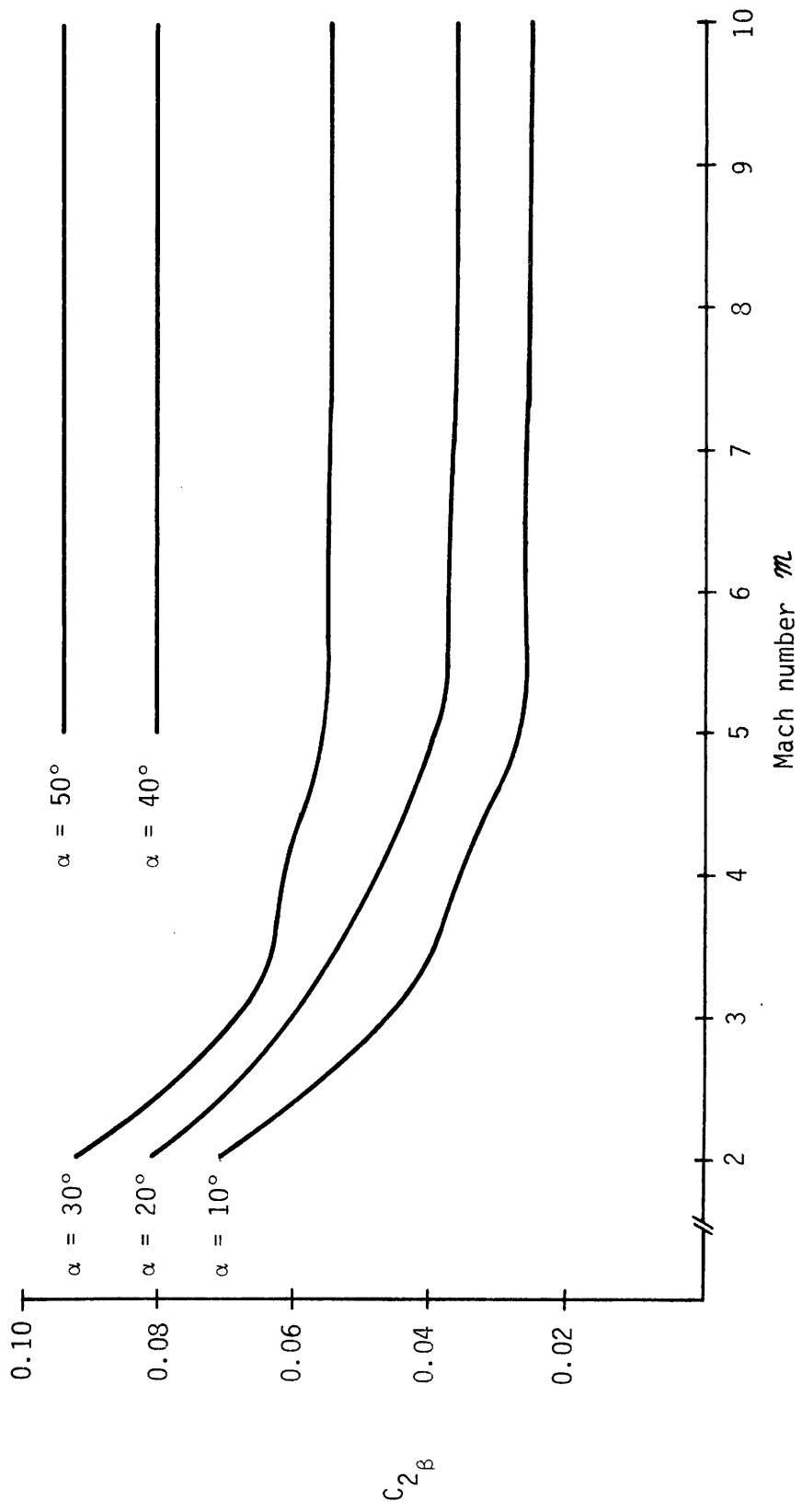
Figure B22. Sideslip Rate Coefficient.

C_{2_β}

$\alpha = 50°$

$\alpha = 40°$

$\alpha = 30°$

$\alpha = 20°$

$\alpha = 10°$

Mach number $\mathcal{M}$
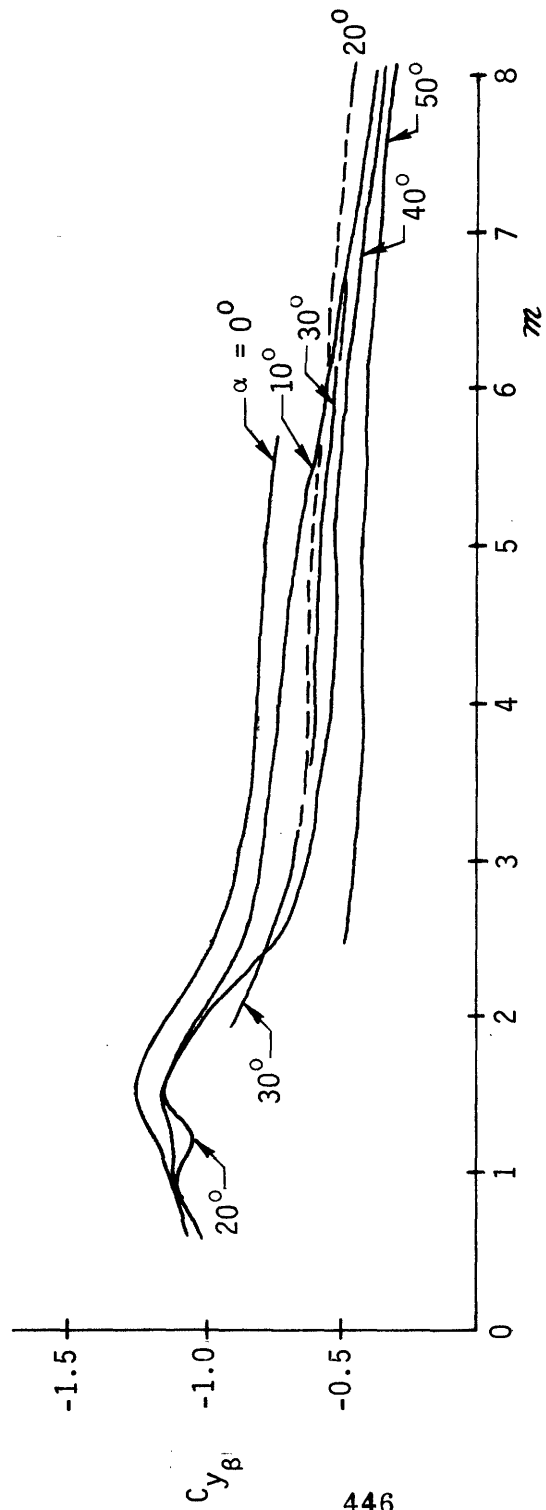
Figure B23. Side Force Derivative Due to Sideslip.

446
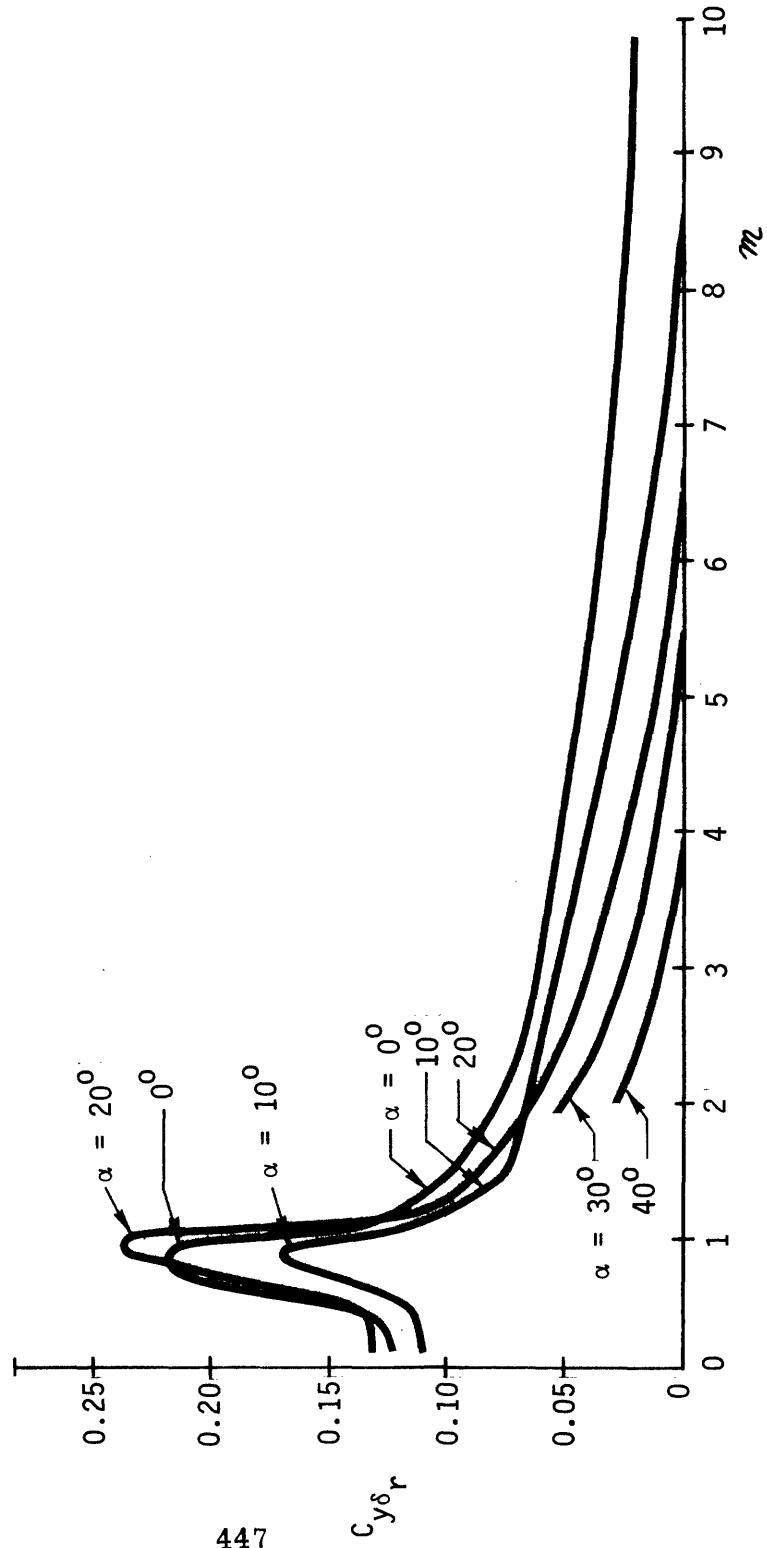
Figure B24. Side Force Derivative Due To Rudder.

447

Table B-4(cont.)

$C_{1\phi}$	0.5	(upper bound)
C_{1_β}	1.0	(upper bound on magnitude)
$C_{2\phi}$	0.1	(upper bound on magnitude)
$C_{2\beta}$	0.1; 0.06	(upper bound; typical value)
C_{y_β}	1.25	(upper bound on magnitude)
C_{y_p}	<1	(conservative upper bound; no value available)
C_{y_r}	<1	(conservative upper bound; no value available)

As noted in Section 4.3.2.1, the first objective of the lateral equation development is the expression of the body rates p and r in terms of the stability-axis variables. One equation relating the two body rates is obtained by combining (4-19a) and (4-24c) to yield:

$$\left[s - \frac{Y_v}{m} \right] \beta - \sigma_1 = g_1 p - g_2 r \tag{B-10}$$

where

$$g_1 = \left[\left(\sin \alpha_T + \frac{Y_p}{mV_T} \right) + \frac{(g/V_T)\cos\theta_o}{s} \right] \tag{a}$$

$$\tag{B-11}$$

$$g_2 = \left[\left(\cos\alpha_T - \frac{Y_r}{mV_T} \right) - \frac{(g/V_T)\sin\theta_o}{s} \right] \tag{b}$$

A second equation relating p and r is given by the definition of the bank rate:

$$s \, \phi_s = p\cos\alpha_T + r\sin\alpha_T \tag{4-27}$$

Using (B-10) and (4-27) to solve for p and r then yields:

$$p = \frac{1}{\Delta} \left\{ (\sin\alpha_T) \left[\left(s - \frac{Y_v}{m}\right) \beta - \sigma_1 \right] + g_2 s \phi_s \right\} \qquad (a)$$

$$\qquad\qquad\qquad\qquad\qquad\qquad\qquad\qquad\qquad\qquad (B-12)$$

$$r = \frac{1}{\Delta} \left\{ -(\cos\alpha_T) \left[\left(s - \frac{Y_v}{m}\right) \beta - \sigma_1 \right] + g_1 s \phi_s \right\} \qquad (b)$$

where

$$\Delta \equiv g_1 \sin\alpha_T + g_2 \cos\alpha_T$$

so that from (B-11),

$$\Delta = 1 + \frac{1}{mV_T} (Y_p \sin\alpha_T - Y_r \cos\alpha_T) - \frac{(g/V_T)\sin\gamma_o}{s} \qquad (B-13)$$

where γ_o is the flight path angle defined by (4-32). Using the stability derivative relations of Appendix A, it follows from (A-14) that:

$$\Delta = 1 + \left(\frac{\bar{q}Sb}{2mV_T^2}\right) \left(C_{y_p} \sin\alpha_T - C_{y_r} \cos\alpha_T\right) - \frac{(g/V_T) \sin\gamma_o}{s}$$

$$\qquad\qquad\qquad\qquad\qquad\qquad\qquad\qquad\qquad\qquad (B-14)$$

Now, a maximum value for the multiplicative constant of the second term is obtained in the following manner:

$$\left(\frac{\bar{q}Sb}{2mV_T^2}\right)_{max} = \frac{\bar{q}_{max}Sb}{2m(V_T^2)_{min}}$$

so that, from Tables B-1 and B-2,

$$\left(\frac{\bar{q}Sb}{2mV_T^2}\right) < 1 \times 10^{-3} \qquad (B-15)$$

In addition, it may be noted that

$$\left| \left(\frac{\bar{q}Sb}{2mV_T^2}\right) \left(C_{y_p} \sin\alpha_T - C_{y_r} \cos\alpha_T\right) \right| < \left| \left(\frac{\bar{q}Sb}{2mV_T^2}\right) \left(|C_{y_p}| + |C_{y_r}|\right) \right|$$

so that using (B-15), and the values in Table B-4,

$$\left| \left(\frac{\bar{q}Sb}{2mV_T^2} \right) \left(C_{y_p} \sin\alpha_T - C_{y_r} \cos\alpha_T \right) \right| < 2 \times 10^{-3} << 1 \qquad \text{(B-16)}$$

Thus, the second term of (B-14) may be conveniently dropped. As discussed in the previous section, the integrated gravity term of (B-14) will contribute little to the vehicle response due to both the small magnitude of the term itself (see (B-3)) and the short-time period of interest. Thus, the third term may also be dropped, so that Δ is approximated by unity. Use of (B-11) in the simplified version of (B-12) then yields the desired result defining the body rates:

$$p = \left[s - \frac{Y_v}{m} \right] (\beta \sin\alpha_T) + \left[\left(\cos\alpha_T - \frac{Y_r}{mV_T} \right) - \frac{(g/V_T)\sin\theta_o}{s} \right] s\phi_s - \sigma_1 \sin\alpha_T \quad \text{(a)}$$

(B-17)

$$r = -\left[s - \frac{Y_v}{m} \right] \left(\beta \cos\alpha_T \right) + \left[\left(\sin\alpha_T + \frac{Y_p}{mV_T} \right) + \frac{(g/V_T)\cos\theta_o}{s} \right] s\phi_s + \sigma_1 \cos\alpha_T \quad \text{(b)}$$

Sideslip Equation[*]

With (p, r) thus defined, the "sideslip equation" may be obtained by multiplying (4-19b) by $(\sin\alpha_T)$ and (4-19c) by $(-\cos\alpha_T)$ and adding, making use of (4-24c), to obtain the following:

$$\lambda_\beta \beta + \left[\left(\sin\alpha_T + \frac{I_{xz}}{I_{zz}} \cos\alpha_T \right) s + \lambda_p \right] p - \left[\left(\cos\alpha_T + \frac{I_{xz}}{I_{xx}} \sin\alpha_T \right) s - \lambda_r \right] r =$$

$$\sigma_2 \sin\alpha_T - \sigma_3 \cos\alpha_T \qquad \text{(B-18)}$$

where

---

[*]This subsection details the development of the equations presented in 4.3.2.1

$$\lambda_\beta \equiv \left[\frac{V_T N_v}{I_{zz}} \cos\alpha_T - \frac{V_T L_v}{I_{xx}} \sin\alpha_T \right] \qquad \text{(a)}$$

$$\lambda_p \equiv \left[\frac{N_p}{I_{zz}} \cos\alpha_T - \frac{L_p}{I_{xx}} \sin\alpha_T \right] \qquad \text{(b)} \qquad \text{(B-19)}$$

$$\lambda_r \equiv \left[\frac{N_r}{I_{zz}} \cos\alpha_T - \frac{L_r}{I_{xx}} \sin\alpha_T \right] \qquad \text{(c)}$$

Using (B-17) to eliminate (p, r), (B-19) becomes, after some manipulation:

$$(a_1 s^2 + a_2 s + a_3)\beta + (b_1 s^2 + b_2 s + b_3) \, \phi_s = (a_1 s + c_1)\sigma_1 + c_2\sigma_2 + c_3\sigma_3 \qquad \text{(B-20)}$$

where the coefficients are defined by:

$$a_1 \equiv 1 + \left(\frac{I_{xz}}{I_{xx}} + \frac{I_{xz}}{I_{zz}} \right) \cos\alpha_T \sin\alpha_T \qquad \text{(a)}$$

$$a_2 \equiv - \left(\frac{Y_v}{m} \right) a_1 + (\lambda_p \sin\alpha_T - \lambda_r \cos\alpha_T) \qquad \text{(b)} \qquad \text{(B-21)}$$

$$a_3 \equiv \lambda_p - \left(\frac{Y_v}{m} \right) \left(\lambda_p \sin\alpha_T - \lambda_r \cos\alpha_T \right) \qquad \text{(c)}$$

$$b_1 \equiv \left(\frac{I_{xz}}{I_{zz}} \cos^2\alpha_T - \frac{I_{xz}}{I_{xx}} \sin^2\alpha_T \right) - \frac{1}{mV_T} \left(Y_r \sin\alpha_T + Y_p \cos\alpha_T \right)$$

$$- \frac{1}{mV_T} \left(Y_r \frac{I_{xz}}{I_{zz}} \cos\alpha_T + Y_p \frac{I_{xz}}{I_{xx}} \sin\alpha_T \right) \qquad \text{(B-22a)}$$

$$b_2 \equiv - \left(\frac{g}{V_T}\right) \left(\cos\gamma_o + \frac{I_{xz}}{I_{zz}} \cos\alpha_T \sin\theta_o + \frac{I_{xz}}{I_{xx}} \sin\alpha_T \cos\theta_o\right)$$

$$+ (\lambda_p \cos\alpha_T + \lambda_r \sin\alpha_T) - \frac{1}{mV_T} (Y_r \lambda_p - Y_p \lambda_r) \qquad \text{(B-22b)}$$

$$b_3 \equiv - \left(\frac{g}{V_T}\right) \left(\lambda_p \sin\theta_o - \lambda_r \cos\theta_o\right) \qquad \text{(B-22c)}$$

$$c_1 \equiv \lambda_p \sin\alpha_T - \lambda_r \cos\alpha_T \qquad \text{(a)}$$

$$c_2 \equiv \sin\alpha_T \qquad \text{(b)} \qquad \text{(B-23)}$$

$$c_3 \equiv -\cos\alpha_T \qquad \text{(c)}$$

Prior to simplification of the above coefficients, it is convenient to redefine λ_β, λ_p, and λ_r of (B-19) in terms of the stability derivatives of Appendix A. Using (A-16) and (A-18) in (B-19) results in the following:

$$\lambda_\beta = \left(\frac{\bar{q}Sb}{I_{zz}}\right) C'_{n_\beta} \qquad \text{(a)}$$

$$\lambda_p = \left(\frac{\bar{q}Sb^2}{2V_T}\right) \left(\frac{1}{I_{zz}}\right) C'_{n_p} \qquad \text{(b)} \qquad \text{(B-24)}$$

$$\lambda_r = \left(\frac{\bar{q}Sb^2}{2V_T}\right) \left(\frac{1}{I_{zz}}\right) C'_{n_r} \qquad \text{(c)}$$

where the "transformed" derivatives (in actuality, dynamic derivatives) are given by:

$$C'_{n_\beta} \equiv C_{n_\beta} \cos\alpha_T - \frac{I_{zz}}{I_{xx}} C_{\ell_\beta} \sin\alpha_T \qquad \text{(a)}$$

$$C'_{n_p} \equiv C_{n_p} \cos\alpha_T - \frac{I_{zz}}{I_{xx}} C_{\ell_p} \sin\alpha_T \qquad \text{(b)} \qquad \text{(B-25)}$$

$$C'_{n_r} \equiv C_{n_r} \cos\alpha_T - \frac{I_{zz}}{I_{xx}} C_{\ell_r} \sin\alpha_T \qquad \text{(c)}$$

Note that the transformation from stability to dynamic derivatives is the same for each state variable. It should also be noted that (B-25) specifies the first of several dynamic derivative subsets to be introduced during this development.

Now to begin simplifying the coefficients of (B-20), it may be noted that

$$\left| \left(\frac{I_{xz}}{I_{xx}} + \frac{I_{xz}}{I_{zz}} \right) \cos\alpha_T \sin\alpha_T \right| < \frac{1}{2} \left\{ \left| \frac{I_{xz}}{I_{xx}} \right| + \left| \frac{I_{xz}}{I_{zz}} \right| \right\}$$

so that from Table B-1, there results:

$$\left| \left(\frac{I_{xz}}{I_{xx}} + \frac{I_{xz}}{I_{zz}} \right) \cos\alpha_T \sin\alpha_T \right| < 8.5 \times 10^{-2} \ll 1 \qquad \text{(B-26)}$$

Thus, a_1 may be approximated by unity:

$$a_1 = 1 \qquad \text{(B-27a)}$$

and a_2 is correspondingly simplified. Further, use of (A-14) and (B-24) gives the following relationship:

$$a_2 = -\left(\frac{\bar{q}S}{mV_T} \right) \left[C_{y_\beta} + \left(\frac{mb^2}{2I_{zz}} \right) C_{1_\beta} \right] \qquad \text{(B-27b)}$$

where, for convenience, the following definition is made:

$$C_{1_\beta} \equiv C'_{n_r} \cos\alpha_T - C'_{n_p} \sin\alpha_T \qquad \text{(B-30a)}$$

In a similar fashion, a_3 may be expanded to yield:

$$a_3 = \left(\frac{\bar{q}Sb}{I_{zz}}\right)\left[C'_{n_\beta} + \left(\frac{\bar{q}Sb}{2mV_T{}^2}\right)C_{y_\beta} C_{1_\beta}\right]$$

However, from (B-15) and Table B-4,

$$\left|\left(\frac{\bar{q}Sb}{2mV_T{}^2}\right) C_{y_\beta} C_{1_\beta}\right| < 1.25 \times 10^{-3} \ll C'_{n_\beta} \qquad \text{(B-31)}$$

so that a_3 is approximated by:

$$a_3 = \left(\frac{\bar{q}Sb}{I_{zz}}\right) C'_{n_\beta} \qquad \text{(B-27c)}$$

To approximate the bank coefficients $(b_i\text{'s})$ of (B-20), (B-22a) may be expanded using (A-14) to yield:

$$b_1 = \frac{I_{xz}}{I_{zz}} \cos\alpha_T \left[\cos\alpha_T - \left(\frac{\bar{q}Sb}{2mV_T{}^2}\right) C_{y_r}\right]$$

$$- \frac{I_{xz}}{I_{xx}} \sin\alpha_T \left[\sin\alpha_T + \left(\frac{\bar{q}Sb}{2mV_T{}^2}\right) C_{y_p}\right]$$

$$- \left(\frac{\bar{q}Sb}{2mV_T{}^2}\right)\left(C_{y_p} \cos\alpha_T + C_{y_r} \sin\alpha_T\right)$$

However, from (B-15) and Table B-4, it follows that:

$$\left|\left(\frac{\overline{q}Sb}{2mV_T^2}\right)C_{y_r}\right| < 1 \times 10^{-3} \; ; \quad \left|\left(\frac{\overline{q}Sb}{2mV_T^2}\right)C_{y_p}\right| < 1 \times 10^{-3}$$

and from Table B-2,

$$\left|\cos\alpha_T\right|_{min} = .76 \; ; \quad \left|\sin\alpha_T\right|_{min} = .17$$

so that

$$\left|\left(\frac{\overline{q}Sb}{2mV_T^2}\right)C_{y_r}\right| \ll \left|\cos\alpha_T\right| \; ; \quad \left|\left(\frac{\overline{q}Sb}{2mV_T^2}\right)C_{y_p}\right| \ll \left|\sin\alpha_T\right| \quad \text{(B-32)}$$

Thus, b_1 is approximated by:

$$b_1 = \left(\frac{I_{xz}}{I_{zz}}\cos^2\alpha_T - \frac{I_{xz}}{I_{xx}}\sin^2\alpha_T\right) - \left(\frac{\overline{q}Sb}{2mV_T^2}\right)\left(C_{y_p}\cos\alpha_T + C_{y_r}\sin\alpha_T\right)$$

$$\text{(B-28a)}$$

Recognizing from Table B-2 that

$$\cos\gamma_o \approx 1 \quad \text{(B-33)}$$

then b_2 may be expanded and simplified using (B-26), (B-32), (B-24), and (A-14), to yield:

$$b_2 = -\left(\frac{g}{V_T}\right) + \left(\frac{\overline{q}Sb^2}{2I_{zz}V_T}\right)C_{1\phi} \quad \text{(B-28b)}$$

where the following definition is used:

$$C_{1\phi} \equiv C'_{n_p}\cos\alpha_T + C'_{n_r}\sin\alpha_T \quad \text{(B-30b)}$$

455

Using (B-24), (B-30a), and (B-33) to expand b_3, the following approximation results:

$$b_3 = \left(\frac{g}{V_T}\right)\left(\frac{\bar{q}S\,b^2}{2\,I_{zz}V_T}\right)C_{1_\beta} \qquad\text{(B-28c)}$$

Finally, c_1 may be similarly expanded:

$$c_1 = -\left(\frac{\bar{q}Sb^2}{2I_{zz}V_T}\right)C_{1_\beta} \qquad\text{(B-29a)}$$

and c_2 and c_3 are given by:

$$c_2 = \sin\alpha_T \qquad\text{(B-29b)}$$

$$c_3 = -\cos\alpha_T \qquad\text{(B-29c)}$$

Now, to express the right-hand side of (4-20) in terms of the control variables, it is necessary to recall the definitions of the σ_i's:

$$\sigma_1 \equiv \frac{Y_{\delta r}}{mV_T}\,\hat{\delta}_r + \frac{Y_{\delta a}}{mV_T}\,\hat{\delta}_a \qquad\text{(a)}$$

$$\sigma_2 \equiv \frac{L_{\delta r}}{I_{xx}}\,\hat{\delta}_r + \frac{L_{\delta a}}{I_{xx}}\,\hat{\delta}_a + u_x \qquad\text{(b)} \qquad\qquad\text{(4-20)}$$

$$\sigma_3 \equiv \frac{N_{\delta r}}{I_{zz}}\,\hat{\delta}_r + \frac{N_{\delta a}}{I_{zz}}\,\hat{\delta}_a + u_z \qquad\text{(c)}$$

With the above relations, and those of (B-29) and the appropriate expressions in Appendix A, the right-hand side of (4-20) becomes:

$$(s + c_1)\sigma_1 + c_2\sigma_2 + c_3\sigma_3 =$$

$$\left(\frac{\overline{q}Sb}{I_{zz}}\right) \left\{ \left(\frac{I_{zz}}{mbV_T}\right) C_{y\delta_r} s - \left[C'_{n\delta_r} + \left(\frac{\overline{q}Sb}{2mV_T^2}\right) C_{y\delta_r} C_{1_\beta} \right] \right\} \hat{\delta}_r$$

$$+ \left(\frac{\overline{q}Sb}{I_{zz}}\right) \left\{ \left(\frac{I_{zz}}{mbV_T}\right) C_{y\delta_a} s - \left[C'_{n\delta_a} + \left(\frac{\overline{q}Sb}{2mV_T^2}\right) C_{y\delta_a} C_{1_\beta} \right] \right\} \hat{\delta}_a$$

$$+ u_x \sin\alpha_T - u_z \cos\alpha_T \tag{B-34}$$

where two additional "dynamic" derivatives are defined for convenience:

$$C'_{n\delta_r} \equiv C_{n\delta_r} \cos\alpha_T - \frac{I_{zz}}{I_{xx}} C_{\ell\delta_r} \sin\alpha_T \tag{d}$$

$$\tag{B-25}$$

$$C'_{n\delta_a} \equiv C_{n\delta_a} \cos\alpha_T - \frac{I_{zz}}{I_{xx}} C_{\ell\delta_a} \sin\alpha_T \tag{e}$$

It should be noted that all five dynamic derivatives defined by (B-25) have the same functional form and thus motivates the general definition given in (4-43).

In order to simplify (B-34), it may be noted from (B-15) and Table B-4 that

$$\left| \left(\frac{\overline{q}Sb}{2mV_T^2}\right) C_{1_\beta} \right| < 1 \times 10^{-3} \ll 1 \tag{B-35}$$

Referring to Figures B-24 and B-13, it may be seen that the two derivatives $C_{y\delta_r}$ and $C'_{n\delta_r}$ are of the same order of magnitude over the envelope of interest. This same magnitude relation is assumed for $C_{y\delta_a}$ and $C'_{n\delta_a}$. Thus,

$$\left| C_{y\delta_r} \right| \sim \left| C'_{n\delta_r} \right| \quad ; \quad \left| C_{y\delta_a} \right| \sim \left| C'_{n\delta_a} \right| \tag{B-36}$$

From (B-35) and (B-36), it follows that

$$\left| \left(\frac{\bar{q}Sb}{2mV_T^2} \right) C_{y\delta_r} C_{1_\beta} \right| << \left| C'_{n\delta_r} \right| \; ; \; \left| \left(\frac{\bar{q}Sb}{2mV_T^2} \right) C_{y\delta_a} C_{1_\beta} \right| << \left| C'_{n\delta_a} \right|$$

(B-37)

Thus, the following approximation to (B-34) can be made:

$$(s+c_1)\, \sigma_1 + c_2\sigma_2 + c_3\sigma_3 = \left(\frac{\bar{q}Sb}{I_{zz}} \right) \left\{ \left(\frac{I_{zz}}{mbV_T} \right) C_{y\delta_r} s - C'_{n\delta_r} \right\} \hat{\delta}_r$$

$$+ \left(\frac{\bar{q}Sb}{I_{zz}} \right) \left\{ \left(\frac{I_{zz}}{mbV_T} \right) C_{y\delta_a} s - C'_{n\delta_a} \right\} \hat{\delta}_a$$

$$+ u_x \sin\alpha_T - u_z \cos\alpha_T$$

(B-38)

The "sideslip equation", (B-20), can now be considerably simplified. Substitution of (B-27), (B-28), (B-29), and (B-38) into (B-20) yields the simplified model of the short-period sideslip dynamics expressed in (4-40) and (4-41). This then completes the derivation of the simplified sideslip dynamic model.

Bank Equation[*]

As was done for the sideslip dynamics, the "bank equation" may be obtained by multiplying (4-19b) by $(\cos\alpha_T)$ and (4-19c) by $(\sin\alpha_T)$ and adding, making use of (4-24c):

$$-\nu_\beta \beta + \left[(\cos\alpha_T - \frac{I_{xz}}{I_{zz}} \sin\alpha_T)s - \nu_p \right] p + \left[\left(\sin\alpha_T - \frac{I_{xz}}{I_{xx}} \cos\alpha_T \right) s - \nu_r \right] r$$

$$= \sigma_2 \cos\alpha_T + \sigma_3 \sin\alpha_T$$

(B-39)

---

[*]This section details the development of the equations presented in 4.3.2.2.

where

$$\nu_\beta \equiv \left[\frac{V_T L_v}{I_{xx}} \cos\alpha_T + \frac{V_T N_v}{I_{zz}} \sin\alpha_T\right] \qquad \text{(a)}$$

$$\nu_p \equiv \left[\frac{L_p}{I_{xx}} \cos\alpha_T + \frac{N_p}{I_{zz}} \sin\alpha_T\right] \qquad \text{(b)} \qquad \text{(B-40)}$$

$$\nu_r \equiv \left[\frac{L_r}{I_{xx}} \cos\alpha_T + \frac{N_r}{I_{zz}} \sin\alpha_T\right] \qquad \text{(c)}$$

As before, the body rates may be eliminated from (B-39) by application of (B-17), so that the bank equation becomes, after some manipulation:

$$(d_1 s^2 + d_2 s + d_3)\,\beta + (e_1 s^2 + e_2 s + e_3)\phi_s = (d_1 s + f_1)\,\sigma_1 + f_2\sigma_2 + f_3\sigma_3 \qquad \text{(B-41)}$$

where the coefficients are defined by:

$$d_1 \equiv \left(\frac{I_{xz}}{I_{xx}} \cos^2\alpha_T - \frac{I_{xz}}{I_{zz}} \sin^2\alpha_T\right) \qquad \text{(a)}$$

$$d_2 \equiv -\left(\frac{Y_v}{m}\right) d_1 + (\nu_r \cos\alpha_T - \nu_p \sin\alpha_T) \qquad \text{(b)} \qquad \text{(B-42)}$$

$$d_3 = -\nu_\beta - \left(\frac{Y_v}{m}\right)\left(\nu_r \cos\alpha_T - \nu_p \sin\alpha_T\right) \qquad \text{(c)}$$

$$e_1 \equiv 1 - \left(\frac{I_{xz}}{I_{xx}} + \frac{I_{xz}}{I_{zz}}\right) \cos\alpha_T \sin\alpha_T - \frac{1}{mV_T}\left(Y_r \cos\alpha_T - Y_p \sin\alpha_T\right)$$

$$- \frac{1}{mV_T}\left(Y_r \frac{I_{xz}}{I_{zz}} \sin\alpha_T - Y_p \frac{I_{xz}}{I_{xx}} \cos\alpha_T\right) \qquad \text{(B-43a)}$$

$$e_2 \equiv -\left(\frac{g}{V_T}\right)\left[\sin\gamma_0 - \left(\frac{I_{xz}}{I_{zz}}\sin\alpha_T\sin\theta_0 - \frac{I_{xz}}{I_{xx}}\cos\alpha_T\sin\theta_0\right)\right]$$

$$- (\nu_p\cos\alpha_T + \nu_r\sin\alpha_T) - \frac{1}{mV_T}\left(Y_r\nu_p - Y_p\nu_r\right) \qquad \text{(B-43b)}$$

$$e_3 \equiv \left(\frac{g}{V_T}\right)(\nu_p\sin\theta_0 - \nu_r\cos\theta_0) \qquad \text{(B-43c)}$$

$$f_1 \equiv (\nu_r\cos\alpha_T - \nu_p\sin\alpha_T) \qquad \text{(a)}$$

$$f_2 \equiv \cos\alpha_T \qquad \text{(b)} \quad \text{(B-44)}$$

$$f_3 \equiv \sin\alpha_T \qquad \text{(c)}$$

Prior to simplification of the above coefficients, it is convenient to redefine ν_β, ν_p, and ν_r in terms of the stability derivatives of Appendix A. Using (B-40), (A-16), and (A-18), there results:

$$\nu_\beta = \left(\frac{\bar{q}Sb}{I_{xx}}\right)C'_{\ell_\beta} \qquad \text{(a)}$$

$$\nu_p = \left(\frac{\bar{q}Sb^2}{2V_T}\right)\left(\frac{1}{I_{xx}}\right)C'_{\ell_p} \qquad \text{(b)} \quad \text{(B-45)}$$

$$\nu_r = \left(\frac{\bar{q}Sb^2}{2V_T}\right)\left(\frac{1}{I_{xx}}\right)C'_{\ell_r} \qquad \text{(c)}$$

where the transformed derivatives (again, dynamic derivatives) are given by:

$$C'_{\ell_\beta} \equiv C_{\ell_\beta} \cos\alpha_T + \frac{I_{xx}}{I_{zz}} C_{n_\beta} \sin\alpha_T \qquad \text{(a)}$$

$$C'_{\ell_p} \equiv C_{\ell_p} \cos\alpha_T + \frac{I_{xx}}{I_{zz}} C_{n_p} \sin\alpha_T \qquad \text{(b)} \quad \text{(B-46)}$$

$$C'_{\ell_r} = C_{\ell_r} \cos\alpha_T + \frac{I_{xx}}{I_{zz}} C_{n_r} \sin\alpha_T \qquad \text{(c)}$$

Again, it should be noted that the transformation from stability to dynamic derivatives is the same for each state variable, although the transformation itself is different from that used to describe the sideslip dynamics, (B-25). This is due to the fact that the above equation set resolves the inertial and aerodyanmic parameters about the velocity vector (bank axis), while (B-25) resolves the same parameters about the sideslip rotation vector.

In order to simplify the coefficients of (B-41), it is convenient to first repeat the definition of d_1 for later reference:

$$d_1 = \left(\frac{I_{xz}}{I_{xx}} \cos^2\alpha_T - \frac{I_{xz}}{I_{zz}} \sin^2\alpha_T \right) \qquad \text{(B-47a)}$$

Making use of (A-14), (B-45), and the above relation, (B-42b) may be expanded as follows:

$$d_2 = -\left(\frac{\bar{q}Sb^2}{2I_{xx}V_T} \right) \left[C_{2_\beta} + \left(\frac{2I_{xx}}{mb^2} \right) \left(\frac{I_{xz}}{I_{xx}} \cos^2\alpha_T - \frac{I_{xz}}{I_{zz}} \sin^2\alpha_T \right) C_{y_\beta} \right]$$

$$\text{(B-50)}$$

where, for convenience, the following definition is made:

$$C_{2_\beta} \equiv C'_{\ell_r} \cos\alpha_T - C'_{\ell_p} \sin\alpha_T \qquad \text{(B-51a)}$$

Now, from Tables B-1 and B-2 it may be seen that

$$\left| \left(\frac{2I_{xx}}{mb^2}\right) \left(\frac{I_{xz}}{I_{xx}} \cos^2\alpha_T - \frac{I_{xz}}{I_{zz}} \sin^2\alpha_T\right) \right| < 1.1 \times 10^{-3}$$

so that from Table B-4, it follows that

$$\left| \left(\frac{2I_{xx}}{mb^2}\right) \left(\frac{I_{xz}}{I_{xx}} \cos^2\alpha_T - \frac{I_{xz}}{I_{zz}} \sin^2\alpha_T\right) C_{y_\beta} \right| < 1.4 \times 10^{-3} << \left| C_{2_\beta} \right|$$

$$(B-52)$$

Thus, (B-50) simplifies to

$$d_2 = -\left(\frac{\overline{q}Sb^2}{2I_{xx}V_T}\right) C_{2_\beta} \qquad (B-47b)$$

Making use of (B-45), (B-51a), and (A-14), d_3 may be expressed as follows:

$$d_3 = -\left(\frac{\overline{q}Sb}{I_{xx}}\right) \left[C'_{\ell_\beta} + \left(\frac{\overline{q}Sb}{2mV_T^2}\right) C_{y_\beta} C_{2_\beta} \right]$$

However, from (B-15) and Table B-4,

$$\left| \left(\frac{\overline{q}Sb}{2mV_T^2}\right) C_{y_\beta} C_{2_\beta} \right| < 1.25 \times 10^{-4} << \left| C'_{\ell_\beta} \right| \qquad (B-53)$$

Thus, d_3 simplifies to:

$$d_3 = -\left(\frac{\overline{q}Sb}{I_{xx}}\right) C'_{\ell_\beta} \qquad (B-47c)$$

To approximate the bank coefficients of (B-41), (A-14) may be
used to expand (B-43a) to yield the following expression for e_1:

$$e_1 = 1 - \frac{I_{xz}}{I_{xx}} \left[\sin\alpha_T + \left(\frac{\overline{q}Sb}{2mV_T^2}\right) C_{y_p} \right] \cos\alpha_T$$

$$- \frac{I_{xz}}{I_{zz}} \left[\cos\alpha_T - \left(\frac{\overline{q}Sb}{2mV_T^2}\right) C_{y_r} \right] \sin\alpha_T$$

$$+ \left(\frac{\overline{q}Sb}{2mV_T^2}\right) (C_{y_p} \sin\alpha_T - C_{y_r} \cos\alpha_T)$$

Use of (B-16) and (B-32) reduces this expression to:

$$e_1 = 1 - \left(\frac{I_{xz}}{I_{xx}} + \frac{I_{xz}}{I_{zz}}\right) \cos\alpha_T \sin\alpha_T$$

Use of (B-26) thus reduces e_1 to unity:

$$e_1 = 1 \qquad\qquad \text{(B-48a)}$$

Making use of (B-40a), (A-14), and (B-32), the expression for
e_2 may be similarly simplified:

$$e_2 = - \left(\frac{g}{V_T}\right) \left[\sin\gamma_0 - \left(\frac{I_{xz}}{I_{zz}} \sin\alpha_T \sin\theta_0 - \frac{I_{xz}}{I_{xx}} \cos\alpha_T \cos\theta_0\right) \right]$$

$$- \left(\frac{\overline{q}Sb^2}{2I_{xx}V_T}\right) C_{2_\phi} \qquad\qquad \text{(B-48b)}$$

where, for convenience, the following definition is made:

$$C_{2_\phi} = C'_{\ell_p} \cos\alpha_T + C'_{\ell_r} \sin\alpha_T \qquad \text{(B-51b)}$$

Use of (B-33), (B-45), and (B-51a) allows for the following approximation of e_3:

$$e_3 = -\left(\frac{g}{V_T}\right)\left(\frac{\bar{q}Sb^2}{2I_{xx}V_T}\right)C_{2_\beta} \qquad \text{(B-48c)}$$

Similarly,

$$f_1 = \left(\frac{\bar{q}Sb^2}{2I_{xx}V_T}\right)C_{2_\beta} \qquad \text{(a)}$$

$$f_2 = \cos\alpha_T \qquad \text{(b)} \qquad \text{(B-49)}$$

$$f_3 = \sin\alpha_T \qquad \text{(c)}$$

Now, to expand the right-hand side of the bank equation, (B-41), use may be made of (4-20), (B-49), and the appropriate expressions in Appendix A, to yield:

$$(d_1s+f_1)\sigma_1 + f_2\sigma_2 + f_3\sigma_3 = \left(\frac{\bar{q}Sb}{I_{xx}}\right)\left\{\left(\frac{I_{xz}}{mbV_T}\right)\left(\cos^2\alpha_T - \frac{I_{xx}}{I_{zz}}\sin^2\alpha_T\right)C_{y\delta_r}s\right.$$

$$\left.+\left[C'_{\ell\delta_r} + \left(\frac{\bar{q}Sb}{2mV_T^2}\right)C_{y\delta_r}C_{2_\beta}\right]\right\}\hat{\delta}_r$$

$$+\left(\frac{\bar{q}Sb}{I_{xx}}\right)\left\{\left(\frac{I_{xz}}{mbV_T}\right)\left(\cos^2\alpha_T - \frac{I_{xx}}{I_{zz}}\sin^2\alpha_T\right)C_{y\delta_a}s\right.$$

$$\left.+\left[C'_{\ell\delta_a} + \left(\frac{\bar{q}Sb}{2mV_T^2}\right)C_{y\delta_a}C_{2_\beta}\right]\right\}\hat{\delta}_a$$

$$+ u_x\cos\alpha_T + u_z\sin\alpha_T \qquad \text{(B-54)}$$

where the remaining bank dynamic derivatives are defined by:

464

$$C'_{\ell\delta_r} \equiv C_{\ell\delta_r}\cos\alpha_T + \frac{I_{xx}}{I_{zz}}C_{n\delta_r}\sin\alpha_T \qquad \text{(d)}$$

$$\text{(B-46)}$$

$$C'_{\ell\delta_a} \equiv C_{\ell\delta_a}\cos\alpha_T + \frac{I_{xx}}{I_{zz}}C_{n\delta_a}\sin\alpha_T \qquad \text{(e)}$$

It should be noted that all five dynamic derivatives defined by (B-46) have the same functional form, and thus motivates the general definition given in (4-47).

In order to simplify (B-54), it may be noted from (B-15) and Table B-4 that

$$\left|\left(\frac{\bar{q}Sb}{2mV_T^2}\right)C_{2_\beta}\right| < 1 \times 10^{-4} << 1 \qquad \text{(B-55)}$$

Referring to Figures B-18 and B-24, it may be seen that the derivative $C'_{\ell\delta_r}$ is typically an order of magnitude smaller than $C_{y\delta_r}$. This same magnitude relation will be assumed between $C'_{\ell\delta_a}$ and $C_{y\delta_a}$, so that:

$$\left|C_{y\delta_r}\right| \sim 10\left|C'_{\ell\delta_r}\right| \quad ; \quad \left|C_{y\delta_a}\right| \sim 10\left|C'_{\ell\delta_a}\right| \qquad \text{(B-56)}$$

From (B-55) and (B-56), it follows that:

$$\left|\left(\frac{\bar{q}Sb}{2mV_T^2}\right)C_{y\delta_r}C_{2_\beta}\right| << \left|C'_{\ell\delta_r}\right| \quad ; \quad \left|\left(\frac{\bar{q}Sb}{2mV_T^2}\right)C_{y\delta_a}C_{2_\beta}\right| << \left|C'_{\ell\delta_a}\right|$$

$$\text{(B-57)}$$

Thus, the following approximation to (B-54) may be made:

$$(d_1 s + f_1)\,\sigma_1 + f_2 \sigma_2 + f_3 \sigma_3 =$$

$$\left(\frac{\bar{q}Sb}{I_{xx}}\right)\left\{\left(\frac{I_{xz}}{mbV_T}\right)\left(\cos^2\alpha_T - \frac{I_{xx}}{I_{zz}}\sin^2\alpha_T\right)C_{y\delta_r} s + C'_{\ell\delta_r}\right\}\hat{\delta}_r$$

$$(B\text{-}58)$$

$$+ \left(\frac{\bar{q}Sb}{I_{xx}}\right)\left\{\left(\frac{I_{xz}}{mbV_T}\right)\left(\cos^2\alpha_T - \frac{I_{xx}}{I_{zz}}\sin^2\alpha_T\right)C_{y\delta_a} s + C'_{\ell\delta_a}\right\}\hat{\delta}_a$$

$$+ u_x \cos\alpha_T + u_z \sin\alpha_T$$

The "bank equation", (B-41), can now be considerately simplified.
Substitution of (B-47), (B-48), (B-49), and (B-58) into (B-41) yields
the simplified model of the short-period bank dynamics expressed
in (4-44) and (4-45). This then completes the derivation of the
simplified bank dynamic model.

Sideslip-Bank Coupling[*]

Additional simplifications may be made to both the sideslip
and bank equations, (4-40) and (4-44), respectively. In particular,
for the coefficients of (4-40), it may be noted from the definition
of b_1 given in (4-41c) that:

$$|b_1| < \left|\frac{I_{xz}}{I_{zz}}\cos^2\alpha_T - \frac{I_{xz}}{I_{xx}}\sin^2\alpha_T\right|_{max} + \left(\frac{\bar{q}Sb}{2mV_T^2}\right)_{max}\left[|C_{y_p}| + |C_{y_r}|\right]$$

so that, from (B-15) and Tables B-1, B-2, and B-4,

$$|b_1| < 2.5 \times 10^{-2} << 1 \qquad\qquad (B\text{-}59)$$

In addition, from the definitions of ω_β^2 and b_3 given by (4-41a) and
(4-41e), respectively, it follows that:

$$\frac{10^2 b_3}{\omega_\beta^2} = 10^2\left(\frac{gb}{2V_T^2}\right)\left(\frac{C_{\ell\beta}}{C'_{n_\beta}}\right)$$

[*]This subsection supports the development of the equations presented
in 4.3.2.3

so that, from Tables B-1, B-2, and B-4,

$$10^2 \frac{|b_3|}{|\omega^2_\beta|} < 0.1$$

Although not as conservative a margin as has been utilized to this point in the development, the above order-of-magnitude difference justifies the following statement of relative magnitudes:

$$10^2 |b_3| << |\omega^2_\beta| \qquad \text{(B-60)}$$

Finally, recognizing from Tables B-1 and B-2 that

$$\left(\frac{I_{zz}}{mbV_T}\right) < 8 \times 10^{-3}$$

and making use of (B-36) and the coefficient definitions given in (4-41g) and (4-41h), it follows that:

$$|\lambda'_{\delta_r}| << |\lambda_{\delta_r}| \quad ; \quad |\lambda'_{\delta_a}| << |\lambda_{\delta_a}| \qquad \text{(B-61)}$$

Section 4.3.2.3 makes use of the above three relations, (B-59), (B-60), and (B-61) in further simplifications to the sideslip equation. Similar relations may be found to aid in simplifying the bank equation: in particular, for the coefficients of (4-44), it may be noted from the definition of d_1 given in (4-45a) and the parameter values given in Tables B-1 and B-2, that:

$$|d_1| < 2.3 \times 10^{-2} << 1 \qquad \text{(B-62)}$$

In addition, from the definitions of d_3 and e_3 given by (4-45c) and (4-45e), respectively, it follows that

$$\frac{10^2 e_3}{d_3} = 10^2 \left(\frac{gb}{2V_T^2}\right)\left(\frac{C_{2\beta}}{C'_{\ell_\beta}}\right)$$

467

so that from Tables B-1, B-2, and B-4,

$$10^2 \frac{|e_3|}{|d_3|} < 3.2 \times 10^{-2}$$

so that the following conclusion holds:

$$10^2 |e_3| << |d_3| \tag{B-63}$$

Further, from the definitions of d_2 and d_3 given by (4-45b) and (4-45c), respectively, it follows that:

$$\frac{d_2}{d_3} = \left(\frac{b}{2V_T} \right) \left(\frac{C_{2_\beta}}{C'_{\ell_\beta}} \right)$$

so that from Tables B-1, B-2, and B-4,

$$\frac{|d_2|}{|d_3|} < 2 \times 10^{-2} << 1$$

so that the following conclusion holds:

$$|d_2| << |d_3| \tag{B-64}$$

Finally, recognizing from Tables B-1 and B-2 that

$$\left| \frac{I_{xz}}{mbV_T} \right| < 1.7 \times 10^{-4}$$

and making use of (B-56) and the coefficient definitions given in (4-45g) and (4-45h), it follows that

$$\left| \nu'_{\delta_r} \right| << \left| \nu_{\delta_r} \right| \quad ; \quad \left| \nu'_{\delta_a} \right| << \left| \nu_{\delta_a} \right| \tag{B-65}$$

As before, Section 4.3.2.3 makes use of the above relations, (B-62) - (B-65), in this case for simplifications to the bank dynamics. This then completes the present level of approximations to be made to the lateral dynamic model.

Appendix C: Trajectory Parameter Histories for Typical Entry Mission

      The objective of this appendix is to provide a graphic description of the entry environment in which the control system is designed to operate, with the specific goals of: (1) introducing the reader to the scope of the design task; (2) providing source material for the parameter limits used in the development of Appendix B; and (3) providing an appropriate context for the simplified model parameter histories described in Section 4.4. Presented here are histories of the important trajectory parameters during entry, obtained from a simplified "3D" guided entry simulation* in which the vehicle's rotational dynamics were of secondary importance. That is, the simulator implemented the vehicle's translational equations of motion, and modelled the closed-loop rotational dynamics (angle-of-attack and bank channels only; sideslip was always assumed zero) by simple rate- and acceleration-limited second-order systems.

      The simulation was initialized after deorbit from a $104°$ inclination angle, 100 mile altitude orbit, with the basic objective of guiding to a target approximately 5400 miles downrange and 560 miles cross range (out of the orbital plane). Two sets of initial conditions are given in Table C-1, one appropriate to the deorbit condition and the other appropriate to the entry interface condition. The elapsed time between these points was 1258 seconds, a "coast" period in which no guidance was attempted because of the lack of any aerodynamic force acting on the vehicle ($\bar{q} = 0$).

      The resultant trajectory is illustrated by the parameter plots of Figures C-1 through C-3, with the bank and angle-of-attack histories providing the guidance shown in Figure C-4. Note that the time base has a zero reference at entry interface, not deorbit. It should be recognized that these plots provide a convenient basis for some of the approximations used in the model development of Appendix B, and also serve

---

* Conducted by F. Marcus of CSDL

470
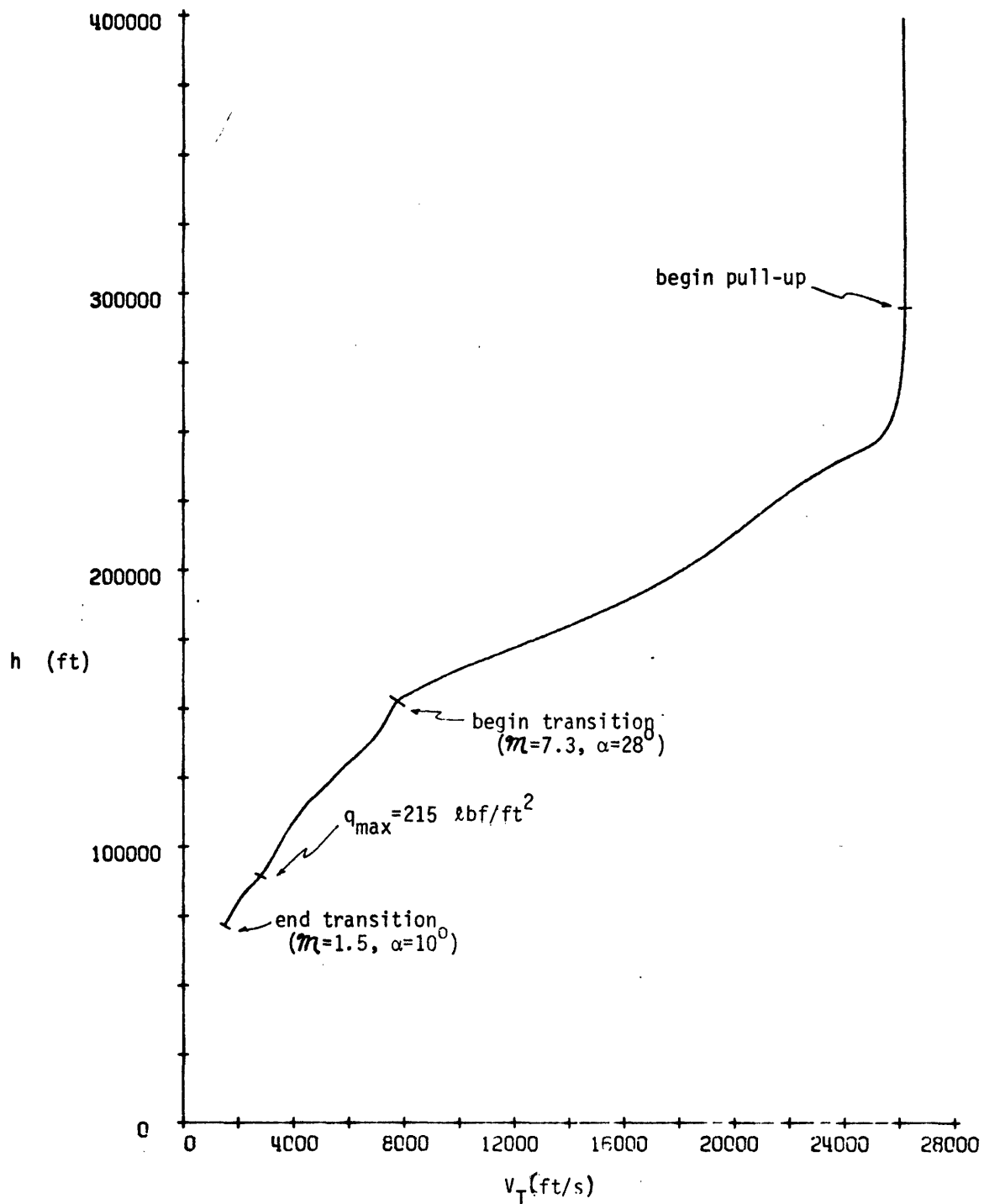
Figure C-1. Altitude vs. Velocity Profile

471
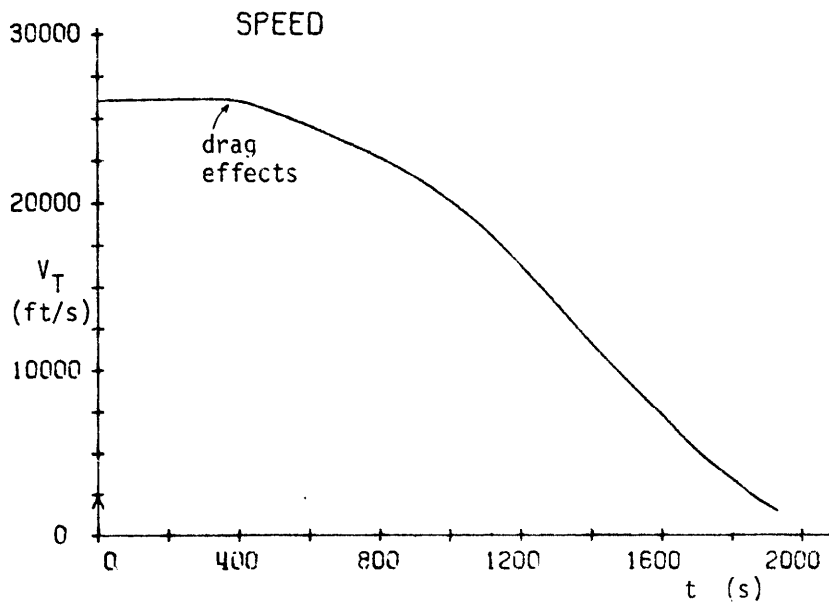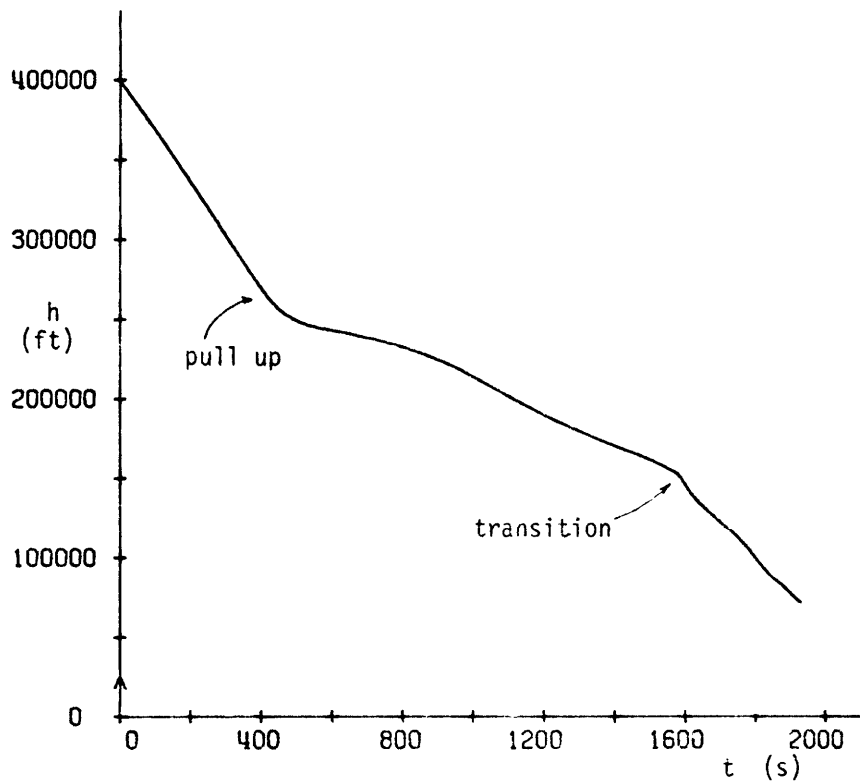
Figure C2.   Altitude and Velocity Histories.
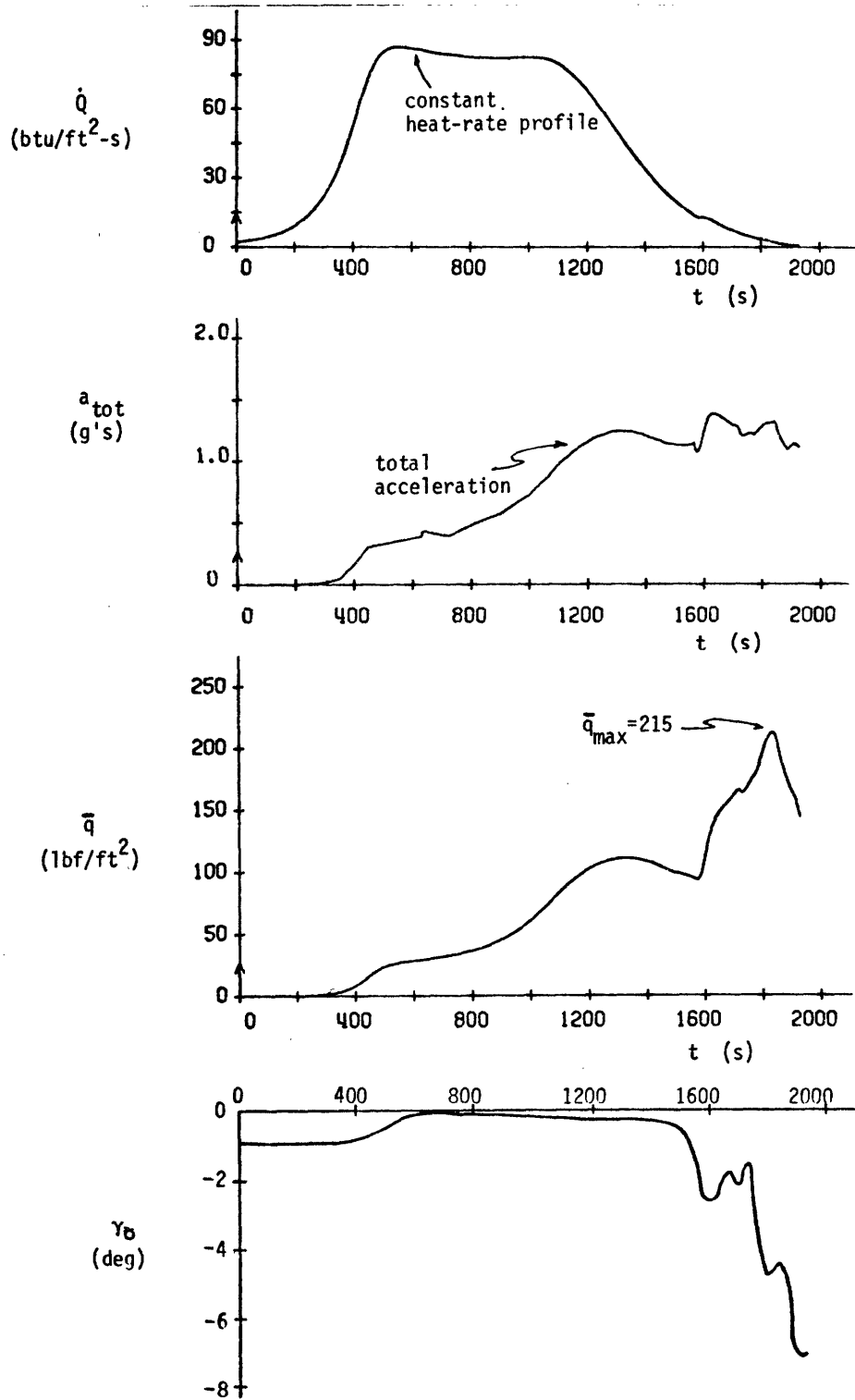
Figure C3. Trajectory Parameter Histories.
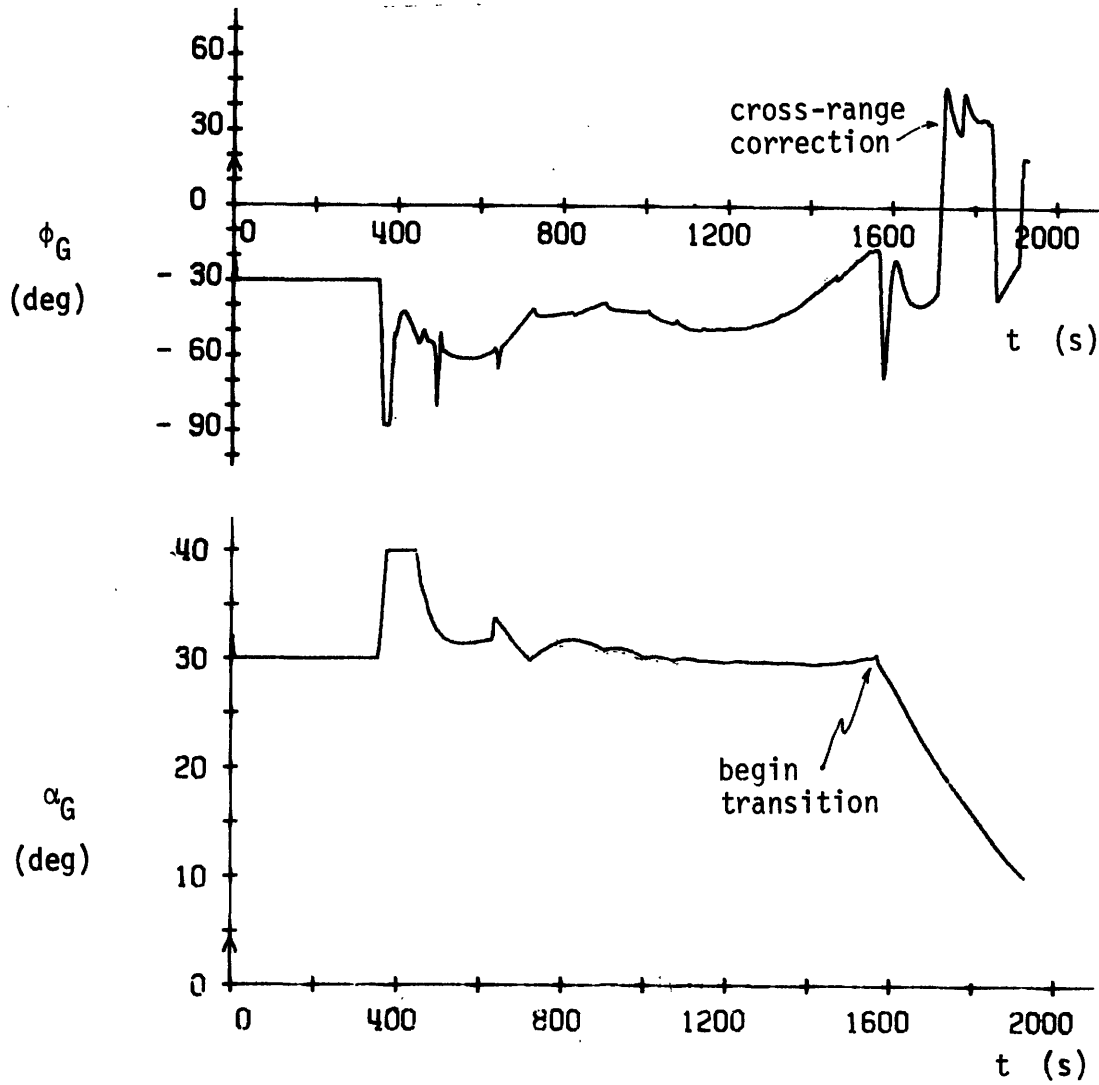
Figure C4. Guidance Commanded Attitude Histories.

Table C-1: Initial Conditions for Simulated Entry

Parameter	Value at deorbit	Value at interface	Dimension
h	630,487	398,096	ft
V_T	26,976	26,062	ft/sec
γ_0	0.00	-0.85	deg
α_T	-	32	deg
longitude	49.19	18.08	deg
latitude	-34.77	47.66	deg

to illustrate the large range in flight conditions encountered during entry. A comparison of these histories with those given in Section 7.2.3 indicates the effect of controller dynamics, although trajectory differences are also caused by the differing targeting conditions.

Appendix D: Sampled-Data Formulation of Equations of Motion[*]

The purpose of this appendix is to derive the sampled-data equation base corresponding to the simplified vehicle model derived in Chapter 4. Because of the inherent non-linearity of the ACPS control authority, the derivation will be concerned only with the aerodynamic control surfaces, specifically the elevator and aileron; the rudder is neglected for purposes of simplicity of illustration of the fundamental characteristics.

This appendix consists of three sections. Section D.1 derives the state-transition equations for the longitudinal and lateral dynamics. Section D.2 then derives the z-transforms of the stability-axis attitude angles and their rates, while Section D.3 derives the corresponding w-transforms.

D.1 State-Transition Equations

This section derives the state-transition equations describing both the lateral and longitudinal dynamics. Section D.1.1 states the general vector difference equation associated with a linear time-invariant vector differential equation. Section D.1.2 then considers the longitudinal equations of motion, while Section D.1.3 covers the lateral equations.

D.1.1 State-Transition Formulation

It is desired to find the vector difference equation associated with the following linear time-invariant system:

$$\underline{\dot{x}} = F\underline{x} + \underline{g}u \qquad (D-1)$$

where $\underline{x}$ is the system-state and u is the input control variable. Taking the Laplace transform of (D-1) yields:

$$\underline{x}(s) = (sI - F)^{-1}\underline{x}_0 + (sI - F)^{-1}\underline{g}u(s) \qquad (D-2)$$

where $\underline{x}_0$ is the initial condition state vector. Since, in the case at

---

[*] This appendix is repeated in modified form from Reference 30.

hand, the command is issued by a digital controller having a sample period of T seconds, it is assumed that the command is a stepwise continuous function, holding a constant value between sample instants. Thus, taking the inverse Laplace transform of (D-2) over the sample interval of T seconds, yields the desired difference equation:

$$\underline{x}_{n+1} = \Phi \underline{x}_n + \underline{\gamma} u_n \tag{D-3}$$

where $\underline{x}_n$ and u_n are the system state and input at the nth sample instant, respectively. The state transition matrix Φ is given by:

$$\Phi = \Phi(T) = \mathscr{L}^{-1} \{(sI - F)^{-1}\} \tag{D-4a}$$

and the control vector $\underline{\gamma}$ is given by:

$$\underline{\gamma} = \underline{\gamma}(T) = \mathscr{L}^{-1} \{\frac{1}{s}(sI - F)^{-1}\underline{g}\} \tag{D-4b}$$

D.1.2 Longitudinal Equation

The simplified differential equation, in the Laplace transform format, describing the response of the angle-of-attack mistrim, $\hat{\alpha}$, to the elevator deflection, $\hat{\delta}_e$, is repeated below from (4-38) of Chapter 4, with modifications:

$$(s^2 + 2\zeta_\alpha \omega_\alpha s + \omega_\alpha^2)\hat{\alpha} = K_{\delta_e} \hat{\delta}_e \tag{D-5}$$

where the elevator time-constant has been neglected for simplicity (see discussion in Section 4.4.1) and the ACPS pitch acceleration is assumed non-existent. To derive the vector state-transition equation, the following state vector is defined:

$$\underline{x} \equiv \begin{bmatrix} \hat{\alpha} \\ \dot{\hat{\alpha}} \end{bmatrix} \tag{D-6a}$$

and the following control variable is defined:

$$u \equiv \delta_e \tag{D-6b}$$

Thus, the vector differential equation is given by (D-1), where, from (D-5),

$$
F = \begin{bmatrix} 0 & 1 \\ -\omega_\alpha^2 & -2\zeta_\alpha\omega_\alpha \end{bmatrix} \quad ; \quad \underline{g} = \begin{bmatrix} 0 \\ K_{\delta_e} \end{bmatrix} \tag{D-6c}
$$

The difference equation corresponding to (D-1) is then given by (D-3), where the state-transition matrix Φ and control vector $\underline{\gamma}$ are found from (D-4) to be:

$$
\Phi = \begin{bmatrix} e^{-aT}(\cos bT + \frac{a}{b}\sin bT) & \frac{1}{b}e^{-aT}\sin bT \\ \\ -\frac{\omega_\alpha^2}{b}e^{-aT}\sin bT & e^{-aT}(\cos bT - \frac{a}{b}\sin bT) \end{bmatrix} \tag{D-7a}
$$

$$
\underline{\gamma} = \frac{K_{\delta_e}}{\omega_\alpha^2} \begin{bmatrix} 1 - e^{-aT}(\cos bT + \frac{a}{b}\sin bT) \\ \\ \frac{\omega_\alpha^2}{b}e^{-aT}\sin bT \end{bmatrix} \tag{D-7b}
$$

where the intermediate variables a and b are defined by:

$$
a = \zeta_\alpha \omega_\alpha \tag{D-7c}
$$

$$
b = \omega_\alpha \sqrt{1 - \zeta_\alpha^2}
$$

An important special case of the above results may be obtained for the situation in which there is negligible damping in the pitch axis (as discussed in Section 4.4.1). For $\zeta_\alpha = 0$, (D-7c) reduces to

$$
a = 0
$$
$$
b = \omega_\alpha \tag{D-8}
$$

478

so that (D-7a) and (D-7b) simplify to:

$$\Phi = \begin{bmatrix} \cos \omega_\alpha T & \dfrac{1}{\omega_\alpha} \sin \omega_\alpha T \\[2ex] -\omega_\alpha \sin \omega_\alpha T & \cos \omega_\alpha T \end{bmatrix}$$ (D-9a)

$$\underline{\gamma} = \dfrac{K_{\delta_e}}{\omega_\alpha^2} \begin{bmatrix} 1 - \cos \omega_\alpha T \\[2ex] \omega_\alpha \sin \omega_\alpha T \end{bmatrix}$$ (D-9b)

Thus, for a sample period of T seconds, the state-transition equation describing the longitudinal dynamics is given by (D-3). The state transition matrix Φ and control vector $\underline{\gamma}$ are given by (D-7). For negligible damping ($\zeta_a = 0$), these simplify to those given in (D-9).

D.1.3 Lateral Equations

The simplified differential equations, in the Laplace transform format, describing the response of bank angle ϕ_s and sideslip angle β to the aileron deflection, $\hat{\delta}_a$, are repeated below from (5-35):

$$(s^2 + \omega_\beta^2)\beta = K_{\beta\delta_a} \hat{\delta}_a$$

$$K_\beta \beta + s^2 \phi_s = K_{\phi\delta_a} \hat{\delta}_a$$ (D-10)

where the rudder has been neglected for simplicity. To define the vector state-transition equation and maintain visibility of the sideslip and bank angle dynamics, use of partitioned vectors and matrices will be made. In particular, the following state vectors are defined:

$$\underline{x}_1 \equiv \begin{bmatrix} \beta \\ \dot{\beta} \end{bmatrix} \quad ; \quad \underline{x}_2 \equiv \begin{bmatrix} \phi_s \\ \dot{\phi}_s \end{bmatrix} \quad ; \quad \underline{x} \equiv \begin{bmatrix} \underline{x}_1 \\ --- \\ \underline{x}_2 \end{bmatrix}$$ (D-11a)

and the following control variable is defined:

$$u \equiv \ddot{\delta}_a \qquad\qquad \text{(D-11b)}$$

Thus, the vector differential equation of (D-1) applies, with the following partitioning:

$$F = \begin{bmatrix} F_{11} & \vdots & 0 \\ \text{-----} & + & \text{-----} \\ F_{21} & \vdots & F_{22} \end{bmatrix} \quad ; \quad \underline{g} = \begin{bmatrix} g_1 \\ \text{----} \\ g_2 \end{bmatrix} \qquad \text{(D-11c)}$$

where the elements of the above are found from (D-10) to be:

$$F_{11} = \begin{bmatrix} 0 & 1 \\ -\omega_\beta^2 & 0 \end{bmatrix} \quad ; \quad F_{21} = \begin{bmatrix} 0 & 0 \\ -K_\beta & 0 \end{bmatrix} \quad ; \quad F_{22} = \begin{bmatrix} 0 & 1 \\ 0 & 0 \end{bmatrix}$$

$$\text{(D-11d)}$$

$$\underline{g}_1 = \begin{bmatrix} 0 \\ K_{\beta \delta_a} \end{bmatrix} \quad ; \quad \underline{g}_2 = \begin{bmatrix} 0 \\ K_{\phi \delta_a} \end{bmatrix} \qquad \text{(D-11e)}$$

The state-transition equation for the lateral dynamics is then given by (D-3), where the state-transition and control matrices are defined by (D-4), and may be partitioned as follows:

$$\Phi = \begin{bmatrix} \Phi_{11} & \vdots & 0 \\ \text{------} & + & \text{-----} \\ \Phi_{21} & \vdots & \Phi_{22} \end{bmatrix} \quad ; \quad \underline{\gamma} = \begin{bmatrix} \gamma_1 \\ \text{---} \\ \gamma_2 \end{bmatrix} \qquad \text{(D-12a)}$$

Prior to substitution of (D-11c), (D-11d), and (D-11e) into (D-4) it is convenient to make use of the following matrix identity:

480

$$\begin{bmatrix} X & 0 \\ \hline Z & Y \end{bmatrix}^{-1} = \begin{bmatrix} X^{-1} & 0 \\ \hline -Y^{-1}ZX^{-1} & Y^{-1} \end{bmatrix} \tag{D-13}$$

provided that X^{-1} and Y^{-1} exist. Now, from (D-11c)

$$(sI-F)^{-1} = \begin{bmatrix} (sI - F_{11}) & 0 \\ \hline -F_{21} & (sI - F_{22}) \end{bmatrix}^{-1}$$

so that, using (D-13),

$$(sI - F)^{-1} = \begin{bmatrix} (sI - F_{11})^{-1} & 0 \\ \hline (sI - F_{22})^{-1}F_{21}(sI - F_{11})^{-1} & (sI - F_{22})^{-1} \end{bmatrix} \tag{D-14}$$

Thus, from (D-11d) and (D-12a), and the definition of Φ in (D-4a), it follows from (D-14) that:

$$\Phi_{11} = \begin{bmatrix} \cos \omega_\beta T & \dfrac{1}{\omega_\beta}\sin \omega_\beta T \\ -\omega_\beta \sin \omega_\beta T & \cos \omega_\beta T \end{bmatrix} \quad ; \quad \Phi_{22} = \begin{bmatrix} 1 & T \\ 0 & 1 \end{bmatrix}$$

$$\tag{D-12b}$$

$$\Phi_{21} = -\dfrac{K_\beta}{\omega_\beta^2} \begin{bmatrix} (1 - \cos \omega_\beta T) & \dfrac{1}{\omega_\beta}(\omega_\beta T - \sin \omega_\beta T) \\ \omega_\beta \sin \omega_\beta T & (1 - \cos \omega_\beta T) \end{bmatrix}$$

Further, using (D-14) and (D-11c),

$$(sI - F)^{-1}\underline{g} = \begin{bmatrix} (sI - F_{11})^{-1}\underline{g}_1 \\ \hline (sI - F_{22})^{-1}\left[F_{21}(sI - F_{11})^{-1}\underline{g}_1 + \underline{g}_2\right] \end{bmatrix} \tag{D-15}$$

Thus, from (D-11e), (D-12a), and the definition of $\underline{\gamma}$ in (D-4b), it follows from (D-15) that:

481

$$\underline{\gamma}_1 = \frac{K_{\beta_{\delta_a}}}{\omega_\beta^2} \begin{bmatrix} 1 - \cos \omega_\beta T \\ \\ \omega_\beta \sin \omega_\beta T \end{bmatrix}$$

$$\underline{\gamma}_2 = \frac{K_{\phi_{\delta_a}}}{\omega_\beta^2} \begin{bmatrix} \left(1 + \dfrac{\omega_\phi^2}{\omega_\beta^2}\right)(1 - \cos \omega_\beta T) - \dfrac{\omega_\phi^2 T^2}{2} \\ \\ \left(1 + \dfrac{\omega_\phi^2}{\omega_\beta^2}\right)(\omega_\beta \sin \omega_\beta T) - \omega_\phi^2 T \end{bmatrix}$$

(D-12c)

where the intermediate variable, ω_ϕ^2, is introduced for convenience, and is defined by[*]:

$$\omega_\phi^2 \equiv \frac{K_{\beta_{\delta_a}}}{K_{\phi_{\delta_a}}} K_\beta - \omega_\beta^2$$

(D-12d)

Thus, for a sample period of T seconds, the state-transition equation describing the lateral dynamics is given by (D-3), where the state-transition matrix Φ and the control vector $\underline{\gamma}$ are given by (D-12).

D.2 z-Transfer Functions

This section derives the z-transfer functions relating the longitudinal and lateral state variables to the appropriate command inputs; specifically, transfer functions are found relating the stability-axis attitudes and rates to the commanded surface deflections. Section D.2.1 states the general z-transform equation associated with the state-transition equation (D-3) of the previous section. Sections D.2.2 and D.2.3 then consider the specific longitudinal and lateral dynamics, respectively.

[*] Note that this parameter is also intimately involved in controllability, as discussed in Section 5.2.2.1.

D.2.1 z-Transform Formulation

It is desired to find the z-transformed vector equation associated with the following state-transition equation:

$$\underline{x}_{n+1} = \Phi \underline{x}_n + \underline{\gamma} u_n \tag{D-3}$$

If $\underline{\lambda}(z)$ is used to represent the z-transform of $\underline{\lambda}_n$, then the following z-transform property may be recalled:

$$\underline{\lambda}_{n+1}(z) = z \underline{\lambda}(z) \tag{D-16}$$

so that transformation of (D-3) and use of (D-16) yields:

$$\underline{x}(z) = (zI - \Phi)^{-1} \underline{\gamma} u(z) \tag{D-17a}$$

or, since u(z) is a scalar, the following transfer function format may be employed:

$$\frac{\underline{x}(z)}{u(z)} = (zI - \Phi)^{-1} \underline{\gamma} \tag{D-17b}$$

D.2.2 Longitudinal z-Transfer Functions

With the longitudinal state-transition matrix Φ defined by (D-7a), it follows that

$$(zI - \Phi)^{-1} = \frac{(K_{\delta_e} / \omega_\alpha^2)}{\Delta}
\begin{bmatrix}
\left[z - e^{-aT}\left(\cos bT - \frac{a}{b}\sin bT\right)\right] & \frac{1}{b}e^{-aT}\sin bT \\[2ex]
-\frac{\omega_\alpha^2}{b}e^{-aT}\sin bT & \left[z - e^{-aT}\left(\cos bT + \frac{a}{b}\sin bT\right)\right]
\end{bmatrix} \tag{D-18a}$$

where the characteristic is given by:

$$\Delta = z^2 - 2ze^{-aT}\cos bT + e^{-2aT} \tag{D-18b}$$

Substitution of (D-18) into (D-17b) and use of the state vector and control variable definitions given in (D-6a) and (D-6b) yields the following:

$$\frac{\hat{\alpha}(z)}{\hat{\delta}_e(z)} = \frac{(K_{\delta_e}/\omega_\alpha^2)}{\Delta}\left\{ z\left[1 - e^{-aT}(\cos bT + \frac{a}{b}\sin bT)\right]\right.$$

$$\left. + e^{-aT}\left[e^{-aT} - (\cos bT - \frac{a}{b}\sin bT)\right]\right\} \tag{D-19}$$

$$\frac{\dot{\hat{\alpha}}(z)}{\hat{\delta}_e(z)} = \frac{(K_{\delta_e}/b)}{\Delta} e^{-aT}\sin bT(z - 1)$$

where Δ is given by (D-18b) and the variables a and b are defined in (D-7c).

The z-transfer functions corresponding to the negligible damping case are obtained by substitution of (D-8) in (D-19), to yield:

$$\frac{\hat{\alpha}(z)}{\hat{\delta}_e(z)} = (K_{\delta_e}/\omega_\alpha^2)(1 - \cos\omega_\alpha T)\left(\frac{z + 1}{z^2 - 2z\cos\omega_\alpha T + 1}\right) \tag{D-20a}$$

$$\frac{\dot{\hat{\alpha}}(z)}{\hat{\delta}_e(z)} = (K_{\delta_e}/\omega_\alpha)(\sin\omega_\alpha T)\left(\frac{z - 1}{z^2 - 2z\cos\omega_\alpha T + 1}\right) \tag{D-20b}$$

Thus, for a sample period of T seconds, the z-transfer functions for the angle-of-attack and the angle-of-attack rate are given by (D-19). For negligible damping ($\zeta_\alpha = 0$), these simplify to those given in (D-20).

D.2.3 Lateral z-Transfer Functions

With the lateral state-transition matrix defined by (D-12a), it follows that:

$$(zI - \Phi)^{-1} = \begin{bmatrix} (zI - \Phi_{11}) & 0 \\ \hline -\Phi_{21} & (zI - \Phi_{22}) \end{bmatrix}^{-1} \tag{D-21}$$

484

so that, using the matrix identity of (D-13), and recalling the partitioning of $\underline{x}$ and $\underline{y}$ given by (D-11a) and (D-12a), the transfer function relation of (D-17b) then yields the following:

$$
\begin{bmatrix} \dfrac{\underline{x}_1(z)/u}{\underline{x}_2(z)/u} \end{bmatrix} = (zI - \Phi)^{-1}\underline{y} = \begin{bmatrix} \dfrac{(zI - \Phi_{11})^{-1}\underline{y}_1}{(zI - \Phi_{22})^{-1}[\,\Phi_{21}(zI - \Phi_{11})^{-1}\underline{y}_1 + \underline{y}_2]} \end{bmatrix} \quad \text{(D-22)}
$$

Recalling the state vector and control variable definitions of (D-11a) and (D-11b), (D-12b) and (D-12c) may be used to expand (D-22), so that the following z-transfer functions are obtained:

$$
\frac{\beta(z)}{\hat{\delta}_a(z)} = \left(\frac{K_{\beta_{\delta_a}}}{\omega_\beta^2}\right)(1 - \cos\omega_\beta T)\left(\frac{z + 1}{\Delta}\right)
$$

$$
\frac{\dot{\beta}(z)}{\hat{\delta}_a(z)} = \left(\frac{K_{\beta_{\delta_a}}}{\omega_\beta}\right)(\sin\omega_\beta T)\left(\frac{z - 1}{\Delta}\right) \quad \text{(D-23a)}
$$

$$
\frac{\phi_s(z)}{\hat{\delta}_a(z)} = \left(\frac{K_{\phi_{\delta_a}}}{\omega_\beta^2}\right)\left(\frac{z + 1}{\Delta(z-1)^2}\right)\left[\left(1 + \frac{\omega_\phi^2}{\omega_\beta^2}\right)(1-\cos\omega_\beta T)(z-1)^2 - \frac{\omega_\phi^2 T^2}{2}\Delta\right]
$$

$$
\frac{\dot{\phi}_s(z)}{\hat{\delta}_a(z)} = \left(\frac{K_{\phi_{\delta_a}}}{\omega_\beta^2}\right)\left(\frac{1}{\Delta(z-1)}\right)\left[\left(1 + \frac{\omega_\phi^2}{\omega_\beta^2}\right)(\omega_\beta\sin\omega_\beta T)(z-1)^2 - \omega_\phi^2 T\Delta\right]
$$

where, as before, ω_ϕ^2 is defined by (D-12d) and

$$
\Delta = z^2 - 2z\cos\omega_\beta T + 1 \quad \text{(D-23b)}
$$

Thus, for a sample period of T seconds, the z-transfer functions for the sideslip and bank angles, and their rates, are given by (D-23).

D.3 w-Transfer Functions

This section derives the w-transfer functions relating the stability-axis attitude angles to the appropriate commanded surface deflection. Section D.3.1 briefly discusses the z/w mapping function, while Sections D.3.2 and D.3.3 present the w-transfer functions for the longitudinal and lateral dynamics, respectively.

D.3.1 w-Transform Function

This section uses the familiar bilinear z-to-w plane mapping given by

$$z = (1 + w)/(1 - w) \qquad (D-24)$$

which will be used in the next two subsections to transform (D-19), (D-20), and (D-23). The system's frequency response is obtained by recalling the s-to-z plane mapping function,

$$z = e^{sT} \qquad (D-25)$$

and restricting the Laplace variable s to a pure imaginary:

$$s = j\omega \qquad (D-26)$$

By substituting (D-25) and (D-26) into (D-24), it is found that the complex variable w must be a pure imaginary, of the form

$$w = j\omega_w \qquad (D-27)$$

where the w-frequency ω_w is related to the s-frequency ω by:

$$\omega_w = \tan(\omega T/2) \qquad (D-28)$$

Thus, for frequency response information, conventional Bode or phase-gain plots may be made of the w-transform, recognizing from (D-28) that $\omega_w = 0$ when $\omega = 0$, and that $\omega_w \to \infty$ as $\omega \to \omega_s/2$, where ω_s is the sampling frequency $(2\pi/T)$.

486

D.3.2 Longitudinal w-Transfer Functions

With the z-transfer function for angle-of-attack defined by (D-19), and the mapping function (D-24), the w-transform is obtained by direct substitution and is given by:

$$\frac{\hat{\alpha}(w)}{\hat{\delta}_e(w)} = \frac{K_{\delta_e}/\omega_\alpha^2}{1 + 2e^{-aT}\cos bT + e^{-2aT}} \frac{N(w)}{D(w)} \tag{D-29a}$$

where

$$N(w) = \left[1 - 2\frac{a}{b}e^{-aT}\sin bT + e^{-2aT}\right]w + \left[1 - 2e^{-aT}\cos bT + e^{-2aT}\right] \tag{D-29b}$$

$$D(w) = w^2 + \left[\frac{2(1-e^{-2aT})}{1+2e^{-aT}\cos bT + e^{-2aT}}\right]w + \left[\frac{1 - 2e^{-aT}\cos bT + e^{-2aT}}{1+2e^{-aT}\cos bT + e^{-2aT}}\right] \tag{D-29c}$$

where the variables a and b are defined in (D-7c).

The w-transform for $\hat{\alpha}$, corresponding to the negligible damping case, is obtained by substitution of (D-8) in (D-29), to yield:

$$\frac{\hat{\alpha}(w)}{\hat{\delta}_e(w)} = K_{\delta_e}\left(\frac{\tilde{\omega}^2}{\omega_\alpha^2}\right)\left(\frac{1-w}{w^2 + \tilde{\omega}^2}\right) \tag{D-30a}$$

where $\tilde{\omega}$ is defined by:

$$\tilde{\omega}^2 \equiv \frac{1 - \cos\omega_\alpha T}{1 + \cos\omega_\alpha T} \tag{D-30b}$$

Thus, for a sample period of T seconds, the w-transfer function for the angle-of-attack is given by (D-29). For negligible damping, this simplifies to that given by (D-30).

D.3.3 Lateral w-Transfer Functions

With the z-transfer functions for sideslip and bank angle defined by (D-23) and the mapping function (D-24), the w- transforms are obtained by direct substitution and are given by:

$$\frac{\beta(w)}{\hat{\delta}_a(w)} = K_{\beta\delta_a}\left(\frac{\hat{\omega}^2}{\omega_\beta^2}\right)\left(\frac{1-w}{w^2+\hat{\omega}^2}\right) \qquad \text{(D-31a)}$$

$$\frac{\phi_s(w)}{\hat{\delta}_a(w)} = K_{\phi\delta_a}\left(\frac{\hat{\omega}^2}{\omega_\beta^2}\right)\frac{(1-w)\left\{\left[1+\omega_\phi^2/\omega_\beta^2-(\omega_\phi T/2)^2/\hat{\omega}^2\right]w^2-(\omega_\phi T/2)^2\right\}}{w^2(w^2+\hat{\omega}^2)}$$

$$\text{(D-31b)}$$

where, as before, ω_ϕ^2 is defined by (D-12d), and $\hat{\omega}$ is defined by:

$$\hat{\omega}^2 \equiv \frac{1-\cos\omega_\beta T}{1+\cos\omega_\beta T} \qquad \text{(D-31c)}$$

Thus, for a sample period of T seconds, the w-transfer functions for the sideslip and bank angles are given by (D-31).

Appendix E: Fuel-Time Optimal Control of a Double-Integrator Plant*

The purpose of this appendix is to derive and discuss an optimal controller for a double-integrator plant, in support of the development of the ACPS phase-plane control logics described in Sections 5.1.1 and 5.2.1. As discussed later in the text (see Section 5.5.1.1), the choice of minimizing a linear combination of control effort and response time provides a practical means, via a simple adjustment of a single parameter, for emphasizing the fuel budget over the response time, or vice versa. It should be noted that the material presented here is freely drawn from the extensive treatment given in Reference 3; however, it is felt appropriate for this appendix to provide a convenient review and summary of this particular optimizing approach used in conjunction with double integrating systems. In particular, the advantages of this approach over the conventional use of a limiter with deadband logic should be clear from this presentation.

This appendix is organized into five sections. Section E.1 presents the formal control problem to be solved, while Section E.2 derives some definitive characteristics of the optimal control. Section E.3 then uses these results to derive the phase-plane logic which specifies the control in a closed-loop form, and which forms the basis for several of the ACPS control laws described in the text. As the basis for the succeeding section, Section E.4 develops the predictive switch time equations for use in an open-loop controller. Finally, Section E.5 discusses some of the performance characteristics of the optimally controlled system and makes note of the additional controls problems which can be solved within the framework presented here, thus enlarging the scope of the solution.

E.1 Problem Statement

The system under consideration is the double integrator plant shown in Figure E-1, and is described by (E-1),   where x_1 and x_2

* This appendix is repeated in modified form from Reference 29.

are the two state variables* to be controlled by the signal u.
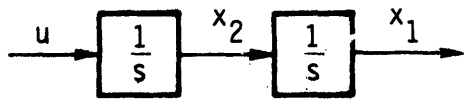
$$\dot{x}_1 = x_2$$
$$\dot{x}_2 = u$$

(E-1)

Figure E-1

The basic objective will be to define a control history u(t) over the time interval t= 0 to t= T, where T is unspecified[†], such that:

i) The system is driven from an arbitrary initial state, where

$$[x_1(0), x_2(0)] = (\xi_1, \xi_2)$$

(E-2)

to a fixed final state, where

$$[x_1(T), x_2(T)] = (0, 0)$$

(E-3)

ii) The control signal is limited by the relation

$$|u(t)| \le U \quad \forall t \in [0, T]$$

(E-4)

iii) The control signal minimizes the following linear combination of response time and control effort:

$$J = KT + \int_0^T |u(t)| dt = \int_0^T [K + |u(t)|] dt$$

(E-5)

where K is a positive weighting constant.

---

* x_1 and x_2 are used rather than ϵ_1 and ϵ_2 to avoid notational ambiguities.

[†] Note here that T is not to be confused with the sample time symbol used in the main text.

490

E.2 Characteristics of the Optimal Control

The first objective of the problem solution is to find the functional form of the control u which will minimize J in (E-5). By definition, the Hamiltonian, formed by adjoining the state equations (E-1) with the cost function integrand (E-5), is given by:

$$\mathcal{H} = p_1 \dot{x}_1 + p_2 \dot{x}_2 + (K + |u|) \tag{E-6}$$

where p_1 and p_2 are the co-state variables. Using (E-1), there results

$$\mathcal{H} = (p_1 x_2 + K) + (p_2 u + |u|) \tag{E-7}$$

To minimize J, $\mathcal{H}$ must be minimized over u, or, equivalently, $(p_2 u + |u|)$ must be minimized over u. It is straightforward to show graphically that the u which minimizes this expression and simultaneously satisfies (E-4) is given by:

$$u = -U[dez(p_2)] \tag{E-8}$$

where the dead-zone function dez (λ), is defined by Figure E-2. The relation between u and p_2 is shown in Figure E-3.
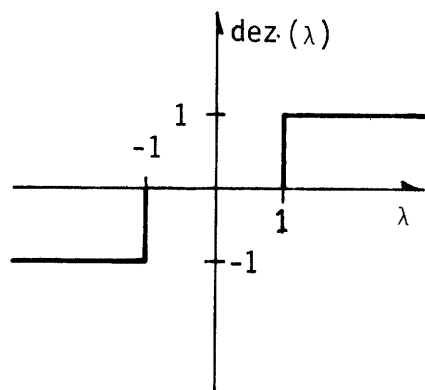
Figure E-2
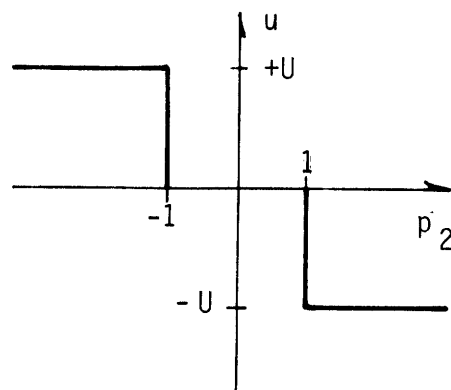
Figure E-3

Because of the indeterminate nature of u when $|p_2(t)| = 1$, it is desirable to show that this singular situation cannot occur over a finite interval of time. It is necessary, then, to determine the functional dependence of p_2 on time. Using the definition of the co-state variables,

$$\dot{p}_i = -\frac{\partial \mathcal{H}}{\partial x_i} \quad (i = 1, 2) \quad \text{(E-9)}$$

there results, from (E-7)

$$\dot{p}_1 = 0$$

$$\dot{p}_2 = -p_1 \quad \text{(E-10)}$$

so that

$$p_1(t) = \pi_1$$

$$p_2(t) = -\pi_1 t + \pi_2 \quad \text{(E-11)}$$

where π_1 and π_2 are undetermined constants. Now, assume that p_2 takes on a singular value for a finite interval of time, so that

$$p_2(t) = 1 \quad \forall \, t \, \epsilon \, [t_1, t_2]$$

Thus, from (E-11), the constants must be given by

$$\pi_1 = 0$$

$$\pi_2 = 1$$

From (E-7), the Hamiltonian is then given by

$$\mathcal{H} = K + u + |u|$$

But for $p_2 = 1$, the control u, from (E-8), must satisfy the following inequality:

$$-U \leq u \leq 0$$

so that

$$u + |u| = 0$$

492

and the Hamiltonian is given by

$$\mathcal{H} = K \neq 0$$

However, this result violates the optimality condition which requires that the Hamiltonian be zero along the optimal trajectory. The same contradiction occurs when $p_2 = -1$ over a finite interval. Consequently, there is no singular control interval where u is indeterminate, so that u(t) must be a piecewise constant function of time, taking on only the values $-U$, 0, and $+U$.

With this characteristic of the control history, it is possible to specify the finite set of control histories which may occur. Given the switching relation of (E-8) and recognizing the linearity of $p_2(t)$ in (E-11), it should be clear that the control u(t) may switch values twice, at most. An example of this situation is given in Figure E-4.
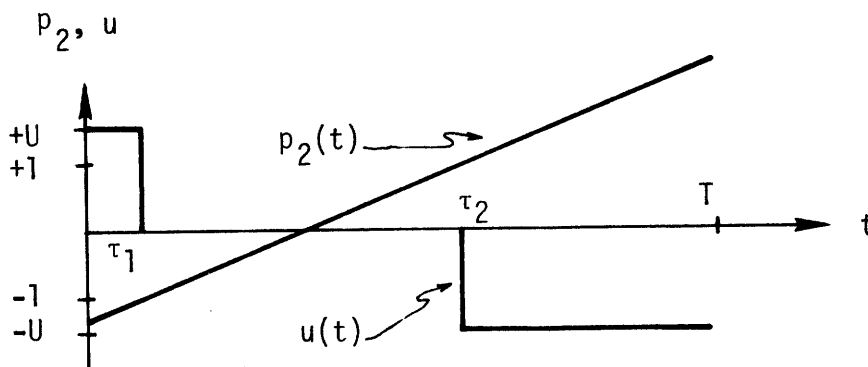
Figure E-4.

Note that in the above example, u(t) takes on the following values:

$$u(t) = +U \qquad \forall\, t \in [0, \tau_1)$$

$$0 \qquad \forall\, t \in (\tau_1, \tau_2)$$

$$-U \qquad \forall\, t \in (\tau_2, T]$$

and may be represented by the following short-hand notation denoting a control sequence:

$$u(t) = \{+U, 0, -U\}$$

Due to the linearity of $p_2(t)$, there are only nine such sequences, so that the control history must be a member of one of the following sequences:

$$\{+U\}, \{+U, 0\}, \{+U, 0, -U\}$$

$$\{-U\}, \{-U, 0\}, \{-U, 0, +U\} \qquad \text{(E-12)}$$

$$\{0\}, \{0, +U\}, \{0, -U\}$$

Thus, to drive the system from (ξ_1, ξ_2) to $(0, 0)$, there are nine control sequences to consider. The problem thus reduces to finding the unique control sequence which will accomplish this task, and at what point within the sequence the switching must occur.

E.3   Derivation of Phase Plane Switch Curves

In order to determine which control sequence will drive the system to the origin from a given initial condition, it is convenient to make use of phase plane trajectory equations. By taking advantage of the piecewise constant nature of $u(t)$, trajectory families may be derived from the state equations (E-1).

Assuming that $u(t)$ is constant over the interval $[0, t]$, then from (E-1), there results:

$$\begin{aligned}
\text{i)} \quad &\text{for } u(t) = 0, &x_1(t) &= \xi_1 + \xi_2 t \\
& &x_2(t) &= \xi_2 \\
\text{ii)} \quad &\text{for } u(t) = \pm U, &\dot{x}_1(t) &= x_2(t) \\
& &\dot{x}_2(t) &= \pm U
\end{aligned} \qquad \text{(E-13)}$$

so that

494

$$\frac{dx_1}{dx_2} = \mp (x_2/U)$$

resulting in

$$x_1(t) = \xi_1 \pm \frac{1}{2U} (x_2^2 - \xi_2^2) \text{ for } u(t) = \pm U \qquad (E\text{-}14)$$

The trajectories of (E-13) and (E-14) may be plotted in the phase plane as shown in Figure E-5, in which a particular family is generated by varying the initial conditions (ξ_1, ξ_2). The arrows indicate direction of travel for increasing time.
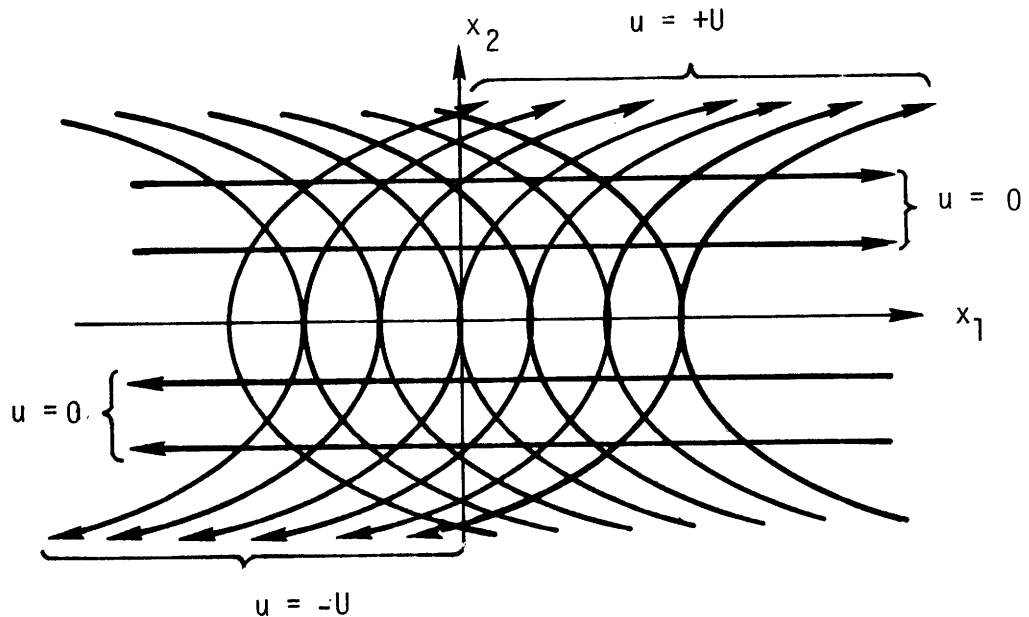
Figure E-5. Phase Plane Trajectories.

From this figure, it can be seen that there are only two trajectories leading to the origin. These are shown in Figure E-6 and denoted as the γ_+ and γ_- curves, to correspond with the control used $(u = \pm U)$.
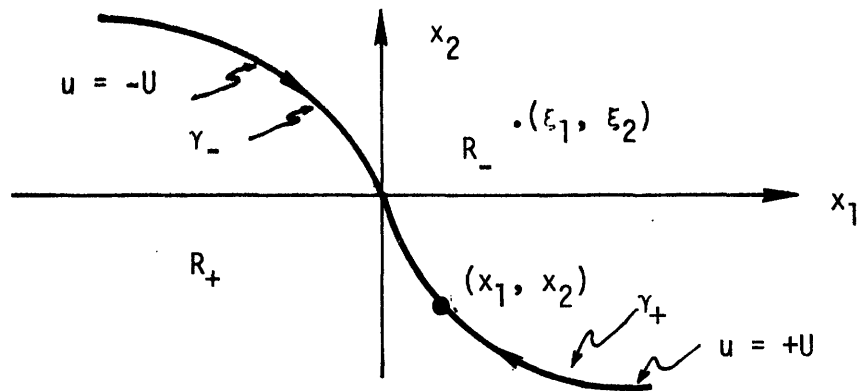
Figure E-6. γ_+ and γ_- Curves.

The equations for these curves may be obtained from (E-14), so that the curve definitions are as follows:

$$\gamma_+ \; : \; x_2 \le 0 \text{ and } x_1 \; = \; \frac{1}{2U}x_2^2 \tag{E-15a}$$

$$\gamma_- \; : \; x_2 \ge 0 \text{ and } x_1 \; = \; -\frac{1}{2U}x_2^2 \tag{E-15b}$$

Now, consider the point (x_1, x_2) on γ_+, as shown in the figure. It should be clear by inspection of the allowable control sequences in (E-12) that the only control sequence which will drive the system to the origin is $\{+U\}$. Thus, part of the optimal control law may be immediately stated:

$$\text{If } (x_1, x_2) \in \gamma_+ \text{, then } u \; = \; +U \tag{E-16a}$$

By symmetry, it should also be clear that:

$$\text{If } (x_1, x_2) \in \gamma_- \text{, then } u \; = \; -U \tag{E-16b}$$

Now, divide the phase plane into two regions, R_- and R_+, as shown in Figure E-6, where

$$\gamma_- \subset R_- \text{ and } \gamma_+ \subset R_+ \tag{E-17}$$

so that the regions may be defined algebraically as follows:

$$R_-: \quad x_1 \geq -\frac{1}{2U} x_2^2 \quad \text{for } x_2 \geq 0$$

$$\text{(E-18a)}$$

$$x_1 > \frac{1}{2U} x_2^2 \quad \text{for } x_2 \leq 0$$

$$R_+: \quad x_1 < -\frac{1}{2U} x_2^2 \quad \text{for } x_2 \geq 0$$

$$\text{(E-18b)}$$

$$x_1 \leq \frac{1}{2U} x_2^2 \quad \text{for } x_2 \leq 0$$

Referring to Figure E-6 consider a point (ξ_1, ξ_2) in R_-. With the allowable control sequences enumerated in (E-12), it is a direct matter to show (either by simple trajectory construction in the phase plane or by algebraic proof) that the only possible control sequences which will drive the system from (ξ_1, ξ_2) to $(0, 0)$ are

$$\{0, U\} \text{ and } \{-U, 0, +U\}$$

Because the former control sequence is a subset of the latter, only the more general sequence $\{-U, 0, U\}$ need be considered. It will be shown below how the sequence $\{0, U\}$ arises as a special case.

Figure E-7 shows a possible trajectory leading from (ξ_1, ξ_2) to $(0, 0)$, using the $\{-U, 0, U\}$ control sequence, and with switching occurring at (α_1, α_2) and (β_1, β_2). Note that the second switch at (β_1, β_2) is specified by both the γ_+ curve (E-15a) and the appropriate switch law (E-16a). The problem here will be to find an analogous curve for (α_1, α_2), and, of course, the corresponding switch law.
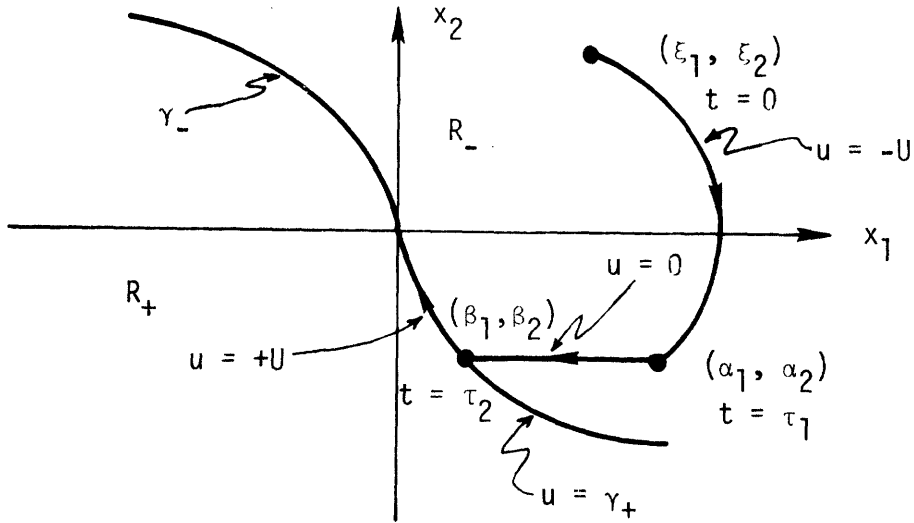
Figure E-7.

The approach to be used here will be to derive the function $f(\alpha_1, \alpha_2)$ which defines the (α_1, α_2) switch curve Γ_+, or

$$\Gamma_+: \quad f(\alpha_1, \alpha_2) \;=\; 0 \tag{E-19}$$

Now, the control switches at times τ_1 and τ_2, so that

$$[x_1(\tau_1), \; x_2(\tau_1)] \;=\; (\alpha_1, \alpha_2)$$

$$[x_1(\tau_2), \; x_2(\tau_2)] \;=\; (\beta_1, \beta_2) \tag{E-20}$$

and

$$
\begin{aligned}
u \;=\; -U \qquad & \forall \, t \, \epsilon \, [0, \tau_1) \\[4pt]
0 \qquad & \forall \, t \, \epsilon \, (\tau_1, \tau_2) \\[4pt]
+U \qquad & \forall \, t \, \epsilon \, (\tau_2, T]
\end{aligned} \tag{E-21}
$$

Since $(\beta_1, \beta_2) \in \gamma_+$, the switch curve definition (E-15a) implies that

$$\beta_1 \;=\; \frac{1}{2U}\, \beta_2^2; \qquad \beta_2 \;\leq\; 0 \tag{E-22}$$

498

Also, from the state equations (E-1) and the control history (E-21), it follows that

$$\beta_2 = \alpha_2 \tag{E-23a}$$

$$\beta_1 = \alpha_1 + \alpha_2(\tau_2 - \tau_1) \tag{E-23b}$$

Combining (E-22) and (E-23), then

$$\frac{1}{2U}\alpha_2^2 = \alpha_1 + \alpha_2(\tau_2 - \tau_1); \quad \alpha_2 \leq 0 \tag{E-24}$$

To find the "coast" time $(\tau_2 - \tau_1)$, (E-8), (E-11), and (E-21) may be utilized to show that

$$p_2(\tau_1) = +1 = -\pi_1\tau_1 + \pi_2$$

$$p_2(\tau_2) = -1 = -\pi_1\tau_2 + \pi_2$$

so that

$$(\tau_2 - \tau_1) = \frac{2}{\pi_1} \tag{E-25}$$

Now, making use of the zero-valued property of the Hamiltonian, at the particular switch time τ_1, results in:

$$\mathcal{H}(\tau_1) = 0 = p_1(\tau_1)x_2(\tau_1) + K + p_2(\tau_1)u(\tau_1) + |u(\tau_1)| \tag{E-26}$$

But

$$p_1(\tau_1) = \pi_1$$

$$p_2(\tau_1) = +1$$

$$x_2(\tau_1) = \alpha_2$$

so that (E-26) becomes

$$\mathcal{H}(\tau_1) = 0 = \pi_1\alpha_2 + K + \left[u(\tau_1) + |u(\tau_1)| \right] \tag{E-27}$$

From (E-8) and (E-21), it follows that

$$0 \geq u(\tau_1) \geq -U$$

so that

$$u(\tau_1) + |u(\tau_1)| = 0$$

and (E-27) then implies

$$\pi_1 = -K/\alpha_2 \qquad \text{(E-28)}$$

Making use of (E-25) and (E-28), (E-24) then becomes

$$\alpha_1 = \frac{1}{2U} \left[\frac{(K/U)+4}{(K/U)} \right] \alpha_2^2 \ ; \quad \alpha_2 \leq 0$$

which is the desired function describing the Γ_+ switch curve of (E-19). Thus, switching from u = -U to u = 0 occurs when $(x_1, x_2) \ \epsilon \ \Gamma_+$, where Γ_+ is defined by:

$$\Gamma_+ : \ x_1 = \frac{1}{2U} \left[\frac{(K/U)+4}{(K/U)} \right] x_2^2 \ ; \quad x_2 \leq 0 \qquad \text{(E-29a)}$$

A totally analogous optimal control sequence and associated switch curve may be derived for the case when $(\xi_1, \xi_2) \ \epsilon \ R_+$ (shown in Figure E-6). The optimal sequence is {+U, 0, -U}, where switching from u = 0 to u = -U occurs along γ_- (in accordance with (E-16b)), and switching from u $\neq$ U to u = 0 occurs along Γ_-, where Γ_- is defined by:

$$\Gamma_- : \ x_1 = -\frac{1}{2U} \left[\frac{(K/U)+4}{(K/U)} \right] x_2^2 \ ; \quad x_2 \geq 0 \qquad \text{(E-29b)}$$

The several results of this section may be summarized by use of phase plane partitioning and the association of a control signal (u = -U, 0, or +U) with each partitioned region. Figure E-8 shows the phase plane partitioned into four regions G_+, G_-, H_+, and H_-. The partitioning curves, γ_+, γ_-, Γ_+, and Γ_-, are defined by (E-15) and (E-29), and are associated with the regions as follows:

$$\gamma_+ \subset G_+; \quad \gamma_- \subset G_-; \quad \Gamma_+ \subset H_+; \quad \Gamma_- \subset H_- \qquad \text{(E-30)}$$
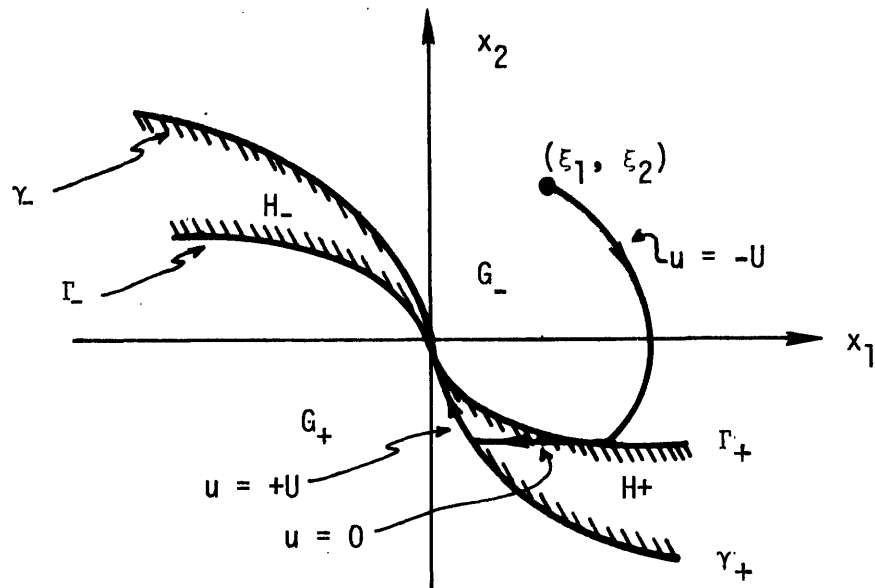
Figure E-8. Phase Plane Switch Curves.

The control laws already derived may then be conveniently summarized as a phase plane switch logic as follows:

If $(x_1, x_2) \in G_+$ then $u = +U$

$\qquad\qquad G_-$ $-U$ (E-31)

$\qquad\qquad (H_+ \cup H_-)$ 0

Figure E-8 also shows a typical optimal trajectory originating in G_-. Note the characteristic "bang-coast-bang" nature of the control, due to the structure of the weighted fuel-time cost function.

The optimal control law has thus been expressed as a three-valued switch logic, regionally defined in the phase plane. It should be clear that since the control is directly determined by system state, or

$$u = u(x_1, x_2)$$

then this approach is particularly appropriate to a closed-loop controller as shown in Figure E-9.
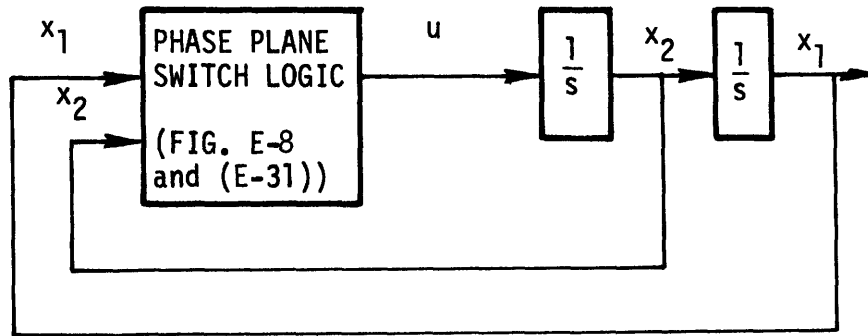
Figure E-9. Closed Loop Controller.

This configuration will then drive the system to the origin in the optimal manner, and is thus a closed-loop solution to the problem as stated in Section E.2.

E.4 Derivation of Predicting Control Logic

Derivation of a predictive, or open-loop, control history $u(t)$ is a rather straightforward application of the results of the previous section. What is required, basically, is a determination of a switch time (τ_i) for each trajectory crossover in the phase plane, as a function of the system's initial conditions (ξ_1, ξ_2).

Shown in Figure E-10 is a typical trajectory originating in G_- and switching at $t = \tau_1$ and $t = \tau_2$. The objective here is to find τ_1 and τ_2 by using the phase plane logic of the previous section.

With $(\xi_1, \xi_2) \epsilon G_-$, the initial control u is determined by (E-31), so that the switch points in the phase plane, (α_1, α_2) and (β_1, β_2), and the control history, $u(t)$, are determined by (E-20) and (E-21), respectively. Thus,

$$u(t) = -U \qquad \forall \ t \ \epsilon \ [0, \tau_1)$$

so that, from the state equations (E-1),

$$\dot{x}_1(t) = x_2(t)$$
$$\dot{x}_2(t) = -U \qquad \forall \ t \ \epsilon \ [0, \tau_1)$$

502
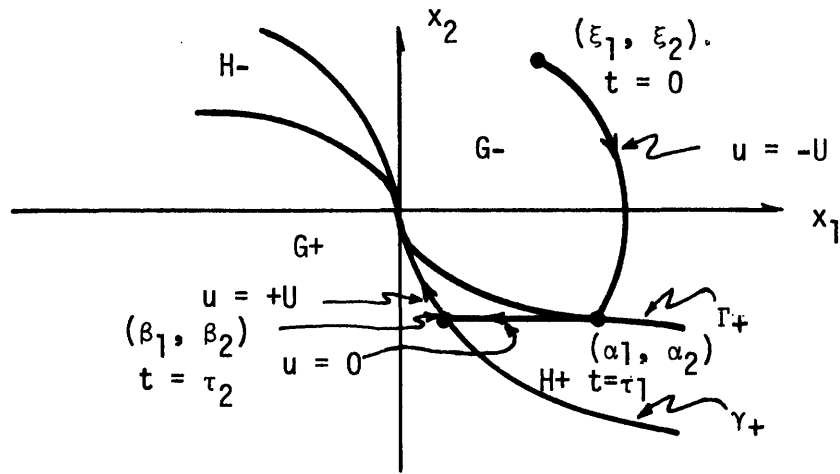
Figure E-10.

implying that

$$x_1(\tau_1) = \alpha_1 = \xi_1 + \xi_2\tau_1 - \frac{1}{2}U\tau_1^2 \qquad \text{(E-32a)}$$

$$x_2(\tau_1) = \alpha_2 = \xi_2 - U\tau_1 \qquad \text{(E-32b)}$$

However, since $(\alpha_1, \alpha_2) \in \Gamma_+$, (E-29a) is applicable, so that

$$\alpha_1 = \frac{1}{2U}\sigma\alpha_2^2 ; \quad \alpha_2 \leq 0 \qquad \text{(E-33)}$$

where σ is defined by

$$\sigma \equiv \left[\frac{(K/U)+4}{(K/U)}\right] \qquad \text{(E-34)}$$

Combining (E-32) and (E-33) results in

$$\xi_1 + \xi_2\tau_1 - \frac{1}{2}U\tau_1^2 = \frac{1}{2U}\sigma(\xi_2 - U\tau_1)^2 \qquad \text{(E-35)}$$

Solving the above quadratic for τ_1 results in:

$$\tau_1 = \hat{\xi}_2 \pm \left[\frac{\hat{\xi}_2^2 + 2\hat{\xi}_1}{(1+\sigma)}\right]^{1/2} \qquad \text{(E-36)}$$

503

where the scaled variables $\hat{\xi}_1$ and $\hat{\xi}_2$ are defined by:

$$\hat{\xi}_i \equiv \xi_i / U \qquad (i = 1, 2) \qquad (E\text{-}37)$$

To remove the ambiguity in (E-36), it may be noted that (E-33) requires that

$$\alpha_2 \leq 0$$

so that, from (E-32b)

$$\tau_1 \geq \hat{\xi}_2$$

thus implying the positive sign in (E-36), or

$$\tau_1 = \hat{\xi}_2 + \left[\frac{\hat{\xi}_2^2 + 2\hat{\xi}_1}{(1+\sigma)} \right]^{1/2} \qquad ; (\xi_1, \xi_2) \in G_- \qquad (E\text{-}38)$$

This, then, is the predicted time for switching from $u = -U$ to $u = 0$, when $(\xi_1, \xi_2) \in G_-$. The time τ_2, at which switching from $u = 0$ to $u = +U$ occurs, may be found by first using (E-25) and (E-28) to yield

$$\tau_2 = \tau_1 - \frac{2\alpha_2}{K}$$

Use of (E-32b) and (E-37) then results in

$$\tau_2 = -\frac{2U}{K} \hat{\xi}_2 + \left(1 + \frac{2U}{K} \right) \tau_1$$

so that substitution of (E-38) yields the following relation for τ_2:

$$\tau_2 = \hat{\xi}_2 + \frac{1}{2}(1+\alpha) \left[\frac{\hat{\xi}_2^2 + 2\hat{\xi}_1}{(1+\sigma)} \right]^{1/2} \qquad ; (\xi_1, \xi_2) \in G_- \qquad (E\text{-}39)$$

Thus, if $(\xi_1, \xi_2) \in G_-$ as shown in Figure E-10, the two switch times τ_1 and τ_2 are given by (E-38) and (E-39), respectively.

Because of the symmetry of the phase plane trajectories, entirely analogous results may be found for $(\xi_1, \xi_2) \in G_+$:

504

$$\tau_1 = -\hat{\xi}_2 + \left[\frac{\hat{\xi}_2^2 - 2\hat{\xi}_1}{1 + \sigma} \right]^{1/2} \quad ; \quad (\xi_1, \xi_2) \in G_+ \qquad \text{(E-40)}$$

$$\tau_2 = -\hat{\xi}_2 + \frac{1}{2}(1 + \sigma)\left[\frac{\hat{\xi}_2^2 - 2\hat{\xi}_1}{1 + \sigma} \right]^{1/2} \quad ; \quad (\xi_1, \xi_2) \in G_+ \qquad \text{(E-41)}$$

Now, if $(\xi_1, \xi_2) \in H_+$, it is clear that after the initial coast period, there is only one switch time of interest. It is desired to find the switch time τ_0 at which switching from u = 0 to u = +U occurs. The state equations prior to switching are:

$$\dot{x}_1(t) = x_2(t)$$
$$\dot{x}_2(t) = 0 \qquad \forall\, t \in [0, \tau_0)$$

so that, referring to Figure E-10,

$$x_1(\tau_0) = \beta_1 = \xi_1 + \xi_2 \tau_0 \qquad \text{(E-42a)}$$

$$x_2(\tau_0) = \beta_2 = \xi_2 \qquad \text{(E-42b)}$$

However, since $(\beta_1, \beta_2) \in \gamma_+$, (E-22) is applicable, so that

$$\beta_1 = \frac{1}{2U}\beta_2^2 \;;\; \beta_2 \le 0 \qquad \text{(E-22)}$$

Combining (E-42) and (E-22) results in:

$$(\xi_1 + \xi_2 \tau_0) = \frac{1}{2U}\xi_2^2$$

or, using (E-37)

$$\tau_0 = \frac{1}{2}\hat{\xi}_2 - \hat{\xi}_1/\hat{\xi}_2 \;;\; (\xi_1, \xi_2) \in H_+ \qquad \text{(E-43)}$$

This, then, is the predicted switch time for $(\xi_1, \xi_2) \in H_+$. An analogous solution may be found for the symmetric region H_-, or:

$$\tau_0 = -\frac{1}{2}\hat{\xi}_2 - \hat{\xi}_1/\hat{\xi}_2 \;;\; (\xi_1, \xi_2) \in H_- \qquad \text{(E-44)}$$

With the various switch times calculated for the control history, the closed-loop control law expressed in (E-31) may now be transformed into a mathematically equivalent open-loop controller, which predicts the desired control sequence. Summarizing the results expressed in (E-34), (E-37)-(E-41), and (E-43)-(E-44), the predictive controller consists of the following logic:

$$\text{If } (\xi_1, \xi_2) \in G_- \cup G_+ \quad \text{then } u = -\Lambda U \quad \forall t \in [0, \tau_1)$$

$$0 \qquad (\tau_1, \tau_2) \qquad \text{(E-45a)}$$

$$+\Lambda U \qquad (\tau_2, T]$$

$$\text{If } (\xi_1, \xi_2) \in H_- \cup H_+ \quad \text{then } u = 0 \quad \forall t \in [0, \tau_0)$$

$$-\Lambda U \qquad (\tau_0, T] \qquad \text{(E-45b)}$$

where the switch times τ_0, τ_1, and τ_2 are defined by:

$$\tau_0 = -\frac{1}{2} |\hat{\xi}_2| - \hat{\xi}_1 / \hat{\xi}_2 \qquad \text{(E-46a)}$$

$$\tau_1 = \Lambda \hat{\xi}_2 + \left[\frac{\hat{\xi}_2^2 + 2\Lambda \hat{\xi}_1}{(1+\sigma)} \right]^{1/2} \qquad \text{(E-46b)}$$

$$\tau_2 = \Lambda \hat{\xi}_2 + \frac{1}{2}(1 + \sigma) \left[\frac{\hat{\xi}_2^2 + 2\Lambda \hat{\xi}_1}{(1 + \sigma)} \right]^{1/2} \qquad \text{(E-46c)}$$

where

$$\hat{\xi}_i \equiv \xi_i / U \qquad (i = 1, 2) \qquad \text{(E-37)}$$

$$\sigma \equiv \left[\frac{(K/U)+4}{(K/U)} \right] \qquad \text{(E-34)}$$

and where Λ is defined by:

If $(\xi_1, \xi_2) \in G_- \cup H_-$ then $\Lambda = 1$

$$(\xi_1, \xi_2) \in G_+ \cup H_+ \qquad \Lambda = -1 \tag{E-47}$$

This then completes the derivation of the predictive controller. Note that the control is a function of initial conditions and time, or

$$u = u(\xi_1, \xi_2, t)$$

in contrast to the state dependent control of the previous section.

E. 5 Effect of Parameter Variation on Controller Performance

The purpose of this section is to describe controller performance as a function of the weighting parameter K in (E-5). Generally, it should be clear from the form of the cost function J, where

$$J = \int_0^T \left[K + |u| \right] dt \; ; \; K > 0 \tag{E-5}$$

that the designer can emphasize the minimization of control effort (with $K \to 0$) or the minimization of response time (with $K \to \infty$).

For a more quantitative relation, it is necessary to determine the equations which specify the terminal time T and the total "fuel" used F, where

$$F = \int_0^T |u| \, dt \tag{E-48}$$

To determine the response time T, suppose that $(\xi_1, \xi_2) \in G_-$. From the optimal control law (either (E-31) or (E-45)) and the state equations (E-1), it is clear that

$$\dot{x}_2(t) = +U \quad \forall \, t \in (\tau_2, T]$$

so that, referring to the trajectory shown in Figure E-10, the endpoints of the last trajectory segment must be related as follows:

$$x_2(T) = 0 = \beta_2 + U(T - \tau_2)$$

implying that

$$T = \tau_2 - (\beta_2 / U) \qquad \text{(E-49)}$$

Use of (E-23a), (E-25), and (E-28) results in

$$T = \tau_1 - \left[\frac{(K/U)+2}{(K/U)}\right]\left(\frac{\alpha_2}{U}\right) \qquad \text{(E-50)}$$

Using (E-32b) and (E-37), the final time T may then be related to the first switch time τ_1, as follows:

$$T = 2\left[\frac{(K/U)+1}{(K/U)}\right]\tau_1 - \left[\frac{(K/U)+2}{(K/U)}\right]\hat{\xi}_2$$

Finally, use of (E-34) and (E-38) reduces this expression to:

$$T = \hat{\xi}_2 + \left(\frac{3+\sigma}{2}\right)\left[\frac{\hat{\xi}_2^2 + 2\hat{\xi}_1}{1+\sigma}\right]^{1/2} \quad ; \quad (\xi_1, \xi_2) \in G_- \qquad \text{(E-51)}$$

Thus, for $(\xi_1, \xi_2) \in G_-$, T is determined by (ξ_1, ξ_2) and K (through (E-34) and (E-37)). Now, suppose $(\xi_1, \xi_2) \in H_+$. If switching from u = 0 to u = +U occurs at t = τ_0 (using the notation of the previous section) then it follows from (E-49) that

$$T = \tau_0 - (\beta_2 / U) \qquad \text{(E-52)}$$

Thus, with

$$\beta_2 = \xi_2 \qquad \text{(E-42b)}$$

and using the expression for τ_0 from (E-43), the response time is then given by:

$$T = -\frac{1}{2}\hat{\xi}_2 - \hat{\xi}_1 / \hat{\xi}_2 \quad ; \quad (\xi_1, \xi_2) \in H_+ \qquad \text{(E-53)}$$

Because of symmetry, results completely analogous to (E-51) and (E-53) may be found for $(\xi_1, \xi_2) \in G_+$ and $(\xi_1, \xi_2) \in H_-$. In summary, the terminal time T for an optimal trajectory is given by:

$$T = T(\xi_1, \xi_2, K) = \Lambda \hat{\xi}_2 + \left(\frac{3+\sigma}{2}\right)\left[\frac{\hat{\xi}_2^2 + 2\Lambda \hat{\xi}_1}{1+\sigma}\right]^{1/2} \quad ; \quad (\xi_1, \xi_2) \in G_- \cup G_+$$

$$\text{(E-54a)}$$

$$= \frac{1}{2}|\hat{\xi}_2| - \hat{\xi}_1/\hat{\xi}_2 \quad\quad ; \quad (\xi_1, \xi_2) \in H_- \cup H_+$$

$$\text{(E-54b)}$$

where Λ, σ, and $(\hat{\xi}_1, \hat{\xi}_2)$ are defined by (E-47), (E-34), and (E-37), respectively.

A similar relation may be derived for the fuel F, as defined by (E-48). Suppose $(\xi_1, \xi_2) \in G_-$, so that the $\{-U, 0, U\}$ control sequence is applicable. The fuel is then given by:

$$F = \int_0^T |u(t)| dt = \int_0^{\tau_1} |-U| dt + \int_{\tau_1}^{\tau_2} |0| dt + \int_{\tau_2}^T |U| dt$$

or,

$$F = U(T - \tau_2 + \tau_1) \quad\quad \text{(E-55)}$$

However, from (E-49),

$$T - \tau_2 = -\beta_2/U$$

so that use of (E-23a), (E-32b), and (E-37) results in

$$T - \tau_2 = -\hat{\xi}_2 + \tau_1$$

which reduces (E-55) to the following:

$$F = U[2\tau_1 - \hat{\xi}_2] \quad\quad \text{(E-56)}$$

Thus, using the switch time expression of (E-38), the total fuel used is then given by:

509

$$F = U \left\{ \hat{\xi}_2 + 2 \left[\frac{\hat{\xi}_2^2 + 2\hat{\xi}_1}{1 + \sigma} \right]^{1/2} \right\} \quad ; \quad (\xi_1, \xi_2) \in G_- \qquad \text{(E-57)}$$

Thus, for $(\xi_1, \xi_2) \in G_-$, F is determined by (ξ_1, ξ_2) and K. Now, suppose $(\xi_1, \xi_2) \in H_+$, so that the $\{0, +U\}$ sequence is applicable, and

$$F = \int_0^T |u(t)| dt = \int_0^{\tau_0} |0| dt + \int_{\tau_0}^T |+U| dt$$

or

$$F = U(T - \tau_0)$$

Use of (E-42b) and (E-52) reduce the above expression to the following:

$$F = -\xi_2 \quad ; \quad (\xi_1, \xi_2) \in H_+ \qquad \text{(E-58)}$$

As before, similar results may be found for $(\xi_1, \xi_2) \in G_+$ and $(\xi_1, \xi_2) \in H_-$, so that the fuel F used along the optimal trajectory is given by:

$$F = F(\xi_1, \xi_2, K) = U \left\{ \Lambda \hat{\xi}_2 + 2 \left[\frac{\hat{\xi}_2^2 + 2\Lambda\hat{\xi}_1}{1 + \sigma} \right]^{1/2} \right\} \quad ; \quad (\xi_1, \xi_2) \in G_- \cup G_+$$

$$\text{(E-59a)}$$

$$F = F(\xi_1, \xi_2, K) = |\xi_2| \quad ; \quad (\xi_1, \xi_2) \in H_- \cup H_+ \qquad \text{(E-59b)}$$

where Λ, σ, and $(\hat{\xi}_1, \hat{\xi}_2)$ are defined by (E-47), (E-34), and (E-37), respectively.

It should be recognized that although T and F are defined explicitly as functions of (ξ_1, ξ_2) and K, they are also dependent on the location of (ξ_1, ξ_2) in the phase plane. Thus, since H_- and H_+ are determined by Γ_- and Γ_+, which are, in turn, determined by K through (E-29), initial condition regional association will depend on K. From (E-15) and (E-29),

it should be clear that

$$\lim_{K \to \infty} \Gamma_+ = \gamma_+ \quad ; \quad \lim_{K \to \infty} \Gamma_- = \gamma_- \qquad \text{(E-60a)}$$

and that

$$\lim_{K \to 0} (\Gamma_+ \cup \Gamma_-) = x_1 - \text{axis} \qquad \text{(E-60b)}$$

where the formal equality signifies point coincidence. This situation is shown graphically in Figure E-11.
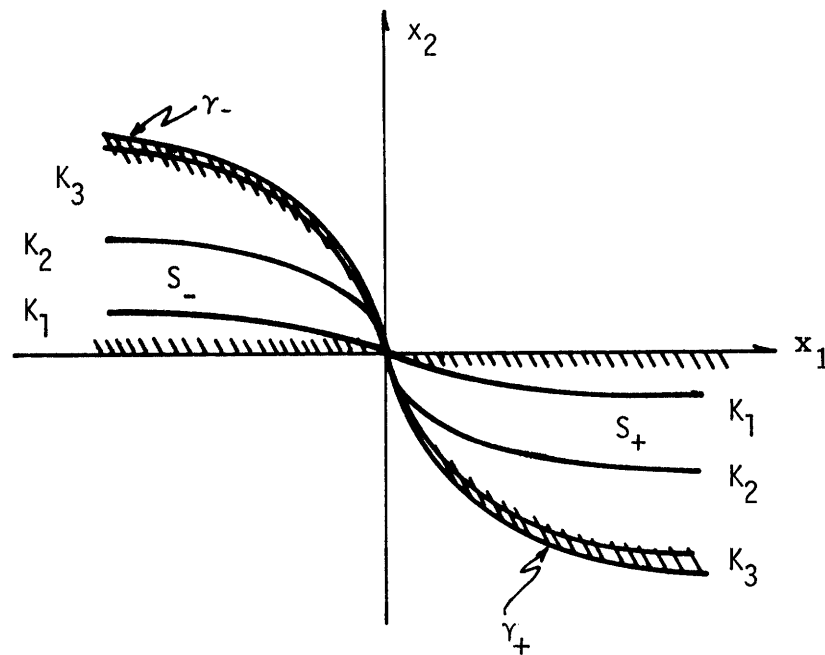
Figure E-11.

For the Γ_+ and Γ_- curve variation shown, the K parameters are chosen to show the limiting behavior, as follows:

$$0 < K_1 < K_2 < K_3 < \infty$$

The regions S_+ and S_- are introduced to define the phase plane area between $(\gamma_+ \cup \gamma_-)$ and the x_1-axis, as shown. The boundary association is given by:

511

$$\left[\gamma_+ \cup (+x_1\text{-axis}) \right] \subset S_+ \quad ; \quad \left[\gamma_- \cup (-x_1\text{-axis}) \right] \subset S_- \qquad \text{(E-61)}$$

With T and F defined explicitly as functions of (ξ_1, ξ_2) and K, and with an understanding of switch region dependence on K, it is now a direct matter to demonstrate the effect of K on system performance. First, it should be noted that for $(\xi_1, \xi_2) \, \epsilon \, (H_- \cup H_+)$, both T and F are independent of K, so that there is no direct parameter sensitivity in this case. However, if $(\xi_1, \xi_2) \, \epsilon \, (G_- \cup G_+)$, direct differentiation of (E-54a) and (E-59a) with respect to K yields:

$$\frac{\partial T}{\partial K} = - \frac{2^{1/2}}{\lambda^{3/2}(\lambda+2)^{3/2} U} (\hat{\xi}_2^2 + 2\Lambda\hat{\xi}_1)^{1/2}$$

$$\text{(E-62)}$$

$$\frac{\partial F}{\partial K} = \frac{2^{1/2}}{\lambda^{1/2}(\lambda+2)^{1/2}} (\hat{\xi}_2^2 + 2\Lambda\hat{\xi}_1)^{1/2}$$

where

$$\lambda \equiv (K/U) \qquad \text{(E-63)}$$

It is clear then that both T and F are monotonic functions of K, or, from (E-62),

$$\frac{\partial T}{\partial K} < 0$$
$$\qquad \qquad \forall K > 0 \quad ; \quad (\xi_1, \xi_2) \, \epsilon \, G_- \cup G_+ \qquad \text{(E-64)}$$
$$\frac{\partial F}{\partial K} > 0$$

Thus, in support of the initial comment of this section, T is minimized as $K \to \infty$ and F is minimized as $K \to 0$. However, the monotonic nature of both T and F in (E-64) leads to another important characteristic of the problem. From (E-54), (E-59), and (E-64), the performance limits, in terms of minimum and maximum T and F, are as follows:

$$T_{min} = \lim_{K \to \infty} T(K) = \Lambda\hat{\xi}_2 + 2^{1/2}(\hat{\xi}_2^2 + 2\Lambda\hat{\xi}_1)^{1/2} \qquad \text{(E-65a)}$$

$$T_{max} = \lim_{K \to 0} T(K) = \infty \qquad \text{(E-65b)}$$

$$F_{min} = \lim_{K \to 0} F(K) = |\xi_2| \qquad \text{(E-65c)}$$

$$F_{max} = \lim_{K \to \infty} F(K) = U[\Lambda\hat{\xi}_2 + 2^{1/2}(\hat{\xi}_2^2 + 2\Lambda\hat{\xi}_1)^{1/2}] \qquad \text{(E-65d)}$$

where $(\xi_1, \xi_2) \in G_- \cup G_+$. Thus, the behavior of T and F with K may be sketched as shown in Figure E-12.
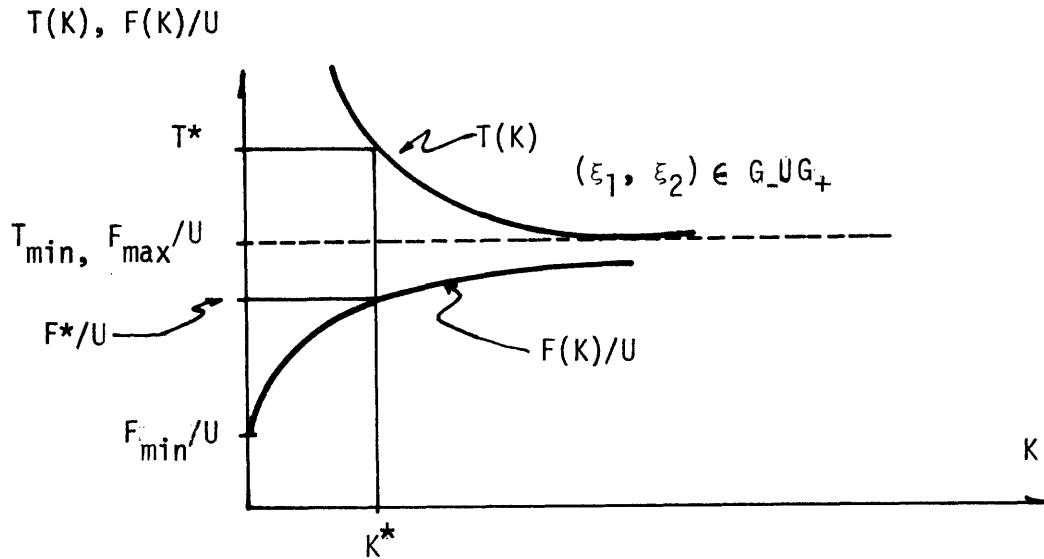
Figure E-12.

The following problem may now be considered. Suppose the parameter K is left free, but that it is specified that the response time T be less than or equal to some T^*, where, for realizability, $T^* > T_{min}$, where T_{min} is given by (E-65). For convenience, define $\tilde{T}$, where

$$\tilde{T} \equiv \frac{1}{2}|\hat{\xi}_2| - \hat{\xi}_1/\hat{\xi}_2 \qquad \text{(E-66)}$$

Now, if $(\xi_1, \xi_2) \in (S_- \cup S_+)$ and if $T^* \geq \tilde{T}$, it should be clear from (E-54b) that the response time specification $(T \leq T^*)$ can be met by choosing K such that $(\xi_1, \xi_2) \in (H_- \cup H_+)$. Further, from (E-59b) and (E-65c), the control effort F is absolutely $\underline{\text{minimized}}$ along the trajectory. Now, if one of the two conditions does not hold, that is, if $(\xi_1, \xi_2) \notin (S_- \cup S_+)$ or if $T^* < \tilde{T}$, then the problem may be solved by assuming $(\xi_1, \xi_2) \in (G_- \cup G_+)$. Referring to Figure E-12, then, if the response time specification $(T \leq T^*)$ is to be met, then K must be chosen such that $K \geq K^*$, where K^* corresponds to T^*. This, in turn, implies that $F \geq F^*$ where F is the resulting control effort and F^* corresponds to K^*. Clearly, then the response time specification is satisfied and the $\underline{\text{minimum}}$ fuel F is used when $K = K^*$.

In summary, then, if an upper bound on T is specified (consistent with (E-65a)), it is always possible to choose a K such that the fuel F will be minimized along the trajectory. Depending on the initial conditions and the upper bound on T, the parameter K is determined either by setting it arbitrarily low or by solving (E-34) and (E-54a) for K. A similar solution (although slightly more complex due to additional inequality constraints) may also be found for the analogous problem in which an upper bound on F is specified (consistent with (E-65c)) and it is desired to minimize T. It should be noted that with a free weighting parameter K, the capability exists for solving a distinctly different problem from the originally proposed free-time, free-fuel problem.

Appendix F: Lateral Controllability

This appendix examines the controllability of the lateral dynamics, in support of the discussion of aerodynamic controllability given in Section 5.2.2.1. The derivations presented here assume only aileron and rudder control are available, and are based on the simplified model descriptions given by (5-35) of Section 5.2.2. The derivations are presented in two sections: Section F.1 discusses the basic two-surface controllability problem, while Section F.2 considers the special case of aileron control with rudder augmentation.

F.1   General Lateral Controllability Criteria

The derivations presented below will be concerned with the formal specification of (Kalman) controllability of the linear time-invariant system describing the simplified lateral dynamics (appropriate to the surface control law synthesis effort) given by (5-35):

$$(s^2 + \omega_\beta^2)\beta = K_{\beta_{\delta_a}} \hat{\delta}_a + K_{\beta_{\delta_r}} \hat{\delta}_r \qquad \text{(a)}$$

$$\text{(5-35)}$$

$$K_\beta \beta + s^2 \phi_s = K_{\phi_{\delta_a}} \hat{\delta}_a + K_{\phi_{\delta_r}} \hat{\delta}_r \qquad \text{(b)}$$

This equation set may be readily put into the more conventional first-degree, four-dimensional vector differential equation, given by

$$\dot{\underline{x}} = F\underline{x} + G\underline{u} \qquad \text{(F-1)}$$

simply by defining the state and control vectors to be

$$\underline{x} \equiv \begin{bmatrix} \beta \\ \dot{\beta} \\ \phi_s \\ \dot{\phi}_s \end{bmatrix} \quad ; \quad \underline{u} \equiv \begin{bmatrix} \hat{\delta}_a \\ \hat{\delta}_r \end{bmatrix} \qquad \text{(F-2)}$$

and the system and control matrices to be[*]:

$$
F \equiv \begin{bmatrix} 0 & 1 & 0 & 0 \\ -\omega_\beta^2 & 0 & 0 & 0 \\ 0 & 0 & 0 & 1 \\ -K_\beta & 0 & 0 & 0 \end{bmatrix} \quad ; \quad G \equiv \begin{bmatrix} 0 & 0 \\ K_{\beta\delta_a} & K_{\beta\delta_r} \\ 0 & 0 \\ K_{\phi\delta_a} & K_{\phi\delta_r} \end{bmatrix} \qquad \text{(F-3)}
$$

The system defined by (F-1), (F-2), and (F-3) is then said to be controllable if and only if the rank of the following matrix equals the dimension of the state, in this case, four:

$$
C = [\, G, \; FG, \; F^2 G, \; F^3 G \,] \qquad \text{(F-4)}
$$

Thus, the question of controllability reduces to an examination of rank (C). Expanding (F-4) through the definitions of (F-3), there results:

$$
C = \begin{bmatrix} 0 & 0 & K_{\beta\delta_a} & K_{\beta\delta_r} & 0 & 0 & -\omega_\beta^2 K_{\beta\delta_a} & -\omega_\beta^2 K_{\beta\delta_r} \\ K_{\beta\delta_a} & K_{\beta\delta_r} & 0 & 0 & -\omega_\beta^2 K_{\beta\delta_a} & -\omega_\beta^2 K_{\beta\delta_r} & 0 & 0 \\ 0 & 0 & K_{\phi\delta_a} & K_{\phi\delta_r} & 0 & 0 & -K_\beta K_{\beta\delta_a} & -K_\beta K_{\beta\delta_r} \\ K_{\phi\delta_a} & K_{\phi\delta_r} & 0 & 0 & -K_\beta K_{\beta\delta_a} & -K_\beta K_{\beta\delta_r} & 0 & 0 \end{bmatrix}
$$

$$
\text{(F-5)}
$$

Thus, with an interchange of rows,

---

[*] Note the implicit assumption of time-invariance in agreement with the discussion in Appendix B.

516

Rank (C) =

$$
\text{Rank}
\begin{bmatrix}
K_{\beta\delta_a} & K_{\beta\delta_r} & 0 & 0 & -\omega_\beta^2 K_{\beta\delta_a} & -\omega_\beta^2 K_{\beta\delta_r} & 0 & 0 \\
K_{\phi\delta_a} & K_{\phi\delta_r} & 0 & 0 & -K_\beta K_{\beta\delta_a} & -K_\beta K_{\beta\delta_r} & 0 & 0 \\
0 & 0 & K_{\beta\delta_a} & K_{\beta\delta_r} & 0 & 0 & -\omega_\beta^2 K_{\beta\delta_a} & -\omega_\beta^2 K_{\beta\delta_r} \\
0 & 0 & K_{\phi\delta_a} & K_{\phi\delta_r} & 0 & 0 & -K_\beta K_{\beta\delta_a} & -K_\beta K_{\beta\delta_r}
\end{bmatrix}
$$

$$(F-6)$$

Now, if both $K_{\beta\delta_a}$ and $K_{\beta\delta_r}$ are zero, then from (F-6), it is clear that the rank of C will be less than or equal to 2. Thus, for the rank of C to be 4, it is necessary that either $K_{\beta\delta_a}$ or $K_{\beta\delta_r}$ be non-zero. Suppose that $K_{\beta\delta_a}$ is non-zero. Then, by elementary row operations,

Rank (C) =

$$
\text{Rank}
\begin{bmatrix}
K_{\beta\delta_a} & K_{\beta\delta_r} & 0 & 0 & -\omega_\beta^2 K_{\beta\delta_a} & -\omega_\beta^2 K_{\beta\delta_r} & 0 & 0 \\
0 & \lambda_1 & 0 & 0 & \eta K_{\beta\delta_a} & \eta K_{\beta\delta_r} & 0 & 0 \\
0 & 0 & K_{\beta\delta_a} & K_{\beta\delta_r} & 0 & 0 & -\omega_\beta^2 K_{\beta\delta_a} & -\omega_\beta^2 K_{\beta\delta_r} \\
0 & 0 & 0 & \lambda_1 & 0 & 0 & \eta K_{\beta\delta_a} & \eta K_{\beta\delta_r}
\end{bmatrix}
$$

$$(F-7)$$

where, for convenient reference, the following two variables are introduced:

$$
\lambda_1 \equiv K_{\phi\delta_r} - K_{\beta\delta_r}\left(\frac{K_{\phi\delta_a}}{K_{\beta\delta_a}}\right) ; \quad \eta \equiv -K_\beta + \omega_\beta^2\left(\frac{K_{\phi\delta_a}}{K_{\beta\delta_a}}\right)
\tag{F-8}
$$

517

By inspection, the necessary and sufficient condition (recalling that $K_{\beta\delta_a} \neq 0$) for rank (C) = 4 is that either $\lambda_1 \neq 0$ or $\eta \neq 0$. Similarly, it may be supposed that $K_{\beta\delta_r}$ is non-zero. With an interchange of the columns of (F-6), it follows that:

Rank (C) =

$$\text{Rank}\begin{bmatrix} K_{\beta\delta_r} & K_{\beta\delta_a} & 0 & 0 & -\omega_\beta^2 K_{\beta\delta_r} & -\omega_\beta^2 K_{\beta\delta_a} & 0 & 0 \\ K_{\phi\delta_r} & K_{\phi\delta_a} & 0 & 0 & -K_\beta K_{\beta\delta_r} & -K_\beta K_{\beta\delta_a} & 0 & 0 \\ 0 & 0 & K_{\beta\delta_r} & K_{\beta\delta_a} & 0 & 0 & -\omega_\beta^2 K_{\beta\delta_r} & -\omega_\beta^2 K_{\beta\delta_a} \\ 0 & 0 & K_{\phi\delta_r} & K_{\phi\delta_a} & 0 & 0 & -K_\beta K_{\beta\delta_r} & -K_\beta K_{\beta\delta_a} \end{bmatrix}$$

$$(F-9)$$

so that, by elementary row operations,

Rank (C) =

$$\text{Rank}\begin{bmatrix} K_{\beta\delta_r} & K_{\beta\delta_a} & 0 & 0 & -\omega_\beta^2 K_{\beta\delta_r} & -\omega_\beta^2 K_{\beta\delta_a} & 0 & 0 \\ 0 & \lambda_2 & 0 & 0 & \nu K_{\beta\delta_r} & \nu K_{\beta\delta_a} & 0 & 0 \\ 0 & 0 & K_{\beta\delta_r} & K_{\beta\delta_a} & 0 & 0 & -\omega_\beta^2 K_{\beta\delta_r} & -\omega_\beta^2 K_{\beta\delta_a} \\ 0 & 0 & 0 & \lambda_2 & 0 & 0 & \nu K_{\beta\delta_r} & \nu K_{\beta\delta_a} \end{bmatrix}$$

$$(F-10)$$

where, for convenient reference, the following two variables are introduced:

$$\lambda_2 \equiv K_{\phi\delta_a} - K_{\beta\delta_a}\left(\frac{K_{\phi\delta_r}}{K_{\beta\delta_r}}\right) \quad ; \quad \nu \equiv -K_\beta + \omega_\beta^2\left(\frac{K_{\phi\delta_r}}{K_{\beta\delta_r}}\right) \qquad \text{(F-11)}$$

By inspection, the necessary and sufficient condition (recalling that $K_{\beta\delta_r} \neq 0$) for rank (C) = 4 is that either $\lambda_2 \neq 0$ or $\nu \neq 0$.

To summarize the results at this point, then, rank (C) = 4 if and only if:

$$\text{either a) } K_{\beta\delta_a} \neq 0 \text{ and } (\lambda_1 \neq 0 \text{ or } \eta \neq 0) \qquad \text{(F-12)}$$

$$\text{or b) } K_{\beta\delta_r} \neq 0 \text{ and } (\lambda_2 \neq 0 \text{ or } \nu \neq 0)$$

This may be restated as:

$$\text{either a) } (K_{\beta\delta_a} \neq 0 \text{ and } \lambda_1 \neq 0) \text{ or } (K_{\beta\delta_r} \neq 0 \text{ and } \lambda_2 \neq 0)$$

$$\text{or b) } K_{\beta\delta_a} \neq 0 \text{ and } \eta \neq 0) \qquad \text{(F-13)}$$

$$\text{or c) } K_{\beta\delta_r} \neq 0 \text{ and } \nu \neq 0$$

With the definition of the following variable,

$$\lambda \equiv K_{\beta\delta_a} K_{\phi\delta_r} - K_{\phi\delta_a} K_{\beta\delta_r} \qquad \text{(F-14)}$$

it is seen from the definitions of (F-8) and (F-11), that

$$(\lambda \neq 0 \text{ and } K_{\beta\delta_a} \neq 0) \iff (\lambda_1 \neq 0 \text{ and } K_{\beta\delta_a} \neq 0)$$

$$\qquad \text{(F-15)}$$

$$(\lambda \neq 0 \text{ and } K_{\beta\delta_r} \neq 0) \iff (\lambda_2 \neq 0 \text{ and } K_{\beta\delta_r} \neq 0)$$

Thus, (F-13) may be restated as follows:

either a) $\lambda \neq 0$ <u>and</u> $(K_{\beta\delta_a} \neq 0$ or $K_{\beta\delta_r} \neq 0)$

or b) $K_{\beta\delta_a} \neq 0$ <u>and</u> $\eta \neq 0$ $\qquad\qquad$ (F-16)

or c) $K_{\beta\delta_r} \neq 0$ <u>and</u> $\nu \neq 0$

Now, suppose λ is non-zero and also suppose that $K_{\beta\delta_a} = K_{\beta\delta_r} = 0$. From (F-14), this would imply that λ is zero, a contradiction. Thus, if λ is non-zero, then either $K_{\beta\delta_a} \neq 0$ or $K_{\beta\delta_r} \neq 0$ (or both). Thus, (F-16) may be simplified, so that the controllability criteria may be summarized as follows:

Rank (C) = 4 $\Leftrightarrow$ either a) $\lambda \neq 0$

$\qquad\qquad$ or b) $K_{\beta\delta_a} \neq 0$ <u>and</u> $\eta \neq 0$ $\qquad$ (F-17)

$\qquad\qquad$ or c) $K_{\beta\delta_r} \neq 0$ <u>and</u> $\nu \neq 0$

where λ, η, and ν are defined by (F-14), (F-8), and (F-11), respectively.

In order to relate these controllability criteria to the aerodynamic properties of the vehicle, it is necessary to use the model parameter definitions of Chapter 4. Recognizing that all of the pertinent model parameters are proportional to dynamic pressure, it should be clear that none of the conditions of (F-17) is satisfied at zero dynamic pressure, as expected. Restricting the controllability analysis to the aerodynamic regime of the entry, then it should also be clear that the dynamic pressure dependence (along with dependence on the vehicle's basic geometric properties) may be dropped in determining the null values of the controllability parameters of (F-17). To state the controllability requirements in terms of the aerodynamic coefficients, it is first convenient to restate (F-17) as follows:

Rank (C) = 4 $\Leftrightarrow$ either a) $\lambda \neq 0$

$\qquad\qquad$ or b) $K_{\beta\delta_a} \neq 0$ <u>and</u> $K_{\beta\delta_a}\eta \neq 0$ $\qquad$ (F-18)

$\qquad\qquad$ or c) $K_{\beta\delta_r} \neq 0$ <u>and</u> $K_{\beta\delta_r}\nu \neq 0$

Use of the definitions given above in (F-14), (F-8) and (F-11), combined
with the model parameter definitions of (4-50) and (4-52), and the
dynamic derivative definitions of (4-43) and (4-47), then allows the
controllability condition to be summarized as follows:

$$\text{Rank (C)} = 4 \Leftrightarrow \text{ either a) } \pi_0 \neq 0$$

$$\text{or b) } C'_{n\delta_a} \neq 0 \underline{\text{ and }} \pi_1 \neq 0 \qquad \text{(F-19)}$$

$$\text{or c) } C'_{n\delta_r} \neq 0 \underline{\text{ and }} \pi_2 \neq 0$$

where the coefficient functions π_i are defined by:

$$\pi_0 \equiv C_{n\delta_r} C_{\ell\delta_a} - C_{\ell\delta_r} C_{n\delta_a} \qquad \text{(a)}$$

$$\pi_1 \equiv C_{n_\beta} C_{\ell\delta_a} - C_{\ell_\beta} C_{n\delta_a} \qquad \text{(b)} \qquad \text{(F-20)}$$

$$\pi_2 \equiv C_{n_\beta} C_{\ell\delta_r} - C_{\ell_\beta} C_{n\delta_r} \qquad \text{(c)}$$

Thus, (F-19) and (F-20) specify the requirements on the aerodynamic
coefficients for the lateral dynamics to be controllable with the surfaces
(presuming non-zero dynamic pressure).

At this point, it should be recognized that there is clearly no
precise point in the entry envelope at which one or more of the control-
lability coefficients takes on the exact value of zero, due to the physical
basis of the coefficients. Thus, it is of interest to consider trends and
limiting behavior of the coefficients. Shown in Figures F-1 through F-5
are contour plots of the five controllability variables of (F-19), display-
ing their dependence on the particular Mach number/trim angle-of-attack
operating point of the vehicle. These plots were generated from the data
of Reference 2, for the forward center-of-gravity configuration, and
cover the low end of the trajectory since this is where coefficient vari-
ation is greatest. The qualitative aspects of these plots, and their im-
plications for control, are discussed in Section 5.2.2.1.

Figure F-1. Contour Plot for π_0.
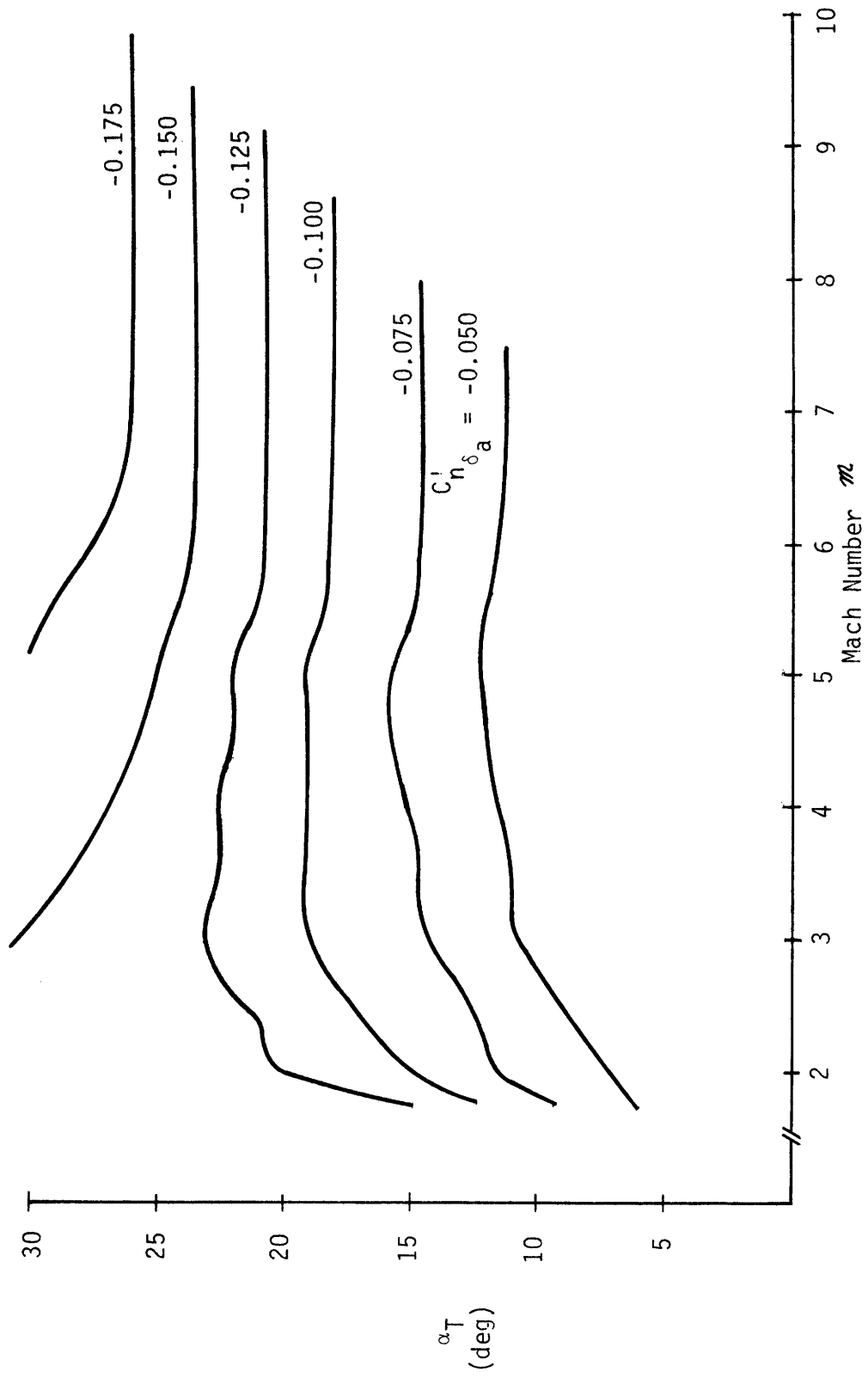
Figure F-2. Contour Plot for $C'_{n_{\delta_a}}$.
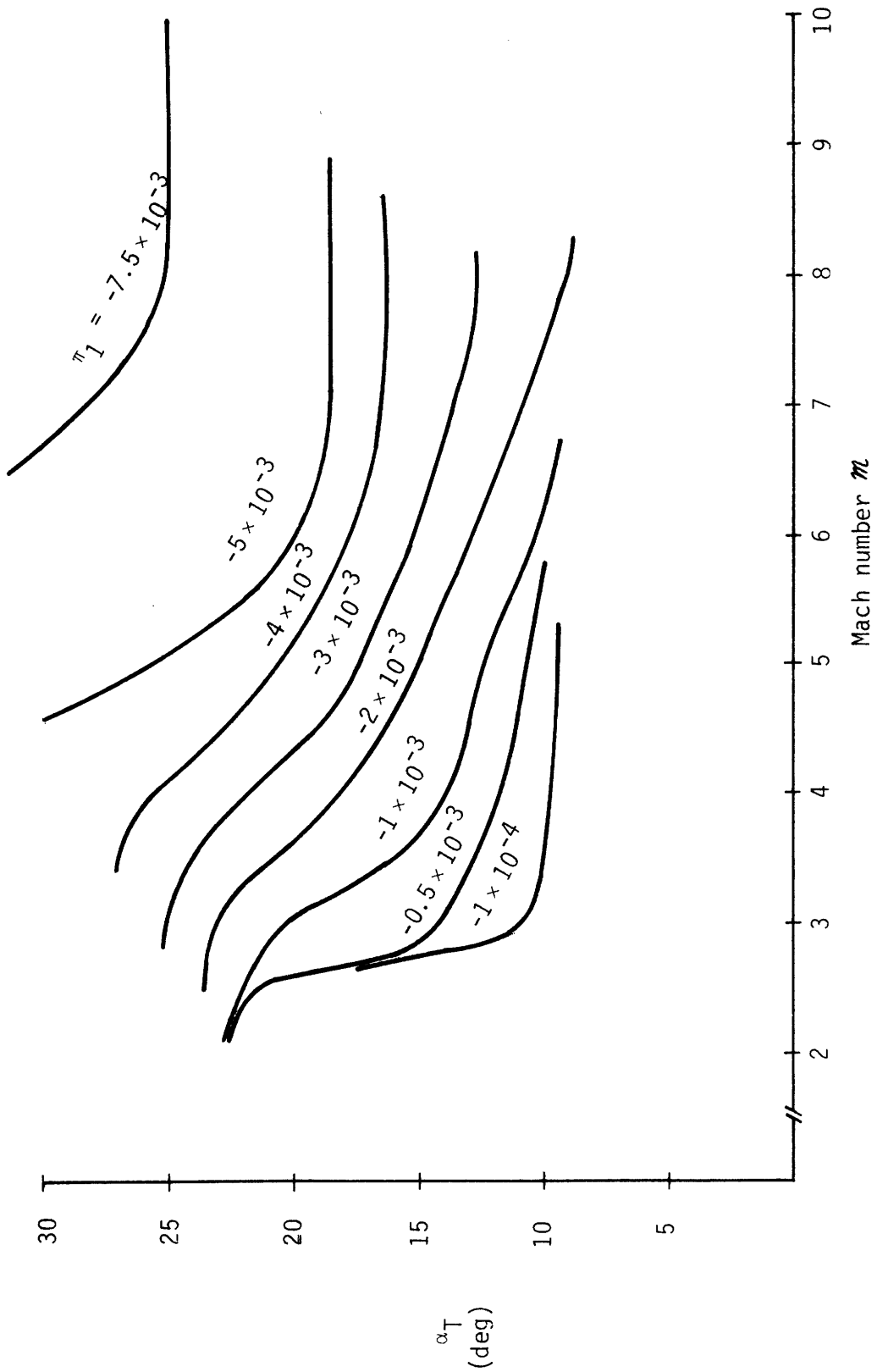
Figure F-3. Contour Plot for π_1.
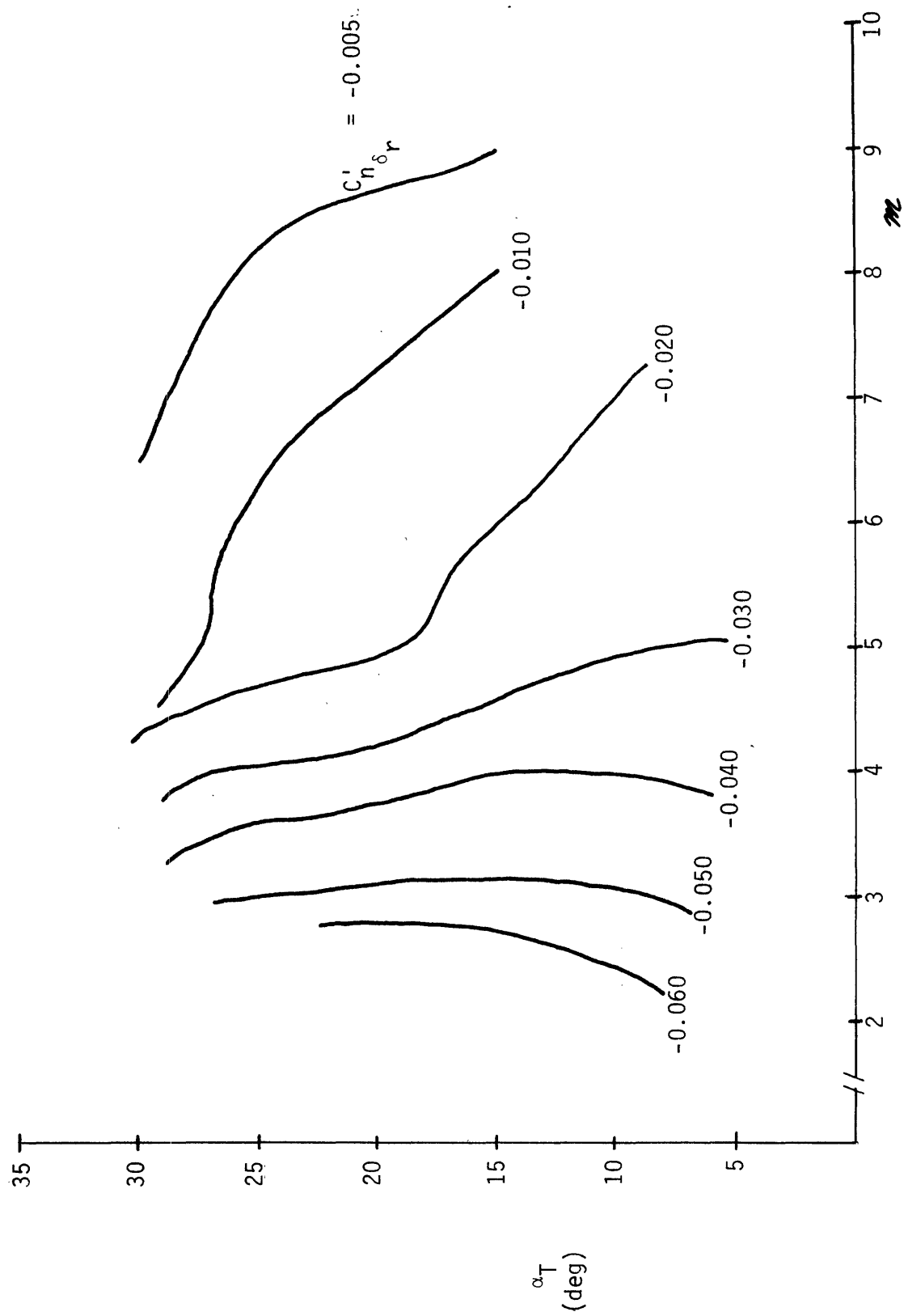
Figure F-4. Contour Plot for $C'_{n_{\delta_r}}$.
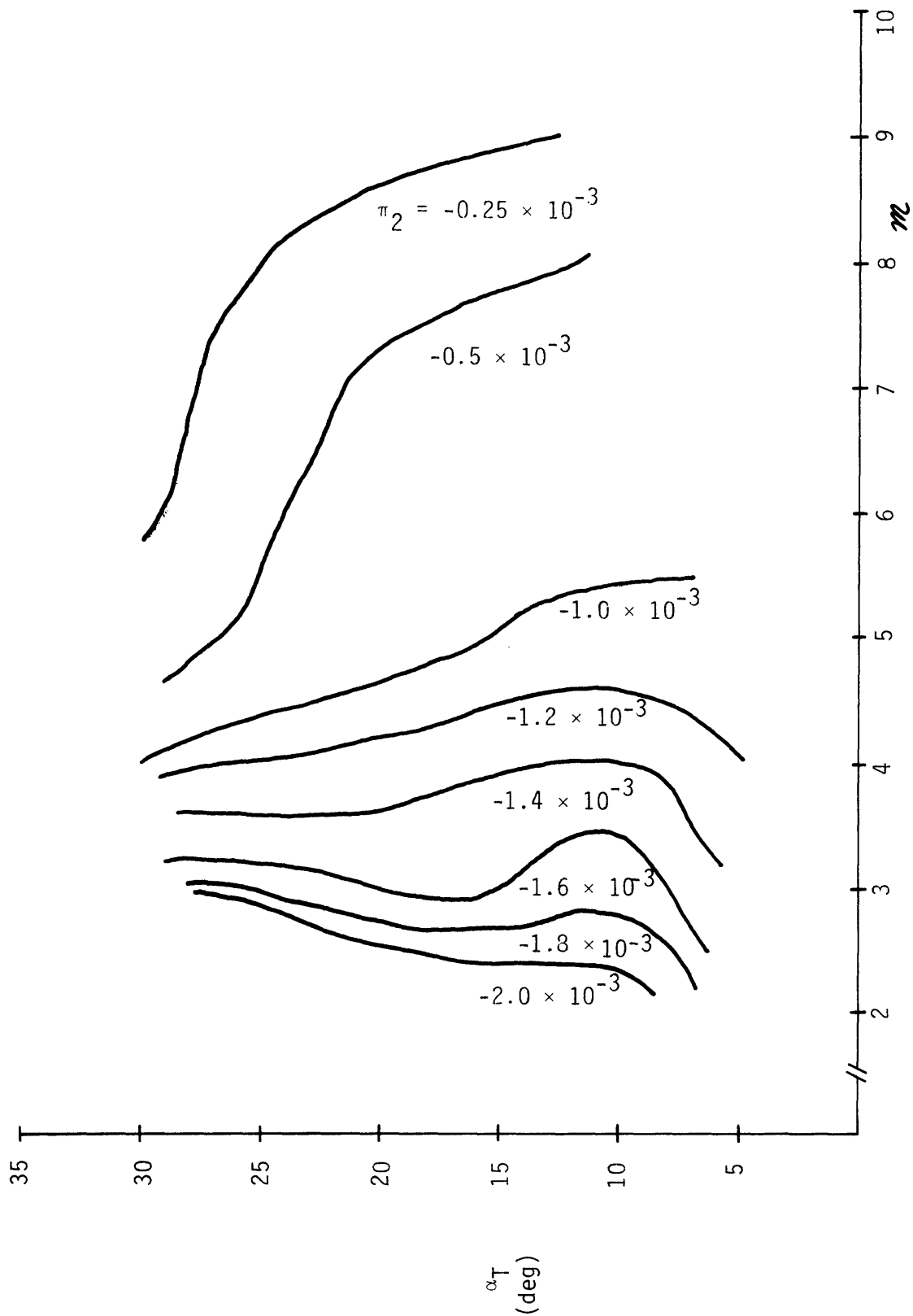
Figure F-5. Contour Plot for π_2.

$\pi_2 = -0.25 \times 10^{-3}$

-0.5×10^{-3}

-1.0×10^{-3}

-1.2×10^{-3}

-1.4×10^{-3}

-1.6×10^{-3}

-1.8×10^{-3}

-2.0×10^{-3}

$\mathcal{M}$

α_T (deg)

F.2 Lateral Controllability with Aileron/Rudder Augmentation

As discussed in the text, rudder augmentation of aileron effectiveness may be accomplished by the use of a simple crossfeed control law:

$$\hat{\delta}_r = C_r \hat{\delta}_a \qquad (5\text{-}42)$$

so that the dynamic equation set of (5-35) becomes:

$$(s^2 + \omega_\beta^2)\beta = \tilde{K}_{\beta\delta_a}\hat{\delta}_a \qquad (a)$$

$$K_\beta\beta + s^2\phi_s = \tilde{K}_{\phi\delta_a}\hat{\delta}_a \qquad (b)$$

$$(5\text{-}43)$$

where the augmented aileron effectiveness parameters $\tilde{K}_{\beta\delta_a}$ and $\tilde{K}_{\phi\delta_a}$ are defined by (5-44) in the text:

$$\tilde{K}_{\beta\delta_a} \equiv K_{\beta\delta_a} + C_r K_{\beta\delta_r} \qquad (a)$$

$$\tilde{K}_{\phi\delta_a} \equiv K_{\phi\delta_a} + C_r K_{\phi\delta_r} \qquad (b)$$

$$(F\text{-}21)$$

To determine the controllability of the system above, it is only necessary to compare it with the system described by (5-35). Clearly, the latter system becomes equivalent to that of (5-43) if the rudder effectiveness is assumed zero and the aileron effectiveness parameters are replaced by the augmented parameters of (5-44). Thus, the controllability conditions of (F-18) apply, with the appropriate substitution of the augmented aileron parameters. Further, recognizing that zero rudder effectiveness implies that (F-18a) and (F-18c) cannot be satisfied, then the following condition must be met for controllability with this configuration:

$$\tilde{K}_{\beta\delta_a} \neq 0 \ \underline{\text{and}} \ \tilde{K}_{\beta\delta_a}\tilde{\eta} \neq 0 \qquad (F\text{-}22)$$

where $\tilde{\eta}$ is defined analogously to η:

$$\tilde{\eta} \equiv -K_\beta + \omega_\beta^2 \left(\frac{\tilde{K}_{\phi\delta_a}}{\tilde{K}_{\beta\delta_a}} \right) \qquad \text{(F-23)}$$

Use of the definitions given in (F-21) and (F-23), combined with the model parameter definitions of (4-50) and (4-52), and the dynamic derivative definitions of (4-43) and (4-47), then allows the controllability condition to be restated as follows: the vehicle is controllable (at non-zero dynamic pressures) using the crossfeed law of (5-42) if and only if

$$\tilde{C}'_{n\delta_a} \neq 0 \ \underline{\text{and}} \ \tilde{\pi}_1 \neq 0 \qquad \text{(F-24)}$$

where the controllability coefficients take on the same augmented form used previously:

$$\tilde{\pi}_1 \equiv C_{n_\beta} \tilde{C}_{\ell\delta_a} - C_{\ell_\beta} \tilde{C}_{n\delta_a} \qquad \text{(F-25)}$$

$$\tilde{C}'_{n\delta_a} \equiv C'_{n\delta_a} + C_r C'_{n\delta_r} \qquad \text{(a)}$$

$$\tilde{C}_{\ell\delta_a} \equiv C_{\ell\delta_a} + C_r C_{\ell\delta_r} \qquad \text{(b)} \qquad \text{(F-26)}$$

$$\tilde{C}_{n\delta_a} \equiv C_{n\delta_a} + C_r C_{n\delta_r} \qquad \text{(c)}$$

As before, contour plots of the augmented controllability coefficients may be made so as to uncover limiting behavior; Figures F-6 and F-7 illustrate the dependence of $\tilde{C}'_{n\delta_a}$ and $\tilde{\pi}_1$ on the Mach number and trim angle-of-attack for a particular (reasonable) value of the crossfeed gain ($C_r = 2$). As with the previous figures, the plots were generated from the data of Reference 2, for the forward center-of-gravity configuration, and cover the low end of the entry trajectory. The qualitative aspects of these plots, and their implications for control, are discussed in Section 5.2.2.1.
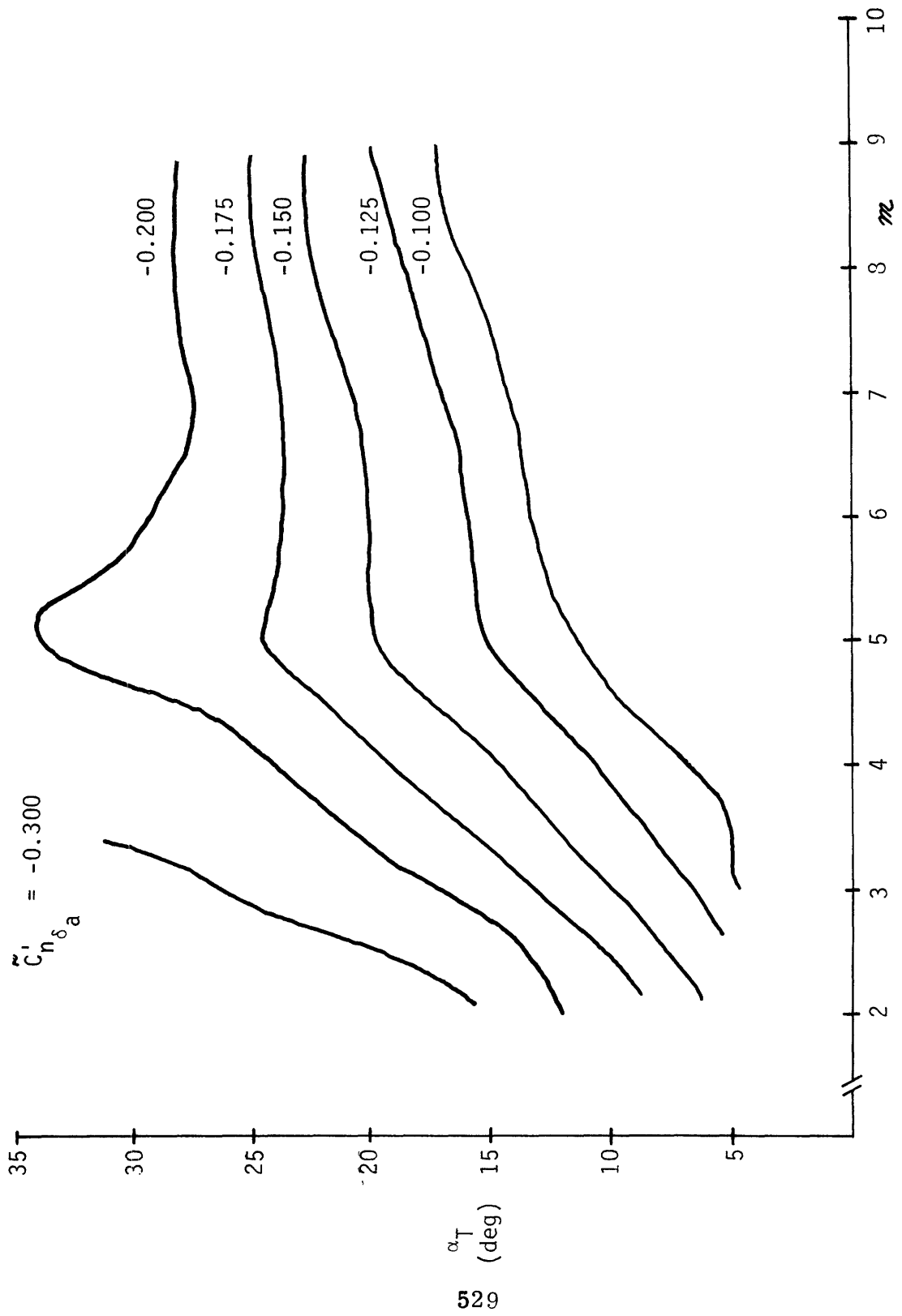
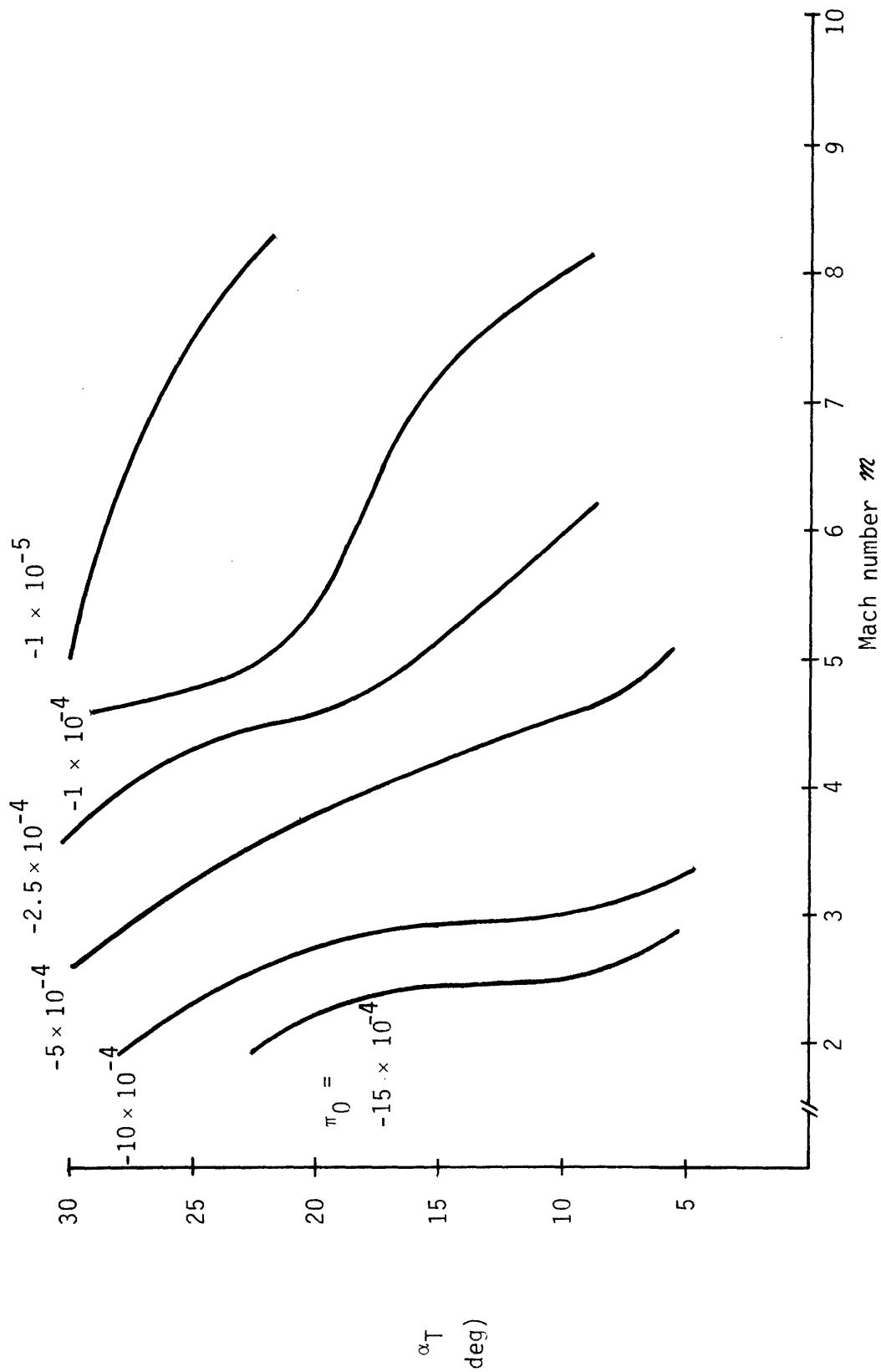Figure F-6. Contour Plot for $\tilde{C}'_{n_{\delta_a}}$.

529
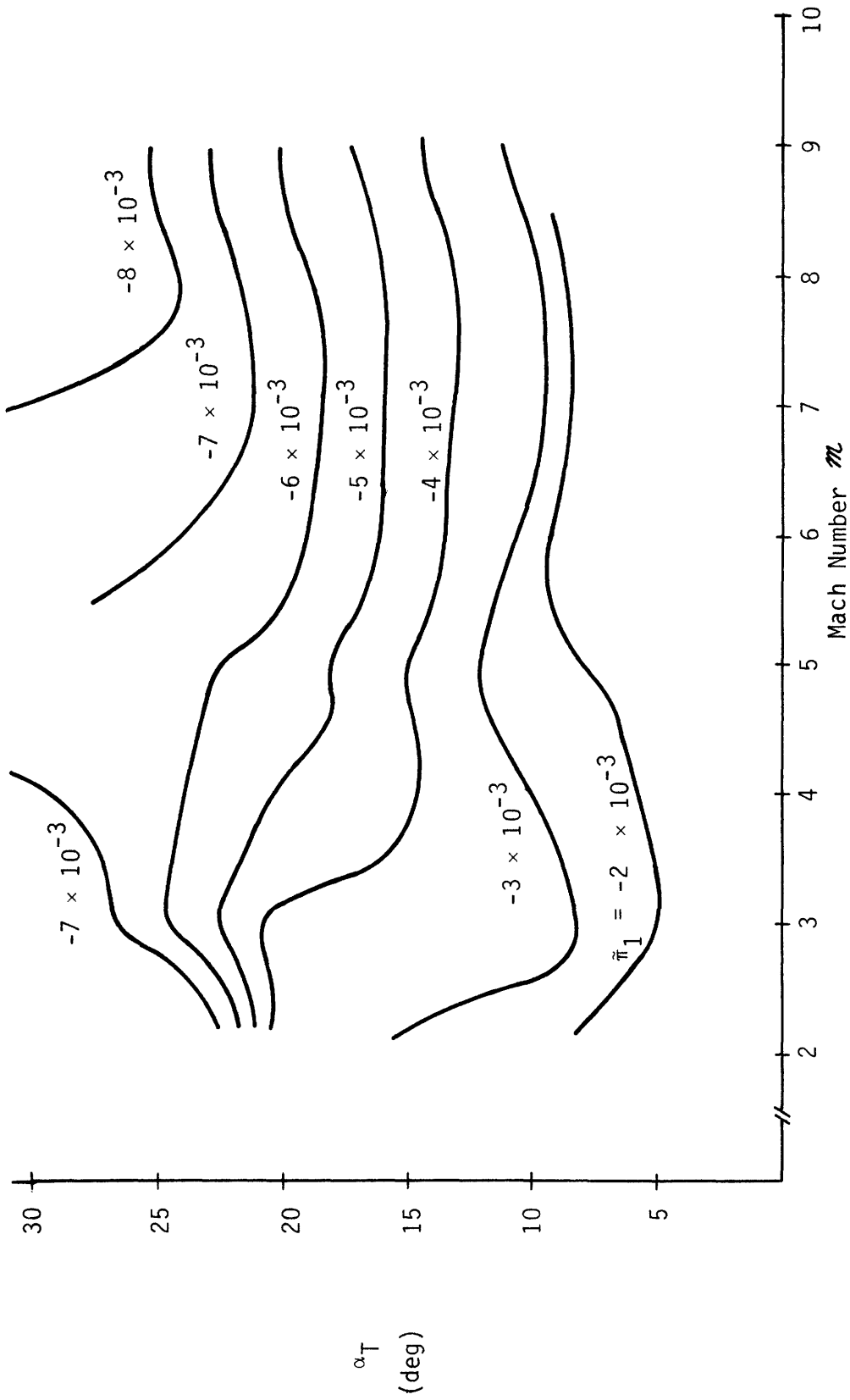
Figure F-7. Contour Plot for $\tilde{\pi}_1$.

Appendix G: Lateral Center-of-Gravity Offset Effects

The purpose of this appendix is to describe the effects on the vehicle's rotational dynamics due to a lateral off-nominal displacement of the center-of-gravity out of the body-axis plane of symmetry. The results presented here support the derivation of the lateral logic given in Section 5.2.2.2.3.

The lateral dynamic model appropriate to this analysis is defined by (5-35) of Chapter 5, which is based on equations derived in Chapter 4 under the assumption of a symmetric vehicle[*]. To allow for an asymmetry, it is necessary to amend (5-35) to include the effects of what may be regarded as disturbance torques; this is readily done by the addition of sideslip and bank angle disturbance accelerations u_β^d and u_ϕ^d, as follows:

$$(s^2 + \omega_\beta^2)\beta = K_{\beta\delta_r}\hat{\delta}_r + K_{\beta\delta_a}\hat{\delta}_a + u_\beta^d \qquad (a)$$

$$K_\beta\beta + s^2\phi_s = K_{\phi\delta_r}\hat{\delta}_r + K_{\phi\delta_a}\hat{\delta}_a + u_\phi^d \qquad (b)$$

(G-1)

The disturbance accelerations may now be defined as functions of the lateral center-of-gravity offset, ℓ. Shown in Figure G-1 is a representation of a (positive) lateral CG displacement out of the body-axis plane of symmetry, which, it is assumed for simplicity[†], contains the vehicle's center-of-pressure (CP). The axial and normal forces acting on the CP, through the moment arm ℓ, give rise to body-axis disturbance torques, which, when divided by the appropriate inertias, result in the following roll and yaw disturbance accelerations:

---

[*] Note that no ACPS firings are modelled; their effect is reintroduced in Section 5.2.2.2.3.

[†] Additional correction terms would be required for an out-of-plane CP, but the end result is essentially the same as the result to be derived here.

531
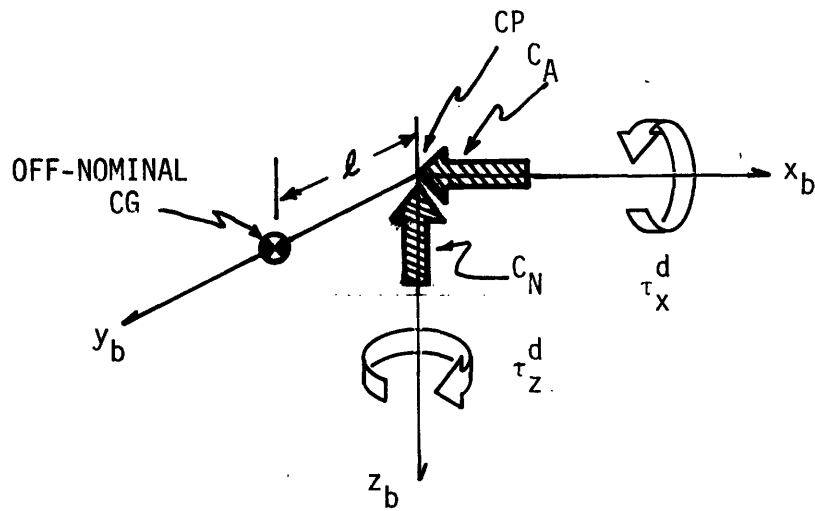
Figure G1.   Positive Y-axis CG Offset
Induced Disturbance Accelerations.
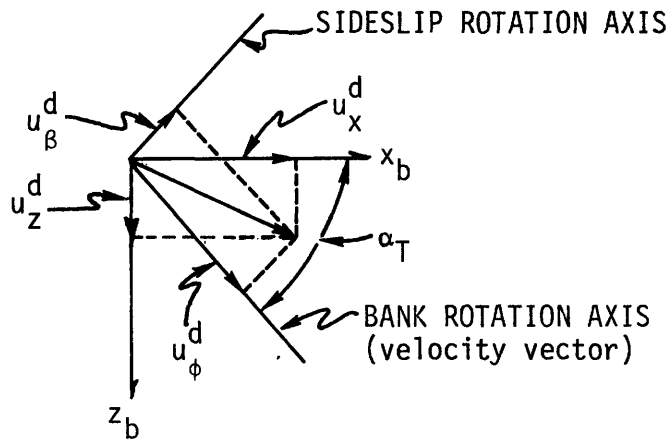
Figure G2.   Relation Between Body and Stability-axis Disturbances.

$$u_x^d = \frac{\overline{q}S\ell}{I_{xx}}C_N \qquad \text{(a)}$$

$$\text{(G-2)}$$

$$u_z^d = -\frac{\overline{q}S\ell}{I_{zz}}C_A \qquad \text{(b)}$$

Assuming that the sideslip angle is small, these body-axis disturbance accelerations may be readily transformed into the stability-axis disturbance accelerations u_β^d and u_ϕ^d, by referring to Figure G-2. A rotation through the trim angle-of-attack, α_T, yields:

$$u_\beta^d = u_x^d \sin\alpha_T - u_z^d \cos\alpha_T \qquad \text{(a)}$$

$$\text{(G-3)}$$

$$u_\phi^d = u_x^d \cos\alpha_T + u_z^d \sin\alpha_T \qquad \text{(b)}$$

Thus, use of (G-2) implies:

$$u_\beta^d = \left(\frac{\overline{q}S\ell}{I_{xx}}\right)C_N \sin\alpha_T \left[1 + \left(\frac{I_{xx}}{I_{zz}}\right)\left(\frac{C_A}{C_N}\right)\cot\alpha_T\right] \qquad \text{(a)}$$

$$\text{(G-4)}$$

$$u_\phi^d = \left(\frac{\overline{q}S\ell}{I_{xx}}\right)C_N \cos\alpha_T \left[1 - \left(\frac{I_{xx}}{I_{zz}}\right)\left(\frac{C_A}{C_N}\right)\tan\alpha_T\right] \qquad \text{(b)}$$

Shown in Figure G-3 are plots showing the values taken on by the (C_A/C_N) terms of (G-4), as the nominal Mach-alpha profile is followed down the trajectory. The profile itself is that given by Figure 5-9, while the inertia data is taken from Appendix B; the functional dependence of the axial and normal force coefficients on Mach number and trim angle-of-attack is defined in Reference 2. As is clear from the magnitudes in the figure, the contribution of the axial coefficient in (G-4b) is negligible, and although the axial coefficient contribution in (G-4b) can reach 25% of the total, its contribution is negligible for the great majority of the entry (i.e., for Mach number > 3). This then
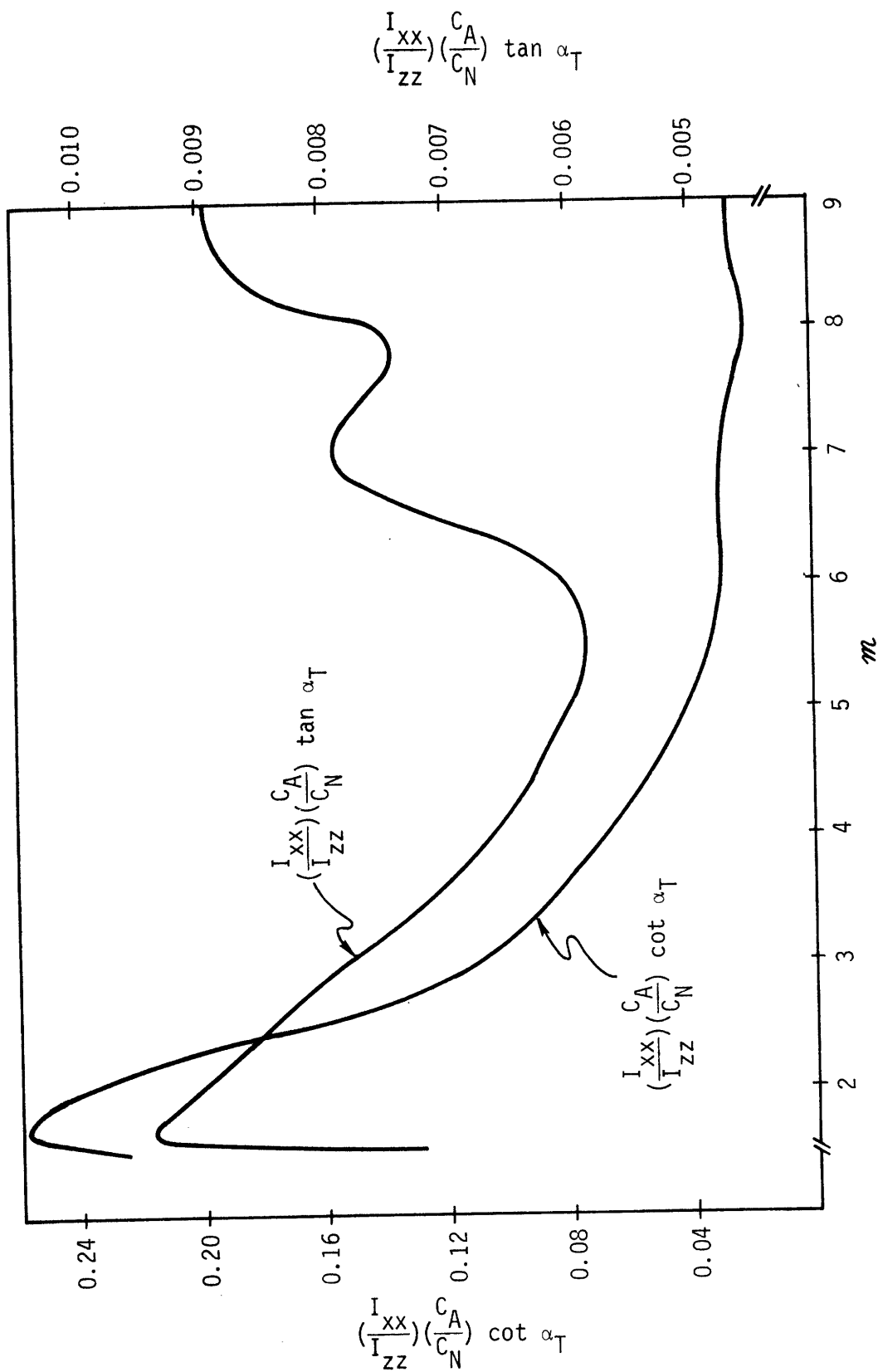
Figure G3.   Axial Force Terms Contributing to Disturbance Accelerations.

provides the motivation for the following simplification of (G-4):

$$u_\beta^d = \frac{\bar{q}S\ell}{I_{xx}}C_N \sin\alpha_T = u_x^d \sin\alpha_T \qquad\text{(a)}$$

$$\qquad\qquad\qquad\qquad\qquad\qquad\qquad\qquad\qquad\text{(G-5)}$$

$$u_\phi^d = \frac{\bar{q}S\ell}{I_{xx}}C_N \cos\alpha_T = u_x^d \cos\alpha_T \qquad\text{(b)}$$

so that the axial coefficient is neglected for the remainder of this analysis. The differential equation specifying the effect of a lateral CG offset is thus obtained from the above relation combined with (G-1):

$$\ddot{\beta} = -\omega_\beta^2\beta + K_{\beta\delta_r}\hat{\delta}_r + K_{\beta\delta_a}\hat{\delta}_a + u_x^d\sin\alpha_T \qquad\text{(a)}$$

$$\qquad\qquad\qquad\qquad\qquad\qquad\qquad\qquad\qquad\text{(G-6)}$$

$$\ddot{\phi}_s = -K_\beta\beta + K_{\phi\delta_r}\hat{\delta}_r + K_{\phi\delta_a}\hat{\delta}_a + u_x^d\cos\alpha_T \qquad\text{(b)}$$

In the presence of a CG offset, then, the trim sideslip angle is found by setting the surface deflections and $\ddot{\beta}$ to zero, so that the "open-loop", or uncompensated, trim is given by:

$$\beta_T^{OL} = (u_x^d\sin\alpha_T)/\omega_\beta^2 \qquad\text{(G-7)}$$

so that, from (G-2) and the definition of ω_β^2 given by (4-50a),

$$\beta_T^{OL} = \left(\frac{\ell}{b}\right)\left(\frac{I_{zz}}{I_{xx}}\right)\left(\frac{C_N}{C_{n_\beta}'}\right)\sin\alpha_T \qquad\text{(G-8a)}$$

where the dynamic derivative C_{n_β}' has been previously introduced and is repeated here from (4-43) for convenient reference:

$$C_{n_\beta}' \equiv C_{n_\beta}\cos\alpha_T - \left(\frac{I_{zz}}{I_{xx}}\right)C_{\ell_\beta}\sin\alpha_T \qquad\text{(G-9)}$$

It should be noted, of course, that this trim sideslip angle gives rise to a bank angle acceleration specified by (G-6b):

$$\ddot{\phi}_s^{OL} = -K_\beta \beta_T^{OL} + u_x^d \cos\alpha_T \qquad (G-10)$$

so that use of (G-8a), (G-2), and the definition of K_β given by (4-52a), then implies that:

$$\ddot{\phi}_s^{OL} = \left(\frac{\overline{q} S \ell}{I_{xx}}\right)\left(\frac{C_{n_\beta}}{C'_{n_\beta}}\right) C_N \qquad (G-8b)$$

Thus, in the absence of surface trim compensation and ACPS firings, (G-8) specifies the effects of a lateral CG offset on the vehicle's dynamics. It should be noted that although the vehicle will establish a trim slip, at β_T^{OL}, there will remain a non-zero bank angle disturbance acceleration, of $\ddot{\phi}_s^{OL}$. Especially significant is the fact that this disturbance is proportional to dynamic pressure.

It is now of interest to consider the use of the aileron and rudder in a trim capacity. Anticipating the introduction of the constant cross-feed control law of (5-42),

$$\hat{\delta}_r = C_r \hat{\delta}_a \qquad (5-42)$$

then (G-5) may be used in (G-1) to yield the following:

$$\ddot{\beta} = -\omega_\beta^2 \beta + \widetilde{K}_{\beta\delta_a} \hat{\delta}_a + u_x^d \sin\alpha_T \qquad (a)$$

$$\ddot{\phi}_s = -K_\beta \beta + \widetilde{K}_{\phi\delta_a} \hat{\delta}_a + u_x^d \cos\alpha_T \qquad (b)$$

(G-10)

where the augmented coefficients $\widetilde{K}_{\beta\delta_a}$ and $\widetilde{K}_{\phi\delta_a}$ reflect the crossfeed law of (5-42) and are defined by (5-43). Requiring that the vehicle be trimmed implies that $\ddot{\beta} = \ddot{\phi}_s = 0$, so that the above equation set implies the following:

$$\beta_T^{CL}/u_x^d = (-\widetilde{K}_{\phi\delta_a}\sin\alpha_T + \widetilde{K}_{\beta\delta_a}\cos\alpha_T)/(K_\beta\widetilde{K}_{\beta\delta_a} - \omega_\beta^2\widetilde{K}_{\phi\delta_a}) \qquad (G-11a)$$

$$\delta_{a_T}/u_x^d = (-K_\beta \sin\alpha_T + \omega_\beta^2 \cos\alpha_T)/(K_\beta \widetilde{K}_{\beta\delta_a} - \omega_\beta^2 \widetilde{K}_{\phi\delta_a}) \qquad \text{(G-11b)}$$

where the "closed-loop", or compensated, trim sideslip, β_T^{CL} is due to the trim aileron (and rudder, by (5-42)) deflection, and the disturbance acceleration u_x^d. Use of (G-2) and the model parameter definitions of (4-50), (4-52), and (5-43) then results in:

$$\beta_T^{CL} = \left(\frac{\ell}{b}\right)C_N(\widetilde{C}'_{n\delta_a}\cos\alpha_T + \frac{I_{zz}}{I_{xx}}\widetilde{C}'_{\ell\delta_a}\sin\alpha_T)/(C'_{n_\beta}\widetilde{C}'_{\ell\delta_a} - C'_{\ell_\beta}\widetilde{C}'_{n\delta_a})$$

$$\text{(G-12a)}$$

$$\delta_{a_T} = -\left(\frac{\ell}{b}\right)C_N(C'_{n_\beta}\cos\alpha_T + \frac{I_{zz}}{I_{xx}}C'_{\ell_\beta}\sin\alpha_T)/(C'_{n_\beta}\widetilde{C}'_{\ell\delta_a} - C'_{\ell_\beta}\widetilde{C}'_{n\delta_a})$$

$$\text{(G-12b)}$$

where the intermediate variables $\widetilde{C}'_{n\delta_a}$ and $\widetilde{C}'_{\ell\delta_a}$ are defined by (5-65). A final application of the dynamic derivative definitions of (4-43) and (4-47) then yields the following expressions for the trim variables:

$$\beta_T^{CL} = \left(\frac{\ell}{b}\right)\frac{C_N\widetilde{C}_{n\delta_a}}{C_{n_\beta}\widetilde{C}_{\ell\delta_a} - C_{\ell_\beta}\widetilde{C}_{n\delta_a}} \qquad \text{(a)}$$

$$\text{(G-13)}$$

$$\delta_{a_T} = -\left(\frac{\ell}{b}\right)\frac{C_N C_{n_\beta}}{C_{n_\beta}\widetilde{C}_{\ell\delta_a} - C_{\ell_\beta}\widetilde{C}_{n\delta_a}} \qquad \text{(b)}$$

where $\widetilde{C}_{\ell\delta_a}$ and $\widetilde{C}_{n\delta_a}$ are the "augmented" aileron effectiveness coefficients defined by (5-65). The familiar looking term in the denominator is, of course, the controllability parameter $\widetilde{\pi}_1$, defined in (5-46).

Thus, (G-13) defines the trim sideslip and aileron corresponding to a given offset ℓ (and implicitly defines the trim rudder through (5-42).

It should be noted that this implies a zero net torque on the vehicle, so that <u>both</u> $\ddot{\beta}$ and $\ddot{\delta}_s$ are zero, in contrast to the no surface trim case defined by (G-8).

Appendix H: Elevator/Aileron Allocation Logic[*]

The purpose of this appendix is to propose one possible solution to the elevator/aileron allocation problem discussed in Section 5.4.2. As noted, even though limiting may be done on the (fictitious) elevator and aileron commands issued by the controller, the command pair may prove to be incompatible with the physical limits of the elevons. The resulting deflections are deleterious to control action not so much due to limiting of the deflections, per se, but due to the elevator/aileron cross-coupling which results. The logic presented here is intended to avoid this situation.

For this problem, it is convenient to work with "pseudo-elevons", defined as follows:

$$\delta_L \equiv \delta_{E_L} - \delta_O$$
$$\delta_R \equiv \delta_{E_R} - \delta_O \tag{H-1}$$

where

$$\delta_O \equiv \frac{1}{2}(\Delta_{max} + \Delta_{min}) \tag{H-2}$$

where Δ_{max} and Δ_{min} are the elevon deflection limits introduced by (5-96) in the text:

$$\Delta_{min} \leq \delta_{E_L}, \ \delta_{E_R} \leq \Delta_{max} \tag{5-96}$$

Thus, the limits on δ_L and δ_R are symmetric, given by

$$-\delta_{max} \leq \delta_L, \ \delta_R \leq \delta_{max} \tag{H-3}$$

where

$$\delta_{max} \equiv \frac{1}{2}(\Delta_{max} - \Delta_{min}) \tag{H-4}$$

---

[*] The material in this appendix is presented in modified form from Reference 28.

With the elevator and aileron deflections defined by (5-95) in terms of the elevon deflections,

$$\delta_e = \frac{1}{2}(\delta_{E_L} + \delta_{E_R}) \qquad \text{(a)}$$

$$\delta_a = \frac{1}{2}(\delta_{E_L} - \delta_{E_R}) \qquad \text{(b)}$$

$$(5\text{-}95)$$

then (H-1) may be used to define them in terms of the "pseudo-elevon" deflections:

$$\delta_e = \frac{1}{2}(\delta_L + \delta_R) + \delta_O \qquad \text{(a)}$$

$$\delta_a = \frac{1}{2}(\delta_L - \delta_R) \qquad \text{(b)}$$

$$(\text{H-5})$$

Shown in Figure H-1 is the (δ_L, δ_R) plane illustrating the symmetric deflection limits of (H-3). In addition, lines of constant elevator and (orthogonal) lines of constant aileron are shown, representing the relation given above in (H-5).

Also shown are the lines associated with a possible command pair $(\tilde{\delta}_e, \tilde{\delta}_a)$ issued by the control logic. Note that the coordinates of the intersection point at A violate the limits set by (H-3), so that this is an unrealizable command pair. Note also that were A inside the limit "box", no elevon allocation problems would exist.

The general approach presented here is best illustrated by describing the solution to this particular example.

Shown in Figure H-2 is the same unrealizable $(\tilde{\delta}_L, \tilde{\delta}_R)$ pair. Clearly, by choosing a (δ_L, δ_R) pair located on the constraint line given by $\delta_L = \delta_{max}$, it is possible to:

i) Satisfy the elevator command at $(\delta_{max}, \delta_R^{max})$ - point B.

ii) Satisfy the aileron command at $(\delta_{max}, \delta_R^{min})$ - point C.

iii) Compromise between commands (i.e., satisfy neither, but minimize the discrepancies between desired aileron and elevator and realizable aileron and elevator) - point D.
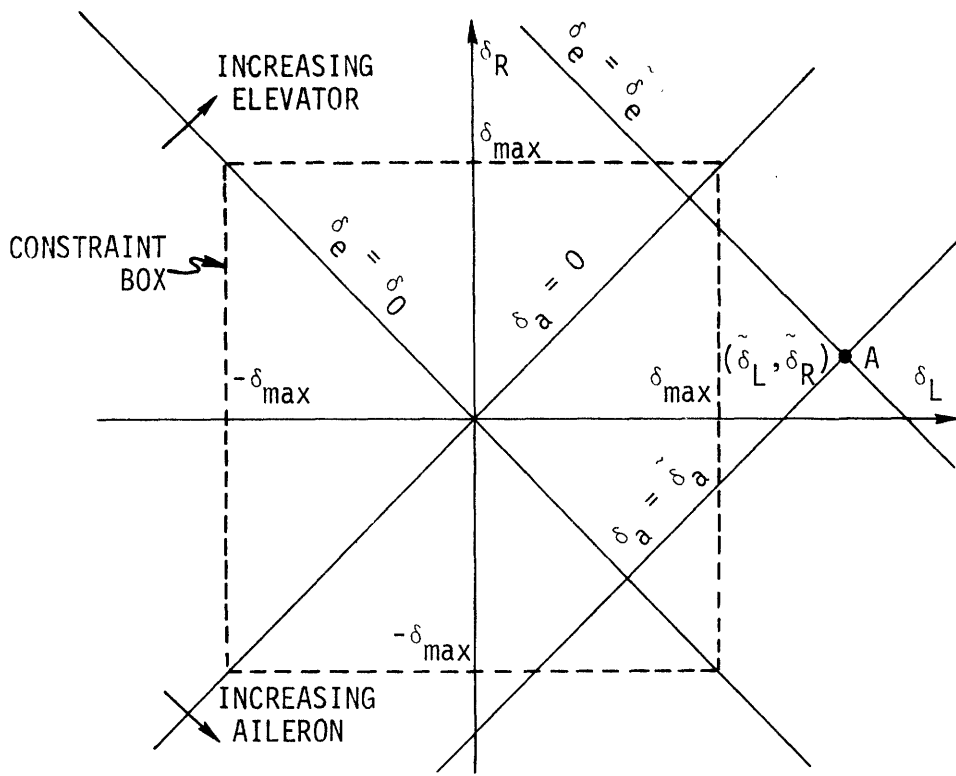
Figure H1. (δ_L, δ_R) Plane, Showing Limits.
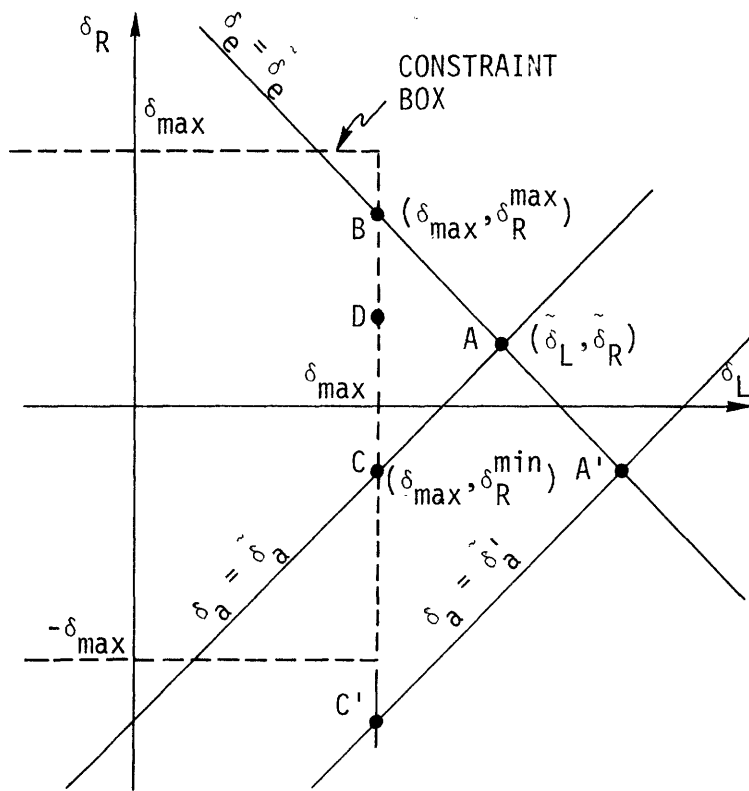
Figure H2. Constrained Solution Points.

The solution may thus be given by:

$$\delta_L = \delta_{max}$$

$$\delta_R = \delta_R^{min} + \lambda(\delta_R^{max} - \delta_R^{min})$$

(H-6)

where the weighting parameter λ:

  i) Satisfies elevator for $\lambda = 1$ (point B)

  ii) Satisfies aileron for $\lambda = 0$ (point C)

  iii) Compromises for $0 < \lambda < 1$ (point D)

The variables $(\delta_R^{max}, \delta_R^{min})$ may be obtained from geometry and are given by:

$$\delta_R^{min} = \tilde{\delta}_R - \Delta$$

$$\delta_R^{max} = \tilde{\delta}_R + \Delta$$

(H-7)

where

$$\Delta = \tilde{\delta}_L - \delta_{max}$$

(H-8)

Prior to generalizing the above results, one more example should be considered. Given the aileron command $\tilde{\delta}_a'$, shown in Figure H-2, having an intersection at C', the calculated δ_R^{min} in (H-7) will be un-realizable, since $\delta_R^{min} < -\delta_{max}$ and (H-3) is violated. Depending on the value of λ, then, the calculated δ_R in (H-6) may also be unrealizable. To avoid this situation, the δ_R obtained from (H-6) should be limited by $\pm \delta_{max}$, or symbolically,

$$\delta_R = LIM(\delta_R, \pm \delta_{max})$$

(H-9)

Now, (H-6) through (H-9) may be generalized for an intersection point A anywhere in the (δ_L, δ_R) plane by an effective rotation into the quadrant just considered, where quadrant definition is specified by the lines $\delta_e = \delta_0$ and $\delta_a = 0$ shown in Figure H-1.

The resulting solution is given in flowchart form in Figure H-3, and ensures a realizable elevon command pair, which, when possible, will satisfy both the elevator and aileron commands. When this is not possible, the program will attempt to satisfy the elevator command, the aileron command, or some compromise between the two, depending on the parameter λ (which, of course, may be regarded as a real-time input variable, rather than a fixed constant). It should be noted that the solution presented here does not attempt to suggest a value for λ; rather, emphasis on elevator or aileron must be specified by the particular control logic design with which this logic interfaces.

START

INPUT
$\delta_e, \delta_a, \lambda$

(δ_e, δ_a) command pair from controller

$0 \leq \lambda \leq 1$; $\lambda = 1$ satisfies elevator command
$\qquad \qquad \qquad$ 0 satisfies aileron command

$\delta_L = (\delta_e + \delta_a) - \delta_o$
$\delta_R = (\delta_e - \delta_a) - \delta_o$

Define intermediate variables
Note: $\delta_o = \frac{1}{2}(\Delta_{max} + \Delta_{min})$; fixed parameter

$|\delta_L| \overset{?}{\leq} \delta_{max}$ yes

Check for possible elevon conflict.
If both commands "small", ignore remainder of logic.
Note: $\delta_{max} = \frac{1}{2}(\Delta_{max} - \Delta_{min})$; fixed parameter

$|\delta_R| \overset{?}{\leq} \delta_{max}$ no

no

yes

(2)

$S_1 = sgn(\delta_a)$
$S_2 = sgn(\delta_e - \delta_o)$

Define (δ_L, δ_R) quadrant

$(\delta_1, \delta_2) = (S_2\delta_L, S_2\delta_R)$

If $S_1 S_2 < 0$, then $(\delta_1, \delta_2) = (\delta_2, \delta_1)$

Rotate quadrant

$\Delta = \delta_1 - \delta_{max}$

$\delta_2^{min} = \delta_2 - \Delta$

$\delta_2^{max} = \delta_2 + \Delta$

$\delta_1 = \delta_{max}$

$\delta_2 = \delta_2^{min} + \lambda(\delta_2^{max} - \delta_2^{min})$

$\delta_2 = LIM (\delta_2, \pm \delta_{max})$

Calculate realizable (δ_1, δ_2)

(1)

Figure H3. Flow Chart for Elevator/Aileron Allocation Logic.

544

Figure H3. Flow Chart for Elevator/Aileron
Allocation Logic (cont)

Appendix I: Lateral Closed-Loop Transfer Functions

This appendix presents a short derivation of the lateral transfer functions relating sideslip and bank to input bank command, for the closed-loop system controlled by the aileron logic of Section 5.2.2.2.1. To do this, it is convenient to separate the lateral state from the desired state by the following vector definitions:

$$\underline{y} \equiv \begin{bmatrix} \beta \\ \phi_s \end{bmatrix} \quad ; \quad \underline{y}_c \equiv \begin{bmatrix} 0 \\ \phi_G \end{bmatrix} \qquad (I\text{-}1)$$

Thus, the state vector of (5-51), used in the transient aileron control law derivation may be expressed as:

$$\underline{x} \equiv \underline{y} - \underline{y}_c \qquad (I\text{-}2)$$

As in the control law development, the lateral dynamics may be recast in the following Laplace transform format:

$$A\underline{y} = \underline{b}\,\hat{\delta}_a \qquad (I\text{-}3)$$

where A and $\underline{b}$ are defined by (5-52) and are repeated here for convenient reference:

$$A \equiv \begin{bmatrix} (s^2 + \omega_\beta^2) & 0 \\ K_\beta & s^2 \end{bmatrix} \quad ; \quad \underline{b} \equiv \begin{bmatrix} \widetilde{K}_{\beta\delta_a} \\ \widetilde{K}_{\phi\delta_a} \end{bmatrix} \qquad (I\text{-}4)$$

Now, from the aileron control law specified by (5-53) and the definitions of (I-1), it follows that

$$\hat{\delta}_a = -\underline{c}'\underline{y} - \underline{c}'\underline{y}_c \qquad (I\text{-}5)$$

where, from (5-54),

$$\underline{c} \equiv \begin{bmatrix} c_{\dot{\beta}}s + c_\beta \\ c_{\dot{\phi}}s + c_\phi \end{bmatrix} \qquad (I\text{-}6)$$

Combining (I-3) and (I-5) then allows the state to be defined as follows:

$$\underline{y} = -(A + \underline{b}\,\underline{c}\,')^{-1}(\underline{b}\,\underline{c}\,')\underline{y}_c \qquad \text{(I-7)}$$

With the feedback gains chosen as in (5-59), so that the closed-loop poles are specified by the design parameters (ζ_i, ω_i), then the determinant of $(A + \underline{b}\,\underline{c}\,')$ is given by:

$$\Delta \equiv |A + \underline{b}\,\underline{c}\,'| = (s^2 + 2\zeta_1\omega_1 s + \omega_1^2)(s^2 + 2\zeta_2\omega_2 s + \omega_2^2)$$

$$\text{(I-8)}$$

Use of (I-1), (I-4), and (I-6) in (I-7) yields the following expressions for the lateral transfer functions:

$$\frac{\beta}{\phi_G} = -\frac{\tilde{K}_{\beta\delta_a}}{\Delta} s^2 (c_{\dot{\phi}} s + c_{\phi}) \qquad \text{(a)}$$

$$\text{(I-9)}$$

$$\frac{\phi}{\phi_G} = -\frac{\tilde{K}_{\phi\delta_a}}{\Delta} (c_{\dot{\phi}} s + c_{\phi}) \left[s^2 - \left(\frac{\tilde{K}_{\beta\delta_a}}{\tilde{K}_{\phi\delta_a}} K_{\beta} - \omega_{\beta}^2 \right) \right] \qquad \text{(b)}$$

Use of (I-8), the gain definitions of (5-59), and the parameter definitions of (5-61) then results in:

$$\frac{\beta}{\phi_G} = \frac{\tilde{K}_{\beta\delta_a}}{\tilde{K}_{\phi\delta_a}} \frac{a_1}{\omega_{\phi}^2} \frac{s^2(a_2 s + 1)}{(s^2 + 2\zeta_1\omega_1 s + \omega_1^2)(s^2 + 2\zeta_2\omega_2 s + \omega_2^2)} \qquad \text{(a)}$$

$$\frac{\phi}{\phi_G} = \frac{a_1}{\tilde{\omega}_{\phi}^2} \frac{(a_2 s + 1)(s^2 - \tilde{\omega}_{\phi}^2)}{(s^2 + 2\zeta_1\omega_1 s + \omega_1^2)(s^2 + 2\zeta_2\omega_2 s + \omega_2^2)} \qquad \text{(b)}$$

$$\text{(I-10)}$$

where, for convenience, the following vehicle parameter is introduced:

$$\tilde{\omega}_\phi^2 \equiv \frac{\tilde{K}_{\beta\delta_a}}{\tilde{K}_{\phi\delta_a}} \, \rho^2 = K_\beta \left(\frac{\tilde{K}_{\beta\delta_a}}{\tilde{K}_{\phi\delta_a}} \right) - \omega_\beta^2 \qquad \text{(I-11)}$$

where ρ^2 is defined by (5-60). Thus, with the feedback gains chosen as described in Section 5.2.2.2, the lateral transfer functions describing closed-loop response to bank commands are given by (I-10). It should be noted from (I-11) that the non-minimum phase nature of the system is intimately linked to vehicle controllability, since, from (F-23), the controllability parameter $\tilde{\eta}$ is related to the transfer function zero, as follows:

$$\tilde{\eta} = -\frac{\tilde{K}_{\phi\delta_a}}{\tilde{K}_{\beta\delta_a}} \, \tilde{\omega}_\phi^2 \qquad \text{(I-12)}$$

Thus, as $\tilde{\eta} \to 0^-$, $\tilde{\omega}_\phi^2 \to 0^+$ (since both $\tilde{K}_{\phi\delta_a}$ and $\tilde{K}_{\beta\delta_a}$ are positive throughout the entry regime of interest), so that (I-10) describes a system approaching degeneracy as the controllability approaches zero. The parallel of this with the open-loop system behavior may be seen by recalling the discussion associated with (5-40) and (5-41) of Section 5.2.2.1.

Appendix J: Control System Flow Charts

  This appendix presents the flow charts describing the FORTRAN implementation of the control system as summarized in Chapter 6. Peripheral routines which are not described here, but are discussed in Reference 25, include: state-estimation, air data, input interface, jet select, and gain scheduling. Shown in Figure J-1 is a diagram of the logic flow of the digital controller, with figure numbers referring to more detailed flow charts of the actual computations. Figures J-2 and J-3 describe longitudinal control, while Figures J-4 and J-5 describe lateral control.
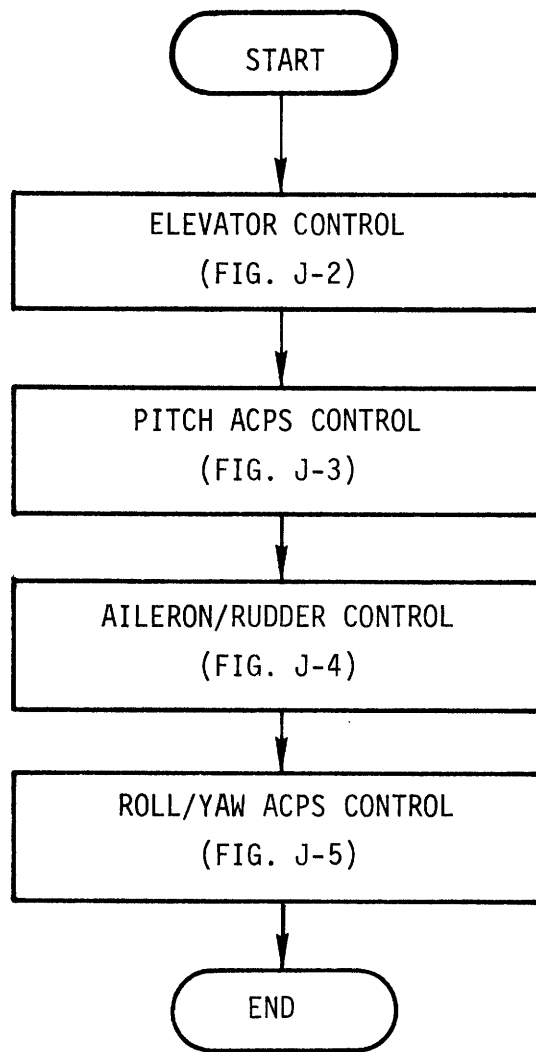
Figure J1. Overall Logic Flow Chart

START — Pick up Inputs from State Estimator

INPUT α_G, α, $\dot{\alpha}$

$(\alpha_G - \alpha)$

$< -\alpha_{max}$: $\alpha_e = -\alpha_{max}$

$\alpha_e = (\alpha_G - \alpha)$

$> \alpha_{max}$: $\alpha_e = \alpha_{max}$

Calculate Elevator Trim

$\bar{q} : \bar{q}_1^*$

$>$: $\delta e_T = \delta e_T + \dfrac{\omega_d^2 K_{\alpha 1} T}{\xi_1 \bar{q}} \, \alpha_e$

$\leqslant$: $\delta_{e_T} = \delta_{e_T} + K_{\alpha_1} T u_y$

δ_{e_T}

$< \Delta_e^{min}$: $\delta_{e_T} = \Delta_e^{min}$

$> \Delta_e^{max}$: $\delta_{e_T} = \Delta_e^{max}$

$\bar{q} : \bar{q}_1^*$

$\leqslant$: $\bar{q} : \bar{q}_1$

$\leqslant$: $\delta_e^c = \delta_{e_T}$, $\lambda_e = 1$

$>$: $\delta_e^{max} = \Delta_e^{max}$, $\delta_e^{min} = \Delta_e^{min}$

$>$: $K_e = m_e (\bar{q} - \bar{q}_1)$
$\delta_e^{max} = (1 - K_e)\delta e_T + K_e \Delta_e^{max}$
$\delta_e^{min} = (1 - K_e)\delta e_T + K_e \Delta_e^{min}$

1

END

Exit to Pitch ACPS Logic (Fig. J-3)

Figure J2. Logic Flow for Elevator Control.

①

Calculate elevator command

$$\delta_e^c = \frac{1}{\xi_1}\left[\frac{\omega_d^2}{\bar{q}}\left(\alpha_e - \frac{2\zeta_d}{\omega_d}\dot{\alpha}\right) - \xi_2\alpha_e\right] + \delta e_T$$

$< \delta e^{min}$ δ_e^c $>> \delta e^{max}$

$\delta_e^c = \delta e^{min}$ $\delta_e^c = \delta e^{max}$

Enter blending logic

$r_1 = (\delta e^{min} - \delta e_T)f_1 + \delta e_T$

$r_2 = (\delta_e^{min} - \delta e_T)f_2 + \delta e_T$

$r_3 = (\delta e^{max} - \delta e_T)f_2 + \delta e_T$

$r_4 = (\delta e^{max} - \delta e_T)f_1 + \delta e_T$

BLENDING SUBROUTINE

If $\delta_e^c < r_1$ or $\delta_e^c > r_4$, $\lambda_e = 1$

If $r_2 < \delta_e^c < r_3$, $\lambda_e = 0$

Otherwise, λ_e unchanged

END   Exit to Pitch ACPS Logic (Figure J-3).

Figure J2. Logic Flow for Elevator Control (cont).

552

START

$\lambda_e : 1$ ≠ → $u_y = 0$ → END

=

$\dot{\alpha} : 0$ <   >

=

$\alpha_e : 0$ <   ≥

$S = -1$ $S = 1$

$\dot{\alpha}^2/2U_y - S\alpha_e : \delta_{\alpha1}$ >   → $u_y = -S$

≤

$\sigma_\alpha \dot{\alpha}^2/2U_y - S\alpha_e : -\delta_{\alpha2}$

<   → $u_y = S$

≥

$u_y = 0$

END

Figure J3.   Logic Flow for Pitch ACPS Control.
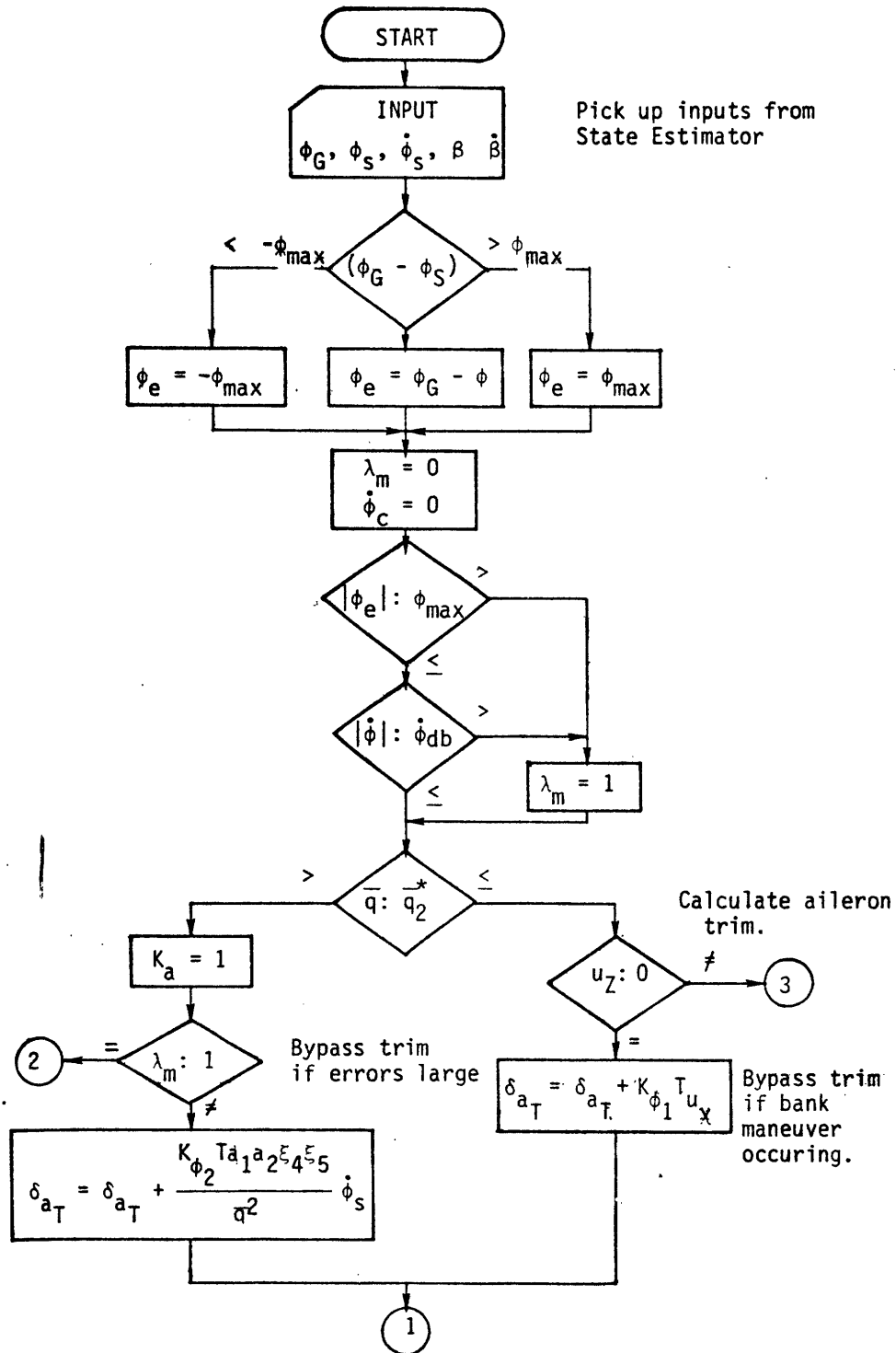
Figure J-4.   Logic Flow for Aileron/Rudder Control.
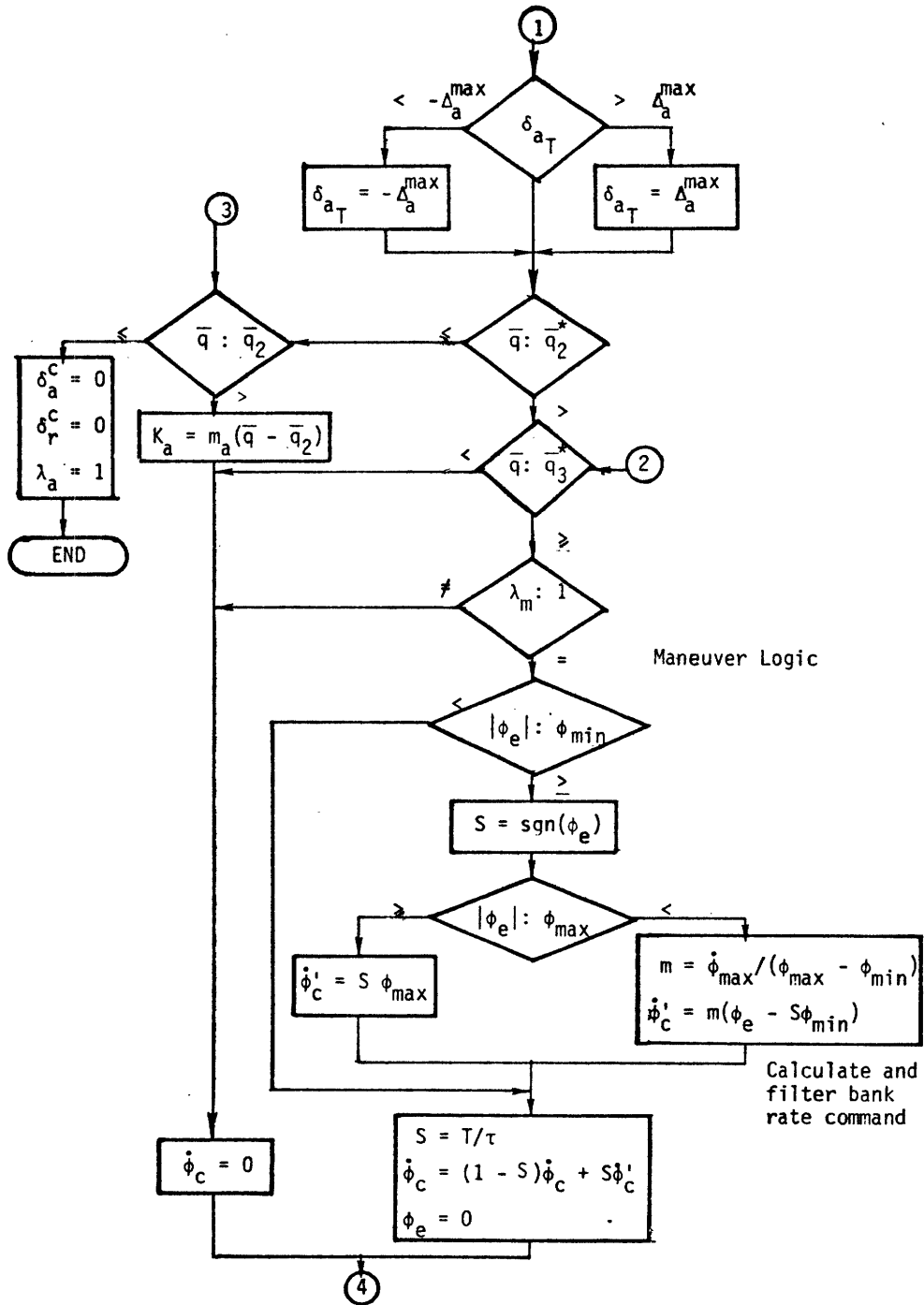
Figure J4   Logic Flow for Aileron/Rudder Control (cont)

555

Calculate aileron command   ④

$$\delta_a^c = \frac{\xi_4}{\bar{q}} \left\{ \left(\frac{a_1 \xi_5}{\bar{q}} \right) \left[\phi_e - a_2(\dot{\phi} - \dot{\phi}_c) + \xi_6(\beta + a_2\dot{\beta}) \right] + a_4\beta + a_3\dot{\beta} \right\} - \xi_3\beta + \delta a_T$$

$$\delta_a^{max} = (1 - K_a)\delta_{a_T} + K_a\Delta_a^{max}$$

$$\delta_a^{min} = (1 - K_a)\delta_{a_T} - K_a\Delta_a^{max}$$

Limit aileron Command

$< \delta_a^{min}$ δ_a^c $> \delta_a^{max}$

$\delta_a^c = \delta_a^{min}$ $\delta_a^c = \delta_a^{max}$

Calculate rudder command $\leqslant$ $\bar{q} : \bar{q}_3^*$

$>$

$\mathscr{m} : \mathscr{m}_1$ $\geqslant$

$<$

$\delta_r^c = 0$ $\delta_r^c = C_{RUD}\delta_a^c$

Limit rudder command

$< -\delta_r^{max}$ δ_r^c $> \delta_r^{max}$

$\delta_r = -\delta_r^{max}$ $\delta_r = \delta_r^{max}$

Enter Blending Logic.

$$r_5 = (\delta_a^{min} - \delta_{a_T})f_3 + \delta_{a_T}$$

$$r_6 = (\delta_a^{min} - \delta_{a_T})f_4 + \delta_{a_T}$$

$$r_7 = (\delta_a^{max} - \delta_{a_T})f_4 + \delta_{a_T}$$

$$r_8 = (\delta_a^{max} - \delta_{a_T})f_3 + \delta_{a_T}$$

⑤

Figure J4   Logic Flow for Aileron/Rudder Control (cont).

Blending Subroutine

If $\delta_a^C < r_5$ or $\delta_a^C > r_8$, $\lambda_a = 1$

If $r_6 < \delta_a^C < r_7$, $\lambda_a = 0$

Otherwise λ_a unchanged

END
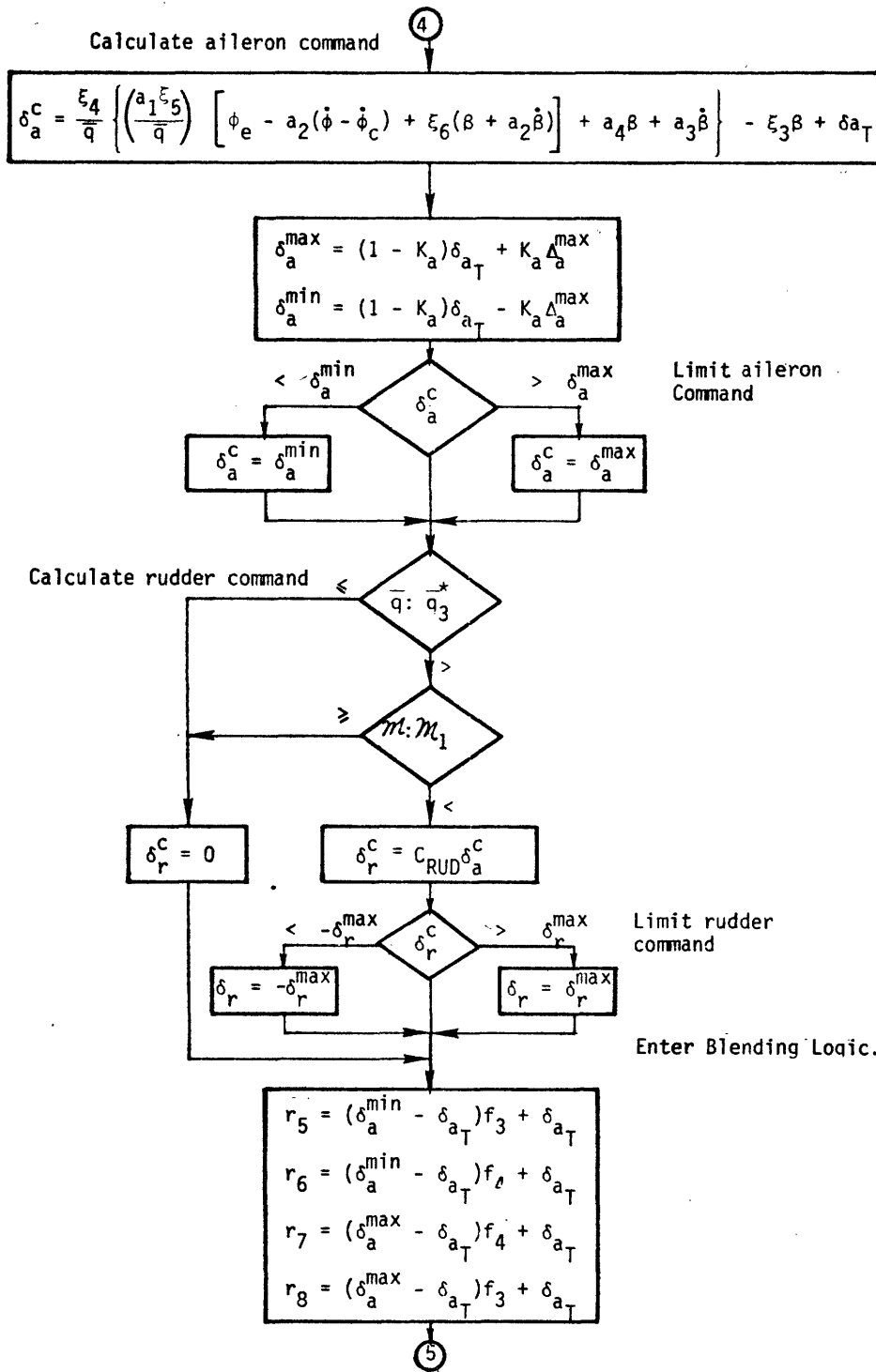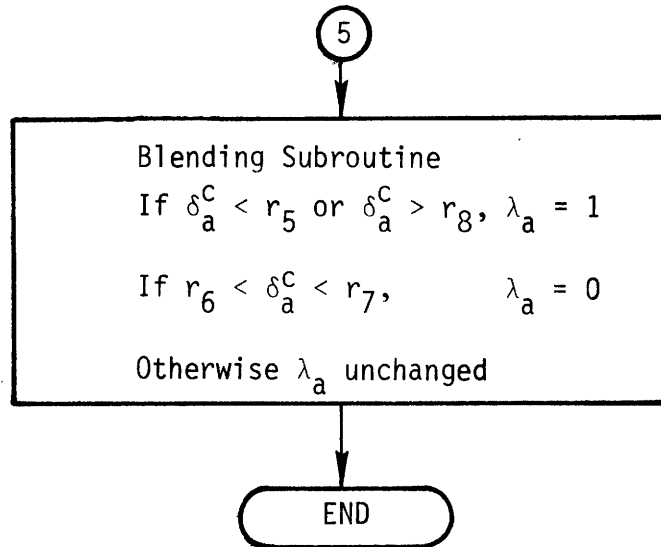
Exit to yaw/roll ACPS logic (Figure J-5).

Figure J4. Logic Flow for Aileron/Rudder Control (cont).
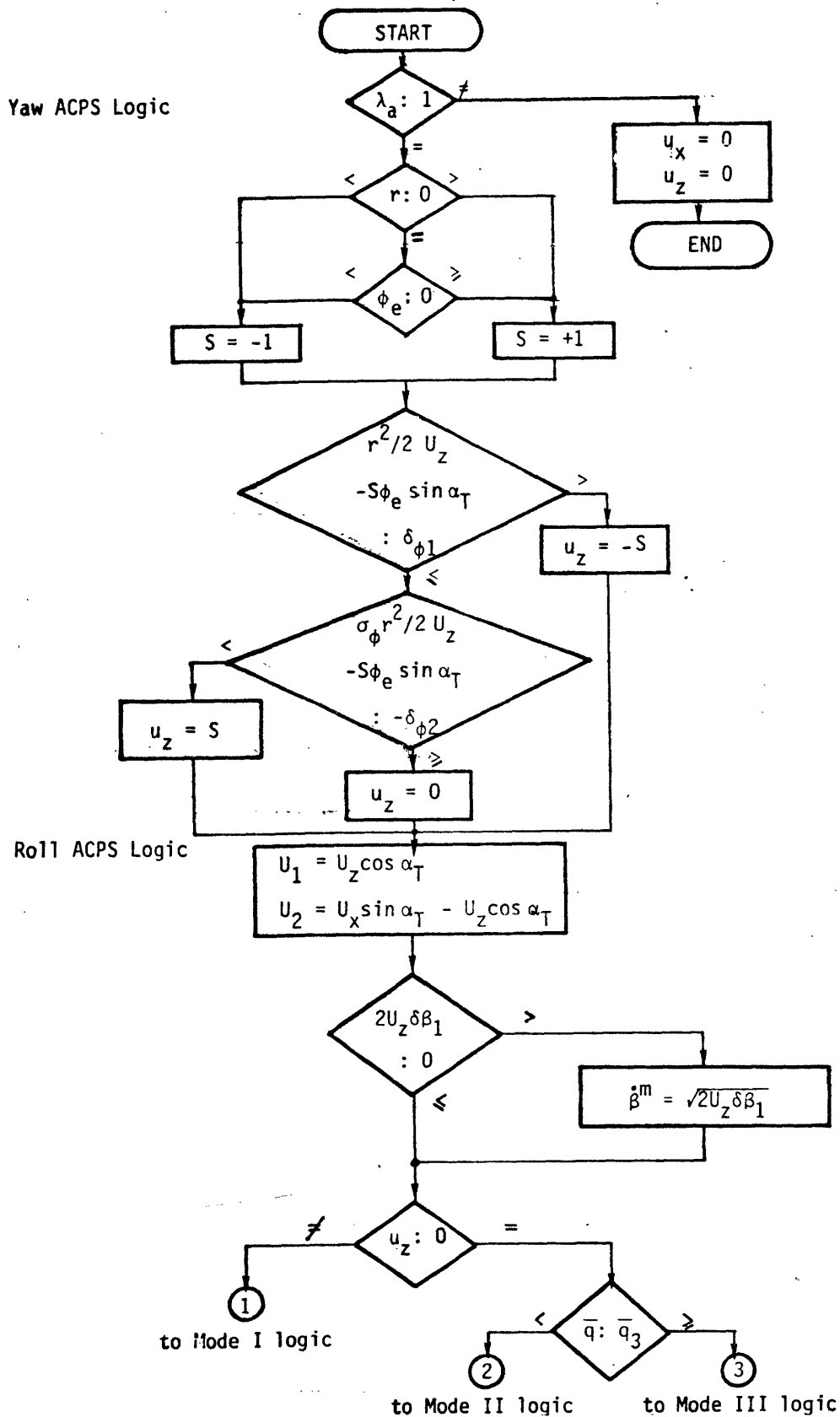
Yaw ACPS Logic

START

$\lambda_a : 1$

$\neq$

$u_x = 0$
$u_z = 0$

END

$=$

$r : 0$

$<$ $=$ $>$

$\phi_e : 0$

$<$ $\geqslant$

$S = -1$

$S = +1$

$\dfrac{r^2/2\, U_z}{-S\phi_e \sin \alpha_T} : \delta_{\phi 1}$

$>$

$u_z = -S$

$\leqslant$

$\dfrac{\sigma_\phi r^2/2\, U_z}{-S\phi_e \sin \alpha_T} : -\delta_{\phi 2}$

$<$

$u_z = S$

$\geqslant$

$u_z = 0$

Roll ACPS Logic

$U_1 = U_z \cos \alpha_T$
$U_2 = U_x \sin \alpha_T - U_z \cos \alpha_T$

$2U_z \delta\beta_1 : 0$

$>$

$\dot{\beta}^m = \sqrt{2U_z \delta\beta_1}$

$\leqslant$

$u_z : 0$

$\neq$ $=$

$\bigcirc 1$

to Mode I logic

$\bar{q} : \bar{q}_3$

$<$ $>$

$\bigcirc 2$ $\bigcirc 3$

to Mode II logic   to Mode III logic

Figure J5. Logic Flow for Yaw/Roll ACPS Control.

558

Mode I

$$\text{sgn}(u_z)\,\dot{\beta} : \dot{\beta}^m$$

$$\mu = -\frac{(\dot{\beta}^{m2} - \dot{\beta}^2)}{2\,U_2}$$

$$\mu = \frac{(\dot{\beta}^{m2} - \dot{\beta}^2)}{2\,U_1}$$

$$\text{sgn}(u_z)\,\beta : \mu$$

$$u_x = 0$$

$$u_x = \text{sgn}(u_z)$$

END

Mode II

$$\dot{\beta} : 0$$

$$\beta : 0$$

$$S = -1 \qquad S = +1$$

$$S\beta + \dot{\beta}^2/2\,U_x \sin\alpha_T : \delta_{\beta 1}$$

$$u_x = -S$$

$$S\beta + \sigma_\beta\,\dot{\beta}^2/2\,U_x \sin\alpha_T : -\delta_{\beta 2}$$

$$u_x = S$$

$$u_x = 0$$

END

Mode III

$$\text{sgn}(\dot{\beta})\,\dot{\beta} : \dot{\beta}^m$$

$$u_x = 0$$

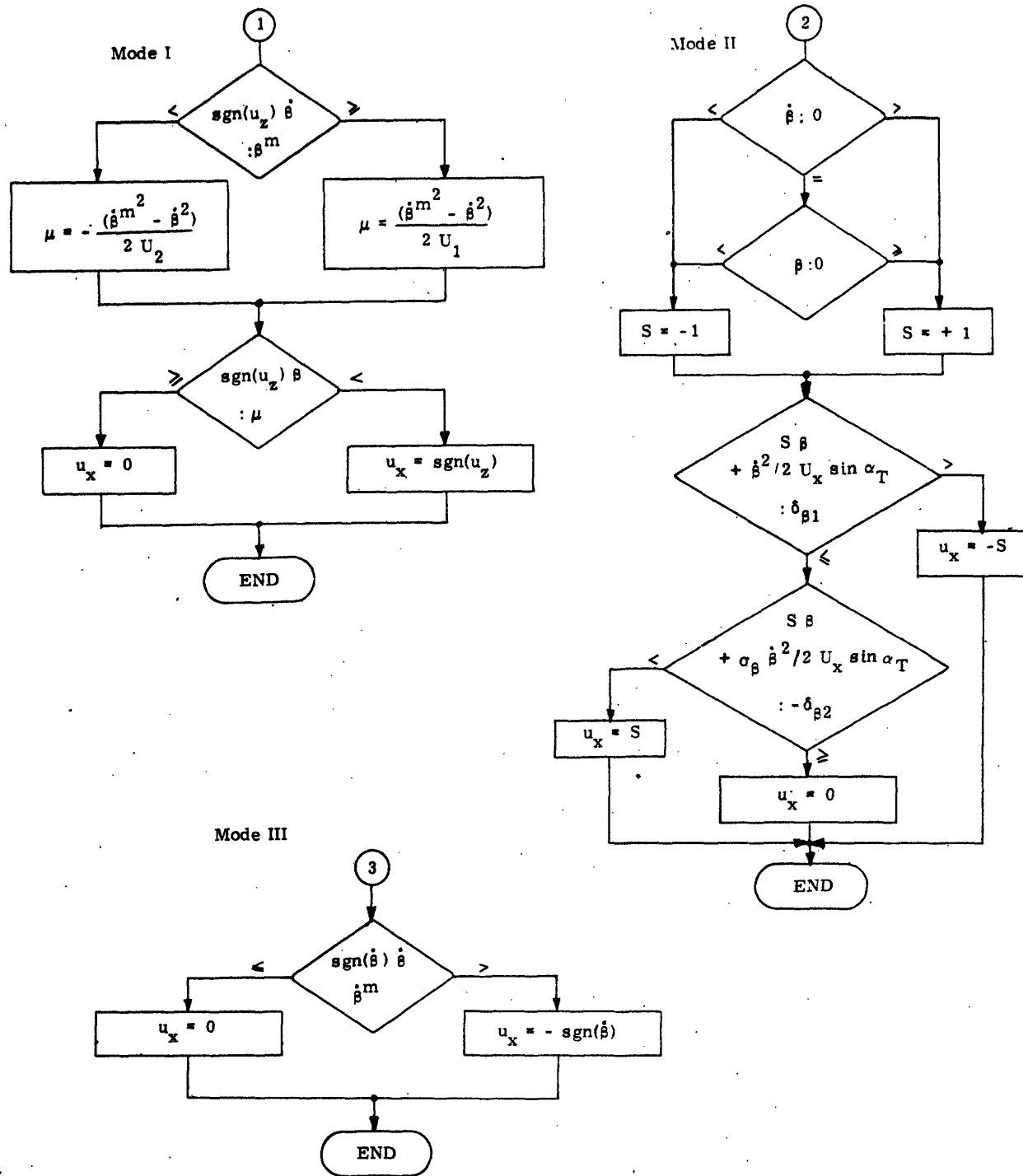$$u_x = -\text{sgn}(\dot{\beta})$$

END

Figure J5.   Logic Flow for Yaw/Roll ACPS Control (cont).

Appendix K: <u>Aerodynamic Coefficient Variations and Lateral</u>
<u>Controllability</u>

The purpose of this appendix is to relate aerodynamic coefficient
variations to changes in lateral controllability, with the specific objec-
tive of defining "worst-case" variations from a controllability point-of-
view. The results presented here support the coefficient sensitivity
testing reported on in Section 7.3.2. The analysis given below is only
first-order, and thus caution must be used in attempting to apply the
results derived here to situations in which coefficient variations are of
the same order of magnitude as the coefficients themselves (as occur
with certain "delta" variations in particular flight regimes). Further-
more, the results are derived for the nominal transition profile, and
any significant trajectory deviation from this may invalidate the results.

The controllability coefficients of interest are defined in Chapter
5 and are repeated here from (5-46) and (5-47), for convenient reference:

$$\tilde{C}'_{n\delta_a} \equiv C'_{n\delta_a} + C_r C'_{n\delta_r} \qquad \text{(a)}$$

$$\qquad \qquad \qquad \qquad \qquad \qquad \text{(K-1)}$$

$$\tilde{\pi}_1 \equiv C_{n_\beta} \tilde{C}_{\ell\delta_a} - C_{\ell_\beta} \tilde{C}_{n\delta_a} \qquad \text{(b)}$$

where, it may be recalled that C_r is the aileron-to-rudder crossfeed
gain. Making use of the intermediate variable definitions given by
(5-47), (4-43), and (4-47), the above coefficients may be expressed
directly in terms of the vehicle's lateral derivatives:

$$\tilde{C}'_{n\delta_a} \approx (C_{n\delta_a} + C_r C_{n\delta_r})\cos\alpha_T - \left(\frac{I_{zz}}{I_{xx}}\right)(C_{\ell\delta_a} + C_r C_{\ell\delta_r})\sin\alpha_T \qquad \text{(a)}$$

$$\tilde{\pi}_1 = -(C_{n\delta_a} + C_r C_{n\delta_r})C_{\ell_\beta} + (C_{\ell\delta_a} + C_r C_{\ell\delta_r})C_{n_\beta} \qquad \text{(b)}$$

$$\qquad \qquad \qquad \qquad \qquad \qquad \text{(K-2)}$$

Thus, Table K-1 may be constructed, relating first-order changes in the controllability coefficients to variations in the aerodynamic coefficients.

Table K-1: Controllability Coefficient Dependence on
Aerodynamic Coefficients

	$C_{n\delta_a}$	$C_{n\delta_r}$	$C_{l\delta_a}$	$C_{l\delta_r}$	C_{n_β}	C_{l_β}
$\dfrac{\partial \tilde{C}'_{n\delta_a}}{\partial x}$	$\cos\alpha_T$	$C_r\cos\alpha_T$	$-\dfrac{I_{zz}}{I_{xx}}\sin\alpha_T$	$-C_r\dfrac{I_{zz}}{I_{xx}}\sin\alpha_T$	-0	0
$\dfrac{\partial \tilde{\pi}_1}{\partial x}$	$-C_{l_\beta}$	$-C_r C_{l_\beta}$	C_{n_β}	$C_r C_{n_\beta}$	$(C_{l\delta_a}+C_r C_{l\delta_r})$	$-(C_{n\delta_a}+C_r C_{n\delta_r})$

The signs of these derivatives may be determined by an examination of the coefficient data of Reference 2. In particular, along the transition profile, it may be seen that:

$$C_{l_\beta} > 0; \quad C_{l\delta_a} > 0; \quad C_{l\delta_r} > 0; \quad C_{n\delta_r} < 0 \qquad \text{(K-3a)}$$

The two derivatives C_{n_β} and $C_{n\delta_a}$ change signs during the transition[*] and are plotted in Figure K-1, so it may be noted that:

$$C_{n_\beta} > 0 \text{ for } \mathcal{M} \lesssim 2.8$$
$$< 0 \qquad \mathcal{M} \gtrsim 2.8 \qquad \text{(K-3b)}$$

However, in Table K-1, the aileron derivative $C_{n\delta_a}$ is combined with

---

[*] Note that they both are zero at approximately the same Mach number, causing the unaugmented controllability coefficient π_1 to go to zero at this point (recall the definition given by (5-39b) and the contour trends of Figure 5-11). This is perhaps the strongest motivation for introducing the crossfeed structure.
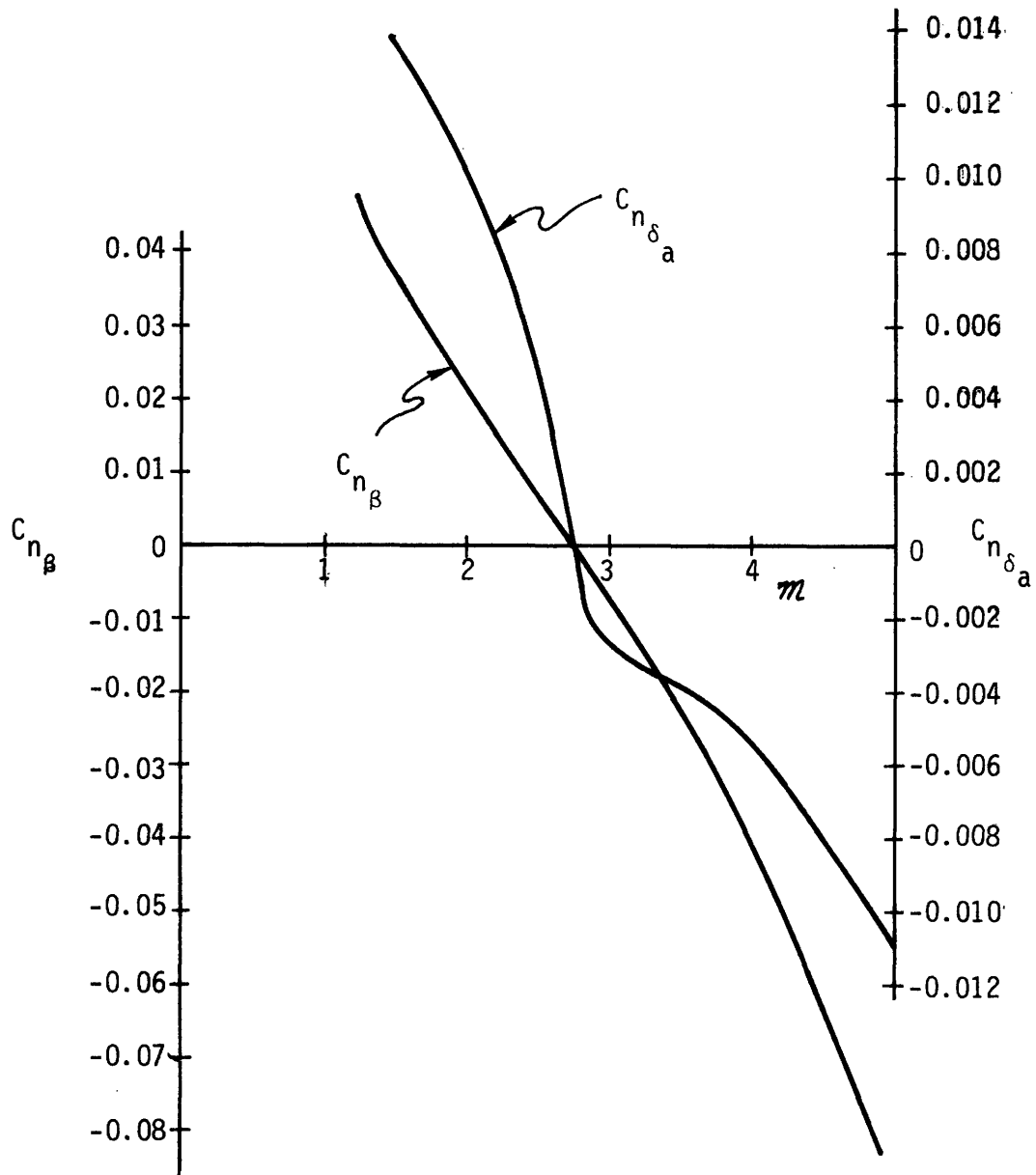
Figure K1. Variation of C_{n_β} and $C_{n_{\delta_a}}$ During Late Entry Pitch-down.

the rudder derivative $C_{n\delta_r}$ through the positive crossfeed gain C_r, so that, as seen from Figure K-2:

$$(C_{n\delta_a} + C_r C_{n\delta_r}) < 0 \qquad \text{(K-3c)}$$

Thus, use of (K-3) allows Table K-1 to be used as a means of determining the sign dependence of variations in the controllability coefficients on variations in the aerodynamic coefficients. More pertinent, however, is the issue of performance degradation with coefficient variation. Assuming a direct correlation between degraded performance and a variation which drives either of the controllability coefficients toward zero, then the gradient information of Table K-1 may be put to use by knowing the nominal signs of the controllability coefficient values. From the contour plots of Figures 5-13 and 5-14, it is seen that both $\tilde{C}'_{n\delta_a}$ and $\tilde{\pi}_1$ are nominally negative; thus, driving their values in the direction of their respective gradients is equivalent to driving their values to zero. Thus, Table K-1 may be combined with (K-3) to provide the desired relation between performance degradation (i.e., controllability loss) and coefficient variation; this is summarized in Table K-2.

Table K-2: <u>Required Coefficient Variations to Degrade</u>
<u>Lateral Controllability</u>*

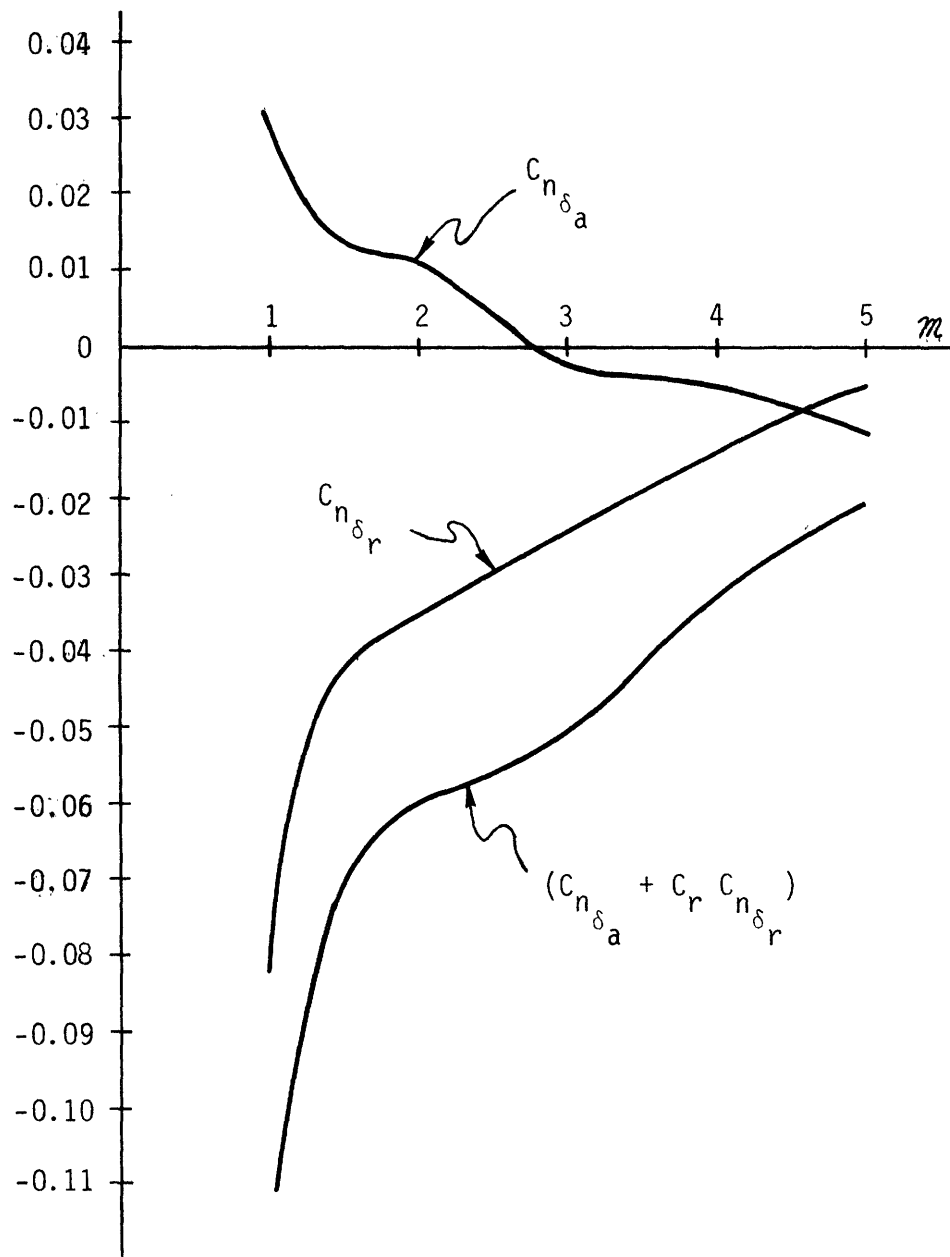| coefficient effect	$C_{n\delta_a}$	$C_{n\delta_r}$	$C_{l\delta_a}$	$C_{l\delta_r}$	C_{n_β}	C_{l_β}
$C'_{n\delta_a} \to 0$	$\Delta > 0$	$\Delta > 0$	$\Delta < 0$	$\Delta < 0$	–	–
$\tilde{\pi}_1 \to 0$	$\Delta > 0$	$\Delta > 0$	$\Delta > 0\ (\mathcal{M} \lesssim 2.8)$ $\Delta < 0\ (\mathcal{M} \gtrsim 2.8)$	$\Delta > 0\ (\mathcal{M} \lesssim 2.8)$ $\Delta < 0\ (\mathcal{M} \gtrsim 2.8)$	$\Delta > 0$	$\Delta > 0$

* along nominal transition profile

Figure K2. Variation of $C_{n_{\delta_a}}$ and $C_{n_{\delta_r}}$ During Late

Entry Pitch-down.

LIST OF REFERENCES

1. *Aerodynamic Design Data Book: Orbiter Vehicle*, Vol. 1, North American Rockwell Corporation, Space Division Data Book SD-72-SH-0060-1D, June 1973.

2. *Aerodynamic Design Data Book: 150K Lightweight Orbiter Vehicle*, North American Rockwell Corporation, Space Division Data Book SD-73-SH-0020, February 1973.

3. Athans, M., and P. L. Falb, *Optimal Control*, McGraw-Hill Book Company, New York, 1966.

4. Baumel, L. S., *SSFS Model Documentation Series: ATM3*, rev. 1, Houston Aerospace Systems Division of Lockheed Electronics Company, Guidance and Dynamics Department Technical Report 62824-133405, 30 November 1971.

5. Brown, F. D., Jr., *Space Shuttle Functional Simulator Executive/ Communicator Flight Software Programmer's/User's Guide*, Houston Aerospace Systems Division of Lockheed Electronics Company, Guidance and Navigation Department Technical Report 67542D-034902, 15 December 1970.

6. Dana, W. H., *Report of Trip to Fly Rockwell International Space Shuttle Reentry Simulator*, NASA Flight Research Center Memo RP:FO, 29 May 1973.

7. Dynamics of Flight (unpublished course notes, University of Michigan College of Engineering, Department of Aeronautical and Astronautical Engineering, 1959).

8. Dynamics of the Airframe, Navy Department Bureau of Aeronautics Report AE-61-4-II, 1952.

9. Erck, J.C., SSFS Model Documentation Series: AERO16, Houston Aerospace Systems Division of Lockheed Electronics Company, Guidance and Dynamics Department Technical Report TR0114, March 1973.

10. Erck, J.C., SSFS Model Documentation Series: GRAV2, rev. 1, Houston Aerospace Systems Division of Lockheed Electronics Company, Guidance and Dynamics Department Technical Report 67542D-123202, 20 August 1971.

11. Etkin, B., Dynamics of Flight, John Wiley and Sons, Inc., New York, 1967.

12. Flying Qualities of Piloted Airplanes, MIL SPEC F-8785, rev. B, January 1970.

13. Harpold, J.C., Control System Requirements for Trajectory Control During Entry, NASA Johnson Space Center Internal Note 73-FM-84, 24 May 1973.

14. Jones, J.E., Analysis of Preprocessor Errors for Computation of Angles of Attack, Bank, and Sideslip from Inertial Data, Charles Stark Draper Laboratory Memo 73-23C-10, 18 July 1973.

15. Jones, J.E., General Variational Equations of Motion for the SSV, Charles Stark Draper Laboratory Memo 73-23C-3, 23 February 1973.

16. Jones, J.E., State Estimator Design for Use with SSV Entry DFCS, Charles Stark Draper Laboratory Memo 73-10C-12, 1 October 1973.

17. Jones, J. E., Stochastic Analysis of Modelling Errors and Parameter Sensitivity in State Estimation, Charles Stark Draper Laboratory Memo 73-23C-2, 30 January 1973.

18. Kelley, E. L., and H. K. Watson, Space Shuttle Flight Control Subsystem, North American Rockwell Corporation, Space Division Specification Document MC621-0043, 5 October 1973.

19. Marcus, F., Shuttle Entry and Transition Phase Guidance, Charles Stark Draper Laboratory Memo 73-23A-48, 21 May 1973.

20. Melville-Jones, B., "Dynamics of the Airplane," Aerodynamic Theory, Vol. V, div. N, N. F. Durand (ed.), Julius Springer, Berlin, 1935.

21. Moul, M. T., and J. W. Paulson, Dynamic Lateral Behavior of High-Performance Aircraft, NACA Langley Aeronautical Laboratory Research Memo RM-L58E16, 6 August 1958.

22. Rausch, J. R., and A. M. Roberge, RCS Jet Flow Field Interaction Effects on the Aerodynamics of the Space Shuttle Orbiter, General Dynamics Corporation, Convair Aerospace Division Report CASD-NAS73-020, November 1973.

23. Schall, M. R., Dispersed Guidance Reference Trajectory for Entry Guidance Selection Committee Study Activity, North American Rockwell Corporation, Space Division Internal Letter 393-150-73-028, 15 August 1973.

24. Suddath, J. H., Accuracy of Estimating α and β Using IMU Data During Shuttle Entry, NASA Manned Spacecraft Center Memo EG2-70-212, 16 December 1970.

25. Weissman, P., Integrated Digital Flight Control System for the Space Shuttle Orbiter, rev. 1, Charles Stark Draper Laboratory Report E-2736, July 1973.

26. White, L. A., SSFS Model Documentation Series: AVEH5, rev. 2, Houston Aerospace Systems Division of Lockheed Electronics Company, Guidance and Dynamics Department Technical Report TR0094, January 1973.

27. Widnall, W. S., Guidance System Operations Plan for Manned CM Earth Orbital and Lunar Missions Using Program COLOSSUS, sec. 3, rev. 1, MIT Instrumentation Laboratory Report R-577, June 1968.

28. Zacharias, G. L., Elevator/Aileron Sharing of Elevons, NASA Manned Spacecraft Center Memo EG2-72-107, 22 June 1972.

29. Zacharias, G. L., Fuel-Time Optimal Control of a Double Integrating Plant, NASA Manned Spacecraft Center Internal Note MSC-EG-71-7, 22 March 1971.

30. Zacharias, G. L., Sampled-Data Formulation of Entry Attitude Equations of Motion, NASA Manned Spacecraft Center Memo EG2-72-160, 17 November 1972.